List of Contributors

J.-M. Bonny, *Structures Tissulaires et Interactions Moléculaires, INRA Theix, 63122 Saint-Genès-Champanelle, France*

I. Ergaz, *Department of Chemistry, Ben-Gurion University of the Negev, Beer-Sheva 84105, Israel*

A. J. Fagan, *Bio-Medical Physics, School of Medical Sciences, College of Life Sciences & Medicine, University of Aberdeen, AB25 2ZD, Scotland, UK*

S. Geresh, *Department of Biotechnology and Engineering, Ben-Gurion University of the Negev, Beer-Sheva 84105, Israel*

R. Glaser, *Department of Chemistry, Ben-Gurion University of the Negev, Beer-Sheva 84105, Israel*

G. Levi-Ruso, *Department of Chemistry, Ben-Gurion University of the Negev, Beer-Sheva 84105, Israel*

D. J. Lurie, *Bio-Medical Physics, School of Medical Sciences, College of Life Sciences & Medicine, University of Aberdeen, AB25 2ZD, Scotland, UK*

G. E. Martin, *Michigan Structure, Elucidation Group, Pfizer Global Research and Development, Pfizer Corporation, Kalamazoo, MI 49001-0199, USA*

P. Medick, *Universität Bayreuth, Experimentalphysik II, 95440 Bayreuth, Germany*

A. Novoselsky, *Department of Biotechnology and Engineering, Ben-Gurion University of the Negev, Beer-Sheva 84105, Israel*

E. A. Rössler, *Universität Bayreuth, Experimentalphysik II, 95440 Bayreuth, Germany*

D. Shiftan, *Department of Chemistry, Ben-Gurion University of the Negev, Beer-Sheva 84105, Israel*

M. Vogel, *Institut für Physikalische Chemie, Westfälische Wilhelms-Universität Münster, Correnstr. 30, 48149 Münster, Germany*

Preface

It is a pleasure for me to introduce Volume 56 of the Annual Reports on NMR. As is customary with this series, the volume contains a number of reports dealing with some of the many areas of application of NMR Spectroscopy.

The first contribution by G.E. Martin covers Small Volume and High Sensitivity NMR Probes; next R. Glaser, I. Ergaz, G. Levi-Ruso, D. Shiftan, A. Novoselsky and S. Geresh deal with Solution and Solid State NMR Studies of Eight- and Nine-Membered Medium Ring *Cis*-Cycloalkene Stereochemistry; A.J. Fagan and D.J. Lurie cover the area of Continuous-Wave NMR Imaging in the Solid State; J.-M. Bonny reports on the Methods and Applications of Quantitative MRI; finally there is an account of Secondary Relaxation Processes in Molecular Glasses studied by NMR Spectroscopy by M. Vogel, P. Medick and E.A. Roessler.

It is my pleasure to express my gratitude to all of these reporters for their timely and comprehensive contributions. My thanks also go to the production staff at Elsevier for the prompt arrival of this volume.

Royal Society of Chemistry
Burlington House
Piccadilly
London, WIJ OBA, UK

G. A. WEBB
February 2005

Contents

Small-Volume and High-Sensitivity NMR Probes

GARY E. MARTIN

Pfizer Global Research and Development, Michigan Structure Elucidation Group, Kalamazoo, MI 49001-0199, USA

Aside from efforts to develop capillary nuclear magnetic resonance (NMR) probes during the 1970s, most NMR samples were traditionally examined using 5 mm probes. Due to low gyromagnetic ratio and/or natural abundance, some larger format NMR probes were developed, these including 8 and 12 mm, and large volume probes of 18 and 22 mm. Large format probes addressed the difficulties of acquiring NMR data for insensitive nuclides when an investigator was not sample limited or dealing with highly insoluble materials. In contrast, for the characterization of scarce samples of natural products, impurities or degradants of pharmaceuticals, metabolites, forensic samples, and other severely sample-limited applications, even conventional 5 mm probes were not well suited to the task of acquiring data for such samples. These considerations led to the development of the first of the 3 mm NMR probes in the early 1990s followed by a succession of progressively smaller format NMR probes down to the 1 mm tube format probes currently available. In parallel, μCoil probes were also developed allowing the use of still smaller sample volumes, albeit in a flow cell rather than a "tube" format, as were magic angle sideways spinning liquids probes such as the Varian

ANNUAL REPORTS ON NMR SPECTROSCOPY
VOLUME 56 ISSN 0066 4103
DOI 10.1016/S0066-4103(05)56001-0

Nano-probe^{TM}. In the late 1990s, the first examples of cryogenic NMR probe technology became available, and these extremely high-sensitivity NMR probes are now becoming more readily available to investigators faced with undertaking the structural characterization of scarce samples. The development of small-volume and high-sensitivity NMR probes is described in this contribution and examples of the application of these probe technologies are reviewed.

1. INTRODUCTION

Nuclear magnetic resonance (NMR) methods are capable of providing a wealth of atom-to-atom connectivity information that has served to make NMR the cornerstone of modern structure elucidation. Unfortunately, NMR is also an inherently insensitive technique. Considerable effort has been expended on the part of thousands of scientists to enhance NMR sensitivity. Efforts have been focused in three primary directions. Magnet technology has been one very major focus. Magnets have progressed from predominantly 60 MHz permanent magnets in use when this author's career in NMR began to the first superconducting NMR magnets at 220 and 300 MHz with voracious appetites for liquid helium, and now to huge 900 MHz magnets that are intended for biomolecular NMR studies and essentially require a gymnasium-sized room to house them. At the same time, the field strength of magnets on instruments for more routine applications have also steadily climbed to the point that most instruments intended for walk-up usage by chemists in the pharmaceutical industry are now 400 or 500 MHz instruments. A second primary area of focus has been in the development of more sophisticated NMR pulse sequences to achieve higher sensitivity. Heteronuclear shift correlation experiments progressed from the fledgling heteronucleus-detected experiments in the early 1980s to the proton- or inverse-detected heteronuclear shift correlation experiments now in widespread usage for chemical structure characterization. The third major area of focus has been on the development of higher-sensitivity NMR probes. Historically, NMR probes have typically been based around an rf coil designed to accommodate a 5 mm NMR tube. With the advent of commercial Fourier transform NMR instruments in the late 1970s, probes evolved from simple 5 mm proton observe capabilities to heteronuclear probes with the heteronuclear or X-coil inboard surrounded by a larger proton-decoupling coil. These designs were quite serviceable through the late 1970s and early 1980s, but with the development of the first proton-detected heteronuclear shift correlation experiments by Müller,[1] Bodenhausen and Ruben,[2] and Bax *et al.*[3] it became obvious that conventional heteronuclear NMR probe designs would be supplanted by what were originally termed "reverse-geometry" NMR probe designs. These are probes with the proton coil closest to the sample for improved proton sensitivity since ^{1}H is the detected nuclide. More recently, "inverse-detection" terminology has come into common usage, the terminology again based on the exchange of the rf coils in the probe design. Modification of NMR probe coil geometry afforded better sensitivity than conventional designs, but sample requirements were still relatively high for

investigators working in severely sample constrained areas of investigation such as the characterization of impurities and degradants of pharmaceuticals, metabolites, etc. This brief history sets the stage for the development of small-volume high-sensitivity conventional NMR probes that occurred through much of the 1990s, which has been followed more recently by the development and commercial availability of cryogenically cooled NMR probes with still higher sensitivity.

2. SMALL-VOLUME CONVENTIONAL NMR PROBES

Small-volume conventional NMR probes encompass the development of 3 mm micro-probes, followed very closely by a 2.5 mm variant. Nearly 6 years after the introduction of 3 mm probes, a 1.7 mm submicro- or SMIDG^{TM} probe was introduced followed, most recently, by the development of a 1.0 mm probe. Given sample handling considerations, it is unlikely that smaller conventional (those using tubes) NMR probes will be developed. This section does not include the development of either magic angle sideways spinning liquids (Nano-probes^{TM}) or what are now generally referred to as μCoil NMR probes. These types of high-sensitivity probe technology are discussed in later sections of this contribution.

2.1. The 3 mm micro-NMR probes

Historically, small-volume NMR probes date back to the 1966 Report of Odelblad, which employed a solenoidal microcoil to study human cervical mucosal secretions.[4] By the early 1970s, Shoolery had begun exploring the use of 1.7 mm capillary NMR probes for the acquisition of ^{13}C data.[5] These early reports essentially set the stage for the start of the development of 3 mm or micro-NMR probes that began in 1991 through a collaboration by the author and his colleagues, then at Burroughs Wellcome, Co., in North Carolina with staff at the Nalorac Corporation. The first experimental results obtained with a 3 mm inverse-detection micro-NMR probe were reported in 1992. Using the simple indoloquinoline alkaloid cryptolepine (**1**) as a model compound for the study, Crouch and Martin[6] were able to demonstrate the acquisition of a heteronuclear multiple-quantum correlation (HMQC) spectrum recorded on 12 μg (0.05 μmol) of the alkaloid dissolved in 145 μL of d_6-dimethyl sulfoxide (d_6-DMSO) in 16 h (Fig. 1). Long-range heteronuclear shift correlation data in the form of a heteronuclear multiple-bond correlation (HMBC) experiment, which is substantially less sensitive than the HMQC experiment, were recorded on a 35 μg (0.15 μmol) sample of the alkaloid in the same volume of deuterated solvent in 21 h. These preliminary results heralded a significant advance in the characterization of small samples by heteronuclear two-dimensional (2D) NMR shift correlation methods. Later in 1992, Crouch and Martin[7] reported a direct comparison of 3 and 5 mm NMR probe performance at 500 MHz. Using a sample of 167 μg (1 μmol; samples were prepared by serial dilution) of the simple alkaloid harmane (**2**)

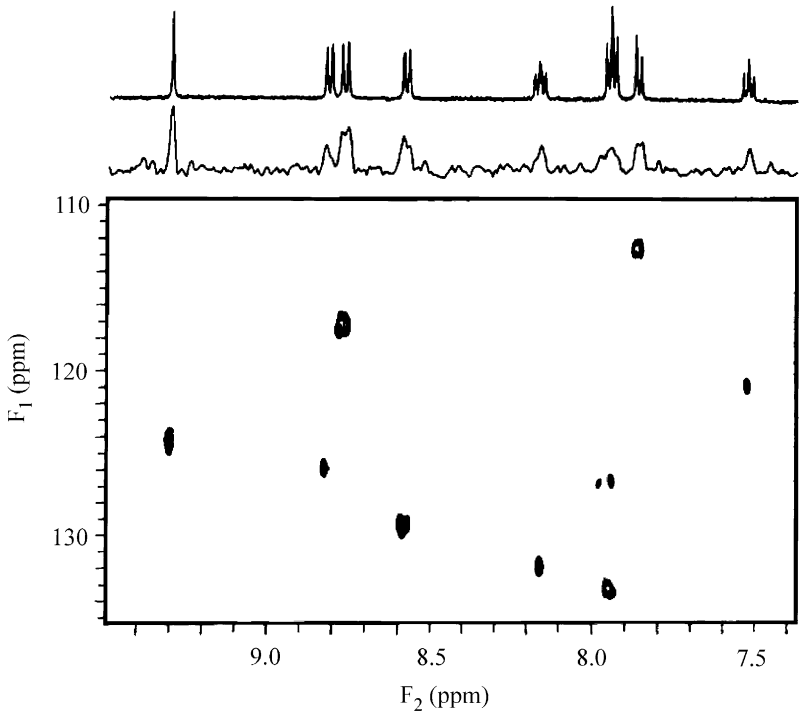

Fig. 1. HMQC spectrum of a 12 µg (0.05 µmol) sample of the indoloquinoline alkaloid cryptolepine (**1**) dissolved in 145 µL of d_6-DMSO. The data were recorded overnight (16 h) at 500 MHz using a 3 mm micro-inverse-detection NMR probe.[6] Both a proton reference spectrum (top trace) and the projection through the F_1 frequency domain (bottom trace) are shown above the contour plot. (Reprinted with permission from Ref. 6. Copyright 1992, American Chemical Society and American Society of Pharmacognosy.)

dissolved in either 160 or 600 µL of d_6-DMSO for 3 or 5 mm NMR sample tubes, respectively, the authors found that it took four times as long to achieve the same signal-to-noise ratio (s/n ratio) in the 5 mm probe as for the 3 mm probe, based on the s/n ratio of a projection through the F_2 frequency domain when identically parameterized HMQC spectra were run. Unfortunately, data were not recorded for the 3 mm sample run coaxially in the 5 mm probe.

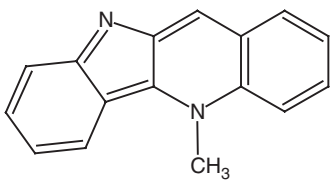

1

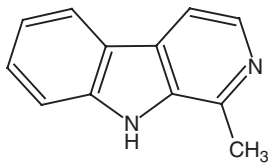

2

Following the initial 1992 reports describing the capabilities of 3 mm micro-NMR probe technology, a 3 mm dual probe was developed with the X-coil inboard for the acquisition of ^{13}C spectra. This 3 mm probe variant made it possible to acquire a ^{13}C-NMR spectrum for submilligram samples overnight at a ^{13}C observation frequency of 100 or 125 MHz. As NMR console designs continued to evolve incorporating pulsed field gradient capabilities, 3 mm micro-probes with gradient capabilities were also developed. Interestingly, based on work done in the laboratories of the author and W. F. Reynolds at the University of Toronto, it has been demonstrated that for ^{1}H–^{13}C heteronuclear shift correlation studies with very small samples, it is preferable to acquire the data without resorting to gradient experiments.[8,9] At higher concentrations, Reynolds and Enriquez[9] demonstrated that t_1 ridges due to incomplete suppression of ^{1}H–^{12}C components of magnetization, or that from protons bound to heteroatoms, constitute the main source of noise in phase-cycled heteronuclear 2D-NMR experiments. Gradient NMR pulse sequences are very effective in suppressing this type of noise, as would be expected. This observation is also consistent with the generally accepted advantage of gradient NMR pulse sequences when only as few as 2 transients/t_1 increment will be recorded. However, it was also shown by Reynolds and Enriquez,[9] that the intensity of the t_1 ridges appears to be directly proportional to the signal strength. Consequently, for very dilute samples, $<\sim$0.25–0.5 μmol in the author's experience, the contribution of t_1 ridges to the total noise in an heteronuclear shift correlation spectrum is relatively minor. Hence, when sufficient numbers of transients are accumulated per t_1 increment (as a rule of thumb, about twice as many transients per t_1 increment as there are steps in the phase cycle), the intrinsically higher sensitivity of phase-cycled experiments vs. gradient-based experiments renders the phase-cycled experiment preferable. While this observation holds for ^{1}H–^{13}C shift correlation experiments at natural abundance, it does not apply to the corresponding ^{1}H–^{15}N long-range correlation experiments in particular. Investigators interested in the acquisition of long-range ^{1}H–^{15}N heteronuclear shift correlation data at natural abundance should utilize gradient pulse sequences for all data acquisition.

The impact of using gradient-based vs. phase-cycled pulse sequences is illustrated in Fig. 2 using a 20 μg sample of the model alkaloid retrorsine (**3**).[10] The results of 8 Hz optimized gradient and phase-cycled HMBC spectra of the 20 μg sample of the alkaloid dissolved in 150 μL of d_4-methanol are contrasted to a reference HMBC spectrum recorded with the same optimization using a 700 μg sample of the alkaloid. The 700 μg spectrum shown in Fig. 2A shows all of the responses that are observable in an 8 Hz optimized HMBC spectrum. B shows the results obtained overnight for the 20 μg sample or retrorsine (**3**) using a conventional, eight step phase-cycled HMBC pulse sequence. A significant number of the possible responses are observed, although some of the observed responses are relatively weak. In contrast, the 8 Hz optimized gradient HMBC (gHMBC) experiment shown in C, with data recorded using parameters identical to those employed in B, shows significantly fewer responses. Those responses that are observed in the gHMBC spectrum shown in C are predominantly the strongest responses observed in the spectrum, with none of the weaker responses visible even when slices through F_2 are examined.

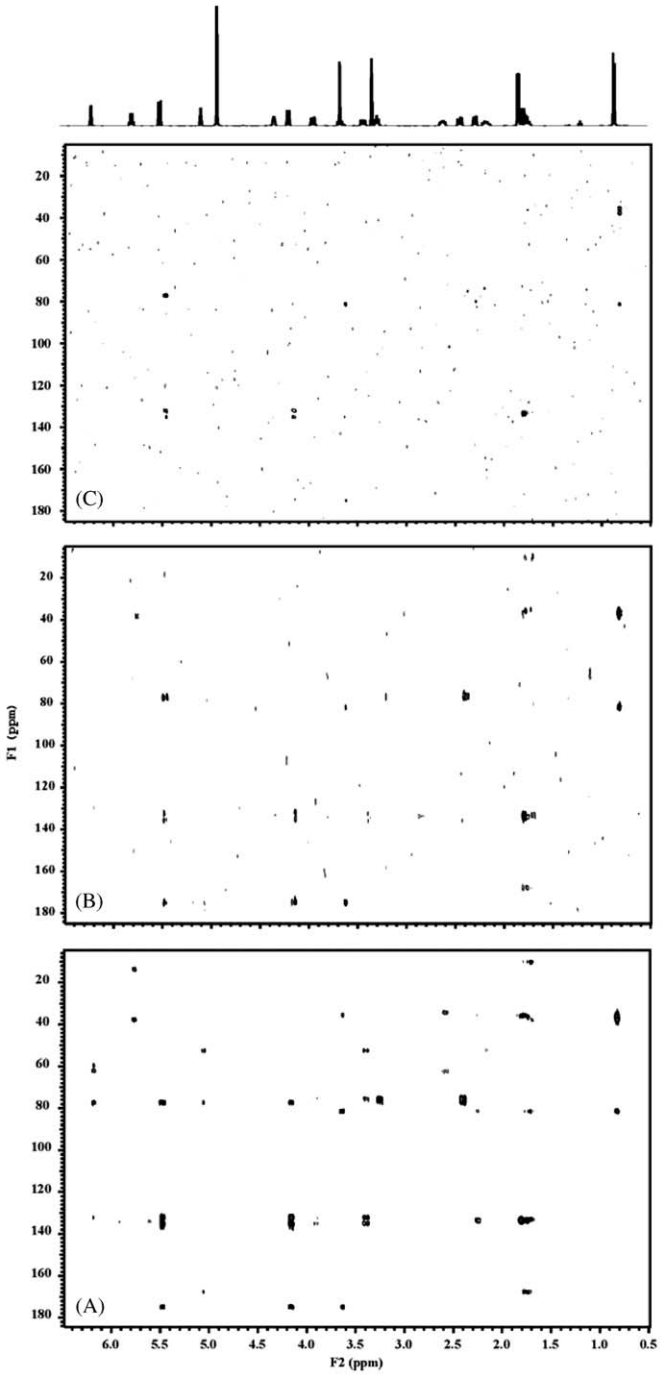
(C)
(B)
(A)
F1 (ppm)
F2 (ppm)
20
40
60
80
100
120
140
160
180
6.0
5.5
5.0
4.5
4.0
3.5
3.0
2.5
2.0
1.5
1.0
0.5

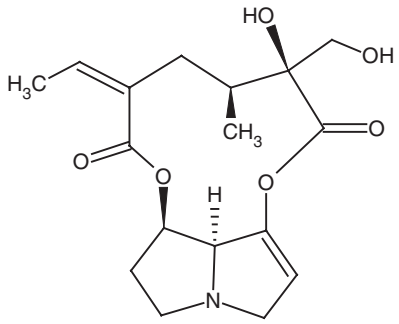

3

While discussing very low-level sample data acquisition, it is also worth commenting on multiplicity-edited pulse sequences used for direct correlation. Multiplicity-edited pulse sequences incorporate additional pulse sequence elements to manipulate the phase of the correlation response as a function of the resonance multiplicity. Cumulatively, the pulse sequence elements added to allow multiplicity-editing cost the investigator about 20–25% in sensitivity in the author's experience. While this is of no consequence when working with milligram samples, for very small samples such as those where one is advised to phase cycle rather than using gradient-based experiments, the signal losses that are encountered in a multiplicity-edited experiment can make the difference between obtaining the data overnight needed to solve a structure vs. having to repeat the experiment over a weekend to obtain suitable data.

As a final note to this section, subsequent to the initial reports of the author and colleagues describing the capabilities of 3 mm NMR probe technology, Bruker Instruments reported the development of 2.5 mm probes with similar capabilities. Practically, the capabilities afforded an investigator by 3 or 2.5 mm probe formats differ very little. For that reason, when applications of micro-probe technology are considered below (Section 6.1), studies employing 3 and 2.5 mm probe technology will be considered together.

Fig. 2. A comparison of gHMBC and phase-cycled HMBC spectra is shown in this figure. Panel A shows the 8 Hz optimized HMBC spectrum obtained using a 700 μg sample of the model alkaloid retrorsine (**3**) dissolved in 150 μL d_4-methanol for comparison to the low-level data shown in Panels B and C. Panel B shows the results obtained overnight with a 20 μg sample of **3**, also dissolved in 150 μL d_4-methanol. The major responses are readily observed and a significant number of the smaller responses are also observed in the contour plot and are readily identifiable when slices through the F_2 frequency domain are examined. Panel C shows the results obtained overnight with the same 20 μg sealed tube using an 8 Hz optimized gHMBC pulse sequence. Only the strongest responses in the spectrum are observed and those are substantially weaker than the corresponding responses in the phase-cycled spectrum shown in Panel B. The much weaker responses visible in Panel B are largely absent from the spectrum presented in Panel C even when slices through the F_2 frequency domain are examined.

2.2. The 1.7 mm submicro- or SMIDG™ NMR probes

Although not developed next in a chronological sense, the next conventional small-volume NMR probe to be developed was the 1.7 mm submicro- or SMIDG™ probe in 1998 in the author's laboratories at Pfizer (then Pharmacia Corporation), again in collaboration with staff at Nalorac Corporation.[11,12] By shrinking the probe dimensions to accommodate a 1.7 mm capillary tube, the required sample volumes correspondingly decrease from ~140 to 160 μL necessary with a 3 mm micro-probe (~70–80 μL using a 3 mm Shigemi tube) to the range of 25–30 μL for the 1.7 mm probe. This reduction in overall sample volume corresponds to a greater than 4-fold increase in sample concentration that can lead to dramatic savings in data acquisition times when dealing with severely limited samples. With care, it is possible to reduce the sample volume to ~20 μL in a 1.7 mm tube, but shimming overhead and the required care in centering the sample relative to the rf coil make it convenient to use a slightly taller sample in most instances.

To illustrate the effects of shrinking the tube volume, Fig. 3 shows a series of three NMR tubes, each containing 1 μmol of the deep violet-colored indoloquinoline alkaloid cryptolepine (**1**). Each of the tubes shown, 5, 3, and 1.7 mm, has the sample of the alkaloid dissolved in what would be the nominal volume for that tube format. As is readily seen from simple inspection of the photograph shown in Fig. 3, the color of the solution in the three tubes goes from a light pink-violet color in the 5 mm tube, to violet in the 3 mm tube, and finally to nearly black in the 1.7 mm tube because of the concentration of the intensely colored alkaloid.

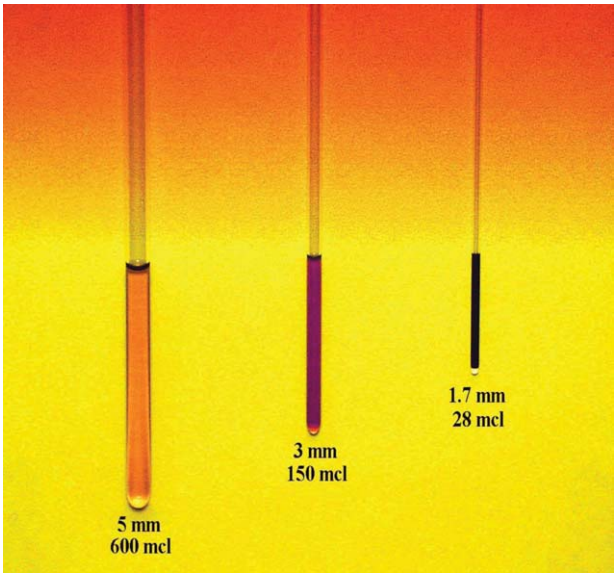

Fig. 3. Photograph showing 5, 3, and 1.7 mm NMR tubes each containing 1 μmol of the deep violet-colored indoloquinoline alkaloid cryptolepine (**3**).

Although the initial studies conducted with the 1.7 mm submicro-probe involved cryptolepine (**1**), the same model compound used in initial studies with the 3 mm micro-probes, a direct comparison between 3 and 1.7 mm probes was not done at the time of the first reports.[11] Using a 0.55 μmol sample of **1**, it was possible to acquire an HMQC direct correlation spectrum in 12 m. For the same sample, HMBC data were acquired in 1.1 h. The gradient HMQC (gHMQC) and HMBC spectra acquired in that first study are shown in Fig. 4(a) and 4(b), respectively. Inverted direct response (IDR) heteronuclear single-quantum correlation total correlation spectroscopy (HSQC-TOCSY) data, an experiment that is considerably less sensitive than HMBC, were also recorded (not shown) on this sample in 3 h. A more interesting low-level performance indication of the 1.7 mm submicro-probes capabilities is seen in the acquisition of heteronuclear shift data for an 8% 11-cryptolepinone impurity (0.04 μmol) of contained in the 0.55 μmol sample of **1** used for these benchmarking studies.[12] The results of a 25.5 h HMQC acquisition are presented in Fig. 5. All of the responses for the impurity in the spectrum were well above the noise floor of the spectrum and readily visible after approximately 12 h of data acquisition. Full HMBC data consistent with the structure were acquired in ~55 h. In practical terms, the ability to acquire data such as those shown in Fig. 5 is a useful capability that can be applied to the identification of impurities and degradation products, metabolites, etc., under favorable circumstances, without having to isolate the minor component for spectroscopic characterization.

A direct comparison of the performance characteristics of 1.7 and 3 mm probes has also been reported that is interesting in that it facilitated a subsequent comparison of the performance of the 1.7 and a 1.0 mm probe later developed by Bruker Instruments (see Section 2.3).[13,14] Using a 1.0 μmol samples of ibuprofen (**4**) in both 1.7 and 3 mm NMR tubes, comparative ^{1}H–^{13}C gradient HSQC (gHSQC) experiments were performed and the results are shown in Fig. 6. The 1.7 mm data were acquired in a scant 3 m, giving an s/n ratio in the experiment of 78:1. The *sec*-butyl methine signal, which is the weakest in both the proton reference spectrum and the contour plot, is still observed with quite usable intensity. In contrast, the 3 mm data, when acquired for 12 m, afforded only a 35:1 s/n ratio and the response for the *sec*-butyl methine proton in the contour plot was of marginal intensity and the response in the proton spectrum barely visible.

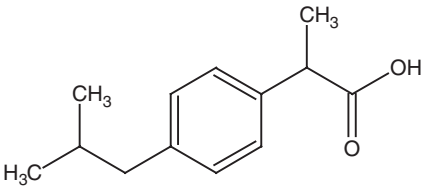

4

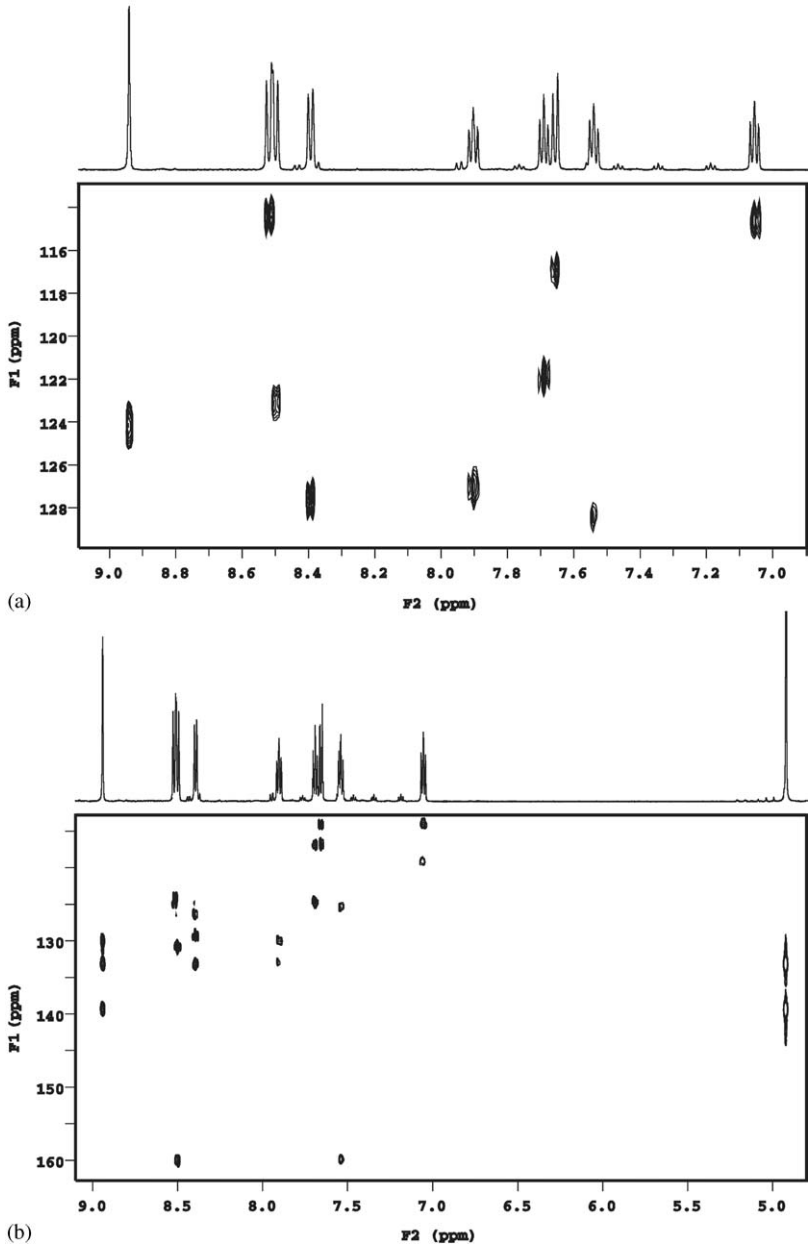

Fig. 4. Spectra acquired for a 0.55 μmol sample of the indoloquinoline alkaloid cryptolepine (**1**) dissolved in 25 μL d_6-DMSO. (a) Proton–carbon (HMQC) direct correlation spectrum recorded in 12 m (16 × 2048 point files, 16 transients/t_1 increment) shown with no linear prediction. (b) Long-range ^{1}H–^{13}C HMBC spectrum of the same sample optimized for 8 Hz. The data were acquired as 64 × 4096 files with 16 transients accumulated/t_1 increment. Data are again shown without any linear prediction. (Reprinted with permission from Ref. 11. Copyright 1998, John Wiley & Sons, Ltd.)

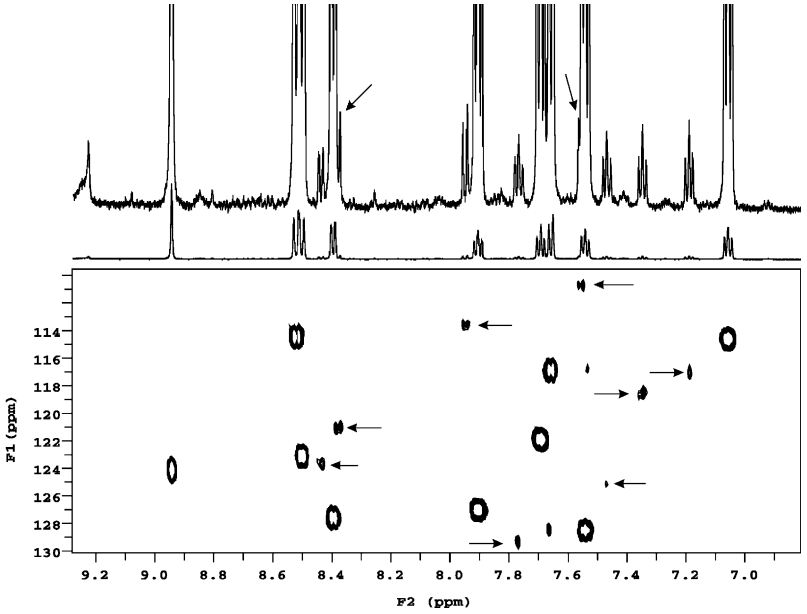

Fig. 5. HMQC spectrum of a 0.55 μmol sample of cryptolepine (**1**) dissolved in 30 μL d_6-DMSO. The data were acquired in a 25.5 h experiment using a 1.7 mm gradient triple resonance submicro-NMR probe at 600 MHz. The minor correlation responses in the spectrum designated by arrows are an 8% (~12 μg) impurity of cryptolepine *N*-oxide present in the sample. All of the impurity responses were visible in a 12 h contour plot. Full HMBC data consistent with the structure were acquired for the impurity in 55 h. (Reprinted with permission from Ref. 12. Copyright 1998, American Chemical Society and American Society of Pharmacognosy.)

Another interesting series of comparative experiments was performed using 1.0 μmol samples of strychnine (**5**) prepared in 1.7 and 3 mm NMR tubes. These spectra are shown in Fig. 7. Panel A shows the results obtained with the 1.7 mm sample with the data acquired using a 600 MHz 1.7 mm submicro- or SMIDG gradient inverse triple resonance NMR probe. The center panel shows the results obtained when the 1.7 mm sample was run coaxially in a conventional 600 MHz 3 mm gradient inverse triple resonance probe. Finally, the right panel in Fig. 7 shows the results obtained using a 3 mm sample in conjunction with the 3 mm gradient inverse triple resonance probe. The proton reference spectra plotted above each of the contour plots were acquired identically and reflect the s/n ratio in the projections through F_2 in the three experiments represented by the contour plots, which were, left to right, 112:1, 75:1, and 62:1, respectively. From these data, it is clear that there is some advantage to be gained in a limited sample situation by using a smaller diameter sample tube in a larger diameter probe, which provides a modest increase in performance (75:1 vs. 62:1 in the example shown in Fig. 7) despite filling factor losses.

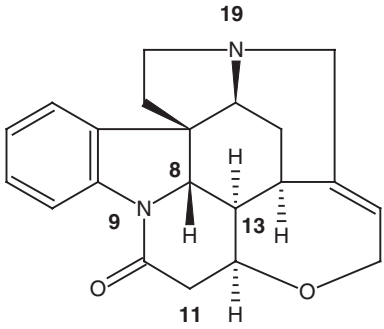

5

Fig. 8 shows the results obtained for a series of natural abundance, 8 Hz optimized ^{1}H–^{15}N gHMBC experiments with a 3 μmol (1 mg) sample of strychnine (**5**) prepared in nominal volumes of 30 and 150 μL in 1.7 and 3 mm NMR tubes, respectively. The 1.7 mm overnight spectrum shown in Fig. 8A shows all of the generally observed responses for the N19 aliphatic nitrogen resonance and two of the three expected responses for the N9 amide resonance. However, when the F_1 slice corresponding to the N9 chemical shift is examined, the H13–N9 correlation response not seen in the contour plot is readily observed. In comparison, the 1.7 mm data acquired overnight using a 3 mm probe shown in B show the appearance of some significant noise spikes in the spectrum (denoted by arrows) as well as some in the projection plotted above the contour plot. If this were an unknown structure with an unestablished empirical formula, care would have to be taken to insure that spurious responses were not misinterpreted. The situation is further exacerbated for the 3 mm sample data shown in C. The s/n ratios for the three experiments are 60:1, 41:1, and 26:1, respectively. Again, there is an appreciably better s/n ratio obtained by running the more concentrated 1.7 mm tube coaxially in the 3 mm probe.

2.3. The 1 mm gradient inverse triple resonance probes

Subsequent to reports from the author's laboratory detailing the performance capabilities of the 1.7 mm submicro-probe, Bruker Instruments announced the development of a 1 mm probe, which is presently the smallest volume conventional (sample tube) NMR probe in commercial production. The sample volume of the 1 mm tubes is approximately 5 μL. Curiously, although Bruker reported data using ibuprofen (**4**) and strychnine (**5**), as were used in the initial reports on the development of the 1.7 mm submicro-NMR probe,[12,13] they reported performance data relative to conventional and cryogenic 5 mm probes, and made no mention of a comparison to 3 or 2.5 mm probes, which would have been a more logical comparison. On this basis, Schlotterbeck and co-workers[14] note that with a 1 mm tube (5 μL volume for the 1 mm probe and 22 μL fill volume when used in the 5 mm

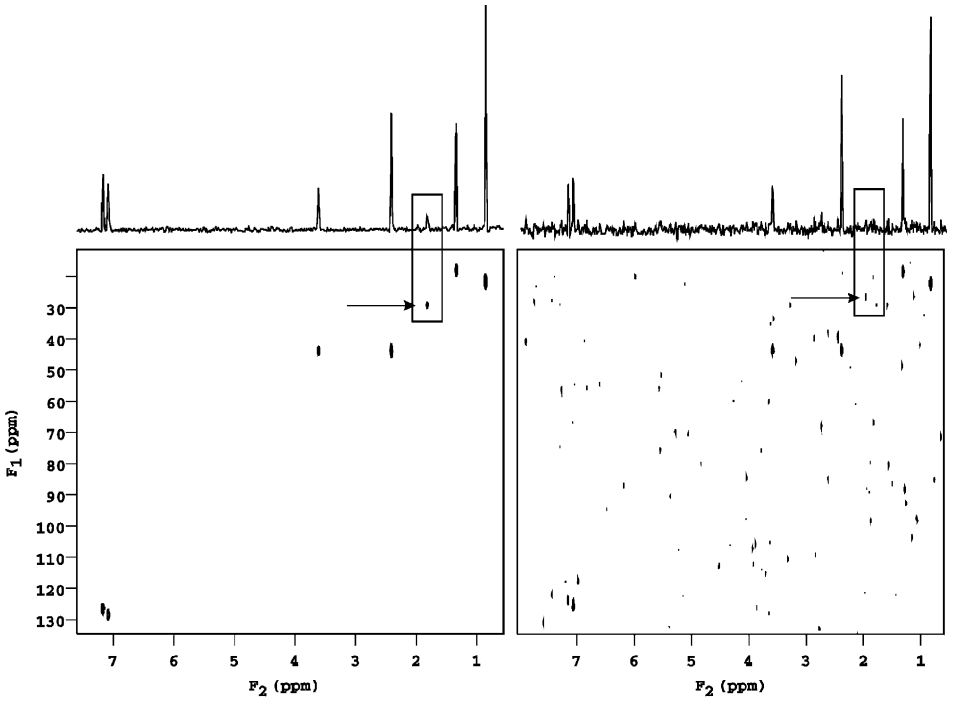

Fig. 6. Comparative 1.0 μmol ^{1}H–^{13}C gHSQC spectra of ibuprofen (**4**). The spectrum shown in the left panel was acquired using a 1.7 mm sample containing the drug in 30 μL d_6-DMSO; data were acquired in 3 m using a 1.7 mm submicro-gradient inverse-detection or SMIDG™ NMR probe at 600 MHz. The data were acquired as 1 transient/each of the 64 t_1 increments used to digitize the second frequency domain. The proton reference spectra plotted above both contour plots were acquired in a single transient. The spectrum plotted over the right panel was subjected to a 3X vertical expansion relative to the spectrum above the left panel. The right panel shows the same quantity of drug dissolved in 150 μL of solvent in a 3 mm NMR tube. The data in the right panel were acquired as 4 transients/each of the 64 t_1 increments in 12 m using a conventional 3 mm gradient inverse triple resonance 600 MHz NMR probe. The s/n ratios of the two experiments were 78:1 for the 1.7 mm spectrum shown in the left panel and 35:1 for the conventional 3 mm spectrum shown in the right panel. The weakest response in both spectra is the *sec*-butyl methine proton (boxed response) but as is readily seen, this response, as well as the multiplet in the proton reference spectrum are both usable in the 1.7 mm data while the corresponding signals in the 3 mm data are marginal at best.

cryogenic probe) containing 172 μg (0.5 μmol), that the 1 mm probe outperforms the cryogenic NMR probe. Relative s/n ratios for the 1 mm tube in the 1 mm probe vs. the 5 mm cryogenic NMR probe were 276:1 vs. 195:1. Based on work in the author's laboratories, there is considerable advantage to using smaller diameter sample tubes in 5 mm cryogenic NMR probes (see Section 5) that arise from increased thermal isolation of the NMR sample relative to the cryogenically cooled rf coils when smaller diameter NMR tube are used *in lieu* of 5 mm samples with a 5 mm cryogenic NMR.

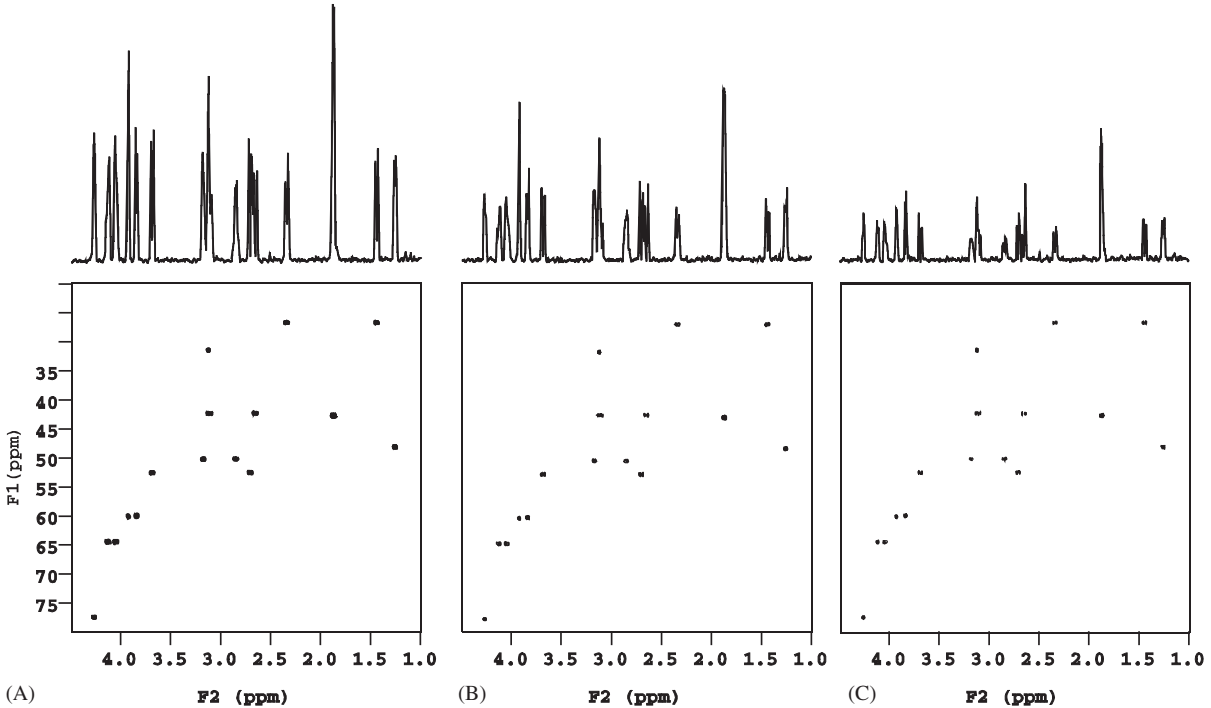

Fig. 7. Comparative 1 μmol spectra of slrychnine (**5**). Panel A shows the results obtained with the 1.7 mm sample with the data acquired using a 600 MHz 1.7 mm submicro- or SMIDG gradient inverse triple resonance NMR probe. The center panel shows the results obtained when the 1.7 mm sample was run coaxially in a conventional 600 MHz 3 mm gradient inverse triple resonance probe. Finally, the right panel in Fig. 7 shows the results obtained using a 3 mm sample in conjunction with the 3 mm gradient inverse triple resonance probe. The proton reference spectra plotted above each of the contour plots were acquired identically and reflect the s/n ratio in the projections through F_2 in the three experiments represented by the contour plots, which were, left to right, 112:1, 75:1, and 62:1, respectively. From these data, it is clear that there is some advantage to be gained in a limited sample situation by using a smaller diameter sample tube in a larger diameter probe, which provides a modest increase in performance (75:1 vs. 62:1 in the example shown in Fig. 7) despite filling factor losses. (Reprinted with permission from Ref. 13 Copyright 1999, John Wiley Sons, Ltd.)

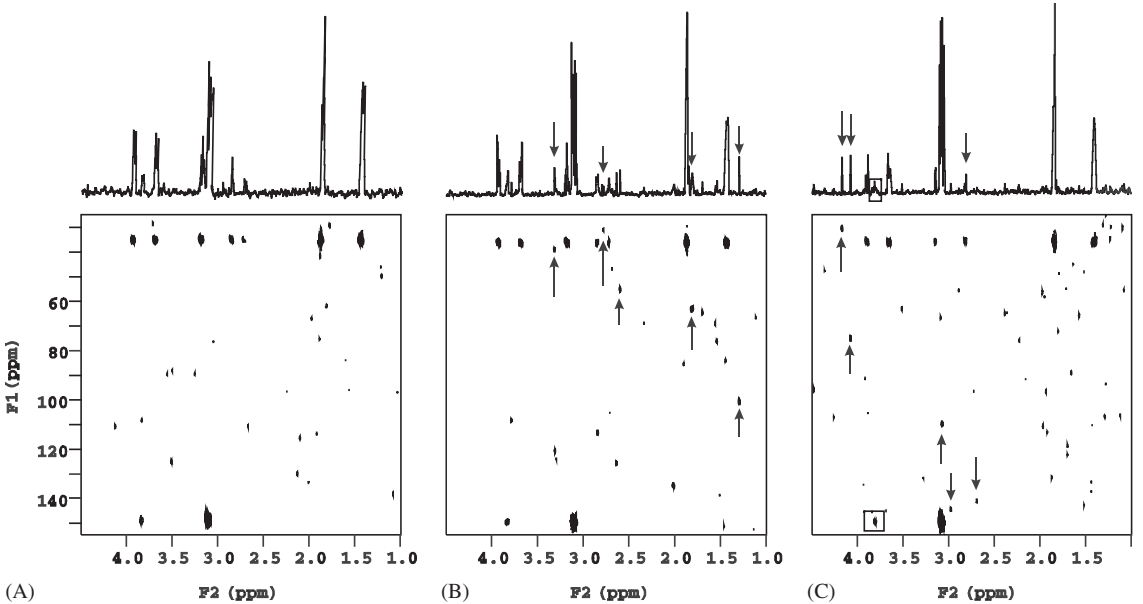

Fig. 8. Comparative 3 μmol (1 mg) spectra of strychnine (**5**). Samples were prepared in either 30 or 150 μL of chloroform-*d* in 1.7 and 3 mm NMR tubes, respectively. Each of the 8 Hz optimized ^{1}H–^{15}N gHMBC spectra shown were acquired at natural abundance by accumulating 1024 transients × 4096 points/each of the 40 t_1 increments, giving an acquisition time of 18 h. The data were identically processed, using linear prediction to 160 files in the second frequency domain and zero filling to afford 2048 × 512 point contour plots shown. The data shown in Panel A were acquired using the 1.7 mm sample with data acquisition in a 600 MHz 1.7 mm gradient inverse-detection or SMIDG™ NMR probe. The s/n ratio in the experiment, taking the open region of the spectrum from 4.5 to 5.5 ppm as representative "noise" was 60:1. All of the expected correlation responses are observed in the contour plot with good intensity with the exception of the H13 resonance (furthest upfield multiple), which was visible in the slice taken at the amide N9 chemical shift. The experiment was repeated with the 1.7 mm sample using a conventional 3 mm 600 MHz gradient inverse triple resonance NMR probe and gave an s/n ratio of 41:1. These results are shown in Panel B, and there are clearly more spurious responses visible in the contour plot. The experiment was repeated a third time using the 3 mm sample paired with the conventional 3 mm probe to afford the data shown in Panel C, with an s/n ratio of 26:1. Spurious responses were more numerous than in Panel B and of greater intensity. It would be strongly preferable for a sample of this size, using conventional 3 mm probe technology, to increase the data accumulation to a weekend duration.

While NMR samples as small as 5 μL can be handled successfully, in the experience of the author, quantitative transfer of a sample this small from the container in which it was prepared to the NMR tube still represents a significant challenge. This is especially true if one is dealing with a rare sample rather than a serially diluted stock solution. Several other considerations also come into play with sample volumes as small as 5 μL. First, there is the issue of solubility. Although the 1 mm probe is intended to work in the low microgram range, Schlotterbeck and colleagues[14] nevertheless reported long-range ^{1}H–^{15}N gHMBC data for a 1 μmol sample (334 μg) of strychnine (**5**). While strychnine is reasonably soluble, samples with more limited solubility could be problematic. A second consideration would be the rate of moisture sorption. A hygroscopic sample or solvent such as d_6-DMSO would mandate preparing and manipulating the sample in a glove box. From the author's own experience with 1.7 mm tubes and sample volumes of 25–30 μL in a glove box, working with a still smaller sample volumes and tubes would be very demanding.

Sample handling problems aside, in their initial report describing the capabilities of a 1 mm probe, Schlotterbeck and co-workers[14] were able to demonstrate rather impressive results. Using ibuprofen (**4**) the authors were able to obtain a ^{1}H–^{13}C gHSQC spectrum on a 5 nmol (1 μg) sample in 20 h and an 8 Hz gHMBC spectrum on 100 nmol (20 μg) in which all responses were visible in 5 h, with an s/n ratio in the contour plot of 9:1. The authors also note that in an attempt to perform these experiments using a 5 mm probe that no data were obtained, which is not particularly surprising. The authors also showed the results obtained with a 2-day ^{1}H–^{15}N gHMBC experiment performed using a 1 μmol (334 μg) sample of strychnine (**5**). The authors note that with the exception of the H20α– and H20β–N19 correlations, that all other correlations were visible in 6 h. These results are comparable to those obtained with an identically sized sample in a 1.7 mm submicro-probe in this author's laboratory over a weekend (65 h).[13]

3. MAGIC ANGLE SIDEWAYS SPINNING LIQUID PROBES

Several years after the commercial introduction of 3 mm micro-NMR probes, another small-volume probe innovation was announced by Varian in the form of the Nano-probe^{TM}. Jim Shoolery, then head of the Varian NMR Applications Laboratory, deserves considerable credit for championing the development of this probe technology within Varian.[15–17] One major objective of the design of the Nano-probe^{TM} was a desire to be able to locate 100% of the NMR sample within the rf coils of the probe. In contrast, conventional NMR probes that utilize tubes typically locate 50–80% of the sample in the rf coil, while flow designs such as the μCoil NMR probes (see Section 4) generally position $<30\%$ of the sample in the confines of the rf coil. The reasoning behind the design of the Nano-probe^{TM} was that by orienting the probe at the magic angle and then spinning the 40 μL sample at several kHz, it would be possible to overcome the inhomogeneities associated with the discontinuity at the cell boundary, averaging all of the magnetic dipoles to zero.[15]

The 40 μL total volume of the nano-cell makes it well suited to applications where the available sample is severely limited. Using a proton Nano-probe™, it was demonstrated in the author's laboratories at Burroughs Wellcome, Co. that it was possible to acquire usable ^{1}H-NMR spectra of samples as small as 75 ng (32 pmol) of cryptolepine (**1**), and a correlation spectroscopy (COSY) spectrum overnight on a 200 ng (85 pmol) sample of the alkaloid.[18,19] The 75 ng proton spectrum is shown in Fig. 9. Due to the tremendous dynamic range, the data were acquired with both the residual water and protio-DMSO resonances suppressed. The ^{13}C satellites from the solvent are roughly twice the intensity of the *N*-methyl resonance (~5.05 ppm) of the cryptolepine, and multiple times more intense than the aromatic proton resonances of the sample. For very low-level sample applications, it may become desirable to consider using ^{13}C depleted deuterated solvents.

The ability of the Nano-probe to put 100% of the sample in the rf coil of the probe makes it useful for acquiring data on trace samples such as metabolites and

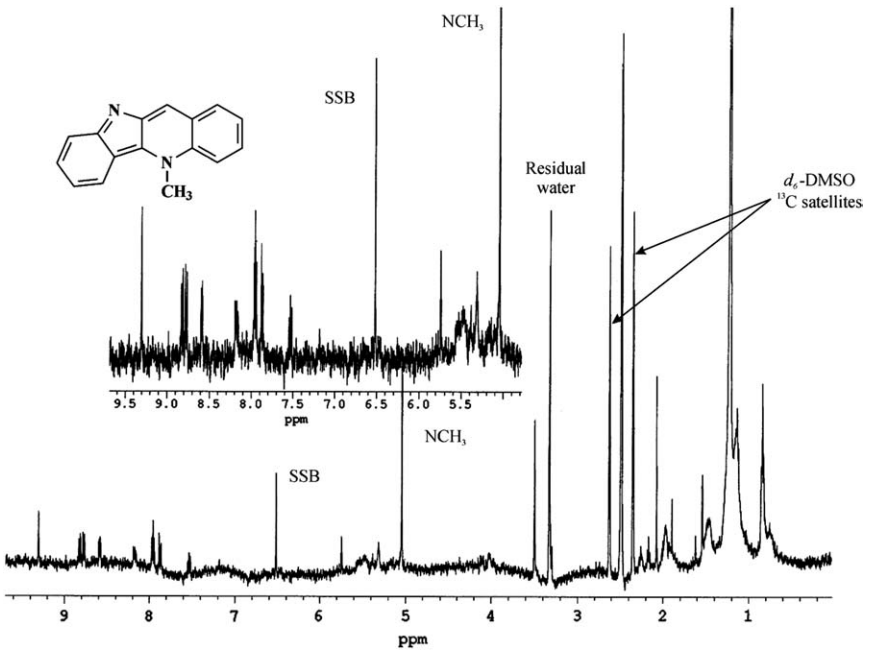

Fig. 9. Proton NMR spectrum of a 75 ng (32 pmol) sample of cryptolepine (**1**) dissolved in 40 μL of 99.996% d_6-DMSO. The data were acquired overnight using a prototype Varian proton Nano-probe™ with the sample spun at approximately 2 kHz. Both the residual water and protio-DMSO were irradiated to suppress their signals during the data acquisition. The suppressed DMSO signal is plotted on-scale for comparison to the ^{13}C satellite lines from the solvent. Relative to the *N*-methyl group of the cryptolepine (**1**) (~5.05 ppm), the unsuppressed ^{13}C satellite lines from the DMSO are observed with approximately twice the intensity of the *N*-methyl signal. The line-labeled SSB is a spinning side band. (Reprinted with permission from Ref. 19. Copyright 2002, John Wiley & Sons, Ltd.)

forensic samples. Fortunately, in many instances with metabolites, it is possible to obtain samples from a few to tens of μg in size, which is well within the detection capability of a Nano-probe. Varian followed the development of the initial homonuclear Nano-probe^{TM} design with both heteronuclear and gradient inverse-detection capability variants. While there has not been a wealth of direct comparison data reported for the Nano-probe^{TM} relative to conventional NMR tube formats, one set of comparative ^{13}C spectra of a 200 μg sample of a secondary fungal metabolite, fumonisin-B_1 (**6**), has appeared.[20] The heteronuclear Nano-probe^{TM} data for **6** shown in Fig. 10 were acquired after an attempt to acquire a ^{13}C reference spectrum in a 3 mm $^{13}C\{^1H\}$ dual probe failed to give a signal for the ketone carbonyl of the molecule (top trace). The sample was concentrated and transferred to a 40 μL nano-cell affording the spectrum shown in the bottom trace of Fig. 10.

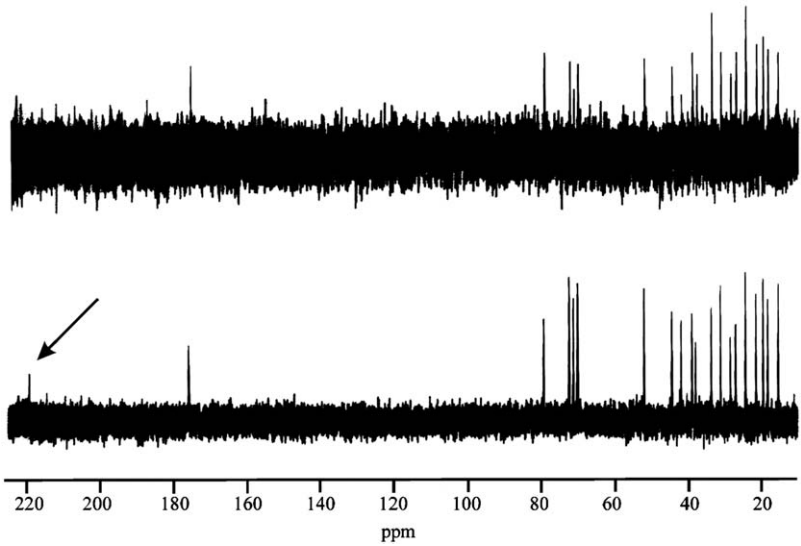

Fig. 10. Comparative overnight ^{13}C spectra of an ~200 μg sample of a secondary fungal metabolite fumonisin B_1 (**6**) in D_2O. The data shown in the top trace were acquired with the sample dissolved in 140 μL of solvent in a 3 mm NMR probe. The data were acquired overnight at 125 MHz using a Nalorac MD-500-3, 3 mm micro-dual NMR probe. The s/n ratio of the experiment was 5.5:1. A ketone carbonyl was expected in the 200–230 ppm region of the spectrum based on mass spectrometric fragmentation data and was not observed in the ^{13}C reference spectrum. In an effort to observe the carbonyl ^{13}C resonance to complete the work, the sample was washed from the 3 mm NMR tube, concentrated to ~20 μL and transferred quantitatively to a 40 μL nano-cell. The overnight data acquisition was repeated using a Varian 500 MHz heteronuclear Nano-probe^{TM} to afford the spectrum shown in the bottom trace. The s/n ratio in the bottom spectrum was 11:1, with the expected carbonyl resonance observed at 219.5 ppm. (Reprinted with permission from Ref. 20. Copyright 1995, American Chemical Society and American Society of Pharmacognosy.)

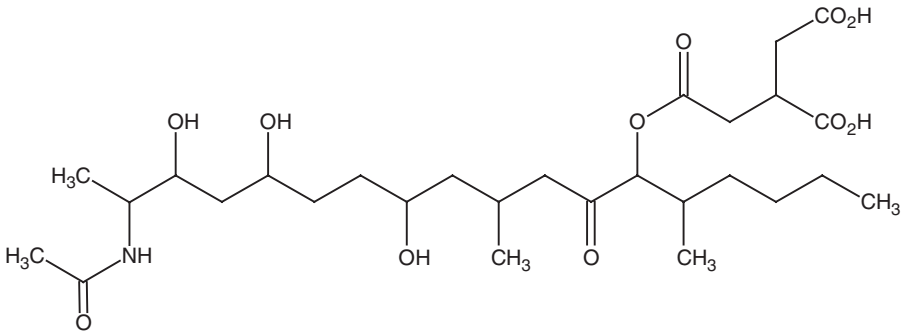

6

Aside from the obvious improvement in the s/n ratio, which arises in part from concentrating the sample from 145 to 40 μL as well as from having all of the sample in the rf coil rather than ~70%, the ketone carbonyl resonance at 219.5 ppm was observed with reasonable signal intensity whereas its presence was questionable at best in the 3 mm micro-dual probe ^{13}C spectrum shown in the top panel. The s/n ratios of the overnight acquisitions were 5.5:1 for the 3 mm micro-dual probe vs. 11:1 for the Nano-probe™. There is no obvious reason why the carbonyl resonance was not observed in the 3 mm micro-dual ^{13}C spectrum, as the relaxation delay between acquisitions was set identically in the two experiments. These data also suggest that on a per-transient basis, that the performance of the Nano-probe™ is perhaps somewhat lower than that of the 3 mm micro-dual probe. This inference is based on the nearly 4-fold concentration difference between the two probe formats. Assuming probe efficiencies were identical, an s/n ratio approaching 22:1 should have been observed for the Nano-probe™ based on the concentration increase.

One other application where Nano-probe technology excels relative to conventional tube or flow NMR probe formats is in the area of heterogeneous samples. One of the early applications demonstrated for the Nano-probe was the acquisition of NMR spectral data for chemically modified polymer beads used in solid-phase-assisted peptide synthesis and related chemical transformations.[21–23] When chemically modified beads are interrogated in a conventional NMR sample tube, the resin bead behaves as an insoluble material and at best very broad and poorly resolved spectra may be recorded. In contrast, when the same beads are placed in a Nano-probe and spun at several kHz at the magic angle, there is sufficient solvation of the pendant chemical moiety and the linker to resin bead nucleus to allow the modified portion to behave as if it is in pseudo solution, which allows reasonable NMR spectra to be recorded. Various factors affect the quality of the NMR data that can be obtained for the pendant molecule, which include the tether length and the solvent used for the measurement.[23] There have been a diverse assortment of applications of Nano-probe™ applications reported in the literature that are discussed in further detail in Section 6.3.

4. μCOIL NMR PROBES

As was noted above, handling samples and the tubes for dealing with volumes smaller than those associated with a 1 mm NMR tube, ~5 μL, would be challenging because of both the tiny sample volumes in addition to the potential fragility of NMR tubes of that size. For this reason, still smaller-volume NMR probes have generally been developed using flow methods, allowing the sample to be pushed into the rf coil region of the probe by either pressurized solvent or compressed gas.

Several early studies reported the results of efforts to record proton NMR spectra at the nL sample volume level in conjunction with online capillary electrophoresis (CE),[24] static and online conventional,[25] and liquid chromatography NMR (LC-NMR) methods.[26] The first report of a more usable high-sensitivity very small-volume NMR probe design, in the opinion of the author, is found in the late 1995 report by Sweedler and colleagues.[27] It was still necessary to immerse the probe design in Fluorinert FC-43 a perfluorinated organic liquid to generate data with usable lineshape and resolution, but, never-the-less, the probe design described in that report ushered in a new area of small-volume high-sensitivity NMR probe research.

The area of μCoil NMR probes has expanded from initial reports in a number of directions. Subramanian and Webb[28] described work on the design of solenoidal microcoils for high-resolution ^{13}C-NMR of small volumes. Using one of these probe designs, the authors reported a limit of detection (defined as an s/n ratio >3.0 by the authors) for unlabeled sucrose of 18 μg (52 nmol) in a 90 m acquisition. The authors also reported the acquisition of a ^{13}C-decoupled HMQC spectrum on 1.6 μg (4.5 nmol) of sucrose in 14 m. Olson *et al.*[29] described an improved nL volume μCoil probe design in which the rf coils were oriented at the magic angle (54.7° relative to the axis of the magnetic field). Multiple solenoidal μCoil probes for high-sensitivity high-throughput NMR spectroscopy were first described in 1999.[30] The concept behind these designs was the optimization of data collection for simultaneous collection of data for multiple samples. A four-coil design was described. Signal cross "contamination" was estimated to be ~0.2% between individual coils. Simultaneous 1D and 2D spectra were shown for samples of fructose, galactose, adenosine triphosphate (ATP), and chloroquine (7 nmol of each compound). The authors also described a "more compact" two-coil designs with observe volumes of 5 and 31 nL for the two coils. 1D- and 2D-NMR spectra were acquired for samples of *n*-butanol (55 nmol) and ethylbenzene (250 nmol). NMR detection using multiple solenoidal microcoils for continuous flow CE has also been reported.[31,32] Due to the extremely small quantity of analyte involved with CE separations, coupled with the inherent insensitivity of NMR measurements, it was necessary to resort to a μCoil to take advantage of the mass sensitivity of this type of probe design to facilitate the acquisition of useful NMR data. In a similar vein, μCoil probes have also been coupled to capillary isotachophoresis (cITP) for the analysis of charged molecules, again for reasons of the mass sensitivity inherent to μCoil probe designs.[33] Applications of various hyphenated μCoil NMR probes are surveyed in Section 6.5.

5. CRYOGENIC NMR PROBES

Radio astronomers have long utilized cryogenic cooling of their receivers to increase s/n ratio and thereby the sensitivity of their measurements. Conceptually, cryogenically cooled NMR probes can be considered an extrapolation from lessons learned in radio astronomy. Early work by Styles and others[34–37] demonstrated that considerable gains in sensitivity could be obtained by decreasing the temperature of the rf coils of the probe and their associated electronics. Design problems inherent to the development of usable cryogenic NMR probes with long-term operability and thermal stability have slowed the commercial introduction of this type of probe technology. Delivery of cryogenic refrigerant to cool the rf coils of an NMR probe located in the bore of a superconducting NMR magnet, with a sample maintained at room temperature only a scant few millimeters separated from the cryogenically cooled region of the probe was one significant challenge. Another challenge was designing the internal components of the cryogenic NMR probes so that capacitors and other portions of the circuitry were not stressed to the breaking point when the probes are thermally cycled from room temperature down to their operating temperature, which is typically in the range of ~25 K in the first commercial examples of these probes.

The s/n ratio in an NMR experiment, which is an expression of sensitivity, has been described for a cryogenic NMR probe[38,39] and can be represented by the equation:

$$\frac{S}{N} \propto \frac{1}{\sqrt{1 + \alpha \frac{R_s}{R_c}}} \tag{1}$$

where R_s is the resistance of the sample, R_c the resistance of the coil, and

$$\alpha = \frac{T_s + T_a}{T_c + T_a} \tag{2}$$

where T_s corresponds to the sample temperature, T_a represents the noise temperature of the preamplifier, and T_c is the rf coil temperature. For a conventional room temperature probe, $\alpha = 1$ and for a cryogenic probe, $\alpha = 7.8$.

The most important factors in determining the s/n ratio or sensitivity of an NMR experiment in a cryogenic NMR probe, insofar as the hardware itself is concerned, are the temperature of the coil, T_c; the resistance of the coil, R_c; the temperature of the sample, T_s; and the resistance added to the coil by the presence of the sample or the sample resistance, R_s. The temperature of the rf coil in a cryogenic NMR probe is typically in the range of 15–30 K; commercial examples of the Varian Cold-probe™ operate at 25 K. The preamplifier noise temperature is generally in the range of 10–15 K and the coil resistance is small compared to a conventional room temperature NMR probe. The first two terms in the expression below provide the basis for the vast improvement in the performance of a cryogenic relative to a conventional NMR probe. The sample temperature, T_s, and sample resistance, R_s,

in contrast, are quite similar for both conventional and cryogenic NMR probes. These terms relate to the s/n ratio according to the expression:[39–43]

$$s/n \sim [T_c R_c + T_a(R_c + R_s) + T_s R_s]^{-0.5} \tag{3}$$

The sample temperature, T_s, unlike the preamplifier and coil temperatures, T_a and T_c, respectively, can generally be varied only over a relatively limited range. The sample resistance, R_s, has been shown to be proportional to sample conductivity,[39] which explains, in part, why the sensitivity of cryogenic NMR probes can be so adversely affected by high-conductivity samples. To a lesser extent, even for small molecules in organic solvents, the choice of solvent can have an impact on the sensitivity of a cryogenic NMR probe, with solvents such as benzene having only a minimal impact on sensitivity while polar solvents such as methanol can have a greater impact on cryogenic NMR probe performance than would running the sample in 100 mM Tris buffer.

Another expression that illustrates how R_s impacts on cryogenic NMR probe performance is:

$$R_s \propto r^4 L(\sigma + \omega\varepsilon_o\varepsilon'')\omega^2 \tag{4}$$

where R_s is proportional to the sample radius, r (inner diameter of the NMR tube), the length of the sample, L, multiplied by the term for the dielectric measurement of the sample ($\sigma + \omega\varepsilon_o\varepsilon''$) times the field, ω^2. When Eq. (4) is considered with respect to the term $T_s R_s$ in Eq. (3), which describes the s/n ratio attainable with a cryogenic NMR probe, it becomes apparent, almost counter-intuitively, that reducing the diameter of the sample and shortening the solvent column in the NMR tube can have a beneficial impact on the performance of a cryogenic NMR probe, despite filling factor losses associated with using smaller diameter tubes. A real-world example would be acquiring data in a 3 mm NMR sample coaxially positioned in a 5 mm cryogenic NMR probe.

In the example of a 3 mm tube being run coaxially in a 5 mm cryogenic NMR probe, the filling factor, η, is defined by the following equation, where:

$$\eta = d_s^2/2D_c^2 \tag{5}$$

For a 5 mm cryogenic NMR probe based on an 8 mm diameter rf coil to allow space for the Dewar, a 5 mm sample tube gives a filling factor of $\eta = 0.138$ vs. 0.045 for a 3 mm sample tube. Thus, the filling factor for the 3 mm sample is approximately 33% that of the 5 mm sample. When a series of NMR samples were prepared in optimal sample volumes in 5, 4, and 3 mm NMR tubes, each tube containing 11.6 μg (0.027 μmol) of the antibiotic clindamycin (**7**) dissolved in 374, 223, and 122 μL, respectively, giving a solvent column in each tube of 27 mm, the transient spectra shown in Fig. 11 were obtained. The s/n ratio for the clindamycin anomeric proton was measured using a 200 Hz "noise" window downfield of the anomeric proton resonance. The s/n ratio of the three experiments was 14.4:1, 20.8:1, and 21.5:1 for the 5, 4, and 3 mm samples, respectively. Repeating the series of experiments with a larger 125 μg sample of clindamycin (**7**) gave proportionately

comparable results of 165:1, 232:1, and 273:1, respectively. These data support the premise that sample resistance, R_s, in Eqs. (3) and (4) has a much more profound impact on the s/n performance of a cryogenic NMR probe containing a constant amount of sample than a 66% decrease of the filling factor, η, defined by Eq. (5), when the sample tube diameter is reduced from 5 to 3 mm.

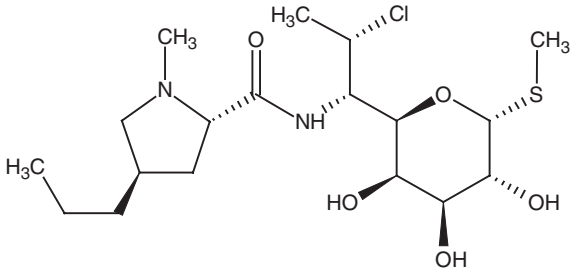

7

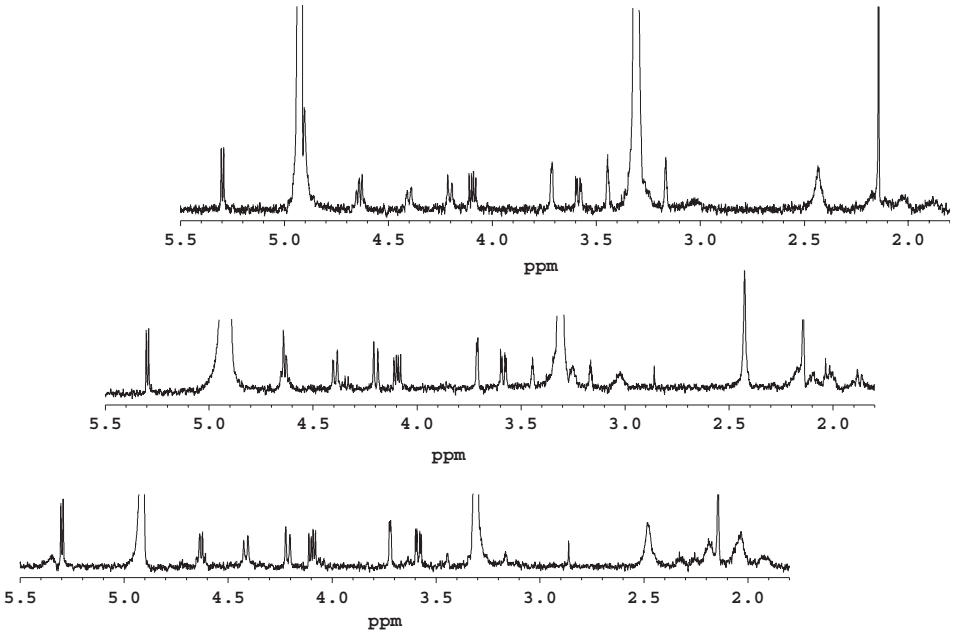

Fig. 11. Eight transient 500 MHz ^{1}H-NMR spectra of an 11.9 μg (0.027 μmol) sample of the antibiotic clindamycin (**7**) prepared in 500 μL of $CDCl_3$ in a 5 mm NMR tube (top trace); 292 μL in a 4 mm tube (middle trace); and 163 μL in a 3 mm tube (bottom trace). All data were acquired using a 500 MHz 5 mm gradient inverse triple resonance Varian Cold-probe^{TM}. The s/n ratio was measured for each spectrum using a 200 Hz region of representative noise downfield of the anomeric proton resonating at ~5.3 ppm. The s/n ratios were 14.4:1, 20.8:1, and 21.5:1 for the 5, 4, and 3 mm tubes, respectively.

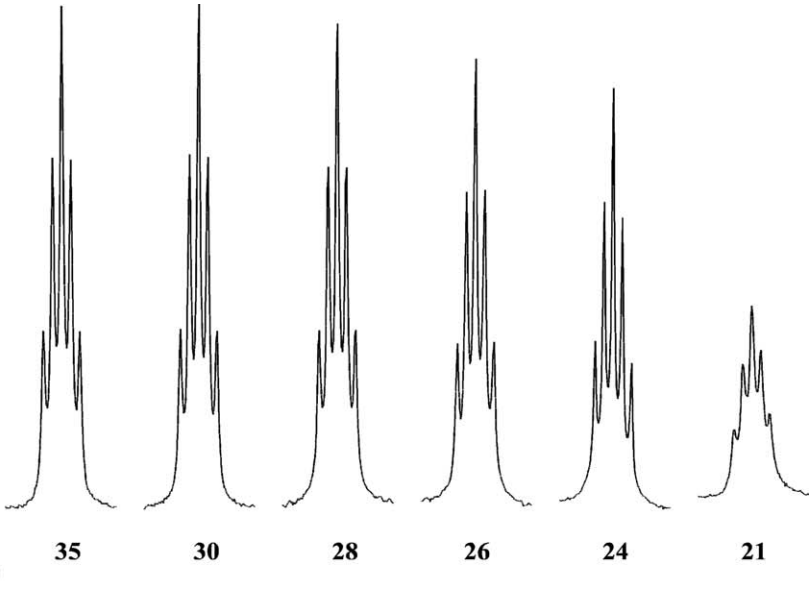

(a)

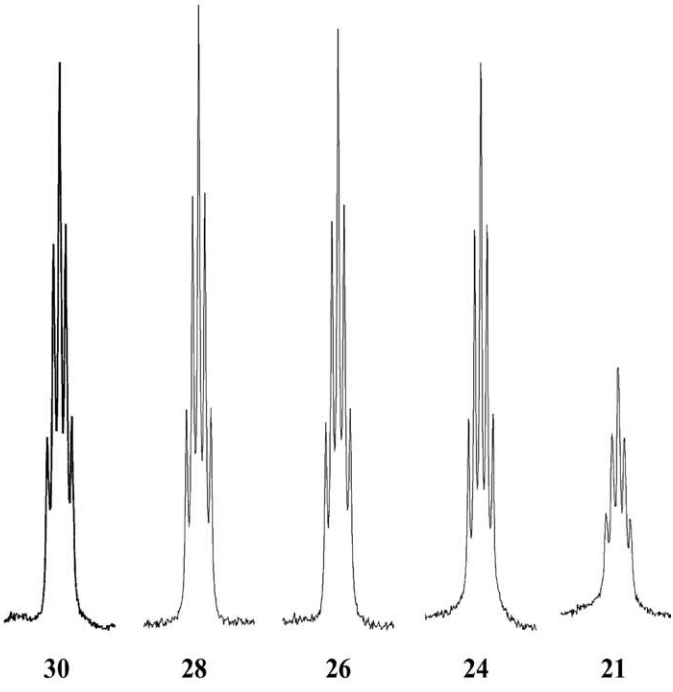

(b)

Eq. (4) also shows that the sample length is a contributor to sample resistance. Work in the author's laboratories to explore the optimal sample volume in 5 and 3 mm tubes has shown that there are differences in how well a 5 mm cryogenic NMR probe can be shimmed as a function of solvent column height, in addition to there being differences between 3 and 5 mm samples in terms of optimal sample column height. Fig. 12 shows a comparison of results obtained with 3 and 5 mm tubes in a 5 mm 500 MHz gradient inverse triple resonance cryogenic NMR probe. The tubes contained d_4-methanol and were first gradient shimmed and then hand shimmed to the best homogeneity possible. It is worth noting that gradient shimming alone was incapable of attaining the optimal shim settings when column heights were successively varied, presumably because of the very large shim current differences for some shims. However, once a shim file was established for a given solvent column height in a given tube format (3, 4, or 5 mm), gradient shimming performed well enough with most real-world samples to be used on a routine basis.

Occasionally, in the author's laboratory, we have found that when a sample is inserted it just does not shim well for no apparent reason. In those instances, spinning the sample for a few seconds, insuring that it is coaxially centered in the probe has generally quickly led to acceptable shim settings.

With the advent of 2D-NMR in general, and inverse-detected 2D-NMR methods in particular, spinning samples have essentially been largely forgotten, the assumption being that probes and magnets are so good that comparable spectra are obtained whether or not a sample is spun. With very scarce samples, it will be desirable to resort to shorter solvent columns to maintain sample concentrations as high as possible for 2D-NMR data acquisition. As will be noted from Fig. 12, shorter columns generally tend to be harder to shim and give less optimal lineshape. However, by spinning the sample, as shown in Fig. 13, a high-quality reference spectrum can be obtained even with a short solvent column, after which the spinner can be turned off and 2D-NMR data acquisition can then be initiated.

One additional aspect of sample preparation that impinges on the performance of a cryogenic NMR probe remains to be discussed. Again, the R_s term that plays an important role in Eqs. (3) and (4) has an important role in this issue of the effects of solvent on cryogenic NMR probe performance. The role of R_s on the effect of

---

Fig. 12. Comparison of the effect of column heights and tube diameters with samples for a 500 MHz gradient inverse triple resonance cryogenic NMR probe. The results obtained in shimming the d_4-methanol multiple for a series of solvent column heights in a 5 mm NMR tube ranging from 35 down to 21 mm is shown in Panel A. The optimal column height is ~30 mm based on these results. The samples were shimmed initially using ^{2}H gradient shimming and then hand shimmed to the final results shown. It was not possible for ^{2}H gradient shimming to provide acceptable results until a shim file had been stored for a given solvent column height. (b) Results obtained in shimming the d_4-methanol multiple for a series of solvent column heights in 3 mm NMR tube ranging from 30 down to 21 mm. The optimal column height is ~28 mm based on these results. It is also worth noting that better homogeneity could be obtained at the minimal column height of 21 mm investigated with both tubes when working in a 3 mm tube.

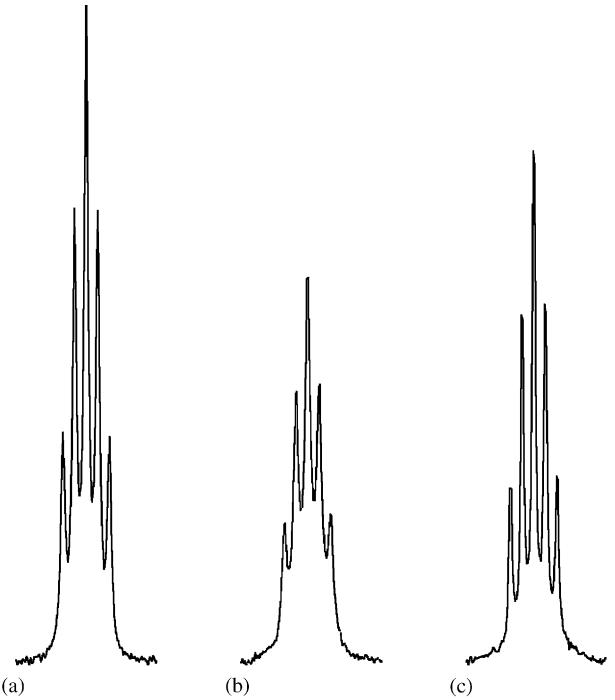

Fig. 13. Results obtained with 4 mm samples in a 500 MHz gradient inverse triple resonance cryogenic NMR probe. (a) Non-spinning resolution of the d_4-methanol multiplet for a 30 mm solvent column in a 4 mm tube. (b) Non-spinning resolution of the d_4-methanol multiplet for a 22 mm solvent column in a 4 mm tube. As expected from Fig. 12, the resolution is lower with a solvent column of this short (the optimal solvent column for a 4 mm tube is 30 mm) is shown in Panel A. (c) Resolution of the d_4-methanol multiplet for a 22 mm solvent column in a 4 mm tube with the sample spinning at ~20 Hz. For very scarce samples when it is necessary to resort to the shortest possible solvent column height to facilitate the acquisition of high-quality 2D-NMR data, it may be beneficial to spin the sample during the acquisition of the proton reference spectra.

solvent on cryogenic NMR probe performance is manifest through the following equation:

$$\frac{N_s^2 - N_{ep}^2}{N_{ep}^2} = \frac{\left(1 + \frac{R_s}{R_c}\right)^{-1}(T_s - T_c)}{(T_c + T_{pa})} \tag{6}$$

where R_s is the sample resistance (Eq. (4)), R_c the coil resistance, T_s the sample temperature, nominally about 298 K; T_c, the rf coil temperature, which is 25 K in most operating commercial cryogenic NMR probes; T_{pa} is the preamplifier temperature which is typically ~15 K; and the terms N_s and N_{ep} are the noise of the sample and the empty probe, respectively.[44] Measuring R_s for commonly used

NMR solvents and examining the effects of solvent on s/n ratio losses in cryogenic NMR probes leads to some rather interesting results that are manifest in part, with 5 vs. 3 mm NMR tubes. These data are shown in Fig. 14. As shown, better results are uniformly obtained with 3 rather than 5 mm NMR tubes, especially for polar solvents such as methanol and with buffers such as 100 mM Tris.

Under favorable circumstances, a cryogenic NMR probehead will deliver a 3- to 4-fold sensitivity gain relative to a conventional NMR probehead in the same configuration (e.g. inverse detection).[45–48] Operationally, to achieve a given s/n ratio in an NMR experiment, the increase in s/n ratio afforded by the cryogenic NMR probe allows an investigator to achieve the target s/n ratio 9–16 times faster than with the corresponding conventional NMR probehead. Thus, when there are no constraints on sample availability, more efficient measurement is one facet of using a cryogenic NMR probe. At the opposite end of the spectrum, the size of a sample that can be successfully interrogated in an allotted time is considerably smaller when an investigator has access to a spectrometer equipped with a cryogenic NMR probe vs. a conventional NMR probe of the same dimension.

To illustrate the performance advantage of a cryogenic NMR probe, a pair of overnight HMBC spectra were acquired for a sealed 3 mm NMR tube containing

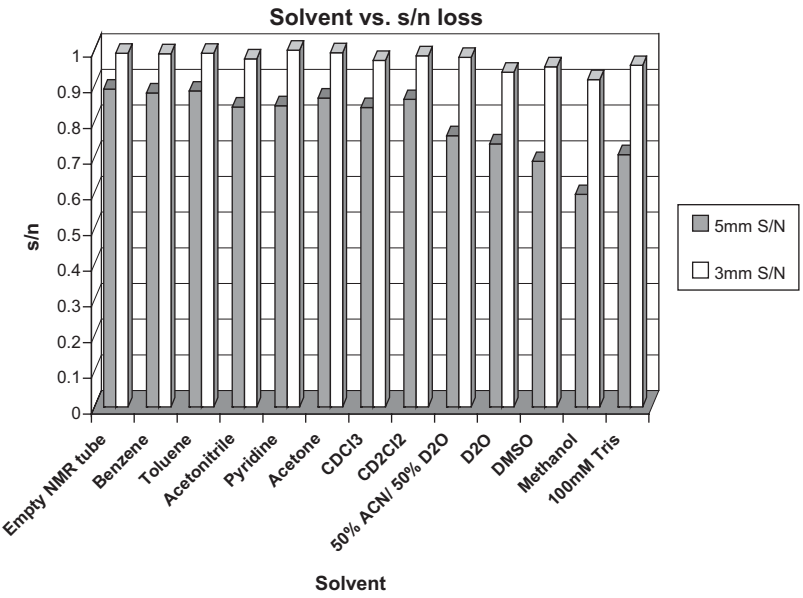

Fig. 14. Plot of solvent vs. s/n ratio losses in 3 and 5 mm NMR tubes in a cryogenic NMR probe. Better probe performance is obtained in all cases with a 3 mm tube rather than a 5 mm tube, even for polar protic solvents such as methanol and 100 mM Tris buffer. (Data generously provided by D. Avizonas and T. de Swiet, Varian NMR Instruments, Palo Alto, CA. Reproduced with permission.)

20 μg of retrorsine (**3**) dissolved in 150 μL of d_4-methanol. The spectra shown in Fig. 15 were each acquired in 15 h with identical parameters and processing. The data acquired in the 5 mm 500 MHz gradient-inverse triple resonance cryoprobe are shown in panel A, and compare favorably in terms of responses observed with data acquired using a 700 μg sample of **3** that were shown in Fig. 2. Using the same sample, panel B shows 15 h HMBC data that were acquired using a 3 mm gradient inverse triple resonance 500 MHz NMR probe. Only the most intense responses are observed. Acquiring a usable HMBC spectrum on a sample of this size with conventional 3 mm NMR probe technology would normally require at least a weekend data accumulation in the experience of this author.

Another area of investigation that is being substantially accelerated by the increasing access to cryogenic NMR probe capabilities is long-range ^{1}H–^{15}N heteronuclear shift correlation at natural abundance. In a 1999 study, Köck *et al.*[49] estimated that in computer-assisted structure elucidation (CASE), the number of structures generated by structure elucidation programs can be reduced by a factor of 100 through the availability of long-range ^{1}H–^{15}N correlation data. In a 2001 study, Crouch and co-workers[50] compared the results obtained using a 2 mg sample of the oxazolidinone antibiotic eperezolid (**8**) in d_3-acetonitrile in a sealed 3 mm NMR tube using 500 MHz conventional 3 and 5 mm cryogenic gradient inverse triple resonance NMR probes to acquire 5–10 Hz optimized CIGAR-HMBC[51] spectra. The spectrum recorded in 4 h for the 2 mg sample of eperezolid (**8**) is shown in Fig. 16(a). All of the expected responses are observed in the spectrum and the s/n ratio on projection through the F_1 (^{15}N) frequency domain (Fig. 16(c)) was 49:1. In contrast, when the same data were acquired using a 5 mm cryogenic NMR probe, the spectrum shown in Fig. 16(b) was acquired in 26 m and gave an s/n ratio on projection through the F_1 frequency domain (Fig. 16(d)) of 101:1. Clearly there are very substantial timesavings available to investigators needing experimental access to long-range ^{1}H–^{15}N heteronuclear shift correlation data at natural abundance when they have access to cryogenic NMR probe capabilities. Other very low-sensitivity 2D-NMR experiments facilitated by cryogenic NMR probe capabilities include experiments such as gHSQC-TOCSY experiments, which have only one-half to one-fourth the sensitivity of HMBC experiments to mention only one. Examples of some of these applications are presented in Section 6.5.

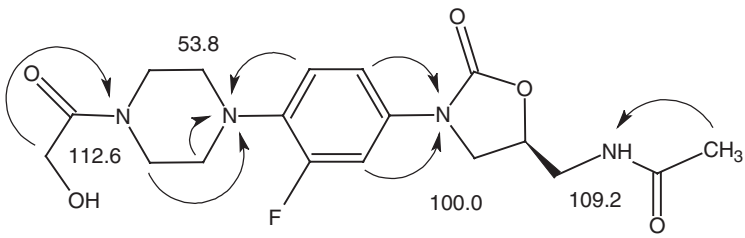

8

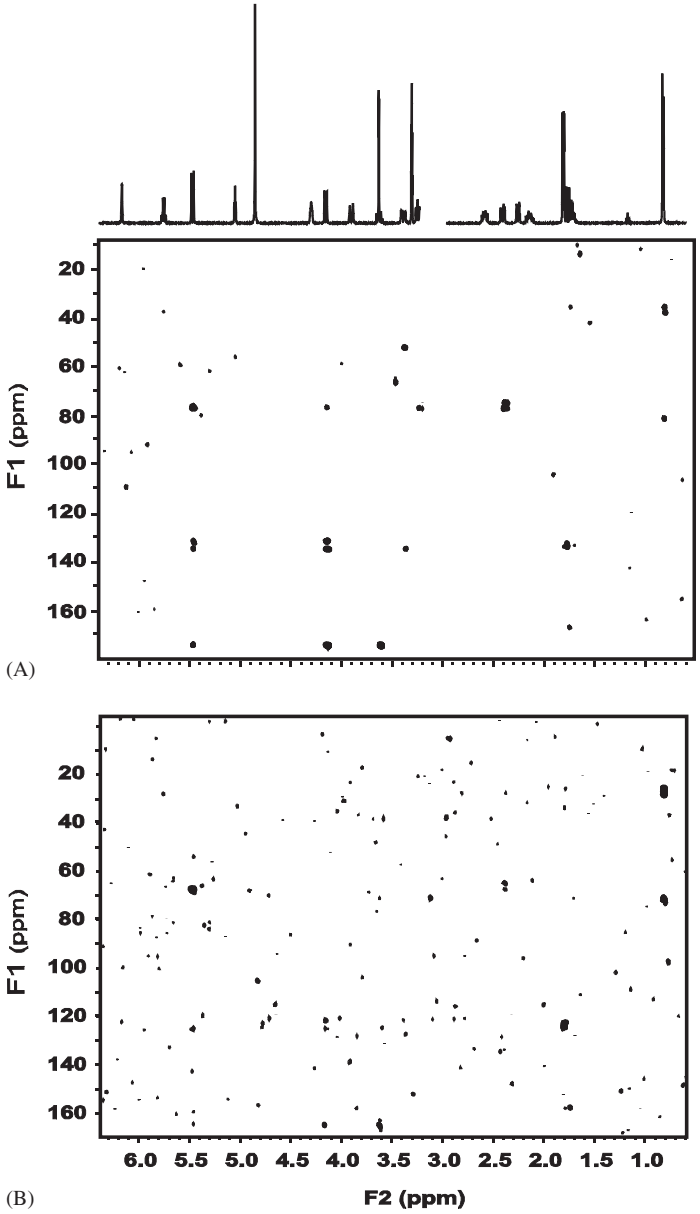

Fig. 15. Comparison of HMBC spectra for a 20 μg sample of retrorsine (**3**) dissolved in 150 μL d_4-methanol in a sealed 3 mm NMR tube. The data shown in both panels are 8 Hz optimized non-gHMBC spectra. The spectrum shown in Panel A was acquired in 15 h using a 5 mm 500 MHz cryogenic gradient inverse triple resonance. Almost all of the expected resonances are observed when these data are compared to those for a 700 μg sample of **3** shown in Fig. 2. In contrast, the spectrum shown in Panel B, which was acquired with identical conditions using a 3 mm gradient inverse triple resonance probe, shows the most prominent responses in the spectrum and only a relatively small number of the other responses expected. For a sample of this size to yield a useful HMBC spectrum, it would be necessary to acquire data for a weekend when using a conventional 3 mm NMR gradient inverse-detection NMR probe.

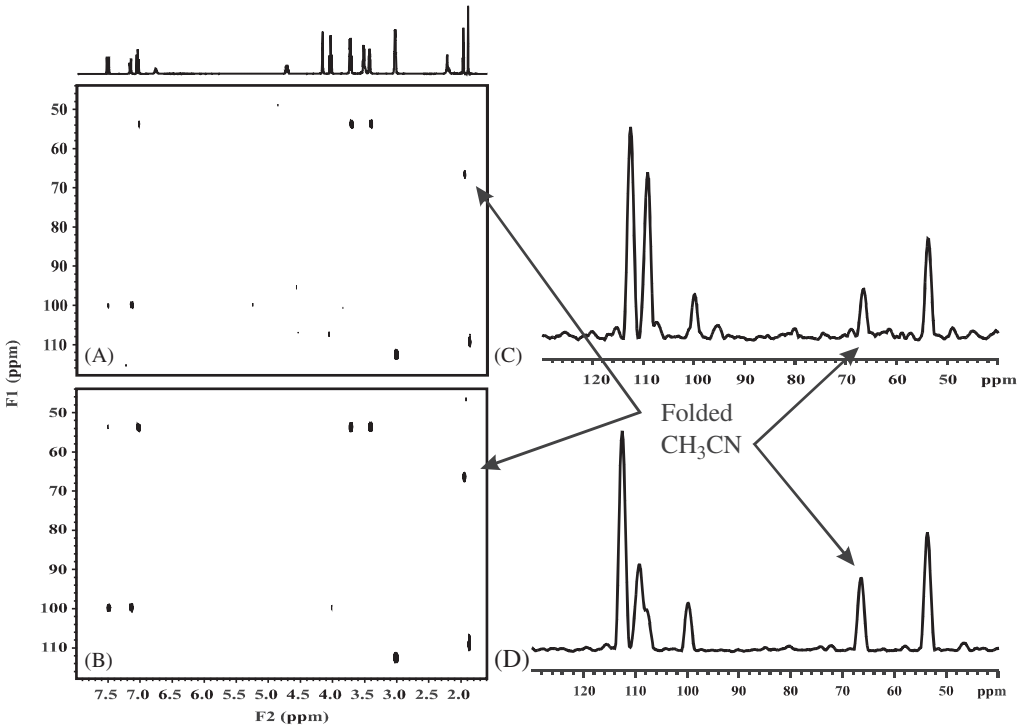

Fig. 16. Long-range ^{1}H–^{15}N gradient 5–10 Hz optimized CIGAR-HMBC spectra of the oxazolidinone antibiotic eperezolid (**8**). Panel A shows the results obtained with a sealed 3 mm tube containing 2 mg of the antibiotic in d_3-acetonitrile with data acquired in 4 h using a 500 MHz Nalorac 3 mm gradient inverse triple resonance NMR probe. All of the expected responses are observed and the spectrum gave an s/n ratio on projection through the F_1 frequency domain of 49:1. The projection is shown in Panel C. The signal from the deuteroacetonitrile was outside of the F_1 window set to accommodate the resonances from the eperezolid (**8**) and was allowed to fold. For comparison, Panel B shows the results obtained with the same sealed sample using a 500 MHz gradient inverse triple resonance Varian Cold-probe^{TM}. The experiment optimization and processing were identical to that used for the data shown in Panel A except that the cryogenic NMR probe data were acquired in only 26 m and gave an s/n ratio on projection through the F_1 frequency domain of 101:1. The projection of the cryogenic NMR probe data is shown in Panel D.

6. APPLICATIONS OF SMALL-VOLUME HIGH-SENSITIVITY AND CRYOGENIC NMR PROBES

It has now been 12 years since the first reported applications of 3 mm micro-NMR probes. As with any technological advance that enjoys widespread acceptance and implementation, referencing the specific use of this technology in early reports is common becoming less frequent with time. This tendency on the part of the research community makes it very difficult to exhaustively literature search for reports using a given technology unless there is a very specific name or acronym involved with the technology that continues to be used thereby facilitating full text searches of the literature. Such is the situation with 3 mm micro-NMR probes – there is no trademarked name or acronym associated with this technology and the use of 3 mm NMR probes is now very widespread. As such, any comprehensive survey of applications of 3 mm NMR probes is virtually impossible. The 1.7 mm SMIDG NMR probes and 1 mm CapNMR probes are more recent additions to the probe compliment of NMR research instruments and thus reports using these technologies are more readily literature searched, as are applications of Nanoprobes™, μCoil probes, and cryogenic NMR probes. For this reason, it is best to state overtly that the survey of applications that follows should not be considered to be exhaustive or comprehensive. Rather, the intent is to provide the reader with a chronological sampling of some of the reports to be found in the literature. There are doubtless many other excellent applications for some of the small-volume high-sensitivity probe formats that have not been cited.

The broad field of small-sample NMR has been the subject of a number of reviews during the past 5 years. In what is probably the earliest review of the field, Sweedler and colleagues surveyed high-resolution NMR measurements with sample volumes in the range of 1–10 nL.[52] Keifer has reviewed applications of various small-volume high-sensitivity NMR probes useful in drug discovery.[53,54] More recently, Sweedler and colleagues reviewed ''microscale'' NMR applications of CE, capillary electrochromatography (CEC) and cITP coupled with μCoil NMR probe technology.[55] A review of applications of high-sensitivity small-volume NMR probes has appeared,[19] as has a more specialized review of applications of high-sensitivity small-volume NMR probes in the characterization of nano-mole quantities of venom toxins.[56] Most recently, Jayawickrama and Sweedler have reviewed hyphenated capillary separations with NMR spectroscopy.[57]

6.1. The 3 and 2.5 mm NMR probe applications

Work in the field of 3 mm micro-NMR began with the initial evaluations of this probe format from the author's laboratories in 1992.[6,7] As is evident from early papers published using 3 mm micro-NMR probe technology, the natural products chemistry community recognized and quickly began to exploit 3 mm probe technology, beginning first within the pharmaceutical industry and spreading to other

disciplines. The papers cited in this review of applications of 3 mm probe technology should by no means be considered exhaustive. As frequently happens, following the development of a new experimental method or technology, the use of that method or capability is reported by investigators. As that capability becomes more commonplace and slips into routine usage, the frequency with which the specific use of the method or technology in question is cited will decline, making exhaustive searches for applications of the method or technology in question progressively more difficult, if not impossible. Such is certainly the case with 3 mm NMR probe technology. These probes have become routinely utilized in laboratories throughout the world. The papers cited herein should not be considered as anything more than representative and by no means inclusive sample of some of the applications of the capabilities of 3 mm NMR probe-equipped spectrometers.

In 1993 shortly after 3 mm micro-probes became commercially available, an application of the use of 3 mm probe technology was reported by Hensens and co-workers at Merck.[58] The enediyne antibiotic neocarzinostatin (**9**) is activated for duplex DNA cleavage by >1000-fold by thiol reagents. Hensens and co-workers utilized both micro-inverse and micro-dual 3 mm NMR probes to characterize the structure and stereochemistry of the novel post-activated drug (**10**).

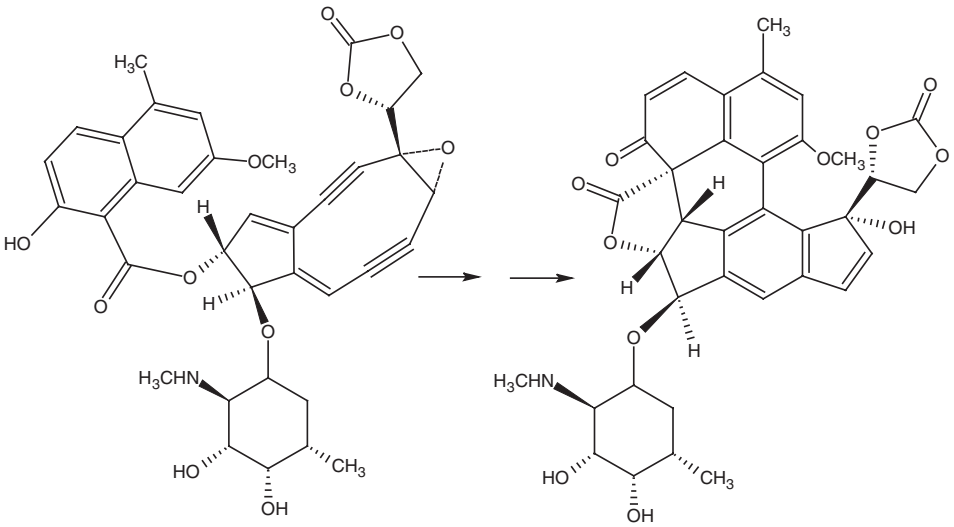

9 **10**

Several applications of 3 mm micro-NMR probe technology were reported in 1994. The first utilized both a 3 mm micro-inverse probe as well as a heteronuclear Nano-probe^{TM} to acquire the NMR data necessary for the characterization of a 30 µg (0.07 µmol) metabolite sample.[59] Following the acquisition of a ^{13}C reference spectrum using a heteronuclear Nano-probe^{TM} the 40 µL sample from the nano-cell was quantitatively transferred to a 3 mm NMR tube and diluted to a total sample

volume of 120 μL to allow the acquisition of a COSY and an HMQC spectrum using a 3 mm micro-inverse probe. Using these data together, it was possible to totally characterize the structure of the metabolite as **11**.

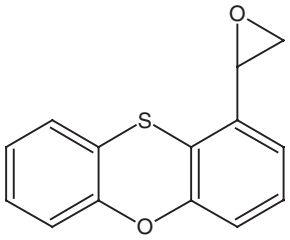

11

Schwartz and co-workers, also at Merck, reported the isolation and elucidation of the structure of pramanicin (**12**) and a related fatty acid that were discovered during a search for novel antifungal agents.[60] The authors reported using a 500 MHz 3 mm micro-inverse probe for the acquisition of the heteronuclear 2D-NMR data to characterize the molecule, including a ^{1}H–^{15}N HMQC spectrum.

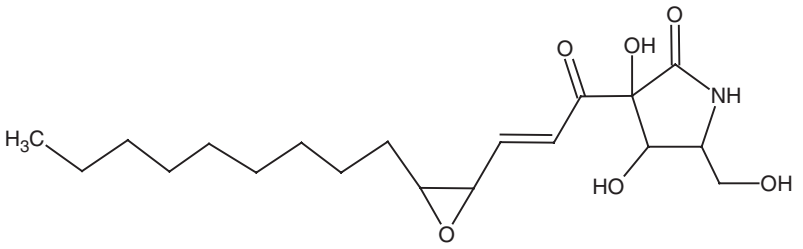

12

In 1995, the structure of fumonisin-B_1 (**6**) was also confirmed using a combination of the 3 mm micro-inverse-detection probe and the heteronuclear Nano-probe™ (see Section 3).[20] The elucidation of the structure of the complex indoloquinoline alkaloid cryptolepicarboline (**13**) was also reported in 1995.[61] Homonuclear and heteronuclear experiments were performed at 500 MHz using 3 mm micro-inverse-detection probes, employing a sample consisting of ~100 μg of the complex alkaloid. The sensitivity of the 3 mm micro-NMR probes allowed the acquisition of both HMQC and HMBC spectra, which were further supplemented by an IDR HMQC-TOCSY experiment. The latter experiment was particularly useful in sequencing the three-protonated four-spin aromatic systems contained in the structure. This study also compared ^{13}C-NMR data acquired using both a 3 mm micro-dual NMR probe and a heteronuclear Nano-probe™, which gave comparable results in this case.

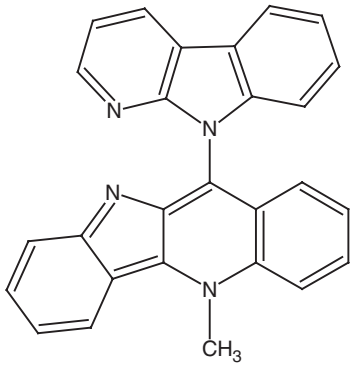

13

Later in 1995, the author and co-workers turned their attention to the proton and carbon NMR spectral assignment problems associated with polyether marine toxins. The assignment of the spectra of brevetoxin-3 (**14**) was used as a model compound[62] with the intent of applying the technology to the much more complicated structure of Caribbean ciguatoxin.[63] Using an 800 μg sample (0.95 μmol) it was possible to acquire a complete ensemble of 2D-NMR spectra, including an IDR HMQC-TOCSY spectrum that was pivotal, in conjunction with the HMBC data, in doing the total ^{1}H and ^{13}C spectral assignment. Applying what was learned from the assignment study of brevetoxin-3 (**14**) the acquisition of data for an ~0.1 μmol sample of Caribbean ciguatoxin was undertaken. To facilitate the acquisition of the data, the sample, dissolved in ~70 μL d_5-pyridine, was put in a 3 mm Shigemi cell (a cell with glass optimized for d_6-DMSO was used as cells optimized for pyridine are not available) for data acquisition. A complete set of HMQC correlations were recorded for the sample but only partial HMBC data could be recorded because of the miniscule size of the sample. Subsequent to the author's 3 mm micro-NMR study, Lewis *et al.*[64] using homonuclear 2D-NMR data recorded with a larger sample in conjunction with the previously reported heteronuclear data[63] were able to assemble the complete structure of Caribbean ciguatoxin-1 (**15**).

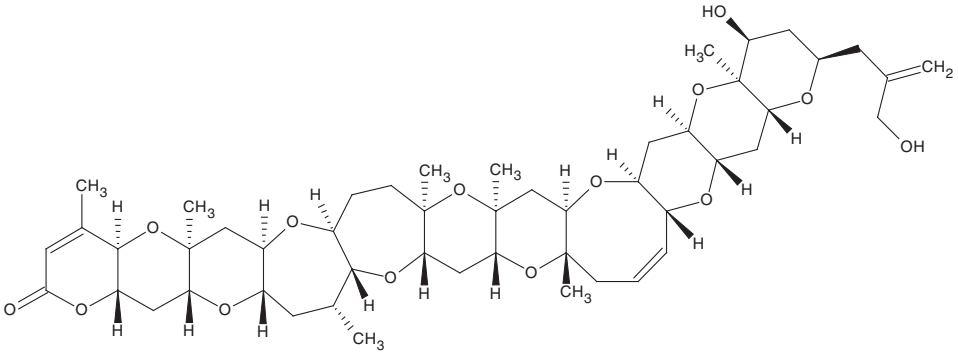

14

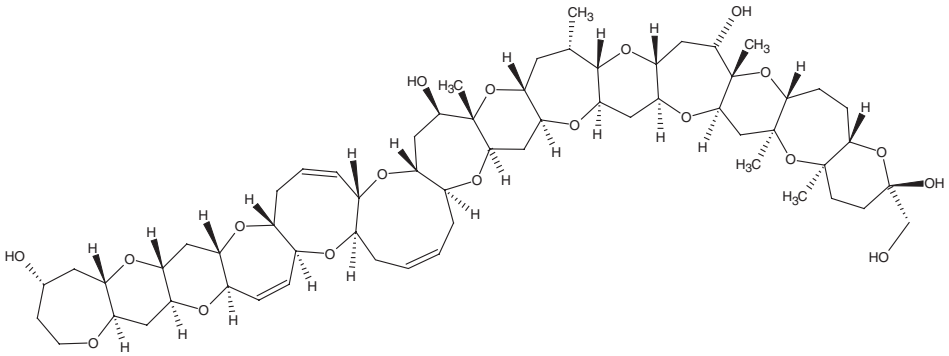

15

There were a several additional studies of members of the indoloquinoline family of alkaloids isolated from *Cryptolepis sanguinolenta* reported that utilized 3 mm micro-NMR probe capabilities reported in 1995. The elucidation of the structure of quindolinone (**16**) was reported next and also utilized 3 mm micro-probe technology for the acquisition of a $^{1}H–^{15}N$ HMQC spectrum on an 800 μg sample of the alkaloid dissolved in 140 μL of solvent in addition to the more commonly acquired $^{1}H–^{13}C$ heteronuclear shift correlation spectra.[65]

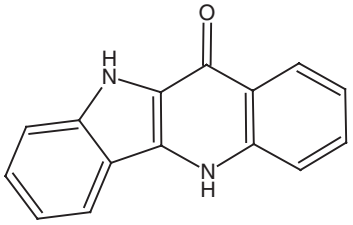

16

Later in 1995, 3 mm probe technology was again utilized in the characterization of an indolobenzazepine, homocryptolepinone (**17**),[66] which may be a biosynthetic constituent of the spiro nonacyclic alkaloid cryptospirolepine (**18**) also produced by *C. sanguinolenta*.[67]

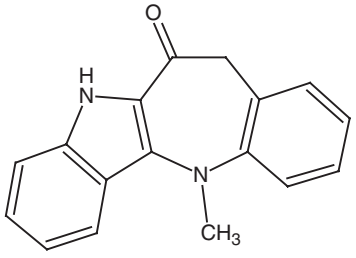

17

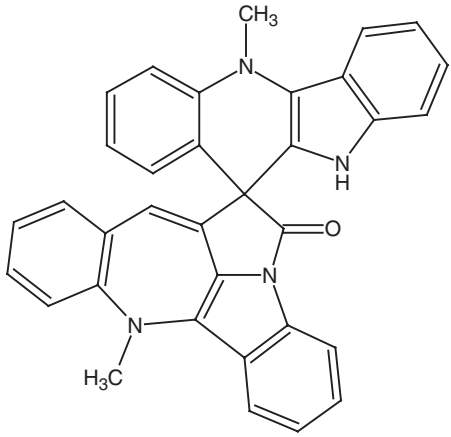

18

Another study reported in late 1995 by Scheuer and co-workers[68] detailed the elucidation of the structure of kauluamine, an unprecedented dimer of manzamine from an Indonesian marine sponge. The bulk of the structure elucidation effort utilized 5 mm probe technology, but the authors reported attempting, unsuccessfully, to acquire INADEQUATE[69,70] data for a 100 mg sample of the molecule using a 3 mm micro-dual probe. The lack of success of that experiment was attributed to ^{13}C linewidth, which were reported to be broad. Finally, Kohn and coworkers[71] reported the use of 3 mm micro-probe technology in their characterization of a 10-bromo-10-descarbonyloxy porfiromycin analog (**19**).

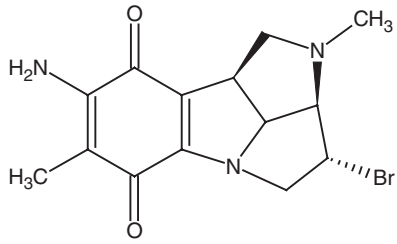

19

In early 1996, 3 mm micro-probe technology played a role in the elucidation of two additional members of the indoloquinoline family of alkaloids, in this case differing in terms of the ring fusion between the indole and quinoline portions of the molecule. Rather than the more common indolo[3,2-*b*]quinoline system, cryptosanguinolentine (**20**) was determined to have an indolo[4,3-*b*]quinoline ring juncture while cryptotackieine (**21**) had an indolo[2,3-*b*]quinoline ring fusion.[72] Long-range ^{1}H–^{13}C connectivity information from the HMBC spectrum, which was accessible through

the use of micro-probe technology, was pivotal in determining the ring fusion orientation of this pair of molecules. The confirmation of the indolo[2,3-*b*]quinoline ring fusion of cryptotackieine more recently has been important in the elucidation of the structure of quindolinocryptotackieine (see Section 6.5).

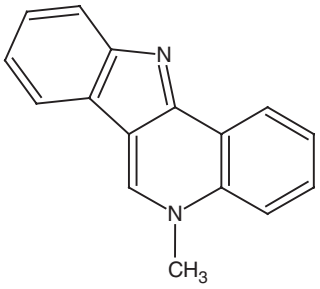

20

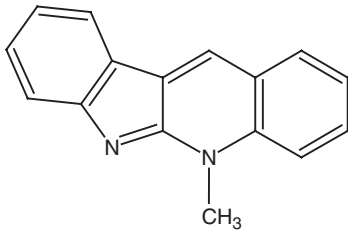

21

Later in 1996 the first example of a dimeric indoloquinoline alkaloid, cryptomisrine (**22**), was isolated and its structure elucidated.[73] Inverse-detected 2D-NMR spectra were recorded using a 3 mm micro-inverse probe; ^{13}C chemical shift data were recorded for the sample using a 3 mm micro-dual probe. In addition to the mass spectral data, a 0.9% nuclear overhauser effect (NOE) observed between the H1 and H9′ protons was used to confirm the structure.

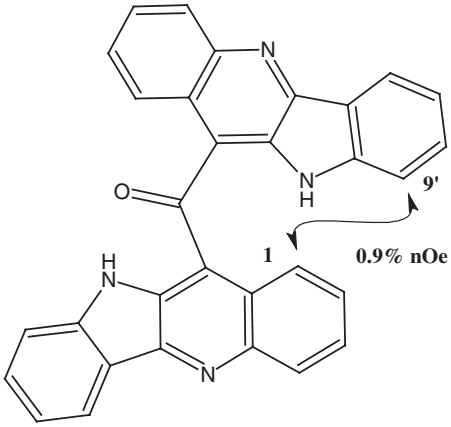

21

Drew and colleagues reported using 3 mm micro-probe capabilities in the characterization of labeled L-(1-^{13}C)- and L-(2-^{13}C)-ascorbic acid.[74] In a more

demanding study, Schneider and co-workers[75] first reported a study of the metabolism of 24-*epi*-castasterone (**22**) and 24-*epi*-brassinolide (**23**) in cell suspension cultures of *Ornithopus satifus*. The authors determined that a series of 20-keto-pregnanes were produced in the cell suspension cultures in multistep metabolic pathways. A subsequent study of **22** in cell suspension cultures of *Lycopersicon esculentum* led to epimerization, hydroxylation, and glucosidation, yielding several new brassinosteroids and brassinosteroid glucosides.[76]

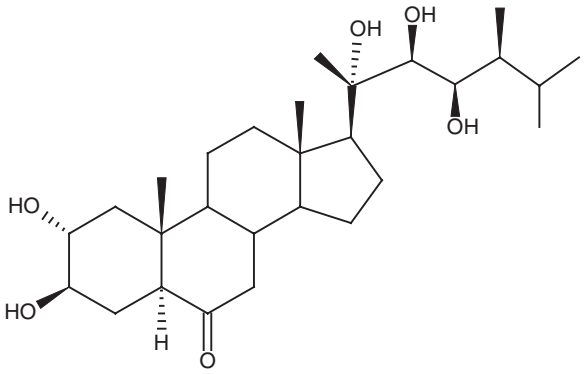

22

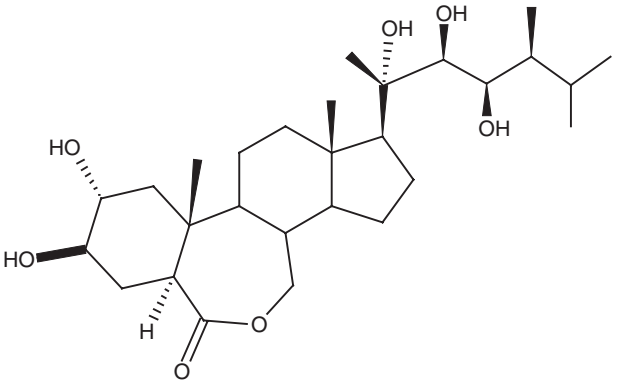

23

Musser and colleagues utilized 3 mm micro-probe technology in a study reporting the identification of a new series of fumonisins containing 3-hydroxypyridine moieties (**24A–C**).[77] A 400 MHz 3 mm micro-dual probe was used to both record ^{13}C spectra as well as for the acquisition of HMQC and HMBC data used in the characterization of these fungal secondary metabolites.

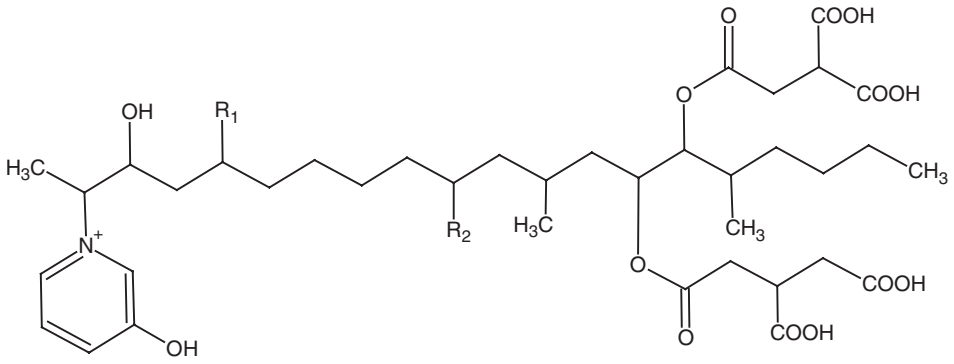

24A $R_1 = R_2 = -OH$

24B $R_1 = -OH$, $R_2 = -H$

24C $R_1 = -H$, $R_2 = -OH$

42

In a very interesting study of the regiospecificity of aminoglycoside phosphotransferases from enterococci and staphylococci, Wright and co-workers[78] examined the phosphorylation of a series of aminoglycoside antibiotics. Phosphorylation of antibiotics such as lividomycin A, neomycin B, butirosin A, and amikacin is an important mechanism for bacteria to overcome the toxicity of these molecules by eliminating the lethal affinity of the compounds for the target ribosome. The portion of this study involving butirosin diphosphate and neomycin monophosphate was conducted using a Bruker 2.5 mm micro-inverse-detection NMR probe.

Fu and Schmitz[80] reported the isolation and characterization of a new brominated diphenyl ether from an unidentified specie of *Dysidae* sponge collected at Satawan Atoll in Micronesia in 1996. In addition to four known brominated diphenyl analogs for which ^{13}C chemical shift data were reported, a new minor metabolite (**25**) was isolated and characterized using a 3 mm micro-dual NMR probe.

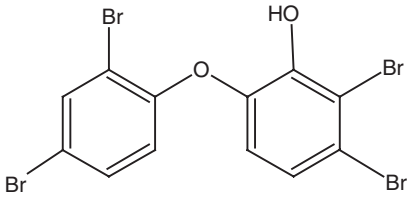

25

In 1997, Reynolds and Enriquez[81] reported a very interesting study that probed the sensitivity limits of ^{13}C-detected 2D-NMR methods using 3 mm microprobe capabilities. The authors pursued this line of investigation specifically for cases of molecules with severely congested ^{13}C spectra. When there are congested regions of the ^{13}C spectrum for a molecule being studied, it can be difficult to attain sufficient resolution in the F_1 frequency domain of ^{1}H-detected heteronuclear 2D-NMR experiments. Using a 500 MHz 3 mm ^{1}H–^{13}C dual NMR probe, the authors concluded that adequate s/n ratios can be achieved with a sample of ~3.5 μmol using a BIRD (Bilinear Rotational Decoupling)-decoupled heteronuclear shift correlation experiment in 4–5 h for molecules with anisochronous methylene groups contained in their structures. The authors used kauradienoic acid (**26**) as a model compound for their study. For ^{13}C-detected long-range connectivity information, the authors resorted to a FLOCK experiment.[82] Using a 3.5 μmol sample of **26** for a 16 h FLOCK experiment was reported to have given poor results. The authors suggested that a sample of this size could be successfully examined using the FLOCK sequence in a weekend long acquisition or that a sample in the range about 15 μmol would be required for an overnight experiment involving a molecule with complex anisochronous methylene proton resonances.

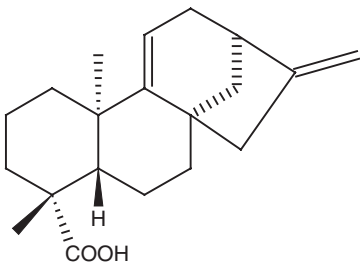

26

Later in 1997, Ondeyka *et al.*[83] reported the isolation and identification of the structure of nodulisporic acid (**27**) using micro-NMR probe technology. Nodulisporic acid is a novel insecticide from *Nodulisporium* sp. and was the first representative of a new class of indole terpenes to be identified. The authors used a combination of ^{1}H-detected homo- and heteronuclear 2D-NMR experiments to assemble the structure in conjunction with a series of three INADEQUATE, each 5 days long, optimized from 40 to 60 Hz that employed a 26 mg sample of **27**. The INADEQUATE data were subjected to computer analysis,[84–86] which identified 32 of 47 possible ^{13}C–^{13}C connectivities.

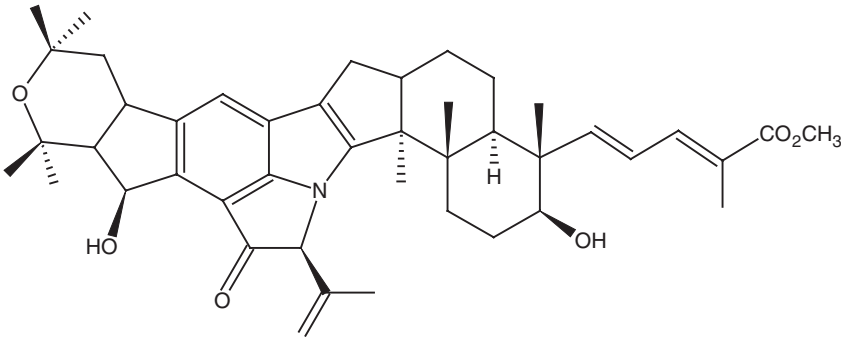

27

Interestingly, the authors also used micro-NMR capabilities to elucidate the structures of two degradation products of nodulisporic acid (**28**).

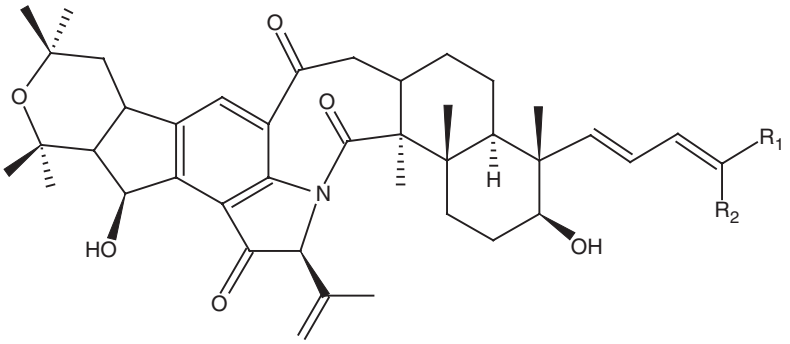

28A $R_1 = -CO_2H$, $R_2 = -CH_3$

28B $R_1 = -CH_3$, $R_2 = -CO_2H$

In a much simpler application of 3 mm micro-probe capability, the structure of granulosin (**29**), a new chromone from *Galipea granulose* was identified using homo- and heteronuclear 2D methods.[87]

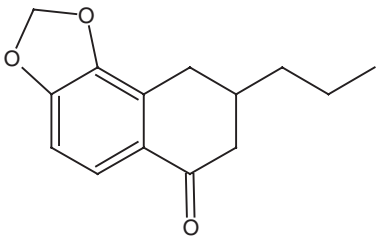

29

In 1998, Serianni and co-workers[88] again resorted to 3 mm micro-NMR probe technology in a report dealing with the detection and quantitation of the cyclic and acyclic forms of ^{13}C-labeled aldopentoses. In a very interesting biosynthetic application, Rowe and co-workers[89] investigated the conversion of δ-(L-amino-adipoyl)-L-cysteinyl-D-valine (**30**) to isopenicillin-*N* (**31**), an important step in the biosynthesis of penicillins and cephalosporins. The authors utilized 3 mm micro-NMR probe capabilities in their work in the analysis of the biosynthetic products of mutants of the enzyme isopenicillin-*N* synthase, the enzyme normally responsible for the conversion of **30** to **31**.

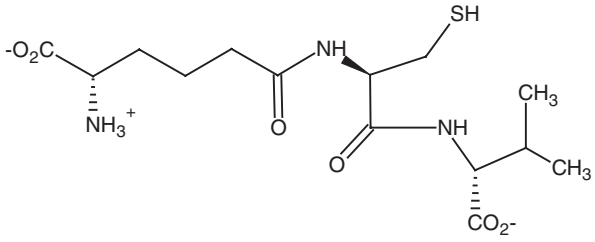

30

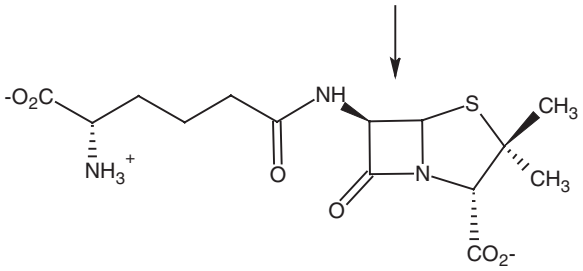

31

The increased sensitivity for dealing with extremely small samples afforded by 3 mm NMR probes was crucial to the success of a comparative biosynthesis study by Spenser and colleagues.[90] The authors compared the biosynthesis of thiamin (vitamin B_1, **32**) in *Esherichia coli* and *Saccharomyces cerevisiae*. In part, a full understanding of the biosynthesis of thiamin has been hampered by the rather dogmatic perception that different microorganisms should have the same biosynthetic pathway. Fortunately, that thinking has since been refuted. The other problem is that thiamin is produced in minute amounts of only from 5 to 27 μg/g of dry weight of the organism, which imposes a severe sensitivity challenge for investigators of these biosynthetic pathways, which the authors circumvented by the use of 3 mm micro-NMR probes.

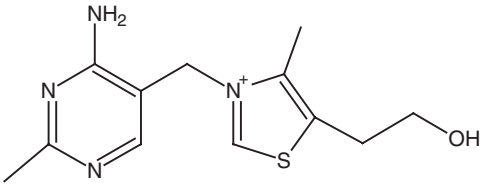

32

Another member indolo[3,2-*b*]quinoline alkaloid, cryptolepinone (**33**) was first isolated in 1993[91], and subsequently isolated and described by two other groups, one of which also described the molecule as the 11-one,[92] while yet another group described the molecule as the 11-ol (**34**).[93] To resolve this structural ambiguity, a sample of the alkaloid was examined by multinuclear 2D-NMR methods (^{1}H, ^{13}C, and ^{15}N using a 3 mm micro-inverse-detection NMR probe.[94] The proton resonance assigned variously as the NH or OH resonance, showed correlations to all four of the quaternary pyrrole carbons in the structure. While the 10-NH resonance can readily show these long-range correlations, it is unlikely that the 11-OH resonance could do so. Further support for the 11-one form of the molecule in d_6-DMSO solution was provided by direct and long-range ^{1}H–^{15}N heteronuclear shift correlation spectra. The quinoline 5-*N*-methyl ^{15}N resonance was observed at 103.4 ppm and, as expected, showed long-range correlations to the H4 and *N*-methyl protons. The other ^{15}N resonance was assigned as the 10-NH on the basis of a direct correlation in a ^{1}H–^{15}N HSQC experiment at 113.1 ppm. Had the molecule been in the 11-ol form, N10 would be expected to resonate in the range of 200–220 ppm similar to cryptolepine.[95]

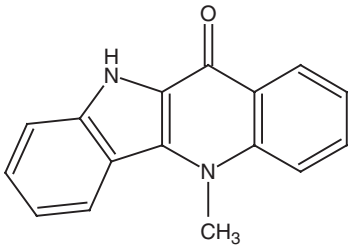

33

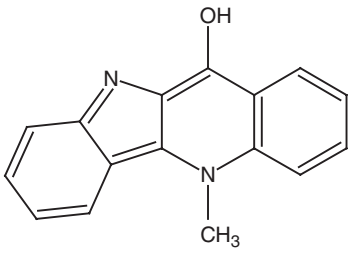

34

In a series of three papers published in 1998, Schmitz and co-workers explored the chemical constituents of Micronesian marine sponges using 3 mm NMR probe technology. In the first of these papers, several imidazole alkaloids and their Zn^{+2} complexes were isolated and characterized from the sponge *Leucetta cf. chagosensis*.[96]

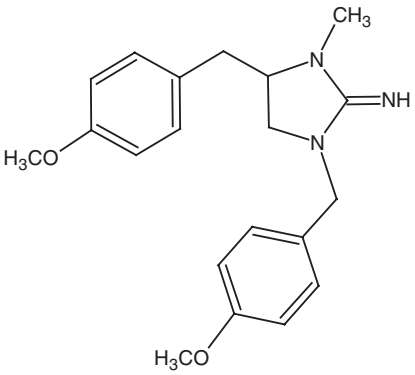

35

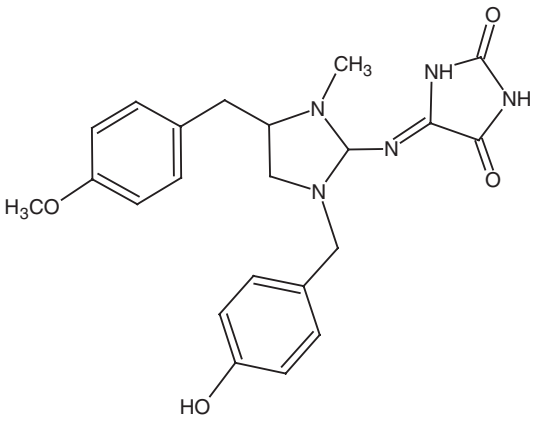

36

In their second 1998 report, Schmitz and co-workers[97] reported the isolation and characterization of a series of 12 new polychlorinated diketopiperazines from the sponge *Dysidae chlorea*. The structure of one of these alkaloids, dysamide-I is shown (**37**).

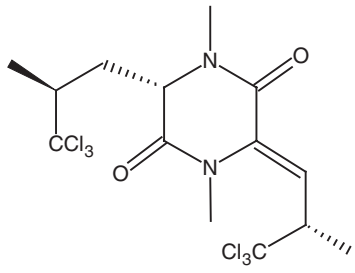

37

In the last of the reports published from this group in 1998, the chemical constituents of the sponge *Phahellia pulcherrima* were investigated, leading to the isolation and identification of seven new diterpene isonitriles and isothiocyanates.[98] The structures were *trans*-decalins with either a tetrahydropyranyl or tetrahydrofuranyl group or a *cis*-decalin with a tetrahydrofuranyl group. The structure of kalihinol-Y (**38**) from the former group is shown.

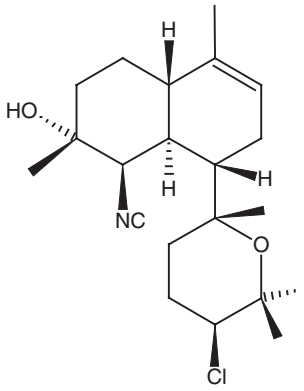

38

The author and colleagues employed 3 mm micro-inverse-detection NMR probe capabilities in an effort to assign the ^{15}N resonances of the cyclic thiopeptide antibiotic sulfomycin-I (**39**).[99] Acquiring the long-range ^{1}H–^{15}N HMBC data in a 3 mm rather than 5 mm probe was advantageous for a molecule such as **39** in that the shorter 90°^{15}N pulse lengths possible with a 3 mm micro-probe gave a broader and

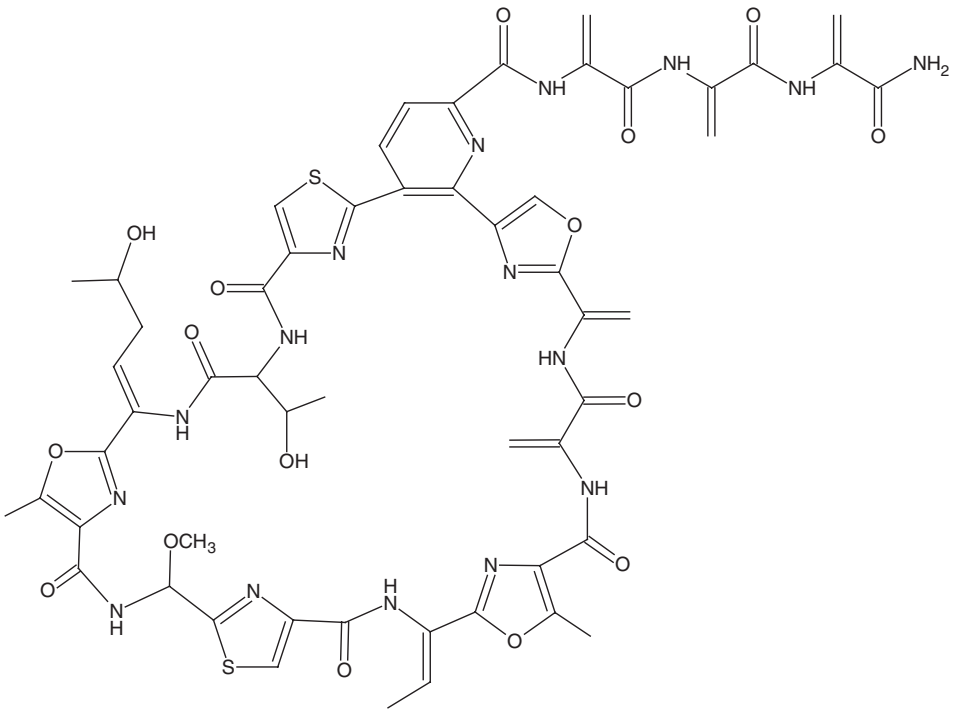

39

more uniform excitation window, which is important in a molecule with a broad diversity of types of nitrogens in its structure. Assigned ^{15}N shifts ranged from ~100 ppm for the terminal D-Ala NH_2 of the side chain to ~315 ppm for one of the thiazole ^{15}N resonances in the structure.

Finally, López and co-workers[100] utilized 3 mm micro-NMR in the course of elucidating the structure of a novel β-hydroxychalcone isolated from the Costa Rican plant *Galipea granulosa*.

Moving into 1999, another report from a group at Oxford focused on the biochemistry of the β-lactam antibiotic family, specifically the inhibition of series proteases by monocyclic β-lactams. Once again this study exploited the sensitivity of 3 mm micro-probe technology.[101]

A number of reports of the characterization of the structure of impurities contained in pharmaceutical preparations also appeared in 1999 beginning with the isolation and characterization of two biologically active isomers of the cardiac glycoside dihydroouabain isolated from a commercial preparation.[102]

An interesting structural challenge was also reported in 1999 by Reynolds and co-workers[103] in dealing with the specific problem of assigning the proton and carbon NMR spectra of a molecule with severe spectral crowding in both the ^1H and ^{13}C spectral domains. The authors, in assigning the spectra of polyprenol-12 (**40**), resorted to the acquisition of ^{13}C-detected heteronuclear shift correlation experiments to obtain sufficient digital resolution in the ^{13}C frequency domain (F_2 in this case, which is directly detected) to derive meaningful assignments from their spectra. The authors also present an interesting discussion of the comparative considerations of using FLOCK[82] vs. correlation through long-range coupling (COLOC)[104] experiments to obtain the requisite long-range shift correlation data.

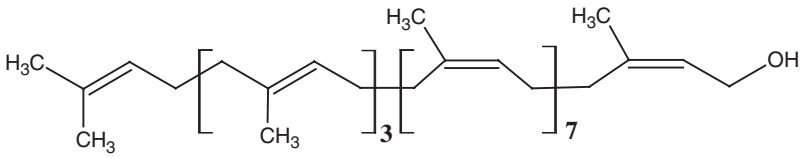

40

Logusch and co-workers[105] further explored the capabilities of 3 mm NMR probe technology in a study of the enzymatic synthesis of a rodent metabolite the pre-emergence herbicide alachlor. Lipopolysaccharides from *Chlamydia trachomatis* serotype L2 were the subject of a study using a 2.5 mm Bruker micro-NMR probe reported by Rundt *et al.*[106] This work represents the first complete structural characterization of a lipopolysaccharide from a *Chlamydial* sp.

Further work in the area of the structural characterization of impurities and degradants of pharmaceuticals was also reported from the author's laboratories in 1999.[107] First, the susceptibility of the morpholine substituent in the oxazolidinone antibiotic linezolid (**41**) was characterized using micro-NMR probe capabilities. Beginning from linezolid (**41**) photo-oxidation produced a transient pink color in

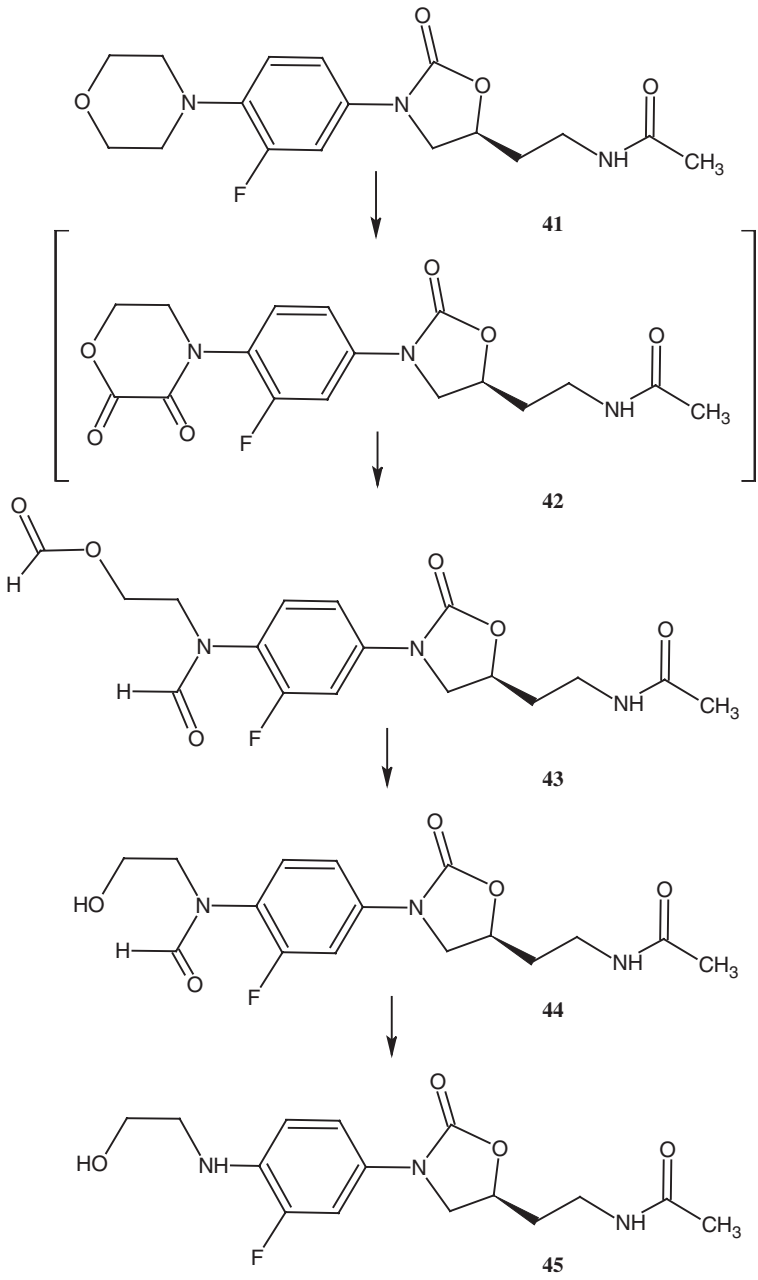

Scheme 1.

solution, presumably due to the morpholine-2,3-dione moiety of **42**, which then underwent oxidative ring cleavage to yield the formate ester degradation product (**43**) which was fully characterized, in part through the observation of the characteristic 223 Hz one-bond coupling of the formyl carbon. In subsequent steps, the formate ester was cleaved to afford the *N*-formyl analog (**44**), which underwent one further degradation step to the secondary amine (**45**) completing the degradation cascade shown in Scheme 1.

In an unrelated study, the structural characterization of the antibiotic novobiocin (**46**) and the related congeners isonovobiocin, decarbamylnovobiocin, and 2″(*O*-carbamyl)novobiocin were reported, providing data from which the structure of novobiocin-2″,3″-carbonate (**47**) was characterized for the first time.[108]

The degradation of cryptolepinone (**33**) which is known to undergo facile air oxidation, was also studied through the use of 3 mm micro-probe capabilities in the author's laboratories.[109]

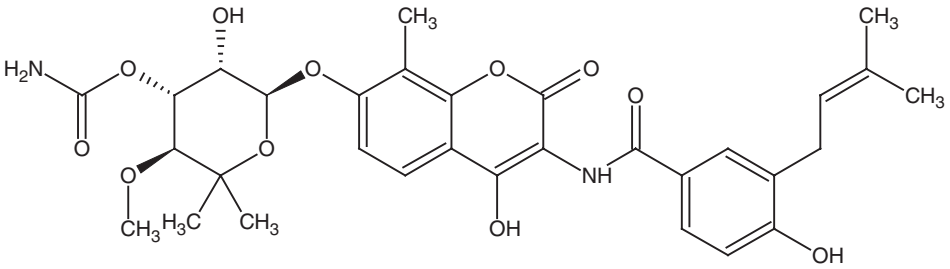

46

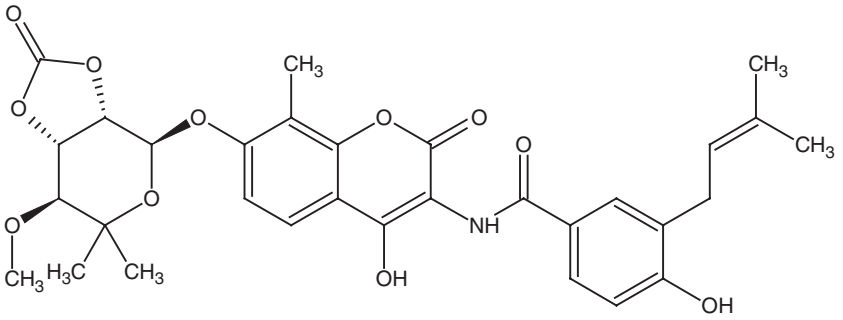

47

In this case, however, the degradants were characterized as a mixture of cryptolepinone (**33**) and cryptolepinone-5-oxide (**48**). To disentangle the collection of correlation responses for this nearly equimolar mixture of aromatic, indoloquinoline alkaloids, the sensitivity of a 3 mm inverse-detection probe was used to advantage to acquire an IDR gHSQC-TOCSY[110,111] spectrum to supplement the more customary assortment of homo- and heteronuclear 2D-NMR shift correlation experiments. The power of this assignment strategy is evidenced by the unequivocal

assignment of the H6–H9 four-spin system of the *N*-oxide (**48**) in which H6 through H9 resonate at 6.97, 6.98, 7.32, and 6.97 ppm, respectively.

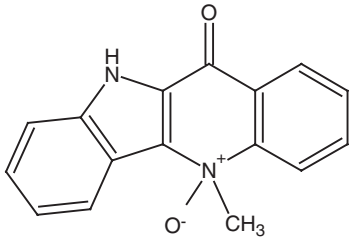

48

Applications of 3 mm probe technology in the characterization of natural product structures continued unabated in 1999, with a number of papers appearing in the *Journal of Natural Products* that employed this technology. The first of these reports also came from the author's laboratory and described the characterization of a new oxobenzylisoquinoline alkaloid, thalprezwalskiinone (**49**) from *Thalictrum prezwalskii*.[112]

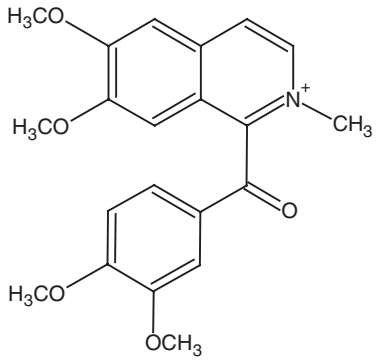

49

Next, Schmitz and co-workers[113] published the first report in an extensive 1999 series of papers focused on marine natural products; their initial study characterized a pair of dibenzo-*p*-dioxins, aplidioxin-A (**50**) and the positionally related isomer, -B,

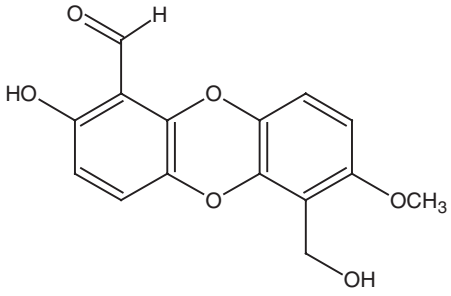

50

from the Ascidian *Aplidopsis ocellata*. Although Ascidians were a source for a wide variety of compounds including aromatic alkaloids, depsipeptides and novel quinones, the isolation of the dibenzo-*p*-dioxins from natural sources is quite uncommon.

In a directly following paper, Schmitz and co-workers reported the isolation and characterization of aurantoside-C (**51**), a novel tetramic acid glycoside from the sponge *Homophymia conferta*.[114] Although the authors elucidated the structure using proton-detected HMQC and HMBC experiments, the nature of the structure of the molecule is such that it might have been advantageous to resort to ^{13}C-detected methods as did Reynolds and co-workers for polyprenol-12.[103]

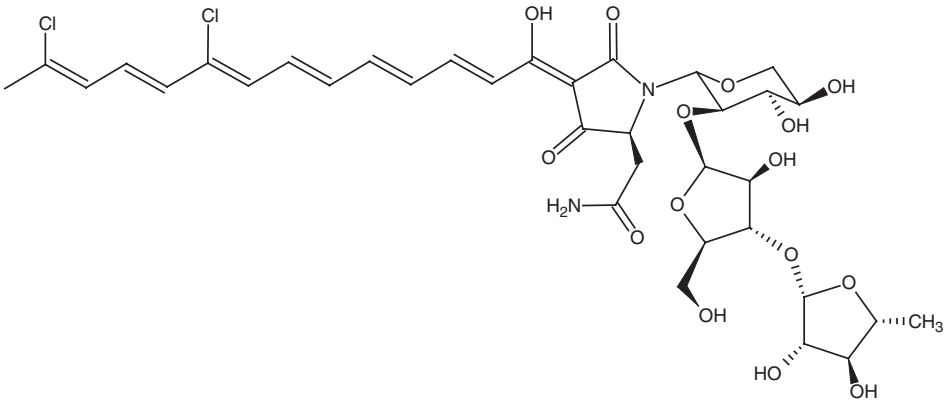

51

Vervoort *et al.*[115] next isolated and characterized a novel cyclized didemnimide alkaloid from the Caribbean Ascidian *Didemnum conchyliatum*. In prior work, the primary author and colleagues isolated and identified four novel alkaloids possessing unprecedented indole–maleimide–imidazole carbon frameworks, which ecological testing suggested served in a predator-deterrent role for the organism. Further fractionation led to a small quantity of a deep purple minor metabolite that required the use of micro-probe technology to facilitate its characterization. The molecule was shown to be related to the previously characterized molecules via cyclization to afford (**52**).

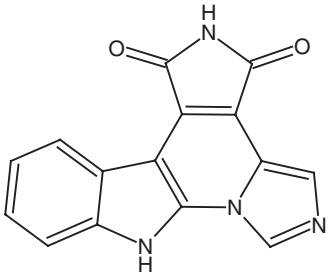

52

Next, Schmitz and colleagues[116] reported the isolation and characterization of malayenolides A–D, series of novel diterpenes from the Indonesian sea pen *Veretillum malayense*. The structures were elucidated using proton-detected 2D-NMR methods in conjunction with the use of 3 mm NMR probe technology. The structure of malayenolide-A (**53**) is shown.

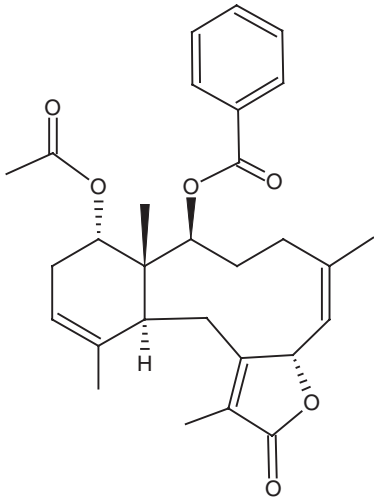

53

Schmitz and co-workers next published a pair of papers that dealt with the isolation and characterization of sesterterpenes from two different sponges. The first of these reports described the structural characterization of phyllofolactones C and D, minor homoscalarane sesterterpenes from the Chinese sponge *Phyllospongia foliascens*.[117] The structure of phyllofolactone-C (**54**) is shown. The second report detailed the characterization of halisulfate-7 (**55**), a sesterterpene sulfate from a sponge, *Coscinoderma* sp.[118]

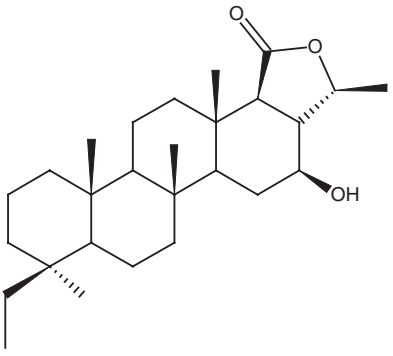

54

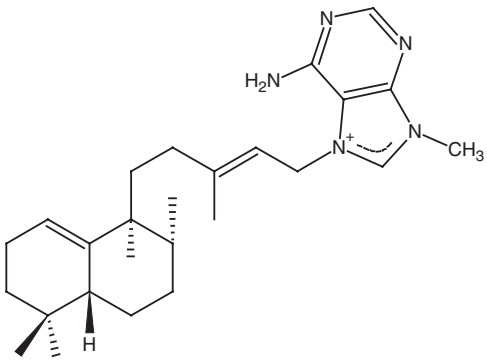

55

Next, Schmitz and co-workers[119] reported the characterization of a pair of novel prenylated paracyclophanes and metacyclophane-type hydroquinones from the tunicate *Aplidium longithorax*. Complete ^{1}H and ^{13}C resonance assignments were made for these complex natural products, again employing 3 mm micro-probe technology. The structure of longitorhol-A (**56**) is shown.

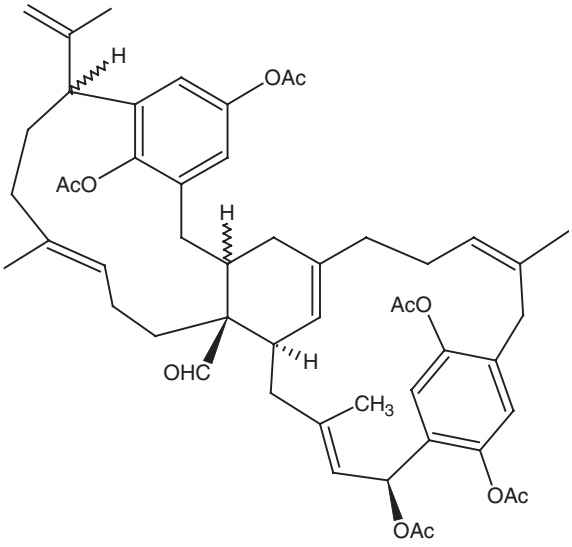

56

In the last of their reports on the characterization of marine natural products to appear in 1999, Fu *et al.*[120] reported the characterization of a series of acetylenic swinholides from a previously undescribed specie of *Theonella* sponge. The structure of one of the new compounds, pellynol E (**57**), is shown. In general, the analogs isolated and characterized differed in the central region of the long methylene chain of **57**.

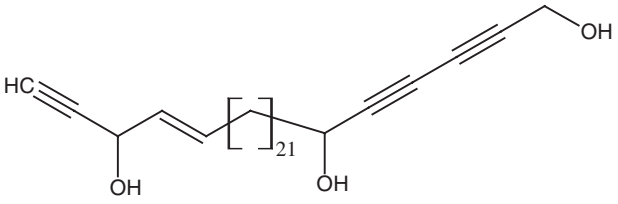

57

In a mechanistic chemistry study, Freeman and Pugh[121] employed the sensitivity advantage of a 3 mm micro-probe to acquire ^{13}C spectra of small, ^{13}C-labeled samples from a study of 4,4-diphenylchclohex-2,5-dienylidene involving rearrangement via an isobenzene pathway. In a paper actually published early in 1999, the

author and colleagues looked at the perturbation of ^{15}N shifts following 5-*N*-oxidation of cryptolepinone (**33**) to afford cryptolepinone 5-oxide (**48**).[122] Although previous work in molecules such as linezolid (**41**) has shown that there are perturbations of the ^{15}N shift of other nitrogen atoms in the molecule, these were not in a conjugated system. In the case of cryptolepine 5-oxide (**47**) 5-*N*-oxidation shifts the 10-NH nitrogen downfield by nearly 24 ppm, the large shift presumably due to the intervening π-bond. Finally, in an application of 3 mm micro-probe technology in the area of environmental chemistry, Kolehmainen and colleagues[123] studied a series of tricyclic polychlorinated C_{10} hydrocarbons and their oxy-derivatives by 2D-NMR methods.

In early 2000, Wilkinson *et al.*[124] reported an interesting study of novel octaketide macrolines related to 6-deoxyerythronolide B, and the evidence that these molecules provide for the iterative operation of erythromycin polyketide synthetase. Bergana and colleagues[125] in a very interesting study examined the range of decomposition products formed from *N*-acetyl-L-glutamine at low pH. The authors employed 3 mm probe technology using either standard 3 mm NMR tubes with sample volumes of 150 µL or Shigemi 3 mm tubes optimized for D_2O containing ~70 µL of solvent. The degradation pathway is shown in Scheme 2.

Work from the author's laboratory in 2000 first focused on the utilization HSQC-TOCSY data acquired using the sensitivity advantage of 3 mm probe technology as a facet of the assignment strategy for the severely congested spectra of polynuclear

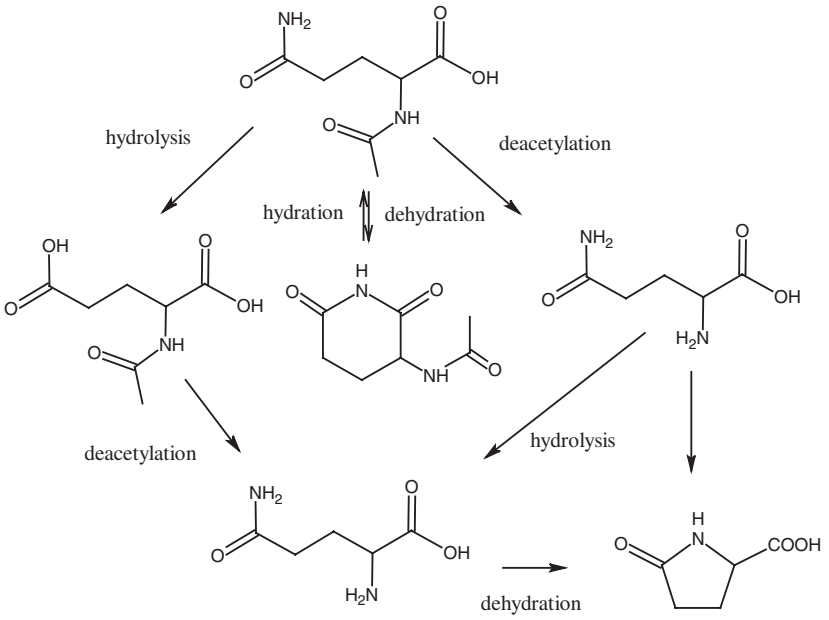

Scheme 2.

aromatics.[126] The total assignment of naphtha[2′,1′:5,6]naphtha[2′,1′:4,5]thieno[2,3-*c*]quinoline (**58**) was used as a model compound for the study.

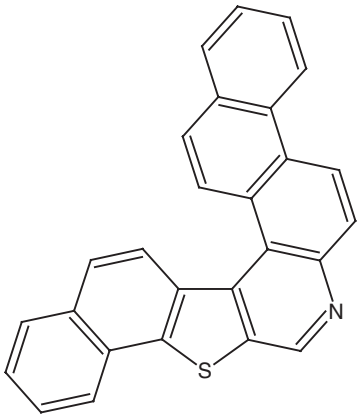

58

The author and a co-worker later exploited 3 mm NMR probe capabilities in a study of the thermal degradation products of the oxazolidinone antibiotic Zyvox® (linezolid, **41**) based on the use of ^{1}H–^{15}N heteronuclear shift correlation experiments.[127] In a study of the structure–function relationships of a new growth hormone-releasing peptide, ghrelin, Bednarek and co-workers[128] at Merck utilized micro-probe capabilities in the characterization of the structures of the minimum sequence of ghrelin necessary for activity. As a result of these efforts, a small spiroindan, MK-0677 (**59**) with oral bioavailability was found to be one of the most potent synthetic analogs with this activity.

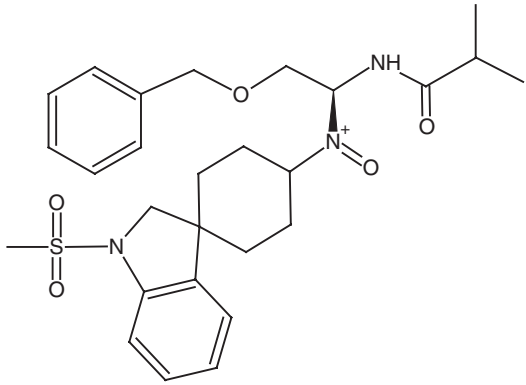

59

An interesting biochemical application of 3 mm probe technology was reported by Williams and Hall[129] in their studies of G[UUCG]C RNA tetraloops. Hölscher

and Schneider[130] reported using a Bruker 2.5 mm micro-probe in the isolation and structural characterization of four new phenalenone-type compounds. The increased sensitivity offered by micro-probe capabilities allowed the authors to do some chemical modification work in this series with subsequent characterization despite limited samples availability. The structure of one of the isolated phenalenones (**60**) is shown.

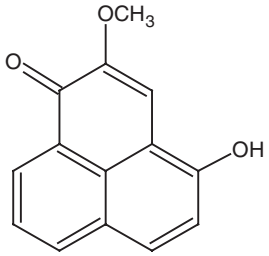

60

Hufford and co-workers[131] in a study of the metabolism of the antifungal copyrine alkaloid sampangine, used micro-probe technology for the characterization of the alkaloid's major metabolite, which was sampangine β-glucuronic acid (**61**).

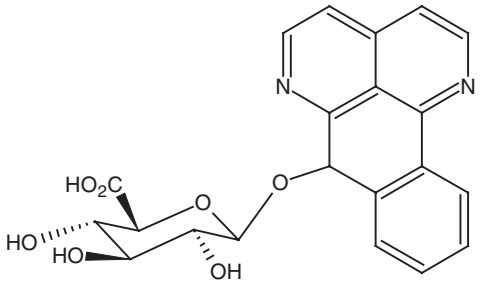

61

Using strychnine (**5**) as a model compound, a comparison study of the performance of conventional 3 mm NMR probes with a 3 mm open cycle cryogenic probe was reported from the author's laboratory in 2000.[132] A full treatment of the comparative performance of the two types of probe technology is presented in Section 6.5. Next, Kwak *et al.*[133] in their only marine natural product application of 2000 reported a study of the sesquiterpene quinols/quinones from the Micronesian sponge *Petrosaspongia metachromia*. The structures of two new sesquiterpenes, pelorol (**62**) and 5-*epi*-smenospongine (**63**), and seven known sesquiterpenes were identified using 3 mm probe technology.

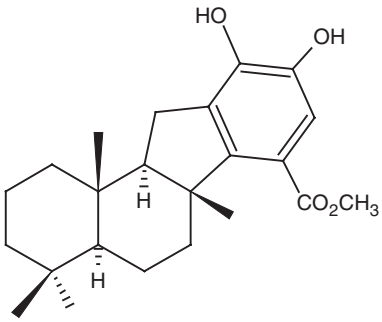

62

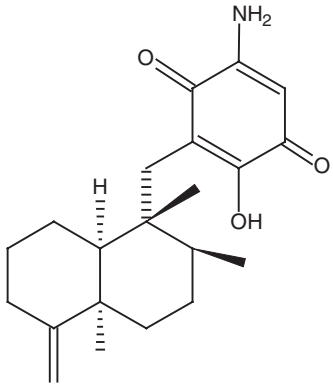

63

Junicke *et al.*[134] employed 3 mm probe capabilities in a study of the carbohydrate complexes of ^{13}C-labeled platinum(IV) through the use of ^{1}H–^{1}H, ^{1}H–^{13}C, and ^{13}C–^{13}C spin–spin coupling constants. The structure of the complex (**64**) is shown.

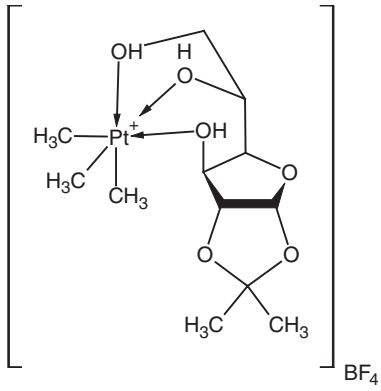

64

In another organometallic study, Satake[135] utilized 3 mm probe capabilities in the characterization of pi-allyl palladium complexes involving *bis*-nitrogen pyridnyl azole ligands as such as pyridinylpyrazoles, pyridinylimidazoles, and pyridinylpyrrole.

Using strychnine (**5**) as a model compound, Martin and Hadden[136] compared the accordion optimized ACCORD-HMBC and IMPEACH-MBC (Improved Performance Accordion Heteronuclear Multiple-Bond Correlation) experiments to gHMBC for the acquisition of long-range ^{1}H–^{15}N heteronuclear shift correlation data. Due to the variability in the size of two- and three-bond ^{1}H–^{15}N coupling constants, the authors reported that the IMPEACH-MBC experiment, optimized over a range of 3–8 Hz, gave the best results in terms of long-range correlation response intensity.

In 2001, Skibo *et al.*[137] reported using a 3 mm micro-dual NMR probe for the acquisition of ^{13}C spectra in a study of recognition and cleavage reactions in the major groove of DNA. Silverman and co-workers utilized 3 mm micro-probes for

both ^{13}C- and inverse-detected NMR experiments in a study that derived spectrometric evidence for the flavin (1-phenylcyclopropylamine inactivator adduct) with monoamine oxidase N.[138] In another biochemically oriented application of 3 mm probe capabilities, Spenser and co-workers reported the results of a study of the biosynthesis of vitamin B_6 in yeast in which the incorporation pattern of glucose was examined.[139]

Not surprisingly, a number of new applications of 3 mm NMR probe capabilities were reported in the area of natural product structure determination during 2001. The first of a number of 2001 papers published in the *Journal of Natural Products* reported the elucidation of the structure of circumdatin G (**65**), a new alkaloid from the fungus *Aspergillus ochraceus*.[140]

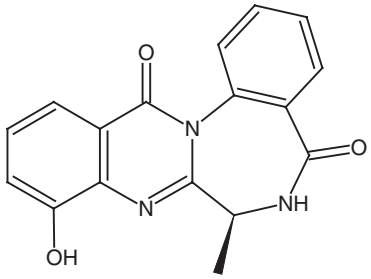

65

In a long-standing collaboration, Blunt and Munro utilized 3 mm probe capabilities in characterizing the structure of a novel, unsymmetrical disulfide metabolite, cortamidine oxide (**66**) from the New Zealand bascidiomycete (mushroom) *Cortinarius* sp.[141] Two other symmetrical dimeric disulfides, **67** and **68**, isolated and characterized by the authors in the same study were suspected to be oxidative degradants of **66**.

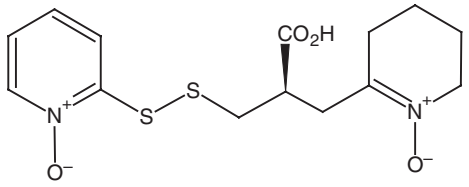

66

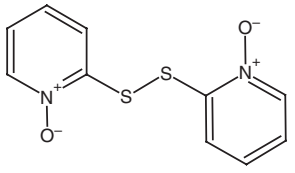

67

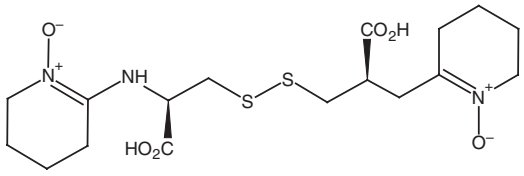

68

Next, the isolation and characterization of a series of briarane diterpenoids was reported from the Western Pacific octocoral *Briareum stechi* by Kwak *et al.*[142] The general structural skeleton shared by a number of the 11 members of the series characterized by the authors is shown by **69**.

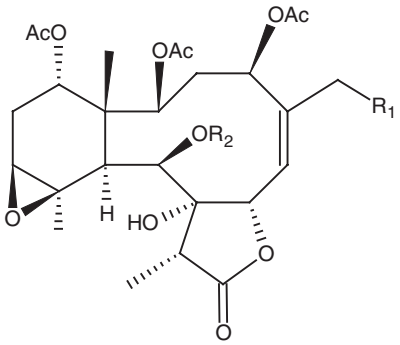

69

In a pair of back-to-back papers, the author and co-workers first reported the isolation and characterization of thalibealine (**70**), a novel tetrahydroprotoberberine–aporphine dimeric alkaloid from *Thalictrum wangii*.[143] That report was followed by a paper reporting the synthesis of thalprezwalskinone (**71**) and a revision of the structure of that alkaloid.[144]

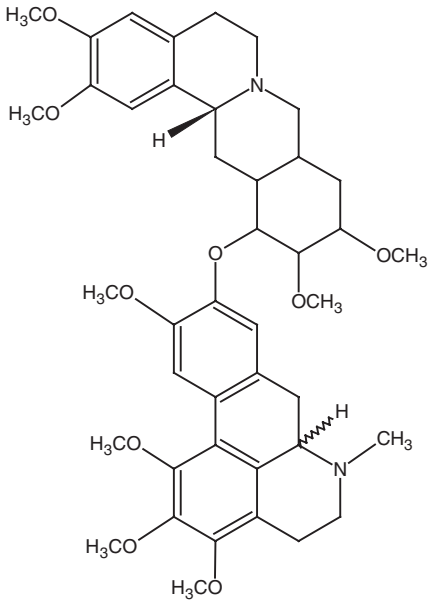

70

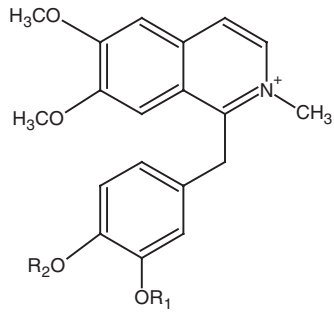

71

Finally, Sidebottom and colleagues at Glaxo Smith Kline and Imperial College reported a method for dereplicating purified natural product structures that utilized 3 mm NMR probe capabilities to minimize sample requirements.[145]

In a review that dealt with the subject of choosing pulse sequences, acquisition parameters and post-acquisition processing considerations, Reynolds and Enriquez[146] also discussed probe considerations for small-size samples. In this role, 3 mm micro-NMR probe technology figured prominently. In a study of the structure, biosynthetic origins, and engineered biosynthesis of calcium-dependent antibiotics from *Streptomyces coelicolor* Micklefield and colleagues[147] made use of the sensitivity of 3 mm micro-NMR probe technology for small-sample data acquisition. In another biochemically oriented study, Duman and Serianni[148] examined the role of endogenous antifreeze protein enhancers in the hemolymph thermal hysteresis activity of the beetle *Dendroides Canadensis*, again taking advantage of 3 mm NMR probe sensitivity and reduced sample requirements.

In the area of natural product characterization, Wall and colleagues utilized 3 mm NMR probe capabilities in the characterization of novel bioactive clerodane diterpenoids from the leaves and twigs of *Casearia sylvestris*.[149] The general structure of the three new clerodanes is shown by **72**, the molecules differing in the length and branching of the alkyl side-chain substituent.

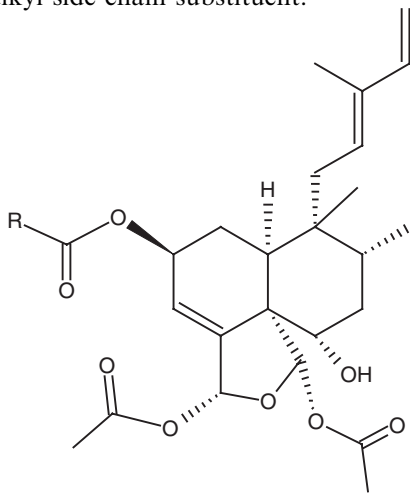

72

In an extension of their 2001 work on the miloides briarane diterpenoids from the Western Pacific octocoral *Brareum stechi*, Kwak *et al.* isolated and characterized the structures of eight additional members of the series related to **69**, making extensive use of the 3 mm NMR probe capabilities.[150] Schneider and colleagues,[151] working with the neotropical plant *Xiphidium caeruleum*, reported the isolation and structural characterization of four new phenylbenzoisochromenones, a new phenylbenzoisoquinolinone, and two new oxabenzocrysenones. The general structures of the phenylphenalenone and oxabenzocrysenone families are shown by **73** and **74**, respectively.

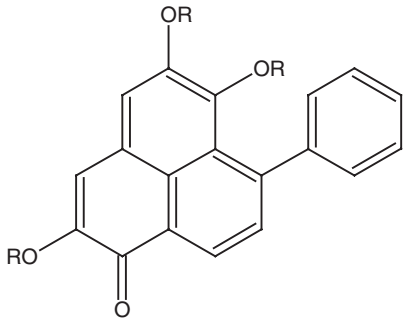

73

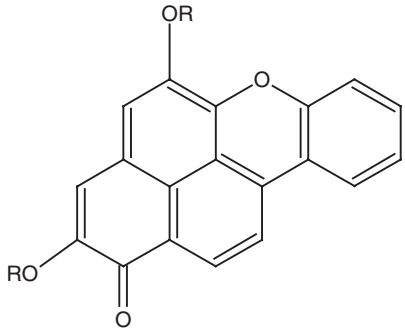

74

A fertile arena for the exploitation of the sensitivity of 3 mm micro NMR probe technology is in the structural characterization of impurities and degradation products of drugs. Synthetic impurities are frequently present at very low levels. Degradation products are frequently the result of various stress challenges imposed on a formulated product according to regulatory guidelines. Occasionally new degradants are observed to form late in such studies when the number or quantity of formulated dosage form may be severely restricted, making it mandatory for investigators to deal with small samples and with requirements for high experimental sensitivity. Along these lines Sigvardson and co-workers[152] reported the isolation and structural identification of a toxic impurity in XP315 (**75**).

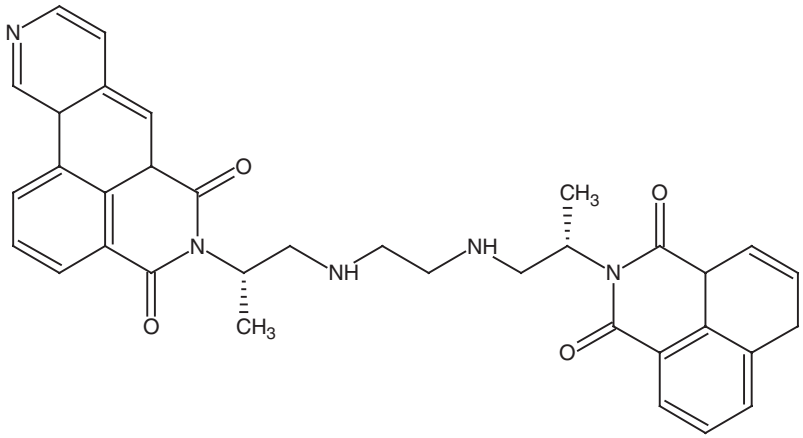

75

One of the challenges inherent to working in this area of structure characterization is that when an impurity is observed, it is difficult to quantitate the impurity present when the structure is unknown. Regulatory guidelines mandate the isolation and identification of impurities or degradants present at $>0.1\%$ in most cases unless the drug is dosed at very high levels, but until the chromophore of the molecule is identified and evaluated, it is difficult to determine whether or not the

relative response factor (RRF) of the impurity and the drug have any relation to one another. In many cases, investigators will opt to isolate and identify only to learn at the end of the exercise that the nature of the impurity is such that it was below the threshold because of RRF considerations. In the case of the toxic impurity observed in XP315, the peak area was $<0.1\%$. When finally isolated, on a

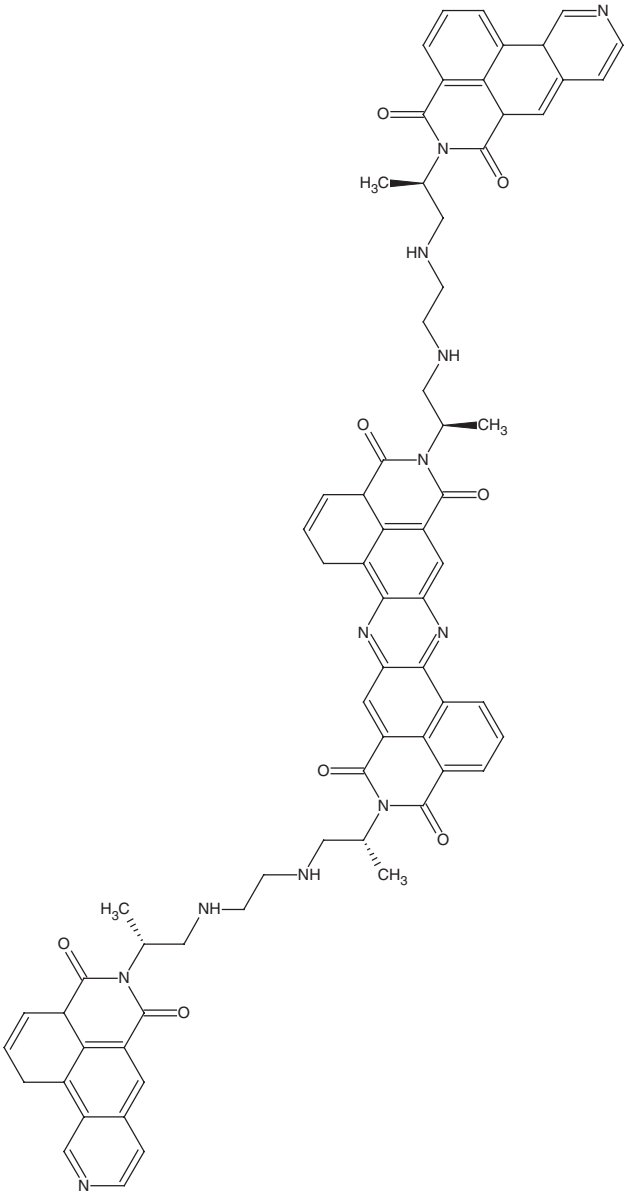

76

weight/weight (w/w) basis, the authors estimated that the C_{70} impurity (**76**) was present in the parent drug at about 0.01% (w/w) level.

Another area of the pharmaceutical sciences where 3 mm NMR probe technology has been utilized is in the confirmation of the structures of synthetically prepared glucuronides intended for use as authentic standards. Soars and co-workers[153] reported the synthesis of glucuronide analogs of seven different drug molecules and employed 3 mm probe technology with an assortment of 2D-NMR experiments for the confirmation of the structures. In a study focused on the addition of hydroxyl radicals to the *ipso* position of alkyl-substituted aromatic compounds, Shuler and co-workers[154] also made use of 3 mm gradient inverse-detection NMR probe capabilities for structure characterization.

Several papers utilizing 3 mm probe capabilities were also published that delved into the area of protein structures. Hepatocyte nuclear factor 4 was studied by a group lead by Williams.[155] It is interesting to note that a 2.7 Å X-ray study showed a fatty acid in the pocket of HNF4γ. Gas chromatography coupled mass spectrometry (GC/MS) and 3 mm NMR studies of extracts from purified HNF4α led to the identification of mixtures of saturated and *cis*-monounsaturated C_{14} to C_{18} fatty acids. Bertini and co-workers[156] utilized 3 mm probe capabilities in the determination of the solution structure of CopC, a cupredoxin-like protein involved in copper homeostasis.

Finally, in a report in tetrahedron, Ferreira and co-workers[157] employed the capabilities of 3 mm micro-NMR probes in a study that established the absolute configuration, conformation, and chiral properties of flavanone-(3→8″)flavone biflavonoids from *Rheedia acuminate*. The general structure of these compounds is shown by **77**. As noted by the authors, the stereochemistry at the 2- and 3-positions remained undetermined and was established for the first time in this study.

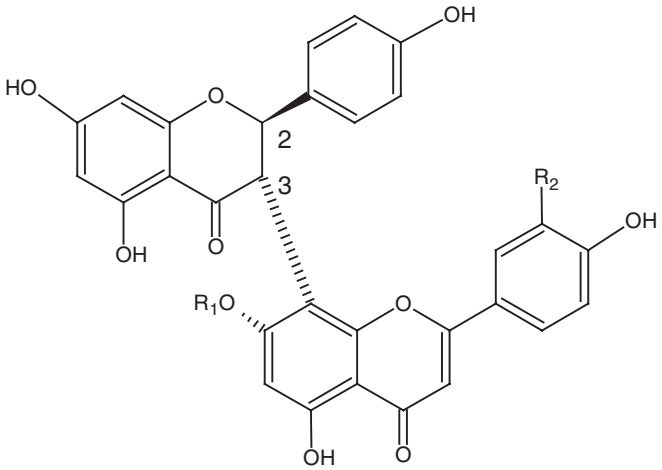

77

In 2003, Burgess and co-workers[158] reported a non-invasive means of evaluating liver function through the use of ^{2}H- and ^{13}C-NMR isotopomer analysis of human.

Acetaminophen and other xenobiotic substances are metabolized by the formation of water-soluble glucuronides that are subsequently removed by renal filtration. When given in combination with stable isotopes such as ^{2}H and ^{13}C, the glucuronides isolated from urine that were analyzed with 3 mm NMR probes provided a chemical biopsy and a convenient means for assessing intermediary liver metabolism.

In a similar biochemically oriented vein, several papers were published during 2003 in the journal *Chemical Research in Toxicology*, representing yet another area of applicability of 3 mm NMR probe capabilities. In the first of these reports, Hankin *et al.*[159] described the results of an investigation into the covalent binding of leukotriene A_4 to DNA and RNA. Later in 2003, Blair and co-workers[160] reported on the characterization of 2′-deoxycytidine adducts derived from 4-oxo-2-nonenal, a novel lipid peroxidation product. Two of the adducts characterized, A_1 and A_2, were consistent with substituted ethano-deoxycytidine structures. The third adduct, B, was characterized as a 7-heptanone-etheno-deoxycytidine adduct (**78**).

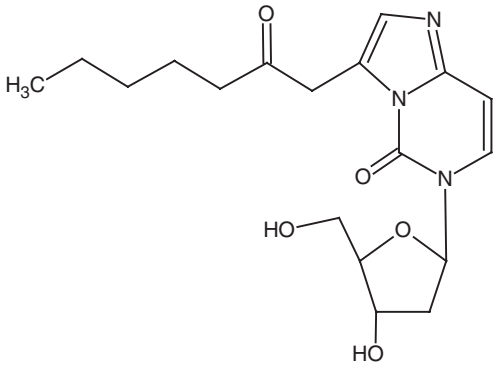

78

In another study, Blair and co-workers[161] reported a novel lipid hydroperoxide-derived modification to arginine, again taking advantage of the sample size and sensitivity of 3 mm probe technology.

The author and co-workers[162] utilized 3 mm probe capabilities in the characterization of an unnatural cyclization product that formed a novel-fused imidazolidinone tetrahydropyrroloindole ring system during the attempted synthesis of roquefortine C. As shown in Scheme 3, rather than the precursor (**79**) cyclizing to afford the N-blocked isoroquefortine C analog (**80**) the reaction instead underwent the unexpected cyclization to afford **81**. Long-range ^{1}H–^{15}N heteronuclear shift correlation data (long-range correlations observed are shown on **81**) were used to confirm the structure of the cyclization product.

In the first of several natural product structure characterization reports published in the *Journal of Natural Products* during 2003, Schmidt *et al.*[163] reported the isolation and characterization of a series of tetramic acids and pyridone alkaloids, militarinones B, C, and D from the insect pathogenic fungus *Poaecilomyces militaris*. The structure of militarinone D (**82**) is shown.

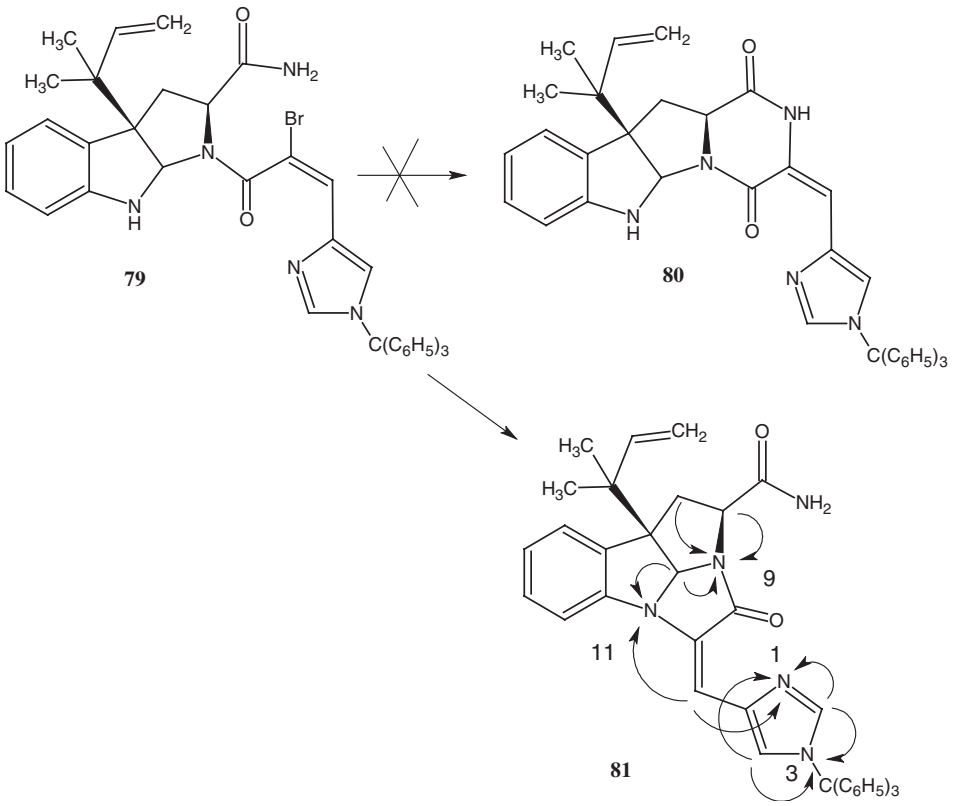

Scheme 3.

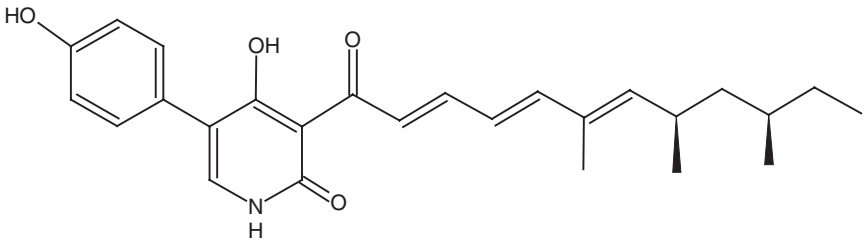

82

Schmitz and co-workers[164] reported the isolation and structural characterization of five new briarane diterpenoids, juncins I–M from the Indian Ocean gorgonian *Junceella junca* Pallas. The general structure of the juncins is shown by **83**.

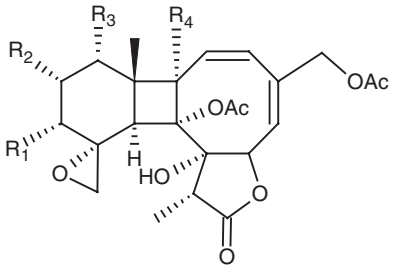

83

Petit and co-workers[165] utilized 3 mm NMR probe technology in the isolation and structural characterization of cribrostatin 6 (**84**), a cancer cell growth inhibitor from the marine sponge, *Cribrochalina* sp. This study was interesting in that the structure of this novel compound was confirmed, in part, using long-range $^{1}H–^{15}N$ gHMBC data acquired from a 2 mg sample of the compound dissolved in 100 μL of solvent in a 3 mm Shigemi NMR tube. The authors specifically used the long-range $^{1}H–^{15}N$ correlation data to differentiate between **84** and **85**. The structure was assigned as **84** on the basis of these data and was subsequently confirmed by an X-ray crystal structure.

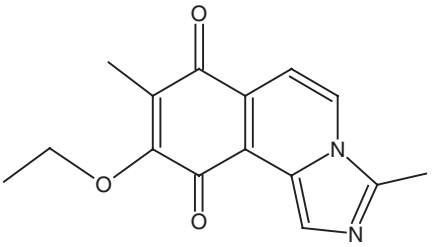

84

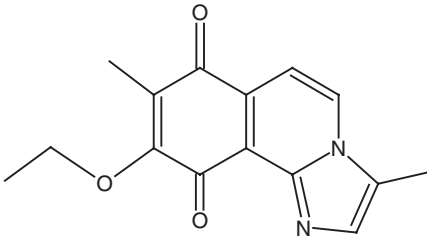

85

In the last of the natural product papers published in the *Journal of Natural Products* of which the author is aware, Daly and co-workers utilized bioassay-guided techniques to direct the isolation of a novel quinolizidine alkaloid, epiquinamide (**86**) from the Ecuadorian poison frog *Epipedobates tricolor*.[166]

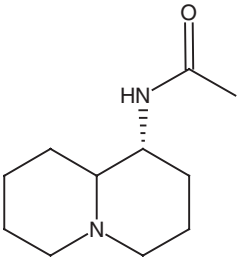

86

Finally, Treutter and co-workers[167] reported a study of the formation of novel flavonoids in apples treated with the 2-oxoglutarate-dependent dioxygenase inhibitor prohexadion-Ca.

Applications of 3 mm probe technology during 2004 were largely oriented toward small-sample structure characterization. Dean and colleagues[168] reported a study of the glucuronidation, oxidative metabolism, and bioactivation of enterolactone in the rhesus monkey that relied on the sensitivity of 3 mm probe capabilities. Vorsa and co-workers[169] reported the characterization of an extensive series of flavonols found in cranberry (*Vaccinium macrocarpon*) powder. Using 2.5 mm probe technology, Hashimoto and co-workers[170] reported a study of the biosynthesis of lambertellols based on the incorporation of ^{13}C-labeled acetate. Pohanka and co-workers[171] employed 2.5 mm probe capabilities in the characterization of a series of enniatins isolated from *Fusarium* sp. strain F31 with the capability of inhibiting the germination of *Botrytis cinerea* spores. Oberlies and large group of colleagues[172] isolated and characterized a number of molecules from the bark of *Diospyros maritima* collected in Indonesia. Among the compounds characterized were a new naphthoquinone (**87**) and a new coumarin (**88**) analog.

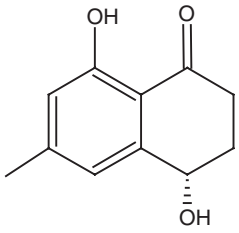

87

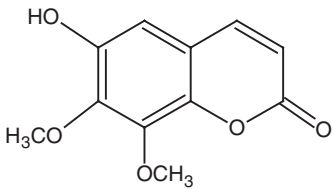

88

Schmitz and co-workers[173] reported the isolation and structural characterization of several cytotoxic lissoclimide-type diterpenes from the mollusks *Pleurobranchus albiguttatus* and *Pleurobranchus forskalii*.

Alsante and co-workers[174] reported an interesting case study for the identification of impurities of pharmaceuticals using a multidisciplinary approach to the problem. The active molecule (**89**) was used as a model system and the characterization of the dimeric structure derived from the active pharmaceutical (**90**) was described.

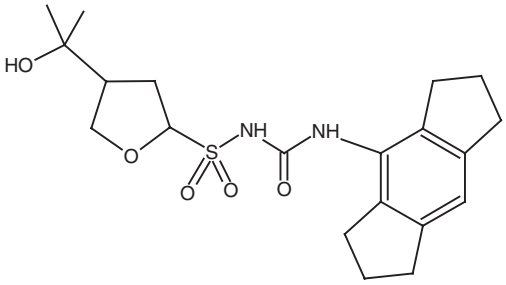

89

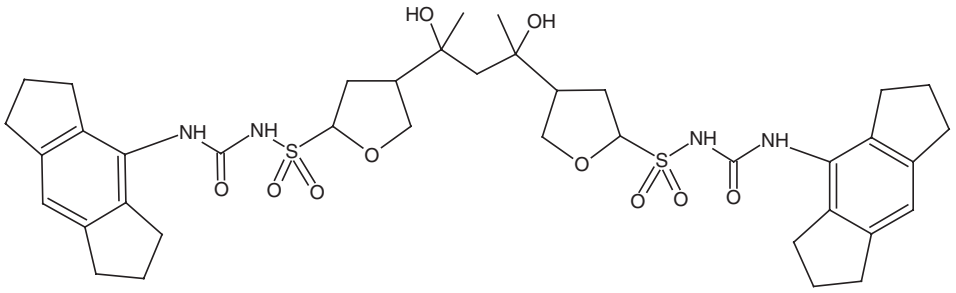

90

Finally, Ireland and co-workers[175] reported the isolation and characterization of a series of diterpene kalihinols, from two *Acanthella cavernosa* sponges with bacterial folate biosynthesis inhibitory activity.

Undoubtedly, applications of 2.5 or 3 mm NMR probe technology in the various forms, in which these probes are offered by vendors, will continue to appear in the published literature. They offer a significant concentration advantage when dealing with smaller samples of natural products, impurities, and degradation products of drugs, metabolites, forensic samples, etc. relative to conventional 5 mm NMR probes. Nevertheless, there are still times when it would be advantageous to have probes capable of dealing with still smaller samples. One approach to this need has been seen in the development of 1.7 and then 1.0 mm conventional small-volume NMR probes, which are discussed in the following section.

6.2. The 1.7 and 1.0 mm NMR probe applications

The need to characterize still smaller samples than is possible with 3 mm microprobes drove the author to collaboratively pursue the development of a 1.7 mm submicro- or SMIDG NMR probe with scientists at Nalorac Corporation. As shown in Fig. 3, which provides a comparison of 5, 3, and 1.7 mm NMR tubes, the sample volume in going from a 5 mm to a 3 mm probe diminishes from ~500 μL for the former to ~140–160 μL for the latter, and less when a 3 mm Shigemi NMR cell is used. Shrinking the probe dimensions to accommodate a 1.7 mm NMR tube leads to a further reduction of sample volume to ~30 μL under normal conditions and to as little as 20 μL if an investigator is willing to deal with more prolonged shimming.

The significant concentration advantage gained by shrinking the sample volume from ~500 μL for a 5 mm tube to ~30 μL for a 1.7 mm correspondingly translates to a considerable performance advantage. The performance gain associated with a 1.7 mm NMR probe can be used either to deal with smaller samples, or by the more rapid acquisition of data when "larger" samples are available. A survey of the results obtainable with 1.7 mm probe technology, as well as the results of comparison studies with a 3 mm micro-NMR probe are discussed in Section 2.2.

There have not been a large number of reported applications of the use of 1.7 mm SMIDG NMR probes in the published literature. In part, this may be due to the

demands of preparing, handling, and transferring such small NMR samples. A 1.7 mm NMR probe was, however, used in a study of the effects of *N*-oxidation on the ^{15}N chemical shifts of the *Strychnos* alkaloids strychnine (**91**) and brucine (**92**).[176] As expected, the 19 *N*-oxide ^{15}N resonances were shifted downfield. In the case of strychnine *N*-oxide (**91**), N19, which normally resonates at 35.0 ppm was shifted downfield to 136.3 ppm (+101.3 ppm). The N19 resonance of brucine *N*-oxide (**92**) shifted downfield from 35.9 ppm to 135.5 ppm (+99.6 ppm). The ^{15}N shifts observed were considerably larger than those observed in previous studies by the authors.[177,178]

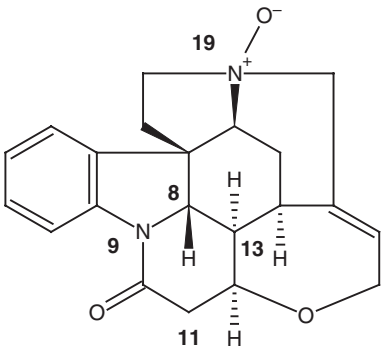

91

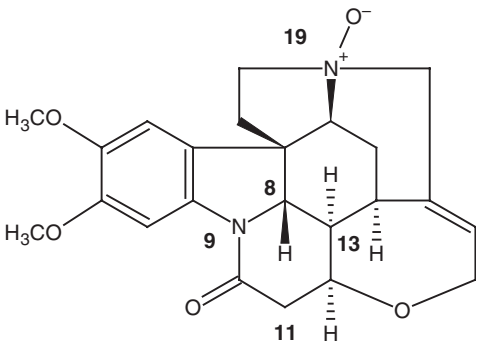

92

The sensitivity of 1.7 mm probe technology was used to advantage in the characterization of a very unstable impurity isolated during the development of the protease inhibitor Tripranovir (PNU-140690).[179] In the last step of the synthesis shown in Scheme 4, the aniline function of the precursor (**93**) is normally reacted with the thionyl chloride group of a trifluromethyl-substituted pyridine to afford the drug (**94**). A pink discoloration of the otherwise white drug product was investigated. The preparatively isolated red impurity was found to be unstable in acetone and to have a half-life of about 12 h in d_4-methanol. A gHSQC spectrum was acquired using a 1.7 mm SMIDG probe followed by an overnight HMBC spectrum which allowed the full characterization of the impurity as the Zincke salt,[180] **95**, formed by the reaction of **93** with ring-opened pyridine used as a scavenger.

In an effort to assign all of the nitrogen resonances of cryptospirolepine (**18**), which was available in relatively limited quantity, a 1.7 mm SMIDG probe was used with 750 μg sample of the alkaloid (Fig. 17).[181] The assignment of the N3 amide resonance in the indolobenzazepine portion of the molecule remained elusive at normal optimization values but was finally assigned with a 2.5 Hz optimized gHMBC spectrum. The necessity of successive reoptimization of the delays in the series of gHMBC experiments performed underscores advantage of using the accordion optimized IMPEACH-MBC experiment for the acquisition of long-range ^{1}H–^{15}N correlation data.[182] Rather than observing a correlation from the proton peri to N3 as might be expected, a correlation was instead observed via four bonds from the H13 vinyl proton as shown by **96**.

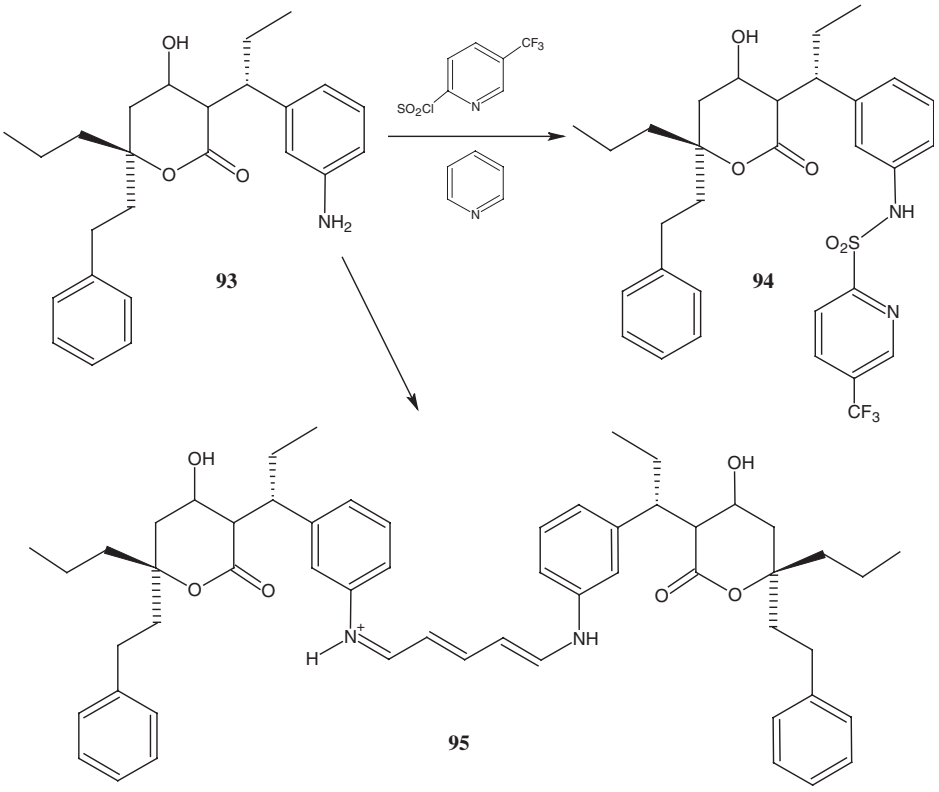
OH
O
O
NH2
93
SO2Cl
CF3
N
OH
O
O
NH
O2S
N
CF3
94
OH
O
O
N+
H
NH
OH
O
O
95

Scheme 4.

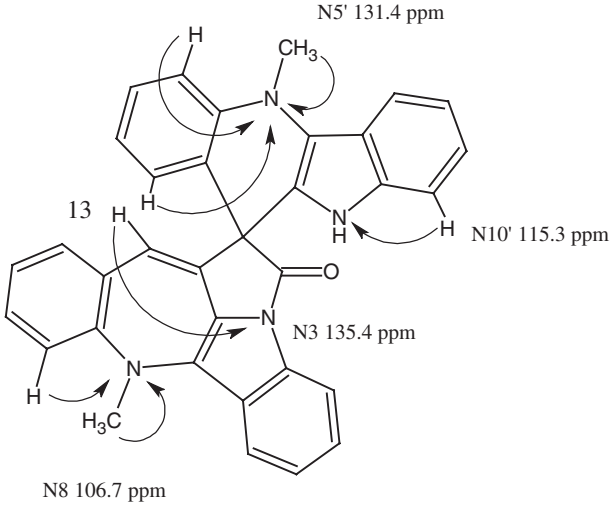
N5' 131.4 ppm
H
CH3
N
13
H
H
N
H
H
N10' 115.3 ppm
O
N
N3 135.4 ppm
N
H
H3C
N8 106.7 ppm

96

The most recent application of 1.7 mm probe technology that the author is aware of was in the characterization of a degradation product of tin ethyl etiopurpurin (SnET2) reported in 2003.[183] During terminal heat sterilization, a photolabile degradant was formed in small quantities in the lipid emulsion formulation. After preparative chromatographic isolation, a sample was prepared in a 1.7 mm NMR tube in the dark for data acquisition. An 8 Hz optimized gHMBC experiment did not give sufficient long-range correlations to assemble the structure of the degradant. There were, however, considerably more correlations observed for the dihydroxycyclopentene ring fused to the B-ring of the molecule in a 2–10 Hz optimized IMPEACH-MBC experiment[184] to allow the structure of the degradant to be confirmed as shown by **97**.

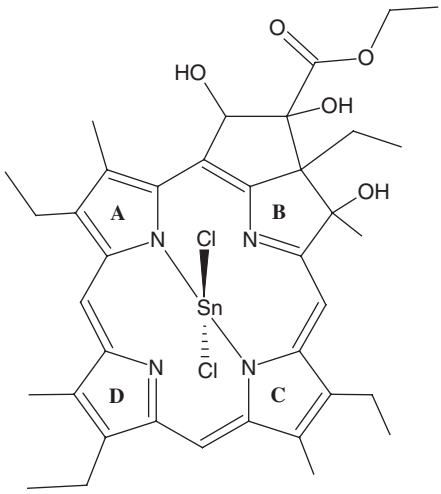

97

Following reports of the development of the 1.7 mm probe by the author and colleagues, workers at Hoffmann-La Roche and Bruker reported the collaborative development of a 1 mm gradient triple resonance NMR probe with a sample volume of ~5 μL.[14] In describing the performance characteristics of the 1 mm probe, the authors do report one interesting comparison of a 1 mm NMR tube containing 172 μg of sucrose for which an s/n ratio measurement was made for the anomeric proton. For a single scan, the authors reported an s/n ratio for the 1 mm probe of 276:1 vs. an s/n ratio measurement of 195:1 for the same tube in a 5 mm cryogenic NMR probe. The authors also reported 2D-NMR benchmarking studies for the 1 mm probe with a 1 μg sample of ibuprofen (**4**) with which they were able to record a ^{1}H–^{13}C gHSQC spectrum in 20 h and a 1 μmol sample of strychnine (**5**) for which they were able to record a ^{1}H–^{15}N gHMBC spectrum in 2 days.

To date, there have been only a few applications of the use of a 1.0 mm NMR probe reported in the literature. The first of these was a metabolic profiling study with rodent biological fluids by Griffin and co-workers.[185] In 2003, O'Neil-Johnson[186] in a paper presented at the New York American Chemical Society meeting

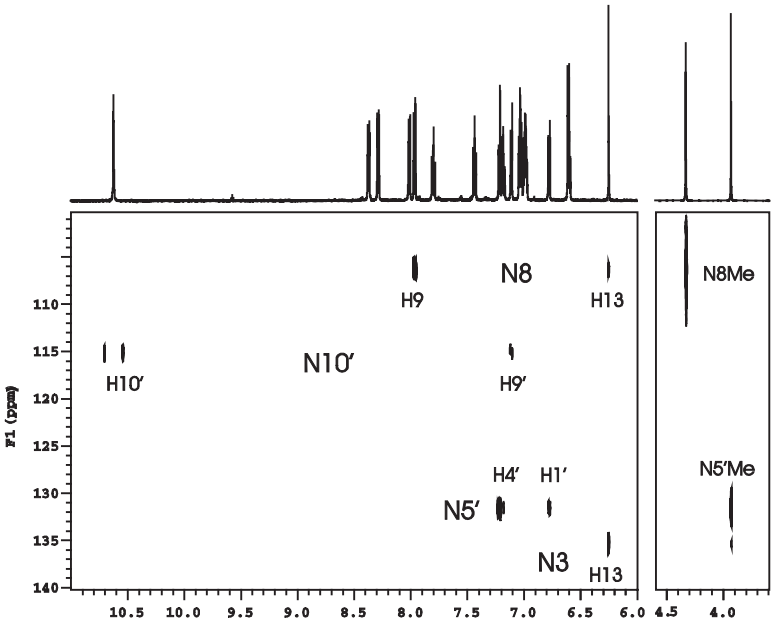

Fig. 17. Long-range ^{1}H–^{15}N gHMBC spectrum of cryptospirolepine (**18**) optimized for 2.5 Hz. The data were acquired using a 750 μg sample of the alkaloid dissolved 30 μL of d_6-DMSO in a 1.7 mm SMIDG NMR probe at 600 MHz. (Reprinted with permission from Ref. 181. Copyright 1999, HeteroCorp.)

posed the question of doing structures with 50 μg samples using 1.0 mm CapNMR probes. This level of probe performance while interesting was well within the performance limits of the 1.7 mm probe based on the characterization of the 8% cryptolepinone impurity contained in samples of cryptolepine (**1**) that were characterized during the development of that probe technology.[12,13] Most recently, Peti and co-workers[187] have reported using a 1.0 mm CapNMR probe for the investigation of microgram quantities of doubly labeled proteins.

There will undoubtedly be more applications of the use of 1.0 mm CapNMR probes reported in the future as they become more widely available. It will also be interesting to see if the label "CapNMR" used in some of the reports published thus far is used on a regular basis in the future, which would, of course, make searching for applications of this probe technology much easier in the future.

6.3. Nano-probe™ applications

Nano-probes were developed nearly in parallel with the now prevalent 3 mm micro-NMR probes. For small-sample applications, Nano-probes have an advantage in that they can locate 100% of a precious sample in the rf coils of the probe.

Furthermore, since the sample cell is spun at high speed, typically ~2 kHz at the magic angle, Nano-probes make it possible to interrogate samples by NMR that would otherwise be intractable. Examples include materials such as polymeric beads to which a substrate molecule is tethered by a linker of some sort. Thus, the first application of the Nano-probe of which the author is aware was in a 1994 collaborative report by authors at Affymax and Varian, that demonstrated the acquisition of high-resolution NMR spectra of a solid-phase synthesis bead.[188] The broad-line widths of the polymeric support (denoted by the circle on **98**) would normally preclude the acquisition of high-resolution NMR data in conventional NMR probes. However by using a Nano-probe, Fitch and co-workers were able to obtain high-resolution data for the non-polymeric portion of the molecule.

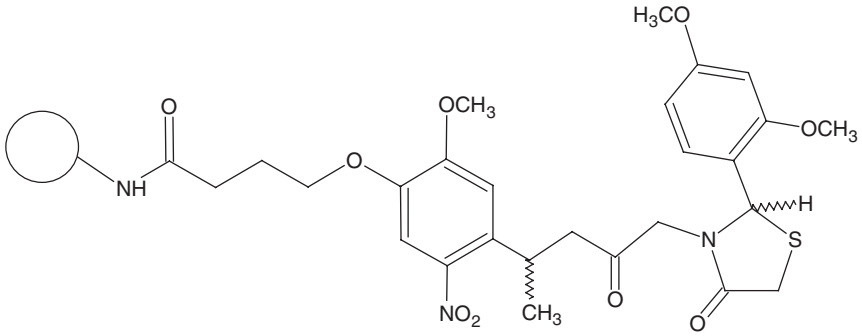

98

In 1995, the author and co-workers reported a comparison of the ^{13}C-NMR spectra acquired for an ~100 μg sample of the alkaloid cryptolepicarboline (**13**) using both a 3 mm micro-dual and heteronuclear Nano-probes.[61] The two probe technologies gave roughly the same s/n ratios with the Nano-probe allowing the acquisition of the spectra in roughly one-third of the time required in a conventional 3 mm probe. Sample volumes were 40 and 140 μL, respectively.

The biological NMR community recognized the potential of Nano-probe technology for dealing with small samples and reported the acquisition of 1D and 2D-NMR data for a series of xylosides available in only 10–25 μg quantities using a 500 MHz Nano-probe.[189]

Keifer and co-workers[17] revisited the problem of acquiring usable high-resolution NMR spectra for molecules tethered to solid-phase synthesis supports in 1995, reporting the results of a comparison of the data obtained for conventional high-resolution, magic angle spinning (MAS), and high-resolution MAS-NMR probes. This work was following in 1996 by the work of Sarkar and co-workers[22] who demonstrated that it is possible to acquire NMR data for molecules bound to a single solid-phase synthesis bead. Later in 1996, Keifer studied the influence of resin structure, tether length, and solvent on the acquisition of high-resolution NMR spectra of solid-phase synthesis resins.[23] Wehler and Westman reported the

utilization of Nano-probe technology as a tool for monitoring the progress of reactions in solid-phase synthesis.[190] A very similar application was also reported by Albert and co-workers.[191]

The capabilities of the Nano-probe were challenged in a completely different fashion in 1996 by a study reporting the characterization of novel steroids from *Trichilia hirta* through the acquisition of INADEQUATE spectra.[192] Using samples of 11 and 9 mg, respectively, INADEQUATE spectra were recorded to establish the structures of **99** and **100**. Data were acquired in ~62 h for each sample and the interpretation of the data was facilitated through the use of FRED software.[84–86]

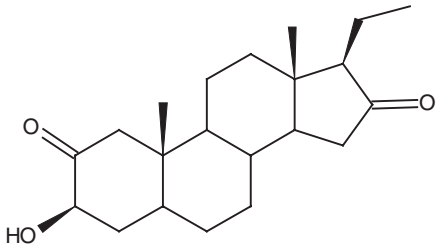

99

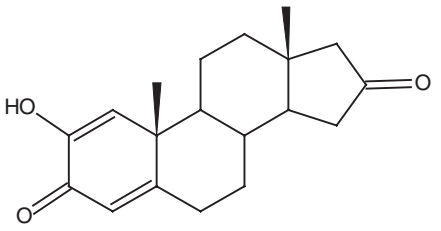

100

Late in 1996, Klein and co-workers[193] reported the characterization of a novel 15-membered macrolide from the blue-green algae *Lyngbya bouillonii* (Cyanophyceae), laingolide (**101**) in which a heteronuclear ^{13}C Nano-probe was utilized to acquire the ^{13}C reference spectrum reported in the study.

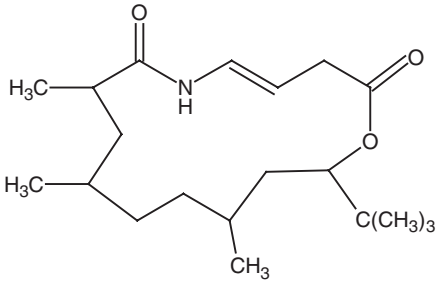

101

Delepierre and co-workers[194] reported the utilization of ^{1}H Nano-probe technology in the characterization of a novel channel blocking peptide toxin from the scorpion *Pandinus imperator* which facilitated the analysis of the very small samples involved in the study. In another biochemical application later in 1997, Chaffotte and co-workers[195] reported a study of the secondary structure recovery during the refolding of reduced hen egg white lysozyme that also utilized Nano-probe technology. Two reviews of the application of Nano-probe technology also appeared in 1997.

The first by Manzi and Keifer discussed the acquisition of NMR data of microgram quantities of complex carbohydrates using Nano-probe technology.[196] Later in 1997, Keifer[197] reviewed the utilization of Nano-probe technology in solid-phase synthesis and combinatorial chemistry.

Delepierre and co-workers reported actively in the area of Nano-probe applications during 1998. First they reported the ^{1}H structural analysis of a novel class of potassium blocking toxins cross-linked by four disulfide bridges rather than three as in previous examples.[198] Two peptides, Pi1 and Pi7, purified from the venom of the scorpion *Panidinus imperator* belong to this class of toxins. Delepierre *et al.*[199] next reported the utilization of Nano-probe technology in the work on the characterization of renatured lysozyme. Delepierre[200] also briefly reviewed the acquisition of high-resolution liquid NMR spectra in MAS Nano-probes in 1998.

The only natural product application of Nano-probe technology of which the author is aware in 1998 was the report of the isolation and unambiguous synthesis of cryptolepinone (**33**) by Bierer and co-workers.[201]

Early in 1999, Keifer[202] reviewed probe designs useful in biotechnological applications, focusing heavily on the capabilities of Nano-probes for dealing with heterogeneous samples, as well as small homogeneous soluble samples, which can be problematic in larger diameter conventional NMR probes unless the investigator resorts to the use of Shigemi NMR cells.

Braekman *et al.*[203] reported the isolation and structural characterization of a modified tetrapeptide, lyngbyapeptin A (**102**) from the blue-green algae *Lyngbya bouillonii* (Cyanophyceae), acquiring the ^{13}C reference spectrum using a heteronuclear Nano-probe on a 500 MHz spectrometer.

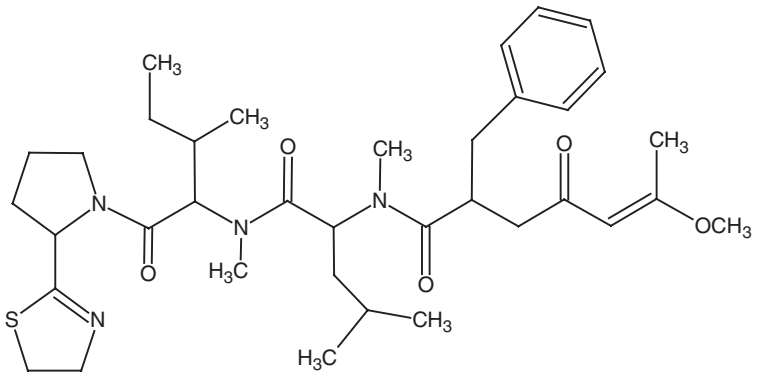

102

Finally, late in 1999, Delepierre *et al.*[204] reported a comprehensive ^{1}H-NMR analysis of the Pi7 peptide from the scorpion *Panadinus imperator*, again using Nano-probe technology to facilitate the acquisition of data with the small samples available.

Perhaps one of the most interesting applications of Nano-probe capabilities in 2000 was seen in the report of Ikeda and co-workers,[205] which dealt with the study of surface-adsorbed molecules on an insoluble pigment. The authors compared the results obtained with a conventional solution NMR probe and a Nano-probe at 600 MHz. As would be expected, the results obtained in the Nano-probe were considerably superior to those in the conventional NMR probe for this type of application. Next, Sefler and Gerritz[206] reported the results of a 1D- and 2D-NMR study done using Nano-probe technology to characterize reaction products bound to Chiron SynPhase crown. Proton, carbon, and COSY spectra were acquired for the analysis, and the authors compared the results with two types of linkers and a variety of solvents, making their work a useful starting point for others working in the field.

The balance of the Nano-probe applications in 2000 were biochemically oriented. First, Varki *et al.*[207] reported a very interesting application of Nano-probe technology in their comparison of the *N*- and *O*-glycans from wild type mouse tissue with those of mice genetically deficient in glycosyltransferases. Next, Wakarchuk *et al.*[208] reported a study of the biosynthesis of ganglioside mimics of *Campylobacter jejuni* OH4384 that relied on a gradient inverse Nano-probe for the acquisition of gHMBC data. In a study of a novel type of arabinoxylan arabinofuranohydrolase isolated from germinated barley, Duus and co-workers[209] utilized Nano-probe technology for the analysis of substrate preference and specificity.

Again in 2001, the majority of Nano-probe papers published were biochemical in orientation. van Halbeek[210] presented the results of a study of glycan profiling of mammalian tissues by homo- and heteronuclear Nano-probe spectroscopy using a gradient inverse-detection version of the Nano-probe referred to as a gHX-Nano-probe. Shao and co-workers[211] utilized Nano-probe technology for the assignment of the proton resonances of a small-peptide OVARC, again taking advantage of the small 40 μL volume of the Nano-cell to facilitate data acquisition for the small samples available for study. Finally, Logan and colleagues[212] utilized tandem MS followed by preparative high-performance LC (HPLC) and Nano-probe NMR capabilities to identify the nature and precise site of glycosylation of the carbohydrates in *Camplyobacter jejuni* Flagellin. Finally, Vliegenthart *et al.*[213] reported a study of the epitope diversity of *N*-glycans from bovine peripheral myelin glycoprotein PO which relied on Nano-probe technology for the acquisition of the NMR data.

The only Nano-probe application report of which the author is aware from 2001 was the demonstration of adiabatic TOCSY MAS in liquids reported by Kupce *et al.*[214] The authors demonstrated that the adiabatic mixing sequences were less susceptible to modulations in TOCSY MAS experiments run in a Nano-probe.

Finally, in the only natural product structure characterization report during 2001 that utilized Nano-probe capabilities, Namikoshi *et al.*[215] reported the isolation and structural characterization of a new macrocyclic trichotehcene, 12,13-deoxyroridin E (**103**) and three known compounds, roridin E, verrucarin A, and verrucarin J.

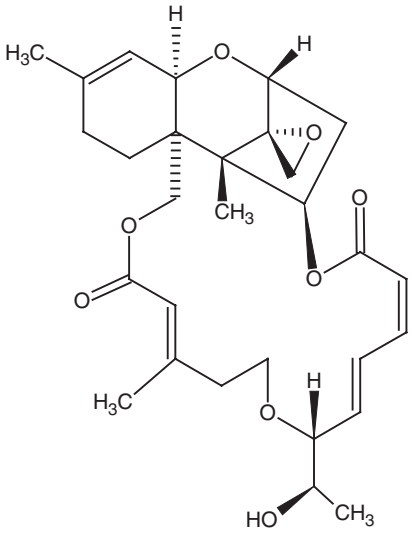

103

Only two reported applications of Nano-probe technology appeared in 2002. The first was a report detailing the solution of the 3D structure of small scorpion toxins present in nano-molar amounts in venom by Delepierre.[216] The other report by Wang *et al.*[217] reviewed the application combined application of LC-NMR and Nano-probe technologies for the analysis of mixtures of natural products.

From 2003 to the present, applications of Nano-probe technology contained in the published literature are relatively few in number, quite possibly because of the high sensitivity of cryogenic NMR probes and the benefits of acquiring data in smaller diameter NMR tubes run coaxially in larger diameter cryoprobes (see Section 6.5). Fung *et al.*[218] reported a novel application of Nano-probe NMR in their efforts to probe the "hard-to-cook" syndrome associated with potatoes in the Middle East. Fenical and co-workers[219] in work also published in 2003 probed the resistance of seaweed to microbial attack by marine fungi. The authors isolated and characterized lobophorolide (**104**), in part through the use of Nano-probe NMR

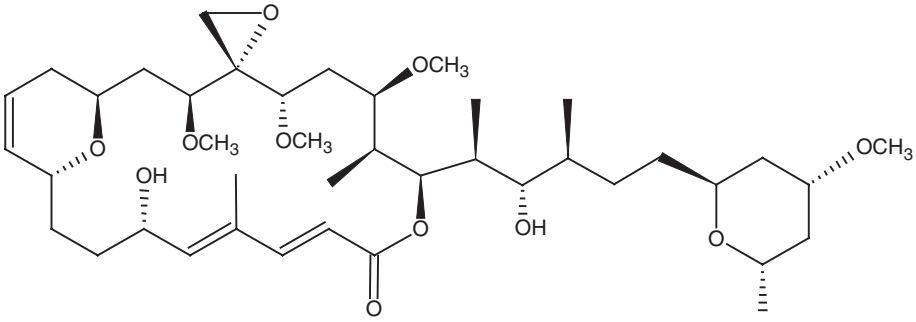

104

measurements, which has antifungal activity that the seaweed was presumed to produce as a chemical defense against attack by marine fungi.

The sole Nano-probe paper published in 2004 of which the author is aware was the study by Claeyssens and co-workers[220] of the enzymatic hydrolysis products of *Nothogenia erinacea* seaweed xylan, which is a linear homopolymer with mixed $\beta-(1\rightarrow 3)/\beta-(1\rightarrow 4)$ linkages. The sequence of the residues was determined from a combination of nuclear overhauser effect spectroscopy (NOESY) correlations between the anomeric protons and a proton of the residue to which it is glycosidically linked and gHMBC data, that were acquired using Nano-probe capabilities. Finally, in early 2005, Bradley *et al.*[221] compared the ability of cryogenic, Nano- and conventional NMR probes to acquire diffusion-ordered spectroscopy (DOSY) spectra of dilute mixtures of compounds.

6.4. The μCoil NMR probe applications

While work on the development of μCoil NMR probes has been proceeding at what might be characterized as a frenetic pace, coupling various separation modalities, for example, CE, cITP, etc., to μCoils for NMR detection, there have been relatively few true applications of μCoil NMR published thus far. This will doubtlessly change, as μCoil probe designs by MRM Corporation are now being tested in various laboratories within the pharmaceutical industry; but for the moment, there remains a dearth of what the author would consider true application reports in the literature.

Perhaps one of the first papers to be published demonstrating the application of μCoil NMR probe capabilities for dealing with the characterization of very small samples is to be found in the report by Subramanian *et al.*[222] in 1999. The authors demonstrated the acquisition of HSQC data which <100 nmol samples of several small molecules. For example, a very usable HSQC spectrum for a 13 μg sample of chloroquine (40 nmol) was acquired in 3.6 h. The authors also showed an HMQC spectrum recorded for a 27 μg sample of progesterone in 1.9 h. The latter spectrum, while certainly usable, could be improved by acquiring HSQC rather than HMQC data, and by increasing the number of files used to digitize the second frequency domain to improve F_1 resolution.

Zeng and co-workers[223] have more recently applied the sensitivity of μCoil NMR probe designs to the problem of acquiring NMR data for small ($\sim$50 μg) samples of material in natural product libraries. The authors demonstrated these abilities using a library of compounds from the stem bark of *Taxus brevifolia*. As high-throughput screening (HTS) is very important for screening large numbers of molecules within the pharmaceutical industry in the search for active new lead molecules, it is quite likely that more interest will be seen in this type of application of μCoil NMR probes.

Sweedler *et al.*[224] have exploited the mass sensitivity of μCoil NMR probes in the development of micromixer-based time-resolved NMR, demonstrating the application of the method to the conformation of the protein ubiquitin. To probe changes in protein conformation based on the elapsed time after a change in solvent composition, two capillary flows are mixed rapidly followed by the acquisition of

NMR spectra of the combined flows as a function of the time following mixing using a μCoil NMR probe. This approach allows the acquisition of time-dependent protein conformational data that would be difficult to acquire by other means. While limited to the acquisition of ^{1}H spectral data for obvious reasons, the method still has interesting potential.

Most recently, Peti *et al.*[225] have demonstrated the potential of μCoil for the chemical shift assignment of aromatic side-chain protons of proteins. Using the conserved hypothetical protein TM0979 from *Thermotoga maritima*, the authors demonstrated the sequence-specific backbone resonance assignments with $<500\,\mu g$ of $^{13}C^{15}N$-doubly labeled protein.

6.5. Cryogenic NMR probe applications

Sensitivity has long been the Achilles' heel of NMR spectroscopy. In an effort to circumvent this shortcoming, magnet technology has been pursued, driving observation frequencies, and unfortunately the price of the technology progressively higher. New experiments have been developed; for example, supplanting of X-detected heteronuclear shift correlation experiments by the much more sensitive proton- or inverse-detected experiments, to further improve sensitivity, and thereby diminish sample requirements and/or observation times. Likewise, probe designs have been refined, and new probe technologies explored, providing the basis for this contribution. While the sensitivity gains inherent to cryogenic NMR probe technology have been known for a considerable time[34–37] it has taken massive effort on the part of probe engineers to develop a robust and reliable cryogenic NMR probe of the type that is now commercially available. Initially, there have been relatively sparse numbers of applications reports that have used this technology, but it is quite likely that there will be burgeoning numbers of applications appearing in the future as regular access to cryogenic NMR probe-equipped instruments becomes routinely available.

It was recognized quite early in the development of cryogenic NMR probes that this technology could have a significant impact on the use of NMR for ligand/protein screening. Fesik and co-workers[226] demonstrated that ^{1}H–^{15}N heteronuclear shift correlation spectra could be acquired in $<10\,m$ using a $50\,\mu M$ protein sample in combination with cryogenic NMR probe technology. Shapiro and Wareing[227] in a general review of high-resolution NMR for screening protein/ligand binding offered the same opinion but did not show data.

In a poster presented at the *40th Experimental NMR Conference* in Orlando in 1999, Pease and co-workers showed the results obtained with a 2.5 mm gradient cryogenic NMR probe in the structural characterization of several drug metabolites.[228] That report was followed by the published report of Logan and co-workers[229] showing the results of a proton cryogenic NMR probe for the acquisition of NOE difference spectra for small samples of the natural product taxol.

Bringmann *et al.*[230] reported utilizing the greatly enhanced sensitivity of a ^{13}C optimized cryogenic NMR probe to acquire ^{13}C–^{13}C 2D INADEQUATE data in a

study of plant alkaloid biosynthetic pathways leading to the alkaloid dioncophylline A (**105**).

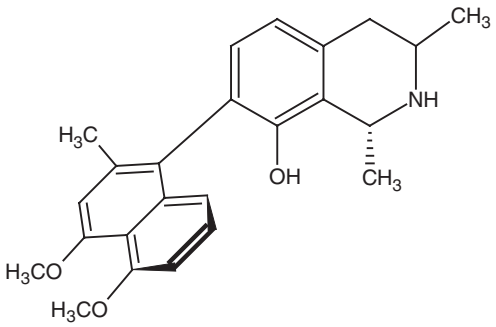

105

Serber *et al.*[231] also utilized a ^{13}C optimized cryoprobe in developing new ^{13}C-detected protein NMR experiments. That communication was followed shortly later by a report by Wand and co-workers[232] describing the optimal use of cryogenic NMR probe technology in the NMR characterization of proteins. Fesik *et al.*[233] described a further application of cryoprobe technology for NMR-based screening of proteins containing ^{13}C-labeled methyl groups later in 2000.

Using strychnine (**5**) as a model compound for the study, the author and coworkers[234] reported a direct comparison of the performance of conventional and 3 mm cryogenic NMR probes for the acquisition of heteronuclear shift correlation data on small samples of natural products. Using a 40 μg sample of strychnine (**5**) prepared by successive serial dilution, it was shown that data comparable to a 17.5 h overnight non-gHSQC spectrum recorded in a conventional 3 mm inverse-detection probe could be acquired in as little as 90 m using a 3 mm cryogenic NMR probe. The 3 mm conventional and cryoprobe comparison spectra are shown in Fig. 18. Additional small-sample applications were reported in several poster presentations. Data acquired using a 500 MHz 3 mm cryoprobe were shown for metabolite samples ranging in size from 10 to 80 μg, the authors reporting eight times the mass sensitivity of a conventional 5 mm NMR probe by Liu and co-workers.[235] O'Neil-Johnson and co-workers demonstrated the sensitivity advantage of 3 mm cryogenic NMR probes for natural product structure elucidation[236] as well as for the support of the microscale synthesis of distamycin (**106**).[237]

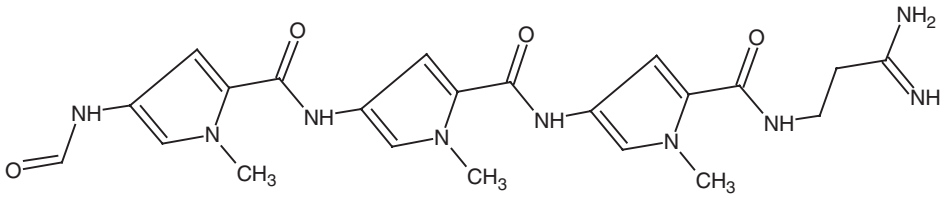

106

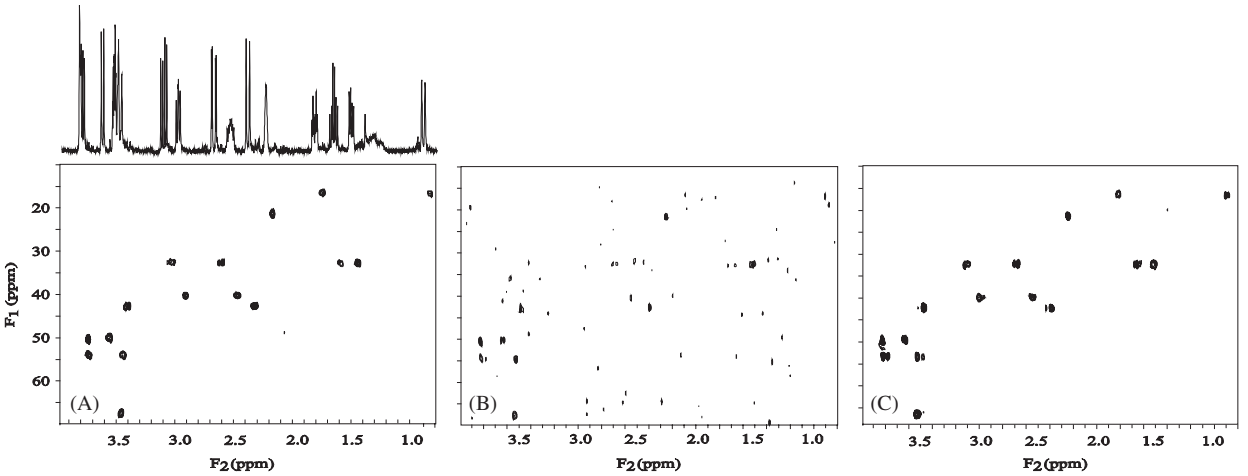

Fig. 18. Comparison spectra for a sealed 3 mm NMR sample tube containing 40 µg (120 nmol) of strychnine (**5**) dissolved in 165 µL $CDCl_3$.[234] All of the spectra were acquired and processed identically. The non-gHSQC spectrum shown in Panel A was acquired in 90 m using a 3 mm inverse-detection cryogenic NMR probe operating with an rf coil temperature of 12 K. The sealed 3 mm sample was used to acquire the 90 m spectrum shown in Panel B in a conventional 3 mm gradient inverse-detection probe. All parameters were identical. Panel C shows the results obtained for the sealed 3 mm sample in a conventional 3 mm NMR probe with an overnight (17.5 h) acquisition. (Reprinted with permission from *J. Nat. Prod.*, **63**, 1049 (2000). Copyright 2000, American Chemical Society and American Society of Pharmacognosy.)

Early in 2001, Serber *et al.*[238] reported additional new carbon-detected pulse sequences for protein NMR structure characterization, further exploiting the sensitivity afforded by a ^{13}C optimized cryogenic probe. Bringmann and Feineis[239] following on the work initially communicated in 2000[230] and again using ^{13}C–^{13}C 2D INADEQUATE data acquired in a ^{13}C optimized cryogenic NMR probe were able to establish a new plant biosynthetic pathway leading to the isoquinoline family of alkaloids.

Using a 5 mm gradient inverse-detection cryoprobe, the author and colleagues[50] demonstrated the considerable sensitivity gain realized when acquiring long-range ^{1}H–^{15}N CIGAR-HMBC data at natural abundance using a sample of the oxazolidinone antibiotic eperezolid (**8**).

Nicholson *et al.*[240] focused their attention on the utilization of the sensitivity advantage of cryogenic NMR probe technology for the acquisition of ^{13}C spectra of urine for metabonomic studies. Prior to their report, all metabonomic studies were ^{1}H detected since it was difficult to justify the time expenditure to obtain sufficiently high s/n ratios to resort to ^{13}C-detected spectra with conventional NMR probe technology. In another novel study, Simon and Sattler[241] used the sensitivity of cryogenic NMR probe technology to advantage in a study of the *de novo* determination of residual dipolar couplings of proteins. Banci *et al.*[242] employed a cryogenic NMR probe for the direct observation of hydrogen bonds in monomeric superoxide dismutase. In a study with far reaching applicability for the biomacromolecular NMR community, Dötsch *et al.*[39] reported a study of low-conductivity buffers. Cryogenic NMR probes have been particularly intolerant of lossy solutions typically encountered with protein and related biomacromolecules, and the results of this study provided investigators in this area with a basis for selecting buffers to obtain optimal results.

A sealed 5 mm NMR sample tube containing a degraded 2.5 mg sample of cryptospirolepine (**18**) was investigated by the author and co-workers using cryogenic NMR probe capabilities.[243] When the sealed tube was cut open and examined chromatographically, there was no cryptospirolepine (**18**) remaining in the sample. Instead, the sample was comprised of a complex mixture of 26 chromatographically separable degradation products, as shown by the chromatogram in Fig. 19. There were two major degradants and numerous smaller degradation products. The largest degradant, ~35% of the total sample, was quickly identified as cryptolepinone (**33**) on the basis of a proton, COSY, and HSQC spectrum. The structure of the second most abundant degradant, labeled DP-2 in Fig. 19 was determined to be cryptoquindolinone (**107**). A complete gamut of 2D-NMR data were acquired using a 5 mm cryogenic NMR probe during the determination of the structure, including a 3–6 Hz optimized ^{1}H–^{15}N CIGAR-HMBC spectrum.

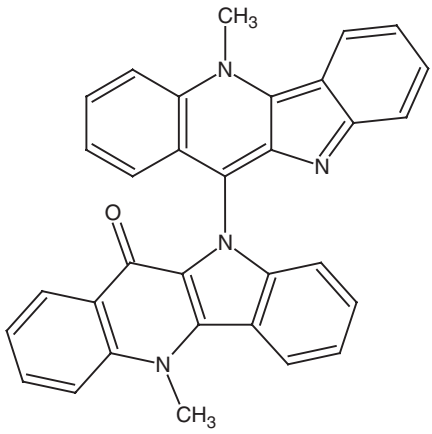

107

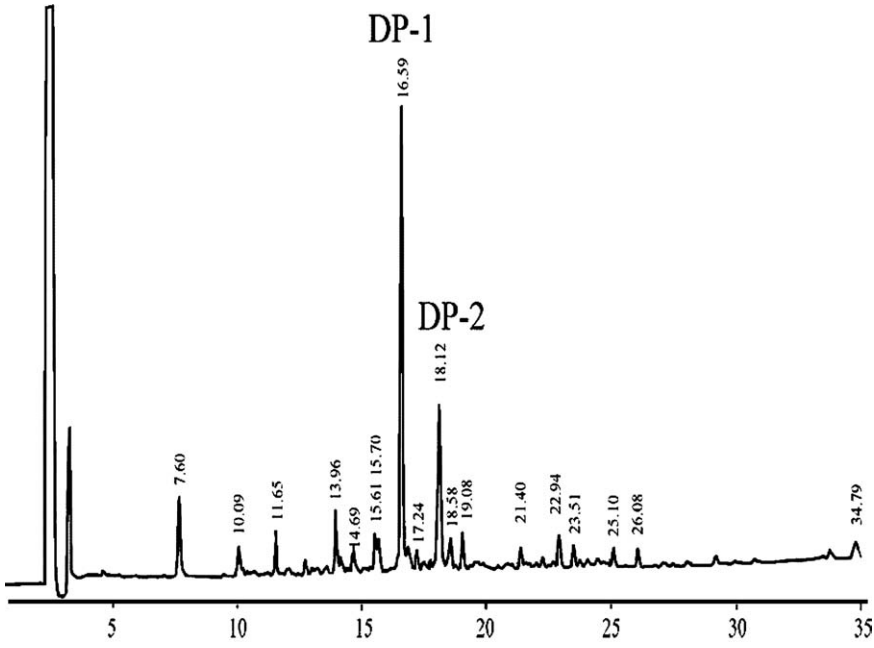

Fig. 19. Reversed-phase HPLC trace of a degraded 2.5 mg sample of the complex indoloquinoline alkaloid cryptospirolepine (**18**) after storage in d_6-DMSO for 10 years under uncontrolled conditions.[243] No trace of the starting alkaloid remains. The two major impurities, labeled DP-1 and DP-2, constituted approximately 50% of the total sample. DP-1 was identified as the known alkaloid cryptolepinone (**33**) on the basis of ^{1}H reference, COSY, and HSQC spectra. The elucidation of the structure of DP-2 required the utilization of a complete gamut of 2D-NMR spectra and the use of cryogenic NMR probe capabilities. (Reprinted with permission from Ref. 243. Copyright 2002, HeteroCorp.)

In another natural product structure determination reported during 2002 that relied on cryoprobe technology, Gustafson *et al.*[244] reported the structure of a new antitumor macrolide lactam, poecillastrin A (**108**) from the sponge *Poecillastra* sp. The study was complicated by the need for extensive ^{1}H–^{13}C HMBC data to assemble the structure and a sample of 800 μg (0.55 μmol).

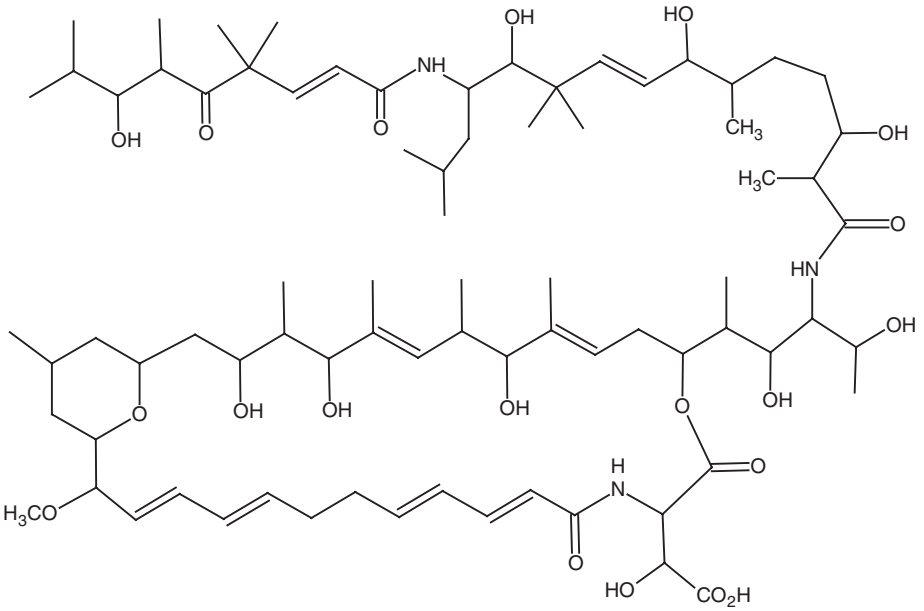

108

In the study of larger molecules, Hernández and LeMaster[245] reported the use of 3D heteronuclear long-range coupling data acquired using cryoprobe technology for the analysis of oligosaccharides. Wüthrich *et al.*[246] reported using cryogenic probe technology in making the side-chain assignments in the membrane protein OmpX in reconstituted micelles. Montelione *et al.*[247] reported using cryogenic probe technology in tandem with a set of integrated computer analysis tools to rapidly determine protein backbone resonance assignments. Brann and co-workers[248] employed a ^{19}F cryoprobe in their studies of the role of domain–domain interactions in the folding of the chaperone PapD. Finally, the last large molecule cryoprobe application of which the author is aware in 2002 was the reported use of reduced dimensionality triple resonance NMR experiments by Montelione[249] for high-throughput protein resonance assignment.

Studies utilizing cryogenic flow or more simply cryoflow probes began to appear in 2003. Corcoran *et al.*[250] first reported on the utilization of cryoflow probe technology for the analysis of acetaminophen metabolites in urine. Their work was followed later that year by an interesting study reported by Exarchou *et al.*[251] that utilized an LC-UV-solid-phase extraction-NMR-MS combination employing a cryoflow probe for the identification of compounds present in Greek oregano.

Griffin, in a review of metabonomics, also notes the impact of cryogenic probe capabilities.[252]

As would be expected, several additional applications of cryoprobe technology in the area of biomacromolecular NMR were also published. Goger *et al.*[253] described the reduction in time required for the acquisition of triple resonance NMR experiments performed on proteins. Later in the year, Craik *et al.*[254] reported a study of the 21 amino acid bacterial peptide microcin J25 that relied on cryoprobe technology. In late 2003, Bertini and co-workers[255] reported the application of cryoprobe-based ^{13}C direct-detection NMR experiments on a paramagnetic oxidized superoxide dismutase.

A number of natural product studies reported in 2003 also utilized cryoprobe technology. Among the studies reported, Griesinger *et al.*[256] addressed the measurement of long-range proton–carbon couplings in natural products in orienting media.

In a study from the author's laboratory, the structure of the complex "dimeric" indoloquinoline alkaloid quindolinocryptotackieine (**109**) was elucidated.[257] The determination of the structure of the C_{31} alkaloid was complicated by severe overlap in both the proton and carbon spectra, leading to the possibility of extensive chemical shift assignment perturbation. The assignment problem was exacerbated when initially undertaken by a sample too small to allow the acquisition of HSQC-TOCSY data. As shown in Fig. 20, the pairing of COSY and HMQC spectra (Panels A and B) acquired using a conventional 3 mm micro-probe, leads to the possibility of any one of three-protonated carbons being assigned as the vicinal neighbor when the COSY coupling partner is in a particularly congested region of the spectrum. In contrast, the IDR HSQC-TOCSY spectrum recorded using a 3 mm sample coaxially in a 5 mm cryogenic probe (Panel C) obviates many of the misassignment problems. Never-the-less, it was still necessary to resort to ACD's Structure Elucidator Computer Software to complete the assembly of the structure.

Fig. 20. Alternative strategies to solve complex structural problems as a function of probe technology. Panels A and B, a COSY and non-gHMQC spectrum, respectively, were acquired a number of years ago using conventional 3 mm micro-inverse-detection NMR probe capabilities. With the sample available at the time, there was not enough sensitivity to do anything more demanding than the acquisition of an HMBC spectrum. In contrast, the gHSQC-TOCSY spectrum shown in Panel C was acquired more recently using significantly less sample despite overall experiment sensitivity that is only one half to one quarter that of an HMBC experiment. The original data show a correlation (shaded box) between a pair of protons in one of the four-spin aromatic spin systems contained in the molecule. The vicinal coupling partner of the resonance furthest upfield resonates in a congested region of the proton spectrum, and the corresponding carbon could presumably be any one of the three ^{13}C resonances in the shaded area of the HMQC spectrum shown in Panel B, leading to a potentially ambiguous assignment. In contrast, the shaded area of the gHSQC-TOCSY spectrum shows that the upfield proton in the COSY spectrum (Panel A) correlates with the proton attached to the carbon resonating at approximately 132 ppm, allowing an unequivocal assignment to be made. While it is not always desirable to run more "exotic" experiments to solve a problem there are cases where the availability of data from such experiments can make certain assignments considerably more straightforward.

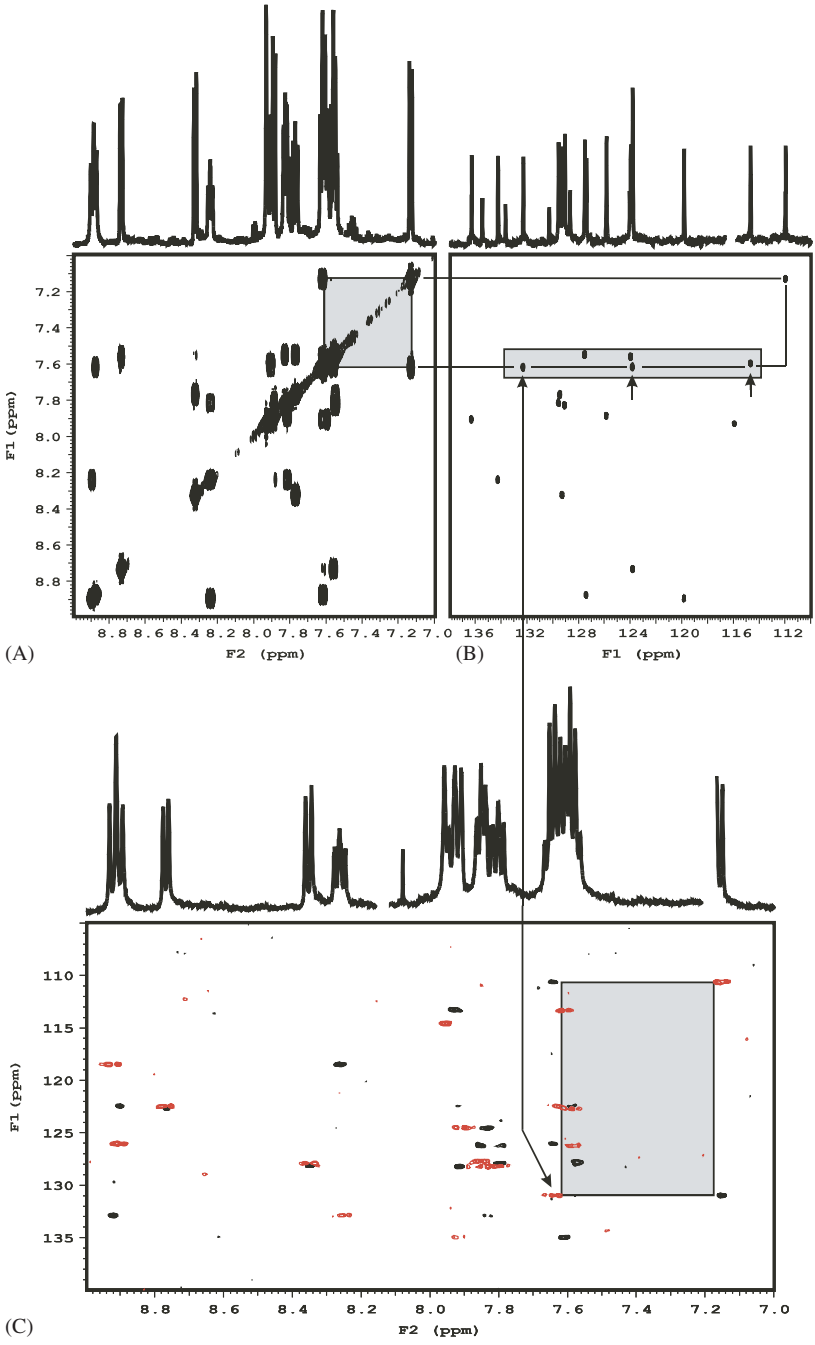
F1 (ppm)
7.2
7.4
7.6
7.8
8.0
8.2
8.4
8.6
8.8
8.8 8.6 8.4 8.2 8.0 7.8 7.6 7.4 7.2 7.0
F2 (ppm)
(A)
136 132 128 124 120 116 112
F1 (ppm)
(B)
F1 (ppm)
110
115
120
125
130
135
8.8 8.6 8.4 8.2 8.0 7.8 7.6 7.4 7.2 7.0
F2 (ppm)
(C)

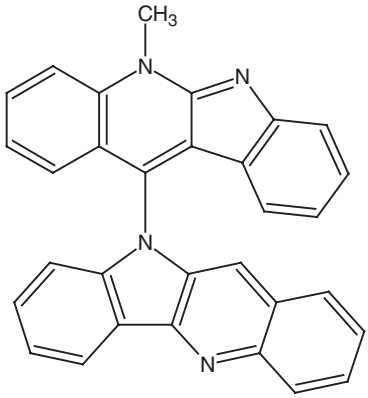

109

A second natural product study reported in 2003 that used the sensitivity of cryogenic probe capabilities and the HSQC-TOCSY experiment to advantage was the report by Preiss *et al.*[258] that detailed the elucidation of the structure of two new asterosaponins from the starfish *Asterias rubens*. The structure of one of the molecules characterized (**110**) of which only 0.3 mg was isolated, is shown.

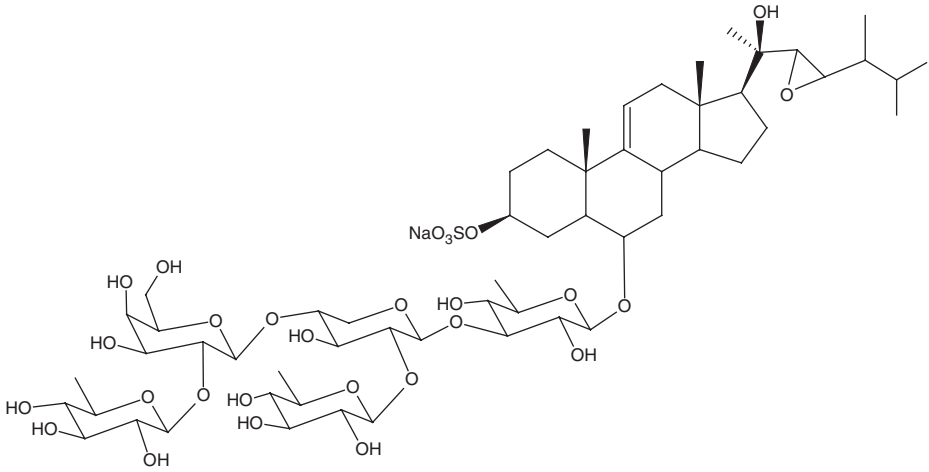

110

Several metabolically oriented reports capitalizing on the sensitivity of cryogenic probe technology also appeared in 2003. Stöckigt *et al.*[259] were able to follow the biosynthesis of ajmaline and its subsequent degradation to raumacline in hybrid cell suspension cultures of *Rawolfia* and *Rhazay* with unlabeled material. Bertini and co-workers[260] utilized the sensitivity of a 600 MHz cryoprobe to follow the degradation of aromatic compounds by a strain of *Pseudomonas putida*. Finally, Griffin

and colleagues[261] used a ^{13}C dual cryoprobe follow the compartmentation of metabolism of doubly labeled alanine.

Moskau and Zerbe[262] in a general review of cryoprobe hardware and performance also detailed ways of quickly recognizing component malfunction in cryogenic probe systems, which from the author's own experience is an area from which others might benefit.

Large molecule cryoprobe applications predominated during 2004. The only other paper of which the author is aware was a study by Godejohann *et al.*[263] involving a study of the metabolism of paracetamol using online LC-SPE-NMR-MS which utilized a cryoflow probe.

Fernandez and Jahnke [264] discussed new approaches for NMR screening in drug discovery involving the use of cryogenic NMR probe technology to improve sensitivity and throughput. Shu and Frieden[265] reported the results of a study of the urea-dependent unfolding of murine adenosine deaminase labeled with 6-^{19}F-tryptophan that employed a ^{19}F cryoprobe. Petros *et al.*[266] described a study of the p53 DNA-binding domain/Bcl-x_L-binding interface using cryoprobe NMR capabilities. Using the capabilities of a ^{13}C optimized cryoprobe, Bertini *et al.*[267] described a ^{13}C–^{13}C NOESY experiment as a supplement to transverse rotating-frame overhauser enhancement spectroscopy (TROSEY) and related experiments for the study of large biomacromolecules. Armengod, Celda and co-workers[268] utilized cryoprobe capabilities in making the backbone ^{1}H, ^{13}C, and ^{15}N resonance assignments for the 18.7 kDa GTPase domain of *E. coli* MnmE protein. Wider *et al.*[269] described the NMR structure of the integral membrane protein OmpX from *E. coli*, followed by a report by Germann *et al.*[270] describing the solution structure of a DNA duplex containing an α-anomeric adenosine. Finally, Volkman *et al.*[271] presented a paper in late 2004, described a procedure for automating protein NMR data collection using cryogenic NMR probes as a part of their efforts to further populate protein fold space.

7. CONCLUSIONS

The development of high-sensitivity NMR probes in various formats and sizes has had considerably increased visibility and interest on the part of the NMR community since the first reports on the development of 3 mm micro-NMR probes in late 1991 from the authors laboratories at what was then the Burroughs Wellcome, Co., in North Carolina. Sensitivity gains have been aggressively pursued and it is now possible, even with conventional small-volume NMR probes to acquire proton spectra of submicrogram quantities of material and inverse-detected 2D-NMR spectra on samples of only a few micrograms in reasonable periods of time. The development of Nano-probes has opened new avenues of investigation for heterogeneous samples and the monitoring of the progress of synthetic reactions on solid-phase support resins. Most recently, cryogenic NMR probe technology has become commercially viable and is now becoming available in increasing numbers of

laboratories throughout the world. Not surprisingly, the highest initial concentrations of these capabilities are in laboratories within the pharmaceutical industry and in laboratories devoted to biomacromolecular NMR. The impact that cryogenic NMR probes of various types will have on the development and metabolism of new drugs, the identification of forensic samples, and on the study of the structures of proteins and nucleic acids will be interesting indeed to follow over the next few years.

REFERENCES

1. L. Müller, *J. Am. Chem. Soc.*, 1979, **101**, 4481.
2. G. Bodenhausen and D. J. Ruben, *Chem. Phys. Lett.*, 1980, **69**, 185.
3. A. Bax, R. H. Griffey and B. L. Hawkins, *J. Magn. Reson.*, 1983, **55**, 301.
4. E. Odelblad, *Nordisk Forening, for Obsterik och Gyynekologi*, Karolinska Institute, Stockholm, 1966.
5. J. N. Shoolery, Small coils for NMR microsamples, G. C. Levy ed., *Topics in Carbon-13 NMR Spectroscopy*, Vol. 3, Wiley Interscience, New York, 1979, pp. 28–38.
6. R. C. Crouch and G. E. Martin, *J. Nat. Prod.*, 1992, **55**, 1343.
7. R. C. Crouch and G. E. Martin, *Magn. Reson. Chem.*, 1992, **30**, S66.
8. G. E. Martin and D. J. Russell, Unpublished results reported in a presentation at the *SMASH Small Molecule NMR Meeting*, Argonne National Laboratory, August, 2000.
9. W. F. Reynolds and R. G. Enriquez, *Magn. Reson. Chem.*, 2001, **39**, 531.
10. D. J. Russell, Unpublished data, 2001.
11. G. E. Martin, R. C. Crouch and A. P. Zens, *Magn. Reson. Chem.*, 1998, **36**, 551.
12. G. E. Martin, J. E. Guido, R. H. Robins, M. H. M. Sharaf, P. L. Schiff Jr. and A. N. Tackie, *J. Nat. Prod.*, 1998, **61**, 555.
13. G. E. Martin and C. E. Hadden, *Magn. Reson. Chem.*, 1999, **37**, 721.
14. G. Schlotterbeck, A. Ross, R. Hochstrasser, H. Senn, T. Kuhn, D. Marek and O. Schett, *Anal. Chem.*, 2002, **74**, 4464.
15. T. Barbara, *J. Magn. Reson.*, 1994, **109A**, 265.
16. J. N. Shoolery, *Prog. NMR Spectrosc.*, 1995, **28**, 37.
17. P. A. Keifer, L. Baltusis, D. M. Rice, A. A. Tymiak and J. N. Shoolery, *J. Magn. Reson.*, 1996, **119A**, 65.
18. G. E. Martin and R. C. Crouch, unpublished data, 1995.
19. G. E. Martin, Microprobes and methodologies for spectral assignments: applications, in *Encyclopaedia of Nuclear Magnetic Resonance*, Vol. 9: Advances in NMR, D. M. Grant and R. K. Harris, eds., John Wiley & Sons Ltd., Chichester, 2002, pp. 98–112.
20. S. M. Musser, R. M. Eppley, E. P. Mazzola, C. E. Hadden, J. P. Shockcor, R. C. Crouch and G. E. Martin, *J. Nat. Prod.*, 1995, **58**, 1392.
21. P. A. Keifer, L. Baltusis, D. M. Rice, A. A. Tymiak and J. N. Shoolery, *J. Magn. Reson., Ser. A.*, 1996, **119**, 65.
22. S. K. Sarkar, R. S. Garigipati, J. L. Adams and P. A. Keifer, *J. Am. Chem. Soc.*, 1996, **118**, 2305.
23. P. A. Keifer, *J. Org. Chem.*, 1996, **61**, 1558.
24. N. Wu, T. Peck, A. G. Webb, R. L. Magin and J. V. Sweedler, *J. Am. Chem. Soc.*, 1994, **116**, 7929.
25. N. Wu, T. L. Peck, A. G. Webb, R. L. Magin and J. V. Sweedler, *Anal. Chem.*, 1994, **66**, 3849.
26. N. Wu, A. Webb, T. L. Peck and J. V. Sweedler, *Anal. Chem.*, 1995, **67**, 3101.
27. D. L. Olson, T. L. Peck, A. G. Webb, R. L. Magin and J. V. Sweedler, *Science*, 1995, **270**, 1967.
28. R. Subramanian and A. G. Webb, *Anal. Chem.*, 1998, **70**, 2454.
29. D. L. Olson, M. E. Lacey and J. V. Sweedler, *Anal. Chem.*, 1998, **70**, 645.
30. Y. Li, A. M. Wolters, P. V. Malawey, J. V. Sweedler and A. G. Webb, *Anal. Chem.*, 1999, **71**, 4815.
31. A. M. Wolters, D. A. Jayawickrama, A. G. Webb and J. V. Sweedler, *Anal. Chem.*, 2002, **74**, 5550.

32. D. A. Jayawickrama and J. V. Sweedler, *Anal. Chem.*, 2004, **76**, 4894.
33. A. M. Wolters, D. A. Jayawickrama, C. K. Larive and J. V. Sweedler, *Anal. Chem.*, 2002, **74**, 4191.
34. P. Styles, N. F. Soffe, C. A. Scott, D. A. Cragg, F. Row, D. White and P. C. J. White, *J. Magn. Reson.*, 1983, **60**, 397.
35. P. Styles., N. F. Soffe. and C. A. Scott., *J. Magn. Reson.*, 1989, **84**, 376.
36. W. A. Anderson, W. W. Brey, A. L. Brooke, B. Cole, K. A. Delin, L. H. Fuks, H. D. W. Hill, M. E. Johanson, V. Y. Kotsubo, R. Nast, R. S. Withers and W. H. Wong, *Bull. Magn. Reson.*, 1995, **17**, 98.
37. H. D. W. Hill, *IEEE Trans. Appl. Superconduct.*, 1997, **7**, 3750.
38. M. Jerosch-Herold and R. K. Kirschman, *J. Magn. Reson.*, 1989, **85**, 141.
39. A. E. Kelly, H. D. Ou, R. Withers and V. Dötsch, *J. Am. Chem. Soc.*, 2002, **124**, 12013.
40. D. I. Hoult and D. E. Richards, *J. Magn. Reson.*, 1976, **24**, 71.
41. D. I. Hoult and P. C. Lauterbur, *J. Magn. Reson.*, 1979, **34**, 425.
42. D. R. Gadian and F. N. H. Robinson, *J. Magn. Reson.*, 1979, **34**, 449.
43. D. Hoult, in *Encyclopaedia of Nuclear Magnetic Resonance*, Vol. 7, 1996, 4256–4266.
44. D. Avizonas and T. de Sweit, Private communication, 2004.
45. P. J. Hajduk, T. Gerfin, J. M. Bohlen, M. Häberli, D. Marek and S. W. Fesik, *J. Med. Chem.*, 1999, **42**, 2315.
46. Z. Serber, C. Richter, D. Moskau, J. -M. Böhlen, T. Gerfin, D. Marek, M. Häberli, L. Baselgia, F. Laukien, A. S. Stern, J. C. Hoch and V. Dötsch, *J. Am. Chem. Soc.*, 2000, **122**, 3554.
47. D. J. Russell, C. E. Hadden, G. E. Martin, A. A. Gibson, A. P. Zens and J. L. Carolan, *J. Nat. Prod.*, 2000, **63**, 1047.
48. Z. Serber, C. Richter and V. Dötsch, *ChemBioChem*, 2001, **2**, 247.
49. M. Köck, J. Junker and T. Lindel, *Org. Lett.*, 1999, **1**, 2041.
50. R. C. Crouch, W. Llanos, K. G. Mehr, C. E. Hadden, D. J. Russell and G. E. Martin, *Magn. Reson. Chem.*, 2001, **39**, 555.
51. C. E. Hadden, G. E. Martin and V. V. Krishnamurthy, *Magn. Reson. Chem.*, 2000, **38**, 143.
52. M. E. Lacey, R. Subramanian, D. L. Olson, A. G. Webb and J. V. Sweedler, *Chem. Rev.*, 1999, **99**, 3133.
53. P. A. Keifer, *Prog. Drug Res.*, 2000, **55**, 137.
54. P. A. Keifer, The NMR "Toolkit" for compound characterization, in *Integrated Drug Discovery Technologies*, H. -Y. Mei and A. W. Czarnik, eds., Marcel Dekker, New York, 2002, pp. 485–541.
55. A. M. Wolters, D. A. Jayawickrama and J. V. Sweedler, *Curr. Opin. Chem. Biol.*, 2002, **6**, 711.
56. M. Delepierre, High-Resolution NMR of Venom toxins in nanomolar amounts, *Persp. Molec. Toxicol.*, A. Menez, ed., John Wiley, Chichester, 2002, pp. 125–139.
57. D. A. Jayawickrama and J. V. Sweedler, *J. Chromatogr., A*, 2003, **100**, 819.
58. O. D. Hensens, G. L. Helms, D. L. Zink, D. -H. Chin, L. S. Kappen and I. H. Goldberg, *J. Am. Chem. Soc.*, 1993, **115**, 11030.
59. R. Wurm, J. P. Shockcor, I. S. Silber, R. C. Crouch and G. E. Martin, *Tet. Lett.*, 1994, **35**, 4019.
60. R. E. Schwartz, G. L. Helms, E. A. Boless, K. E. Wilson, R. A. Giacobbe, J. S. Tkacz, G. F. Bills, J. M. Liesch, D. L. Zink, J. E. Curotto, B. Ramanik and J. C. Onishi, *Tetrahedron*, 1995, **50**, 1675.
61. M. H. M. Sharaf, P. L. Schiff Jr., A. N. Tackie, C. H. Phoebe Jr., L. Howard, C. Meyers, C. E. Hadden, S. K. Wrenn, A. O. Davis, C. W. Andrews, D. Minick, R. L. Johnson, J. P. Shockcor, R. C. Crouch and G. E. Martin, *Magn. Reson. Chem.*, 1995, **33**, 767.
62. R. C. Crouch, G. E. Martin, R. W. Dickey, D. G. Baden, R. E. Gawley, K. S. Rein and E. P. Mazzola, *Tet. Lett.*, 1995, **36**, 8409.
63. R. C. Crouch, G. E. Martin, S. M. Musser, H. R. Grenade and R. W. Dickey, *Tet. Lett.*, 1995, **36**, 6827.
64. R. J. Lewis, J. -P. Vernoux and I. M. Brereton, *J. Am. Chem. Soc.*, 1998, **120**, 5914.
65. R. C. Crouch, A. O. Davis, T. D. Spitzer, G. E. Martin, M. H. M. Sharaf, P. L. Schiff Jr., C. H. Phoebe Jr. and A. N. Tackie, *J. Heterocycl. Chem.*, 1995, **32**, 1077–1080.
66. M. H. M. Sharaf, P. L. Schiff Jr., A. N. Tackie, C. H. Phoebe Jr., A. O. Davis, C. W. Andres, R. C. Crouch and G. E. Martin, *J. Heterocycl. Chem.*, 1995, **32**, 1631.

67. A. N. Tackie, G. L. Boye, M. H. M. Sharaf, P. L. Schiff Jr., R. C. Crouch, T. D. Spitzer, R. L. Johnson, J. Dunn, D. Minick and G. E. Martin, *J. Nat. Prod.*, 1993, **56**, 653.
68. I. I. Ohtani, T. Ichiba, M. Isobe, M. Kelly-Borges and P. J. Scheuer, *J. Am. Chem. Soc.*, 1995, **117**, 10743.
69. A. Bax, R. Freeman and S. P. Kempsell, *J. Am. Chem. Soc.*, 1980, **102**, 4849.
70. A. Bax, R. Freeman and T. H. Frenkiel, *J. Am. Chem. Soc.*, 1981, **103**, 2102.
71. D. Choi, B. Yoo, K. L. Colson, G. E. Martin and H. L. Kohn, *J. Org. Chem.*, 1995, **60**, 3391.
72. M. H. M. Sharaf, P. L. Schiff Jr., A. N. Tackie, C. H. Phoebe Jr. and G. E. Martin, *J. Heterocycl. Chem.*, 1996, **33**, 239.
73. M. H. M. Sharaf, P. L. Schiff Jr., A. N. Tackie, C. H. Phoebe Jr., R. L. Johnson, D. Minick, C. W. Andrews, R. C. Crouch and G. E. Martin, *J. Heterocycl. Chem.*, 1995, **33**, 789.
74. K. N. Drew, T. J. Church, B. Basu, T. Vuorinen and A. S. Serianni, *Carbohydr. Res.*, 1996, **284**, 135.
75. A. Kolbe, B. Schneider, A. Porzel and G. Adam, *Phytochemistry*, 1996, **41**, 163.
76. T. Hai, B. Schneider, A. Porzel and G. Adam, *Phytochemistry*, 1996, **41**, 197.
77. S. M. Musser, M. L. Gay, E. P. Mazzola and R. D. Plattner, *J. Nat. Prod.*, 1996, **59**, 970.
78. P. R. Thompson, D. W. Hughes and G. D. Wright, *Biochemistry*, 1996, **35**, 8686.
80. X. Fu and F. J. Schmitz, *J. Nat. Prod.*, 1996, **59**, 1102.
81. W. F. Reynolds and R. G. Enriquez, *Magn. Reson. Chem.*, 1997, **35**, 614.
82. K. A. Carpenter, W. F. Reynolds, J. -P. Yang and R. G. Enriquez, *Magn. Reson. Chem.*, 1992, **30**, S35.
83. J. G. Ondeyka, G. L. Helms, O. D. Hensens, M. A. Goetz, D. L. Zink, A. Tsipouras, W. L. Hoop, L. Slayton, A. W. Dombrowski, J. D. Polishook, D. A. Ostlind, N. N. Tsou, R. G. Ball and S. B. Singh, *J. Am. Chem. Soc.*, 1997, **119**, 8809.
84. R. Dunkel, C. L. Mayne, J. Curtis, R. J. Pugmire and D. M. Grant, *J. Magn. Reson.*, 1990, **90**, 290.
85. R. Dunkel, C. L. Mayne, R. J. Pugmire and D. M. Grant, *Anal. Chem.*, 1992, **64**, 3133.
86. R. Dunkel, M. L. Mayne, M. P. Foster, C. M. Ireland, D. Li, D. L. Owen, R. J. Pugmire and D. M. Grant, *Anal. Chem.*, 1992, **64**, 3150.
87. J. A. López, W. Barillas, J. Gomez-Laurito, G. E. Martin, A. J. Al-Rehaily, M. A. Zemaitis and P. L. Schiff Jr., *J. Nat. Prod.*, 1997, **60**, 24.
88. K. N. Drew, J. Zajicek, G. Bondo, B. Bose and A. S. Serianni, *Carbohydr. Res.*, 1998, **307**, 199.
89. C. J. Rowe, C. P. Shorrock, T. D. W. Claridge and J. D. Sutherland, *Chem. and Biol.*, 1998, **5**, 229.
90 K. Himmelcirk, B. G. Sayer and I. D. Spenser, *J. Am. Chem. Soc.*, 1998, **120**, 3581.
91. M. H. M. Sharaf, Ph.D. Thesis, University of Pittsburgh, Pittsburgh, PA, 1993, 177–192.
92. M. M. Cooper, J. A. Lovell and J. A. Soule, *Tet. Lett.*, 1996, **37**, 4283.
93. A. Paulo, E. T. Gomes and P. J. Houghton, *J. Nat. Prod.*, 1995, **58**, 1485.
94. M. H. M. Sharaf, P. L. Schiff Jr., A. N. Tackie and G. E. Martin, *J. Heterocycl. Chem.*, 1998, **35**, 1365.
95. G. E. Martin, R. C. Crouch, M. H. M. Sharaf and P. L. Schiff Jr., *J. Nat. Prod.*, 1996, **56**, 2.
96. X. Fu, F. J. Schmitz, R. S. Tanner and M. Kelly-Borges, *J. Nat. Prod.*, 1998, **61**, 384.
97. X. Fu, M. L. G. Ferreira, F. J. Schmitz and M. Kelly-Borges, *J. Nat. Prod.*, 1998, **61**, 1226.
98. D. Wolf and F. J. Schmitz, *J. Nat. Prod.*, 1998, **61**, 1524.
99. G. E. Martin, F. W. Crow, B. D. Kaluzny, J. G. Marr, G. D. Fate and T. J. Gilbertson, *Magn. Reson. Chem.*, 1998, **36**, 635.
100. J. A. López, W. Barila, J. Gomez-Laurito, G. E. Martin, F. -t. Lin, A. J. Al-Rehaily, M. A. Zemaitis and P. L. Schiff Jr., *Planta Med.*, 1998, **64**, 76.
101. R. C. Wimouth, S. Kassamally, N. J. Westwood, R. J. Sheppard, T. D. W. Claridge, R. T. Aplin, P. A. Wright, G. J. Pritchard and C. J. Schofield, *Biochemistry*, 1999, **38**, 7989.
102. H. M. A. M. Qazzaz, M. A. El-Masri, N. J. Stolowich and R. Vales Jr., *Biochem. Biophys. Acta*, 1999, **1472**, 486.
103. W. F. Reynolds, S. McLean, H. Jacobs and W. H. Harding, *Can. J. Chem.*, 1999, **77**, 1922.
104. H. Kessler, C. Griesinger, J. Zarbock and H. R. Loosli, *J. Magn. Reson.*, 1984, **57**, 331.
105. S. J. Lgusch, P. C. C. Feng, H. Fujiwara, W. C. Hutton and S. J. Wratten, *J. Agric. Food Chem.*, 1999, **47**, 2125.

106. S. Rundt, B. Lidner, H. Brade and O. Holst, *J. Biol. Chem.*, 1999, **274**, 16819.
107. G. E. Martin, R. H. Robins, P. B. Bowman, W. K. Duholke, K. A. Farley, B. D. Kaluzny, J. E. Guido, S. M. Sims, T. J. Thamann and B. E. Thompson, *J. Heterocycl. Chem.*, 1999, **36**, 265.
108. F. W. Crow, W. K. Duholke, K. A. Farley, C. E. Hadden, D. A. Hahn, B. D. Kaluzny, C. S. Mallory, G. E. Martin, R. F. Smith and T. J. Thamann, *J. Heterocycl. Chem.*, 1999, **36**, 365.
109. C. E. Hadden, W. K. Duholke, J. E. Guido, R. H. Robins, G. E. Martin, M. H. M. Sharaf and P. L. Schiff Jr., *J. Heterocycl. Chem.*, 1999, **36**, 525.
110. T. Domke, *J. Magn. Reson.*, 1991, **95**, 174.
111. R. C. Crouch, A. O. Davis and G. E. Martin, *J. Heterocycl. Chem.*, 1995, **33**, 889.
112. A. J. Al-Rehaily, M. H. M. Sharaf, M. A. Zemaitis, C. -y. Gao, G. E. Martin, C. E. Hadden, T. J. Thamann, F. -t. Lin and P. L. Schiff Jr., *J. Nat. Prod.*, 1999, **62**, 146.
113. D. Wolf, F. J. Schmitz, M. B. Hossain and D. van der Helm, *J. Nat. Prod.*, 1999, **62**, 167.
114. D. Wolf, F. J. Schmitz, F. Qiu and M. Kelly Borges, *J. Nat. Prod.*, 1999, **62**, 170.
115. H. C. Vervoort, W. Fenical and P. A. Keifer, *J. Nat. Prod.*, 1999, **62**, 389.
116. X. Fu, F. J. Schmitz and G. C. Williams, *J. Nat. Prod.*, 1999, **62**, 584.
117. X. Fu, L. Zeng, J. Su and F. J. Schmitz, *J. Nat. Prod.*, 1999, **62**, 644.
118. X. Fu, M. L. G. Ferreira, F. J. Schmitz and M. Kelly, *J. Nat. Prod.*, 1999, **62**, 1190.
119. X. Fu, M. L. G. Ferreira and F. J. Schmitz, *J. Nat. Prod.*, 1999, **62**, 1306.
120. X. Fu, F. J. Schmitz and M. Kelly, *J. Nat. Prod.*, 1999, **62**, 1336.
121. P. K. Freeman and J. K. Pugh, *J. Org. Chem.*, 1999, **64**, 3947.
122. G. E. Martin, C. E. Hadden, J. R. Blinn, M. H. M. Sharaf, A. N. Tackie and P. L. Schiff Jr., *Magn. Reson. Chem.*, 1999, **37**, 1.
123. E. Kolehmainen, J. Koivisto, K. Laihia, R. Kauppinen and J. Passivirta, *Magn. Reson. Chem.*, 1999, **37**, 359.
124. B. Wilkinson, G. Foster, B. A. M. Rudd, N. L. Taylor, A. P. Blackaby, P. J. Sidebottom, D. J. Cooper, M. J. Dawson, A. D. Buss, S. Gaisser, I. U. Böhm, C. J. Rowe, J. Cortés, P. F. Leadlay and J. Staunton, *Chem. Biol.*, 2000, **7**, 111.
125. M. M. Bergana, J. D. Holdon, I. L. Reyzer, M. K. Snowden, J. H. Baxter and F. L. Pound, *J. Agric. Food Chem.*, 2000, **48**, 6003.
126. C. E. Hadden, G. E. Martin, J. -K. Luo and R. N. Castle, *J. Heterocycl. Chem.*, 2000, **37**, 821.
127. C. E. Hadden, P. B. Bowman, W. H. Duholke, J. E. Guido, B. D. Kaluzny, R. H. Robbins, D. J. Russell, S. M. Sims, T. J. Thamann and G. E. Martin, *J. Heterocycl. Chem.*, 2000, **37**, 1623.
128. M. M. Bednarek, S. D. Feighner, S. -S. Pong, K. K. McKee, D. L. Hreniuk, M. V. Silva, V. A. Warren, A. D. Howard, L. H. Y. Van der Ploeg and J. V. Heck, *J. Med. Chem.*, 2000, **43**, 4370.
129. D. J. Williams and K. B. Hall, *J. Molec. Biol.*, 2000, **297**, 1045.
130. D. Hölscher and B. Schneider, *J. Nat. Prod.*, 2000, **63**, 1027.
131. K. Y. Orabi, L. A. Walker, A. M. Clark and C. D. Hufford, *J. Nat. Prod.*, 2000, **63**, 685.
132. D. J. Russell, C. E. Hadden, G. E. Martin, A. A. Gibson, A. P. Zenz and J. L. Carolan, *J. Nat. Prod.*, 2000, **63**, 1047.
133. J. H. Kwak, F. J. Schmitz and M. Kelly, *J. Nat. Prod.*, 2000, **63**, 1153.
134. H. Junicke, A. S. Serianni and D. Steinborn, *J. Org. Chem.*, 2000, **65**, 4153.
135. A. Satake, *J. Syn. Org. Chem. Jpn.*, 2000, **58**, 736.
136. G. E. Martin and C. E. Hadden, *Magn. Reson. Chem.*, 2000, **38**, 251.
137. E. B. Skibo, C. Xing and T. Groy, *Bioorg. Med. Chem.*, 2001, **9**, 2445.
138. D. J. Mitchell, D. Nikolic, E. Rivera, S. O. Sablin, S. Choi, R. B. van Breemen, T. P. Singer and R. B. Silverman, *Biochemistry*, 2001, **40**, 5447.
139. R. N. Gupta, T. Hemscheidt, B. G. Sayer and I. D. Spenser, *J. Am. Chem. Soc.*, 2001, **123**, 11353.
140. J. -R. Dai, B. K. Carte, P. J. Sidebottom, A. L. S. Yew, S. -B. Ng, Y. Huang and M. S. Butler, *J. Nat. Prod.*, 2001, **64**, 125.
141. G. M. Nicholas, J. W. Blunt and M. H. G. Munro, *J. Nat. Prod.*, 2001, **64**, 341.
142. J. H. Kwak, F. J. Schmitz and G. C. Williams, *J. Nat. Prod.*, 2001, **64**, 754.
143. T. A. Al-Wowiriny, M. A. Zemaitis, C. -y. Gao, C. E. Hadden, G. E. Martin, F. -t. Lin and P. L. Schiff Jr., *J. Nat. Prod.*, 2001, **64**, 819.

144. T. A. Al-Howiriny, M. A. Zemaitis, C. -y. Gao, C. E. Hadden, G. E. Martin, F. -t. Lin and P. L. Schiff Jr., *J. Nat. Prod.*, 2001, **64**, 823.
145. J. Bradshaw, D. Butina, D. J. Dunn, R. H. Green, M. Hajek, M. M. Jones, J. C. Lindon and P. J. Sidebottom, *J. Nat. Prod.*, 2001, **64**, 1541.
146. W. F. Reynolds and R. G. Enriquez, *J. Nat. Prod.*, 2002, **65**, 221.
147. Z. Hojati, C. Milne, B. Harvey, L. Gordon, M. Borg, F. Flett, B. Wilkinson, P. J. Sidebottom, B. A. M. Rudd, M. A. Hayes, C. P. Smith and J. Micklefield, *Chem. Biol.*, 2002, **9**, 1175.
148. J. G. Duman and A. S. Serianni, *J. Insect Phys.*, 2002, **48**, 103.
149. N. H. Oberlies, J. P. Burgess, H. A. Navarro, R. E. Pinos, C. R. Fairchiled, R. W. Peterson, D. D. Soejarto, N. R. Farnsworth, A. D. Kinghorn, M. C. Wani and M. E. Wall, *J. Nat. Prod.*, 2002, **65**, 95.
150. J. H. Kwak, F. J. Schmitz and G. C. Williams, *J. Nat. Prod.*, 2002, **65**, 704.
151. S. Opitz, D. Hölscher, N. J. Oldham, S. Bartram and B. Schneider, *J. Nat. Prod.*, 2002, **65**, 1122.
152. K. W. Sigvardson, S. P. Adams, T. B. Barnes, K. F. Blom, J. M. Fortunak, M. J. Haas, K. L. Reilly, A. J. Repta and G. A. Nemeth, *J. Pharm. Biomed. Anal.*, 2002, **27**, 327.
153. M. G. Soars, E. L. Mattiuz, D. A. Jackson, P. Kulanthaivel, W. J. Ehlhardt and S. A. Wrighton, *J. Pharmacol. Toxicol. Meth.*, 2002, **47**, 161.
154. R. H. Schuler, G. Albarran, J. Zajicek, M. V. George, R. W. Fessenden and I. Carmichael, *J. Phys. Chem. A*, 2002, **106**, 12178.
155. G. B. Wisely, A. B. Miller, R. G. Davis, A. D. Thornquest Jr., R. Johnson, T. Spitzer, A. Sefler, B. Shearer, J. T. Moore, A. B. Miller, T. M. Willson and S. P. Williams, *Structure*, 2002, **10**, 1225.
156. F. Arnesano, L. Banci, I. Bertini and A. R. Thompsett, *Structure*, 2002, **10**, 1337.
157. X. -C. Li, A. S. Joshi, B. Tan, H. N. El Sohly, L. A. Walker, J. K. Zjawiony and D. Ferreira, *Tetrahedron*, 2002, **58**, 8709.
158. S. C. Burgess, B. Weis, J. G. Jones, E. Smith, M. E. Merritt, D. Margolis, A. D. Sherry and C. R. Malloy, *Anal. Biochem.*, 2003, **312**, 228.
159. J. A. Hankin, D. N. M. Jones and R. C. Murphy, *Chem. Res. Toxicol.*, 2003, **16**, 551.
160. M. Pollack, T. Oe, S. H. Lee, M. V. S. Elipe, B. H. Arison and I. A. Blair, *Chem. Res. Toxicol.*, 2003, **16**, 893.
161. T. Oe, S. H. Lee, M. V. S. Elipe, B. H. Arison and I. A. Blair, *Chem. Res. Toxicol.*, 2003, **16**, 1598.
162. C. E. Hadden, D. J. Richard, M. M. Joullié and G. E. Martin, *J. Heterocycl. Chem.*, 2003, **40**, 359.
163. K. Schmidt, U. Riese, Z. Li and M. Hamburger, *J. Nat. Prod.*, 2003, **66**, 378.
164. A. S. R. Anjaneyulu, V. L. Rao, V. G. Sastry, M. J. R. V. Venugopal and F. J. Schmitz, *J. Nat. Prod.*, 2003, **66**, 507.
165. G. R. Petit, J. C. Collins, J. C. Knight, D. L. Herald, R. A. Nieman, M. D. Williams and R. K. Pettit, *J. Nat. Prod.*, 2003, **66**, 544.
166. R. W. Fitch, H. M. Garraffo, T. F. Spande, H. J. C. Yeh and J. W. Daly, *J. Nat. Prod.*, 2003, **66**, 1345.
167. S. Roemmelt, N. Zimmermann, W. Rademacher and D. Treutter, *Phytochem.*, 2003, **64**, 709.
168. B. Dean, S. Chang, G. A. Doss, C. King and P. E. Thomas, *Arch. Biochem. Biophys.*, 2004, **429**, 244.
169. I. O. Vveden Skaya, R. T. Rosen, J. E. Guido, D. J. Russell, K. A. Mills and N. Vorsa, *J. Agric. Food Chem.*, 2004, **52**, 188.
170. T. Murakami, Y. Takahashi, E. Fukushi, J. Kawabata, M. Hashimoto, T. Okuno and Y. Harada, *J. Am. Chem. Soc.*, 2004, **126**, 9214.
171. A. Pohanka, K. Capieau, A. Broberg, J. Stenlid, E. Strenström and L. Kenne, *J. Nat. Prod.*, 2004, **67**, 851.
172. J. -Q. Gu, T. N. Graf, D. Lee, H. -B. Chai, Q. Mi, L. B. S. Kardono, F. M. Setyowati, R. Ismail, S. Riswan, N. R. Fransworth, G. A. Cordll, J. M. Pezzuto, S. M. Swanson, D. J. Kroll, J. O. Falkinham III, M. E. Wall, M. C. Wani, A. D. Kinghorn and N. H. Oberlies, *J. Nat. Prod.*, 2004, **67**, 1156.
173. X. Fu, A. J. Palomar, E. P. Hong, F. J. Schmitz and F. A. Valeriote, *J. Nat. Prod.*, 2004, **67**, 1415.

174. K. M. Alsante, P. Boutros, M. A. Couturier, R. C. Friedmann, J. W. Harwood, G. J. Horan, A. J. Jensen, Q. Lium, L. L. Lohr, R. Morris, J. W. Raggon, G. L. Reid, D. P. Santafianos, T. R. Sharp, J. L. Tucker and G. E. Wilcox, *J. Pharm. Sci.*, 2004, **93**, 2296.
175. T. te S. Bugni, M. P. Singh, L. Chen, D. A. Arias, M. K. Harper, M. Greenstein, W. M. Maiese, G. P. Concepción, G. C. Mangalindan and C. M. Ireland, *Tetrahedron*, 2004, **60**, 6981.
176. C. E. Hadden, B. D. Kaluzny, R. H. Robins and G. E. Martin, *J. Heterocycl. Chem.*, 1999, **37**, 325.
177. K. A. Farley, P. B. Boman, J. C. Brumfield, F. W. Crow, W. K. Duholke, J. E. Guido, R. H. Robins, S. M. Sims, R. F. Smith, T. J. Thamann, B. S. Vonderwell and G. E. Martin, *Magn. Reson. Chem.*, 1998, **36**, S11.
178. G. E. Martin, C. E. Hadden, J. R. Blinn, M. H. M. Sharaf, A. N. Tackie and P. L. Schiff Jr., *Magn. Reson. Chem.*, 1999, **36**, 1.
179. G. E. Martin, B. A. Pearlman, R. H. Robins, F. W. Crow, W. K. Duholke, J. E. Guido, C. E. Hadden, B. D. Kaluzny and T. J. Thamann, *J. Heterocycl. Chem.*, 1999, **36**, 1107.
180. T. Zincke, *Liebigs Ann. Chem.*, 1903, **330**, 361.
181. C. E. Hadden, G. E. Martin, A. N. Tackie and P. L. Schiff Jr., *J. Heterocycl. Chem.*, 1999, **36**, 1115.
182. G. E. Martin and C. E. Hadden, *Magn. Reson. Chem.*, 2000, **38**, 251.
183. C. E. Hadden, W. K. Duholke, B. D. Kaluzny, P. E. Sanders, T. J. Thamann, K. Rosenqvist, G. E. Martin, B. C. Robinson and M. N. Masuno, *J. Heterocycl. Chem.*, 2003, **40**, 389.
184. C. E. Hadden, G. E. Martin and V. V. Krishnamurthy, *J. Magn. Reson.*, 1999, **140**, 274.
185. J. L. Griffin, A. W. Nicholls, H. C. Keun, R. J. Mortishire-Smikth, J. K. Nicholson and T. Kuehn, *Analyst*, 2002, **127**, 582.
186. M. O'Neil-Johnson, Can I get a structure on 50 micrograms? Metabolites, natural products and proteins using a CapNMR probe, *226th ACS National Meeting*, New York, NY, September 7–11, 2003, Abstract CHED-123.
187. W. Peti, J. Norcross, G. Eldridge and M. O'Neil-Johnson, *J. Am. Chem. Soc.*, 2004, **126**, 5873.
188. W. L. Fitch, G. Detre, C. P. Holmes, J. N. Shoolery and P. A. Keifer, *J. Org. Chem.*, 1994, **59**, 7955.
189. A. Manzi, P. V. Salimath, R. C. Spiro, P. A. Keifer and H. H. Freeze, *J. Biol. Chem.*, 1995, **270**, 9154.
190. T. Wehler and J. Westman, *Tetrahedron Lett.*, 1996, **37**, 4771.
191. M. Pursch, G. Schlotterbeck, L. -H. Tseng, K. Albert and W. Rapp, *Angew. Chem. Int. Ed.*, 1996, **35**, 2867.
192. D. C. Chauret, T. Durst, J. T. Amason, P. Sanchez-Vindas, L. San Roman, L. Poveda and P. A. Keifer, *Tetrahedron Lett.*, 1996, **37**, 7875.
193. D. Klein, J. -C. Braekman, D. Daloze, L. Hoffmann and V. Demoulin, *Tetrahedron Lett.*, 1996, **37**, 7519.
194. M. Delepierre, A. Prochnicka-Chalufour and L. D. Possani, *Biochemistry*, 1997, **36**, 2649.
195. P. Roux, M. Delepierre, M. E. Goldberg and A. -F. Chaffotte, *J. Biol. Chem.*, 1997, **272**, 24843.
196. A. E. Manzi and P. A. Keifer, New frontiers in nuclear magnetic resonance spectroscopy: use of a nano NMR probe for the analysis of microgram quantities of complex carbohydrates, in *Techniques in Glycobiology*, T. R. Reid and R. T. Arland Jr., eds., Dekker, NY, 1997, pp. 1–16.
197. P. A. Keifer, *Drug Discov. Today*, 1997, **2**, 468.
198. M. Delepierre, A. Prochnicka-Chalufour and L. D. Possani, *Toxicon*, 1998, **36**, 1599.
199. M. Delepierre, P. Roux, A. -F. Chaffotte and M. E. Goldberg, *Magn. Reson. Chem.*, 1998, **36**, 645.
200. M. Delepierre, *J. Chim. Phys.*, 1998, **95**, 235.
201. D. M. Fort, J. Litvak, J. L. Chen, Q. Lu, P. -W. Phuan, R. Cooper and D. E. Bierer, *J. Nat. Prod.*, 1998, **61**, 1528.
202. P. A. Keifer, *Curr. Opin. Biotech.*, 1999, **10**, 34.
203. D. Klein, J. -C. Braekman, D. Daloze, L. Hoffmann, G. Castillo and V. Demoulin, *Tetrahedron Lett.*, 1999, **40**, 695.
204. M. Delepierre, A. Prochnick-Chalufour, J. Boisbouvier and L. D. Possani, *Biochemistry*, 1999, **38**, 16756.
205. T. Mohri, Y. Nakahara, W. Zhang, T. Muneishi, Y. Jiyaji and I. Ikdea, *Chem. Lett.*, 2000, 988.
206. A. M. Sefler and S. W. Gerritz, *J. Comb. Chem.*, 2000, **2**, 127.

207. A. E. Manzi, K. Norgard-Sumnicht, S. Argade, J. D. Marth, H. van Halbeek and A. Varki, *Glycobiology*, 2000, **10**, 669.
208. M. Gilbert, J. -R. Brisson, M. -F. Karwaski, J. Michniwicz, A. –o. M. Cunningham, Y. Wu, N. M. Young and W. W. Wakarchuk, *J. Biol. Chem.*, 2000, **275**, 3896.
209. H. Ferré, A. Broberg, J. Ø. Duus and K. K. Thomsen, *Eur. J. Biochem.*, 2000, **267**, 6633.
210. H. van Halbeek, Glycan profiling of mammalian tissues and cells by homo- and heteronuclear nano-NMR spectroscopy, *221st ACS National Meeting*, San Diego, CA, April 1–5, 2001, Abstract POLY 394.
211. R. -r. Shao, H. -y. Hu, Y. -n. Chen and G. -q. Song, *Bopuxue Zazhi*, 2001, **18**, 235.
212. P. Thibault, S. M. Logan, J. F. Kelly, J. -R. Brisson, C. P. Ewing, T. J. Trust and P. Guerry, *J. Biol. Chem.*, 2001, **276**, 34862.
213. R. G. Gallego, J. L. Jiménez Blanco, C. W. E. M. Thijssen-van Zuylen, C. H. Gotfredsen, H. Voshol, J. Ø. Duus, M. Schachner and J. F. G. Vliegenthart, *J. Biol. Chem.*, 2001, **276**, 30844.
214. E. Kupce, P. A. Keifer and M. Delepierre, *J. Magn. Reson.*, 2001, **148**, 115.
215. M. Namikoshi, K. Akano, S. Meguro, I. Kasuga, Y. Mine, T. Takahashi and H. Kobayashi, *J. Nat. Prod.*, 2001, **64**, 396.
216. M. Delepierre, High-resolution NMR of venom toxins in nanomolar amounts, published in *Perspectives in Molecular Technology*, A. Menez ed., John Wiley & Sons Ltd, Chichester, 2002, pp. 125–139.
217. Y. -h. Wang, W. -y. He, X. -m. Li, B. Li, X. Liu and M. Lin, *Bopuxue Zazhi*, 2002, **19**, 325.
218. A. Fung, R. E. Stark and H. Lujan-Upton, Investigating "hard to cook" syndrome in potatoes using two-dimensional NMR techniques, *226th ACS National Meeting*, New York City, September 7–11, 2003, Abstract AGFD-090.
219. J. Kubanek, P. R. Jensen, P. A. Keifer, M. C. Sulards, D. O. Collins and W. Fenical, *Proc. Natl. Acad. Sci., USA*, 2003, **100**, 6916.
220 W. Nerinckx, A. Broberg, J. Ø. Duus, P. Ntarima, L. A. S. Parolis, H. Parolis and M. Claeyssens, *Carbohydr. Res.*, 2004, **339**, 1047.
221. S. A. Bradley, J. Paschal and P. Kulanthaivel, *Magn. Reson. Chem.*, 2005, **43**, 31.
222. R. Subramanian, J. V. Sweedler and A. G. Webb, *J. Am. Chem. Soc.*, 1999, **121**, 2333.
223. G. R. Eldridge, H. C. Verboort, C. M. Lee, P. A. Cremin, C. T. Williams, S. M. Hart, M. G. Goering, M. O'Neil-Johnson and L. Zeng, *Anal. Chem.*, 2002, **74**, 3963.
224. M. Kakuta, D. A. Jayawickrama, A. M. Wolters, A. Manz and J. V. Sweedler, *Anal. Chem.*, 2003, **75**, 956.
225. W. Peti, J. Norcross, G. Eldridge and M. O'Neil-Johnson, *J. Am. Chem. Soc.*, 2004, **126**, 5873.
226. P. J. Hajduk, T. Gerfin, J. -M. Boehlen, M. Häberli, D. Marek and S. W. Fesik, *J. Med. Chem.*, 1999, **42**, 2315.
227. M. J. Shapiro and J. R. Wareing, *Curr. Opin. Drug Disc. Devel.*, 1999, **2**, 396.
228. J. Pease, R. Witehrs, R. Nast, A. Deese, P. Calderon, S. Mehta, T. Kelly and F. Laukien, Application of a 2.5 mm CryoProbe to Metabolite Studies, *40th Experimental NMR Conference*, Orlando, FL, February 28–March 5, 1999, Abstract W&Th P202.
229. T. M. Logan, N. Murali, G. Want and C. Jolivet, *Magn. Reson. Chem.*, 1999, **37**, 762.
230 G. Bringmann, M. Wohlfarth, H. Rischer, M. Grüne and J. Schlauer, *Angew. Chem., Int. Ed.*, 2000, **39**, 1464.
231. Z. Serber, C. Richter, D. Moskau, J. -M. Böhlen, T. Gerfin, D. Marek, M. Häberli, L. Baselgia, F. Laukien, A. S. Stern, J. C. Hoch and V. Dötsch, *J. Am. Chem. Soc.*, 2000, **122**, 3554.
232. P. F. Flynn, D. L. Mattiello, H. D. W. Hill and A. J. Wand, *J. Am. Chem. Soc.*, 2000, **122**, 4823.
233. P. J. Hajduk, D. J. Augeri, J. Mack, R. Mendoza, J. Yang, S. F. Betz and S. W. Fesik, *J. Am. Chem. Soc.*, 2000, **122**, 7898.
234. D. J. Russell, C. E. Hadden, G. E. Martin, A. A. Gibson, A. P. Zens and J. L. Carolan, *J. Nat. Prod.*, 2000, **63**, 1047.
235. Y. Liu, J. Pease, B. Potts, A. Deese, Y. D. Liu, M. O'Neil-Johnson, R. Withers and R. Nast, Analysis of mass-limited pharmaceutical samples: practical demonstration of a 3 mm cryogenic NMR probe, *SMASH – Small Molecule NMR Meeting*, Argonne, IL, July 16–19, 2000, Abstract 21.

236. M. O'Neil-Johnson, R. Withers, R. Nast, B. Potts, A. Deese, J. Pease and Y. Liu, Natural products characterization: analysis of mass-limited samples using 3 mm microCryoProbe, *221st ACS National Meeting*, San Diego, CA, April 1–5, 2001, Abstract MEDI-357.
237. D. Boger, M. O'Neil-Johnson, S. Wolkenberg and G. Eldridge, MicroScale synthesis: the total synthesis of distamycin, *221st ACS National Meeting*, San Diego, CA, April 1–5, 2001, Abstract ORGN-321.
238. Z. Serber, C. Richter and V. Dötsch, *Chembiochem*, 2001, **2**, 247.
239. G. Bringmann and D. Feineis, *J. Exp. Botany*, 2001, **52**, 363.
240 H. C. Keun, O. Beckonert, J. L. Griffin, C. Richter, D. Moskau, J. C. Lindon and J. K. Nicholson, *Anal. Chem.*, 2002, **74**, 4588.
241. B. Simon and M. Sattler, *Angew. Chem., Int. Ed.*, 2002, **41**, 437.
242. L. Banci, I. C. Felli and R. Kümmerle, *Biochemistry*, 2002, **41**, 2913.
243. G. E. Martin, C. E. Hadden, D. J. Russell, B. D. Kaluzny, J. E. Guido, W. K. Duholke, B. A. Stiemsma, T. J. Thamann, R. C. Crouch, K. Blinov, M. Elyashberg, E. R. Martirosian, S. G. Molodtsov, A. J. Williams and P. L. Schiff Jr., *J. Heterocycl. Chem.*, 2002, **39**, 1241.
244. M. A. Rashid, K. R. Gustafson, R. C. Crouch, A. Groweiss, L. K. Pannell, Q. N. Van and M. R. Boyd, *Org. Lett.*, 2002, **4**, 3293.
245. G. Hernández and D. M. LeMaster, *Magn. Reson. Chem.*, 2002, **40**, 169.
246. C. Hilty, C. Fernández, G. Wider and K. Wüthrich, *J. Biomol. NMR*, 2002, **23**, 289.
247. D. Monleón, K. Colson, H. N. B. Mosely, C. Anklin, R. Oswald, T. Szyperski and G. T. Montelione, *J. Struct. Funct. Genom.*, 2002, **2**, 93.
248. J. G. Brann, J. Pinkner, S. J. Hultgren and C. Frieden, *Proc. Nat. Acad. Sci., USA*, 2002, **99**, 709.
249. T. Szyperski, D. C. Yeh, D. K. Sukumaran, H. N. B. Mosely and G. T. Montelione, *Proc. Nat. Acad. Sci., USA*, 2002, **99**, 8009.
250. M. Sparul, A. S. Freund, R. E. Nast, R. S. Withers, W. E. Mass and O. Corcoran, *Anal. Chem.*, 2003, **75**, 1546.
251. V. Exarchou, M. Godejohann, T. A. van Beek, I. P. Gerothanassis and J. Vervoort, *Anal. Chem.*, 2003, **75**, 6288.
252. J. L. Griffin, *Curr. Opin. Chem. Biol.*, 2003, **7**, 648.
253. M. J. Goger, J. M. McDonnell and D. Cowburn, *Spectroscopy*, 2003, **17**, 161.
254. K. J. Rosengren, R. J. Clark, N. L. Daly, U. Göransson, A. Jones and D. J. Craik, *J. Am. Chem. Soc.*, 2003, **125**, 12464.
255. W. Bermel, I. Bertini, I. C. Felli, R. Kümmerle and R. Pierattelli, *J. Am. Chem. Soc.*, 2003, **125**, 16423.
256. L. Verdier, P. Sakhaii, M. Zweckstetter and C. Griesinger, *J. Magn. Reson.*, 2003, **163**, 353.
257. K. Blinov, M. Elyashberg, E. R. Martirosian, S. G. Molodtsov, A. J. Williams, A. N. Tackie, M. H. M. Sharaf, P. L. Schiff Jr., R. C. Cruch, G. E. Martin, C. E. Hadden, J. E. Guido and K. A. Mills, *Magn. Reson. Chem.*, 2003, **41**, 577.
258. M. Sandvoss, A. Preiss, K. Levsen, R. Weisemann and M. Spraul, *Magn. Reson. Chem.*, 2003, **41**, 949.
259. C. Hinse, C. Richter, A. Provenazni and J. Stöckigt, *Bioorg. Med. Chem.*, 2003, **11**, 3913.
260. I. Bertini, A. Provenazni, M. S. Viezzoli, D. H. Pieper and K. N. Timmis, *Magn. Reson. Chem.*, 2003, **41**, 615.
261. J. L. Griffin, H. Keun, C. Richter, D. Moskau, C. Rae and J. K. Nicholson, *Neurochem. Intl.*, 2003, **42**, 93.
262. D. Moskau and O. Zerbe, *Meth. Prin. Med. Chem.*, 2003, **16**, 67.
263. M. Godejohann, L. -H. Tseng, U. Braumann, J. Fuchser and M. Spraul, *J. Chromatogr. A*, 2004, **1058**, 191.
264 C. Fernandez and W. Jahnke, *Drug. Discov. Today: Tech.*, 2004, **1**, 277.
265. Q. Shu and C. Frieden, *Biochemistry*, 2004, **43**, 1432.
266. A. M. Petros, A. Gunasekara, N. Xu, E. T. Olejniczak and S. W. Fesik, *FEBS Lett.*, 2004, **559**, 171.
267. I. Bertini, I. C. Felli, R. Kümmerle, D. Moskau and R. Pierattelli, *J. Am. Chem. Soc.*, 2004, **126**, 464.

268. D. Monleón, L. Yim, M. Martínez-Vicente, M. E. Armengod and B. Celda, *J. Biomol. NMR*, 2004, **28**, 307.
269. C. Fernández, C. Hilty, G. Wider, P. Güntert and K. Wüthrich, *J. Mol. Biol.*, 2004, **336**, 1211.
270. J. M. Aramini, S. H. Cleaver, R. T. Pon, R. P. Cunningham and M. W. Germann, *J. Mol. Biol.*, 2004, **338**, 77.
271. B. F. Volkman, F. C. Peterson and B. L. Lytle, *56th Southeast Regional ACS Meeting*, Research Triangle Park, NC, November 10–13, 2004, Abstract GEN-300.

Continuous-Wave NMR Imaging in the Solid State

ANDREW J. FAGAN* AND DAVID J. LURIE

Bio-Medical Physics, School of Medical Sciences, College of Life Sciences & Medicine, University of Aberdeen, AB25 2ZD, Scotland, UK

*Current aaddress: Trinity College Institute of Neuroscience, Lloyd Building, Trinity College, Dublin 2, Ireland

ANNUAL REPORTS ON NMR SPECTROSCOPY
VOLUME 56 ISSN 0066 4103
DOI 10.1016/S0066-4103(05)56002-2

A novel nuclear magnetic resonance (NMR) technique for imaging materials exhibiting extremely short T_2 relaxation times is described and some examples of its application to materials of scientific and industrial interest are presented. The technique employs continuous-wave (CW) radio-frequency irradiation of the sample together with continual detection, and thus the experimental dead-time inherent in pulsed techniques is effectively eliminated. The mechanisms which broaden the NMR linewidths of materials in the solid state and liquids in confined geometries are described, and the resulting difficulties which these broad linewidths pose to NMR imaging (NMRI) are outlined. A brief review of existing NMRI techniques is then presented. The CW-NMR approach to imaging is expounded, and the CW-NMRI system is described in detail. 1-D and 2-D images of the ingress of water (^1H imaging) and brine (^{23}Na imaging) into various cementitious materials are presented, together with images of the solid ^{27}Al phase of a high-temperature refractory cement. The inter- and self-diffusion coefficients of a clay mineral, bentonite, were successfully measured, and the 2-D and 3-D imaging performance of the system was demonstrated on phantoms of poly(methyl methacrylate) (PMMA; Perspex/Plexiglas).

1. INTRODUCTION

The development of nuclear magnetic resonance imaging (NMRI) techniques has traditionally focussed on imaging in the liquid state, in particular imaging the free water distribution in biological tissues. This has led to numerous important applications, culminating in the revolution in diagnostic imaging capabilities made possible with the introduction of whole-body magnetic resonance image (MRI) scanners into hospitals in the 1980s. Developments in NMRI in the solid state have likewise received much attention since the first NMR experiments in the 1940s, however progress in this area has lagged considerably behind its medical counterpart. In solids, or solid-like materials where atomic motion is very restricted, the NMR lines are broad and spin–spin relaxation times, T_2, are short compared to those normally found in liquids. This presents a very severe problem for the application of imaging techniques to such materials.[1–4]

The essential feature of an NMRI system is the ability to encode the spatial information in a time of the order of T_2. In liquids, T_2s are of the order 30–300 ms (corresponding to linewidths in the range 1–10 Hz), which is long enough to enable images to be generated using commercially available hardware. The situation is drastically different in solids, with linewidths ranging from 10 to 100 kHz, T_2 relaxation times of less than 30 μs are typical. This difference stems predominately from intranuclear line-broadening mechanisms, which are averaged to zero in liquids by rapid random isotropic motion, but which are not averaged to zero in solids because the atoms are more rigidly bound within the structure. The application of NMRI techniques to the study of porous media poses additional

challenges: the presence of paramagnetic impurities; susceptibility-induced field gradients and chemical-shift anisotropies, all result in enhanced relaxation and, hence, broader resonance lines. Furthermore, the presence of liquids in such confined geometries can lead to adsorption phenomena on internal pore surfaces which shorten relaxation values compared to those found in the bulk liquid, to the extent that solid imaging techniques are required.

The maximum achievable spatial resolution of an NMR image is directly proportional to both the T_2 of the material under investigation and the magnitude of the applied field gradients. Consequently, for a solid-state imaging system to achieve the same resolution as a liquid state imaging system, the field gradients must be increased to compensate for the decreased T_2 values. For example, it is difficult to produce them over large sample volumes ($> 10\,cm^3$), and to switch large field gradients within the time needed for some imaging experiments. A further problem with the use of large field gradients is that the receiver bandwidth must be increased to accommodate the spread in resonant frequencies, and therefore the signal-to-noise ratio (SNR), which scales with the square root of the receiver bandwidth, can be reduced by several orders of magnitude in the resultant image. This illustrates the fundamental problem and the technical difficulties of dealing with much shortened timescales.

These problems can be overcome, to some degree, by decreasing the effective NMR linewidth of the sample using techniques which reduce the line-broadening mechanisms within the sample, so that lower strength field gradients may be used (called 'line-narrowing' techniques). This can be achieved by using a range of special multi-pulse radio-frequency (RF) irradiation methods[5–10] or by physically spinning the sample at the magic angle.[11–13] An alternative approach to solid-state NMRI which has been exploited in several techniques involves the application of sufficiently large magnetic field gradients to produce spatial localisation on the resonant spins, thereby retaining the broad linewidths which contain useful information from the T_2 relaxation phenomenon which broaden the lines.[14–18] However, various practical and/or technical problems have limited the success of these varied approaches to NMRI in the solid state, and to date no one technique has emerged as an all-round gold standard.

The technique described in this chapter utilises continuous-wave (CW) detection, originally developed for electron paramagnetic resonance (EPR) experiments but adapted here to the study of materials in the solid state by NMR. In EPR, materials with electron T_2 relaxation times less than 1 μs are typically encountered. The signal from the sample under investigation is detected by recording the change in the electrical characteristics of the RF resonator as the sample is swept through resonance by a time-varying magnetic field applied across the sample. Indeed, swept-field CW-NMR with magnetic field modulation and lock-in detection was ubiquitous in the early years of NMR, being used to perform spectroscopy on solids as early as 1949.[19] More recent applications of this method include the study of crystallinity in stretched[20] and plasticised[21] rubber. Lauterbur *et al.* suggested that slow passage NMR together with magnetic field gradients might be useful for imaging substances with very short relaxation times.[22] However, it was not until 1996 that the first paper describing just such an approach to NMRI was published by Lurie *et al.*[23]

Solid-state NMRI has many potential application areas. To date, NMRI of solids has revealed its potential to probe the porosity of ceramics, rocks and other heterogeneous systems,[24,25] to give insight into chemical and physical changes in elastomers under stress and during the ageing process,[15,26] and to study polymerisation reactions and local dynamics of elastomers below the transition temperature.[27] Techniques have been developed to study the drying mechanisms of thin, coating layers, such as those found in the application of paints and glues,[28] to image the diffusion of liquids into solids,[29,30] and to study the hydration and hardening of cement paste.[31,32] Biomedical materials such as bones, teeth and dental cement have also been studied using NMR techniques.[33–35]

2. LINE-BROADENING MECHANISMS

The narrow linewidths of liquids allow one to observe weak spin interactions such as the indirect spin–spin (J) coupling and the isotropic chemical shift (δ). In the solid state, however, linewidths are broadened considerably by much stronger interactions, involving mainly the dipole–dipole interaction (typically 10–100 kHz), chemical-shift anisotropy (~1 kHz), the quadrupole interaction (~250 kHz) and the effect of paramagnetic impurities. For these reasons the J and δ interactions are generally not observed in solids.[2]

The Hamiltonian describing the energy of interaction of a solid in an NMRI experiment is given by:

$$H = H_{\text{ext}} + H_{\text{int}}, \tag{1}$$

where H_{ext} represents all external influences on the spin system (static field B_0, RF field B_1 and field gradients G) and H_{int} represents interactions internal to the spin system (the direct nuclear dipole–dipole, chemical-shift (both isotropic and anisotropic), quadrupole and indirect spin–spin (J-coupling) interactions).[36] The H_{ext} term usually dominates the evolution of the spin system during periods of strong RF irradiation of the sample, whereas the H_{int} term (together with the field-gradient contribution to H_{ext}) dominates during periods of free precession, provided that the system is viewed in a frame rotating at the Larmor frequency of the spin under consideration. In general, the dipole–dipole and anisotropic chemical-shift interactions dominate H_{int} and thus are responsible for line broadening in solids. Quadrupolar interactions are only of concern in materials with nuclear spin $I > 1/2$, whereas the J-coupling interaction is generally too weak to be observed. Magnetic susceptibility-induced field gradients which vary with position in heterogeneous materials also influence the spin system, tending to further broaden the observed linewidths.

2.1. The dipole–dipole interaction

The dipole–dipole interaction is the through-space coupling of one magnetic spin with the local field of its neighbours. The interaction depends on the magnitude and

orientation of the magnetic moments, and also on the length and orientation of the vector describing their relative positions. The Hamiltonian describing the energy acquired by a nuclear magnetic moment $\boldsymbol{\mu}_i = \hbar\gamma\mathbf{I}_i$ (where the nuclear spin angular momentum operator $\mathbf{I}_i = \mathbf{I}_{ix} + \mathbf{I}_{iy} + \mathbf{I}_{iz}$) when placed in the local fields generated by a collection of other nuclear spins $\Sigma\boldsymbol{\mu}_j$ can be written as

$$H_{\mathrm{D}} = \frac{\mu_0\hbar}{4\pi} \sum_{i<j} \gamma_i\gamma_j \left(\frac{\mathbf{I}_i \cdot \mathbf{I}_j}{r_{ij}^3} - \frac{3[\mathbf{I}_i \cdot \mathbf{r}_{ij}][\mathbf{I}_j \cdot \mathbf{r}_{ij}]}{r_{ij}^5} \right). \tag{2}$$

The situation with a pair of spins is illustrated in Fig. 1, where the static field B_0 is along the z-axis. To first order and neglecting terms in the expansion of Eq. (2) which lead to a change in nuclear quantum numbers of 1 or 2 (i.e. $\Delta m = \pm 1$ and ± 2 transitions), the effect of H_{D} is to split the Zeeman levels into many closely spaced energy levels, thereby causing a distribution of resonant frequencies and consequently a broad line. Eq. (2) has been simplified by the van Vleck formula:[2]

$$H_{\mathrm{D}} = \frac{\mu_0\hbar}{8\pi} \sum_{i<j} \frac{\gamma_i\gamma_j}{r_{ij}^3} (1 - 3\cos^2\theta_{ij})[3I_{zi}I_{zj} - \mathbf{I}_i\mathbf{I}_j]. \tag{3}$$

One can see from Eq. (3) that the van Vleck dipolar Hamiltonian is the product of a spatial part and a spin part. In liquids, the rapid isotropic molecular tumbling motion, which occurs at frequencies well above the dipolar linewidth, averages the spatial part $(1-3\cos^2\theta_{ij})$ to zero, thus nulling the dipolar broadening. In solids, the spins are constrained to vibrate and rotate about their mean positions, resulting in an effective dipolar Hamiltonian which is generally non-zero, and consequently in

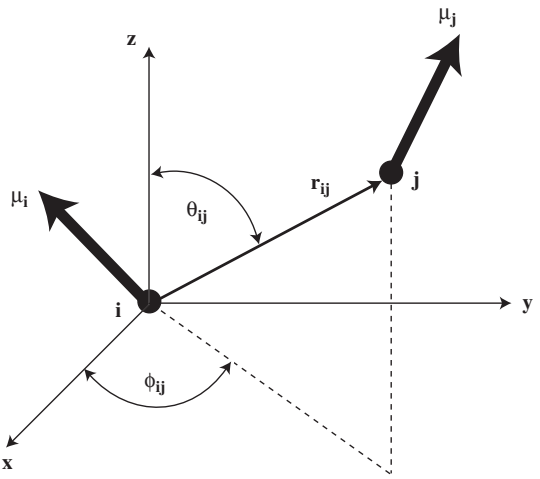

Fig. 1. Geometry of the magnetic dipole–dipole interaction. θ_{ij} and Φ_{ij} are the polar and azimuthal angles respectively of the internuclear vector r_{ij}.

broad lines. The NMR lineshape is approximately Gaussian,[37] in contrast to the Lorentzian line associated with liquids. The linewidth is characteristically of order:[38]

$$\Delta f = \frac{\mu_0 \gamma^2 \hbar}{8\pi^2 r^3}, \tag{4}$$

for the homonuclear case, and with r the nearest neighbour separation, and assuming an internuclear distance of 0.15 nm, this gives $\Delta f = 35$ kHz.

2.2. The chemical-shift interaction

The chemical shift can be defined as the shielding interaction between the electron clouds and the nuclear spin angular momenta; it is isotropic in liquids but has rotational anisotropy in solids. The spin Hamiltonian describing the interaction is therefore tensorial in nature:

$$H_{\mathrm{CS}} = -\mathbf{I} \cdot \mathbf{S} \cdot \mathbf{B}_0 = -\gamma \mathbf{I} \cdot \boldsymbol{\sigma} \cdot \mathbf{B}_0, \tag{5}$$

where $\mathbf{S}$ is the shielding tensor and $\boldsymbol{\sigma}$ is the chemical-shift tensor.

Unlike the situation with the dipolar interaction, which averages to zero in liquids due to the rapid molecular tumbling motion, the isotropic rotation leaves a residual chemical-shift Hamiltonian:

$$H_{\mathrm{CS}} = -\sigma_{\mathrm{i}} \omega_0 I_z, \tag{6}$$

where σ_{i} is the isotopic chemical shift given by the diagonal sum $(\sigma_{xx} + \sigma_{yy} + \sigma_{zz})/3$. For solids, the full chemical-shift Hamiltonian is[37]

$$H_{\mathrm{CS}} = -\sigma_{\mathrm{i}} \omega_0 I_z - (3\cos^2\beta - 1)(\sigma_{zz} - \sigma_{\mathrm{i}})\omega_0 I_z/2, \tag{7}$$

where β is the polar angle between the polarising field direction and the principle axis system of the chemical-shift tensor. The additional term in Eq. (7) is the anisotropic chemical shift which contributes to line broadening in solids.

2.3. The quadrupole interaction

For nuclear spins with spin quantum number $I > 1/2$, the nuclear charge distribution about the centre of gravity of the nucleus is not spherically symmetric. This asymmetry in the nuclear charge distribution gives rise to an electric quadrupole moment, Q, which interacts with electric-field gradients (EFG) established by electrons surrounding the nucleus. Although this is an electrical interaction, it depends on the magnetic quantum number and so affects the NMR spectrum.

The quadrupole interaction Hamiltonian for a single spin is

$$H_{\mathrm{Q}} = \mathbf{I}_i \cdot \mathbf{Q} \cdot \mathbf{I}_i, \tag{8}$$

where

$$\mathbf{Q} = \frac{eQ}{2I(2I-1)\hbar}\ \mathbf{V}, \tag{9}$$

and **Q** is the nuclear quadrupole moment of spin I and **V** is the EFG tensor. For the case of an axially symmetric EFG tensor, the secular part of the quadrupole Hamiltonian is given by:[2]

$$H_{\mathrm{Q}} = \frac{eQV_{33}}{8I(2I-1)}\ (3\cos^2\beta - 1)(3I_z^2 - I(I+1)). \tag{10}$$

2.4. Magnetic susceptibility effects

When applying solid-imaging techniques to highly heterogeneous material systems, the heterogeneity of the diamagnetic susceptibility also contributes significantly to line broadening. Susceptibility broadening arises because a localised region with susceptibility different to the surroundings perturbs the applied magnetic field both in and around itself. The geometry of the heterogeneity and its orientation relative to B_0 influence the degree of perturbation of the field, with the largest effects occurring at boundaries and in high fields. This creates two problems: the first is image distortion arising from different nuclei experiencing different magnetic fields; the second is attenuation of the signal and hence line broadening arising from diffusion of nuclei across the susceptibility-induced field gradients.

The offset magnetic field outside a cylinder of radius a and susceptibility χ_2, which is embedded in a material of susceptibility χ_1 and placed in a magnetic field of strength B_0 such that the long axis of the cylinder is orthogonal to the field, is given by:

$$\Delta B = \frac{(\chi_2 - \chi_1)a^2 \cos 2\varphi}{2r^2}\ B_0, \tag{11}$$

where r is the distance from the cylinder axis and φ is the angle between the vector $\boldsymbol{r}$ and B_0. Taking the materials as air and water, the susceptibility difference is -9×10^{-6}, so that for ^{1}H NMR at $B_0 = 7.05\,\mathrm{T}$ (the field strength used in our own experiments), the maximum field offset is $32\,\mu\mathrm{T}$, equivalent to $1.36\,\mathrm{kHz}$. Such offset fields give rise to gradients of the order of several hundred T/m in the vicinity of micron-sized cavities within porous materials. Diffusion through these field gradients attenuates the NMR signal at time t by a factor $\exp(-\gamma^2 G^2 D t^3/3)$, where G is the gradient and D is the diffusion coefficient.

Paramagnetic impurities in samples such as concretes and rocks can be present at considerable concentrations and thus can also give rise to line broadening. This can happen in two ways:[38] (i) a magnetic nuclear–electron dipolar interaction, which provides an efficient relaxation mechanism due to the very large electron magnetic moment (compared to that of the nuclear moment) and (ii) short (contact) and long range electronic shielding, which leads to gradients in paramagnetic susceptibility

across the sample, with similar (although larger) effects to that due to the diamagnetic contribution to susceptibility broadening.

3. OVERVIEW OF SOLID IMAGING TECHNIQUES

Detailed reviews of solid-state imaging techniques have been presented previously (e.g. see Jezzard *et al.*,[2] Demco and Blumich[3,39] and Blumich[40]), and thus only a brief overview is given here. Although 'soft' solid materials such as elastomers exhibiting linewidths less than 3 kHz can be imaged using Fourier imaging on modern solid-state NMRI systems, more specialised techniques are required to image nuclei in rigid matter. In general, two imaging strategies have been adopted: either the gradient strength can be increased or the linewidth can be reduced. Techniques utilising the former approach include stray-field imaging (STRAFI), the use of strong oscillating gradients, single point imaging (SPI) using pure phase encoding and multiple-quantum (MQ) imaging. Techniques utilising the latter approach include magic angle spinning (MAS), magic-angle rotating-frame (MARF) imaging, imaging with multi-pulse line narrowing and magic-echo imaging. By way of comparison, while the large gradient techniques adopt a brute force approach to overcome the broad linewidths present in solids, line-narrowing techniques attempt to replicate the conditions existing in liquids which suppress many of the principal line-broadening mechanisms. In effect, the spins in the solid are made to act as if they were undergoing rapid isotropic thermal motion by introducing, via external forces, a time dependence into the effective Hamiltonian describing the system such that the spins sample all directions of spin space in turn. Indeed, this time-dependence can be introduced in the spatial and/or the spin parts of the van Vleck Hamiltonian given in Eq. (3).

3.1. STRAFI

The idea of using the large static field gradients present in the fringe field of solenoidal superconducting magnets to image solids was first expounded by Samoilenko *et al.*[14] By using such large field gradients, which typically measure 60 T/m for 9.4 T magnets, spatial resolutions of the order of 10 μm are achievable in materials with linewidths of the order of 30 kHz. The resultant broad spread in resonant frequencies, of the order of 25 MHz cm^{-1} for ^{1}H nuclei, means that even for moderately sized samples, the RF pulses do not have sufficient bandwidth to encompass the entire range of resonant frequencies to allow for imaging of the entire length of the sample. Every RF pulse, shaped or not, will excite resonance in a thin slice perpendicular to the gradient direction, and because the gradient direction cannot be changed, the sample must be mechanically moved through the gradient in order to excite the next slice. In this way, a 1-D profile of the sample is acquired in the direction of the gradient in a stepwise fashion. The measured

magnetisation corresponds directly to the sample's spin density, and therefore no Fourier transformation (FT) of the data is required. The 2- and 3-D image data sets can be acquired by combining sample rotation and translation, with image reconstruction of a sufficient number of profiles performed by using back projection. However, mechanical complexities and time constraints associated with such sample manipulations have rendered STRAFI a predominately 1-D imaging technique, with experimental set-up typically optimised to this end.[38]

Several variations of the original STRAFI method have been reported. Frequency-swept experiments, in which the NMR spectrometer frequency was swept such that the sensitive slice moved through the sample, have been carried out on sufficiently thin samples.[28] Another variation was reported by Mallett *et al.*, who used a magnetic field sweep facility to move the sensitive slice through the sample.[41] These experiments eliminated problems associated with positional reproducibility and backlash or misalignment in the sample travel. For 3-D imaging of samples which could not be rotated and for which high resolution was only required in 1-D (e.g. initially wet planar coatings of paint and varnish), Godward *et al.* developed a system which uses STRAFI in conjunction with pulsed orthogonal gradients.[42] The realisation that the use of a superconducting solenoid magnet with a very high central field homogeneity is not necessary for STRAFI has led to the development of two magnet designs specifically targeted to STRAFI work. The first is the NMR MObile Universal Surface Explorer (NMR-MOUSE), a portable magnet and spectrometer system developed by Blumich *et al.*[43,44] This system uses an asymmetrical permanent magnet producing a field of 0.41 T and an RF coil placed between the magnet pole pieces with its axis perpendicular to the surface of the magnet. The stray field outside the magnet has a maximum field gradient of 14 T/m, and can be used to probe to depths of several millimetres. The second example is a novel high-gradient permanent magnet designed for the profiling of planar films and coatings by Glover *et al.* (GARField).[45] This magnet provides a typical operating field of 0.8 T with a homogeneous gradient of 20 T/m within a useable interpole access of 20 mm.

3.2. Imaging with oscillating gradients

The oscillating-gradients technique uses the same brute force approach as STRAFI, i.e., applying large gradients to overcome the broad linewidths in order to acquire an image with good spatial resolution. In STRAFI, the RF pulses are necessarily applied in the presence of the gradient, which leads to ill-defined excitation slices within the sample. However, it is often desirable to irradiate the sample with no applied gradient, and then to observe the signal in the presence of a gradient. The difficulty here is to switch the large gradients and allow them to settle in a short timescale compared to the T_2^* of the sample. A solution to this problem was demonstrated by Cottrell *et al.*,[16] who used a sinusoidal variation in order to apply a rapidly varying time-dependent gradient. The power required for the application of large gradients was reduced by making the gradient coils part of a tuned circuit.

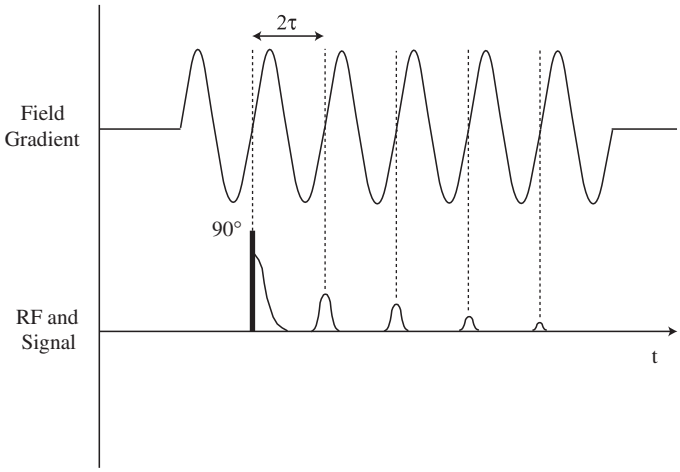

Fig. 2. A typical timing diagram used with the oscillating-gradient technique to produce gradient echoes. (Adapted from Ref. 16.)

Furthermore, they applied the initial 90° RF pulse at a zero crossing of a sinusoid, so that the RF power requirement was simply that associated with a solid.

A typical timing diagram used in this experiment is outlined in Fig. 2. The first half-cycle of the field gradient after the 90° pulse encodes the spatial information on the free induction decay (FID). The gradient is then reversed in the second half-cycle with a gradient echo forming after one period of the gradient oscillation. Provided that $2\tau < T_2^*$ further gradient echoes will continue to form at times $2n\tau$, the amplitudes decreasing successively as determined by T_2^*. A suitable choice of gradient permits the echo formation clear of the 90° pulse dead-time and there is no 180° pulse to further obscure the signal. Schemes for 2-D[46] and 3-D[47] imaging were subsequently developed, the latter employing doubly resonant-gradient coils to allow for imaging using standard 3DFT techniques.

Although the inclusion of the gradient coils into a resonant circuit allows an increase in the gradient strength (typically 1–10 T/m), it is still significantly lower than that used in STRAFI. Furthermore, technical limitations on the oscillation period ($TE_{min} \sim 200\,\mu s$) limit the shortest measurable relaxation time.[16] Hence the oscillating-gradient scheme has proved to be suitable for imaging soft solids (rubber and soft polymers) with linewidths of up to 3 kHz,[48,49] although the technique has been used in combination with multi-pulse line-narrowing techniques to extend the range of applications to stronger dipolar solids.[50]

3.3. Single point imaging (SPI)

Single point imaging was first suggested by Emid[51] as a method for minimising the effect of all line-broadening mechanisms while using modest gradient strengths. The

evolution of the magnetisation in the gradient is detected by measuring only one data point of the FID at a fixed time τ after the excitation pulse. As this time is fixed and the gradient strength is incremented between successive experiments, only the evolution of the spins due to the gradients is observed; the evolution due to dipolar interactions, chemical shifts and other line-broadening mechanisms is constant and therefore is not observed. The spatial resolution is only limited by the magnitude of the applied gradient.

The SPI technique tends to be very hard on the gradient amplifiers because of the need to use large gradients when imaging solids, but also because the time during which the gradients phase encode the signal is necessarily less than the T_2^* of the sample under investigation, and hence rapid gradient switching is required. To alleviate this problem somewhat, the gradients are turned on and allowed to stabilise before applying the RF pulse. Consequently, the RF pulses are applied in the presence of a gradient, and therefore extremely short, broadband pulses are required in order to excite the full range of frequencies across the sample. As only one point in k-space is acquired after each excitation, acquisition times tend to be very long, and therefore small flip angles are typically used in order to allow for the use of short t_R values without saturation (subject to duty-cycle limitations of the gradient set). Several techniques aimed at reducing the image acquisition time of the basic SPI experiment have been described, including the turbo spin-echo SPI technique of Beyea *et al.*,[24] which obtained multiple phase encoded k-space data points with each RF excitation pulse train, and the multi-point k-space mapping techniques of Cho and Ro[52] and Fernandez-Seara *et al.*,[53] which extend one phase-encoding gradient in time, allowing for the acquisition of n k-space points per excitation.

Despite these improvements, the SPI technique is inherently slow and, furthermore, the intense, rapidly switched gradient pulses it uses can lead to excessive gradient vibration. The single point ramped imaging with T_1 enhancement (SPRITE) technique, developed by Balcom *et al.* in 1996, overcomes these problems and enables the introduction of quantitative T_1 contrast into images.[54] Unlike the SPI sequence, the magnetic-field gradients in the SPRITE sequence are not switched on/off for each acquisition. Instead, the primary phase-encode gradient G_z is ramped in equally spaced discrete steps (typically 0.5–5 ms in duration), while conventional phase-encoding gradients are applied in the secondary directions (G_x and G_y). A broadband RF pulse with flip angle α is applied at each step of G_z, and a single data point is measured on each resulting FID after a time t_p. Gradient vibrations are reduced due to the lower dB/dt inherent in the technique. A marked time improvement is achieved with samples where T_1 relaxation times are on the order of the gradient rise time.[55,56] Gradient steps are typically limited to 0.5–5 ms in duration in order to remain within the duty cycle limits of the gradient amplifiers. T_1 contrast is introduced into the images by partial saturation of magnetisation components that have longitudinal relaxation times longer than the gradient switching time. Improvements to the sensitivity (both SNR and acquisition speed) of the basic SPRITE sequence using two centric scanning acquisition strategies have recently been described. The SPIRAL-SPRITE technique reported by Szomolanyi

et al.[57] employs a spiral *k*-space scanning strategy, and is carried out by applying sinusoidally ramped X and Y gradients with a constant Z gradient. The Conical-SPRITE technique reported by Halse *et al.*[58] employs a system of spiral trajectories mapped to a conical surface, with the X and Y gradients varied sinusoidally and the Z gradient stepped in a linear ramp.

3.4. Multiple quantum (MQ) imaging

An MQ coherence of order p can exist in a coupled spin system, and in a quadrupolar nucleus under certain conditions, when the system contains states $|i>$ and $|j>$ whose magnetic quantum numbers differ by $M_i - M_j = \pm p$. In this case, the oscillation frequency due to such transitions is p times larger than the Larmor frequency ω_0. In general, NMR experiments detect single quantum coherences, i.e. $p = \pm 1$. Higher order coherences do not produce magnetic dipole radiation and thus cannot be detected directly by a conventional dipole antenna used to detect single-quantum resonances, and instead are detected by their influence on observable single quantum coherences.[2] Furthermore, although very high-order coherences can be induced in dipolar solids, the intensity of the NMR signal decreases strongly with increasing p. The interest in MQ coherences for solid imaging arises because the rate of phase evolution of an MQ coherence of order p in a field gradient is enhanced by a factor p. This means that the frequency resolution is enhanced by a factor p, and thus one could conceivably obtain good spatial resolution in a broad linewidth material without the need to use very large gradients. Furthermore, MQ coherences in solids can be less sensitive to certain spin interactions, leading to narrower linewidths and potentially still better spatial resolution.[40]

A typical MQ coherence imaging pulse sequence comprises four distinct steps: preparation, evolution, reconversion and detection. A range of multi-pulse sequences exist for exciting different order MQ coherences during the preparation period.[59,60] The excited coherences then evolve for a time t_1 under the influence of the applied space-encoding gradient to allow for imaging, before being re-converted to single quantum coherences and detected in the usual manner. Phase cycling schemes can also be used to extract different coherence orders. MQ imaging was first shown for dipolar-coupled protons in adamantane by Garroway *et al.*[17] Coherences of order up to $p = 20$ were observed, although amplification of the effective gradient strength was only achieved up to $p = 14$ due to the decrease in signal intensity as p increased. The technique was later applied to spectroscopic deuteron solid-state imaging, where deuterated polymers exhibiting linewidths of the order of 250 kHz were imaged with sub-millimetre resolution using double quantum coherences.[61] MQ techniques have also found use in conjunction with magic angle spinning (MAS) techniques,[62–64] wherein the MQ coherences were used to improve spectral resolution, to suppress signals from isolated spins-1/2 and to estimate local molecular structure through internuclear distances and molecular torsion angles.[65] Furthermore, the possibility of exciting and

detecting proton double quantum coherences in inhomogeneous static and RF magnetic fields was investigated by Wiesmath *et al.*[66] using the NMR-MOUSE system.

3.5. Magic angle spinning (MAS) imaging

Early work by Andrew *et al.*[67] and Lowe[68] in 1959 demonstrated how the dipolar part of the interaction Hamiltonian could be averaged to zero by spinning the sample about the magic angle axis (54.74° to B_0). However, this technique was not used in imaging experiments on solid materials until 1988, when Cory *et al.* successfully resolved two pieces of silicone rubber samples separated by 1 mm by rotating them at 2 kHz.[11] MAS is a line-narrowing technique which eliminates homonuclear and heteronuclear dipolar coupling, as well as chemical-shift anisotropy, while retaining the isotropic chemical shift. It effectively averages the spatial part of the van Vleck Hamiltonian in Eq. (3) to zero. However, the MAS rotation frequency must exceed the dipolar coupling strength for the dipolar contribution to be fully averaged, a condition which is seldom met for solid imaging since typical rotational frequencies are <20 kHz.[40] A further problem is that spinning sidebands are observed if the spinning frequency is smaller than the anisotropy of the interaction.[1] Nevertheless, MAS imaging is very suitable for imaging heterogeneous materials, since it conserves the isotropic chemical shift. In homogeneous materials, MAS techniques are often used in conjunction with other more efficient methods for homonuclear dipolar decoupling. The MAS technique has some drawbacks related to the existence of centrifugal forces (10^5 g typical) which can cause deformation, fracture and separation of materials, and to the restriction in the geometry (preferably axially symmetric samples are imaged) and size of the sample ($\sim$10 mm), together with technically demanding hardware.

Several approaches to imaging using MAS have been proposed, but the most extensively used experiments employ rotor-synchronised rotating gradients, in which the gradients are rotated synchronously with the spinning sample so that the gradients appear stationary in the sample frame.[1] Both frequency and phase-encoding procedures have been used to generate images for ^1H[12] and ^2H.[69] When imaging rare nuclei like ^{13}C, the signal can be enhanced by cross-polarisation from ^1H to ^{13}C, while the detection is done in the presence of high-power heteronuclear decoupling.[70]

3.6. Magic angle rotating frame (MARF) imaging

MARF imaging is another technique which uses the concept of a magic angle to produce line narrowing. This experiment, originally developed by Lee and Goldberg,[71] is based on the evolution of the spins around an effective RF field, $\mathbf{B_{eff}}$, tilted at the magic angle as seen in the rotating frame, while the sample remains

static. It works on the spin part of the interaction Hamiltonian, averaging to zero bilinear interactions such as the dipolar interaction when ϑ is set to the magic angle and reducing linear interactions such as the chemical-shift anisotropy (which are scaled as $\cos\vartheta$). The MARF technique produces better dipolar decoupling compared to the MAS method, since the Hamiltonian modulation frequencies can be an order of magnitude higher with MARF. However, the SNR is intrinsically low, while the ability to produce the magic angle conditions at every point in the sample depends strongly on the precision and stability of field gradients applied across the sample, which can be difficult to achieve in practice at the required magnitudes.[39]

The effective field $\mathbf{B_{eff}}$ is generated using a combination of a static-field gradient G_{0x} and an RF-field gradient G_{1x}, both of which are applied in the laboratory frame along the B_0 and $\mathbf{B}_1$ directions, respectively, and are needed to ensure that $\mathbf{B_{eff}}$ varies linearly in amplitude but at constant orientation. To maintain the orientation of the effective field at the magic angle at all positions in the sample, the gradient amplitudes must be set such that $G_{1x}/G_{0x} = \sqrt{2}$. This condition limits the resolution of the method because of the relatively low values of the RF-field gradient which can be achieved experimentally.

Two detection schemes are possible. In the first scheme, used in the original Lee–Goldberg experiment,[71] the signal is detected in the rotating frame after the application of a 90° RF detection pulse following the evolution for a variable time t_1 in the spin-lock $\mathbf{B_{eff}}$ field at the magic angle.[25] A dephasing delay $t_d \gg T_2$ is used before applying the 90° pulse to remove any transverse magnetisation, and thus only the desired longitudinal magnetisation is measured. Single point detection is then used, while projections at different angles can be measured by gradient or sample rotation. The second is a direct detection scheme, first demonstrated by Medfed and Atsarkin,[72] which uses a spin-echo sequence to generate transverse magnetisation in the tilted rotating frame, precessing about the z'-axis with frequency ω_{eff}, which is in the audio frequency (AF) range. Therefore, a separate AF coil is required to generate the spin-echo pulses, which is decoupled from the RF coil by aligning it along the z-axis in the laboratory frame. Mechanical oscillations in the AF coil in this direct detection scheme can be problematic. The former, indirect, detection method obviates the need for the AF channel, and although it is more time consuming and provides the same line narrowing, it nevertheless gives a higher SNR because the signal is detected in the rotating frame (i.e., higher excitation frequency used, ω_0 compared to ω_{eff}). Several improvements have been made to the basic indirect MARF technique over the past few years, resulting in T_2,[25] $T_{1\rho}$[73] and $T_{2\rho}$[74] weighted contrast in images of various polymers.

3.7. Imaging with multi-pulse line narrowing

Multiple pulse (MP) sequences work on the spin part of the interaction Hamiltonian, and are based on the original ideas of Ostroff and Waugh[75] and

Mansfield and Ware[76] of extending the time domain signal of dipolar coupled systems by applying a cyclic train of 90° pulses. An MP sequence typically consists of a train of several hundred RF pulses comprising repeated sets of n pulses,[2] with $4 \leqslant n \leqslant 48$. If the sequence is applied at a rate sufficiently rapid compared with the value of the linewidth to be narrowed, it will average to zero dipolar interactions within the sample, while the chemical-shift interaction is either scaled or eliminated, depending on the type of MP sequence used.

Solid imaging using MP sequences involves difficult experimental set-up and is very demanding of the hardware, requiring high-powered pulses with excellent phase and amplitude stability. The free induction decay signal is sampled between pulses, and hence the overall efficiency of the sequence depends on the quality of the RF pulses. Furthermore, low quality-factor RF coils must be used to allow for the generation of RF pulses with the required short rise and fall times, which reduces the sensitivity and hence the spatial resolution. These issues, among others, have limited the widespread use of MP sequences for solid imaging. The first MP sequence was the WAHUHA sequence developed by Waugh *et al.*[77] Many of the pulse sequences developed since then have been based around this one, with various modifications aimed at improving the spatial resolution. Examples include the MREV-8 sequence developed by Mansfield[78] and the BR-24 sequence developed by Burum and Rhim.[79] Indeed, a form of the MREV-8 sequence was used in the first paper in which MP-line narrowing was applied to imaging in 1975[80] (1-D profiling), and also the first 2-D image in 1985.[5]

The space-encoding gradients need to be introduced into the MP sequence in such a way that they do not influence the line-narrowing efficiency of the sequence. The approach used with the MREV-8 sequence is to apply the RF pulses in the presence of static-field gradients, allowing for the introduction of T_1 or $T_{1\rho}$ contrast into the images by storing the magnetisation along $\mathbf{B}_0$ (Zeeman storage) or $\mathbf{B_1}$ (spin-locking) respectively.[5] However, the spin evolution under the influence of the gradients which invariably results from this approach leads to non-uniform resolution across the image, and a balance must therefore be struck between gradient strength and offset dependence for optimising the spatial resolution. An improvement in dipolar decoupling efficiency and image resolution is obtained when oscillating rather than continuous gradients are used. Off-resonance effects can be minimised if the RF pulses are applied at the zero crossings of the gradients, although problems with non-uniform spatial resolution still exist. However, second-averaging techniques have been used to eliminate the phase shifts in the rotating frame causing the off-resonance effects.[6,81]

The best spatial resolution is obtained when ultra-short (2–5 μs) gradient pulses are applied in the windows of a time suspension (i.e. all interactions are suppressed) MP sequence incorporating second-averaging techniques,[82] albeit at the expense of demanding gradient hardware. Yet another variation is the combination of MP and MAS techniques, resulting in a combined rotation and multiple-pulse spectroscopy (CRAMPS) experiment, first implemented by Cory *et al.*[83] and later extended to incorporate the magic echo-based sequence TREV-8.[84,85] The advantage of such an approach is that the large dipole interaction can be removed by the MP sequence,

while the chemical-shift anisotropy broadening can be removed by MAS (pulse techniques alone cannot be used to separate the contributions of isotropic and anisotropic chemical shifts, so both are removed or both are preserved).

3.8. Magic-echo imaging

The line-narrowing techniques discussed thus far only work effectively for isolated coupled spin pairs; if more than two spins couple, refocusing of the homonuclear dipole–dipole interaction is incomplete. Complete refocusing can, however, be done in these situations using the magic echo, even after a time as long as T_2, which allows more time for gradient switching, which in turn significantly improves the spatial encoding potential with rigid solids.[10] The dipole–dipole interaction scales with the second Legendre polynomial $P_2(\cos\theta) = (3\cos^2\theta - 1)/2$ (*cf.* Eq. (3)), and thus $P_2 = (1 \text{ or } -1/2)$ for $\theta = (0^\circ \text{ or } 90^\circ)$ respectively. Therefore, complete refocusing occurs if the spin system evolves for a time [2τ under $\theta = 0^\circ$ *and* 4τ under $\theta = 90^\circ$].

The most successful magic-echo scheme that has been developed for imaging experiments is the magic-sandwich echo (MSE) sequence, first reported by Rhim *et al.*[86] This original MSE pulse sequence consisted of many $n180^\circ_x$ and $n180^\circ_y$ pulses sandwiched by 90°_y and 90°_{-y} pulses, illustrated in Fig. 3a. The sign of the homonuclear dipolar Hamiltonian is reversed during the sandwich period of RF irradiation, resulting in a negative dipolar evolution with the strength of the dipole coupling reduced by a factor of 2. By setting the duration of this negative evolution equal to 4τ, where τ is the initial positive evolution period, an echo occurs

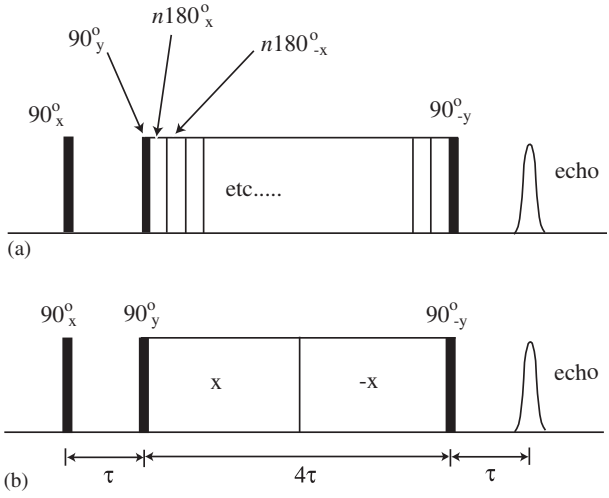

Fig. 3. (a) The original MSE sequence. (Adapted from Ref. 86.); (b) 180° pulses replaced by continuous-RF irradiation. (Adapted from Ref. 8.)

at 6τ, in the absence of any RF field. The requirement of using $n180^\circ$ pulses can be removed by using instead two continuous-RF irradiations with reversed phases (Fig. 3b).[8]

Two approaches to spatial encoding exist: frequency encoding using time suspension MP sequences incorporating magic echoes, similar to the MP sequences using solid echoes discussed in the previous section; and using pure phase encoding. The first approach uses stroboscopic measurement of multiple magic echoes, with spatial encoding performed by gradient pulses of constant strength applied in the windows of the multiple-MSE pulse sequence.[9] The free-evolution windows are long compared to solid echo-based MP sequences, so gradient switching is comparatively easy. The second approach uses the same principles as SPI discussed earlier: because the echo time and the gradient-pulse time are kept constant, the spin system only evolves under the influence of the variable gradient amplitude (ignoring transverse relaxation effects). This magic echo phase-encoding imaging (MEPSI) experiment was first reported by Hafner *et al.* in 1991, and later extended to 3-D imaging with the addition of a third phase-encoding gradient, with a consequently large increase in image acquisition time.[87]

3.9. CW-NMRI

Despite the range of techniques that have been developed to image materials in the solid state, no one technique has emerged as an all-round gold standard. STRAFI is an inherently 1-D technique, and has consequently found application predominately in imaging materials where the process of interest has been reduced to 1-D (e.g. profiling perpendicular to thin films), where high-resolution imaging of the in-plane processes are not so critical. The SPI/SPRITE technique, while perhaps the most successful technique to date from the point of view of its range of applications reported in the literature, like the STRAFI technique imposes a lower limit on the shortest T_2 value which can be studied. Line-narrowing techniques, by their very nature, lose useful information from the T_2 relaxation phenomena that broaden the lines, often require the application of high-RF power and place restrictions on sample size. Together with the complexity of the experimental set-up and the severe instrumentation requirements, their application to the imaging of solid materials has been limited.

An alternative approach to solid imaging is the CW-NMRI technique, which uses continuous-RF irradiation and detection in the presence of continuously applied, moderately strong gradients. This technique offers a number of advantages compared to other solid imaging techniques:

- The use of CW-RF irradiation and detection eliminates the equipment dead-time inherent in all other techniques, thus effectively removing the limit on the shortest value of T_2 that can be investigated.
- The problems associated with rapid gradient switching are avoided through the use of continuously applied gradients.

- The use of magnetic field modulation together with phase-sensitive detection using a lock-in amplifier renders CW-NMRI an extremely narrow-bandwidth detection technique, and thus the penalty inherent in all other techniques of a reduced SNR with increasing gradient strength (due to the increased frequency bandwidth) is removed.
- The RF power requirement in CW-NMRI is a factor of 10^3 to 10^6 lower compared to the other solid imaging techniques, thus making it practicable to envisage examination of full-size structural components which might prove problematic for conventional pulsed techniques due to excessive RF power requirements.

A prototype system capable of producing 2-D images of rigid polymers has been described previously,[88] while an upgraded system was used to study a range of heterogeneous materials such as cements and rocks.[89]

4. CW-NMRI

4.1. CW-NMR spectroscopy

In the CW-NMR experiment, the magnetic field B_0 is swept slowly through resonance by the application of a ramped, offset magnetic field while the sample is continually irradiated at a fixed frequency.[23,88,89] The steady-state solutions to the Bloch equations (see e.g. Ref. 36) are valid in this experiment provided the magnetic field sweep is sufficiently slow (the 'slow passage' condition), i.e. provided that equilibrium is maintained between the RF field and the nuclear magnetisation. If the resonance is traversed too rapidly, the magnetisation becomes saturated and consequently the measured signal diminishes. The slow passage condition is satisfied when,

$$\frac{dB_0}{dt} \ll \gamma(\Delta B_{1/2})^2, \tag{12}$$

where $\Delta B_{1/2}$ is the linewidth in field units. Typically, field sweep rates of the order of $1.6 \times 10^{-2}\,\mathrm{Ts}^{-1}$ are used, well below $\gamma(\Delta B_{1/2})^2 \sim 1$ to $10^3\,\mathrm{Ts}^{-1}$ which is typical for the solid materials studied by the CW-NMRI system.[89,90]

To understand the CW-NMRI experiment, it is useful to consider the basic CW-NMR spectrometer illustrated schematically in Fig. 4. With a sample placed in a resonator located in a magnetic field, a signal from an RF source is applied to one of the terminals of a hybrid junction. This device serves to split an input signal into two, with each component following a different path to the output terminal where they are recombined. When the resonator is matched to $50\,\Omega$, the incident RF power is equally split between the resonator and the $50\,\Omega$ load, and no signal appears at the output terminal. The magnetic field applied across the sample is then swept using a time-varying ramped magnetic field and at resonance the spins absorb energy, which changes the impedance of the resonator and leads to an impedance

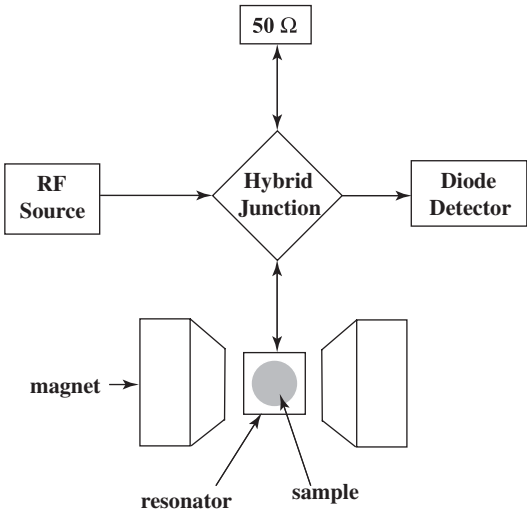

Fig. 4. Block diagram of the CW-NMR spectrometer.

mismatch across the hybrid junction. This mismatch causes power to be transmitted through the junction to its output terminal, where it is passed to the detector. A plot of detector output versus magnetic field would therefore show the sample's magnetic resonance absorption spectrum.

A diode detector is used to rectify and smooth the RF power to a direct current (DC) voltage. The change in signal as resonance is achieved is often very small ($\sim$10 μV) compared to the electrical noise present in the system, and therefore an audio frequency (AF) modulation is superimposed on the ramped magnetic field, with lock-in detection used to extract the signal with the same frequency as the modulation and at a fixed relative phase. This 'phase-sensitive' detection by a lock-in amplifier essentially represents a very narrow-bandwidth detection scheme, and since the detected noise scales with the square root of the bandwidth, there is a resultant large increase in the measured SNR using magnetic field modulation techniques. The output from the lock-in amplifier is proportional to the change in signal reflected from the resonator as the field is swept, i.e. it is the first derivative of the absorption mode signal.

4.2. Magnetic field modulation

With the magnetic field modulation superimposed on the ramped magnetic field, the time-dependent magnetic field experienced by the sample can be expressed as

$$\begin{aligned} B(t) &= B_0 + B_{\text{ramp}} + B_{\text{mod}}, \\ &= B_0 + \Delta B_0(t/t_0 - 1/2) + (1/2)B_{\text{m}} \sin \omega_{\text{m}} t, \end{aligned} \tag{13}$$

where

B_{ramp} is the ramped field and equal to $\Delta B_0(t/t_0 - 1/2)$;
B_{mod} is the sinusoidal modulation field with amplitude $(1/2)B_{\text{m}}$;
ω_{m} is the modulation frequency; and
the magnetic field $(B_0 + B_{\text{ramp}})$ is swept over the range ΔB_0 from $(B_0 - \Delta B_0/2)$ to $(B_0 + \Delta B_0/2)$.

To satisfy slow passage conditions, ω_{m} must be sufficiently small such that there are several cycles of the modulation frequency during the passage between the half-amplitude points of the resonance line, i.e.

$$\omega_{\text{m}} \ll \gamma \Delta B_{1/2}. \tag{14}$$

Under these conditions, the magnetic field $(B_0 + B_{\text{ramp}})$ can be considered to be effectively constant. The mechanism whereby the magnetic field modulation is transformed to RF power modulation is illustrated in Fig. 5. The field modulated sine wave $\sin \omega_{\text{m}} t$ is converted by the non-linear lineshape to a complex signal $S(B)$ that is a superposition of the fundamental modulation frequency ω_{m} and a large

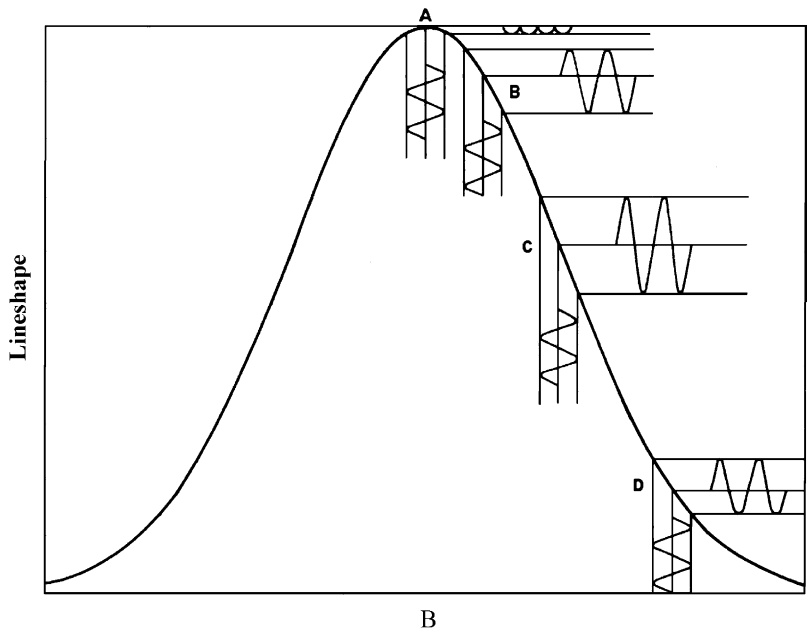

Fig. 5. The signal (horizontal) produced at various points on the resonant line due to the magnetic field modulation (vertical). (Adapted from Ref. 91.)

number of harmonics of ω_m:

$$S(B) = \sum_{n=0}^{\infty} [a_n(B) \cos n\omega_m t + b_n(B) \sin n\omega_m t]. \quad (15)$$

The measured signals deriving from different points on the resonance line shown in Fig. 5 are composed of different combinations of the fundamental and harmonic terms in the Fourier series expansion of Eq. (15). Thus the signal from the inflection point C on the resonant curve in Fig. 5 is composed primarily of the fundamental $\sin \omega_m t$, while that at the centre point A is composed primarily of the second harmonic $\cos 2\omega_m t$. The signal from points B and D contain the fundamental, second and higher harmonics in the Fourier series, but are inverted and phase shifted with respect to each other. Likewise, signals from corresponding points on different sides of the curve are phase shifted by 180° with respect to each other. By way of illustration, the signal arriving at the detector is illustrated in Fig. 6a with no field modulation and Fig. 6b with field modulation, where S_1 represents the signal amplitude resulting from the B_1 field at frequency ω_0, while S_m represents the amplitude of the modulation envelope at frequency ω_m. In the situation depicted in Fig. 6b, the RF frequency ω_0 is modulated primarily by the fundamental $\sin \omega_m t$ term of Eq. (15), which occurs for signals deriving from point C in Fig. 5. The detector strips off the RF component and passes the AF envelope component to the lock-in amplifier.

The use of magnetic field modulation with lock-in detection influences the measured shape and amplitude of the absorption spectra, both being dependent on the modulation amplitude B_m. Analyses of these effects have been made by a number of authors based upon the assumption of either a Lorentzian or a Gaussian lineshape (for a review, see Ref. 91). Myers and Putzer[92] derived an expression for the measured signal assuming a Gaussian lineshape, which is typical of the solid materials studied by the CW-NMR system. They began by expressing a generalised Gaussian lineshape in terms of magnetic field units, substituting in Eq. (13) and

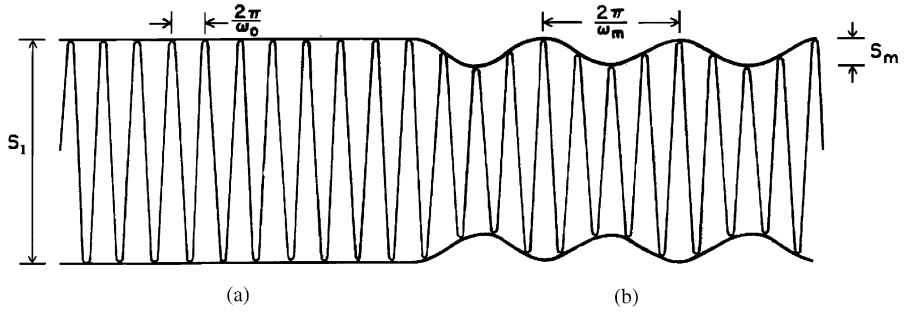

Fig. 6. Signal arriving at the detector (a) with no field modulation; (b) with field modulation. (Adapted from Ref. 91.)

expanding it as a Fourier series:

$$g(B) = 2T_2 \exp\left[-0.693\left(\frac{B - B_0}{(1/2)\Delta B_{1/2}}\right)^2\right]$$
$$= 2T_2 \exp\left[-0.693\left(\frac{B_{\text{ramp}} + (1/2)B_{\text{m}} \sin \omega_{\text{m}} t}{(1/2)\Delta B_{1/2}}\right)^2\right]$$
$$= 2T_2\left[a_0 + \sum_{n=1}^{\infty}(a_n \sin n\omega_{\text{m}} t + b_n \cos n\omega_{\text{m}} t)\right]. \quad (16)$$

Only the fundamental (first harmonic) component given by the Fourier coefficient a_1 is detected in the CW-NMR experiment (since we are employing lock-in detection at the modulation frequency ω_{m}):

$$a_1 = \exp(-(sB_{\text{ramp}})^2) \sum_{n=0}^{\infty} \frac{(sB_{\text{m}}/2)^{2n+1}}{2^{2n}} \left(\frac{(2n+1)!}{(n)!(n+1)!}\right)$$
$$\times \sum_{k=n+1}^{2n+1} \frac{(-1)^k}{(k)!} \left(\frac{(k)!}{(2k-2n-1)!(2k-2n)!}\right)(2sB_{\text{ramp}})^{2k-2n-1}, \quad (17)$$

where $s = 2(\ln 2)^{1/2}/\Delta B_{1/2}$. The effect of the magnetic field modulation on the measured lineshapes is illustrated in the plot of Eq. (17) in Fig. 7 for several values of B_{m} normalised to the linewidth $\Delta B_{1/2}$.[93] The severe line broadening which results from the use of an excessive B_{m} is clearly evident. The corresponding maximum signal amplitude as a function of B_{m} is illustrated in Fig. 8, normalised to the signal amplitude in the absence of field modulation. As B_{m} increases, the signal increases linearly at

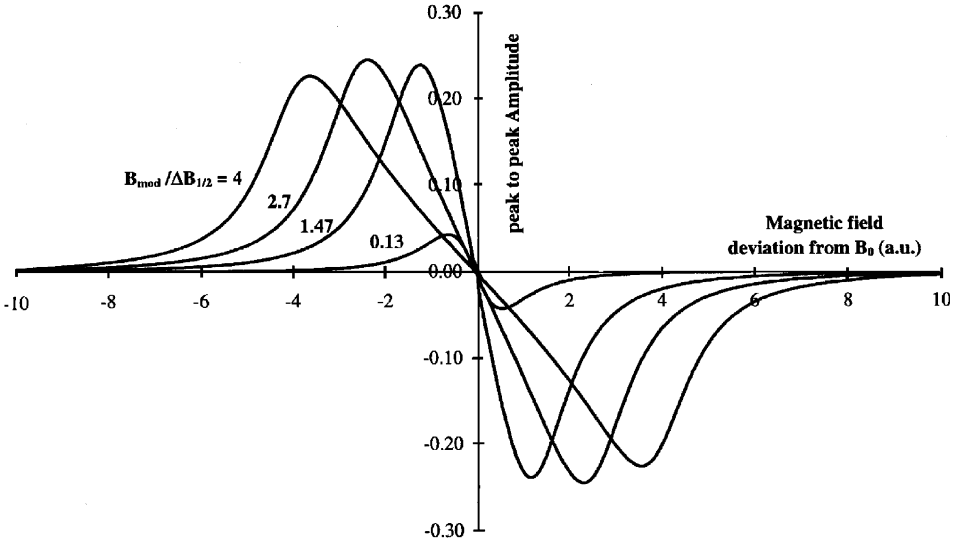

Fig. 7. Effect of magnetic field modulation on the measured lineshape according to Eq. (17).

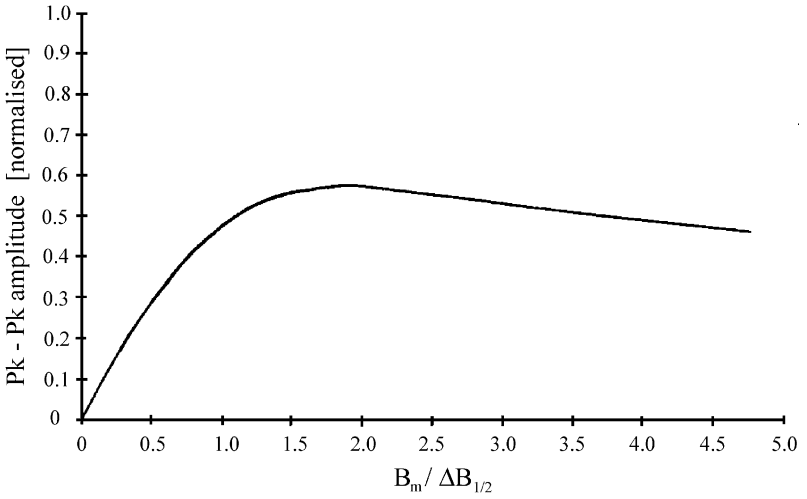

Fig. 8. Variation in the signal amplitude with B_m, normalised to the signal amplitude in the absence of field modulation according to Eq. (17).

first, but levels off and reaches a maximum of ~0.57 at a field of $B_m/\Delta B_{1/2} \sim 1.8$, with a steady decrease thereafter. Despite this loss of signal when using field modulation, the large decrease in the measured noise due to the use of narrow bandwidth phase-sensitive detection results in a net improvement in SNR.

4.3. Spatial localisation

If a linear magnetic-field gradient $G_x = dB_z/dx$ is superimposed on the main static field B_0, the resonant frequency of a nucleus within the sample will depend on its position along the direction of the applied gradient

$$\nu(x) = (\gamma/2\pi)(B_0 + xG_x). \tag{18}$$

This is the basis of frequency encoding, which is used exclusively in CW-NMR imaging. The application of such a magnetic-field gradient confines the spins that come into resonance to a plane perpendicular to the gradient direction. The effect of the ramped magnetic field B_{ramp} is then to sweep this plane of resonance across the sample in the direction of the gradient. Because magnetic field modulation is employed, the signal from the lock-in amplifier is proportional to the change in the number of spins that are in the plane of resonance. Therefore, the trace over time is the first derivative of the spin density of the sample projected onto the axis of the gradient. Rotating the gradient direction in a fixed plane around the sample results in a series of projections, from which a two-dimensional image can be reconstructed using filtered back-projection. Rotating this plane extends reconstruction of the image to three-dimensions. For 2-D imaging, the gradient direction can be rotated

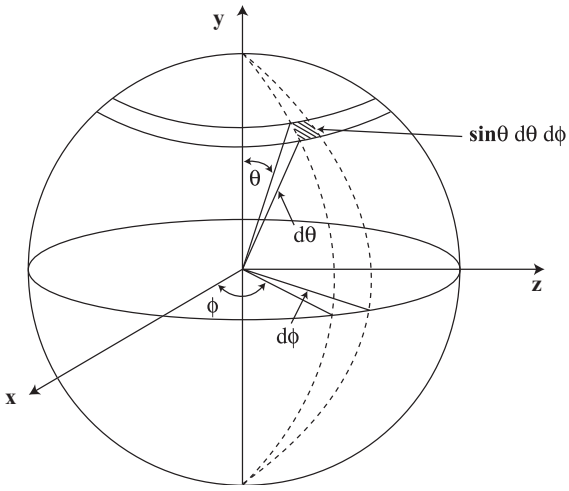

Fig. 9. Co-ordinate system for 3-D imaging sequence, illustrating the acquisition scheme for isotropic resolution.

by using a linear combination of two orthogonal gradients G_x and G_y such that

$$G = G_x \sin\theta + G_y \cos\theta, \tag{19}$$

where G is the gradient strength. For 3-D imaging, the gradient direction must be rotated in both polar and azimuthal directions to cover four octants in 3-D space. Furthermore, to ensure isotropic resolution, the gradient orientations must be uniformly distributed over the surface of a sphere. Hence, since the elemental area on the surface of a sphere is proportional to $\sin\theta\,d\theta\,d\phi$, as illustrated in Fig. 9, the polar angle θ must be stepped uniformly (i.e. $\Delta\theta = \text{constant}$), but the azimuthal angle ϕ must be incremented as $1/\sin\theta$ (i.e. $\Delta\phi = \Delta\theta/\sin\theta$). Using the co-ordinate system defined in Fig. 9, the gradient strengths must therefore be varied as

$$\begin{aligned} G_z &= G \sin\vartheta \sin\phi, \\ G_x &= G \sin\vartheta \cos\phi, \\ G_y &= G \cos\vartheta. \end{aligned} \tag{20}$$

To cover four octants during 3-D imaging experiments, only the top hemisphere needs to be scanned requiring inversion of the G_z and G_x gradient directions, and hence θ is varied from 0° to 90°, while ϕ is varied from 0° to 360°.

The maximum achievable spatial resolution $(\Delta x)^{-1}$ in CW-NMRI is determined by the natural linewidth $\Delta\nu_{1/2}$ of the material being studied and by the magnitude of the applied gradient G:

$$(\Delta x)^{-1} = \gamma G (2\pi\Delta\nu_{1/2})^{-1}. \tag{21}$$

$\Delta\nu_{1/2}$ can be approximated by $(\pi T_2)^{-1}$ for Lorentzian lineshapes and $(2.13\ T_2)^{-1}$ for Gaussian lineshapes.[94] Therefore, for solid-state materials with Gaussian

lineshapes, we have

$$(\Delta x)^{-1} \approx 0.34\gamma G T_2. \tag{22}$$

Thus, at a gradient strength of 300 mT/m, this corresponds to a maximum theoretical spatial resolution of approximately 0.36 mm for a rigid polymer such as poly(methyl methacrylate) (PMMA) exhibiting a T_2 of 16 μs.

5. SYSTEM HARDWARE

5.1. Overview

A block diagram of the CW-NMRI system is presented in Fig. 10. The system is based around a 7 T, 183 mm diameter horizontal bore superconducting magnet (Oxford Instruments, UK), with a computer (800 MHz PC) controlling certain elements of the system electronics via a GPIB IEEE 488 instrument bus and running the sequence control and data acquisition/processing software. A multifunction data

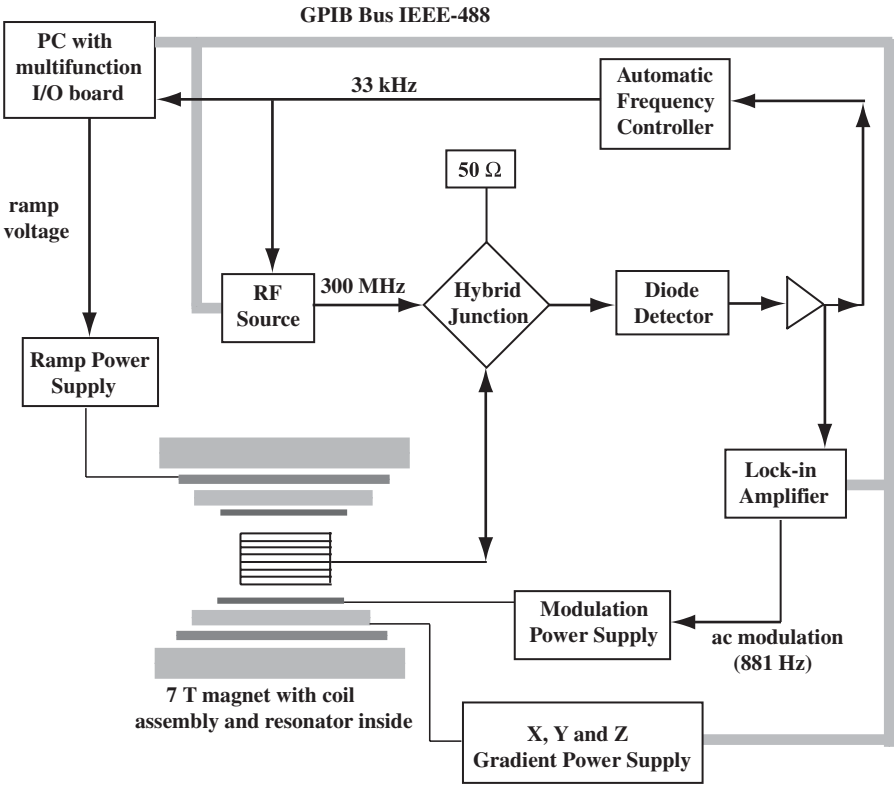

Fig. 10. Block diagram of the principal components in the CW-NMRI system.

input/output (I/O) board (National Instruments, USA, Model PCI-MIO-16E-4) was used to enable the I/O of a range of digital and analogue signals to/from the PC for various aspects of experimental control and monitoring. An on-board data buffer together with the in-built timing functionality was used to output all ramp patterns in a precisely time-controlled fashion. A shielded connection block (National Instruments, USA, Model SCB-68) was used as an interface between the I/O board and the equipment rack. The RF was supplied by a synthesiser (Hewlett Packard, USA, Model HP8647A) and applied to one terminal of a hybrid junction (Lorch Electronics, USA, Model JH280E). The two neighbouring ports of the hybrid junction were connected to a 50 Ω load and the resonator, while the signal appearing on the output was sent to a diode detector and low-noise pre-amplifier unit built in-house, before being passed to the lock-in amplifier (Stanford Research Systems, USA, Model 830 DSP).

All of the software needed to run the CW-NMRI experiment was developed using the LabVIEW programming language (Laboratory Virtual Instrument Engineering Workbench, National Instruments, USA). LabVIEW uses a hierarchical and modular structure, with higher-level programs (VIs) passing data or parameter lists to lower-lying sub-VIs. Sub-VIs function as stand-alone executables, which aids with the debugging and development of complicated programmes. Furthermore, LabVIEW contains a range of library functions specifically aimed at data acquisition and instrument control, rendering it particularly suitable for the current application. Another useful feature of LabVIEW is the fact that it is a dataflow programming language (by comparison with conventional linear, text-based languages), which means that it can execute multiple operations in parallel, lending greater efficiency to the overall sequence control.

5.2. Coil assembly

The gradient, offset and modulation magnetic fields were produced using a custom-built water-cooled coil assembly (Laplacian Ltd., UK), which employed proprietary stream function designs with power dissipation minimisation to produce large gradient fields (maximum 400 mT/m for the Z and 300 mT/m for the X/Y gradients), together with two nested solenoids producing the ramped offset magnetic field (maximum ± 16 mT) and the superimposed AF modulation field (maximum ± 400 μT). Overall, the unit had outer and inner diameters of 180 and 90 mm respectively. The modulation coil was placed on the inside layer of the assembly to minimise its inductance and hence current requirements, while the offset coil was placed on the outside to minimise its coupling to the modulation coil. All magnetic fields were homogeneous to within 5% over a cylindrical volume of diameter 50 mm and length 70 mm. Commercial power supplies (Advance Hivolt, UK, Models AP90100 and AP5060) were used to power the gradient and offset coils (with maximum current capabilities of 90 and 50 A respectively), while a home-built AF power supply was used to drive the modulation coil up to a maximum frequency of 15 kHz. Temperature sensors were placed at various

Table 1. Physical characteristics of the coil assembly

Parameter	Modulation	Ramp	X Gradient	Y Gradient	Z Gradient
Number of Layers	1	2	2	2	2
Number of Turns	20	225	–	–	152
Average Radius [mm]	49	73.3	50.8	53.4	69.5
Thickness [mm]	1	3.9	2	2	3.9
Current [A]	3.4	11.8	86	92	33.4
Ohmic voltage [V]	0.7	7.2	5.6	6.0	13.9
Resistance at 25°C	0.178	0.525	0.056	0.056	0.356
Ohmic power [W]	2	85	482	552	464
Inductance [μH]	13	–	–	–	–
Maximum field [mT]	±0.4	±16	–	–	–
Maximum gradient [mT/m]	–	–	300	300	300
Wire length [m]	6.2	103.6	–	–	66.4
Calibration factor [mT/m/A] or [mT/A]	0.0706	0.8841	3.53	3.28	9.34
Efficiency $\times 10^{-7}$/radius^2 [Tm/A] (see Ref. 99)	–	–	91.1	93.5	451

hotspots within the assembly and continually monitored during experiments. The physical characteristics of the coil assembly are listed in Table 1.

5.3. Resonators

All of the resonators used with the CW-NMRI system were based on an 8- or 12-leg birdcage design described previously.[88] In each case, it was necessary to avoid using materials in the construction of the resonators which contained the nuclei of interest, since these would be detected by the system and hence contribute a significant background signal. Thus, PTFE was typically used to provide structural support, while specialised non-magnetic capacitors were used throughout (fixed capacitances formed using miniature chip ceramic capacitors (Tekelec, France) or appropriately shaped strips of CuFlon (Polyflon, USA), which is comprised of copper electroplated onto both sides of a thin dielectric of PTFE; and Voltronics variable capacitors (Voltronics, USA)). The resonators were placed directly into RF shields made from copper sheets of thickness 0.5 mm and length 200 mm, with a resultant outer diameter of 81 mm. It was necessary to split the shields along their length to prevent the AF magnetic field modulation causing eddy currents, which would introduce acoustic interference and would also prevent the modulation from penetrating the shield to the sample. This split was typically closed to RF penetration by forming a capacitor comprising the shield itself and a strip of copper (width 18–80 mm, thickness 40–80 μm depending on the resonant frequency) bridging the gap, with a strip of PTFE (thickness 55 μm) in between acting as a dielectric.

5.4. Automatic frequency controller

In a CW-NMRI experiment, it is essential to ensure that the resonator is maintained exactly on-tune in order to eliminate the dispersive component of the RF susceptibility and thus only detect the absorption component. However, factors such as thermal expansion, sample loading and microphonics can lead to drifting of the resonator's frequency, and therefore it is vital to be able to track such frequency drifts. In practice, this was achieved by dynamically controlling the frequency transmitted by the RF synthesiser using a home-built automatic frequency controller (AFC)[95] so as to equalise the transmitted frequency and the resonator's central frequency. This was implemented using a feedback loop from the output of the hybrid junction to the RF synthesiser (Fig. 10). By effectively operating at a different frequency in this manner, the static field B_0 needs to be adjusted to maintain the resonance condition, i.e. ω_0 is effectively changed to follow drifting of the resonator during the course of an experiment. This adjustment of the static field B_0 was done by adding a DC offset shift to the ramped magnetic field when sweeping through the resonant peak.

The AFC controls the operating frequency by imposing a frequency modulation (FM) at 33 kHz onto the signal transmitted by the RF synthesiser (300 MHz for ^{1}H work). At resonance, the 33 kHz FM is converted to a 66 kHz amplitude modulation (AM) of the reflected signal (see Fig. 11c). If the resonator drifts away from resonance, the signal from the hybrid junction will contain AM components at both 33 and 66 kHz (Fig. 11a–c). The amplitude of the 33 kHz component increases as the resonator drifts further from resonance, while its phase is sensitive to the direction of the drift. Part of this reflected signal is then fed back into the AFC, where it inputs to a phase-sensitive detector (PSD). The PSD compares this signal with a reference signal deriving from the source of the original 33 kHz modulation, and outputs a DC error signal proportional to the frequency drift of the resonator.

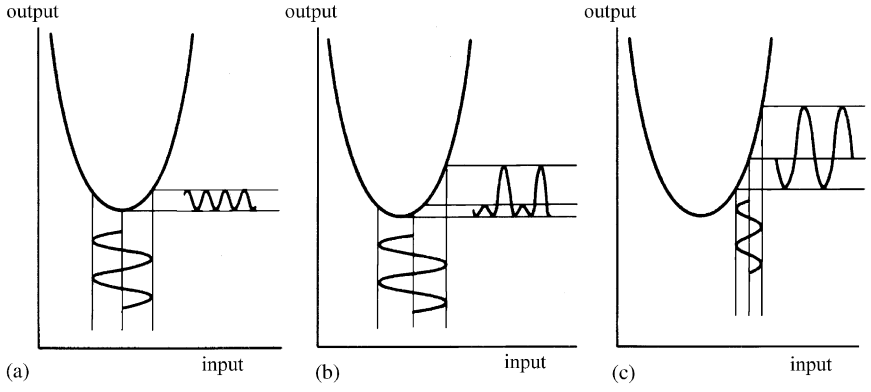

Fig. 11. Response to the 33 kHz modulation of the AFC: (a) on resonance; (b) close to resonance; and (c) far-off resonance (adapted from Ref. 91).

This DC error signal is added to the 33 kHz modulation signal, and applied to the 'DC FM' input of the RF synthesiser. The RF synthesiser's transmitted frequency can be varied by ± 50 kHz with the application of a ± 1 V DC error signal, which corresponds to a magnetic field of ± 1.16 mT at 300 MHz.

5.5. Detector

Before describing the operation of the detector circuit, it is instructive to summarise the various signals along different pathways in the CW-NMRI system. These are illustrated in Fig. 12.

The 15 V DC signal added to the output of the AFC is stripped from the other components using the capacitor *C* and is used to power the detector and pre-amplifier circuitry. Meanwhile, the 300 MHz and 33 kHz components pass onto the hybrid junction without attenuation because of the greater impedance presented by the resistor *R* compared to the capacitor. The output from the hybrid junction to the detector contains the 300 MHz and 33 kHz components, together with the absorption signal at 881 Hz (variable up to 15 kHz). The detector strips off the 300 MHz component and outputs the 33 kHz component, the 881 Hz absorption signal, plus a 'DC bias' voltage which indicates the actual operating bias voltage of the diode detector. These signals arrive at the AFC, which removes the DC component (which can be monitored at the AFC) before forwarding the 881 Hz and 33 kHz components to the lock-in amplifier. The PSDs in the lock-in amplifier and AFC are only sensitive to the 881 Hz and 33 kHz components respectively, and disregard the rest.

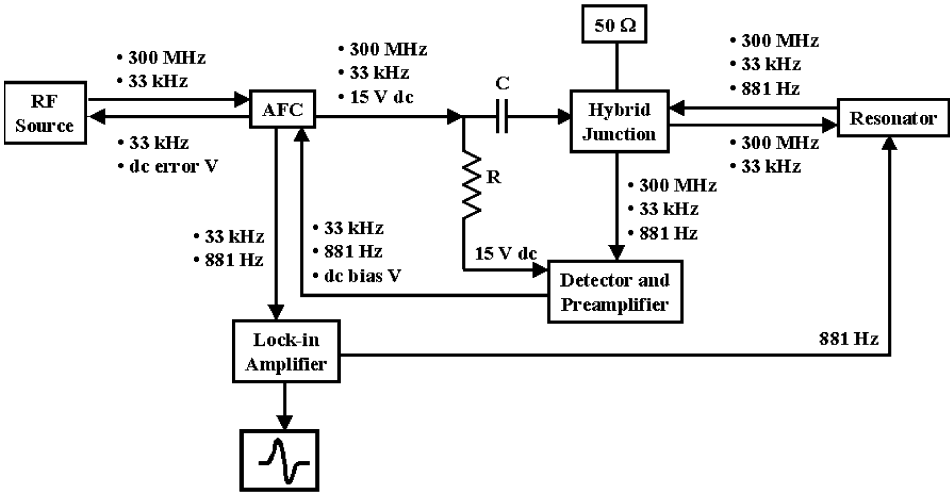

Fig. 12. Block diagram showing the various signals along different pathways in the CW-NMRI system (for ^{1}H work).

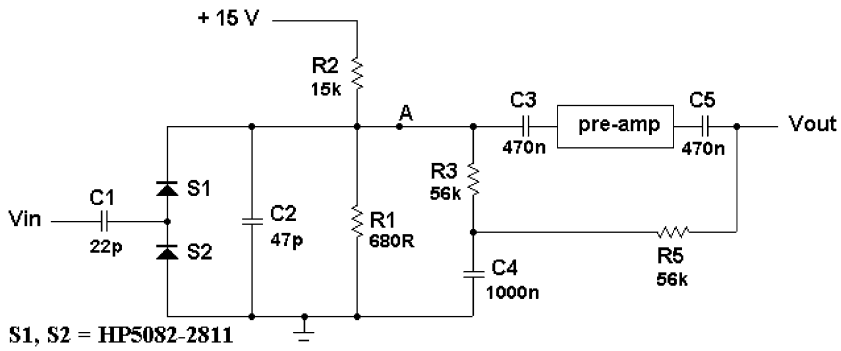

Fig. 13. Schematic diagram of the diode detector circuit.

The main elements in the diode detector are illustrated in Fig. 13. A diode detector essentially takes an RF signal, rectifies it, filters it to remove the high-frequency component, and outputs a DC signal proportional to the RF input level. The detector built for the CW-NMRI system uses a pair of Schottky diodes S_1 and S_2 in bi-phase arrangement, which doubles the output signal compared to using just one diode since both half cycles of the RF waveform are detected. Resistors R_1 and R_2 set the required bias for the diodes. Capacitor C_1 couples the incoming signal to the circuit, while C_2 forms an RC circuit (with R_1) with a time constant of ~32 ns, which effectively smoothes the rectified RF signal to a DC level proportional to the input RF power. The 33 kHz and 881 Hz signals superimposed on the 300 MHz carrier wave are not rectified, nor do they 'see' this RC circuit because of its short time constant and so pass through it unaffected. Thus the signal arriving at point A consists of the 33 kHz and 881 Hz components with a superimposed DC component. This DC component is prevented from entering the pre-amplifier circuit by C_3, and instead follows the path directly to the output. The 33 kHz and 881 Hz signals are prevented from following the DC component because of the large impedance presented to them by R_3, and therefore pass into the pre-amplifier. The amplified components are finally added to the DC bias voltage at the output. The detector and pre-amplifier circuit was encased in a die-cast alloy box which was placed as close as possible to the resonator.

5.6. Support frame

The resonator/shields were mechanically decoupled from the main gradient, ramp and modulation coil assembly by sliding them into a 1.6-m-long fibreglass tube (1 mm wall thickness, inner diameter 83 mm) which was suspended within the coil assembly using two support frames built at either end of the magnet (Fig. 14a). The frames did not touch either the coil assembly or the magnet at any point and furthermore were mounted on vibration-dampening feet, in an effort to minimise

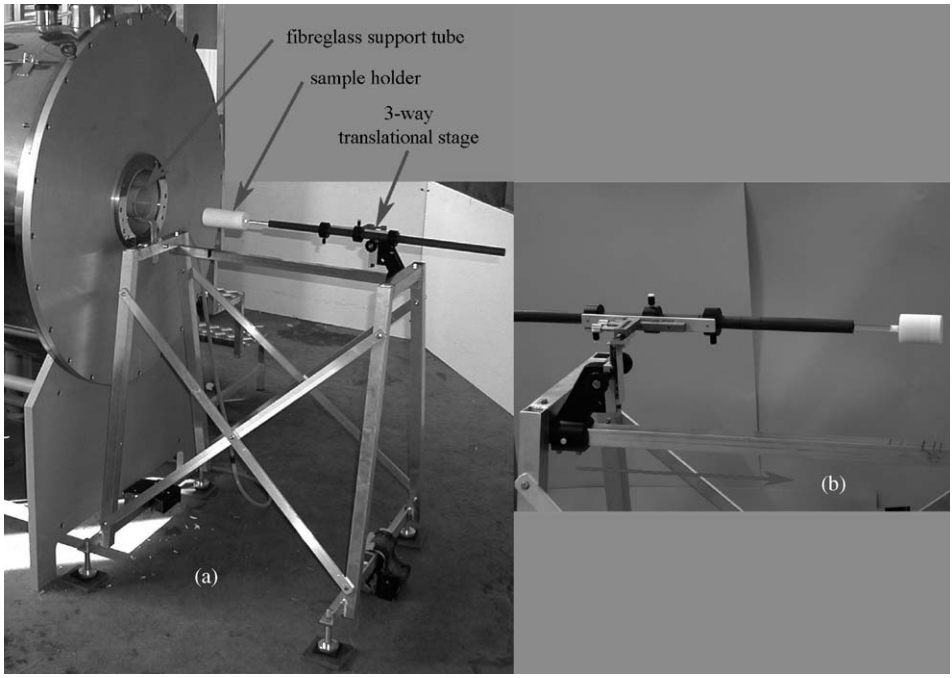

Fig. 14. (a) Photograph of the frame supporting the shield/resonator and sample holder; (b) close-up of the 3-way translational stage for accurate positioning of the sample.

microphonic effects due to vibrations originating in the modulation coil. A system for suspending and accurately positioning samples within the magnet was also incorporated into the support frame. Sample holders were typically made from PTFE to avoid background signal pick-up and attached to a three-way translational stage on the positioning platform via a quartz rod (Fig. 14b).

6. APPLICATIONS

6.1. Imaging of cementitious materials

The deterioration over time of reinforced concrete structures is of major economic significance throughout the world. The presence of water and water transport is known to play a key role in determining the pore structure and long-term durability of cement materials, which constitute the key component of concretes. For example, an excess of water during fabrication leads to large pore sizes and hence a high permeability in the material. This results in enhanced water ingress, which causes problems on a number of fronts: direct physical attack via freeze–thaw mechanisms; chemical leaching of the calcium hydroxide phase in the cement by the hydration of

calcium silicates; direct damage caused by salt crystallisation and effects of various dissolved ion species, e.g. dissolved sulphate ions directly attacking calcium aluminate phases, and dissolved chloride ions corroding the steel in reinforced structures.[96] Bridges and coastal structures are particularly exposed to the ingress of salty water, while de-icing on motorways via salt gritting can also cause significant problems. However, the movement of dissolved ions such as sodium and chloride within cements is still not fully understood, while the reactions which may take place between them and the cement material itself or additives within the cement are equally vague. It is therefore of considerable interest to characterise water content and transport in cement materials in a spatially resolved, non-invasive and non-destructive manner which will allow time-course studies to be carried out.

The CW-NMRI system was used to study the penetration of water and brine into samples fabricated from Ordinary Portland Cement (OPC), using various water/cement (w/c) ratios and curing conditions to produce a range of samples with differing pore size distributions. In general, one-dimensional profiling experiments were carried out on cylindrically shaped samples measuring up to 44 mm in diameter and 60 mm in length, with a typical acquisition time of 4 min per profile.

6.1.1. *Water penetration*

A sample with a w/c ratio of 0.4 by weight (which is at the threshold water content required for complete hydration of OPC) was cured for 28 days in a dry desiccator with a relative humidity of $<5\%$. All surfaces of the sample except the top face were sealed with Parafilm, to promote evaporation of water through this surface only. This was done to disrupt the hydration process in this part of the sample and hence introduce some inhomogeneity into the cured sample. Following the cure period, the Parafilm was removed and the sample was dried in an oven for 48 h at 105°C in order to remove all evaporable water. Water penetration studies were then carried out as described below.

One-dimensional profiling experiments carried out on the sample during curing and drying are illustrated in Fig. 15. It can be seen that there is a gradual decrease in intensity on the left-hand side of the profile, consistent with a loss of water from this part of the sample through evaporation from the exposed face. It should be noted that the CW-NMRI technique detects water protons in all environments within the sample, i.e. capillary water, gel water *and* chemically combined water. Consequently, any decrease in the measured intensity results from a loss of water from the sample, rather than a loss of signal due to an increasing proportion of chemically combined water as the hydration progresses. The maximum non-uniformity measured along the sample occurred after 14 days of curing, after which the profile began to level off as water diffused from the right side of the sample and was eventually lost through evaporation. There was no further decrease in intensity or indeed sample mass after 24 h of drying, and hence the 24-h profile is a measure of the chemically combined water content within the sample. Note the residual slope to the left-hand side in this profile, indicating an inhomogeneous cure along the axis of the sample. At this point, the sample exhibited a T_2^* of $\sim$10 μs.

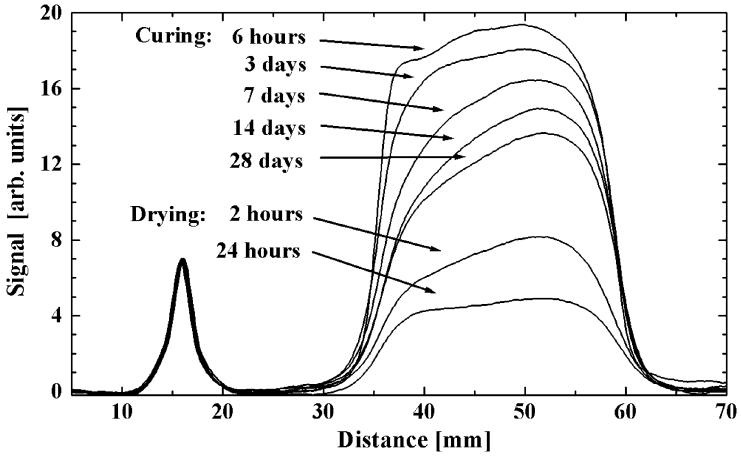

Fig. 15. Profiles of an inhomogeneously cured w/c = 0.4 sample for different curing and drying times. A gradient of 140 mT/m was used. The unsealed face was on the left side. The peak to the left of the sample is from a reference material.

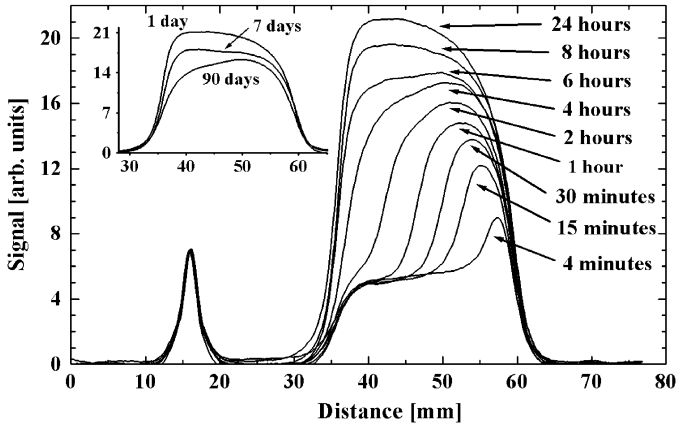

Fig. 16. Water penetration into a w/c = 0.4 sample as a function of soaking time, reaching a peak after 24 h of soaking – the water reservoir was on the right side. The insert shows the decrease in intensity after 7 and 9 days of soaking, indicating the establishment of a dynamic equilibrium within the sample between water absorption from the reservoir on the right and evaporation on the left.

Fig. 16 shows the penetration of water into the cured and dried sample. The sample's orientation was as before, with the exposed face to the left side. The water reservoir was on the right side and was removed while profiling. A water front can be seen moving across the sample, reaching the left side after approximately 6 h of soaking. Thereafter, the intensity of the profile increased over a period of tens of hours, consistent with the gradual filling of smaller pores within the sample. Two

effects can be discerned. Firstly, the intensity peaks after 24 h of soaking, but exhibits a fall-off to the right, indicating enhanced uptake of water in the left part of the sample. This is consistent with an incomplete hydration in this region of the sample due to water evaporation during the curing process, which would result in a more porous structure and hence an enhanced uptake of water. Secondly, the intensity of the profile decreased following further soaking, reaching a steady state after about 90 days (see insert in Fig. 16). This situation represents a dynamic equilibrium in the sample between uptake of water from the reservoir on the right and loss of water via evaporation from the left face.

The sample was dried completely and a second water penetration experiment was carried out. The maximum uptake of water occurred once again after 24 h of soaking; however, the slope of the profile was less pronounced, as illustrated in Fig. 17. Furthermore, the peak intensity was lower in the second experiment, which is evidence of a smaller pore size distribution in the sample, suggesting that some degree of rehydration took place in this sample during the course of the first water penetration study. This result was further verified by mercury intrusion porosimetry.

2-D imaging of water penetration into a sample of OPC is illustrated in Fig. 18. This sample, measuring $32 \times 30 \times 12$ mm, was cured for 28 days in a wet environment (relative humidity $>95\%$) to ensure a homogeneous cure, and dried at 105°C for 48 h to remove all evaporable water. The sample was then completely sealed except for the left face, which was exposed to a water reservoir. The water reservoir was removed for imaging, and an acquisition time of 15 min was used for each image (there was negligible penetration of the absorbed water into the sample while the water reservoir was removed). It can be seen in Fig. 18 that the water has almost fully penetrated across the sample after approximately 1 h of soaking, with a

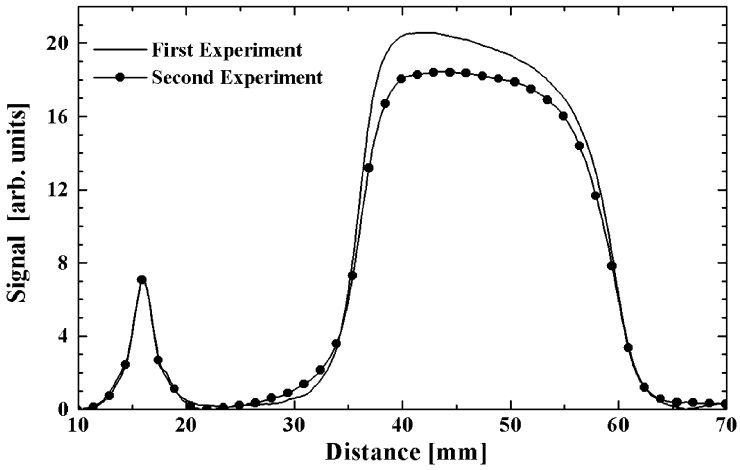

Fig. 17. Comparison of the peak water uptake into the w/c = 0.4 sample during the first and second water penetration experiments.

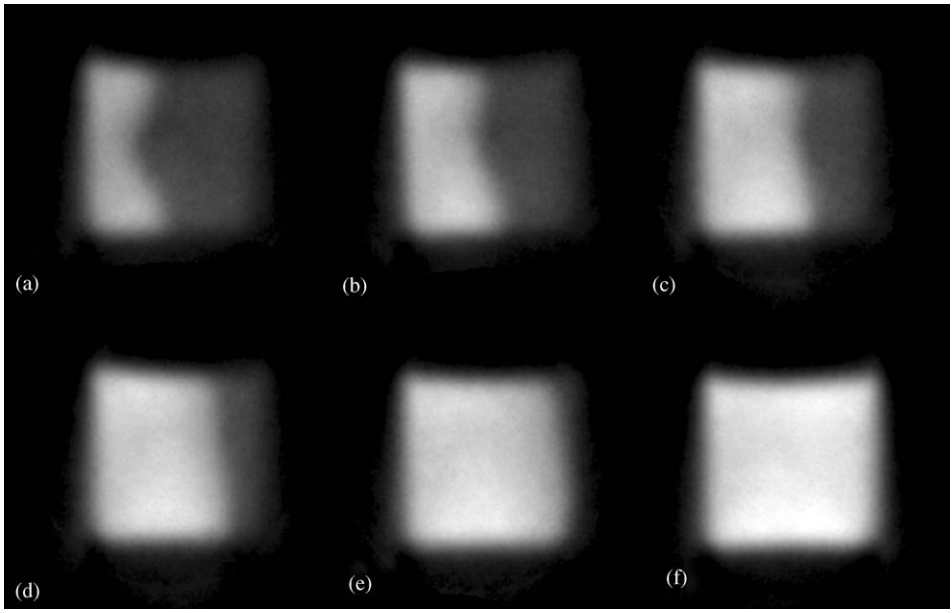

Fig. 18. Water penetration into a cement sample following soaking times of: (a) 5 min; (b) 10 min; (c) 15 min; (d) 30 min; (e) 60 min; (f) 5 h. Image acquisition times = 15 min. (Reproduced from Ref. 89 with permission from Elsevier.)

further increase in intensity after prolonged soaking, again consistent with the filling of smaller pores within the sample. Note that the signal in the right part of Fig. 18a derives solely from the chemically combined water in the sample, with a T_2^* of approximately 10 μs. The imbibed water exhibited a T_2^* of approximately 30 μs.

6.1.2. *Brine penetration*

The penetration of brine into a range of OPC samples (with w/c ratios of 0.3, 0.4 and 0.5) was studied. The samples were cured for 28 days in a wet environment (relative humidity >95%) to ensure a homogeneous cure, and dried at 105°C for 48 h to remove all evaporable water. After drying, the samples were immediately placed into a saturated solution of NaCl for 4 days, after which the samples were fully saturated. The samples were then removed from the solution and imaged. The resulting 1-D profiles are presented in Fig. 19, where an increase in the signal is observed as the w/c ratio is increased, due to the increased pore sizes and hence increased uptake.

In a second set of experiments, the rate of penetration of a brine solution into a cement sample was measured as a function of soaking time. The sample, which had a w/c ratio of 0.4, was heated in an oven at 105°C for 4 days to remove all evaporable water, and then sealed on all sides except the end face which was dipped in a saturated salt solution. The resulting 1-D profiles illustrated in Fig. 20 show the progression of the ^{23}Na front into the sample with prolonged soaking times.

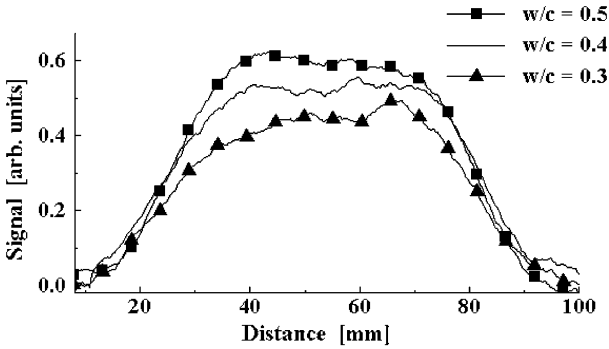

Fig. 19. Profiles of the ^{23}Na concentration in OPC samples with w/c ratios of 0.3, 0.4 and 0.5 soaked in brine, showing enhanced uptake for larger w/c values. (Reproduced from Ref. 98 with permission from Elsevier.)

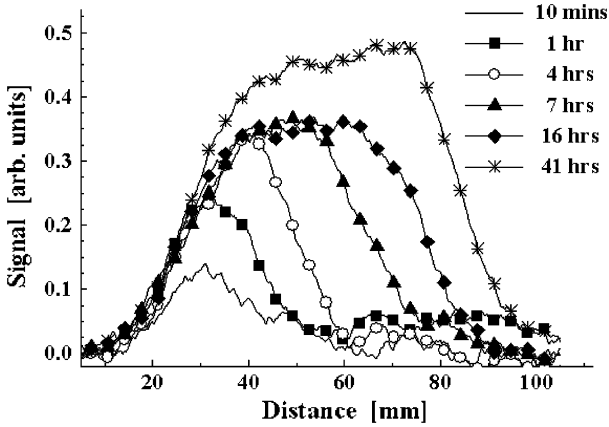

Fig. 20. Profiles of the ingress of ^{23}Na into an OPC sample as a function of soaking time. (Reproduced from Ref. 98 with permission from Elsevier.)

6.1.3. *Imaging of solid ^{27}Al in cement*

In addition to their binding properties, modern cements are characterised by a range of physical properties such as their rate of hardening, their resistance to ageing and temperature extremes, their rheological properties, and their interaction with the fillers and additives typically used in the mix. These properties are determined by the mineralogical composition of the cement, which are generally tailored to suit the particular application. For example, for high-temperature refractory applications, cements with high content of Al_2O_3 have been developed which afford the cement a very quick setting time and extremely high temperature resistance. Understanding the extent of the hydration reaction of the various components within these materials can aid in determining their long-term

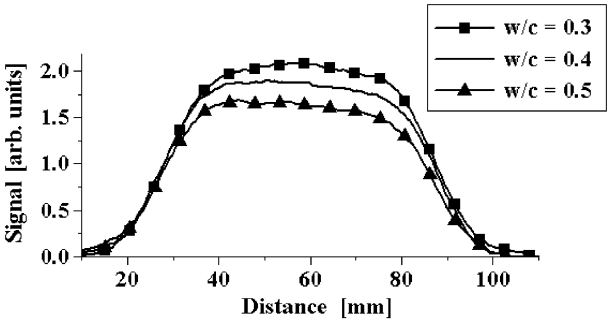

Fig. 21. 1-D profiles of the ^{27}Al content in cylindrical Secar 80® cement samples (Reproduced from Ref. 98 with permission from Elsevier.)

durability, and hence the ability to image the various phases in the cement is highly desirable.

A series of samples with w/c ratios of 0.3, 0.4 and 0.5 were made using a high-temperature refractory cement called Secar 80® (Lafarge Aluminates, France). This calcium aluminate cement consists of approximately 80% Al_2O_3 and 17% CaO, together with trace amounts of other elements (for comparison, OPC contains only ~12% $Ca_3Al_2O_6$ and ~8% $Ca_4Al_2Fe_2O_{10}$). The samples, measuring 44 mm in diameter and 60 mm in length, were cast in cylindrical moulds and cured for 28 days in an environment with a relative humidity of >95%. Spectroscopic evaluation of the ^{27}Al-containing phase of the fully cured samples indicated a T_2 relaxation time of 49 ± 1 μs. The 1-D profiles presented in Fig. 21 are of the ^{27}Al chemically combined within the Al_2O_3 phase in the cement. The decrease in the measured ^{27}Al signal of these samples as the w/c ratio is increased is clearly evident, demonstrating that the CW-NMRI system is sensitive to differences in the local cement concentration. It is interesting to note the slope to the right side (which corresponds to the top of the samples) for the w/c = 0.4 and 0.5 samples, which indicates that some degree of sedimentation may have taken place during the early stages of the cure.

A section of dimension $60 \times 34 \times 32$ mm was cut from the w/c = 0.3 sample. Two holes with diameters 6 and 8 mm were drilled through the sample, and a 2-D image (Fig. 22a) was acquired using an acquisition time of 16 h. The image was deconvolved with the sample's zero-gradient spectrum using a modified Weiner filter algorithm, resulting in an improvement in spatial resolution (Fig. 22b).

6.2. Diffusion of water in clay minerals

The three-layered clay mineral montmorillonite (bentonite) is characterised by a low-hydraulic conductivity and a capacity to bind water molecules and positively charged ions (cations). As such, water-saturated compacted bentonite powder is used as a hydrological barrier in areas such as waste disposal, for example around land-fill sites where the desire is to prevent leakage of contaminants from the land-

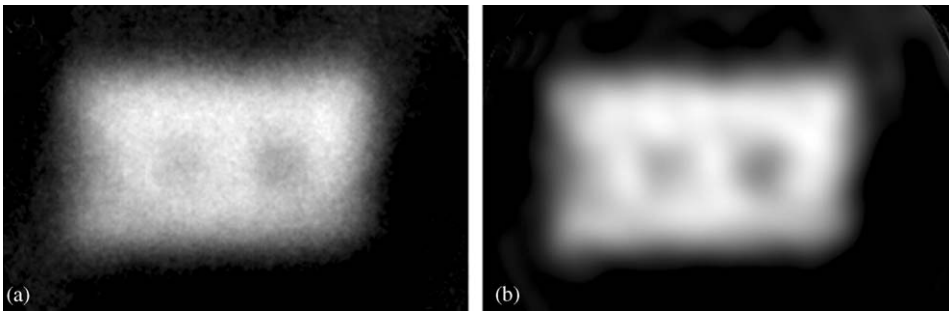

Fig. 22. (a) Raw and (b) deconvolved image of the ^{27}Al component in a Secar 80® cement sample, illustrating a 6 mm of the left side and a 8 mm hole on the right side. (Reproduced from Ref. 98 with permission from Elsevier.)

fill into the surrounding environment. It is also used in underground nuclear waste repositories as a barrier to radionuclide diffusion, where a layer of water-saturated, compacted bentonite is coated on the outside of a steel canister containing the radioactive waste. Here, the interest is in preventing ground-water from penetrating through to the canister, where dissolved elements may corrode the steel, but also in preventing dissolved radionuclides from leaking out in the event of a compromised canister. The excellent sorption capacity of bentonite for cationic radionuclides is key in this regard. However, bentonite is generally ineffective in adsorbing anionic contaminants such as the long-lived ^{129}I and ^{99}Tc. The migration of such contaminants is expected to be dominated by diffusion processes, and thus it is of considerable interest to measure the diffusion coefficient of water in compacted bentonite.

Conventional MRI has been successfully used to measure diffusion coefficients in a broad range of materials using field-gradient diffusometry techniques. However, such an approach is not possible for samples of bentonite due to the extremely short transverse relaxation times which this material exhibits, particularly for samples with relatively low water contents in the region of 20–30%, which is the water content typically used in the environmental technology applications mentioned above. An alternative approach to diffusometry via NMR employed in the present work is the observation of the temporal evolution of 1-D substance profiles by CW-NMRI, which can be used to determine the diffusion coefficient of the substance of interest. However, in contrast to field-gradient NMR, this approach cannot be used to observe pure self-diffusion, but rather one is constrained to study either diffusion processes along a moisture gradient (inter-diffusion) or the propagation of a stable isotope tracer profile (i.e. the diffusive mixing between ordinary water and deuterium oxide in the case of water self-diffusion in clay).

Clay samples were prepared in PTFE containers with an inner diameter of 30 mm and a length of 50 mm. Laboratory grade bentonite powder was obtained from Sigma-Aldrich (Poole, UK) and mixed in powder form with the appropriate quantities of water or heavy water (D_2O). After mixing, the moistened powder was filled in several layers into the sample container. Each layer was condensed into a

homogeneous clay mass by heavily stamping with a rounded metal bar for several minutes. To create an inter-diffusion scenario along a moisture gradient, a sample consisting of a homogeneous bentonite layer with a water content of 20 wt% was brought into contact with a reservoir of laboratory tissue paper soaked with several millilitres of deionised water. In a separate experiment, the self-diffusion of water between two bentonite layers prepared with light and heavy water was studied. The water content in this case was chosen to be 30 wt% for the light water and 33.3 wt% for the heavy water.

The results of these experiments are presented in Fig. 23. The profiles in Fig. 23a show the concentration-driven diffusion water front moving into the bentonite sample. The right side of the sample was confined at the bottom of the sample container, and hence swelling of the sample as it progressively absorbed more water is evident at the interface between the bentonite and tissue. In Fig. 23b, some residual H_2O content is evident on the left side of the sample despite heating the bentonite powder at 70°C for 3 days in an attempt to remove all evaporable water. The absorption of atmospheric water by the highly hygroscopic bentonite powder and pick-up from ^1H in OH groups within the alumina layers of the bentonite account for this signal. Nevertheless, the gradual diffusion of the H_2O through the sample is clear.

In both cases, an analysis of the diffusion front as a function of time shows a t^2 dependence of the front line which indicates Fickian diffusion and allows for the determination of a diffusion coefficient according to $x^2 = 2Dt$ from the slope of the curves in Fig. 24. The inter-diffusion coefficient was measured at $[1.15 \pm 0.05] \times 10^{-9}\,m^2/s$, while the self-diffusion coefficient was measured at $[8.4 \pm 0.5] \times 10^{-10}\,m^2/s$, which is the same order of magnitude as that recorded for non-swelling technical-grade kaolinite at similar water content.[97] This indicates

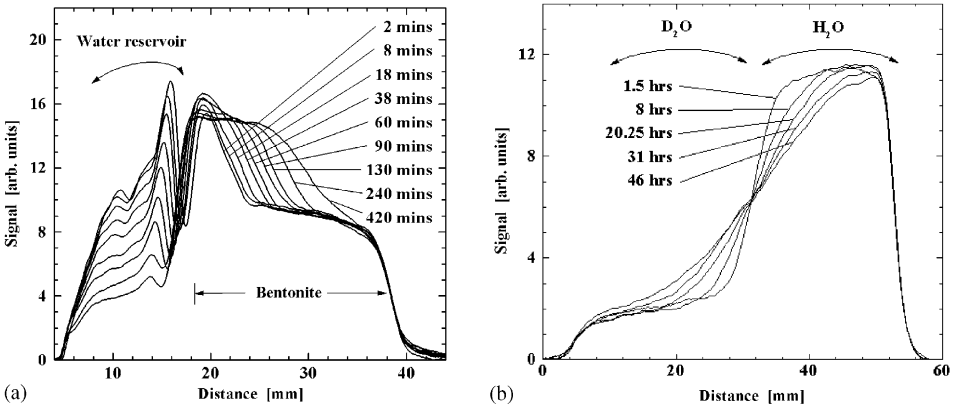

Fig. 23. Diffusion profiles of water into bentonite: (a) diffusion of water from a reservoir (left-hand side) into bentonite clay with initially 20% w/b water; (b) diffusion of water between two bentonite clay layers initially prepared D_2O and H_2O as indicated. (Reproduced from Ref. 90 with permission from Elsevier.)

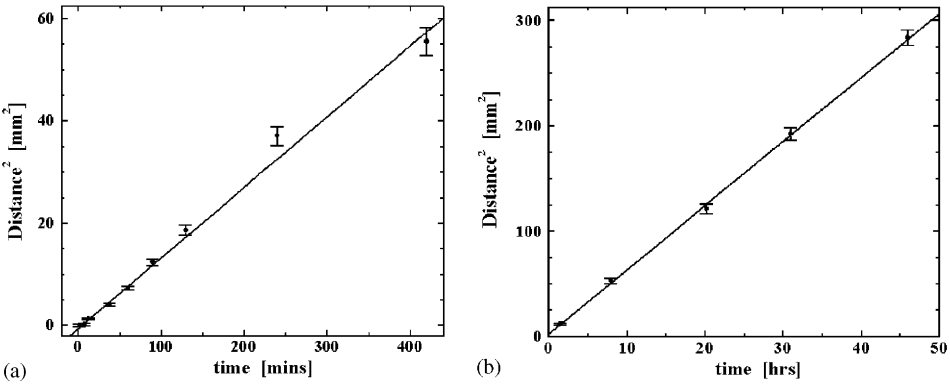

Fig. 24. Determination of the diffusion coefficients from the observed diffusion fronts shown in Fig. 23: (a) Diffusion along moisture gradient; (b) self-diffusion scenario for 30% w/b moisture content. (Reproduced from Ref. 90 with permission from Elsevier.)

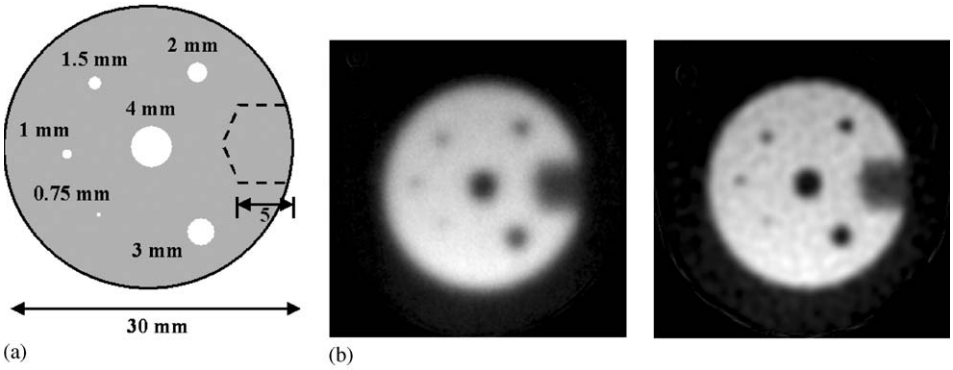

Fig. 25. (a) Schematic diagram of the PMMA resolution phantom; (b) raw and deconvolved images. (Reproduced from Ref. 98 with permission from Elsevier.)

that the difference in molecular dynamics between bentonite and kaolinite clays (which is quite obvious from the different NMR relaxation behaviour of both materials) does not lead to a strong effect on the long-range diffusive transport behaviour of the water molecules and that the tortuosities encountered by the molecules are similar.

6.3. Imaging of a rigid polymer

The imaging performance of the CW-NMRI system can be demonstrated by showing 2- and 3-D images of a rigid polymer such as poly (methyl methacrylate) (PMMA) (Perspex/Plexiglas). Spectroscopic investigations carried out on this

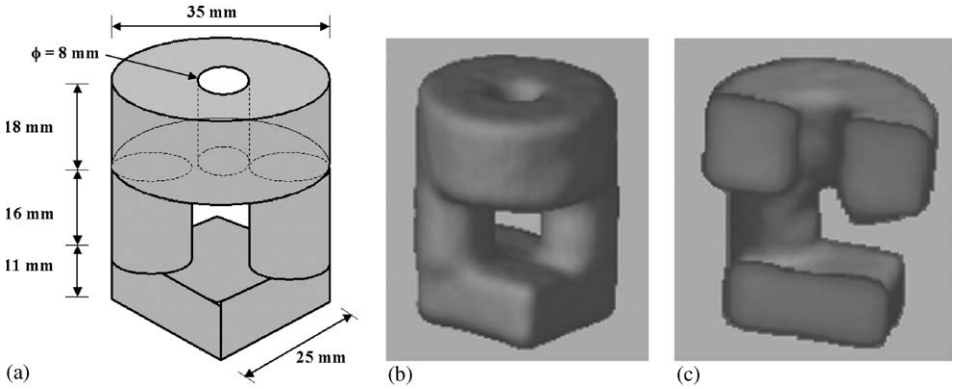

Fig. 26. Schematic and 3-D surface rendered views of the PMMA 3-D phantom. (Reproduced from Ref. 98 with permission from Elsevier.)

material indicated the presence of both crystalline and semi-amorphous phases (relative proportions 80:20), with T_2^* values of 16.3 and 26.9 μs, respectively. The maximum achievable spatial resolution for this material is illustrated by reference to Fig. 25. The resolution phantom, shown schematically in Fig. 25a, was imaged using a gradient strength of 300 mT/m and an acquisition time of 1.8 h. The 1 mm hole is just resolved in the raw image of Fig. 25b, while the 0.75 mm hole is resolved in the deconvolved image in Fig. 25c. A 3-D phantom, shown schematically in Fig. 26a, was imaged using a gradient strength of 300 mT/m. In total, 5102 1-D line projections were acquired at different angles around the sample, resulting in an acquisition time of 8.5 h. 3-D surface rendered views of the phantom are presented in Figs. 26(b) and (c).

7. CONCLUDING REMARKS

The work carried out in this research has shown that CW-NMRI is a valuable addition to the armoury of techniques available for the non-invasive imaging of solid materials by magnetic resonance. Although there exists scope for further improvements to the system, most notably in reducing imaging time (several strategies are currently being considered), the advantages inherent to the CW approach to NMR imaging have already rendered amenable to study a broad range of materials, and should lead to CW-NMRI becoming a standard technique in this field.

ACKNOWLEDGEMENTS

The authors would like to thank Dr Gareth Davies and Prof. Jim Hutchison for help with various aspects of experimental design and construction, Prof. Fredrik

Glasser for help and advice with the cement studies, Dr Nikolaus Nestle (TU, Darmstadt) for collaboration with the bentonite work, and Dr Yuanmu Deng (Ohio State University) for help with the reconstruction of the 3-D dataset. We are also indebted to Mr. Eddie Stevenson and Mr Peter Frew for workshop assistance. This work was funded by the UK Engineering and Physical Sciences Research Council (Grant Number GR/R02269/01).

REFERENCES

1. P. Blumler and B. Blumich, *NMR Imaging of Solids*, Vol. 30, Springer, Berlin, 1994, 208.
2. P. Jezzard, J. J. Attard, T. A. Carpenter and L. D. Hall, *Progr. Nucl. Magn. Reson. Spectrosc.*, 1991, **23**, 1.
3. D. E. Demco and B. Blumich, *Concept Magn. Reson.*, 2000, **12**, 188.
4. E. R. Andrew and E. Szczesniak, *Progr. Nucl. Magn. Reson. Spectrosc.*, 1995, **28**, 11.
5. G. C. Chingas, J. B. Miller and A. N. Garroway, *J. Magn. Reson.*, 1986, **66**, 530.
6. D. G. Cory, J. B. Miller, R. Turner and A. N. Garroway, *Mol. Phys.*, 1990, **70**, 331.
7. D. G. Cory, *Solid State Nucl. Magn.*, 1996, **6**, 347.
8. K. Takegoshi and C. A. McDowell, *Chem. Phys. Lett.*, 1985, **116**, 100.
9. S. Matsui, *Chem. Phys. Lett.*, 1991, **179**, 187.
10. S. Hafner, D. E. Demco and R. Kimmich, *Solid State Nucl. Magn. Reson.*, 1996, **6**, 275.
11. D. G. Cory, J. W. M. van Os and W. S. Veeman, *J. Magn. Reson.*, 1988, **76**, 543.
12. S. Hafner and H. W. Spiess, *Concept Magn. Reson.*, 1998, **10**, 99.
13. F. De Luca and B. Maraviglia, *J. Magn. Reson.*, 1986, **67**, 169.
14. A. A. Samoilenko, D. Y. Artemov and L. A. Sibeldina, *JETP Lett.*, 1988, **47**, 417.
15. P. J. McDonald and B. Newling, *Rep. Progr. Phys.*, 1998, **61**, 1441.
16. S. P. Cottrell, M. R. Halse and J. H. Strange, *Meas. Sci. Technol.*, 1990, **1**, 624.
17. A. N. Garroway, J. Baum, M. G. Munowitz and A. Pines, *J. Magn. Reson.*, 1984, **60**, 337.
18. B. H. Suits and D. White, *Solid State Commun.*, 1984, **50**, 291.
19. H. S. Gutowsky, G. B. Kistiakowsky and E. M. Purcell, *J. Chem. Phys.*, 1949, **17**, 972.
20. E. von Meerwall, R. B. Creel, C. F. Griffin, E. DiCato, F. T. Lin and F. M. Lin, *J. Appl. Polym. Sci.*, 1977, **21**, 1489.
21. J. Pacanovsky, F. N. Kelley and E. von Meerwall, *J. Polym. Sci. Polym. Phys.*, 1994, **32**, 1339.
22. P. C. Lauterbur, C. S. Dulcey, C. M. Lai, M. A. Feiler, W. V. House, D. Kramer, C.-N. Chien and R. Dias, *Proceedings of 18th AMPERE Congress Nottingham*, 1974, **1**, 27.
23. D. J. Lurie, S. J. McCallum, J. M. S. Hutchison and M. Alecci, *MAGMA*, 1996, **4**, 77.
24. S. D. Beyea, B. J. Balcom, I. V. Mastikhin, T. W. Bremner, R. L. Armstrong and P. E. Grattan-Bellew, *J. Magn. Reson.*, 2000, **144**, 255.
25. F. De Luca, N. Lugeri, S. Motta, G. Cammisa and B. Maraviglia, *J. Magn. Reson. A*, 1995, **115**, 1.
26. M. Klinkenberg, P. Blumler and B. Blumich, *J. Magn. Reson. A*, 1996, **119**, 197.
27. P. Barth, S. Hafner and W. Kuhn, *J. Magn. Reson. A*, 1994, **110**, 198.
28. P. M. Glover, P. J. McDonald and B. Newling, *J. Magn. Reson.*, 1997, **126**, 207.
29. D. E. Axelson, A. Kantzas and A. Nauerth, *Solid State Nucl. Magn. Reson.*, 1996, **6**, 309.
30. M. R. Halse, H. J. Rahman and J. H. Strange, *Physica B*, 1994, **203**, 169.
31. M. Bogdan, B. J. Balcom, T. W. Bremner and R. L. Armstrong, *J. Magn. Reson. A*, 1995, **116**, 266.
32. T. Nunes, E. W. Randall, A. A. Samoilenko, P. Bodart and G. Feio, *J. Phys. D: Appl. Phys.*, 1996, **29**, 805.
33. B. J. Balcom, *Spatially Resolved Magnetic Resonance*, Wiley-VCH, Weinheim, Germany, 1998 75.
34. M. A. Baumann, G. M. Doll and K. Zick, *Oral. Surg. Oral. Med. O.*, 1993, **75**, 517.
35. C. H. Lloyd, S. N. Scrimgeour, G. Hunter, J. A. Chudek, D. M. Lane and P. J. McDonald, *J. Mater. Sci. -Mater. M.*, 1999, **10**, 369.

36. A. Abragam, *The Principles of Nuclear Magnetism*, Oxford University Press, New York, 1961.
37. P. T. Callaghan, *Principles of Nuclear Magnetic Resonance Microscopy*, Clarendon Press, Oxford, 1991.
38. P. J. McDonald, *Progr. Nucl. Magn. Reson. Spectrosc.*, 1997, **30**, 69.
39. D. E. Demco and B. Blumich, *Concept Magn. Reson.*, 2000, **12**, 269.
40. B. Blumich, *NMR Imaging of Materials*, Clarendon Press, Oxford, 2000.
41. M. J. D. Mallett, M. R. Halse and J. H. Strange, *J. Magn. Reson.*, 1998, **132**, 172.
42. J. Godward, E. Ciampi, M. Cifelli and P. J. McDonald, *J. Magn. Reson.*, 2002, **155**, 92.
43. G. Eidmann, R. Savelsberg, P. Blumler and B. Blumich, *J. Magn. Reson. A*, 1996, **122**, 104.
44. B. Blumich, P. Blumler, G. Eidmann, A. Guthausen, R. Haken, U. Schmitz, K. Saito and G. Zimmer, *Magn. Reson. Imaging*, 1998, **16**, 479.
45. P. M. Glover, P. S. Aptaker, J. R. Bowler, E. Ciampi and P. J. McDonald, *J. Magn. Reson.*, 1999, **139**, 90.
46. Y. M. Daud and M. R. Halse, *Physica B*, 1992, **176**, 167.
47. M. J. D. Mallett, S. L. Codd, M. R. Halse, T. A. P. Green and J. H. Strange, *J. Magn. Reson. A*, 1996, **119**, 105.
48. J. H. Strange, *Philos. Trans. Roy. Soc. A*, 1990, **333**, 427.
49. S. L. Codd, M. J. D. Mallett, M. R. Halse, J. H. Strange, W. Vennart and T. van Doom, *J. Magn. Reson. B*, 1996, **113**, 214.
50. J. B. Miller and A. N. Garroway, *J. Magn. Reson.*, 1989, **82**, 529.
51. S. Emid, *Physica B & C*, 1985, **128**, 79.
52. Z. H. Cho and Y. M. Ro, *Magn. Reson. Med.*, 1994, **32**, 258.
53. M. A. Fernandez-Seara, S. L. Wehrli and F. W. Wehrli, *J. Magn. Reson.*, 2003, **160**, 144.
54. B. J. Balcom, R. P. MacGregor, S. D. Beyea, D. P. Green, R. L. Armstrong and T. W. Bremner, *J. Magn. Reson. A*, 1996, **123**, 131.
55. S. D. Beyea, B. J. Balcom, P. J. Prado, A. R. Cross, C. B. Kennedy, R. L. Armstrong and T. W. Bremner, *J. Magn. Reson.*, 1998, **135**, 156.
56. P. J. Prado, B. J. Balcom, S. D. Beyea, R. L. Armstrong and T. W. Bremner, *Solid State Nucl. Magn. Reson.*, 1997, **10**, 1.
57. P. Szomolanyi, D. Goodyear, B. Balcom and D. Matheson, *Magn. Reson. Imaging*, 2001, **19**, 423.
58. M. R. Halse, D. J. Goodyear, M. MacMillan, P. Szomolanyi, D. Matheson and B. J. Balcom, *J. Magn. Reson.*, 2003, **165**, 219.
59. R. R. Ernst, G. Bodenhausen and A. Wokaun, *Principles of Nuclear Magnetic Resonance in One and Two Dimensions*, Clarendon Press, Oxford, 1987.
60. G. Bodenhausen, *Progr. Nucl. Magn. Reson. Spectrosc.*, 1980, **14**, 137.
61. E. Gunther, B. Blumich and H. W. Spiess, *Mol. Phys.*, 1990, **71**, 477.
62. H. Geen, R. Graf, A. S. D. Heindrichs, B. S. Hickman, I. Schnell, H. W. Spiess and J. J. Titman, *J. Magn. Reson.*, 1999, **138**, 167.
63. A. Jerschow, J. W. Logan and A. Pines, *J. Magn. Reson.*, 2001, **149**, 268.
64. C. Filip, X. Filip, M. Bertmer, D. E. Demco and B. Blumich, *J. Magn. Reson.*, 2001, **150**, 184.
65. T. Karlsson, M. Eden, H. Luthman and M. H. Levitt, *J. Magn. Reson.*, 2000, **145**, 95.
66. A. Wiesmath, C. Filip, D. E. Demco and B. Blumich, *J. Magn. Reson.*, 2001, **149**, 258.
67. E. R. Andrew, A. Bradbury and R. G. Eades, *Nature*, 1959, **183**, 1802.
68. I. J. Lowe, *Phys. Rev. Lett.*, 1959, **2**, 285.
69. E. Gunther, B. Blumich and H. W. Spiess, *Chem. Phys. Lett.*, 1991, **184**, 251.
70. U. Scheler, G. Schauss, B. Blumich and H. W. Spiess, *Solid State Nucl. Magn. Reson.*, 1996, **6**, 375.
71. M. Lee and W. I. Goldberg, *Phys. Rev.*, 1965, **140**, A1261.
72. A. E. Medfed and V. A. Atsarkin, *JETP Lett.*, 1977, **25**, 215.
73. F. De Luca, A. Gargaro, B. Maraviglia, G. H. Raza and C. Casieri, *Magn. Reson. Imaging*, 1998, **16**, 435.
74. F. De Luca, E. De Vita, G. H. Raza and C. Casieri, *J. Magn. Reson.*, 1999, **139**, 126.
75. E. D. Ostroff and J. S. Waugh, *Phys. Rev. Lett.*, 1966, **16**, 1097.
76. P. Mansfield and D. Ware, *Phys. Lett.*, 1966, **22**, 133.

77. J. S. Waugh, L. M. Huber and U. Haeberlen, *Phys. Rev. Lett.*, 1968, **20**, 180.
78. P. Mansfield, *J. Phys. C: Solid State*, 1971, **4**, 1444.
79. D. P. Burum and W. K. Rhim, *J. Chem. Phys.*, 1979, **71**, 944.
80. P. Mansfield and P. K. Grannell, *Phys. Rev. B*, 1975, **12**, 3618.
81. D. G. Cory, *Magnetic Resonance Microscopy*, VCH, Weinheim, Germany, 1992, p. 49.
82. J. B. Miller, D. G. Cory, L. G. Butler and A. N. Garroway, *Magn. Reson. Imaging*, 1992, **10**, 789.
83. D. G. Cory, A. M. Reichwein, J. W. M. van Os and W. S. Veeman, *Chem. Phys. Lett.*, 1988, **143**, 467.
84. Y. H. Sun, J. C. Xiong, H. Lock, M. L. Buszko, J. A. Haase and G. E. Maciel, *J. Magn. Reson. A*, 1994, **110**, 1.
85. M. Buszko and G. E. Maciel, *J. Magn. Reson. A*, 1994, **110**, 7.
86. W. K. Rhim, A. Pines and J. S. Waugh, *Phys. Rev. B*, 1971, **3**, 684.
87. S. Hafner, P. Barth and W. Kuhn, *J. Magn. Reson. A*, 1994, **108**, 21.
88. G. R. Davies, D. J. Lurie, J. M. S. Hutchison, S. J. McCallum and I. Nicholson, *J. Magn. Reson.*, 2001, **148**, 289.
89. A. J. Fagan, G. R. Davies, J. M. S. Hutchison and D. J. Lurie, *J. Magn. Reson.*, 2003, **163**, 318.
90. A. J. Fagan, N. Nestle and D. J. Lurie, *Magn. Reson. Imaging*, 2005, **23** (2), 317.
91. C. P. Poole, *Electron Spin Resonance: A Comprehensive Treatise on Experimental Techniques*, 2nd edition, Wiley-Interscience, New York, 1983.
92. O. E. Myers and E. J. Putzer, *J. Appl. Phys.*, 1959, **30**, 1987.
93. S. J. McCallum, Ph.D. Thesis, University of Aberdeen, Aberdeen, 1998.
94. C. P. Poole and H. A. Farach, *Relaxation in Magnetic Resonance*, Academic Press, London, 1971.
95. M. Alecci, S. J. McCallum and D. J. Lurie, *J. Magn. Reson. A*, 1995, **117**, 272.
96. A. Chowdhury, A. Gillies, P. J. McDonald and M. Mulheron, *Magn. Concrete Reson.*, 2001, **53**, 347.
97. N. Nestle, NMR studies of transport and remediation processes in soil and sediments, in: *Soil and Sediment Remediation*, P. Lens, T. Grotenhuis and H. Tabak, eds, IWAP Publishing, London, (in press) 2005.
98. A. J. Fagan, G. R. Davies, J. M. S. Hutchison, F. P. Glasser and D. J. Lurie, *J. Magn. Reson*. (in press).
99. R. Turner, *Magn. Reson. Imaging*, 1993, **11**, 903.

Solution- and Solid-State NMR Studies of Eight- and Nine-Membered Medium Ring *Cis*-Cycloalkene Stereochemistry

ROBERT GLASER[1], ITZHAK ERGAZ[1], GANIT LEVI-RUSO[1], DROR SHIFTAN[1], ARTEM NOVOSELSKY[1] AND SHIMONA GERESH[2]

[1]*Department of Chemistry, Ben-Gurion University of the Negev, Beer-Sheva 84105, Israel*
[2]*Department of Biotechnology Engineering, Ben-Gurion University of the Negev, Beer-Sheva 84105, Israel*

ANNUAL REPORTS ON NMR SPECTROSCOPY
VOLUME 56 ISSN 0066 4103
DOI 10.1016/S0066-4103(05)56003-4

Solution-state ^{13}C and ^{1}H nuclear magnetic resonance (NMR) spectroscopy (including nuclear overhauser effect studies); density functional theory quantum mechanical conformational modeling (and resultant calculations of ^{13}C shielding constants and $\mathbf{J}_{HH}$ spin–spin coupling constants) were combined with solid-state cross-polarization/magic angle spinning ^{13}C-NMR spectroscopy of samples whose structures are known by X-ray crystallography to help unravel the extra complications present in **cis**-*cyclooctene and* **cis**-*cyclononene medium ring stereochemical investigations. The stereochemistry of medium rings is considerably more complicated than that of the common rings (five to seven members) due to the presence of chiral conformations. An achiral cycloalkane conformation has only two sub-types: a* **reference** *conformation and a ring-inverted (***inverso***) conformation in which corresponding torsion angles exhibit sign-inverted values. The reference and its ring-invertomer lose their structural degeneracy and become diastereomeric when* **axial** *and* **equatorial** *substituents on a stereogenic ring atom in one conformation exchange their orientations in the other. The reference and ring-inverted structures of chiral conformations (e.g. those for* **cis**-*cyclooctene) represent a pair of* **reference/inverso** *enantiomers. Chiral conformations of heteroatom substituted* **cis**-*cyclooctenes result in the formation of two pairs of enantiomers differing in the directionality (tropicity) of the heteroatom vis-à-vis the double bond (i.e. a* **reference/inverso** *pair and a reversed tropicity diastereomeric* **retro/retro-inverso** *pair). Labeling of a ring atom in a chiral conformation* **cis**-*cyclooctene with a single substituent makes that ring atom stereogenic. This causes all four of these isomers to be diastereomeric, and each now has an enantiomeric partner. The theoretical possibility of stereochemically labeled chiral medium rings having diastereomeric conformational subtypes, differing in the stereogenic elements of ring chirality and/or substituent tropicity, was shown to exist in practice for some of the 2,5-benzoxazocine and 2,6-benzoxazonine skeletons reported in this study. These*

were characterized by both solution- and solid-state NMR spectroscopy together with X-ray crystallography.

1. INTRODUCTION

It goes without saying that nuclear magnetic resonance (NMR) spectroscopy is one of the prime tools for stereochemical studies. In this report, we will be presenting some of the solution- and solid-state NMR results that we have used to investigate the conformations of *cis*-cycloalkene medium rings. Since most readers are probably not very familiar with this subject, it is advantageous to briefly present an overview of some of the salient general features of medium ring stereochemistry prior to commencing with a description of NMR studies on this compound class. The 'small' (three to four members) and 'common' rings (five to seven members) typically exhibit achiral stable conformations. But, such is not the case for the medium rings (eight to eleven members). Our interest has been the stereochemistry of medium ring *cis*-cycloalkenes in general, and, in particular, the structures of *cis*-cyclooctenes and *cis*-cyclononenes. The larger size of medium rings enables the existence of more conformational possibilities, thus providing a greater challenge for the researcher. For example, within a theoretical calculated energy window of *ca*. 29 kJ from their global minima, eight- and nine-membered *cis*-cycloalkene rings have four[1,2] and thirteen[2,3] energy-accessible conformations, respectively. All four of the *cis*-cyclooctene conformations are chiral, while this is true for eleven of the thirteen *cis*-cyclononenes. While many eight- and nine-membered saturated rings are chiral and exhibit C_2 symmetry, their unsaturated analogs are usually totally asymmetric (i.e. C_1 symmetry). These molecules have a double bond as an obvious point of reference. Since the double bonds in these C_1 symmetry chiral rings are not bisected by any symmetry element, pairs of diastereotopic ring atoms exist in which each member of the pair resides in a different side of the double bond. Moreover, each member of the pair has *chirotopic*[4] site symmetry with only the presence of an *identity* symmetry element, and thus the two protons ligated to this ring atom are also *diastereotopic* and hence *anisochronous*. For example, there are four diastereotopic allylic sites for *cis*-cyclooctene: A,B on C(1) and C,D on C(6). These are depicted in the two enantiomers (**1** and **1-*bar***) for the *Boat–Chair* (BC) global minimum conformation of *cis*-cyclooctene that will be used for a brief discussion of some of the special stereochemical features relating to *cis*-cycloalkene medium rings. Similar to X-ray crystallography, a 'bar' descriptor will be used to denote an enantiomeric relationship, and its use is illustrated in the *inverso* isomer **1-*bar*** compared to the arbitrarily chosen *reference* structure **1**. We use this 'bar' notation both for enantiomeric structures and for *externally enantiotopic* sites (e.g. ring atoms 6 and 6-*bar* in enantiomers **1** and **1-*bar***). Drawings **1** and **1-*bar*** (and others to follow) are 2D iconic projections of 3D models (either from calculation or X-ray crystallography).[5]

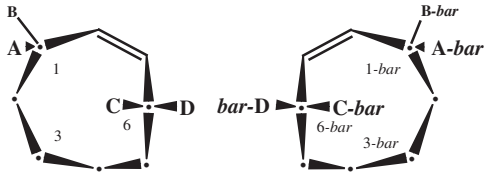

(*reference*)-BC **1** (*inverso*)-BC **1-*bar***

One of the interconversion modes for *cis*-cyclooctene utilizes a transition state in which a torsion angle of one bond moves through a zero-degree value resulting in the exchange of *axial*/*equatorial* descriptors for protons ligated to each of the two moving ring atoms. Kolossváry and Guida[6] have described such an interconversion as '*kayaking*' since it reminded them of the coordinated movement of the double-bladed paddle in the kayak rower's arms. A kayaking movement about the C(3)–C(4) bond in (*reference*)-BC **1** converts it into the *externally enantiotopic* C(4-*bar*)–C(3-*bar*) bond in (*inverso*)-BC **1-*bar***, and results in a (A,C-*bar*)(B,D-*bar*)(C,A-*bar*) and (D,B-*bar*) site exchange permutation, see Fig. 1.[1] This is an *enantiomerization* process whereby the diastereotopic sides of the double bond in a static conformation now become *dynamically enantiotopic*. The time-averaged symmetry (see **2** in Fig. 1) of corresponding sites in **1** and **1-*bar*** is related by a symmetry operation which inverts the handedness of exchanged subunits, i.e. an operation of the 'second kind'.

We have recently discussed the situation where one of the members of a diastereotopic pair is exchanged with a stereochemical label, e.g. a generic 'Z'-label in place of C(1) or C(6).[1] In this case, four isomers (two diastereomeric D,L-pairs: **3,3-*bar***

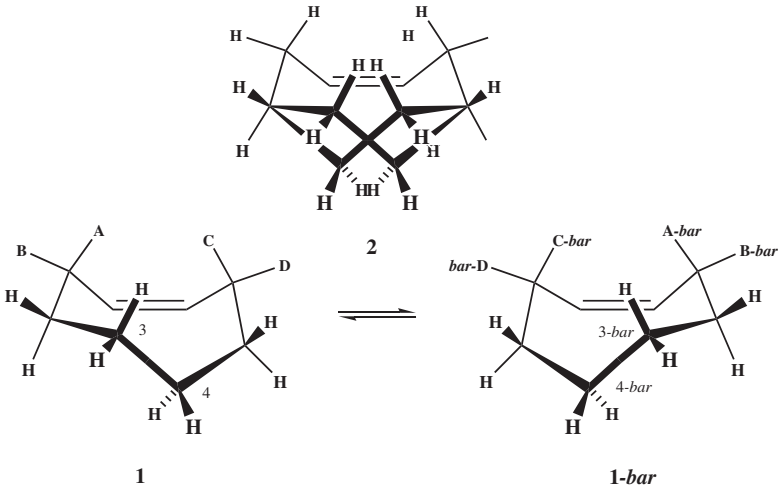

1 **1-*bar***

Fig. 1. Enantiomerization of *cis*-cyclooctene BC conformations (**1** and **1-*bar***) via a kayaking mechanism to afford a (A,C-*bar*)(B,D-*bar*)(C,A-*bar*), and (D,B-*bar*) site exchange permutation. Time-averaged structure depicted as **2**.

and **4**,**4-*bar***) are possible due to the existence of two stereogenic[4] elements: *label tropicity* (directionality of Z vis-à-vis the double bond) as well as *ring chirality*.[1] We have affixed '*retro*/*inverso*' descriptors[1] to these drawings in an analogous manner to that used before for protein stereochemistry.[7] The Z to double bond tropicity is clockwise when viewed in the orientation depicted for the diastereomeric **3** and **4-*bar*** drawings shown below, while it is counterclockwise in the corresponding **3-*bar*** and **4** enantiomers. Thus, '*inverso*' and '*retro*' respectively denote inverted ring chirality, and reversed label tropicity relative to those found for the arbitrarily defined '*reference*' arrangement and orientation. Due to their arbitrary assignments, the reference conformation (as opposed to (*R, S*) descriptors or (+, −) signs for torsion angles) must always be defined in each study. In addition, the orientation of the ring must be defined (usually by illustration) since the tropicity of an arrow bent into a circle is reversed when viewed from the opposite face of the plane.

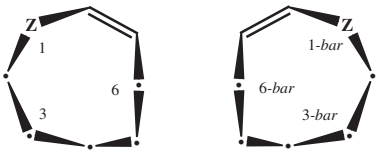

(*reference*)-BC **3** (*retro-inverso*)-BC **3-*bar***

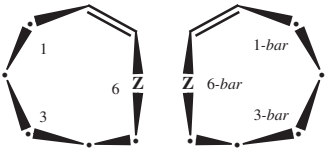

(*retro*)-BC **4** (*inverso*)-BC **4-*bar***

Six entries are to be found in the Cambridge Structural Database[8] for the same C_2 symmetry conformation for a series of *cis*-cyclooctene substituted analogs determined by X-ray crystallography. But, Saunders and Jiménez-Vázques[2] did not report a C_2 symmetry conformation in their MM3[9] molecular mechanics stochastic conformational search for the parent unsubstituted *cis*-cyclooctene. Using this C_2 symmetry conformation for *cis*-cyclooctene as the MM3 input structure, we found it to change into another conformation.[1] The geometry does not change (i.e. the same input and output conformation) under semi-empirical AM1 and density functional theory (DFT) B3LYP/6-311 + g(2d,p) geometry optimization techniques;[10] however, the DFT frequency calculation shows it to have one negative (imaginary) vibrational frequency. This means that the unsubstituted compound is really an intermediate rather than a true minimum-energy structure on the energy hypersurface.[1] If the ring is unlabeled (just methylene carbons as in Fig. 2), then rotation about the C_2 symmetry axis in intermediate **5** relates two homomeric Twist–Boat–Chair (TBC, **6**) conformations and results in an (A,D)(B,C) site-permutation. This is a *topomerization*

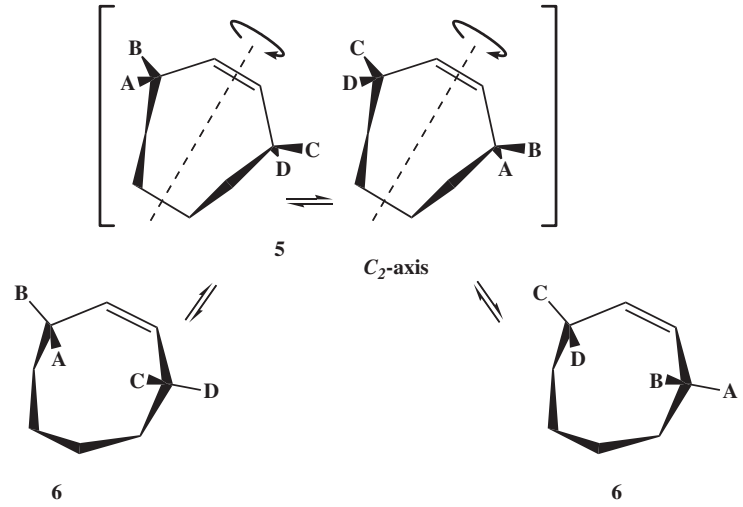

Fig. 2. Topomerization of A,B sites with C,D sites in *cis*-cyclooctene TBC conformation (**6**) via a C_2-symmetry intermediate (**5**) to afford an (A,D)(B,C) site exchange permutation.

process (exchange of place) since both sides of the C_2-intermediate double bond are *internally homotopic* (they are related by a symmetry operation which preserves their handedness, i.e. an operation of the 'first kind'). If the ring now has a Z-label, then this process is a *diastereomerization* that interconverts the (*reference*)-TBC (**7**) and (*retro*)-TBC (**8**) conformations, and results in a reversal of label tropicity.[1] These TBC conformations eventually lead to the (*reference*)-BC (**3**) and (*retro*)-BC (**4**) diastereomers.[1] Pathways involving a combination of the two mechanisms (enantiomerization and topomerization) are necessary for complete site-equivalence.[11,12] These two processes were clearly seen in the dynamic NMR of *cis*-cyclooctene-d_{13} (22.2 and 34.3 kJ/mol)[13] and also in 1-fluorocyclooctene (25.5 and 33.4 kJ/mol)[14] with the topomerization[12] affording the lower barrier.

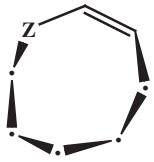

(*reference*)-TBC **7**

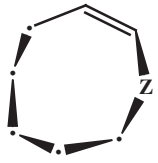

(*retro*)-TBC **8**

If the non-stereogenic Z-labeled ring atom is now replaced by a *chirotopic* stereogenic carbon ring atom (e.g. –CH(*R*)–), then one can envision four possible diastereomeric D,L-pairs (see the **9–12** (*S*)-configuration diastereomers) for each conformation. For any particular conformation, one should expect significant differences in population for *retro*/*inverso* diastereomers since only two of them usually place the *R*-group in less sterically demanding *equatorial* positions (e.g. **10** and **11**), while *transannular* non-bonding interactions should disfavor **9** and especially **12**.

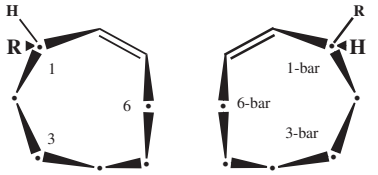

(*reference,S*)-BC **9** (*retro-inverso,S*)-BC **10**

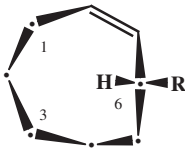

(*retro,S*)-BC **11**

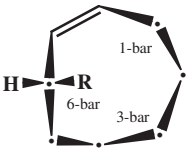

(*inverso,S*)-BC **12**

The compounds in this report usually contain a chirotopic stereogenic carbon ring atom, and were prepared as racemic mixtures. Hypothetically, if the BC conformation prevails, then one can imagine two enantiomers in solution: (*reference*,*S*)-BC **9** and (*retro-inverso*,*R*)-BC **9-*bar***. Since this stereochemistry is complicated, it will be helpful if we refer to the descriptor for only one enantiomer. Therefore, in an arbitrary but consistent manner in this report, we will always define the *reference* ring chirality and label tropicity to be that of the (*S*)-enantiomer. For example, suppose a racemic mixture of (*reference*,*S*)-BC **9** and (*retro-inverso*,*R*)-BC **9-*bar*** affords crystals belonging to an achiral space group so that both enantiomers in the 'racemic compound' are present in the crystal lattice. Let us further suppose that dissolution of these crystals will give the same solution-state conformation. We will write that 'the solid-state (*reference*,*S*)-BC **9**

conformation is maintained upon dissolution of the crystals (rather than being interconverted into another diastereomeric conformation)'. By the above statement we imply that the (*retro-inverso*,*R*)-BC **9-*bar*** conformation for the enantiomer is also maintained when going from the solid- to the solution-state, but we will not specifically state this. We have already seen that two conformational interconversion modes change either the ring chirality or the label tropicity. There exist other interconversion mechanisms that preserve both these stereogenic elements but change only the conformation. We will soon discuss these. If the new conformation of the (*S*)-enantiomer can be formed from the (*reference*,*S*)-BC **9** conformation without changing the ring chirality or the label tropicity, then we will keep the '(*reference*,*S*)' descriptor for the new conformation. If the new conformation for the (*S*)-enantiomer has a change of either the ring chirality, label tropicity, or both, then we will use the appropriate (*inverso*,*S*)-, (*retro*,*S*)-, or (*retro-inverso*,*S*)-descriptors, and once again to simplify things, we will not mention the presence of the (*R*)-enantiomer.

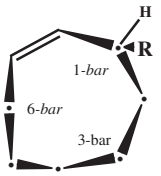

(*retro-inverso,R*)-BC 9-*bar*

In the common rings, protons are usually perpendicular to the mean plane of the ring or are oriented outward. This is not the situation for medium rings. In this case, some ring atoms have both substituents pointing outward (e.g. C(5) in **13**). These have identically signed *synclinal* (*gauche,* +g/+g, or −g/−g) endocyclic torsion angles on either side, and have been described by Dale[11] as *corner atoms*. To eliminate close contacts between larger-than-proton substituents with their transannular proton neighbors, *gem*-disubstituted ring atoms exist in conformations where they are corner atoms, and each substituent is assigned the same *isoclinal* (equally oriented) descriptor. They are *ideally isoclinal* if a conformation enables a C_2-axis to pass through the corner atom since now they are symmetry equivalent (internally homotopic). Structure **14** (a side orientation of **10**) shows one proton on *non-corner* atom number 6 oriented toward the ring center where it suffers close contacts with two transannular proton neighbors residing on C(1 and 3). Using Anet's[15] general definition of *axial*/*equatorial* descriptors for rings of any size, these inward pointing protons are usually *axial*. Their geminal neighbor may be either a proton or a larger group (e.g. 'R' in **14**), because it points outward and is usually affixed an *equatorial* descriptor. Since transannular close contacts exist for all medium ring conformations, nuclear overhauser effect (NOE) intensity enhancements will be quite beneficial in assigning the conformation of medium rings.

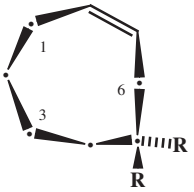

(*retro*)-BC 13

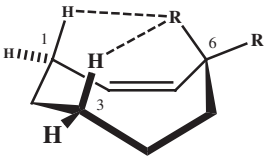

(*retro,S*)-BC 14

2. METHODS

2.1. NMR experiments

Chemical shifts in solution-state spectra are relative to tetramethylsilane (TMS) based on internal TMS for $CDCl_3$, or the residual $CHDCl_2$ isotopomer (δH 5.32 and δC53.8) for CD_2Cl_2. Chemical shifts in solid-state cross-polarization/magic angle spinning (cp/mas) spectra are relative to TMS using external glycine as a secondary reference standard (carbonyl δC 176.03). If the compound was a crystalline solid, both solution-state ^{1}H- and ^{13}C-NMR, and solid-state (^{13}C cp/mas) studies were undertaken, plus a single crystal X-ray crystallographic structure analysis. A typical solution-state protocol included a high-resolution ^{1}H spectrum to enable as complete an analysis of J_{HH} coupling constants in multiplets as possible. This was followed by homonuclear decoupling experiments to ascertain connectivity within the spin-systems and the identity of the particular coupling constant removed by a decoupling irradiation. NOE experiments followed. Overlapping multiplets were sometimes resolved by a 'NOE spectral editing' experiment. A requisite for this was that a terminal transition of the overlapping two multiplets resulted from only one of the two nuclei. Irradiation of this terminal transition with very low power usually excited all the transitions within only a single multiplet of the overlapping pair, and afforded a negatively phased signal in an NOE-DIFFERENCE spectrum. ^{13}C{^{1}H}, DEPT-135, and when appropriate DEPT-90, experiments were then run. Finally, heteronuclear multiple-quantum correlation (HMQC) (and sometimes heteronuclear multiple-bond correlation, HMBC) experiments were performed to ascertain ^{13}C–^{1}H one-bond correlations (or those from multiple-bonds involving quaternary carbon atoms).

For our stereochemical studies, we desire to measure solid-state cp/mas ^{13}C-NMR isotropic chemical shift values from samples whose conformations were determined by X-ray crystallography. Therefore, it is important that the cp/mas ground crystallite sample originates from the same crystals grown for X-ray analysis. Unground crystal samples with observable reflective faces are preferred over microcrystals due to the problem of *crystalline polymorphism*. When all the crystals look morphologically the same, the spectroscopist has a better feeling that they might hopefully all be the same polymorph. However, this is not always the case.[16]

Polymorphism is the existence of different crystalline forms, i.e. different crystals of the same material. Different crystals mean different packing arrangements and, consequently, different magnetic environments for the molecule. It is an important field of endeavor for the pharmaceutical industry, since, if the crystals are different by symmetry argument, then all their physical properties dependent on the solid state (including their rates of dissolution, cp/mas NMR, etc.) must be different. In addition, the polymorphic form of the active pharmaceutical ingredient used in a tablet may be patented. Different polymorphs may also be found in the same crystallization vessel,[16] and when this occurs, they are known as 'concomitant polymorphs'. Polymorphs may have the same or different conformations. When the conformations are different they are known as 'conformational polymorphs'. Prior to rotor filling, the crystalline sample was carefully crushed to a fine powder without recourse to excessive pressure and grinding (both produce heat which might cause a solid-state transition from one polymorphic form to another). In this report we will discuss two conformational polymorphs.

The solid-state protocol of ^{13}C cp/mas experiments which were used included Variable Amplitude Cross-Polarization (VACP), SELTICS, SELTICS-NQS, Cross Polarization Polarization Inversion (CPPI), and sometimes T_1 determination. While ^{13}C assignments in solution-state spectra are usually straightforward based on HMQC and the DEPT experiments, the assignments are sometimes less exact when using a cp/mas accessory (Bruker BL-4 probehead) for a high-resolution spectrometer (Bruker DMX-500 rather than a dedicated solids spectrometer). Therefore, we used a series of solid-state experiments to at least ascertain the multiplicity of protons ligated to the ^{13}C nuclei. Both VACP and SELTICS provide signals from all of the carbon hybridization types (i.e. from quaternary, sp, sp^2, and sp^3 nuclei), and differ in that the VACP spectrum shows spinning side-bands (ssb's), while the SELTICS spectrum does not. Typical VACP experiments were usually run with >10 kHz spin-rates while all other solid-state experiments were performed at 5–6 kHz. The higher the spin-rate, the farther away and lower intensity are the ssb's arising from anisotropic nuclei (typically from sp^2-hybridized nuclei (i.e. aromatic and carbonyl carbons)). Thus, VACP spin rates were chosen so that the ssb's appeared within empty windows in the frequency domain spectrum. Moreover, lower spin-rates produce less rotor friction, and consequently lower rotor sample internal temperatures. Using the lead nitrate thermometer technique[17] with our probe, it was found that the 4 mm rotor sample temperature was actually *ca.* 1 °C cooler than that in a non-spinning rotor at a 5.0 kHz spin-rate (spin-air cooling overcame rotor friction heating).[18] This is an important consideration when studying hydrated/solvated crystalline samples that, in some cases, might undergo solid-state phase transitions upon increasing the spin-rate.[18]

With the exception of the CPPI experiment, all of our pulseprograms used a 'ramp' for variable proton power amplitudes (i.e. a VACP subsequence). For many of our particular benzannelated eight- and nine-membered rings (but in our experience, not necessarily for all of them nor for other compound types), the relative intensities of quaternary carbon signals appearing in the SELTICS spectrum were

often of the same order of magnitude as those originating from other carbons. However, this was not always the case for quaternary signals in the VACP spectra (they usually afforded markedly lower intensities than other aromatic signals). This was helpful in assignment of quaternary aromatic carbon signals, since they could not always be unequivocally located in the NQS (Non-Quaternary and non-methyl Suppression) spectrum. The NQS experiment has a T_2 or dipolar dephasing delay inserted prior to FID acquisition and enabled nuclei with inefficient dipolar relaxation mechanisms to still provide relatively strong signals in the FID. Dipolar relaxation of quaternary ^{13}C-nuclei via ^{1}H neighbors is inefficient since these nuclei are devoid of directly ligated protons, while methyl carbons typically relax via a spin-rotation mechanism. Thus, quaternary and methyl signals had relatively high intensities in the NQS spectrum (dipolar dephasing delay periods of 40–60 μs) while those from other carbon types were either absent or very low in intensity.

Another useful spectral editing experiment was 'CPPI' developed by Zilm.[19] Using this experiment with a relatively short cross-polarization period, a *methylene-only* ^{13}C spectrum was observed whose phase was negative. The final experiment in our solids protocol was a single delay T_1 experiment. Nuclei in the solid-state obviously cannot reorientate at rates approaching their Larmor frequencies, since they only undergo thermal vibrations with relatively low frequencies. Thus, their efficient T_2 relaxation is counteracted by notoriously long T_1 time constants. But, of all the hybridization types, the T_1 of methyl carbons is relatively the shortest due to usually unimpeded rotation about the C–CH_3 bond. By performing one rapid inversion recovery delay experiment with a T_1 delay of 10–15 s, methyl carbon signals usually disappeared from the solid-state spectrum while all others remained. Thus, by using the above-mentioned solid-state NMR protocol, the carbon hybridization type could be determined. In some cases, this is sufficient to unequivocally assign the chemical shift to a particular nucleus. In cases where this could not be done, assignments were made by comparison with similar solution-state or scaled calculated values.

Finally, solution-state chemical shifts often are weighted time-averages arising from equilibria between low-energy conformations. The combined cp/mas NMR/X-ray crystallography approach permits one to obtain chemical shifts from nuclei in known conformations. These solid-state ^{13}C isotropic chemical shifts of nuclei in conformational polymorphs have enabled deconvolution of solution-state weighted time averaged values to ascertain the predominant conformation in a particular solvent.[20]

2.2. Computational techniques

The NMR data were usually sufficient to ascertain the predominant conformation in solution. Once a conformational working hypothesis was made, it was extremely helpful to compare computational models for the various conformations. The advent of relatively low cost personal computers and commercial programs with

efficient algorithms make the calculation of high-quality models a viable technique. Initially, simple molecular mechanics (MM2 and MM3) or semi-empirical molecular orbital (AM1) models were used for a proposed conformational hypothesis. Models of conformations could be eliminated which clearly did not agree with the magnitudes of experimentally measured vicinal coupling constants and NOE effects. Once the conformational hypothesis was confirmed, the final calculated model was geometry optimized using a higher level of theory, e.g. DFT B3LYP/6-311 + g(2d,p).[10] Using this basis set, quantum mechanical based isotropic magnetic shielding tensors, and even more important, total spin–spin *J*-coupling constants were then calculated. On the basis of experimentally determined chemical shifts for rigid molecules of known conformation, an empirical linear scaling factor ($\delta^{13}_{\text{calcd}}\text{C} = -0.966765 \times \sigma^{13}_{\text{calcd}} + 175.37$) for the gauge-independent atomic orbital (GIAO) isotropic magnetic shielding tensors (σ_{calcd}) was determined by plotting $\delta_{\text{exptl}}{}^{13}\text{C}$ versus $\sigma_{\text{calcd}}{}^{13}\text{C}$, and this was then used for comparison of $\delta_{\text{calcd}}{}^{13}\text{C}$ with $\delta_{\text{exptl}}{}^{13}\text{C}$.

3. REPRESENTATIVE EXAMPLES OF NMR STUDIES ON 2,5-BENZOXAZOCINE MEDIUM RING STEREOCHEMISTRY

3.1. (1*RS*,5*RS*)- and (1*RS*,5*SR*)-5-methyl-1-phenyl-3,4,5,6,-tetrahydro-1*H*-2,5-benzoxazocine hydrochloride [nefopam hydrochloride *equatorial* and *axial N*-methyl diastereomers] (15) and (18), respectively

Nefopam hydrochloride is a non-narcotic analgesic drug.[21] A racemic mixture of nefopam hydrochloride crystallized as a racemic compound in an achiral crystal in which the eight-membered ring of one of the enantiomers has a (*reference*,1*S*,5*S*)-Boat–Boat (BB) conformation **15** (see Fig. 3).[22] Using the carbon ring atom of the –CH(Ph)– moiety as stereogenic label, a *reference*-descriptor has been affixed to **15** since the ring is related to (*reference*,*S*)-BC **9**. A flip of C(2) in **9** from one side of the ring to the other interconverts BC to BB. The X-ray crystallographically determined torsion angles for the (*reference*,1*S*,5*S*)-BB enantiomer **15** are also provided in the graphical representation. In this conformation, the *N*-methyl group is located at a corner position of the ring, and is assigned a *nearly isoclinal* descriptor using Anet's[15] general definition of substituent descriptors. Nevertheless, one would like to provide an *N*-methyl *axial*/*equatorial* descriptor for the crystalline-state (*reference*,1*S*,5*S*)-BB diastereomer **15**. Since the $-\text{OCH}_2\text{CH}_2\text{N}^+\text{H}(\text{CH}_3)\text{C}-$ fragment is common to both nefopam and *N*-methylmorpholine salts, we have referred to the dispositions of H(32), H(42), and *N*-methyl group of crystalline **15** as being *equatorially* oriented relative to the local environment of this fragment. The phenyl group is in a *pseudoequatorial* position and eclipses the geminal C–H bond in the crystal conformation.

Since nefopam HCl is a hydrohalide salt, its crystals exhibit some solubility even in a chlorinated organic solvent (e.g. very sparingly soluble in methylene

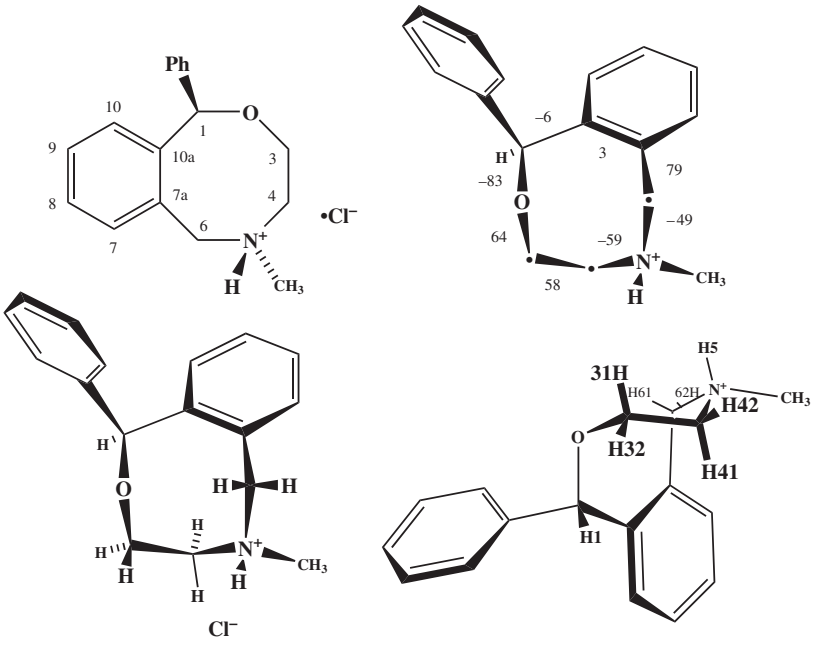

(*reference*,1*S*,5*S*)-BB **15**

Fig. 3. Crystallographically determined torsion angles (deg) and different orientations of the (*reference*,1*S*,5*S*)-BB conformation for nefopam hydrochloride (**15**) *equatorial N*-methyl diastereomer.

chloride-d_2). With modern pulse NMR spectrometers, this means that a high quality ^{1}H-NMR spectrum can be obtained for resolution enhancement in about 1k of scans. Dissolution of the *equatorial N*-methyl (*reference*,1*S*,5*S*)-BB salt crystals in the chlorinated solvent results in an epimerization at nitrogen (the well-known *prototropic shift/nitrogen inversion*).[23,24] Two *N*-methyl diastereomeric species in the ratio of 3 : 2 were observed at the slow exchange limit (SEL) for interconversion in ^{1}H- and ^{13}C-NMR spectra. Due to the *ca.* 9.3 pk_a[25] of typical ammonium salts, the $^+$N–H bond in **15** is labile in the presence of trace quantities of water vapor in the solvent. While changing the solvent from CD_2Cl_2 to D_2O can sometimes change the predominant *N*-methyl diastereomer,[24] a similar ratio of these same two species was observed in acidic D_2O.[26] There are advantages to using CD_2Cl_2 rather than D_2O in NMR studies of protonated amines. While some protonated amine salts show two *N*-methyl diastereomers at the SEL even in neutral D_2O,[27] this is not generally the case. The two species are usually in fast exchange unless a few drops of acid are added.[23,24] On the other hand, slow $^+$N–H bond breaking and bond making is usually the case in CD_2Cl_2. The advantage of having the *N*-methyl diastereomers in slow exchange in CD_2Cl_2 is that the $^+$N–H bond has a long enough lifetime on the NMR time-scale so that vicinal coupling constants involving

the $^{+}$N–H proton can be observed in the ^{1}H-NMR spectrum. Measurement of these coupling constants is one of the factors enabling the assignment of configuration for the *N*-methyl group (this can be confirmed by NOE experiments). Obviously, this is not possible for the $^{+}$N–D bond in acidic D_2O solution. Slow exchange for the $^{+}$N–H proton also enables it to be homonuclear decoupled as well as irradiated for NOE experiments.

Selected solution-state ^{1}H- and ^{13}C-NMR, and solid-state cp/mas ^{13}C-NMR parameters are given in Table 1. The diastereotopic protons ligated to C(3) are part of an apparent four-spin system (eight transitions), while those on C(4) are readily differentiated since they are part of an apparent five-spin system. Another feature is the $\Delta\delta$ anisochronicity of 0.59 ppm (major species) and 2.05 ppm (minor species) for the diastereotopic protons on C(6), due to the close proximity of H(61) (*endo*) to its transannular O(2) neighbor and the orientation of the *N*-methyl group.

It now remains to interpret the solution-state NMR results to ascertain the predominant conformation of each species and its configuration at nitrogen. Since the cp/mas ^{13}C chemical shifts are similar to those from either solution-state species, it is reasonable to assume (as a first working hypothesis) that the (*reference*,1*S*)-BB conformation found in the crystal is the same predominant conformation for each species. However, this hypothesis must still be proven for each species, since there are numerous occasions when the solid- and solution-state conformations are different. The minor species H(61,62) protons are broadened at room temperature, and sharpen up at 232 K. Therefore, the minor species clearly appears to be in conformational equilibrium. Since no other species was noted in the low temperature ^{1}H-NMR spectrum, it was reasonable to assume that a 'hidden partner' (i.e. a species with very low population) was involved which shortened the lifetime on the NMR time-scale. At this stage one should not exclude the possibility that the major species is also in conformational equilibrium, and is perhaps at the fast exchange limit (FEL) for conformational exchange since line broadening was not observed for it (see below). It will be shown later that in the case of **15**, the hidden partner conformation can arise from segmental motion involving both the C(3)–C(4) and C(4)–N(5) bonds. The large 11.9 and 11.3 Hz ^{3}J(31–41) coupling constants for the major and minor species, respectively, strongly suggests an *antiperiplanar*-type (*ca.* 180°) arrangement. This enables them to each be assigned as *J*(ax–ax) within the –OCH_2CH_2N– fragment, i.e. the H(31) and H(41) *trans*-protons reside on opposite faces of the ring and are *diaxial*. Similarly, the 2.2 and 3.1 Hz ^{3}J(32–42) values for the major and minor species, respectively, fit a *synclinal* arrangement and these are assigned as *J*(eq–eq). H(32) and H(42) must also reside on opposite faces of the ring, and these *trans*-protons are *diequatorial*. This spatial arrangement implies that the O(2)–C(3)–C(4)–N(5) dihedral angle is approximately *synclinal*. The observation of large *antiperiplanar*-type and smaller *synclinal*-type values for the two coupling constants involving *trans*-protons suggests that each one cannot represent an average arising from an equally populated mixture of conformations. An important question to be answered is: 'are the ^{3}J(31–41) values as large as they would be (and the ^{3}J(32–42) values as small as they would be) if only one conformation exists in

Table 1. Selected solution-state ^{1}H- and ^{13}C-NMR (CD_2Cl_2) and solid-state cp/mas ^{13}C-NMR spectral parameters for (1*RS*,5*RS*)- and (1*RS*,5*SR*)-nefopam hydrochloride *equatorial* and *axial N*-methyl diastereomers (**15**) and (**18**), respectively[a]

Atom	(1*RS*,5*SR*) major species (**18**) $\delta(^{1}H)^{b}$	(1*RS*,5*RS*) minor species (**15**) $\delta(^{1}H)^{b}$	Atom	(1*RS*,5*SR*) major species (**18**) $\delta(^{13}C)^{b}$	(1*RS*,5*RS*) minor species (**15**) $\delta(^{13}C)^{b}$	cp/mas (**15**) $\delta(^{13}C)^{c}$
H(1)	5.81	5.75	C(1)	86.30	85.81	84.13
H(31)	4.49	4.73	C(3)	64.91	66.33	65.89[d]
H(32)	4.09	3.98	C(4)	48.69	51.18	49.81[d]
H(41)	3.29	2.96	C(6)	58.46	57.02	54.53[d]
H(42)	2.82	3.15	N$\underline{C}H_3$	40.49	41.65	41.56[e]
H(5)	12.92	13.34	C(7)	135.19	–	134.18
H(61)	5.01	5.96	C(9)	130.56	–	–
H(62)	4.42	3.91	C(7a)	–	–	122.42[e,f]
H(7)	7.67	–	C(10a)	142.71[f]	–	144.15[e,f]
H(8)	7.45	–	C(*ipso*)	141.49[f]	–	143.48[e,f]
H(9)	7.45	–				
NC$\underline{H}_3$	2.98	2.64				

HH	$J_{HHexptl}$[g,h]	$J_{HHexptl}$[g,i]	BB_{axNMe} $J_{HHcalcd}$[j]	TCC_{eqNMe} $J_{HHcalcd}$[j]	BB_{eqNMe} $J_{HHcalcd}$[j]	TCC_{axNMe} $J_{HHcalcd}$[j]
31–32	–14.0 [–14.2]	–13.8 [–14.2]	–14.24	–13.99	–14.29	–13.90
31–41	11.9 [10.9]	11.3 [9.4]	11.85	2.32	11.74	2.48
31–42	4.4 [5.0]	3.1 [4.2]	5.20	2.75	4.78	2.51
32–41	4.7 [5.3]	3.4 [4.0]	5.79	1.32	5.01	1.07
32–42	2.2 [1.4]	3.1 [3.0]	0.38	10.57	0.54	10.55
41–42	–14.6 [–13.2]	–13.8 [–13.1]	–13.20	–12.95	–13.10	–13.04
41–5	1.8 [3.0]	7.7 [7.8]	2.94	3.46	10.04	0.88
42–5	3.0 [3.4]	2.7 [2.6]	2.72	9.87	1.69	5.17
5–61	7.7 [7.5]	2.9 [4.3]	7.62	6.43	5.49	0.71
5–62	4.0 [4.8]	<1 [3.7]	5.33	0.31	3.25	5.11
5-CH_3	4.7 [5.5]	3.9 [5.6]	5.50	5.25	5.59	5.74
61–62	–11.9 [–11.4]	–12.9 [–11.7]	–11.36	–11.79	–11.66	–12.00

[a] Major : minor species 3 : 2, solution-state data from Ref. 21.
[b] ppm from internal TMS, 200 MHz [^{1}H] and 50 MHz [^{13}C], ambient temperature.
[c] SELTICS cp/mas, 125.7 MHz, 5.0 kHz spin-rate, ppm using external glycine carbonyl δ 176.03.
[d] Observed in CPPI.
[e] Observed in SELTICS-NQS.
[f] Assigned by analogy to DFT $\delta^{13}C_{calcd}$ values for *equatorial N*-methyl (*reference*,1*S*,5*S*)-**BB**: 119.36 [C(7a)], 145.38 [C(10a)], 137.51 [C(*ipso*)].
[g] Hz, 0.1 Hz estimated standard deviation for coupling constants not involving the N–H proton.
[h] Weighted average of DFT calculated coupling constants: 90% BB_{axNMe} + 10% TCC_{eqNMe} given in square brackets.
[i] Weighted average of DFT calculated coupling constants: 75% BB_{eqNMe} + 25% TCC_{axNMe} given in square brackets.
[j] Hz, DFT calculated.

solution?' In other words, do we have only a 'rock stable' single conformation for the solution-state major species, or this there an FEL conformational equilibrium where one contributor is very predominant?

The O(2)–C(3)–C(4)–N(5) dihedral angle (θ) can be calculated using the four vicinal coupling constants of the dimethylene fragment and Lambert's[28] equation: $\cos\ \theta = \sqrt{(3/(4R+2))}$, where $R = J(trans)_{av}/J(cis)_{av}$ at the FEL for conformational interchange, or $R = [J(\mathrm{ax}-\mathrm{ax}) + J(\mathrm{eq}-\mathrm{eq})]/[J(\mathrm{ax}-\mathrm{eq}) + J(\mathrm{eq}-\mathrm{ax})]$ at the SEL. By using a ratio of four coupling constants, electronegativity and orientation effects in the O(2)–C(3)–C(4)–N(5) fragment are canceled out. The solution-state O(2)–C(3)–C(4)–N(5) dihedral angle was estimated by this method to be 53° and 58° for the major and minor species, respectively. For the purpose of comparison, by X-ray crystallography, this angle is 48° and 58° in the chiral crystals of (1*S*,5*S*)-nefopam HCl monohydrate and in the anhydrate racemic compound, respectively. Both crystals have the same (*reference*,1*S*,5*S*)-BB solid-state conformation and configuration at nitrogen (*equatorial N*-methyl). Comparison of the two solid-state structures shows only minor differences in the bonding parameters (bond lengths, bond angles, and torsion angles). These minor differences are expected since the disparate local environment of molecules in a chiral crystal versus that for a racemic compound does not permit them to be *ideally* the same via a symmetry exchange. Thus, the phrase 'same conformation for two or more molecules' implies a small range of values for corresponding torsion angles. In other words, since the local environments of the eight-membered ring are different in a chiral crystal, in a racemic compound crystal, in the solvated species in solution, in a biological host, and at the bottom of the potential energy well in calculated structures, one expects minor differences in all corresponding torsion angles since symmetry does not constrain them to be ideally the same.

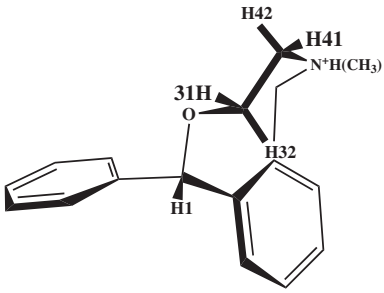

(*reference*,1*S*,5*S*)-TCC **16**

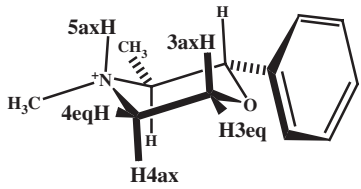

17

Upon dissolution of the (*reference*,1*S*)-BB **15** crystals, one can envision a second conformational model for the $-OCH_2CH_2N^+H(CH_3)C-$ fragment: the Twist–Chair–Chair (*reference*,1*S*)-TCC **16**. In either conformation, each *equatorial* proton

is *antiperiplanar* to an electronegative atom. Specifically, H(42) (in **15**) and H(41) (in **16**) are *antiperiplanar* to O(2), while H(32) (in **15**) and H(31) (in **16**) are *antiperiplanar* to N(5). The BB/TCC conformations are known to interconvert via a flip of ring atom C(4) from one side of the octagonal ring to the other.[29] When this occurs, there is an exchange of *axial*/*equatorial* orientations for protons on C(3), C(4), and N(5). As a result, *J*(ax–ax) in BB is averaged with *J*(eq–eq) in TCC, and *J*(eq–eq) in BB is averaged with *J*(ax–ax) in TCC, etc. Another consequence of this atom flip is that the oppositely signed *synclinal* torsion angles on either side of C(4) have their signs inverted.

The chemical anorexic drug (diet pill) (+)-*N*-methylphendimetrazine bitartarate (**17**) is conformationally biased in favor of *diequatorial* phenyl and *C*-methyl substituents. It can be used to illustrate a $-OCH_2CH_2N^+H(CH_3)-$ fragment whose 58°[30] X-ray crystallographically measured O(2)–C(3)–C(4)–N(5) dihedral angle is comparable to those values measured for the chiral and achiral nefopam HCl crystals. To measure the two *N*-methyl diastereomers at the SEL (*ca.* 17 : 1 *equatorial* : *axial* ratio), the bitartarate anion of the weak acid had to first be exchanged for an anion of a strong acid (e.g. a mesylate).[31] The experimentally measured vicinal coupling constants for the *N*-methylphendimetrazine *equatorial N*-methyl major species in CD_2Cl_2 are (Hz): 12.2 [*J*(3ax–4ax)], 2.2 [*J*(3ax–4eq)], 3.8 [*J*(3eq–4ax)], and 1.1 [*J*(3eq–4eq)].[31] For the sake of comparison, Lambert's[28] equation predicts an estimated 58° for the solution-state O(2)–C(3)–C(4)–N(5) dihedral angle. Therefore, the *N*-methylphendimetrazine results suggest that the coupling constants for both the major and minor species of nefopam HCl in CD_2Cl_2 represent weighted time-averaged values between the BB and TCC conformations at fast exchange, with one predominating for each species.

Since medium rings are larger than normal rings, conformational interconversions such as the C(4) atom flip usually take place by segmental motion where only some of the ring atoms change their positions. The problem is that, as a first approximation, the experimental vicinal coupling constants appear to fit either model. So, which conformation is predominant in solution? Comparison of the two conformations (**15** and **16**) shows that 'equatorial' H(32) is close to benzhydrylic H(1) in (*reference*,1*S*)-BB (**16**) while 'axial' H(32) is close to H(1) in (*reference*,1*S*)-TCC (**17**). NOE difference experiments provide a definitive answer: {δ 5.81, H(1) major} affords a 3.9% intensity enhancement into the δ 4.09 proton on C(3) which is *equatorially* disposed as seen by the magnitudes of its coupling constants to vicinal neighbors. Similarly, {δ 4.09, *equatorial* H(32) major} affords a 3.4% intensity enhancement into δ 5.81 H(1) major; while {δ 5.75, H(1) minor} affords a 3.9% intensity enhancement into δ 3.98 *equatorial* H(32) minor; and {δ 3.98, *equatorial* H(32) minor} affords a 3.3% intensity enhancement into δ 5.75 H(1) minor. Thus, the predominant conformational contributor in CD_2Cl_2 solution is the (*reference*,1*S*)-BB structure for both species. The experimental coupling constants in Table 1 suggest that the quantity of the minor (*reference*,*S*)-TCC conformational component in the major species is slightly smaller than that in the minor species.

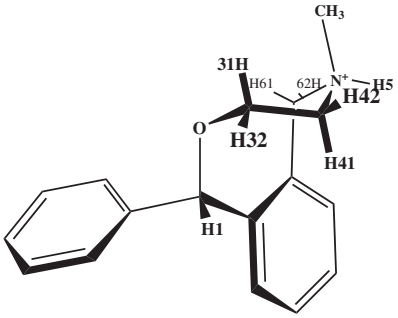

(*reference*,1*S*,5*R*)-BB **18**

Now one must tackle the configuration at nitrogen for both solution-state species. This will tell us which one is similar to the solid-state structure. Inspection of the crystalline-state **15** structure in Fig. 3 shows the following relationships: the *N*–H(5) proton is *antiperiplanar* to *axial* H(41) and *synclinal* to *equatorial* H(42), to *endo* H(61), and also to *exo* H(62). The minor species 7.7 Hz *J*(41–5), 2.7 Hz *J*(42–5), 2.9 Hz *J*(5–61), and <1 Hz *J*(5–62) values are all consistent with an *equatorial* configuration for the *N*-methyl group (i.e. the same as in crystal structure **15**). On the other hand, an *equatorial N*–H would be *antiperiplanar* to *endo* H(61) and *synclinal* to *axial* H(41), to *equatorial* H(42), and also to *exo* H(62). Finally, the major species 7.7 Hz *J*(5–61), 1.8 Hz *J*(41–5), 3.0 Hz *J*(42–5), and 4.0 Hz *J*(5–62) values are all consistent with an *axial* configuration for the *N*-methyl group (see **18**). DFT B3LYP/6-311 + g(2d,p) models show the *axial N*-methyl (*reference*,*S*)-BB diastereomer to be 2.1 kJ lower in energy than the *equatorial N*-methyl epimer.

To provide more insight into a possible conformational equilibrium for the two solution-state species, four DFT B3LYP/6-311 + g(2d,p) models (the C(4) atom flip related BB_{axNMe}/TCC_{eqNMe} pair, and the C(4) atom flip related BB_{eqNMe}/TCC_{axNMe} pair) were used as input structures for NMR = spin–spin calculations to obtain $J_{HHcalcd}$ coupling constants (also performed at the B3LYP/6-311 + d(2d,p) level). Their values are listed in Table 1. The best fit of the experimentally measured *major* species vicinal coupling constants with $J_{HHcalcd}$ values calculated for BB_{axNMe} mixed with corresponding C(4) atom flip TCC_{eqNMe} values was for an estimated weighted average of 90% BB_{axNMe} + 10% TCC_{eqNMe}. Similarly, the best fit of the experimentally measured *minor* species vicinal coupling constants with $J_{HHcalcd}$ values calculated for BB_{eqNMe} mixed with corresponding C(4) atom flip TCC_{axNMe} values was for an estimated weighted average of 75% BB_{eqNMe} + 25% TCC_{axNMe}. While the agreement between $J_{HHexptl}$ and weighted-average $J_{HHcalcd}$ values is far from perfect, nevertheless, it does provide an estimation of a possible conformational equilibrium, providing that the identities of the two partners are known. This quantum mechanics estimation should be better than those based on empirical considerations. After the crude estimated ratios are determined, one can qualitatively state that the weighted-average $J_{HHcalcd}$ coupling constants are consistent

with a predominant *axial N*-methyl (*reference*,1*S*,5*R*)-BB and *equatorial N*-methyl (*reference*,1*S*,5*S*)-BB conformation for the respective major and minor species. Furthermore, it can be said that the contribution to the conformational equilibrium of the *equatorial N*-methyl (*reference*,1*S*,5*R*)-TCC partner for the major solution-state species appears to be smaller than that by the *axial N*-methyl (*reference*,1*S*,5*S*)-TCC partner for the minor species. In other words, it is probably safer to provide a qualitative interpretation of the estimated conformational ratios, rather than place high reliance on the actual numerical weighted-average ratios themselves.

Can one use the DFT J_{HHcalcd} values to provide reasonable estimations of the endocyclic O–C–C–N dihedral angle using Lambert's equation? The answer is affirmative since this angle for $\mathrm{BB_{axNMe}}$ and $\mathrm{BB_{eqNMe}}$ was calculated to be 47° and 49° based on J_{HHcalcd} values, respectively, while it is 41° and 45° in the respective DFT models themselves. Similarly, the O–C–C–N dihedral angle for $\mathrm{TCC_{eqNMe}}$ and $\mathrm{TCC_{axNMe}}$ is 63° and 65° based on the J_{HHcalcd} coupling constants, respectively, while it is 70° and 72° in the respective DFT models themselves. Therefore, the Lambert equation calculated O–C–C–N dihedral angles for the BB conformation are slightly smaller than an *ideal synclinal* 60° value while those for the TCC conformation are slightly larger, and these results are indeed consistent with X-ray crystallographically measured results of eight-membered rings having the two conformations.

3.2. 5,5-Dimethyl-1-phenyl-3,4,5,6-tetrahydro-1*H*-2,5-benzoxazocinium halide [nefopam methohalide] (methiodide, 19) (methobromide, 21) and (methochloride, 22)

Nefopam methiodide (**19**) was the first in a series of methohalide quaternary ammonium salts to be prepared.[32,33] The ^{1}H-NMR parameters are listed in Table 2. The assignment of an *axial N*-methyl descriptor to the δ 3.78 methyl group was based upon a 2.3% NOE intensity enhancement into δ 4.62 *axial* H(31) upon {δ3.78 *axial* $\mathrm{NC}\underline{H}_3$}. The connectivity of protons in the benzo ring was determined by homonuclear decoupling experiments. The termini of this fragment were assigned by the observation of a 7.5% NOE intensity enhancement into δ 7.60 H(7) upon {δ 4.80 *exo* H(62)}, and a 4.1% NOE intensity enhancement into δ 4.80 *exo* H(62) upon {δ 7.60 H(7)}. Only one species was observed in the ^{1}H-NMR spectrum, but the line-widths were slightly broader ($W_{1/2} = 3.3$ Hz) than those for diethyl ether ($W_{1/2} = 1.0$ Hz) present in a trace amount in the solution.[32] NOE difference experiments showed that the major conformational contributor was the (*reference*,*S*)-BB structure for one of the enantiomers, since the benzhydrylic proton was found to be close to *equatorial* H(32). A 4.2% intensity enhancement for δ 4.15 *equatorial* H(32) was measured upon {H(1), δ 5.82}, and a 7.1% intensity increase for δ 5.82 H(1) was measured upon {*equatorial* H(32), δ 4.15}. However, while this line broadening was obviously indicative of a conformational equilibrium, it appeared to be predominantly to one side (BB) as seen by the 'extreme' magnitudes for the *trans*-coupling constants: large 12.8(1) J(31–41) [J(ax–ax)] and small <1 J(32–42)

Table 2. Selected solution-state ^{1}H-NMR ($CDCl_3$) parameters for nefopam methiodide (**19**)[a]

Atom	$\delta(^1H)$[b]	H–H	$J_{HHexptl}$[c]	BB $J_{HHcalcd}$[d]	TCC $J_{HHcalcd}$[d]
H(1)	5.82	31–32	–14.5	–14.29	–13.97
H(31)	4.62	31–41	12.8	11.68	2.72
H(32)	4.15	31–42	3.8	5.06	2.50
H(41)	3.30	32–41	4.3(2)	5.69	0.97
H(42)	3.95	32–42	<1	0.48	10.36
H(61)	5.79	41–42	–14.0(2)	–13.20	–13.08
H(62)	4.80	61–62	–12.4	–11.61	–12.19
H(7)	7.60	7–8	7.3		
H(8)	7.41	7–9	1.6		
H(9)	7.45	8–9	7.5		
H(10)	7.20	8–10	1.7		
NC$\underline{H}_3$(ax)	3.78	9–10	7.4		
NC$\underline{H}_3$(eq)	3.49	*Ortho–meta*	7.8		
H(*ortho*,*ortho*′)	7.11	*Ortho–para*	1.8		
H(*meta*,*meta*′)	7.32				
H(*para*)	7.32				

[a]Experimental data from Ref. 32, 200 MHz.
[b]ppm from internal TMS, ambient temperature.
[c]Hz, *ca.* 0.1 Hz estimated standard deviation (esd) of coupling constants unless stated in parenthesis.
[d]Hz, DFT calculated.

[*J*(eq–eq)]. B3LYP/6-311 + g(2d,p) calculations showed that the BB conformational model for the quaternary ammonium cation is lower in energy by 8.1 kJ than that calculated for TCC.

Nefopam methiodide crystallized as a racemic compound in an achiral crystal, and showed a disordered structure (see **20**) with one enantiomer having a (*reference*,*S*)-BB conformation molecule superimposed upon a (*reference*,*S*)-TCC conformation (3 : 2 ratio).[33] The decimal fraction of an atom's total electron density at each disordered site is a crystallographic refined parameter, and is referred to as an *occupancy factor*. Using the same **19** data crystal, these occupancy factors were found to be temperature dependent: BB : TCC occupancy factor ratios of 0.657(5) : 0.343(5) (193 K) and 0.592(7) : 0.408(7) (293 K).[29] The temperature dependence of the occupancy factors testifies to a dynamic conformational equilibrium *within the crystal lattice* as BB molecules interconvert into TCC and vice versa. Interconversion occurs via a C(4) atom flip from one side of the octagonal ring to the other, and is the same mechanism proposed for the solution-state conformational equilibrium of **19**, as well as for the analogous tertiary ammonium salt **15** mentioned above. DFT B3LYP/6-311 + g(2d,p) calculations[10] were performed on the (*reference*,*S*)-BB and (*reference*,*S*)-TCC conformations, and the geometry optimized structures were used as input for NMR = spin–spin calculations (also at the B3LYP/6-311 + d(2d,p) level).

The calculated coupling constants for each conformational model are also listed in Table 2. The set of four $^{3}J_{\mathrm{HHcalcd}}$ values from the O(2)–C(3)–C(4)–N(5) fragment in the (*reference*,*S*)-BB model agrees with the experimentally measured solution-state values with a root-mean-squared (RMS) difference of only 1.1 Hz, while the RMS = 0.9 Hz if the geminal values for this fragment are also included. This strongly suggests that (*reference*,*S*)-BB is the predominant conformation in solution. The DFT calculations also show the electronegativity effect expected for J(32–42) [J(eq–eq)] in the BB conformation.

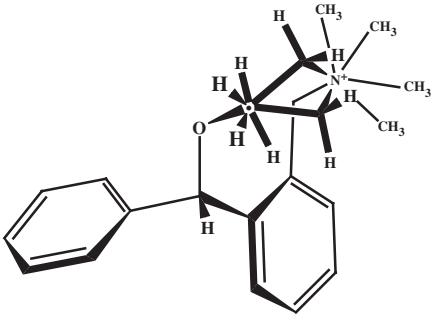

(*reference*,*S*)-BB/TCC 20

The methobromide (**21**) and methochloride (**22**) analogs were subsequently prepared, and crystallized. Fig. 4 gives torsion angles in the X-ray structure of **22**. Since packing efficiency (minimization of void space) is very important in crystallography, one might expect different space groups and packing motifs in the above series of increasing anion diameter. Fortuitously, these quaternary salts also afforded crystals in the same $P2_1/c$ space group and the same packing motif as found for the larger methiodide **19**.[29] The methobromide crystal also showed a temperature dependent BB/TCC disorder: 0.961(5) : 0.039(5) (193 K), 0.780(5) : 0.220(5) (293 K), and 0.755(6) : 0.245(6) (343 K), while the methochloride crystal contained only the more compact BB conformation in the lattice.[29] The TCC occupancy factors for data sets collected at various temperatures for the MeI and MeBr salts were found to be linearly correlated with the intermolecular (TCC)$\mathrm{Me}_{\mathrm{eq}}$–$\underline{H}\cdots\underline{H}$–$\mathrm{Me}_{\mathrm{ax}}$(TCC) distance between abutting methyl group protons in 2_1-screw-axis-related neighbors. The y-intercept of the linear relationship predicted a 0% TCC occupancy factor at *ca.* 2.53 Å for the above distance.[29] In other words, there will not be enough void space in the lattice to accommodate two 2_1-screw axis related adjacent TCC molecules when the intermolecular (TCC)$\mathrm{Me}_{\mathrm{eq}}$–$\underline{H}\cdots\underline{H}$–$\mathrm{Me}_{ax}$(TCC) distance between abutting methyl group protons becomes less than *ca.* 2.53 Å. For the methochloride crystal, a 2.31 Å close intermolecular (TCC)$\mathrm{Me}_{\mathrm{eq}}$–$\underline{H}\cdots\underline{H}$–$\mathrm{Me}_{\mathrm{ax}}$(TCC) distance between adjacent 2_1-screw symmetry ammonium cations was estimated by molecular modeling superimposition of a TCC conformation upon the BB conformation within the **22** lattice. Since this is smaller than the minimum 2.53 Å distance, required for two adjacent more extended TCC molecules, the

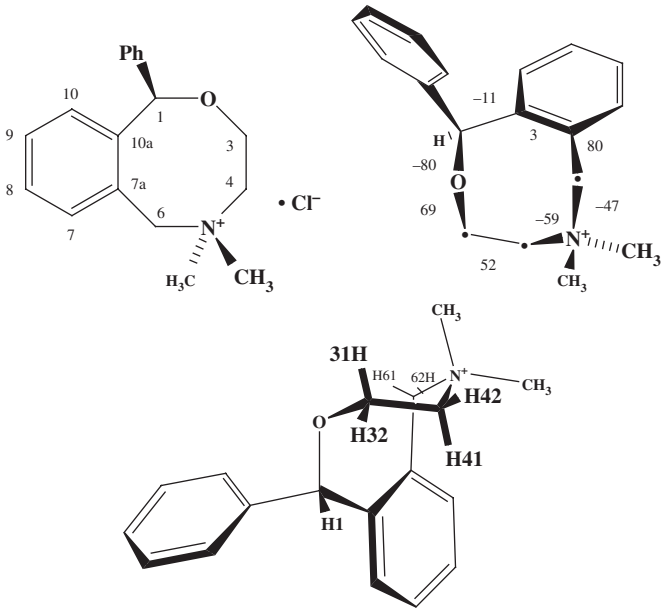

(*reference,S*)-BB 22

Fig. 4. Crystallographically determined torsion angles (deg) and different orientations of the (*reference*,1*S*,5*S*)-BB conformation for nefopam methochloride (**22**).

existence of only the more compact BB conformation in crystalline **22** may now be rationalized.[29]

A cp/mas VACP ^{13}C-NMR study was made of these three *pseudopolymorphic* crystals (**19**, **21**, and **22**).[29] The prefix 'pseudo' is affixed to 'polymorph' to describe this series of nefopam methohalide crystals since the anions therein are different. The results of this solid-state ^{13}C-NMR study are presented in Table 3 along with the solution-state ^{13}C chemical shifts. The cp/mas ^{13}C-NMR spectra of crystalline **19**, **21**, and **22** are illustrated in Fig. 5. It is seen that the C(4) peak (δ 58.51) in the cp/mas ^{13}C-NMR spectrum of the methochloride (**22**) is sharp due to the sole presence of the immobile BB conformation quaternary ammonium cation in the crystal. However, the C(4) peak (δ 59.42) in the methobromide (**21**) spectrum was markedly lower in intensity and broad, and in the methiodide (**19**) spectrum it was just a broad shoulder at δ 62.[29] Therefore, as the C(4) nucleus becomes more site-disordered in the crystal due to conformational interconversion, its cp/mas peaks show lower intensities and greater line-broadening.

An extensive solid-state cp/mas study was undertaken to determine T_1 time-constants of ^{13}C nuclei in the crystalline methochloride salt (**22**), and the results are reported in Fig. 6.[29] Local magnetic fields from the two sets of rapidly rotating methyl proton magnetic dipoles (estimated to revolve at *ca.* 10^9 rotations/s in the solid)[34] provide a distance-dependent relaxation mechanism for the neighboring

Table 3. Selected solution- and solid-state cp/mas ^{13}C-NMR spectral parameters for nefopam methohalide quaternary ammonium salts (**19**,**21** and **22**)[a]

Atom	Methiodide (**19**) cp/mas $\delta(^{13}C)$	$(CDCl_3)$[b] $\delta(^{13}C)$	Methobromide (**21**) cp/mas $\delta(^{13}C)$	Methochloride (**22**) cp/mas $\delta(^{13}C)$	minimum distance T_1[c] [r(C…H–Me)]
C(1)	84.69	(86.39)	85.58	86.02	375 [4.26]
C(3)	66.15[d]	(65.24)	66.08[d]	66.50[e]	81 [2.70]
C(4)	62[f] vv brd	(58.37)	59.42[g] v brd	58.51[e]	29 [2.56]
C(6)	66.15[d]	(68.17)	66.08[d]	67.52[e]	37 [2.60]
C(7)	135.13	(135.08)	135.18	136.71	111 [2.88]
C(8)	–	(128.54)	–	129.16	203 [3.81]
C(9)	–	(131.15)	–	130.3(4)[h]	⩾271 [4.50]
C(10)	–	(129.29)	–	–	–
C(7a)[i]	123.44	(124.27)	123.52	123.71[j]	138 [2.80]
C(10a)[i]	145.07	(143.43)	145.36	146.47[j]	241 [3.71]
NCH_{3ax}	49.62 brd	(50.86)	50.31 brd	49.94[j]	0.1 [–]
NCH_{3eq}	53.82 brd	(53.09)	52.50 brd	52.73[j]	0.1 [–]
C(*ipso*)[i]	142.68	(140.76)[k]	143.16	143.46[j]	323 [5.12]
C(*ortho*)	–	(127.64)			
C(*meta*)	–	(128.89)			
C(*para*)	–	(128.66)			

[a] ppm, 125.76 MHz, external spectral reference: glycine δC(= O) 176.03, VACP {TPPM-^{1}H}, spin-rate 12.75 KHz, 295 K, data from Ref. 29.

[b] $CDCl_3$ solution-state δ-values for **19** in parenthesis, internal spectral reference: tetramethylsilane (TMS), protonated carbon assignments by $^{13}C/^1H$ 2D-HMQC.

[c] T_1 values (s), carbon distance (Å) to closest methyl-proton given in square brackets.

[d] Unresolved broadened peak.

[e] Observed in CPPI spectrum.

[f] Very low intensity broad hump.

[g] Low intensity very broadened peak.

[h] Mean δ-value for 130.66, 130.29, and 129.93 δ (3C, 271 s T_1) close peaks which are not resolved in the T_1 experiment; estimated standard deviation of last digit is given in parenthesis; assignment based upon T_1 value.

[i] Assignment based on GIAO δC_{calcd} values calculated from a BB-conformation DFT/B3LYP model.

[j] C_{quat} or C_{methyl} observed in 60 μs dipolar dephasing delay NQS spectrum.

[k] Assignment based upon $^{13}C/^1H$(long-range) 2D-HMBC.

carbon nuclei in the solid-state. The rotatable *N*-methyl carbons[34] in **22** exhibit characteristically short T_1 values of only *ca.* 0.1 s (as opposed to much longer solid-state values typical for immobile carbons). It is seen that within a series of carbon nuclei having the same proton multiplicity, the T_1 constants were observed to dramatically shorten for nuclei residing closer to the rotating protons in the *gem*-dimethylammonium moiety of the BB-molecule.[29] As a result of this effect, the T_1 values were found to be useful in assigning some of the cp/mas carbon signals for this molecule. For example, there are three aromatic quaternary carbon signals in the SELTICS-NQS spectrum, and their T_1 values are markedly different: 138 s (δ123.71), 241 s (δ 146.47), and 323 s (δ 143.46). This enabled the chemical shifts to

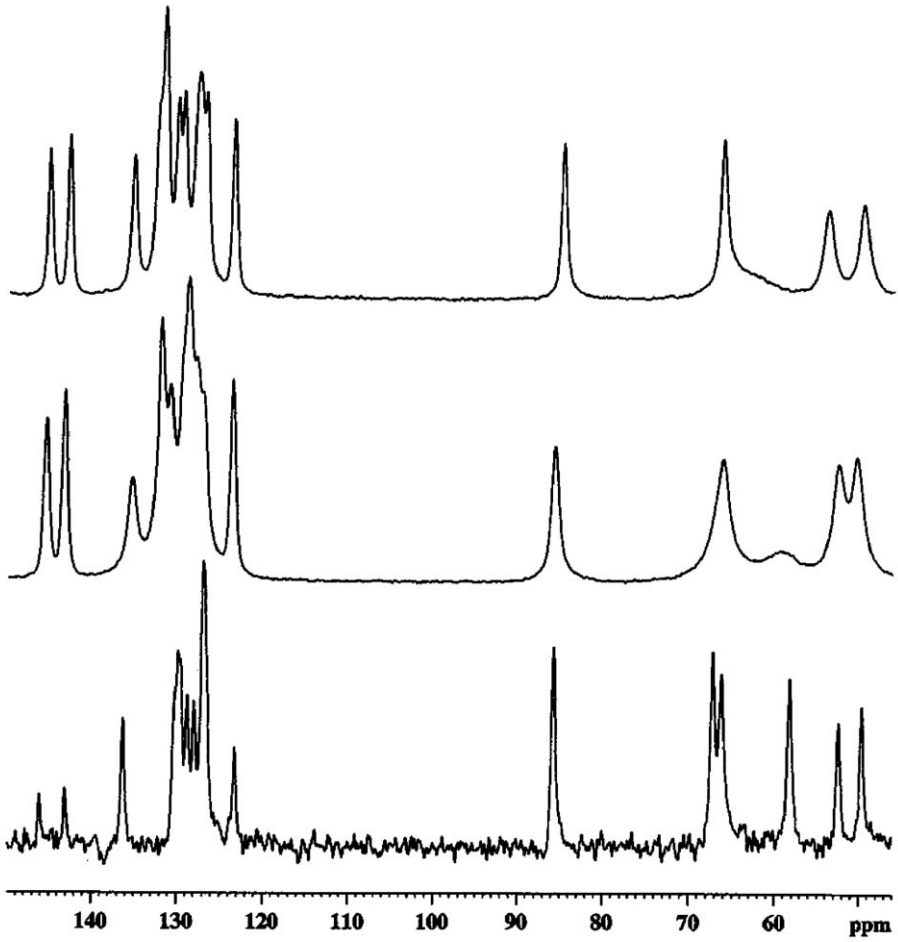

Fig. 5. (Top) Solid-state VACP cp/mas ^{13}C-NMR spectra of nefopam methiodide (**19**), (middle) nefopam methobromide (**21**), and (bottom) nefopam methochloride (**22**) measured from crystalline samples having BB : TCC occupancy factors of 0.59 : 41, 0.78 : 22, and 1.00 : 0.00, respectively.

be assigned as C(7a), C(10a), and C(*ipso*) since the respective distances of these quaternary carbons from the nearest methyl proton were *ca.* 2.8, 3.7, and 5.1 Å in the X-ray model. The assignments of these solid-state quaternary signals are consistent with the $\delta^{13}C_{calcd}$ values of δ 123.56 C(7a), 146.24 C(10a), and 136.40 C(*ipso*) calculated from scaled DFT GIAO isotropic magnetic shielding tensors (σ_{calcd}).

Three methylene carbon signals are found in the CPPI spectrum: (δ) 67.52, 66.50 and 58.51, and their respective T_1 values are: (s) 37, 81, and 29. The C(4) and C(6)

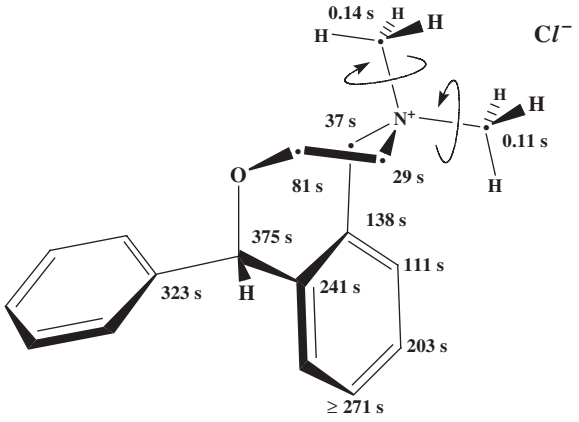

Fig. 6. Solid-state T_1 relaxation times of ^{13}C nuclei in crystalline nefopam methochloride (**22**) lengthen as the distance from the nucleus to the rotating methyl protons increases.

methylene nuclei together with N(5) define a plane which bisects the space between the two *N*-methyl groups, and thus they both reside in very close vicinity to the two rotors. On the other hand, C(3) is close to only one methyl (i.e. C(3) is *synclinal* to one methyl group but *antiperiplanar* to the second one). Without the T_1 data, it would be tenuous to assign C(3) and C(6) in the solid-state cp/mas spectrum. However, since the T_1 of the δ 66.50 nucleus is approximately two times longer than that for the δ 67.52 methylene, these chemical shifts can now be assigned as C(3) and C(6), respectively. These cp/mas chemical shift assignments are consistent with the ordering of DFT $\delta^{13}C_{calcd}$ values of 71.65 C(6), 64.01 C(3), and 59.38 C(4).

Finally, three of the four benzo-ring aromatic methine carbon signals are resolved in the T_1 cp/mas experiment: (d) 136.71, 129.16, and 130.3(4), and their respective T_1 values are: (s) 111, 203, and $\geqslant$271. These solid-state T_1 values are consistent with *ca.* 2.9, 3.8, and 4.5 Å distances from the nearest methyl group proton, and enable their respective assignments to be C(7), C(8), and C(9). Now that most of the ^{13}C cp/mas chemical shifts have been assigned, the close correspondence of these values to those in the solution-state spectrum provided further evidence (in addition to the NOE results noted above) that the predominant conformation in solution is (*reference*,*S*)-BB.

3.3. 1-Phenyl-3,4,5,6-tetrahydro-1*H*-2,5-benzoxazocine hydrochloride [*N*-desmethylnefopam hydrochloride] (23)

N-desmethyl-nefopam (**23**) is a metabolite of the parent drug, and it too crystallizes as a racemic compound in an achiral crystal. One of the enantiomers in the crystal has the (*reference*,*S*)-BB conformation (see Fig. 7 for torsion angles in X-ray

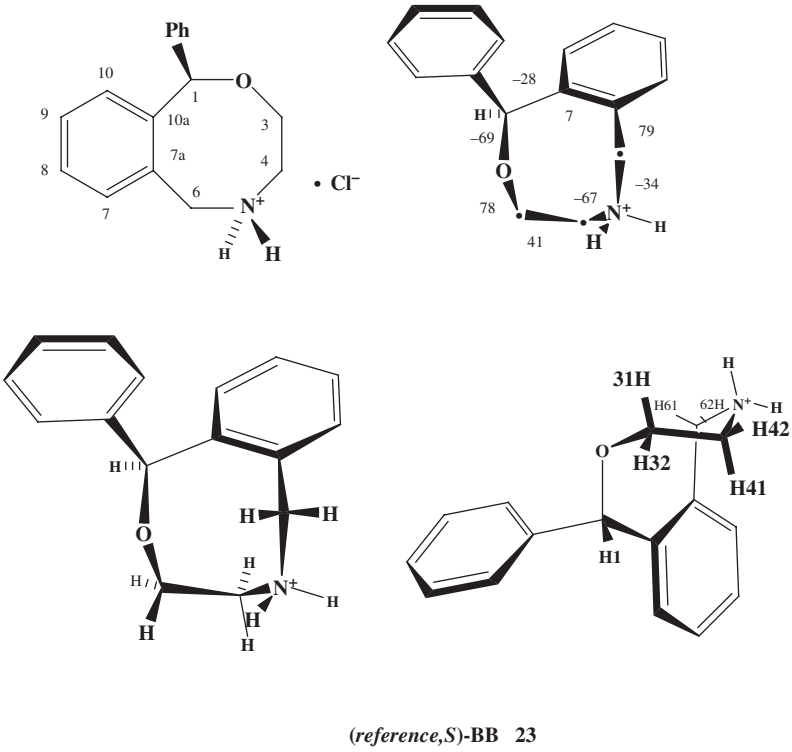

(*reference,S*)-BB **23**

Fig. 7. Crystallographically determined torsion angles (deg) and different orientations of the (*reference*,1*S*)-BB conformation for *N*-desmethyl nefopam hydrochloride (**23**).

structure). The H(41,42) signals were strongly second order in the $CDCl_3$ spectrum, and the two N–*H* protons were in fast exchange. The signals from the O(2)–C(3)–C(4)–N(5) fragment of the spectrum were simulated using the *gNMR 4.1*[36] program and the ^1H and ^{13}C selected spectral parameters are listed in Table 4. Also in this case, the relative magnitudes of the vicinal coupling constants involving the two sets of *trans* protons enabled assignment of *axial* and *equatorial* descriptors to H(31,41) and H(32,42), respectively. Inspection of the vicinal coupling constants strongly suggested a BB/TCC conformational equilibrium with an increase in the amount of TCC conformation compared that of the corresponding tertiary or quaternary ammonium salts. A 1.3% NOE intensity enhancement into the δ 4.04 *equatorial* H(32) was measured upon {δ 5.76 H(1)}, thus suggesting that the BB conformation is the predominant contributor to the equilibrium. The B3LYP/6-311 + g(2d,p) calculations show that the BB and TCC conformational models for **23** are really quite close in energy and that the TCC-model is even slightly more stable (1.0 kJ) than its BB counterpart. Of course, the effects of solvation on conformer stability are not taken into consideration in these calculations.

Table 4. Selected solution-state ^{1}H- and ^{13}C-NMR and solid-state cp/mas ^{13}C-NMR spectral parameters for *N*-desmethyl-nefopam hydrochloride (**23**)[a]

Atom	$\delta(^1H)$[b]	H–H	$J_{HHexptl}$[c]	[BB : TCC = 65 : 35] $J_{HHcalcd}$[d]	BB $J_{HHcalcd}$[d]	TCC $J_{HHcalcd}$[d]
H(1)	5.76 {5.75}	31–32	{−13.4}	[−14.0]	−14.10	−13.91
H(31)	4.48 {4.50}	31–41	{9.2}	[8.3]	11.68	2.00
H(32)	4.04 {4.05}	31–42	{3.6}	[4.4]	5.23	2.83
H(41)	3.19 {3.20$_5$}[e]	32–41	{3.2}	[4.0]	5.38	1.44
H(42)	3.19 {3.22$_9$}[e]	32–42	{4.9}	[4.0]	0.34	10.74
H(51)	10.34 {9.89}[f]	41–42	{−14.1}	[−13.0]	−13.07	−12.91
H(52)	9.89 {9.89}[f]	51–61	3.3(2)	[3.9]	5.53	0.15
H(61)	5.26 {5.26}	51–62	2.6(5)	[2.0]	0.23	6.24
H(62)	4.39 {4.40}	52–61	8.9(4)	[7.6]	7.42	7.91
H(7)	7.53 {7.55}	52–62	3.9(5)	[4.0]	6.00	0.29
H(8)	– {7.36}	61–62	−12.3(3)	[−11.5]	−11.34	−11.79
H(9)	– {7.36}					
H(10)	– {7.14}					

	CD_2Cl_2 $\delta(^{13}C)$[b]	cp/mas $\delta(^{13}C)$[g]
C(1)	85.77 {85.24}	86.27
C(3)	66.93 {66.31}	63.49[h]
C(4)	42.48 {42.35}	46.74[h,i]
C(6)	48.65 {48.25}	47.20[h,i]
C(7)	– {134.39}	–
C(8)	– {128.86}[j]	–
C(9)	– {129.95}	–
C(10)	– {129.00}[j]	–
C(7a)	– {127.41}[i]	131.35[i,k]
C(10a)	– {141.85}[i,l]	141.69[i,k]
C(*ipso*)	– {141.20}[i,l]	138.65[i,k]
C(*ortho*)	– {127.27}	
C(*meta*)	– {128.61}	
C(*para*)	– {128.08}	

[a]Data for CD_2Cl_2 solvent, 200 MHz for ^{1}H and 50 MHz for ^{13}C from Ref. 35; data for $CDCl_3$ 500.1 MHz for ^{1}H and 125.76 MHz for ^{13}C given in braces.
[b]ppm from internal TMS, ambient temperature.
[c]Hz, *ca.* 0.1 Hz estimated standard deviation (esd) of coupling constants unless stated in parenthesis.
[d]Hz, DFT calculated, 65 : 35 weighted average of BB : TCC values given in square brackets.
[e]$\Delta\nu = 12.17$ Hz.
[f]Very broad.
[g]125.76 MHz, SELTICS cp/mas, 5.0 kHz spin-rate, ppm using external glycine carbonyl δ 176.03.
[h]Observed in CPPI.
[i]Assignment by analogy to (*ref,S*)-BB conformation DFT $\delta C(4)_{calcd}$ 44.67, $\delta C(6)_{calcd}$ 58.90, $\delta C(7a)_{calcd}$ 121.03, $\delta C(10a)_{calcd}$ 145.40, and $\delta C(ipso)_{calcd}$ 136.90.
[j]Assignments may be interchanged.
[k]Observed in SELTICS-NQS.
[l]Assignments may be interchanged.

Quantum mechanical calculations of the coupling constants (B3LYP/6-311 + g(2d,p)) for the two conformations are also listed in Table 4. A *ca.* 2 : 1 ratio of BB : TCC calculated coupling constants provides weighted averaged values (also in Table 4) in reasonable agreement with those found by experiment. The results from this investigation of a series of similar octagonal rings with secondary, tertiary, or quaternary ammonium salt moieties, seem to show that the higher the degree of *N*-methylation, the greater is the amount of BB conformation in CD_2Cl_2 solution. On the other hand, solvation interactions are clearly not present in the crystal lattice, and now in the case of the quaternary ammonium salt analogs, the population of the TCC conformation in the BB : TCC equilibrium is dependent upon the void volume between adjacent 2_1-axis related neighbors. Bottom line: Kurt Mislow[37] has coined the phrase ... 'what something is depends on where it is.'

3.4. (1*RS*,3*RS*,5*RS*)- and (1*RS*,3*RS*,5*SR*)-3,5-dimethyl-1-phenyl-3,4,5,6-tetrahydro-1*H*-2,5-benzoxazocine hydrochloride [(1*RS*,3*RS*,5*RS*)- and (1*RS*,3*RS*,5*SR*)-3-methyl-nefopam hydrochloride *equatorial* and *axial N*-methyl diastereomers] (24) and (25), respectively

The (1*RS*,3*RS*) and (1*RS*,3*SR*) diastereomers of 3-methyl-nefopam have the methyl group *trans* or *cis* to phenyl, respectively, and were present in the reaction mixture. They were separated, single crystals of each of the hydrochloride salts were grown, and then subjected to X-ray crystallographic structure determination.[38] The solution of the *trans* C(3)-methyl isomer contained two *N*-methyl diastereomers: the (1*RS*,3*RS*,5*RS*) racemic mixture, and the epimeric (1*RS*,3*RS*,5*SR*) racemic mixture. Crystallization of this solution resulted in spontaneous resolution to afford a conglomerate of chiral crystals.[38] Each single crystal contained either the (1*R*,3*R*,5*R*)- or the (1*S*,3*S*,5*S*)-enantiomer. The *C*- and *N*-methyl groups were ligated to 'corner'[11] atoms on a (*reference*,1*S*,3*S*,5*S*)-BB conformation for one of the crystals (see Fig. 8 for X-ray crystallographically determined torsion angles of **24**).[38] Relative to the $-OCH(CH_3)CH_2N-$ fragment, we may again refer to both methyl groups as being *equatorial* within the context of this local environment. Not surprisingly, dissolution of the crystalline tertiary ammonium salt in CD_2Cl_2 afforded epimerization at nitrogen. The two *N*-methyl species were in the ratio of 3 : 2. Selected ^1H and ^{13}C solution-state NMR spectral parameters for the two species **24** and **25** as well as the solid-state cp/mas chemical shifts for **24** are provided in Table 5. Some of the signals in the minor species were very broad at 298 K, while those for the major species were sharp. These minor species signals sharpened up at 230 K, but as with nefopam itself (**15**), no additional species was observed at this temperature.[39] The H(3) proton in both solution-state species has an *axial* disposition within the $-OCH(CH_3)CH_2N-$ fragment as evidenced by *antiperiplanar* type 12.3(3) Hz (major) and 10.8 Hz (minor) vicinal coupling constant values to one of the geminal protons ligated to C(4). The coupling constants for the major species (**25**) were very similar to those noted for corresponding values measured for the major species of nefopam itself (**18**) (*axial N*-methyl BB diastereomer).

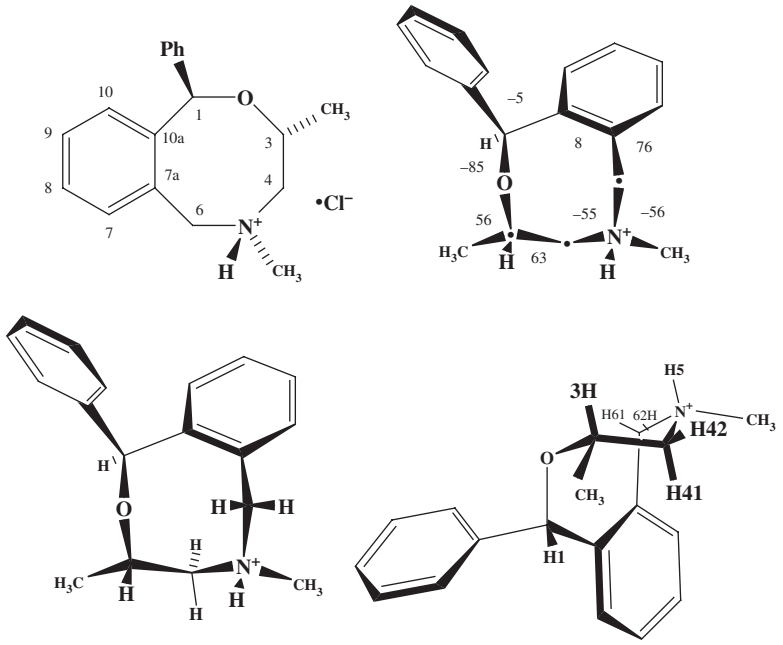

(*reference*,1*S*,3*S*,5*S*)-BB 24

Fig. 8. Crystallographically determined torsion angles (deg) and different orientations of the (*reference*,1*S*,3*S*,5*S*)-BB conformation for (1*RS*,3*RS*,5*RS*)-3-methyl-nefopam hydrochloride (**24**) *equatorial N*-methyl diastereomer.

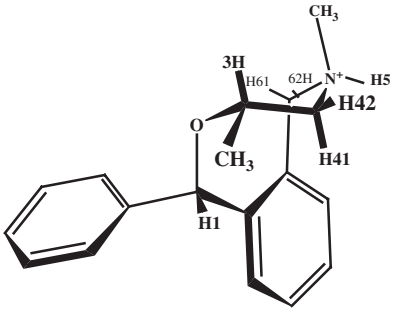

(*reference*,1*S*,3*S*,5*R*)-BB 25

The NOE results are consistent with a BB solution-state conformational preference. A 1.4% intensity increase into δ 1.44 major C(3)–C$\underline{H}_3$ is measured upon {δ 5.98 major H(1)}, and a 2.3% intensity increase into δ 5.98 major H(1) is measured

Table 5. Selected solution-state ^{1}H- and ^{13}C-NMR (CD_2Cl_2) and solid-state cp/mas ^{13}C-NMR spectral parameters for (1*RS*,3*RS*,5*RS*)- and (1*RS*,3*RS*,5*SR*)-3-methyl-nefopam hydrochloride respective *equatorial* (**24**) and *axial* (**25**) *N*-methyl diastereomers[a]

Atom	(1*RS*,3*RS*,5*SR*) major species (**25**) $\delta(^{1}H)$[b]	(1*RS*,3*RS*,5*RS*) minor species (**24**) $\delta(^{1}H)$[b]	Atom	(1*RS*,3*RS*,5*SR*) major species (**25**) $\delta(^{13}C)$[b]	(1*RS*,3*RS*,5*RS*) minor species (**24**) $\delta(^{13}C)$[b]	cp/mas (**24**) $\delta(^{13}C)$[c]
H(1)	5.98 {5.94}	5.94 {5.90}	C(1)	77.63	77.32	76.19
H(3)	4.70 {4.72}	.[d] {4.88}	C(3)	68.11	70.20	69.72
H(41)	2.96 {~2.9}	.[d] {~2.9}	C(4)	52.55	–	51.74[e,f]
H(42)	2.76 {~2.9}	.[d] {~2.9}	C(6)	57.70	56.42	52.22[e,f]
H(5)	12.76 {12.01}	13.20 {12.35}	C$\underline{C}H_3$	16.40	16.75	16.17[g]
H(61)	4.92 {4.99}	.[d] {6.05}	N$\underline{C}H_3$	40.08	42.20	40.41[g]
H(62)	4.39 {4.36}	3.91 {3.91}	C(7)	–	–	134.02[h]
C$C\underline{H}_3$	1.44 {1.41}	1.41 {1.38}	C(9)	–	–	131.40[h]
N$C\underline{H}_3$	2.99 {3.02}	2.65 {2.67}	C(7a)	–	–	123.40[g]
	–	–	C(10a)	–	–	144.80[e,g]
	–	–	C(*ipso*)	–	–	142.55[e,g]

HH	$J_{HHexptl}$[i]	$J_{HHexptl}$[i]	BB_{axNMe} $J_{HHcalcd}$[j]	BB_{eqNMe} $J_{HHcalcd}$[j]
31-C$\underline{H}_3$	6.5(1) {6.5(1)}	6.5(1) {6.7(1)}	6.14	6.12
3–41	12.1(3) {11.8(5)}	.[d] {~10.8}	10.73	10.52
3–42	4.6(2) {3.5(5)}	.[d]	5.05	4.69
41–42	−14.4(3) {−}	.[d]	−13.10	−12.96
41–5	2.1(3) {−}	.[d]	2.75	9.77
42–5	2.7(2) {−}	.[d]	2.95	1.38
5-C$\underline{H}_3$	4.9(1) {4.9(1)}	4.9(1) {4.8(1)}	5.49	5.69
5–61	7.8(3) {8.3(1)}	.[d] {3.0(2)}	7.43	5.95
5–62	5.1(1) {4.9(2)}	.[d] {<1}	5.59	0.25
61–62	−11.6(1) {−11.6(2)}	−12.9(1) {−13.0(1)}	−11.41	−11.70

[a] CD_2Cl_2 solvent, 298 K, 300 MHz for ^1H and 75 MHz for ^{13}C, data from Ref. 39, major : minor species 3 : 2 {230 K low temperature values given in braces, 400 MHz}.
[b] ppm from internal TMS.
[c] 125.76 MHz, SELTICS cp/mas, 5.0 kHz spin-rate, ppm using external glycine carbonyl δ 176.03.
[d] Not measured owing to severe line broadening.
[e] Assignments may be interchanged.
[f] Observed in CPPI.
[g] Observed in SELTICS-NQS.
[h] Assigned by analogy with assignments for the solid **22** quaternary ammonium salt.
[i] Hz, estimated standard deviation of last digit given in parenthesis.
[j] Hz, DFT calculated.

upon {δ 1.44 major C(3)–C$\underline{H}_3$}. The *axial* orientation of the major species *N*-methyl is forthcoming from the observation of an 8.3(1) Hz *antiperiplanar*-like magnitude for ^3J(5–61) and *synclinal*-like 2.1(3) Hz ^3J(41–5), 2.7(2) Hz ^3J(42–5), and 4.9(1) Hz ^3J(5–62) values. The assignment of a 1,3-type *cis-diaxial* relationship between the major *N*-methyl and H(3) moieties is further strengthened by the finding of a 2.3% intensity increase into δ 4.70 major *axial* H(3) upon {δ 2.99 major NC$\underline{H}_3$}. The table also shows that assignment of a predominant BB solution-state conformation for both the major and minor species is clearly in excellent accord with the quantum mechanical calculated coupling constants listed for an *axial N*-methyl BB model and *equatorial N*-methyl BB model, respectively. It is very apparent that there is a rigid geometry for the solution-state major species. A comparison of the DFT calculated coupling constants with those few measured at low temperature for the minor species, suggests that the minor species is also rigid.

In addition, a 5.5% intensity increase into δ 5.94 minor H(1) measured upon {δ 1.41 minor C(3)–C$\underline{H}_3$} testifies to a predominant BB solution-state conformation also for the minor species. Like the minor species of nefopam (**15**), the minor species *N*-methyl group is also *equatorial* as evidenced by two *synclinal*-type vicinal coupling constants involving the *N*–H proton and the geminal protons on C(6) [3.0(2) Hz ^3J(5–61) and <1 Hz ^3J(5–62)]. For the nefopam (**15**) minor species, $\Delta\delta$ for the diastereotopic geminal H(61,62) protons was 2.05 ppm while it was only 0.59 ppm for the major species (**18**). Similar $\Delta\delta$-values are noted for the (1*RS*,3*RS*,5*RS*) minor species (**24**) ($\Delta\delta$ 2.14 ppm) and for the (1*RS*,3*RS*,5*SR*) major species (**25**) ($\Delta\delta$ 0.53 ppm). It is thus apparent, that the solution-state minor species predominant conformation and *N*-methyl configuration corresponds to that observed in the crystal, similar to the case described above for nefopam HCl (**15**). Finally, the δ 77.63 and 77.32 C(1) chemical shifts for the major (**25**) and minor (**24**) species versus δ 86.06 and 85.45 values for the corresponding species [(**18**) and (**15**)] in nefopam HCl can be readily explained by the well-known *gamma-gauche* effect (e.g. cp/mas δ 76.19 value correlated with a 69° C(1)–O(2)–C(3)–$\underline{C}$H$_3$ dihedral angle in the solid-state structure).

3.5. (1*RS*,3*SR*,5*SR*)- and (1*RS*,3*SR*,5*RS*)-3,5-dimethyl-1-phenyl-3,4,5,6-tetrahydro-1*H*-2,5-benzoxazocine hydrochloride [(1*RS*,3*SR*,5*SR*)- and (1*RS*,3*SR*,5*RS*)-3-methyl-nefopam hydrochloride *equatorial* and *axial N*-methyl diastereomers] (26) and (27), respectively

What about the (1*RS*,3*SR*)-epimeric diastereomers that contain a C(3)-methyl *cis* to the phenyl group? Like their *trans* analogs discussed above, a solution of the *cis* compound should contain the two *N*-methyl diastereomers as a (1*RS*,3*SR*,5*RS*) racemic mixture (see **26** in Fig. 9) and a (1*RS*,3*SR*,5*SR*) racemic mixture (see **27** in Fig. 10). The mixture of two racemic diastereomers crystallizes as a racemic compound of only **27** in an achiral crystal. Torsion angles for the (1*S*,3*R*,5*R*)-enantiomer are given in X-ray structure **27**. X-ray crystallographic structure analysis of these crystals shows them to have two symmetry unrelated molecules in

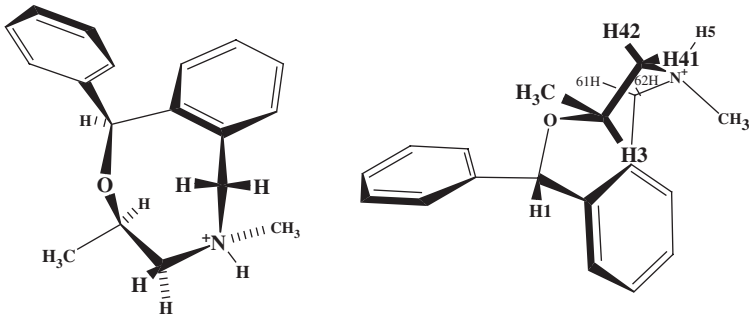

(*reference*,1*S*,3*R*,5*S*)-TCC **26**

Fig. 9. Different orientations of the (*reference*,1*S*,3*R*,5*S*)-TCC conformation for (1*RS*,3*SR*,5*RS*)-3-methyl-nefopam hydrochloride (**26**) *axial N*-methyl diastereomer.

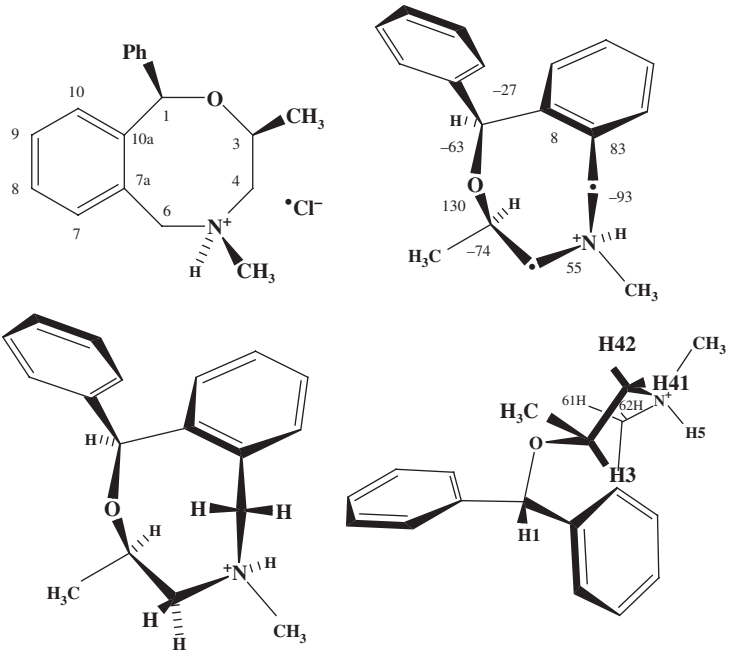

(*reference*,1*S*,3*R*,5*R*)-TCC **27**

Fig. 10. Crystallographically determined torsion angles (deg) and different orientations of the (*reference*,1*S*,3*R*,5*R*)-TCC conformation for (1*RS*,3*SR*,5*SR*)-3-methyl-nefopam hydrochloride (**27**) *equatorial N*-methyl diastereomer.

the asymmetric unit. Both **27** molecules have the same (but not *ideally* identical) (*reference*,*S*)-TCC conformation for one of the enantiomers in the crystal in which the *C*- and the *N*-methyl groups are both *equatorial* and each resides at a 'non-corner' position. The entire extended array of molecules in the crystal lattice is constructed by duplicating a repeat unit (known as the *unit cell*) using only the *translation* symmetry operation. The *asymmetric unit* contains the minimum amount of molecular material needed to construct the unit cell using *all* the symmetry operations of the crystal space group with the exception of translation. It is the same as the unit cell if the space group contains only the symmetry operations of *identity* and *translation*. It will be a fraction of the unit cell if the space group contains additional symmetry operations other than *identity* and *translation*. Two molecules in the asymmetric unit must have different magnetic environments since there is no symmetry requirement that they be identical. The presence of two molecules in the asymmetric unit is readily ascertained in a cp/mas spectrum since each nucleus gives two single-intensity lines (or sometimes single double-intensity lines). Such is the case for the cp/mas ^{13}C-NMR spectrum of solid **27** (see chemical shifts in Table 6).

A comparison of the (*reference*,1*S*,3*S*,5*S*)-BB (see **24** in Fig. 8) X-ray crystallographically determined geometry with that of the (*reference*,1*S*,3*R*,5*R*)-TCC diastereomer (see **27** in Fig. 10) shows that four endocyclic dihedral angles change from *synclinal* values in BB to *anticlinal* (*ca.* 120°) or *orthogonal* values in TCC. Thus, the 56° C(1)–O(2)–C(3)–C(4), 69° C(1)–O(2)–C(3)–$\underline{C}H_3$, 56° C(4)–N(5)–C(6)–C(7a), and 69° $\underline{C}H_3$–N(5)–C(6)–C(7a) angles in BB (**24**), open up to larger 130°, 110°, 91°, and 144° values, respectively, in TCC (**27**). When comparing cp/mas ^{13}C-NMR spectra from these two solid samples, one expects to observe *gamma-gauche* effects for chemical shifts of terminal nuclei defined by these angles. This is indeed the case, since the chemical shifts for these nuclei are: (δ) 76.19 [C(1)], 16.17 [C$\underline{C}H_3$], 51.74 (or 52.22) [C(4)], 40.41 [N$\underline{C}H_3$], and 123.40 [C(7a)] in the BB spectrum (**24**, see Table 5), versus (δ) 86.19/82.51 [C(1)], 19.19/17.46 [C$\underline{C}H_3$], 60.84/58.98 [C(4)], 45.78/44.89 [N$\underline{C}H_3$], and 130.48 [C(7a)] in the TCC spectrum (**27**, see Table 6).

Dissolution of the (*reference*,1*S*,3*R*,5*R*)-TCC crystals in CD_2Cl_2 afforded two *N*-methyl diastereomers in the ratio of 7 : 6.[38] It is seen that H(3) in **27** is *antiperiplanar* to H(42) while it is *synclinal* to H(41) (i.e. respective 171° and 71° dihedral angles). While the ^3J(3–42) coupling constant is larger than that of ^3J(3–41) for both *N*-methyl diastereomeric solution-state species, these values certainly appear to be averaged [6.6(1) Hz and 2.3(1) Hz, respectively, for major species **26**, and 8.5(1) Hz and 2.2(1) Hz, respectively, for minor species **27**]. If the predominant solution-state conformations of the major and minor species are TCC, then one expects *axial* H(3) to be close to H(1). This is confirmed by NOE-DIFFERENCE experiments. It was found that {δ5.82, H(1) major} afforded a 2.9% intensity enhancement into δ 4.14 *axial* H(3) major; and {δ 4.14, *axial* H(3) major} gave a 4.3% intensity increase into δ 5.82 H(1) major. Similarly, {δ 5.89, H(1) minor} gave a 5.9% intensity increment into δ 4.33 *axial* H(3) minor. These NOE results are in line with a preponderance of the TCC conformation for both solution-state species. The lower ^3J(3–42) time-averaged value for the major species versus

Table 6. Selected solution-state ^{1}H- and ^{13}C-NMR (CD_2Cl_2), and solid-state cp/mas ^{13}C-NMR parameters for (1*RS*,3*SR*,5*RS*)- and (1*RS*,3*SR*,5*SR*)-3-methyl-nefopam hydrochloride *axial* and *equatorial* *N*-methyl diastereomers (**26**) and (**27**), respectively[a]

Atom	(1*RS*,3*SR*,5*RS*) major species (**26**) $\delta(^{1}H)$[b]	(1*RS*,3*SR*,5*SR*) minor species (**27**) $\delta(^{1}H)$[b]	Atom	(1*RS*,3*SR*,5*RS*) major species (**26**) $\delta(^{13}C)$[b]	(1*RS*,3*SR*,5*SR*) minor species (**27**) $\delta(^{13}C)$[b]	cp/mas (**27**) $\delta(^{13}C)$[c]
H(1)	5.82	5.89	C(1)	84.83	83.95	86.19, 82.57
H(3)	4.14	4.33	C(3)	70.39	70.46	71.08, 70.30
H(41)	2.93	3.32	C(4)	57.70	60.57	60.84, 58.98
H(42)	3.30	2.82	C(6)	56.04	58.54	58.98, 55.73
H(5)	13.07	12.60	C$\underline{C}H_3$	20.21	20.43	19.19, 17.46[d]
H(61)	5.61	5.15	N$\underline{C}H_3$	40.78	45.74	45.78, 44.89[d]
H(62)	4.05	4.13	C(7)	–	–	138.52, 136.44
H(7)	7.32	–	C(7a)	–	–	130.48[d]
C$\underline{C}H_3$	1.50	1.37	C(10a)	–	–	142.98, 142.31[d]
N$\underline{C}H_3$	2.56	2.94	C(*ipso*)	–	–	140.30[d]

HH	$J_{HHexptl}$[e,f]	$J_{HHexptl}$[e,g]	BB_{eqNMe} $J_{HHcalcd}$[h]	TCC_{axNMe} $J_{HHcalcd}$[h]	BB_{axNMe} $J_{HHcalcd}$[h]	TCC_{eqNMe} $J_{HHcalcd}$[h]
31-C$\underline{H}_3$	6.6 [6.0]	6.5 [6.0]	6.27	5.94	6.63	5.96
3–41	2.3 [2.0]	2.2 [1.9]	4.81	0.72	7.85	1.26
3–42	6.6 [6.6]	8.5 [8.3]	0.67	9.16	0.77	9.12
41–42	−14.0 [−12.8]	−13.1 [−12.7]	−13.05	−12.67	−13.41	−12.61
41–5	4.8(4) [3.7]	3.2 [3.4]	9.88	1.02	3.22	3.46
42–5	3.5 [4.1]	7.9(2)[9.2]	1.73	5.09	2.71	9.88
5-C$\underline{H}_3$	5.0 [5.7]	4.9 [5.6]	5.64	5.75	5.55	5.58
5–61	1.5 [2.1]	7.2 [5.9]	5.22	0.72	0.16	6.50
5–62	3.4 [3.8]	< 1 [0.9]	0.45	5.17	6.01	0.32
61–62	−13.3 [−11.9]	−12.7 [−11.7]	−11.66	−11.97	−11.54	−11.74

[a] CD_2Cl_2 solvent, 298 K, 300 MHz for ^{1}H and 75 MHz for ^{13}C, data from Ref. 39, major : minor species 7 : 6.
[b] ppm from internal TMS.
[c] 125.76 MHz, SELTICS cp/mas, 5.0 kHz spin-rate, ppm using external glycine carbonyl δ 176.03.
[d] SELTICS-NQS experiment, assigned by analogy with assignments for the solid **23** quaternary ammonium salt.
[e] Hz, *ca.* 0.1 Hz estimated standard deviation (esd) of coupling constants unless stated in parenthesis.
[f] TCC_{axNMe} : BB_{eqNMe} 70 : 30 ratio of $J_{HHcalcd}$ values given in square brackets.
[g] TCC_{eqNMe} : BB_{axNMe} 90 : 10 ratio of $J_{HHcalcd}$ values given in square brackets.
[h] Hz, DFT calculated.

that for the minor species suggests that the former has a higher concentration of the smaller conformational contributor than the latter. DFT $J_{HHcalcd}$ values were calculated in order to provide a rough estimate of a TCC/BB conformational equilibrium for both the major and minor species, and are reported in Table 6. On the basis of weighted averaged values, the *axial N*-methyl TCC is the predominant conformation for the major solution-state species on the basis of an estimated TCC_{axNMe} : BB_{eqNMe} equilibrium of about 70 : 30, while the *equatorial N*-methyl TCC is the predominant conformation for the minor solution-state species on the basis of an estimated TCC_{eqNMe} : BB_{axNMe} equilibrium of about 90 : 10. It appears that a *cis*-to-phenyl placement of a 3-methyl group on our eight-membered ring makes these (1*RS*,3*SR*)-diastereomers conformationally more mobile than their *trans*-to-phenyl (1*RS*,3*RS*)-counterparts.

The orientation of the *N*-methyl group is forthcoming from the vicinal coupling constants involving the *N*–H proton. In the solid-state *equatorial N*-methyl TCC ring model (**27**), dihedral angles involving H(5) and its H(41) and H(42) neighbors are 58° and 176°, respectively, while those relating H(5) to the H(61) *endo* and H(62) *exo* pair are 146° and 95°, respectively. The solution-state values for the minor species are consistent with these angles: 3.2(1) Hz ^3J(41–5), 7.9(2) Hz ^3J(42–5), 7.2(1) Hz ^3J(5–61), and <1 Hz ^3J(5–62). Additional evidence showing that the minor species conformational equilibrium contains a predominant *equatorial N*-methyl TCC structure is the finding of a 1.2% intensity increase into the δ 4.33 minor *axial* H(3) upon {δ 12.60 minor H(5)}. Furthermore, there is a slightly better agreement of the *equatorial N*-methyl TCC cp/mas ^{13}C chemical shifts with corresponding values for the minor *N*-methyl diastereomer, than with those for the major one. An *axial* orientation for the major species *N*-methyl is also seen by an NOE-DIFFERENCE experiment: a 1.8% intensity increase into the δ 4.14 major *axial* H(3) upon {δ2.56 major N$\underline{C}H_3$}.

3.6. 4-Methyl-6-phenyl-3,4-dihydro-2*H*,6*H*-1,5,4-benzodioxazocine (28)

The substituted 1,5,4-benzodioxazocine (**28**) is a known compound.[40] It was reinvestigated since proton spin–spin coupling constants, and a crystal structure did not appear in the literature. The racemic mixture of **28** crystallized as a racemic compound in an achiral space group crystal.[41] The (*reference*,1*S*,3*R*)-TCC conformation was observed for one of the enantiomers in the crystal, and the stereolabile *N*-methyl group was found to occupy an *equatorial* position. The X-ray crystallographically determined torsion angles of **28** are given in Fig. 11 (ring atom numbers used are consistent with those for other eight-membered rings in this report rather than with the compound name). Table 7 lists ^{1}H and ^{13}C selected spectral parameters. The close agreement between DFT calculated coupling constants for the (*reference*,1*S*,3*R*)-TCC model and their experimentally measured counterparts strongly suggest that the eight-membered ring maintained the same crystalline-state conformation when crystals were dissolved in $CDCl_3$. In addition, the close correspondence between experimentally measured aliphatic ^{13}C chemical shifts and the

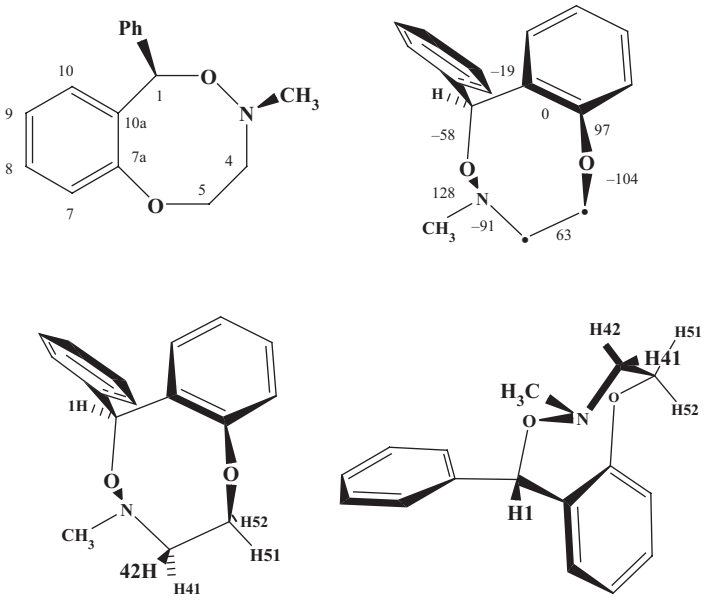

(*reference*,1*S*,3*R*)-TCC 28

Fig. 11. Crystallographically determined torsion angles (deg) and different orientations of the (*reference*,1*S*,3*R*)-TCC conformation for **28**.

Table 7. Selected solution-state ^{1}H- and ^{13}C-NMR ($CDCl_3$) spectral parameters for 4-methyl-6-phenyl-3,4-dihydro-2*H*,6*H*-1,5,4-benzodioxazocine (**28**)[a]

Atom	$\delta(^{1}H)^{b}$	H–H	$J_{HHexptl}{}^{c}$	TCC $J_{HHcalcd}{}^{d}$	Atom	$CDCl_3$ $\delta(^{13}C)_{exptl}{}^{b}$	TCC $\delta(^{13}C)_{calcd}{}^{e}$
H(1)	5.92	41–42	−14.0	−13.01	C(1)	85.6	88.85
H(41)	2.65	41–51	1.1	0.95	C(4)	59.7	59.46
H(42)	3.35	41–52	3.7	3.74	C(5)	75.1	75.51
H(51)	4.49	42–51	4.2	4.21	$\underline{C}H_3$	47.5	44.47
H(52)	4.08	42–52	11.9	10.72	C(7)	128.8	123.40
H(7)	7.40	51–52	−12.2	−11.82	C(8)	124.5	126.43
H(10)	7.01	7–8	7.9(3)	7.07	C(9)	129.1	121.92
	–	7–9	1.7(3)	0.83	C(10)	127.9	127.82
	–	8–10	1.5	1.15	C(7a)	135.5	138.23
	–	9–10	6.3	6.89	C(10a)	158.5	160.00
	–	–	–	–	C(*ipso*)	141.0	143.52

[a] 200.1 MHz for ^{1}H (data from Ref. 41) and 67.89 MHz for ^{13}C (data from Ref. 40).
[b] ppm from internal TMS, ambient temperature.
[c] Hz, *ca.* 0.1 Hz estimated standard deviation (esd) of coupling constants unless stated in parenthesis.
[d] Hz, DFT calculated.
[e] ppm, DFT B3LYP/6-311 + g(2d,p) geometry optimization followed by NMR = spin–spin, scaling equation: $\delta(^{13}C)_{calcd} = -0.966765 * \sigma(^{13}C)_{calcd} + 175.37$.

DFT calculated scaled values points to an *equatorial N*-methyl group also in solution. It is apparent that the eight-membered ring of **28** with its stereolabile *equatorial N*-methyl is much more conformationally homogeneous than that of **26** or **27** with its stereostable *equatorial C*-methyl moiety (in which the predominant TCC conformation is in equilibrium with a minor quantity of BB). This difference in conformational behavior may be rationalized in terms of a very strong conformational constraint originating from the interaction between non-bonding electrons on the two adjacent heteroatoms. The *anticlinal* C(1)–O(2)–N(3)–C(4) and C(1)–O(2)–N(3)–$\underline{C}H_3$ torsion angles, result in the nitrogen lone-pair of electrons being *anticlinal* to each one of the two lone-pairs on oxygen. This arrangement affords an optimum minimization of repulsion between non-bonding electron pairs on adjacent atoms.[41] An *axial N*-methyl arrangement on the TCC ring or interconversion of TCC into BB, would force the non-bonding electron pair on nitrogen to be closer to one or both of the lone-pairs on oxygen. When the X-ray crystallographically determined structure of the nine-membered analog (see **29** in Fig. 12)[40] is now analyzed, it is not surprising to find this same strong electronic torsional constraint also affording an *anticlinal* C(1)–O(2)–N(3)–C(4) torsion angle in the (*retro-inverso*,1*S*,3*R*)-Twist–Chair–Boat (TCB) type 1^3 conformation (for the meaning of 'type' see section on nine-membered ring compound **36**).

Using Lambert's[28] equation and the experimentally measured vicinal coupling constants, the N(3)–C(4)–C(5)–O(6) dihedral angle is estimated to be 54°. A value

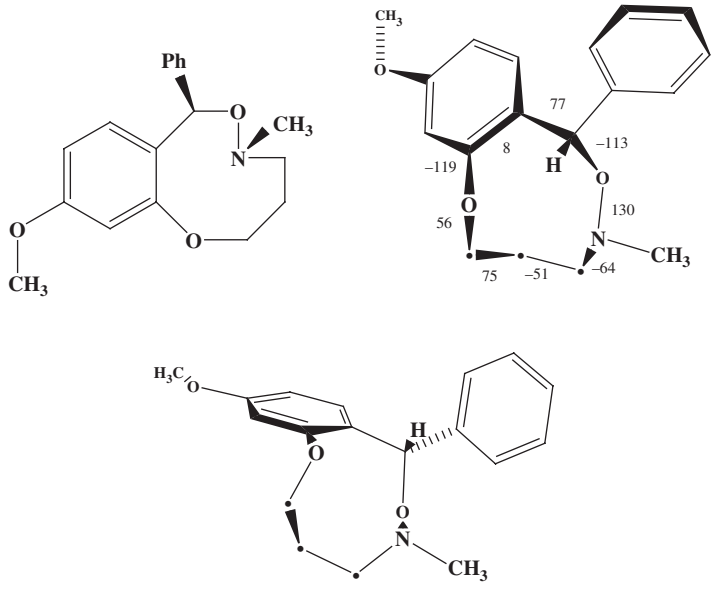

(*retro-inverso*,1*S*,3*R*)-TCBtype1 29

Fig. 12. Crystallographically determined torsion angles (deg) and different orientations of the (*retro-inverso*,1*S*,3*R*)-TCB type 1 conformation for **29**.

of 52° is calculated using the DFT calculated $^3J_{HH}$ values. This angle is 63° and 55° in the X-ray crystallographic and DFT models, respectively.

3.7. 1-Phenyl-3,4,5,6-tetrahydro-1*H*-2,5-benzoxazocine-5-carbonitrile (30)

Compound **30**[42] is a crystalline solid. While it is a known compound, the J_{HH} coupling constants for the $-OCH_2CH_2N-$ fragment were not reported, nor was its stereochemistry investigated. It was remade and crystallized as a racemic compound in an achiral crystal. X-ray crystallography has shown it to have the (*reference*,*S*)-TCC conformation for one of the enantiomers in the crystal (see Fig. 13 for torsion angles in the X-ray structure). The phenyl ring now eclipses the C(1)–C(10a) bond rather than the C(1)–H(1) bond as it does in crystalline nefopam HCl (**15**). Selected ^{1}H- and ^{13}C-NMR ($CDCl_3$), and cp/mas spectral parameters are listed in Table 8. Once again, the 9.7 Hz *antiperiplanar*-type magnitude for ^3J(32–42) enabled us to assign *axial* descriptors for these protons within the $-OCH_2CH_2N-$ fragment. A 4.0% NOE intensity enhancement into the δ 3.81 *axial* H(32) was measured upon

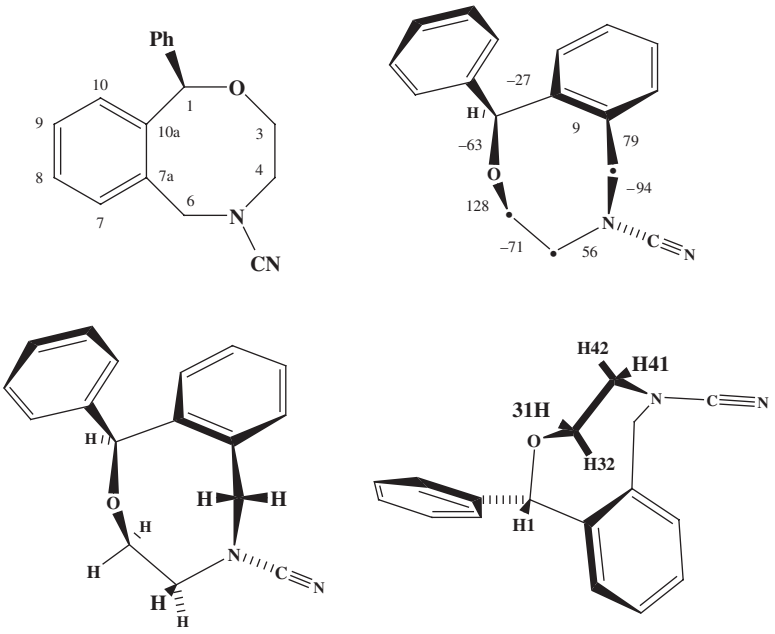

(*reference,S*)-TCC **30**

Fig. 13. Crystallographically determined torsion angles (deg) and different orientations of the (*reference*,*S*)-TCC conformation for 1-phenyl-3,4,5,6-tetrahydro-1*H*-2,5-benzoxazocine-5-carbonitrile (**30**).

Table 8. Selected solution-state ^{1}H- and ^{13}C-NMR ($CDCl_3$) and solid-state cp/mas ^{13}C-NMR spectral parameters for 1-phenyl-3,4,5,6-tetrahydro-1*H*-2,5-benzoxazocine-5-carbonitrile (**30**)[a]

Atom	$\delta(^{1}H)$[b]	H–H	$J_{HHexptl}$[c]	TCC $J_{HHcalcd}$[d]	Atom	$CDCl_3$ $\delta(^{13}C)$[b]	cp/mas $\delta(^{13}C)$[e]
H(1)	5.74	31–32	−12.1	−11.3	C(1)	85.12	83.94
H(31)	4.09	31–41	3.7	2.3	C(3)	68.23	69.61[f]
H(32)	3.81	31–42	2.4	2.1	C(4)	51.53	50.51[f]
H(41)	3.23	32–41	1.9	1.5	C(6)	53.85	50.51[f]
H(42)	3.44	32–42	9.7	9.8	C(7)	133.17[g]	133.77
H(61)	4.97	41–42	−14.5	−14.1	C(8)	128.58[g]	
H(62)	4.12	61–62	−13.8	−13.6	C(9)	129.86[g]	132.41
H(7)	7.27	–	–	–	C(10)	129.13[g]	
H(10)	7.08	–	–	–	C(7a)	133.07[h,i]	137.14[h,i]
	–	–	–	–	C(10a)	139.08[h,i]	137.67[h,i]
	–	–	–	–	C(*ipso*)	141.48[h,i]	142.47[h,i]
	–	–	–	–	C(*ortho*)	127.29	
	–	–	–	–	C(*meta*)	128.58	
	–	–	–	–	C(*para*)	127.94	
	–	–	–	–	CN	117.93	117.73

[a] 500.1 MHz for ^{1}H and 125.76 MHz for ^{13}C.
[b] ppm from internal TMS, ambient temperature.
[c] Hz, *ca.* 0.1 Hz estimated standard deviation (esd).
[d] Hz, DFT calculated.
[e] SELTICS cp/mas, 5.0 kHz spin-rate, ppm using external glycine carbonyl δ 176.03.
[f] Observed in CPPI.
[g] Putative assignment.
[h] Observed in SELTICS-NQS.
[i] Assignment by analogy to (*ref,S*)-TCC conformation DFT scaled $\delta C(7a)_{calcd}$ 136.85, $\delta C(10a)_{calcd}$ 138.26, and $\delta C(ipso)_{calcd}$ 143.87.

{δ 5.74 H(1)}; and a 6.3% NOE intensity increase into δ 5.74 H(1) upon {δ 3.81 H(32)} testifies that the predominant conformation in solution is TCC. Since the 9.7 Hz ^{3}J(32–42) value was larger than the 6.6 and 8.5 Hz values measured for ^{3}J(3–42) in **26** and **27**, respectively, this suggested that the preponderance of the TCC conformational contributor to the conformational equilibrium in solutions of **30** was greater than that for **26** and **27**. Other NOE experiments defined the ^{1}H termini of the benzo ring: a 5.1% NOE intensity enhancement into the δ 7.09 H(terminal benzo) was measured upon {δ5.74 H(1)}; and a *ca.* 3% NOE intensity increase was noted into δ 7.27 H(terminal benzo) upon {δ 4.12 *exo* H(62)}. This enabled them be assigned as H(10) and H(7), respectively. The finding of δ H(7) > δH(10) had also been found for the quaternary (**19**) and secondary (**23**) nefopam analogs.

The similarity of solid-state cp/mas ^{13}C chemical shifts for **30** and the DFT $J_{HHcalcd}$ coupling constants compared to corresponding values measured in the

relevant solution-state spectra was consistent with the presence of a TCC conformation in solution with little, if any, contribution from a second conformational partner. Using Lambert's equation, the O–C–C–N dihedral angle in solution is calculated to be 63° [$J_{HHexptl}$] versus 64° [$J_{HHcalcd}$], 71° [X-ray], and 69° [DFT-model].

3.8. 1-Phenyl-3,4,5,6-tetrahydro-1*H*-2,5-benzothiazocine-5-carbonitrile (31,32)

Replacement of the oxygen ring atom in **30** by sulfur affords a thia-analog with two different solid-state conformations (see **31**,**32** in Figs. 14 and 15). X-ray crystallography of the crystals showed spontaneous resolution had occurred in which the conglomerate of enantiomorphic chiral crystals contained two symmetry independent molecules of identical configuration in the asymmetric unit of each chiral crystal.[1] This is similar to the case for the chiral crystals of **27**, but now there are two different conformations instead of only one. One of the chiral crystals showed both

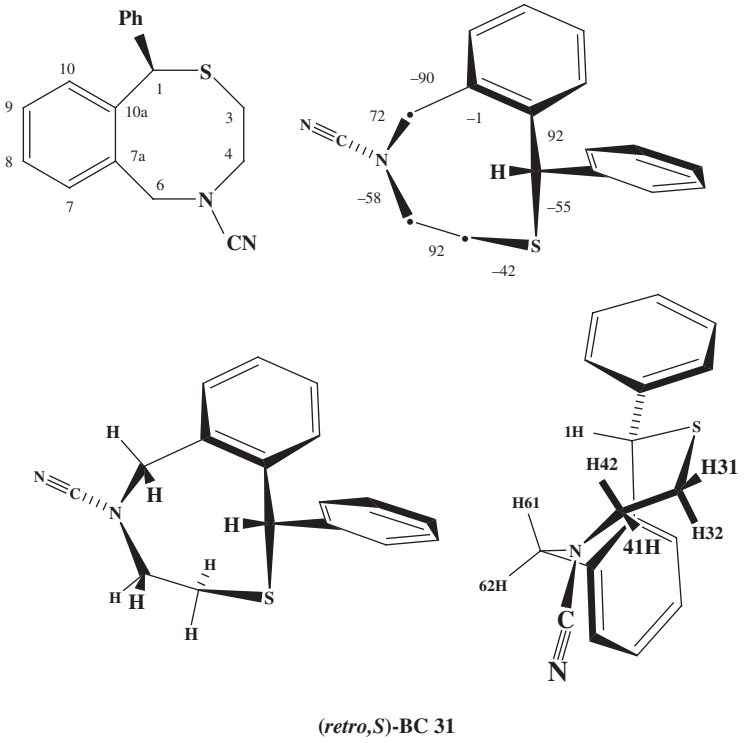

(*retro,S*)-BC **31**

Fig. 14. Crystallographically determined torsion angles (deg) and different orientations of the (*retro*,*S*)-BC conformation (**31**) for 1-phenyl-3,4,5,6-tetrahydro-1*H*-2,5-benzothiazocine-5-carbonitrile.

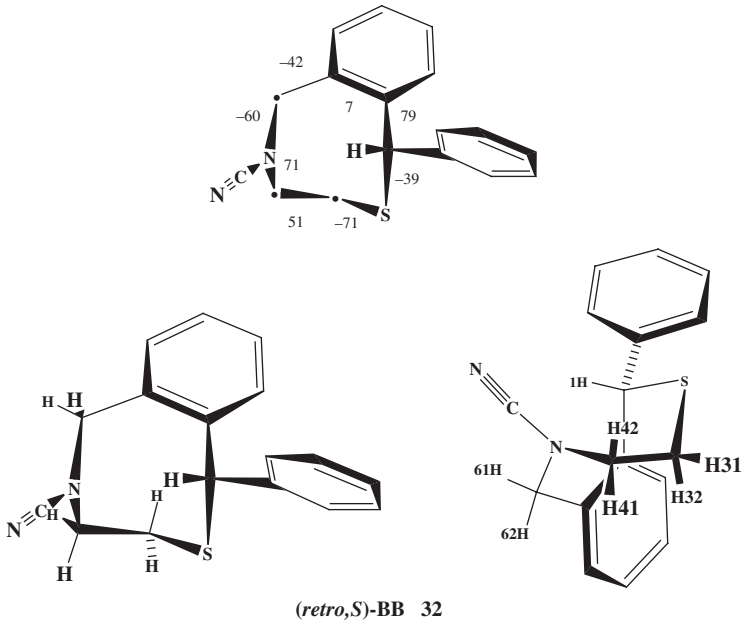

(*retro,S*)-BB 32

Fig. 15. Crystallographically determined torsion angles (deg) and different orientations of the (*retro*,*S*)-BB conformation for 1-phenyl-3,4,5,6-tetrahydro-1*H*-2,5-benzothiazocine-5-carbonitrile (**32**).

the (*retro*,*S*)-BC (**31**) and the (*retro*,*S*)-BB (**32**) conformations. The phenyl ring was *equatorially* disposed in both conformations. Compare the endocyclic torsion angles given in the iconic structures of (*reference*,*S*)-BB (**15**) and (*retro*,*S*)-BB (**32**). Corresponding torsion angles for **15** (see Fig. 3) are similar in respective signs and magnitudes to those for **32** (see Fig. 15), and thus the chirality of the two rings is the same. The orientation of iconic structures **15** and **32** is also the same, but the tropicity from phenyl to benzo is clockwise in **15** and counterclockwise in **32**. Therefore, **32** is assigned the (*retro*,*S*)-BB descriptor, while that for **32** is (*reference*,*S*)-BB.[1] The (*retro*,*S*)-BC (**31**) and (*retro*,*S*)-BB (**32**) conformations are related by a flip of N(5) from one side of the mean plane to the other.[1] There is crystallographic precedence for this type of atom flip interconversion mode.[1] As a result, the 1,3-type *cis-diaxial* relationship between H(42) and H(61) in **15**, becomes a 1,3-type *cis-diequatorial* one in **32**, while the reverse happens to the H(41) and H(62) protons.[1]

Selected solution-state ^{1}H- and ^{13}C-NMR, and solid-state cp/mas ^{13}C parameters have been listed in Table 9. It is seen that some of the aliphatic carbons (and some of the aromatic also, not listed) gave double signals in the cp/mas spectrum. H(31) was assigned as *trans* to H(41) (they are on opposite faces of the ring), and H(32) was assigned as *trans* to H(42) on the basis of the magnitudes of their respective 6.4 Hz ^{3}J(31–41) and 8.6 Hz ^{3}J(32–42) values. In addition, a 6.9% NOE intensity

Table 9. Selected solution-state ^{1}H- and ^{13}C-NMR ($CDCl_3$) and solid-state cp/mas ^{13}C-NMR spectral parameters for 1-phenyl-3,4,5,6-tetrahydro-1*H*-2,5-benzothiazocine-5-carbonitrile (**31**,**32**)[a]

Atom	$\delta(^{1}H)$[b]	H–H	$J_{HHexptl}$[c]	[BC : BB = 60 : 40] $J_{HHcalcd}$[d]	BC $J_{HHcalcd}$[d]	BB $J_{HHcalcd}$[d]
H(1)	5.83	31–32	−15.9	[−15.2]	−15.37	−14.85
H(31)	2.75	31–41	6.4	[6.0]	9.40	0.83
H(32)	2.38	31–42	3.2	[3.2]	1.01	6.40
H(41)	3.70	32–41	2.8	[2.4]	0.74	4.90
H(42)	3.51	32–42	8.6	[8.3]	6.09	11.57
H(61)	4.34	41–42	−14.8	[−14.6]	−15.51	−13.17
H(62)	4.63	61–62	−14.7	[−14.7]	−14.55	−14.89

Atom	$CDCl_3$ $\delta(^{13}C)$[b]	cp/mas $\delta(^{13}C)$[e]
C(1)	47.8	45.84, 49.28
C(3)	30.2	29.34[f]
C(4)	54.5	57.47, 56.56[f,g]
C(6)	53.6	50.30[g,h]
CN	117.93	–
C(*ipso*)	–	139.83[i]

[a] 500.1 MHz for ^{1}H and 125.76 MHz for ^{13}C.
[b] ppm from internal TMS, ambient temperature.
[c] Hz, *ca.* 0.1 Hz estimated standard deviation (esd) of coupling constants.
[d] Hz, DFT calculated, 60 : 40 weighted average of BC : BB values given in square brackets.
[e] SELTICS cp/mas, 5.0 kHz spin-rate, ppm using external glycine carbonyl δ 176.03.
[f] Observed in CPPI.
[g] Assignments may be interchanged.
[h] *Ca.* double-intensity.
[i] Observed in SELTICS-NQS.

increase in δ 4.63 H(61) was measured upon {δ 5.83 H(1)}, an 8.1% intensity enhancement in δ 5.83 H(1) was measured upon {δ 4.63 H(61)}, and a 1.5% intensity enhancement in δ 5.83 H(1) was measured upon {δ 3.51 H(42)} showing that H(1), H(42), and H(61) were all located on the same face of the ring. In the X-ray determined structure of (*retro*,*S*)-BC (**31**), H(61) and H(42) are 1.95 and 2.82 Å, respectively away from H(1).

For the other face of the ring, a 5.8% intensity enhancement in δ 3.70 H(41) was measured upon {δ 4.34 H(62)}, and a 4.9% intensity enhancement in δ 4.34 H(62) was measured upon {δ 3.70 H(41)} which is compatible with the 1,3-type *cis-diaxial* relationship between H(41) and H(62) found in (*retro*,*S*)-BB (**32**). These NOE results can be reconciled by proposing a conformational equilibrium between **31** and **32** in solution. Coupling constants were calculated by DFT B3LYP/6-311 + g(2d,p) geometry optimization of both conformations followed by the NMR = spin–spin calculation. Inspection of Table 9 shows that a *ca.* 3 : 2 mixture of BC : BB afforded

a reasonably good weighted average fit between the calculated values versus the experimental ones.

3.9. (1*RS*,3*SR*)-1-phenyl-3,4,5,6-tetrahydro-3,5,5-trimethyl-1*H*-2,5-benzoxazocinium chloride [(1*RS*,3*SR*)-3-methyl-nefopam methochloride] (33)

The racemic quaternary ammonium salt crystallized in two conformational pseudopolymorphic forms. They are pseudopolymorphs (and not true polymorphs) since their molecular composition is different (one was an anhydrate (**33**) while the other was a dihydrate (**34**)).[1] The torsion angles are given in Figs. 16 and 17 for the respective X-ray structures. Crystallization of the racemic mixture via acetone diffusion into an ethanolic solution of the salt afforded spontaneous resolution yielding a conglomerate of anhydrate chiral crystals (**33**).[1] The molecular conformation in one of the chiral crystals was (*reference*,1*S*,3*R*)-TCC. Evaporation of the racemic mixture afforded achiral crystals containing a racemic compound in the form of a dihydrate and exhibiting another conformation: (*retro-inverso*,1*S*,3*R*)-BC illustrated as (**34**). The dihydrate crystals have two molecules in the asymmetric unit. In this

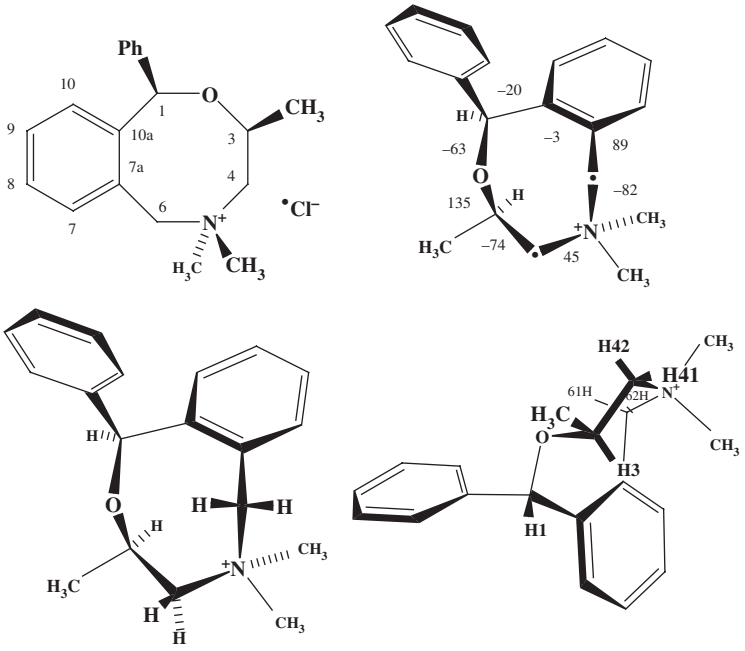

(*reference*,1*S*,3*R*)-TCC **33**

Fig. 16. Crystallographically determined torsion angles (deg) and different orientations of the (*retro*,1*S*,3*R*)-TCC conformation (**33**) for (1*RS*,3*SR*)-3-methyl-nefopam methochloride.

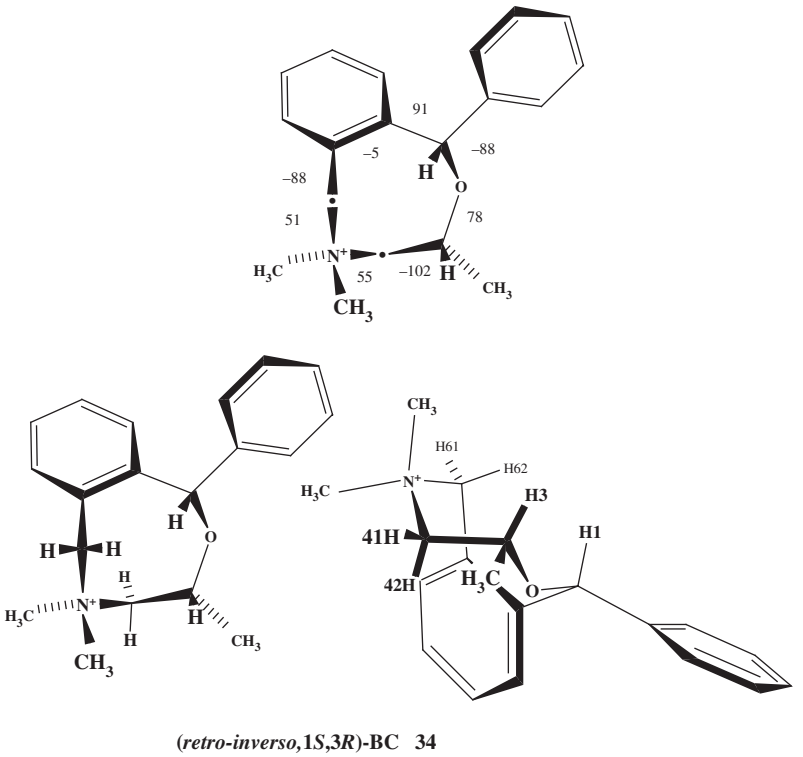

(*retro-inverso*,1*S*,3*R*)-BC 34

Fig. 17. Crystallographically determined torsion angles (deg) and different orientations of the (*retro-inverso*,1*S*,3*R*)-BC conformation (**34**) for (1*RS*,3*SR*)-3-methyl-nefopam methochloride.

conformation, the phenyl and *C*-methyl groups both reside at non-corner positions and are each *equatorial*, while the two *N*-methyl groups are located at a corner position and are approximately *isoclinal*.

Selected ^{1}H and ^{13}C solution-state ($CDCl_3$), and solid-state cp/mas ^{13}C-NMR parameters for the quaternary ammonium salt are listed in Table 10. The termini of the benzo fragment were differentiated by the finding of a 6.8% intensity increase into δ 4.77 H(62) *exo* upon {δ 8.12 H(7)}. The two *N*-methyl groups were differentiated by the observance of a 7.1% intensity increment into δ 4.16 H(3) *axial* upon {δ 3.35 NC$\underline{H}_3$ *axial*}. The lists of solid-state ^{13}C chemical shifts of the two pseudopolymorphs are seen to be different (especially those for C(1)). The C(1)–O(2)–C(3)–C(4) dihedral angle was 135° and 78° in crystalline (*reference*,1*S*,3*R*)-TCC (**33**) and (*retro-inverso*,1*S*,3*R*)-BC (**34**), respectively. Thus, also in this case, the cp/mas chemical shifts of δ 84.34 (for **33**) and δ 76.87 (for **34**) can be easily rationalized in terms of a *gamma-gauche* effect.

In the (*reference*,1*S*,3*R*)-TCC (**33**) conformation X-ray structure, H(3) is *synclinal* to H(41) and *antiperiplanar* to H(42). On the other hand, H(3) is *orthogonal* to H(41)

Table 10. Selected solution-state ^{1}H- and ^{13}C-NMR ($CDCl_3$), and solid-state cp/mas ^{13}C-NMR spectral parameters for (1*RS*,3*SR*)-3-methyl-nefopam methochloride (**33**)[a]

Atom	$\delta(^{1}H)$[b]	Atom	$CDCl_3$ $\delta(^{13}C)$[b]	Anhydrate (*ref,S*)-TCC cp/mas $\delta(^{13}C)$[b,c]	Dihydrate (*ret-inv,S*)-BC cp/mas $\delta(^{13}C)$[b,c]
H(1)	5.88	C(1)	83.97	84.34	76.87
H(3)	4.16	C(3)	68.19	68.49	71.11
H(41)	3.86	C(4)	71.00	71.23[d,e]	69.29[d,f]
H(42)	3.46	C(6)	66.64	65.81[d,e]	62.69[d,f]
H(61)	5.55	$C\underline{C}H_3$	19.73	19.71[g]	22.79[g]
H(62)	4.77	$N\underline{C}H_{3ax}$	50.79	49.81[g]	52.37[g]
$CC\underline{H}_3$	1.45	$N\underline{C}H_{3eq}$	57.57	56.55[g]	52.37[g]
$NC\underline{H}_{3ax}$	3.35	C(7)	137.66	139.66[h]	135.65[h]
$NC\underline{H}_{3eq}$	3.84	C(8)	129.03	–	–
H(7)	8.12	C(9)	131.40	134.58[h]	–
H(8)	7.48	C(10)	129.89	–	–
H(9)	7.48	C(7a)	125.55[e]	125.81[e,g,h]	129.80[f,g,h]
H(10)	7.24	C(10a)	141.22[e]	144.12[e,g,h]	145.66[f,g,h]
H(*ortho*)	7.11	C(*ipso*)	139.92[e]	141.77[e,g,h]	141.85[f,g,h]
H(*meta*)	7.31	C(*ortho*)	127.50		
H(*para*)	7.31	C(*meta*)	128.82		
	–	C(*para*)	128.59		

HH	$J_{HHexptl}$[i]	(*ref,S*)-TCC $J_{HHcalcd}$[j]	(*ret-inv,S*)-BC $J_{HHcalcd}$[j]
3-$C\underline{H}_3$	6.5	5.96	6.26
3–41	–	0.93	0.43
3–42	8.6(4)	8.89	4.35
41–42	−13.4	−12.78	−13.86
61–62	−12.5	−12.16	−12.84
7–8	6.9	6.94	6.81
9–10	6.9	7.06	7.25
Ortho–meta	6.6	7.02	7.04

[a] 500.1 MHz for ^{1}H and 125.76 MHz for ^{13}C, H(1) $W_{1/2} = 4.75$ Hz preliminary results in $CDCl_3$, 298 K [will be repeated at low temperature].
[b] ppm from internal TMS.
[c] SELTICS cp/mas, 5.0 kHz spin-rate, ppm using external glycine carbonyl δ 176.03.
[d] Observed in CPPI.
[e] Assignment by analogy to (*ref,S*)-TCC conformation DFT scaled $\delta C(4)_{calcd}$ 72.68, $\delta C(6)_{calcd}$ 70.30, $\delta C(7a)_{calcd}$ 123.31, $\delta C(10a)_{calcd}$ 143.70, and $\delta C(ipso)_{calcd}$ 138.02.
[f] Assignment by analogy to (*retro-inverso,S*)-BC conformation DFT $\delta C(4)_{calcd}$ 72.23, $\delta C(6)_{calcd}$ 65.95, $\delta C(7a)_{calcd}$ 121.86, $\delta C(10a)_{calcd}$ 146.13, and $\delta C(ipso)_{calcd}$ 136.24.
[g] Observed in SELTICS-NQS.
[h] Putative assignment.
[i] Hz, *ca.* 0.1 Hz estimated standard deviation (esd) of coupling constants unless stated in parenthesis.
[j] Hz, DFT calculated.

and *anticlinal* (143°) to H(42) in the (*retro-inverso*,1*S*,3*R*)-BC (**34**) X-ray structure. The line-width of the signals from the C(4) geminal protons resulted in the measurement of only one of the two vicinal coupling constants. Its 8.6(4) Hz value suggests that it is the $^{3}J(3\text{–}42)_{\text{exptl}}$ value. This value was in agreement with the DFT 8.9 Hz $^{3}J(3\text{–}42)_{\text{calcd}}$ value for the (*reference*,1*S*,3*R*)-TCC conformational model, while it differed from the 4.4 Hz value calculated for the (*retro-inverso*,1*S*,3*R*)-BC model. A 3.8% intensity increase into δ 4.16 H(3) *axial* was found upon {δ 5.88 H(1)}, and a 7.0% intensity increment into δ 5.88 H(1) upon {δ 4.16 H(3) *axial*}. Unfortunately, the observation of NOE intensity enhancements between H(1) and H(3) can fit either model. However, there is a good match when one compares the solution-state ^{13}C chemical shifts with corresponding values from the cp/mas ^{13}C spectrum of crystalline (*reference*,1*S*,3*R*)-TCC. On the other hand, the C(1) cp/mas chemical shift from the (*retro-inverso*,1*S*,3*R*)-BC dihydrate pseudopolymorphic crystal exhibited a marked *gamma-gauche* effect. The RMS in the list of seven aliphatic ^{13}C chemical shifts in the solution-state spectrum versus those in the solid-state (*reference*,1*S*,3*R*)-TCC or (*retro-inverso*,1*S*,3*R*)-BC cp/mas spectra is 0.65 and 3.78 ppm, respectively. This strongly suggests that the (*reference*,1*S*,3*R*)-TCC

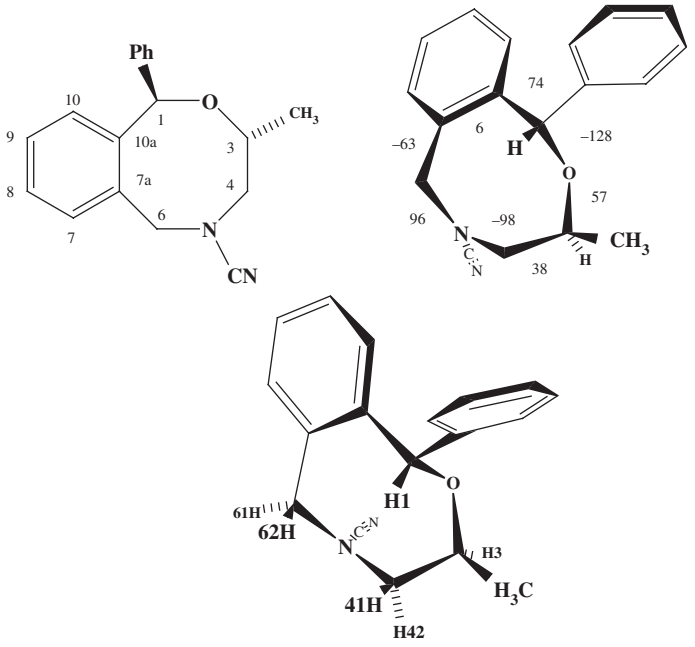

(*retro-inverso*,1*S*,3*S*)-TBC **35**

Fig. 18. Crystallographically determined torsion angles (deg) and different orientations of the (*retro*,1*S*,3*S*)-TBC conformation for (1*RS*,3*RS*)-3-methyl-1-phenyl-3,4,5,6-tetrahydro-1*H*-2,5-benzoxazocine-5-carbonitrile (**35**).

conformation predominated in $CDCl_3$ solution when either of these two crystals was dissolved.

3.10. (1*RS*,3*RS*)-3-Methyl-1-phenyl-3,4,5,6-tetrahydro-1*H*-2,5-benzoxazocine-5-carbonitrile (35)

Racemic (1*RS*,3*RS*)-3-methyl-1-phenyl-3,4,5,6-tetrahydro-1*H*-2,5-benzoxazocine-5-carbonitrile (**35**) crystallized as a racemic compound in an achiral space group.[1] X-ray structure analysis showed that one of the enantiomers in the crystal was bent into the (*retro*,*S*)-TBC conformation (for torsion angles of the X-ray structure, see Fig. 18).[1] TBC is a relatively rare *cis*-cyclooctene conformation, and is the fourth and highest energy conformation for *cis*-cyclooctene within an energy window of 33.4 kJ from the ground state.[1] Selected ^{1}H and ^{13}C solution-state and ^{13}C cp/mas

Table 11. Selected solution-state ^{1}H- and ^{13}C-NMR ($CDCl_3$), and solid-state cp/mas ^{13}C-NMR spectral parameters for (1*RS*,3*RS*)-3-methyl-1-phenyl-3,4,5,6-tetrahydro-1*H*-2,5-benzoxazocine-5-carbonitrile (**35**)[a]

Atom	$\delta(^1H)^b$	H–H	$J_{HHexptl}{}^c$	TBC $J_{HHcalcd}{}^j$	Atom	$CDCl_3$ $\delta(^{13}C)^b$	cp/mas $\delta(^{13}C)^d$
H(1)	6.03	3-C$\underline{H}_3$	6.5	5.98	C(1)	76.73	73.44
H(3)	4.20	3–41	9.3	9.88	C(3)	72.42	71.07
H(41)	3.17_4	3–42	2.9	5.46	C(4)	54.54[e]	57.34[g,f]
H(42)	3.15_7	41–22	–15.1	–14.99	C(6)	54.64[e]	53.45[g,f]
H(61)	4.88	61–62	–13.2	–14.96	C$\underline{C}$H$_3$	18.05	17.40
H(62)	4.52	–	–	–	$\underline{C}$(7)	132.13	132.48[g,f]
CC$\underline{H}_3$	1.18	–	–	–	C(8)	128.61	
	–	–	–	–	C(9)	129.18	139.66[g]
	–	–	–	–	C(10)	129.18	
	–	–	–	–	C(7a)	132.63	138.44[h]
	–	–	–	–	C(10a)	141.37[g]	143.31[g,h]
	–	–	–	–	C(*ipso*)	140.66[g]	140.61[g,h]
	–	–	–	–	C(*ortho*)	127.66	
	–	–	–	–	C(*meta*)	128.48	
	–	–	–	–	C(*para*)	127.91	
	–	–	–	–	CN	118.15	117.24

[a] 500.1 MHz for ^{1}H and 125.76 MHz for ^{13}C, $CDCl_3$, 298 K, aliphatic region simulated by *gNMR* program (36).
[b] ppm from internal TMS.
[c] Hz, *ca.* 0.1 Hz estimated standard deviation (esd), unless stated otherwise.
[d] SELTICS cp/mas, 5.0 kHz spin-rate, ppm using external glycine carbonyl δ 176.03.
[e] Assignment may be reversed.
[f] Observed in CPPI.
[g] Assignment may be reversed.
[h] Observed in SELTICS-NQS.

spectral parameters are given in Table 11. The geminal protons on C(4) were very strongly coupled ($\Delta\upsilon = 8.5$ Hz) in the 500 MHz ^{1}H-NMR spectrum, and necessitated spectral simulation using *gNMR*.[36] As a result of the simulation, the ^3J(3–41) and ^3J(3–42) coupling constants were calculated to be 9.3 and 2.9 Hz, respectively. The magnitudes of these parameters were consistent with 161° and 44° dihedral angles involving the respective pairs of vicinal protons in the X-ray model. However, NOE experiments were not conclusive, putatively due to the second order nature of the spectrum. Both the δ 76.73 solution-state and δ 73.44 cp/mas δ C(1) chemical shifts were consistent with a *gamma-gauche* effect expected for the 57° C(1)–O(2)–C(3)–C(4) and 70° C(1)–O(2)–C(3)–$\underline{C}H_3$ *synclinal* dihedral angles measured in the crystalline structure. The similarity between solution-state ($CDCl_3$) and cp/mas ^{13}C chemical shifts suggests that the solution-state structure is predominantly the (*retro*,*S*)-TBC conformation.

4. REPRESENTATIVE EXAMPLES OF NMR STUDIES ON 2,6-BENZOXAZONINE MEDIUM RING STEREOCHEMISTRY

4.1. 1-Phenyl-1,3,4,5,6,7-hexahydro-2,6-benzoxazonine hydrochloride [*N*-desmethyl-2,6-homonefopam hydrochloride] (36)

Nine-membered ring analogs of nefopam have also been studied as part of this project. Stereochemical investigations of these larger rings are more of a challenge due to the greater number of conformational possibilities available for consideration. On the other hand, there are now a larger number of vicinal coupling constants providing structural information. The first nine-membered ring to be discussed in this section is a secondary ammonium salt, *N*-desmethyl-2,6-homonefopam hydrochloride (**36**). Since the trivial name 'homonefopam' is not specific, e.g. it can refer to either a 2,5-benzoxazonine (two methylenes between the oxygen and nitrogen) or a 2,6-benzoxazonine skeleton (three methylenes between the oxygen and nitrogen), these two examples of constitutional isomers can be referred to as 2,5- or 2,6-homonefopam. Secondary ammonium salts, such as **36**, are advantageous for stereochemical studies since vicinal coupling constants involving the two N–H protons enable Lambert's equation to be used to estimate the dihedral angle for each of the two endocyclic bonds involving nitrogen (i.e. CH_2–$^+NH_2$–CH_2).

The racemic mixture of **36** crystallized as a racemic compound in an achiral space group crystal. Analysis of its X-ray crystallographically determined structure shows one of the enantiomers to have a (*reference*,*S*)-TCBtype3[3] conformation as depicted in the iconic drawing for **36** (see Fig. 19). Conformational families exist for *cis*-[3] or *trans*-[44] cyclononenes. The various members of a family maintain similar torsion angles for six of the nine bonds compared to those measured for their cyclononane saturated parent.[3] Double bonds are formed from either *synclinal* or *antiperiplanar*-type bonds in the parent. Conversion of a single bond to a double bond will usually

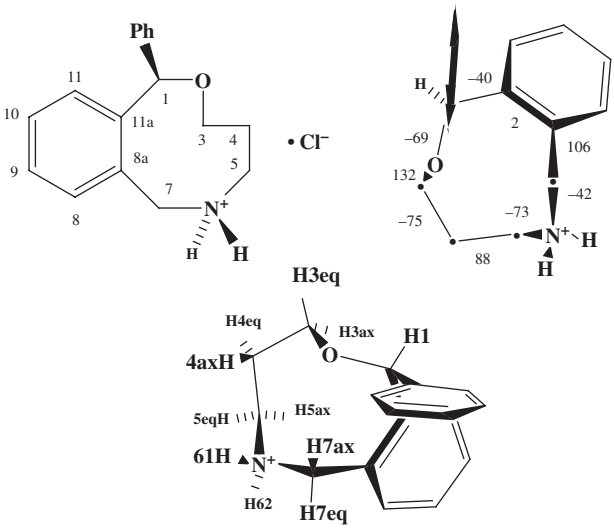

(*reference,S*)-TCBtype3 36

Fig. 19. Crystallographically determined torsion angles (deg) and different orientations of the (*reference*,*S*)-TCB type 3 conformation for *N*-desmethyl-2,6-homonefopam hydrochloride (**36**).

remove at least one transannular interaction. Bonds adjacent to either side of the double bond keep their signs, but change their magnitudes vis-à-vis corresponding torsion angles in the parent. Thus, a double bond can be placed at a number of positions on a medium ring, and still maintain a conformation very similar to that of its saturated parent. For example, any one of the four different *synclinal* torsion angles in the TCB conformation of cyclononane can be converted to a *synperiplanar* value to yield one of four different *cis*-cyclononene conformations (each having a different set of six endocyclic torsion angles that are similar to those of the parent). To differentiate between them, they were described as 'TCBtypes1–4', where 'type1' was the lowest calculated energy member in the series.[3] In most cases, the energy ranking order remained the same independent of the computational method that was chosen.[3]

Both C(1) (the benzhydrylic carbon) and N(6) resided at corner positions on the TCBtype3 nine-membered ring. Since the geminal protons on N(6) are *isoclinal*, they were only assigned as H(61) and H(62) without appending *axial* or *equatorial* descriptors. On the other hand, the geminal pairs on C(3),C(4),C(5), and C(7) may all be assigned their appropriate *axial* and *equatorial* descriptors according to Anet's[15] method.

Table 12 lists the solution-state (CD_2Cl_2) ^1H and ^{13}C selected spectral parameters, the solid-state ^{13}C cp/mas chemical shifts, as well as the scaled DFT $\delta(^{13}C)_{calcd}$ and $J_{HHcalcd}$ calculated values. The TCBtype3 $\delta(^{13}C)_{calcd}$ and cp/mas

$\delta(^{13}C)_{exptl}$ values are in very good agreement with corresponding values measured in the solution-state spectrum. This strongly suggests a predominant TCBtype3 conformation also for the solution-state. This is further strengthened by the good agreement between all the TCBtype3 $J_{HHcalcd}$ DFT calculated values versus those from experiment. For example, the TCBtype3 conformation for **36** may be characterized by four *antiperiplanar* magnitude $J_{HHexptl}$ coupling constants: (Hz) 10.1 ^3J(3ax–4ax), 10.0 ^3J(4ax–5ax), 9.2 ^3J(5ax–61ax), and 8.7 ^3J(62ax–7ax) which are all similar to their $J_{HHcalcd}$ DFT calculated counterparts: (Hz) 10.8 ^3J(3ax–4ax), 10.5 ^3J(4ax–5ax), 10.2 ^3J(5ax–61ax), and 7.1 ^3J(62ax–7ax). The TCBtype3 conformation is defined in part by four characteristic adjacent *synclinal* endocyclic dihedral angles involving bonds from C(3) to C(7). Table 12 also shows that these four *synclinal* dihedral angles calculated by Lambert's[28] equation using the $J_{HHexptl}$

Table 12. Selected solution-state ^{1}H- and ^{13}C-NMR (CD_2Cl_2), and solid-state cp/mas ^{13}C-NMR spectral parameters for *N*-desmethyl-2,6-homonefopam hydrochloride (**36**)[a]

Atom	$\delta(^1H)^b$	Atom	CD_2Cl_2 $\delta(^{13}C)^b$	cp/mas $\delta(^{13}C)^c$	TCBtype3 $\delta(^{13}C)_{calcd}{}^d$
H(1)	5.71	C(1)	83.98	83.41	86.58
H(3ax)	3.47	C(3)	68.60	67.20[e]	65.49
H(3eq)	4.20	C(4)	26.80	28.42[e]	31.69
H(4ax)	2.22	C(5)	44.21	40.29[e,f]	47.66
H(4eq)	1.94	C(7)	45.77	43.84[e,f]	55.23
H(5ax)	2.59	C(8)	133.96	–	132.21
H(5eq)	3.40	C(9)	129.47	–	131.03
H(61)	9.15	C(10)	129.63	–	133.42
H(62)	10.33	C(11)	130.54	–	132.97
H(7ax)	4.79	C(8a)	130.24	128.77[g,h]	127.03
H(7eq)	4.14	C(11a)	141.93	145.23[g,h]	145.57
H(8)	7.78	C(*ipso*)	140.56	141.99[g,h]	138.10
H(9)	7.43	C(*ortho*)	127.03		
H(10)	7.40	C(*meta*)	128.62		
H(11)	7.19	C(*para*)	127.93		

H–H	$J_{HHexptl}{}^i$	TCBtype3 $J_{HHcalcd}{}^j$	Dihedral angle	$\theta_{exptl}{}^k$	$\theta_{calcd}{}^l$	$\theta_{X\text{-}ray}{}^m$	$\theta_{DFT}{}^n$
3ax–3eq	–11.6	–11.41	O(2)–C(3)–C(4)–C(5)	62°	58°	75°	67°
3ax–4ax	10.1	10.79	C(3)–C(4)–C(5)–N(6)	72°	74°	88°	81°
3ax–4eq	2.0	2.05	C(4)–C(5)–N(6)–C(7)	72°	75°	73°	80°
3eq–4ax	3.0	3.76	C(5)–N(6)–C(7)–C(8a)	44°	34°	42°	32°
3eq–4eq	4.5	2.11					
3eq–5eq	0.5	0.60					
4ax–4eq	–16.4	–16.26					
4ax–5ax	10.0	10.46					
4ax–5eq	2.1	1.18					
4eq–5ax	<1	0.70					

(*continued*)

Table 12. Continued

H–H	$J_{HHexptl}$[i]	TCBtype3 $J_{HHcalcd}$[j]	Dihedral angle	θ_{exptl}[k]	θ_{calcd}[l]	$\theta_{X\text{-}ray}$[m]	θ_{DFT}[n]
4eq–5eq	6	6.27					
5ax–5eq	–12.8	–13.77					
5ax–61	9.2	10.19					
5ax–62	<1	0.74					
5eq–61	2	0.75					
5eq–62	6	5.60					
61–7ax	5.0	5.96					
61–7eq	1.2	0.26					
62–7ax	8.7	7.08					
62–7eq	5.6	6.56					
7ax–7eq	–12.9	–11.82					
8–9	7.4	6.78					
8–10	1.5	0.80					
9–10	7.4	6.74					
9–11	1.6	0.85					
10–11	7.1	6.88					

[a] 500.1 MHz for ^{1}H and 125.76 MHz for ^{13}C, CD_2Cl_2, 298 K, aliphatic region simulated by *gNMR* program (Ref. 36).
[b] ppm from internal TMS.
[c] SELTICS cp/mas, 5.0 kHz spin-rate, ppm using external glycine carbonyl δ 176.03.
[d] DFT B3LYP/6-311 + g(2d,p) geometry optimization followed by NMR = spin–spin, scaling equation: $\delta(^{13}C)_{calcd} = -0.966765 * \sigma(^{13}C)_{calcd} + 175.37$.
[e] Observed in CPPI.
[f] Assignment may be reversed.
[g] Observed in SELTICS-NQS.
[h] Assigned by analogy to DFT values.
[i] Hz, *ca.* 0.1 Hz estimated standard deviation (esd), unless value is a whole integer.
[j] DFT calculation for TCBtype3 conformation.
[k] Lambert's equation using $J_{HHexptl}$ values.
[l] Lambert's equation using DFT $J_{HHcalcd}$ values.
[m] Value from X-ray crystallographically determined structure.
[n] Value from DFT calculated model for TCBtype 3 conformation.

values compare quite favorably with those calculated from the DFT $J_{HHcalcd}$ values, or measured from the X-ray structure, or the DFT model.

Finally, NOE experiments are also consistent with a predominant (*reference*,*S*)-TCBtype3 solution-state conformation. 1,3-Type *cis-diaxial* arrangements were seen by a 2.4% intensity increase into δ 3.47 H(3ax) upon {δ .59 H(5ax)} on one face of the ring, and also a 2.6% intensity increment into δ 2.22 H(4ax) upon {δ 9.2 H(61)} on the other face. The H(8) terminus of the benzo proton spin-system was assigned by a 2.1% intensity increase into δ 4.14 H(7eq) upon {δ 7.78 H(8)}. In the (*reference*,*S*)-TCBtype3 conformation, H(3ax) is closer than H(3eq) to H(1). This is consistent with a 4.2% intensity increment into δ 3.47 H(3ax) upon {δ 5.71 H(1)}. The (*reference*,*S*)-TCBtype3 conformation of **36** contains a 'W'-type coplanar H(3eq)–C(3)–C(4)–C(5)–H(5eq) arrangement as evidenced by an RMS deviation of

the five atoms from the mean plane of only 0.154 Å (X-ray structure) and 0.098 Å (DFT-model), respectively. The coplanarity of this fragment was maintained in solution, as evidenced by measurement of a long-range 0.5 Hz ^4J(3eq–5eq) coupling constant. In summary, the solid-state (*reference*,*S*)-TCBtype3 conformation of **36** is maintained upon dissolving the crystals in CD_2Cl_2.

4.2. (1*RS*,3*SR*)-3-Methyl-1-phenyl-1,3,4,5,6,7-hexahydro-2,6-benzoxazonine hydrobromide [(1*RS*,3*SR*)-*N*-desmethyl-3-methyl-2,6-homonefopam hydrobromide] (37)

^{1}H-NMR analysis of the crude reaction product showed that synthesis of 3-methyl-1-phenyl-1,3,4,5,6,7-hexahydro-2,6-benzoxazonine hydrobromide (**37**) afforded only the (1*RS*,3*SR*)-diastereomer and not the expected mixture with a (1*RS*,3*RS*)-component in spite of the fact that there are two stereogenic chirotopic carbon atoms C(1) and C(3) in the structure. The racemic mixture of **37** crystallized as a racemic compound in an achiral space group crystal. Analysis of its X-ray crystallographically determined structure showed one of its enantiomers to have a (*reference*,*S*)-TCBtype3[3] conformation as depicted in the iconic drawing for **37** (see Fig. 20). Selected ^{1}H- and ^{13}C-NMR spectral parameters are reported in Table 13. Perusal of

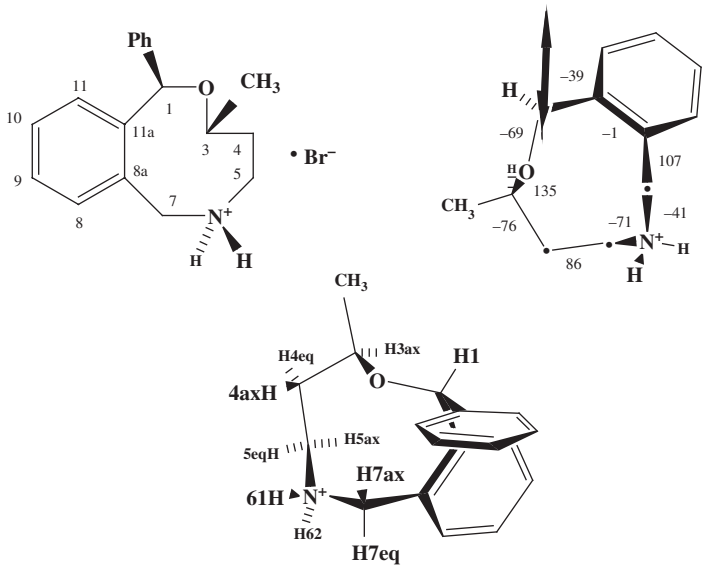

(*reference*,1*S*,3*R*)-TCBtype3 **37**

Fig. 20. Crystallographically determined torsion angles (deg) and different orientations of the (*reference*,1*S*,3*R*)-TCB type 3 conformation for (1*RS*,3*SR*)-*N*-desmethyl-3-methyl-2,6-homonefopam hydrobromide (**37**).

the coupling constants and chemical shift values shows strong similarities to those of the unsubstituted parent compound [(*reference*,*S*)-TCBtype3 for the (1*S*)-enantiomer of **36**]. Specifically, the measurement of four *antiperiplanar* value coupling constants: two involving H(4ax) and its vicinal neighbors on either side, and two involving each of the geminal protons on atom number 6 [H(61) and H(62)] and vicinal neighbors on either side are characteristic of the TCBtype3 conformation

Table 13. Selected solution-state ^{1}H- and ^{13}C-NMR (CD_2Cl_2), and solid-state cp/mas ^{13}C-NMR spectral parameters for (1*RS*,3*SR*)-*N*-desmethyl-3-methyl-2,6-homonefopam hydrobromide (**37**)[a]

Atom	$\delta(^{1}H)$[b]	Atom	CD_2Cl_2 $\delta(^{13}C)$[b]	cp/mas $\delta(^{13}C)$[c]	TCBtype3 $\delta(^{13}C)_{calcd}$[d]
H(1)	5.69	C(1)	83.04	82.46	84.21
H(3ax)	3.68	C(3)	75.41	73.84	74.11
C$\underline{H}_3$	1.30	C(4)	33.28	34.55[e]	37.95
H(4ax)	2.09	C(5)	43.00	39.77[e]	47.04
H(4eq)	1.89	$\underline{C}H_3$	21.08	23.03[f]	17.69
H(5ax)	2.54	C(7)	46.27	42.96[e]	55.29
H(5eq)	3.35	C(8)	134.26	–	131.96
H(61)	8.97	C(9)	129.51	–	130.29
H(62)	10.36	C(10)	129.72	–	132.99
H(7ax)	4.76	C(11)	130.27	–	132.42
H(7eq)	4.11	C(8a)	130.27	128.76[f]	123.15
H(8)	7.77	C(11a)	142.41	144.99[f,g,h]	146.25
H(9)	7.43	C(*ipso*)	142.41	141.59[f,g,h]	138.25
H(10)	7.40	C(*ortho*)	127.03		
H(11)	7.18	C(*meta*)	128.68		
	–	C(*para*)	128.01		

H–H	$J_{HHexptl}$[i]	TCBtype3 $J_{HHcalcd}$[j]	Dihedral angle	θ_{exptl}[k]	θ_{calcd}[l]	$\theta_{X\text{-}ray}$[m]	θ_{DFT}[n]
3ax–4ax	9.2	9.37	C(3)–C(4)–C(5)–N(6)	72°	73°	86°	81°
3ax–4eq	1.6	2.19	C(4)–C(5)–N(6)–C(7)	87°	77°	71°	84°
3ax-C$\underline{H}_3$	6.3	5.75	C(5)–N(6)–C(7)–C(8a)	34°	56°	41°	29°
4ax–4eq	–16.0(3)	–15.97					
4ax–5ax	9.7(3)	10.46					
4ax–5eq	1.7(2)	1.22					
4eq–5ax	$\leqslant$1	0.71					
4eq–5eq	7.0	6.20					
5ax–5eq	–14.1(2)	–13.77					
5ax–61	9.7(3)	9.82					
5ax–62	$\leqslant$1	0.54					
5eq–61	$\leqslant$1	0.53					
5eq–62	3.2(3)	6.10					

(*continued*)

Table 13. Continued

H–H	$J_{HHexptl}$[i]	TCBtype3 $J_{HHcalcd}$[j]	Dihedral angle	θ_{exptl}[k]	θ_{calcd}[l]	$\theta_{X\text{-}ray}$[m]	θ_{DFT}[n]
61–7ax	5.3	6.44					
61–7eq	$\leqslant 1$	0.25					
62–7ax	8.3	6.61					
62–7eq	5.3(5)	6.87					
7ax–7eq	–12.7(2)	–11.94					
8–9	7.3	6.76					
8–10	1.6	0.80					
9–10	7.4	6.75					
9–11	1.6	0.85					
10–11	7.4	6.86					

[a] 500.1 MHz for ^{1}H and 125.76 MHz for ^{13}C, CD_2Cl_2, 298 K.
[b] ppm from internal TMS.
[c] SELTICS cp/mas, 5.0 kHz spin-rate, ppm using external glycine carbonyl δ 176.03.
[d] DFT B3LYP/6-311 + g(2d,p) geometry optimization followed by NMR = spin–spin, scaling equation $\delta(^{13}C)_{calcd} = -0.966765 * \sigma(^{13}C)_{calcd} + 175.37$.
[e] Observed in CPPI.
[f] Observed in SELTICS-NQS.
[g] Assignment may be reversed.
[h] Assigned by analogy to DFT values.
[i] Hz, *ca.* 0.1 Hz estimated standard deviation (esd), unless stated in parenthesis otherwise.
[j] DFT calculation for TCBtype3 conformation.
[k] Lambert's equation using $J_{HHexptl}$ values.
[l] Lambert's equation using DFT $J_{HHcalcd}$ values.
[m] Value from X-ray crystallographically determined structure.
[n] Value from DFT calculated model for TCBtype3 conformation.

[(Hz) 9.2 ^{3}J(3ax–4ax), 9.7(3) ^{3}J(4ax–5ax), 9.7(3) ^{3}J(5ax–61ax), and 8.3 ^{3}J(62ax–7ax)]. In addition, the *synclinal* and *antiperiplanar* type coupling constants involving H(3) and its two vicinal neighbors on C(4) clearly testify to an *equatorial* disposition for the C(3)-methyl group and assignment of (1*RS*,3*SR*)-stereochemistry for the solution-state molecule. The estimation by Lambert's method of 72° C(3)–C(4)–C(5)–N(6), 87° C(4)–C(5)–N(6)–C(7), and 42° C(5)–N(6)–C(7)–C(8a) dihedral angle values from the experimentally measured coupling constants are also in agreement with the proposed solution-state TCBtype3 conformation. These values are comparable with the respective 86°, 71°, and 34° values in the X-ray crystallographically determined model. Corresponding values in the DFT-model are 81°, 84°, and 29°.

The C(3) ring atom of the unsubstituted parent compound **36** is located at a 'non-corner' position on the TCBtype3 nine-membered ring. In other words, one of its geminal protons [H(3ax)] points inward while the other one [H(3eq)] is directed outward. The production of 3-methyl diastereomers should afford two different conformations for the (1*RS*,3*RS*) and (1*RS*,3*SR*) diastereomers, since if only one

non-corner C(3) conformation existed for both, then a methyl group pointing inward [instead of H(3ax)] would be sterically very unfavorable. Since ring closure in the synthesis is under thermodynamic control, the finding of a (*reference*,1*RS*,3*RS*)-TCBtype3 *equatorial* C(3)-methyl structure is not a surprise. What is a surprise is the extremely high degree of diastereoselectivity in its production, since one would have expected a measurable amount of the (1*RS*,3*RS*)-product having a different conformation.

4.3. (1*RS*,5*RS*)-6-Methyl-1-phenyl-1,3,4,5,6,7-hexahydro-2,6-benzoxazonine hydrogenfumarate [(1*RS*,5*RS*)-2,6-homonefopam hydrogenfumarate] (38a) and mesylate [(1*RS*,5*RS*)-2,6-homonefopam mesylate] (38b)

The racemic (1*RS*,6*RS*) and racemic (1*RS*,6*SR*) *N*-methyl diastereomers of 6-methyl-1-phenyl-1,3,4,5,6,7-hexahydro-2,6-benzoxazonine were present in the reaction mixture. The hydrogenfumarate salt crystallized as a racemic compound in an achiral space group crystal containing only the (1*RS*,6*RS*)-diastereomers (**38a**) in which the *N*-methyl group at the labile stereogenic nitrogen was *antiperiplanar* to H(5ax).[43] The X-ray crystallographically determined torsion angles of the (1*S*,6*S*)-enantiomer of **38a** are shown in Fig. 21.[43] The (1*S*,6*S*) enantiomer in the crystal had

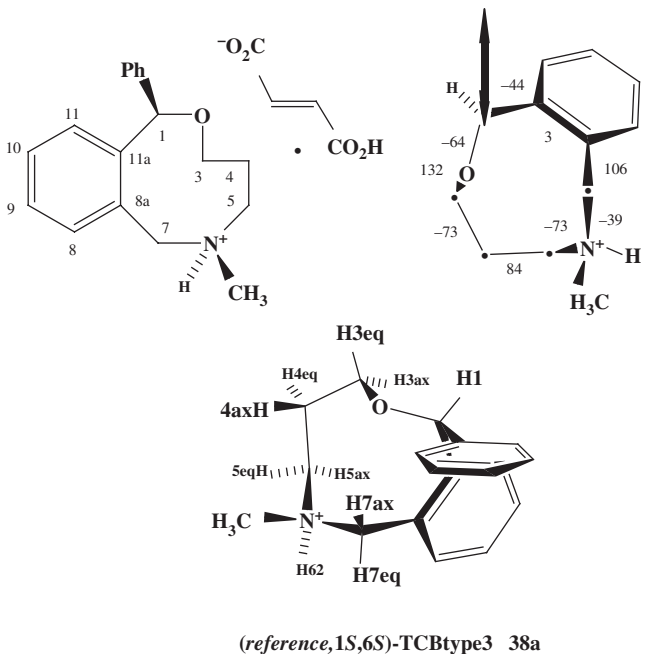

(*reference*,1*S*,6*S*)-TCBtype3 38a

Fig. 21. Crystallographically determined torsion angles (deg) and different orientations of the (*reference*,1*S*,6*S*)-TCB type 3 conformation for (1*RS*,6*RS*)-2,6-homonefopam hydrogenfumarate (**38a**).

a (*reference*,1*S*,6*S*)-TCBtype3 conformation similar to those noted for the secondary ammonium salts **36** and **37** discussed above.[43] To increase the lifetime of the solution-state protonated species on the NMR time-scale, the hydrogenfumarate salt was converted into a mesylate (**38b**), and then dissolved in CD_2Cl_2 to afford two *N*-methyl diastereomers in the ratio of 87 : 13.[43] Only the solution-state NMR parameters of the major species are listed in Table 14, since the minor species appears to be conformationally inhomogeneous.

The three *antiperiplanar* type coupling constants: two involving H(4ax) and its vicinal neighbors on either side, and one involving a geminal proton on atom C(6) [H(62)] and its vicinal neighbor on C(7) are characteristic of the TCBtype3 conformation [(Hz) 11.8 ^3J(3ax–4ax), 12.5 ^3J(4ax–5ax), and 8.5 ^3J(62ax–7ax)]. The (ppm) 3.38 H(3ax), 2.18 H(4ax), 2.71 H(5ax), and 4.51 H(7ax) protons were therefore assigned *axial* descriptors. As noted before, the substituent positions on N(6) are *isoclinal* in the TCBtype3 conformation. The H(62) N–*H* proton is approximately *synclinal* to both H(5ax) and H(5eq), while being approximately *antiperiplanar* to H(7ax) as shown by the <1 Hz ^3J(5ax–62ax), 3.8 Hz ^3J(5eq–62eq), and 8.5 Hz ^3J(62ax–7ax) coupling constants. This is consistent with a solution-state TCBtype3 conformation in which the *N*-methyl group is *antiperiplanar* to H(5ax) in the major species. Therefore, within the local environment of the C(3)–N(6) fragment, the major species *N*-methyl group would be expected to exhibit a 1,3-type *cis-diaxial* interaction with H(4ax). The finding of a 24.79 ppm value for major species C(4) in **38b** versus 26.80 ppm in *N*-desmethyl **36** may signify a *gamma-gauche* effect for the former. Finally, the DFT calculated coupling constants for a TCBtype3 conformation *N*-methyl group *antiperiplanar*-to-H(5ax) model are also listed in Table 14, and are in excellent agreement with those measured in solution for the major species. Therefore, the configuration at nitrogen and the nine-membered ring conformation of the major solution-state species are the same as in the solid-state. Substitution of *cis*-to-phenyl H-atoms on C(3) or N(6) of the 1-phenyl-2,6-benzoxazonine (*reference*,*S*)-TCBtype3 skeleton (**36**) by methyl groups appears not to change the conformational preference.

The estimation by Lambert's method of 62° O(2)–C(3)–C(4)–C(5) and 76° C(3)–C(4)–C(5)–N(6) dihedral angle values using the experimentally measured coupling constants were also in agreement with the proposed solution-state TCBtype3 conformation. Using the DFT calculated coupling constants, the corresponding values were 60° and 74°. These values were comparable with the respective 73° and 84° values in the X-ray crystallographically determined model, and with the 69° and 82° values in the DFT model.

4.4. 6,6-Dimethyl-1-phenyl-1,3,4,5,6,7-hexahydro-2,6-benzoxazonium iodide [2,6-homonefopam methiodide] (39)

The racemic mixture of 6,6-dimethyl-1-phenyl-1,3,4,5,6,7-hexahydro-2,6-benzoxazonium iodide (**39**) crystallized as an anhydrate racemic compound in a monoclinic achiral space group crystal. The racemic mixture of the corresponding

Table 14. Selected solution-state ^{1}H- and ^{13}C-NMR (CD_2Cl_2) spectral parameters for (1*RS*,6*RS*)-2,6-homonefopam mesylate (**38b**) major *N*-Methyl diastereomer[a]

Atom	$\delta(^{1}H)^{b}$	Atom	CD_2Cl_2 $\delta(^{13}C)^{b}$	TCBtype3 $\delta(^{13}C)_{calcd}{}^{c}$
H(1)	5.67	C(1)	86.61	86.47
H(3ax)	3.38	C(3)	68.85	65.38
H(3eq)	4.21	C(4)	24.79	25.09
H(4ax)	2.18	C(5)	51.78	55.50
H(4eq)	1.66	C(7)	56.07	61.61
H(5ax)	2.71	C(8)	135.96	130.45
H(5eq)	3.15	C(9)	129.62	130.39
NC$\underline{H}_3$	2.79	N$\underline{C}$H$_3$	41.24	39.12
H($\underline{6}$2)	12.52	C(*ortho*)	127.65	125.07
H(7ax)	4.51	C(*meta*)	130.73	128.40
H(7eq)	4.17	C(*para*)	128.79	129.52
H(8)	8.12			
H(9)	7.55			
H(10)	7.52			
H(11)	7.40			

H–H	$J_{HHexptl}{}^{d}$	TCBtype3 $J_{HHcalcd}{}^{e}$	Dihedral angle	$\theta_{exptl}{}^{f}$	$\theta_{calcd}{}^{g}$	$\theta_{X\text{-}ray}{}^{h}$	$\theta_{DFT}{}^{i}$
3ax–3eq	−11.4	–11.41	O(2)–C(3)–C(4)–C(5)	62°	60°	73°	69°
3ax–4ax	11.8	10.87	C(3)–C(4)–C(5)–N(6)	76°	74°	84°	82°
3ax–4eq	1.8	1.91					
3eq–4ax	3.4	3.61					
3eq–4eq	3.3	3.31					
3eq–5eq	0.6	0.59					
4ax–4eq	–16.9	–16.53					
4ax–5ax	12.5	10.82					
4ax–5eq	1.1	1.01					
4eq–5ax	<1	0.80					
4eq–5eq	6.6	6.61					
5ax–5eq	–14.3	–13.77					
5ax–6$\underline{2}$	<1	2.15					
5eq–6$\underline{2}$	3.8	4.00					
6$\underline{2}$–7ax	8.5	8.24					
6$\underline{2}$–7eq	5.0	5.15					
6$\underline{2}$-C$\underline{H}_3$	5.0	5.55_{av}					
7ax–7$\underline{e}$q	–12.4	–12.02					

[a] 500.1 MHz for ^{1}H and 50.3 MHz for ^{13}C, CD_2Cl_2, 298 K, ratio of 87 : 13 for major : minor *N*-methyl diastereomers, aliphatic region simulated by *gNMR* program (Ref. 36), data from Ref. 43.

[b] ppm from internal TMS.

[c] DFT B3LYP/6-311 + g(2d,p) geometry optimization followed by NMR = spin–spin, scaling equation $\delta(^{13}C)_{calcd} = -0.966765 * \sigma(^{13}C)_{calcd} + 175.37$.

[d] Hz, *ca.* 0.1 Hz estimated standard deviation (esd), unless value is a whole integer.

[e] Hz, DFT calculation for TCBtype3 conformation.

[f] Lambert's equation using $J_{HHexptl}$ values.

[g] Lambert's equation using DFT $J_{HHcalcd}$ values.

[h] Value from X-ray crystallographically determined structure.

[i] Value from DFT calculated model for TCBtype3 conformation.

quaternary ammonium salt chloride analog crystallized as a dihydrate in a triclinic achiral space group crystal with two molecules in the asymmetric unit. Despite residence in crystals with different space groups and with different degrees of hydration, the (*S*)-enantiomer in the two salts exhibited the same (*retro-inverso*,*S*)-TBC solid-state conformation. In this conformation, the phenyl group was located in an *equatorial* position on the nine-membered ring, while protons ligated to C(3) or methyl groups attached to N(6) represent two sets of *isoclinal* atoms or groups. Each of the geminal pairs of protons ligated to C(4), C(5), and C(7) has an *axial* and an *equatorial* partner according to Anet's[15] definitions. X-ray crystallographically determined torsion angles for the (*retro-inverso*,*S*)-TBC solid-state conformation are given in iconic structure **39** shown in Fig. 22.

The solid-state ^{13}C cp/mas for crystalline **39**, and the quantum mechanical calculated ^{13}C chemical shifts and J_{HH} coupling constants for a TBC model are listed in Table 15. Comparison of the ^{13}C chemical shift values in the cp/mas spectrum versus corresponding values for those from the quantum mechanical calculation shows them to be similar. Dissolution of either quaternary ammonium salt in $CDCl_3$ solution affords two species (88 : 12) in which the major species has undergone a conformational change to a (*reference*,*S*)-TCBtype3 structure, while the

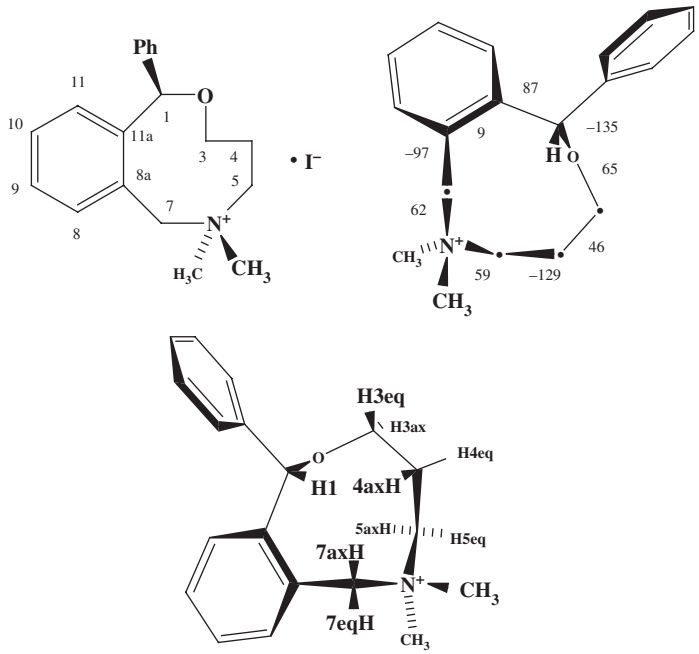

(*retro-inverso,S*)-TBC **39**

Fig. 22. Crystallographically determined torsion angles (deg) and different orientations of the (*retro-inverso*,*S*)-TBC conformation (**39**) for 2,6-homonefopam methiodide.

geometry of the minor one is unknown. DFT calculated torsion angles for the solution-state TCBtype3 model are given in iconic structure **40** (see Fig. 23).

The C(1) chemical shifts in the solution-state $^{13}C\{^1H\}$ NMR spectrum are significantly different versus corresponding values in the cp/mas spectrum. This is apparently the result of a *gamma-gauche* effect since dihedral angle C(1)–O(2)–C(3)–C(4) is 136° in the TCBtype3 model (see Fig. 23), versus only 65° and 71° in the TBC X-ray (see Fig. 22) and DFT-models, respectively. It is noted that the *gem-N*-methyl groups resided in sterically free 'corner' positions in both conformations. The relative disposition of H(4ax) vis-à-vis its vicinal neighbors was different for the two conformations. The conformation of the TBC model (**39**) was characterized by H(4ax) disposed as *antiperiplanar* to H(3ax) (165°) and *anticlinal* to both its proton neighbors on C(5) (112° and 130°), while H(4eq) was *synperiplanar* (9°) to H(5eq). On the other hand, as we have already seen, H(4ax) in TCBtype3 was *antiperiplanar* to both H(3ax) and H(5ax). Thus, one expects to

Table 15. Selected solution-state ^1H- and ^{13}C-NMR ($CDCl_3$), and solid-state cp/mas ^{13}C-NMR spectral parameters for 2,6-homonefopam methiodide (**39**)[a]

Atom	$\delta(^1H)$[b]	Atom	$CDCl_3$ $\delta(^{13}C)$[b]	TCBtype3 $\delta(^{13}C)_{calcd}$[c]	cp/mas $\delta(^{13}C)$[d]	TBC $\delta(^{13}C)_{calcd}$[c]
H(1)	5.68	C(1)	85.18	86.12	71.99	76.24
H(3ax)	3.61	C(3)	68.00	65.53	64.48[e]	63.33
H(3eq)	4.24	C(4)	25.40	27.64	20.46[e]	21.11
H(4ax)	2.26	C(5)	64.11	64.32	57.65[e]	57.80
H(4eq)	1.84	C(7)	66.13	69.96	61.32[e]	65.50
H(5ax)	3.06	N$\underline{C}H_3$(ax)	53.60	49.49	49.07[f]	49.78
H(5eq)	4.00	N$\underline{C}H_3$(eq)	55.03	55.65	50.67[f]	50.95
H(7ax)	4.84	C(8)	134.92	131.74	135.49	132.62
H(7eq)	5.13	C(9)	129.49	129.48	–	128.25
H(8)	7.74	C(10)	131.07	132.89	–	134.09
H(9)	7.56	C(11)	131.52	133.12	–	132.19
H(10)	7.56	C(8a)	126.72[g]	125.43	127.96[f,g]	121.02
	7.42	C(11a)	142.34[g]	145.92	144.98[f,g]	145.60
NC$\underline{H}_3$(ax)	3.58	C(*ipso*)	140.20[g]	138.61	138.84[f,g]	135.29
NC$\underline{H}_3$(eq)	3.67	C(*ortho*)	126.29	125.03		
	–	C(*meta*)	128.48	128.23		
	–	C(*para*)	128.48	129.36		

H–H	$J_{HHexptl}$[h]	TCBtype3 $J_{HHcalcd}$[i]	Dihedral angle	θ_{exptl}[j]	θ_{calcd}[k]	$\theta_{X\text{-}ray}$[l]	θ_{DFT}[m]
3ax–3eq	–11.6	–11.29	O(2)–C(3)–C(4)–C(5)	58°	58°	46°	68°
3ax–4ax	10.1	11.15	C(3)–C(4)–C(5)–N(6)	73°	72°	129°	81°
3ax–4eq	2.8	2.12					
3eq–4ax	3.8	3.85					

(*continued*)

Table 15. Continued

H–H	$J_{HHexptl}$[h]	TCBtype3 $J_{HHcalcd}$[i]	Dihedral angle	θ_{exptl}[j]	θ_{calcd}[k]	$\theta_{X\text{-}ray}$[l]	θ_{DFT}[m]
3eq–4eq	4.3	2.16					
4ax–4eq	–17.1	–16.55					
4ax–5ax	10.9	10.86					
4ax–5eq	<1	1.33					
4eq–5ax	<1	1.00					
4eq–5eq	6.6	6.49					
5ax–5eq	–13.8	–13.82					
7ax–7eq	–13.0	–12.52					
8–9	7.2	6.90					
8–10	1.7	0.81					
9–10	–	6.70					
9–11	1.9	0.90					
10–11	7.0	6.90					

[a] 500.1 MHz for ^{1}H and 125.76 MHz for ^{13}C, $CDCl_3$, 298 K, aliphatic region simulated by *gNMR* program (Ref. 36).
[b] ppm from internal TMS.
[c] DFT B3LYP/6-311 + g(2d,p) geometry optimization followed by NMR = spin–spin, scaling equation $\delta(^{13}C)_{calcd} = -0.966765 * \sigma(^{13}C)_{calcd} + 175.37$.
[d] SELTICS cp/mas, 5.0 kHz spin-rate, ppm using external glycine carbonyl δ 176.03.
[e] Observed in CPPI.
[f] Observed in SELTICS-NQS.
[g] Assigned by analogy to DFT values.
[h] Hz, *ca.* 0.1 Hz estimated standard deviation (esd), unless value is a whole integer.
[i] DFT calculation for TCBtype3 conformation.
[j] Lambert's equation using $J_{HHexptl}$ values.
[k] Lambert's equation using DFT $J_{HHcalcd}$ values for TCBtype3 conformation.
[l] Value from X-ray crystallographically determined structure (TBC conformation).
[m] Value from DFT calculated model for TCBtype3 conformation.

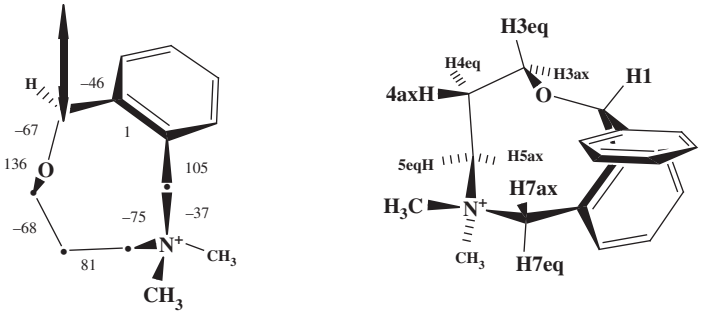

(*reference,S*)-TCBtype3 **40**

Fig. 23. DFT quantum mechanically calculated torsion angles (deg) and different orientations of a (*reference,S*)-TCB type 3 conformation model (**40**) 2,6-homonefopam methiodide.

measure three large coupling constants involving H(4ax) if TCBtype3 is the solution-state conformation: 10.1 Hz [^3J(3ax–4ax)], 10.9 Hz [^3J(4ax–5ax)], and –17.1 Hz [^2J(4ax–4eq)]. In the DFT-TCBtype3 model, these corresponding values were: (Hz) 11.15, 10.86, and –16.55. Finally, a 4.9% NOE intensity increase was measured for 3.61 ppm H(3ax) upon {5.68 ppm, H(1)}. In the TCBtype3 model, H(1) and H(3ax) are *syn* and are located at a relatively close distance of 2.43 Å, while they are on opposite faces of the nine-membered in the TBC model.

Using Lambert's[28] equation, the experimentally measured vicinal coupling constants provide 58° and 73° *synclinal* values for the respective O(2)–C(3)–C(4)–C(5) and C(3)–C(4)–C(5)–N(6) dihedral angles which are in excellent agreement with the 58° and 72° values in the TCBtype3 model. These angles are 46° and 129° in the X-ray determined TBC conformation. Therefore, the solution-state predominant TCBtype3 conformation of the quaternary ammonium salt is the same as that found for the tertiary and secondary ammonium salt analogs, in spite of the fact that the solid-state quaternary conformation is TBC.

4.5. (1*RS*,3*RS*)-3-Methyl-1-phenyl-1,3,4,5,6,7-hexahydro-2,6-benzoxazonine-6-carbonitrile (41)

Synthesis of 3-methyl-1-phenyl-1,3,4,5,6,7-hexahydro-2,6-benzoxazonine-6-carbonitrile afforded (1*RS*,3*RS*)- and (1*RS*,3*SR*)-diastereomers that were separated by silica-gel chromatography. The (1*RS*,3*RS*)-diastereomer **(41)** was not crystallizable in our hands. However, ^{1}H and ^{13}C-NMR spectroscopic measurements of **41** in $CDCl_3$ solution clearly showed a similar (*retro-inverso*,*S)*-TBC solution-state conformation for one of the enantiomers as that found for solid-state **39**. DFT quantum mechanically determined torsion angles for a (*retro-inverso*,*S)*-TBC model of **41** are presented in Fig. 24. Strong coupling between H(5ax) and H(5eq) ($\Delta\upsilon = 7.24$ Hz) in the 500 MHz ^{1}H-NMR ($CDCl_3$) spectrum necessitated spectral simulation.[36] Selected ^{1}H- and ^{13}C-NMR parameters for **41** are listed in Table 16.

The 76.01 ppm value for the benzhydrylic C(1) nucleus is characteristic of a *gamma-gauche* effect in accord with a *synclinal* 63° C(1)–O(2)–C(3)–C(4) dihedral angle for the TBC DFT-model. In addition, the *antiperiplanar* 10.9 Hz ^3J(3ax–4ax) and *synperiplanar* 9.8 Hz ^3J(4eq–5eq) coupling constants are also indicative of a TBC conformation. Protons H(1), H(4ax), and H(7ax) are located on the same face of the (*retro-inverso*,*S)*-TBC nine-membered ring and are oriented into its interior where they suffer transannular close contacts: e.g. 2.245 Å H(1)...H(4ax) and 1.974 Å H(1)...H(7ax) non-bonding distances in the TBC DFT-model. NOE intensity enhancements of 3.0% into 6.04 ppm H(1) upon {1.86 ppm, H(4ax)}; 6.1% into 6.04 ppm H(1) upon {4.42 ppm, H(7ax)}; and 3.9% into 4.42 ppm, H(7ax) upon {6.04 ppm, H(1)} were all consistent with a (*retro-inverso*,*S)*-TBC solution-state conformation. Finally, using the vicinal coupling constants involving the C(4)–C(5) bond, Lambert's equation estimates an *anticlinal* 122° C(3)–C(4)–C(5)–N(6) dihedral angle which is in good agreement with the 128° value measured in the DFT model.

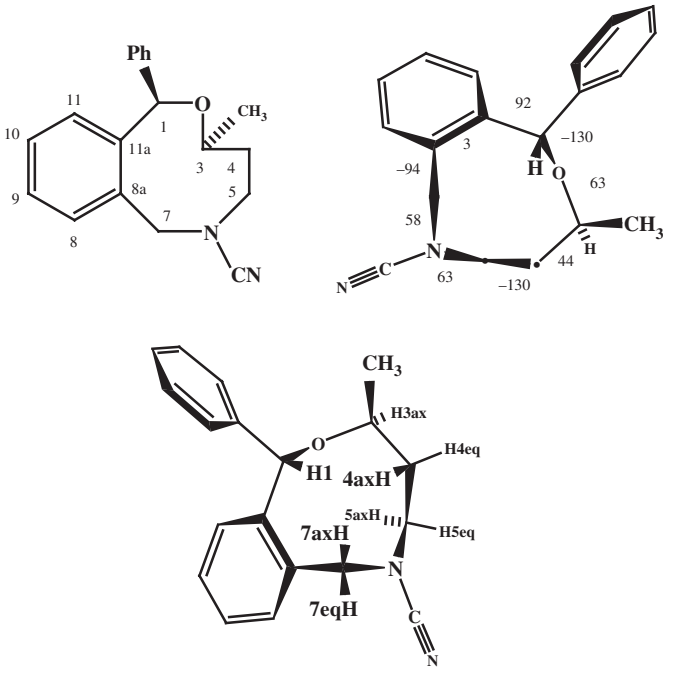

(*retro-inverso*,1*S*,3*S*)-TBC **41**

Fig. 24. DFT quantum mechanically calculated torsion angles (deg) and different orientations of a (*retro-inverso*,1*S*,3*S*)-TBCconformation model for (1*RS*,3*RS*)-3-methyl-1-phenyl-1,3,4,5,6,7-hexahydro-2,6-benzoxazonine-6-carbonitrile (**41**).

4.6. 1-Phenyl-1,3,4,5,6,7-hexahydro-2,6-benzoxazonine-6-carbonitrile (42)

The racemic mixture of 1-phenyl-1,3,4,5,6,7-hexahydro-2,6-benzoxazonine-6-carbonitrile (**42**) crystallized as a racemic compound in an achiral space group crystal.[3] There are two molecules in the asymmetric unit, and both show the (*reference*,*S*)-Skew–Chair–Boat type 2 (SCBtype2) conformation for the same enantiomer.[3] X-ray crystallographically determined torsion angles for the (*reference*,1*S*, 3*R*)-SCBtype2 solid-state conformation are given in iconic structure **42** for one of the molecules (see Fig. 25). In this conformation, the phenyl group was almost *isoclinal* with only a very small amount of *pseudoequatorial* character. The C(4) atom resided at a 'corner' position, and thus the geminal protons on C(4) were *isoclinal* and were assigned *proR*/*proS* descriptors for the (*S*)-enantiomer. The three geminal pairs of protons [ligated to C(3), C(5), and C(7)] each have an *axial* and an *equatorial* partner according to Anet's[15] definitions. Strong coupling between H(5ax) and H(5eq) necessitated spectral simulation of the ^{1}H-NMR spectrum.[36] Selected solution-state ^{1}H and ^{13}C spectral parameters, solid-state cp/mas and DFT ^{13}C chemical shifts of **42** are listed in Table 17. It is noted that the experimentally measured and simulated –10.1 Hz ^{2}J(3ax–3eq) coupling constant was relatively

Table 16. Selected solution-state ^{1}H- and ^{13}C-NMR ($CDCl_3$) spectral parameters for (1*RS*,3*RS*)-3-methyl-1-phenyl-1,3,4,5,6,7-hexahydro-2,6-benzoxazonine-6-carbonitrile (**41**)[a]

Atom	$\delta(^{1}H)$[b]	Atom	$CDCl_3$ $\delta(^{13}C)$[b]	TBC $\delta(^{13}C)_{calcd}$[c]
H(1)	6.04	C(1)	76.01	69.53
H(3ax)	3.58	C(3)	70.59	74.48
H(4ax)	1.86	C(4)	35.71	30.21
H(4eq)	1.65	C(5)	51.72	44.17
H(5ax)	3.42_8	C(7)	56.07	49.19
H(5eq)	3.44_2	$\underline{C}H_3$	22.12	18.90
H(7ax)	4.41_8	CN	117.56	116.54
H(7eq)	4.52_1			
$C\underline{H}_3$	1.05			
H(11)	6.82			

H–H	$J_{HHexptl}$[d]	TBC $J_{HHcalcd}$[e]	Dihedral angle	θ_{exptl}[f]	θ_{calcd}[g]	θ_{DFT}[h]
3ax-CH_3	6.5	5.97	C(3)–C(4)–C(5)–N(6)	122°	127°	128°
3ax–4ax	10.9	11.34				
3ax–4eq	2.4	4.75				
4ax–4eq	−15.5	−15.76				
4ax–5ax	5.8	1.48				
4ax–5eq	3.3	3.76				
4eq–5ax	3.7	4.70				
4eq–5eq	9.8	11.67				
5ax–5eq	−14.9	−12.93				
7ax–7eq	−14.5	−14.59				

[a] 500.1 MHz for ^{1}H and 125.76 MHz for ^{13}C, $CDCl_3$, 298 K, aliphatic region simulated by *gNMR* program (Ref. 36).
[b] ppm from internal TMS.
[c] DFT B3LYP/6-311 + g(2d,p) geometry optimization followed by NMR = spin–spin, scaling equation $\delta(^{13}C)_{calcd} = -0.966765 * \sigma(^{13}C)_{calcd} + 175.37$.
[d] Hz, *ca.* 0.1 Hz estimated standard deviation (esd).
[e] DFT calculation for TBC conformation.
[f] Lambert's equation using $J_{HHexptl}$ values.
[g] Lambert's equation using DFT $J_{HHcalcd}$ values for TBC conformation.
[h] Value from DFT calculated model for TBC conformation.

small in magnitude for two geminal protons (however, the –9.22 Hz DFT calculated value was also small).

The (*reference*,*S*)-SCBtype2 conformation of **42** is characterized by each *isoclinal* proton on C(4) having one large *antiperiplanar* magnitude coupling constant with a vicinal neighbor [11.3 Hz ^{3}J(3ax–4_{proR}) and 11.2 Hz ^{3}J(4_{proS}–5ax)]. While the (*retro-inverso*,*S*)-TBC conformation of **41** also has each C(4) geminal proton showing a large magnitude coupling constant with a vicinal neighbor, the two conformations can be readily differentiated by NMR spectroscopy. In the (*retro-inverso*,*S*)-TBC

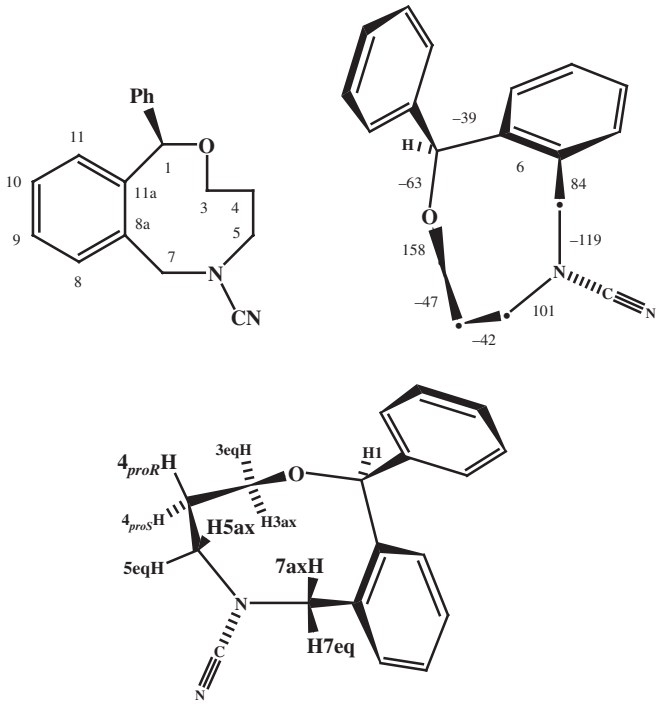

(*reference,S*)-SCBtype2 42

Fig. 25. Crystallographically determined torsion angles (deg) and different orientations of the (*reference*,*S*)-SCB type 2 conformation for 1-phenyl-1,3,4,5,6,7-hexahydro-2,6-benzoxazonine-6-carbonitrile (**42**).

conformation of **41** H(1), H(4ax), and H(7ax) all suffer close contacts as seen by NOE experiments mentioned above. However, in the (*reference*,*S*)-SCBtype2 conformation of **42**, H(1) is close to H(3eq) and is on the opposite face of the ring from H(7ax). This is consistent with a 1.2% NOE intensity enhancement into 3.89 ppm H(3eq) upon {5.69 ppm, H(1)}, and a 1.4% intensity increase into 5.69 ppm H(1) upon {3.89 ppm H(3eq)}. In the (*reference*,*S*)-SCBtype2 conformation, H(7ax) is close to H(5ax). This agrees with a 1.7% NOE intensity increase into 3.36 ppm H(5ax) upon {4.35 ppm, H(7ax)}, and a 1.8% NOE intensity increment into 4.35 ppm H(7ax) upon {3.36 ppm H(5ax)}. Another characteristic difference between the two conformations involves their C(1) chemical shifts. The cp/mas C(1) value for (*retro-inverso*,*S)*-TBC crystalline **39** is 71.99 ppm versus 81.47 ppm for (*reference*,*S*)-SCBtype2 conformation crystalline **42**, in accord with a *gamma-gauche* effect expected for a 63° C(1)–O(2)–C(3)–C(4) dihedral angle in **39** but not for a 158° angle in **42**.

Inspection of the cp/mas and DFT calculated ^{13}C chemical shifts (versus corresponding values measured in the solution-state spectrum) very strongly suggests

Table 17. Selected solution-state ^{1}H- and ^{13}C-NMR ($CDCl_3$), and solid-state cp/mas ^{13}C-NMR spectral parameters for 1-phenyl-1,3,4,5,6,7-hexahydro-2,6-benzoxazonine-6-carbonitrile (**42**)[a]

Atom	$\delta(^{1}H)$[b]	Atom	$CDCl_3$ $\delta(^{13}C)$[b]	cp/mas $\delta(^{13}C)$[c]	SCBtype2 $\delta(^{13}C)_{calcd}$[d]
H(1)	5.69	C(1)	83.33	81.47	85.62
H(3ax)	3.45	C(3)	63.97	62.36[e]	62.13
H(3eq)	3.89	C(4)	27.62	26.72[e]	28.69
H(4_{proR})	1.98	C(5)	51.42	50.65[e]	51.43
H(4_{proS})	1.86	C(7)	55.78	56.13[e]	56.06
H(5ax)	3.36_7	CN	117.83	117.16	114.45
H(5eq)	3.48_1	C(8a)	132.90[f]	131.95[f,g]	135.64
H(7ax)	4.35	C(11a)	139.22[f]	138.08[f,g]	139.40
H(7eq)	4.20	C(*ipso*)	141.13[f]	142.46[f,g]	143.53

H–H	$J_{HHexptl}$[h]	SCBtype2 $J_{HHcalcd}$[i]	Dihedral angle	θ_{exptl}[j]	θ_{calcd}[k]	$\theta_{X\text{-}ray}$[l]	θ_{DFT}[m]
3ax–3eq	–10.1	–9.22	O(2)–C(3)–C(4)–C(5)	50°	45°	47°	44°
3ax–4_{proR}	11.3	11.08	C(3)–C(4)–C(5)–N(6)	52°	46°	42°	47°
3ax–4_{proS}	4.6	5.15					
3eq–4_{proR}	5.9	6.66					
3eq–4_{proS}	2.2	0.52					
4_{proR}–4_{proS}	–14.6	–13.40					
4_{proR}–5ax	4.1	4.84					
4_{proR}–5eq	2.9	0.86					
4_{proS}–5ax	11.2	11.13					
4_{proS}–5eq	5.4	6.40					
5ax–5eq	–14.6	–13.97					
7ax–7eq	–13.4	–13.36					

[a] 500.1 MHz for ^{1}H and 125.76 MHz for ^{13}C, $CDCl_3$, 298 K, aliphatic region simulated by *gNMR* program (Ref. 36).
[b] ppm from internal TMS.
[c] SELTICS cp/mas, 5.0 kHz spin-rate, ppm using external glycine carbonyl δ 176.03.
[d] DFT B3LYP/6-311 + g(2d,p) geometry optimization followed by NMR = spin–spin, scaling equation $\delta\ (^{13}C)_{calcd} = -0.966765 * \sigma(^{13}C)_{calcd} + 175.37$.
[e] Observed in CPPI.
[f] Assigned by analogy to DFT values.
[g] Observed in SELTICS-NQS.
[h] Hz, *ca.* 0.1 Hz estimated standard deviation (esd).
[i] Hz, DFT calculation for SCBtype2 conformation.
[j] Lambert's equation using $J_{HHexptl}$ values.
[k] Lambert's equation using DFT $J_{HHcalcd}$ values for SCBtype2 conformation.
[l] Value from X-ray crystallographic model.
[m] Value from DFT calculated model for SCBtype2 conformation.

that the SCBtype2 solid-state conformation is maintained upon dissolution of crystalline **42** in $CDCl_3$ solution. In addition, the experimentally measured vicinal coupling constants for the C(3)–C(4) and C(4)–C(5) bonds enabled an estimate of 50° and 52° for the respective endocyclic *synclinal* dihedral angles which compared well with 47° and 42° values in the X-ray crystallographic model, and with 44° and 47° values in the DFT model. These same dihedral angles were estimated to be 44° and 47°, respectively, using the DFT calculated coupling constants.

4.7. (1*RS*,3*SR*)-3-Methyl-1-phenyl-1,3,4,5,6,7-hexahydro-2,6-benzoxazonine-6-carbonitrile (43)

The racemic mixture of (1*RS*,3*SR*)-3-methyl-1-phenyl-1,3,4,5,6,7-hexahydro-2,6-benzoxazonine-6-carbonitrile (**43**) crystallized as a racemic compound in an achiral space group crystal.[3] *Cis*-to-phenyl substitution of a methyl at C(3) did not change the solid-state (*reference*,*S*)-SCBtype2 conformation of the parent nine-membered

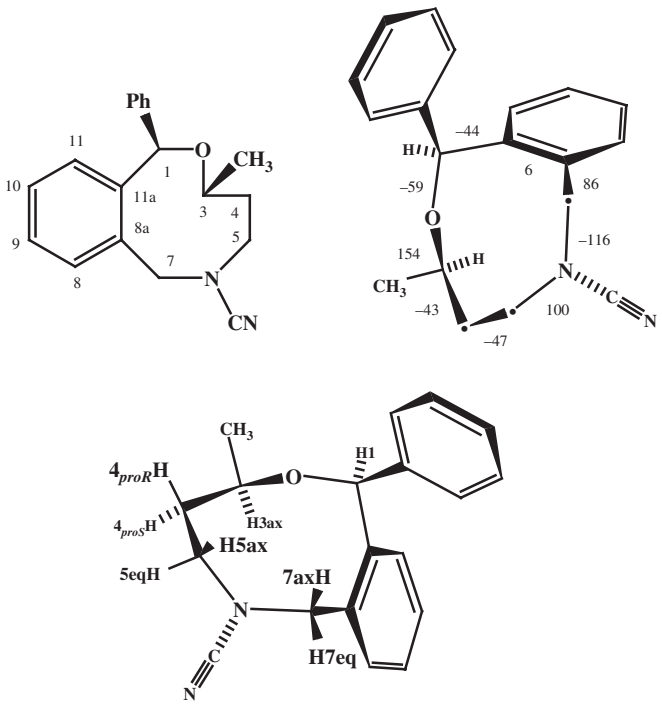

(*reference*,1*S*,3*R*)-SCBtype2 **43**

Fig. 26. Crystallographically determined torsion angles (deg) and different orientations of the (*reference*,1*S*,3*R*)-SCB type 2 conformation for (1*RS*,3*SR*)-3-methyl-1-phenyl-1,3,4,5,6,7-hexahydro-2,6-benzoxazonine-6-carbonitrile (**43**).

Table 18. Selected solution-state ^{1}H- and ^{13}C-NMR ($CDCl_3$), and solid-state cp/mas ^{13}C-NMR spectral parameters for (1*RS*,3*SR*)-3-methyl-1-phenyl-1,3,4,5,6,7-hexahydro-2,6-benzoxazonine-6-carbonitrile (**43**)[a]

Atom	$\delta(^{1}H)$[b]	Atom	$CDCl_3$ $\delta(^{13}C)$[b]	cp/mas $\delta(^{13}C)$[c]	SCBtype2 $\delta(^{13}C)_{calcd}$[d]
H(1)	5.69	C(1)	81.01	79.39	82.49
H(3ax)	3.53	C(3)	69.08	68.45[e]	67.96
H(4_{proR})	1.63	C(4)	35.45	34.93[e]	36.67
H(4_{proS})	1.83	C(5)	50.60	49.88[e]	51.37
H(5ax)	3.27_8	C(7)	55.54	55.88[e]	55.67
H(5eq)	3.28_4	CN	117.92	117.56	114.56
H(7ax)	4.23	$\underline{C}H_3$	18.69	17.37	15.82
H(7eq)	4.08	$\underline{C}$(8a)	–	133.12[f,g]	135.47
$C\underline{H}_3$	1.21	C(11a)	–	137.98[f,g]	138.77
	–	C(*ipso*)	–	142.61[f,g]	143.40

H–H	$J_{HHexptl}$[h]	SCBtype2 $J_{HHcalcd}$[i]	Dihedral angle	θ_{exptl}[j]	θ_{calcd}[k]	$\theta_{X\text{-}ray}$[l]	θ_{DFT}[m]
3ax-$C\underline{H}_3$	6.0	5.46	C(3)–C(4)–C(5)–N(6)	58°	48°	47°	49°
3ax–4_{proR}	10.5	9.51					
3ax–4_{proS}	4.2	5.04					
4_{proR}–4_{proS}	–14.5	−13.43					
4_{proR}–5ax	4.0	4.51					
4_{proR}–5eq	3.2	1.09					
4_{proS}–5ax	12.9	11.23					
4_{proS}–5eq	3.4	5.99					
5ax–5eq	–14.6	–13.96					
7ax–7eq	–13.3	–13.41					

[a] 500.1 MHz for ^{1}H and 125.76 MHz for ^{13}C [data taken from Ref. 3], $CDCl_3$, 298 K, aliphatic region simulated by *gNMR* program (Ref. 36).
[b] ppm from internal TMS.
[c] SELTICS cp/mas, 5.0 kHz spin-rate, ppm using external glycine carbonyl δ 176.03.
[d] DFT B3LYP/6-311 + g(2d,p) geometry optimization followed by NMR = spin–spin, scaling equation $\delta(^{13}C)_{calcd} = -0.966765 * \sigma(^{13}C)_{calcd} + 175.37$.
[e] Observed in CPPI.
[f] Assigned by analogy to DFT values.
[g] Observed in SELTICS-NQS.
[h] Hz, *ca.* 0.1 Hz estimated standard deviation (esd).
[i] Hz, DFT calculation for SCBtype2 conformation.
[j] Lambert's equation using $J_{HHexptl}$ values.
[k] Lambert's equation using DFT $J_{HHcalcd}$ values for SCBtype2 conformation.
[l] Value from X-ray crystallographic model.
[m] Value from DFT calculated model for SCBtype2 conformation.

ring since the methyl resides in an *equatorial* position. X-ray crystallographically determined torsion angles for the (*reference*,1*S*,3*R*)-SCBtype2 solid-state conformation are given in iconic structure **43** (see Fig. 26). As with the parent compound **42**, strong coupling between H(5ax) and H(5eq) necessitated spectral simulation of the ^{1}H-NMR spectrum.[36] Selected solution-state ^{1}H and ^{13}C spectral parameters, solid-state cp/mas and DFT scaled ^{13}C chemical shifts of **43** are listed in Table 18.

As with parent **42**, each *isoclinal* proton on C(4) had one large *antiperiplanar* magnitude coupling constant involving a vicinal neighbor [10.5 Hz ^{3}J(3ax–4_{proR}) and 12.9 Hz ^{3}J(4_{proS}–5ax)]. These coupling constants, together with a C(1) chemical shift of 81.01 ppm, were characteristic of a (*reference*,1*S*,3*R*)-SCBtype2 conformation for **43**. Also, in the case of this (1*RS*,3*SR*)-3-methyl analog, comparision of the cp/mas and DFT calculated ^{13}C chemical shifts with corresponding values measured in the solution-state spectrum very clearly suggested that the SCBtype2 solid-state conformation was maintained upon dissolution of crystalline **43** in $CDCl_3$ solution. In addition, the experimentally measured vicinal coupling constants for the C(4)–C(5) bond enabled an estimate of 58° for the C(3)–C(4)–C(5)–N(6) *synclinal* dihedral angle which compared reasonably well with a 47° value in the X-ray crystallographic model, and with 49° in the DFT model. This same dihedral angle was estimated to be 48° using the DFT calculated coupling constants.

5. CONCLUSIONS

A series of eight- and nine-membered rings having 2,5-benzoxazocine and 2,6-benzoxazonine skeletons were prepared with systematic changes in the number and type of substituents. Most of the samples were crystalline solids that enabled the growing of single crystals, and subsequent structure determination using X-ray crystallography. Some of the chemical shifts measured in the solid-state cp/mas ^{13}C-NMR spectra from these crystals could be correlated with a particular ring conformation. The medium-ring solid samples were dissolved and their conformations were then studied by solution-state NMR methods. In addition, DFT quantum mechanical geometry optimization calculations were performed to provide models for the calculation of ^{13}C shielding constants and total nuclear spin–spin coupling constants. Comparisons of solution-state NMR parameters with those from the solid-state and DFT calculations were used to ascertain if the solid-state conformation was maintained in solution. The solution- and solid-state conformations were the same in many cases. In other instances, the solution-state conformation either changed from that of the solid-state, or it was in an FEL conformational equilibrium with usually one conformation predominating in the mixture.

Lambert's equation using the experimental vicinal coupling constants enabled good estimations of endocyclic dihedral angles within the solution-state solvated molecules. These values were generally in reasonable agreement with those calculated by the same equation but now based upon DFT calculated spin–spin coupling constants. This enabled the following conclusions to be drawn:

- The current level of 'theory' in calculation of spin–spin coupling constants by quantum mechanical methods appears to be relatively good.
- The calculated conformational geometry and that inferred by NMR experiment were similar to each other (despite the fact that the molecule in the computer is in a 'vacuum' and at the bottom of the potential energy well (i.e. at 0 K – no vibrations), whereas the solution-state molecule is at ambient temperature and solvated).
- Lambert's equation gave very reasonable estimations of solution-state dihedral angles for fragments of the XCH_2–CH_2Y type within medium rings. In addition, these estimated dihedral angles were also found to be quite similar to those measured in X-ray crystallographically determined structural models, in spite of the fact that, also here, one is comparing a different situation, i.e. molecules within a crystal lattice.

The theoretical possibility of stereochemically labeled chiral medium-rings having diastereomeric conformational subtypes differing in the stereogenic elements of ring chirality and/or substituent tropicity, was shown to exist in practice for some of the 2,5-benzoxazocine and 2,6-benzoxazonine skeletons reported in this study. These were characterized by both solution- and solid-state NMR spectroscopy together with X-ray crystallography, with the eventual goal of using this knowledge to control ring stereochemistry. Unfortunately, very detailed conformational analyses could not be presented within the size limitations of this chapter.

ACKNOWLEDGMENTS

This chapter is dedicated to the memory of the late Prof. Shimona Geresh, the Ph.D. research co-advisor to G. L.-R. and I. E. Her knowledge and wisdom in organic synthesis was an invaluable asset to the projects mentioned in this report. With great sorrow we note her passing on October 15, 2004.

REFERENCES

1. R. Glaser, I. Ergaz, G. Levi-Roso, A. Novoselsky, D. Shiftan and S. Geresh, manuscript in preparation.
2. M. Saunders and H. A. Jiménez-Vázques, *J. Comput. Chem.*, 1993, **14**, 330.
3. R. Glaser, D. Shiftan, G. Levi-Roso, I. Ergaz and S. Geresh, *J. Org. Chem.*, 2002, **67**, 5486.
4. K. Mislow and J. Siegel, *J. Am. Chem. Soc.*, 1984, **106**, 3319.
5. *CSChem3D Pro 5.0* and *CSChemDraw Ultra 5.0*, Cambridge Soft Inc., Cambridge, MA, 2000.
6. I. Kolossváry and W. C. Guida, *J. Am. Chem. Soc.*, 1993, **113**, 2107.
7. M. Goodman and M. Chorev, *Acct. Chem. Res.*, 1979, **12**, 1 and reference therein.
8. (a) *Cambridge Structural Database version 5.25*, Cambridge Crystallographic Data Center, Cambridge, UK, Nov. 2033; (b) F. H. Allen, *Acta Crystallogr.*, 2002, **B58**, 380.
9. (a) N. L. Allinger, Y. H. Yuh and J. H. Lii, *J. Am. Chem. Soc.*, 1989, **111**, 8551; (b) J. H. Lii and N. L. Allinger, *ibid*, 1989, **111**, 8566; (c) J. H. Lii and N. L. Allinger, *ibid*, 1989, **111**, 8576.
10. *Gaussian 03W, Revision B.04*, Gaussian, Inc., Pittsburgh, PA, 2003.
11. J. Dale, *Top. Stereochem.*, 1976, **9**, 199.

12. F. A. L. Anet and R. Anet, *Dynamic Nuclear Magnetic Resonance Spectroscopy*, L. M. Jackman and F. A. Cotton, eds., Academic Press, New York, 1975, pp. 547–619.
13. F. A. L. Anet, *Conformational Analysis*, G. Chiurdoglu ed., Academic Press, New York, 1971, p. 15.
14. F. J. Weigert and D. R. Strobach, *Org. Magn. Reson.*, 1970, **2**, 303.
15. F. A. L. Anet, *Tetrahedron Lett.*, 1990, **31**, 2125.
16. R. Glaser, J. F. Blount and K. Mislow, *J. Am. Chem. Soc.*, 1980, **102**, 2777.
17. A. Bielecki and D. P. Burum, *J. Magn. Reson.*, 1995, **A116**, 215.
18. R. Glaser, D. Shiftan and M. Drouin, *Can. J. Chem.*, 2000, **78**, 212.
19. X. Wu and K. W. Zilm, *J. Magn. Reson.*, 1993, **A102**, 205 and *ibid.* 1993, **A104**, 119.
20. R. Glaser, D. Shiftan and M. Drouin, *J. Org. Chem.*, 1999, **64**, 9217.
21. *The Merck Index*, S. Budavari, ed., 12th edition, Merck, Rahway, NJ, 1996, 1105 and references therein.
22. R. Glaser, G. Frenking, G. H. Loew, D. Donnell, S. Cohen and I. Agranat, *J. Chem. Soc., Perkin Trans.*, 1989, **2**, 113.
23. G. L. Closs, *J. Am. Chem. Soc.*, 1959, **81**, 5456.
24. R. Glaser, Q. -J. Peng and A. S. Perlin, *J. Org. Chem.*, 1988, **53**, 2172.
25. D. W. Newton and R. B. Kluza, *Principles of Medicinal Chemistry*, W. O. Foye, ed., 2nd edition, Lea and Febinger, Philadelphia, PA, 1981, pp. 901–908.
26. R. Glaser, G. Frenking, G. H. Loew, D. Donnell and I. Agranat, *New J. Chem.*, 1988, **12**, 953.
27. R. Glaser, I. Adin, D. Shiftan, Q. Shi, H. M. Deutsch, C. George, K. -M. Wu and M. Froimowitz, *J. Org. Chem.*, 1998, **63**, 1785.
28. J. B. Lambert, *J. Am. Chem. Soc.*, 1967, **89**, 1836.
29. R. Glaser, A. Novoselsky, D. Shiftan and M. Drouin, *J. Org. Chem.*, 2000, **65**, 6345.
30. R. Glaser, I. Adin, M. Drouin and A. Michel, *Struc. Chem.*, 1994, **5**, 197.
31. R. Glaser, *Magn. Reson. Chem.*, 1989, **27**, 1142.
32. R. Glaser, A. Peleg and S. Geresh, *Magn. Reson. Chem.*, 1990, **28**, 389.
33. R. Glaser, A. Michels and M. Drouin, *Can. J. Chem.*, 1990, **68**, 1128.
34. K. Schmidt-Rohr and H. W. Spiess, *Multidimensional Solid-State NMR and Polymers*, Academic Press, London, 1994, 174.
35. R. Glaser, S. Geresh, J. Blumenfeld, D. Donnell, N. Sugisaka, M. Drouin and A. Michel, *J. Pharm. Sci.*, 1993, **82**, 276.
36. P. H. M. Budzelaar, *gNMR version 4.1*, Cherwell Scientific Ltd., Oxford, UK, 1999.
37. K. Mislow, Princeton University, NJ, private communication to the author, 1978.
38. R. Glaser, J. Blumenfeld, S. Geresh, D. Donnnell, J. H. Rosland, K. Hole and K. Maartmann-Moe, *J. Pharm. Sci.*, 1993, **82**, 886.
39. R. Glaser, J. Blumenfeld and S. Geresh, *Magn. Reson. Chem.*, 1993, **31**, 845.
40. J. Bremner, E. J. Browne, L. M. Englehardt, I. W. K. Gunawardana and A. H. White, *Aust. J. Chem.*, 1988, **19**, 293.
41. R. Glaser, I. Adin, M. Drouin and J. B. Bremner, *New J. Chem.*, 1995, **19**, 1099.
42. J. B. Bremner and N. Thirasasana, *Aust. J. Chem.*, 1982, **35**, 2307.
43. R. Glaser, D. Shiftan and M. Drouin, *Struct. Chem.*, 1995, **6**, 25.
44. R. Glaser and A. Hadad, manuscript in preparation.

Methods and Applications of Quantitative MRI

JEAN-MARIE BONNY

INRA QuaPA, Centre expérimental de Theix, 63122 Saint Genes, Champanelle, France

The general objective of quantitative magnetic resonance imaging (MRI), or parametric mapping, consists of reconstructing synthetic images in which each voxel bears the value of a physical parameter selected a priori. Due to the large degrees of freedom in the choice of acquisition parameters, MRI is versatile and is thus able to quantify different types of physico-chemical parameters. While the steps that result in such mapping are closely dependent on the context, the present chapter attempts to describe, in a natural order, different strategies for obtaining an exploitable parametric map; i.e., the modeling of acquired data in terms of noise and signal, the optimization of the measurement protocol parameters and the actual methods of reconstruction that lead from the acquisition space to the parametric space.

1. INTRODUCTION

The general objective of quantitative magnetic resonance imaging (MRI) is to take visual analysis a step further and quantify a set of parameters from different acquisitions that can be analyzed *a posteriori* using statistical methods. The exploitation of the anatomic content of images serves a broad range of applications. Attributes can be calculated to characterize morphology or texture, for example. In our present definition, quantitative MRI has a narrower scope: it consists of reconstructing other images in which each voxel bears the value of a physical parameter selected *a priori*; in other words, parametric mapping.

ANNUAL REPORTS ON NMR SPECTROSCOPY
VOLUME 56 ISSN 0066 4103
DOI 10.1016/S0066-4103(05)56004-6

Due to the large degrees of freedom in the choice of acquisition parameters (type of sequence, delays, flip angles, use of magnitude or phase reconstruction, etc.), MRI is versatile and is thus able to quantify different types of physical and chemical parameters. The obvious utility of such parametric mapping is to associate spatial and quantitative information. Moreover, it ensures theoretically that the signal variation is due specifically to the variation in the considered parameter. It is thus helpful for interpretation because signal modification in a "weighted" MRI rarely results from the variation of a single parameter; e.g., a drying process induces both a reduction of moisture and a modification of water mobility. It is thus helpful to use quantitative approaches to separate possible concomitant contributions of the different intrinsic parameters in a single MRI. This is the case for example when T_2*-mapping is needed to separate the different contributions of the composite signal of a SPRITE sequence during a drying process.[1]

This chapter presents, in a natural order, the different steps for obtaining an exploitable parametric map; i.e., the modeling of acquired data in terms of noise and signal (Section 2), the optimization of the measurement protocol parameters (Section 3) and the actual methods of reconstruction that lead from the acquisition space to the parametric space (Section 4). The last part looks at certain applications and the current limits of these approaches (Section 5).

2. DEFINITION OF A MODEL FOR THE DATA

The modeling of the acquired data is a fundamental step because it determines the choice of the reconstruction technique and the quality of the parametric map obtained. This phase is delicate because it depends on both methodologic factors (sequence used) and the properties of the tissue being studied.

2.1. True response

For a given sequence, Bloch equations give the relationship between the explanatory variables, $\mathbf{x}$, and the true response, η. The p-dimensional vector, $\boldsymbol{\theta}$, corresponds to the unknown parameters that have to be estimated; $\mathbf{x}$ stands for the m-dimensional vector of experimental factors, i.e., the sequence parameters, that have an effect on the response. These factors may be scalar ($m = 1$), as previously described in the T_1-mapping protocol, or vector ($m > 1$); e.g., the direction of diffusion gradients in a diffusion tensor experiment.[2] The model $\eta(x; \boldsymbol{\theta})$ is generally non-linear and depends on the considered sequence. Non-linearity is due to the dependence of at least one first derivative $\partial\eta(x; \boldsymbol{\theta})/\partial\boldsymbol{\theta}_i$ on the value of at least one parameter, θ_i. The model integrates intrinsic parameters of the tissue (e.g., relaxation times, apparent diffusion coefficient), and also experimental nuclear magnetic resonance (NMR) factors which are not sufficiently controlled and so are unknown.

This is the case in T_1 mapping using an inversion recovery sequence and collecting n images at different inversion delays ($x = TI$). In this case,

$$\eta(x;\boldsymbol{\theta}) = k \cdot \mathrm{ABS}[1 - 2\theta_2 \exp(-x/\theta_1)], \tag{1}$$

Where θ_1 and θ_2 are, respectively, the intrinsic T_1 and an experimental factor accounting for a spatially dependent imperfect spin inversion. In some cases, generic parametric models (e.g., polynomial series) can be used to identify complicated responses, such as the free induction decay (FID) signal dephasing induced by the presence of magnetic field inhomogeneities.[3]

The validation is an essential step for checking the validity of the parametric model in the case of practical data. It is usually carried out by performing measurements on phantoms in the range of x judged of interest by the experimenter.[4–6] This approach is often tedious, especially when $m>1$, because the space of the experimental factors has to be scanned. In addition, the test objects often display characteristics that are remote from those of biologic tissues. For this reason, phantoms with more complex behavior have been proposed.[7,8]

2.2. Noise

After Fourier transform reconstruction, noise affecting both real and imaginary parts of MR complex images is generally considered as additive, uncorrelated, and with a spatially constant zero-mean Gaussian probability density function (pdf).[9] In practice, this is justified when fitting the model to complex data only if the information is contained in both magnitude and phase, which is the case for chemical shift imaging,[10,11] for the 3-point Dixon method for water and fat decomposition,[12] and in temperature mapping based on water proton chemical shift.[13,14] To obviate the handling of bi-spectral data, phase $y = \tan^{-1}(y_i/y_r)$ or magnitude $y = \sqrt{y_r^2 + y_i^2}$ reconstructions are usually performed. In most cases, the information of interest is carried by the magnetization amplitude, and so a magnitude reconstruction is performed to discard phase. Alternatively, phase reconstruction can be performed to discard magnitude. In general, phase data are rarely reconstructed mainly because this requires also applying an unwrapping method to improve dynamics and facilitate the interpretation of phase information.[15] Parametric mapping using phase information is preferentially derived from complex data, as in phase-encoded temperature[13,14] or flow-mapping[16,17] methods. Since noise affecting complex images is additive and stationary, noise properties do not depend on the value of the true signal. Conversely, when phase and magnitude transformations are applied, noise is no longer additive, but its impact depends in a complicated manner on the value of the true signal.

When a magnitude reconstruction is performed, the pdf of noisy magnitude signal y is given by the following Rice distribution:[18,19]

$$P_{Rice}(y;\eta(x;\boldsymbol{\theta}),\ \sigma) = \frac{y}{\sigma^2}\ \exp\left[-\frac{1}{2}\left(\frac{y}{\sigma}\right)^2 + \frac{1}{2}s^2\right] I_0\left[\frac{y}{\sigma}s\right], \tag{2}$$

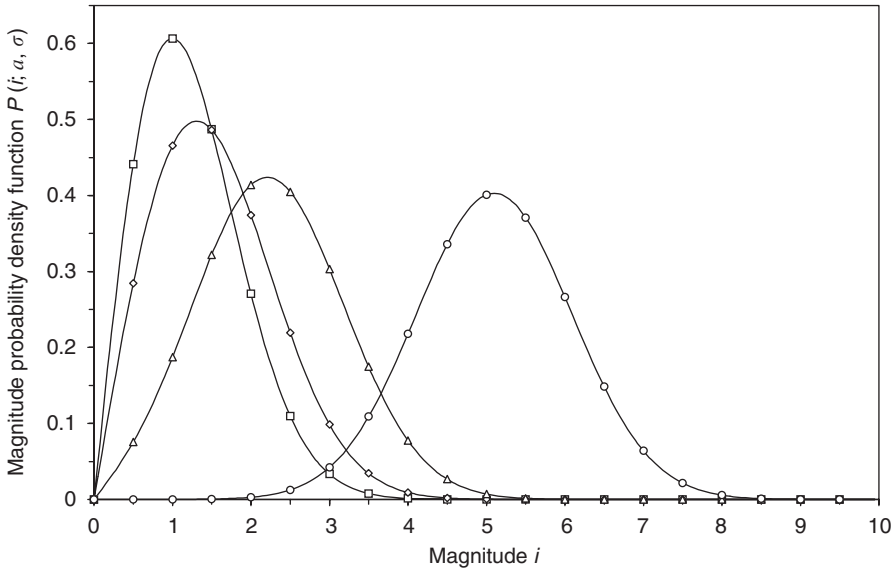

Fig. 1. Rice distribution of magnitude for several SNR ( ) S/N = 0, (◇) 1, (Δ) 2 and (○) 5. From Ref. 29, with permission.

where σ^2 is the variance of the noises corrupting the real and imaginary images, $s = \eta(x;\boldsymbol{\theta})/\sigma$ is the true signal-to-noise ratio (SNR), and I_0 is the zero-order modified Bessel function. It expresses the rectification of noisy signal to positive values. It is important to note that the statistical properties of noisy magnitude depend on the value of true amplitude $\eta(x;\boldsymbol{\theta})$ as shown in Fig. 1. In particular, the expectation value for the Rician distribution differs from the value of the true signal, which leads to systematic errors (bias), especially at low SNR.[20] For higher SNR (>3), Rice distribution can be considered as a Gaussian distribution with variance σ^2.[21,22] However, whatever the SNR, noisy magnitude is not strictly centered on $\eta(x;\boldsymbol{\theta})$ because[23]

$$E[P_{Rice}(y;\eta(x;\boldsymbol{\theta}),\sigma)] = \sigma\sqrt{\frac{\pi}{2}}\exp\left(-\frac{s^2}{4}\right)\left[\left(1+\frac{s^2}{2}\right)I_0\left(\frac{s^2}{4}\right)+\frac{s^2}{2}I_1\left(\frac{s^2}{4}\right)\right]$$
$$\approx \sqrt{\eta(x;\boldsymbol{\theta})^2+\sigma^2}. \tag{3}$$

When a phase reconstruction is performed, the pdf of noisy phase signal y is given by the following distribution:[24]

$$P_{Phase}(y;a,\sigma,\eta(x;\boldsymbol{\theta})) = \frac{1}{2\pi}\exp\left[-\frac{1}{2}\left(\frac{a}{\sigma}\right)^2\right]\left[1+\kappa\sqrt{\pi}\exp(\kappa^2)(1+\operatorname{erf}\kappa)\right], \tag{4}$$

with

$$\kappa = \frac{1}{\sqrt{2}}\frac{a}{\sigma}\cos[y-\eta(x;\boldsymbol{\theta})], \tag{5}$$

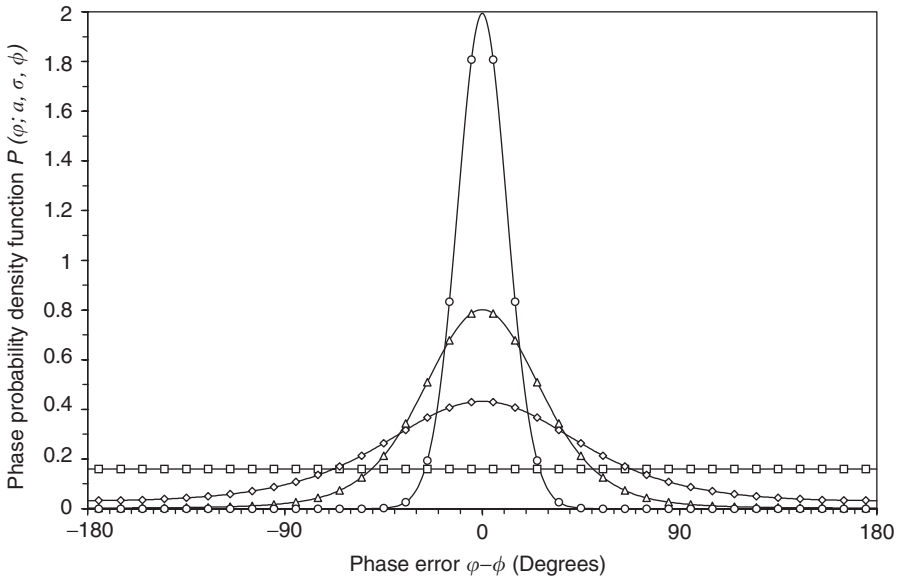

Fig. 2. The pdf of phase versus phase error (i.e., the deviation of noisy phase φ from its true value ϕ) for several SNR ( ) $a/\sigma = 0$, ($\diamond$) 1, (Δ) 2 and ($\circ$) 5. From Ref. 29, with permission.

where a denotes the true amplitude. It should be noted that the previous pdf depends on both the phase difference $(y - \eta)$, representing the deviation of noisy phase y from its true value η and the value of the SNR (more precisely magnitude-to-noise) $\frac{a}{\sigma}$. This means that the amplitude of stochastic deviations of y around the true value η is not spatially invariant. For large SNR, and as shown in Fig. 2, the phase pdf can be considered as a zero-mean Gaussian distribution with variance $(\sigma/a)^2$.[21,25] Also, contrary to magnitude reconstruction, the symmetry of phase pdf ensures that no bias is introduced by noise when a true model is fitted to noise phase samples.

2.3. Estimation of noise variance

The estimation of noise variance is important for:

- Segmenting background (noise-alone regions) from object (mixture of signal and noise), which is useful to avoid degrading the parametric map with aberrant values in the background.
- Estimating the SNR in each voxel, which is helpful for quantifying the performance of an acquisition process and for stating which kind of pdf can be considered for the noisy signal; e.g., Rice or Gaussian behavior for the noisy magnitude.
- Testing the fit.[26,27]

The most popular approach is supervised because a region of interest has to be defined in the background of the images in order to extract n samples. Afterward, the choice of the estimator depends on what kind of data is available. For complex images, the optimal maximum likelihood (ML) estimator of σ^2 is given by[28]

$$\hat{\sigma}^2 = \frac{1}{2n}\sum_{j=1}^{n}(y_{r,j}^2 + y_{i,j}^2), \tag{6}$$

where $y_{r,j}$ and $y_{i,j}$ correspond, respectively, to the real and imaginary parts of the jth sample ($j = 1,\ldots,n$). For magnitude images, the corresponding estimator is[29]

$$\hat{\sigma}^2 = \frac{1}{2n}\sum_{j=1}^{n} y_j^2, \tag{7}$$

where y_j refers here to the magnitude of the jth sample. Since it has been demonstrated recently that the mean-squared errors of the two estimators are the same,[28] the choice between the two approaches can be guided by practical arguments. In many cases, the magnitude reconstruction is performed by default, whereas complex data must be specifically reconstructed. It is certainly more important to know whether it is easier to define the regions belonging to the background in complex images than in module images. Owing to the spatial variations of the phase, which have different sources,[30] the complex images are marred by characteristic bands that modulate the signal in the regions of the object. Additional work then becomes necessary to validate the positioning of the region of interest on the two images, because the hypo-intense regions can translate particular phase values ($k\pi$ for the real part, $k\pi/2$ for the imaginary part), rather than areas belonging to the background (see Fig. 3). In conclusion, the main limitation of these methods is their operator dependency for characterizing the background region that has to be positioned outside the artifact areas (movement in particular). There is no validated general approach that allows such automatic positioning because the methods of object/background segmentation mostly use the value of σ^2 as *a priori* knowledge. The only non-supervised method is proposed by Sijbers *et al.*,[31] but it needs two images acquired *stricto sensu* in the same conditions.

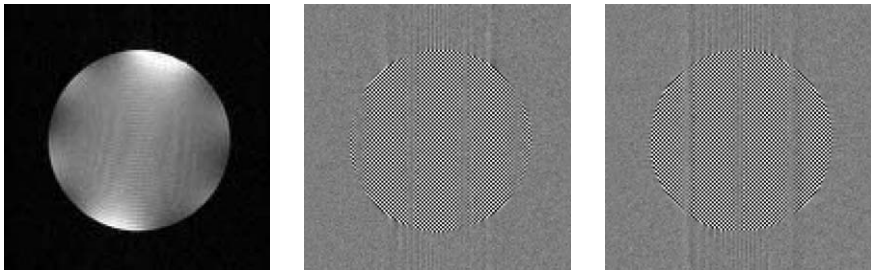

(Magnitude) (Real part) (Imaginary part)

Fig. 3. Magnitude and complex reconstructions obtained from the same raw data.

3. DESIGN OF THE QUANTITATIVE EXPERIMENT

A general measurement protocol consists of collecting n noisy samples by changing the value of the explanatory variables. To a vector $\mathbf{x}$ then corresponds a vector of measurements $\mathbf{y}$ in each voxel of the image. This section presents several strategies for choosing $\mathbf{x}$ in order to optimize the quality of estimation *a priori*.

3.1. Lower bounds of the estimation variance

To optimize or compare measurement protocols, an index of quality must be quantified for each estimated parameter. For a parameter taken separately, the performance of estimation is a function of both the variance (or precision) and the bias (or accuracy) of the estimate. The covariance matrix of each unbiased estimator $\hat{\boldsymbol{\theta}}$ checks the inequality of Frechet–Cramér-Rao:[24]

$$\mathrm{cov}(\hat{\boldsymbol{\theta}}) = \mathbf{E}[(\hat{\boldsymbol{\theta}} - \boldsymbol{\theta})(\hat{\boldsymbol{\theta}} - \boldsymbol{\theta})^T] \geqslant I^{-1}(\boldsymbol{\theta}). \tag{8}$$

Provided the estimator is unbiased, this expression indicates that the diagonal elements of the inverse information matrix, the Cramer-Rao bound (CRB), give the highest attainable variance of the unknown parameters. For zero-mean noise and a correct model η, no difference is expected between the values of the estimates and the true values. These minimal variances depend on the pdf of the signal, because the Fisher information matrix $\mathbf{I}$ is given by

$$\mathbf{I} = \mathrm{E}\left[\left(\frac{\partial \ln L(\mathbf{y};\boldsymbol{\theta})}{\partial \boldsymbol{\theta}}\right)\left(\frac{\partial \ln L(\mathbf{y};\boldsymbol{\theta})}{\partial \boldsymbol{\theta}}\right)^T\right], \tag{9}$$

where L is the likelihood function defined as the joint density of the n noisy observations:

$$L(\mathbf{y};\boldsymbol{\theta}) = \prod_{k=1}^{n} P(y_k;\boldsymbol{\theta}) = P(y_1;\boldsymbol{\theta}) \cdots P(y_n;\boldsymbol{\theta}). \tag{10}$$

Let us consider the case of n magnitude samples. In this case the likelihood function is equal to the product of the Rice pdf, which yields the following expression of the (i, j)th entry of the information matrix:[32]

$$I_{ij} = \sum_{k=1}^{n} \frac{\lambda_k}{\sigma_k^2} \frac{\partial \eta(x_k;\boldsymbol{\theta})}{\partial \theta_i} \frac{\partial \eta(x_k;\boldsymbol{\theta})}{\partial \theta_j}, \tag{11}$$

where σ_k^2 denotes the variance of the noises corrupting the kth complex image. The term λ_k is a weighting factor that depends on the magnitude-to-noise ratio $s_k = \eta(x_k;\boldsymbol{\theta})/\sigma_k$ of the kth sample:

$$\lambda_k = -s_k^2 + \int_0^{+\infty} \left[\frac{y}{\sigma_k} \frac{I_1}{I_0}\left(\frac{y}{\sigma_k} s_k\right)\right]^2 P_{Rice}(y;\eta(x_k;\boldsymbol{\theta}),\sigma_k)\, dy, \tag{12}$$

where I_1 is the first-order modified Bessel function ($I_1 = I_0'$). The latter approaches unity as the magnitude-to-noise ratio increases (see Fig. 4). When $\lambda_k = 1$, the Fisher matrix takes the form of the curvature matrix which corresponds to the case of zero-mean additive Gaussian noise. When this condition is met, it may be possible to derive an analytical expression of CRB (e.g., Refs. 22,33,34). When Rician effects have to be taken into account, the derivation of analytical expressions of CRB is intractable due to the integral formulation of λ_k which has to be calculated numerically. For this purpose, the main difficulty arises from the evaluation of the ratio of modified Bessel functions $\frac{I_1}{I_0}$ (x), for which Hill has proposed a practical procedure.[21]

Fig. 5 represents the CRB of θ_2 for the following mono-exponential model:

$$\eta(x; \boldsymbol{\theta}) = \theta_1 \exp(-x/\theta_2). \tag{13}$$

The region near the minimum of the υ-shape indicates the range in which the parameter θ_2 may be estimated with a low uncertainty. At low SNR (= 10) and when the exponential curve is sampled at two points $\mathbf{x} = [10, 80]^{\mathrm{T}}$, the minimal bound is equal to ~34%, which is unacceptable in many practical situations. To reduce this value and enlarge the region of acceptable variance, an obvious solution is to increase the SNR. When Rician effects can be neglected, the CRB are inversely proportional to the SNR. In the example presented in Fig. 5, a Rician effect produces an increase of CRB for low θ_2 that is difficult to assess visually. Also, the minimum of CRB is not the same for the two conditions of SNR in contrast to the case of zero-mean additive Gaussian noise; CRB reaches a minimum for $\theta_2 \approx 71$ ms when $\theta_1/\sigma = 100$ and $\theta_2 \approx 75$ ms when $\theta_1/\sigma = 10$. Fig. 5b allows also to forecast the effect of a more dense sampling, which induces a global decrease of CRB and a broadening of the region of acceptable variance.

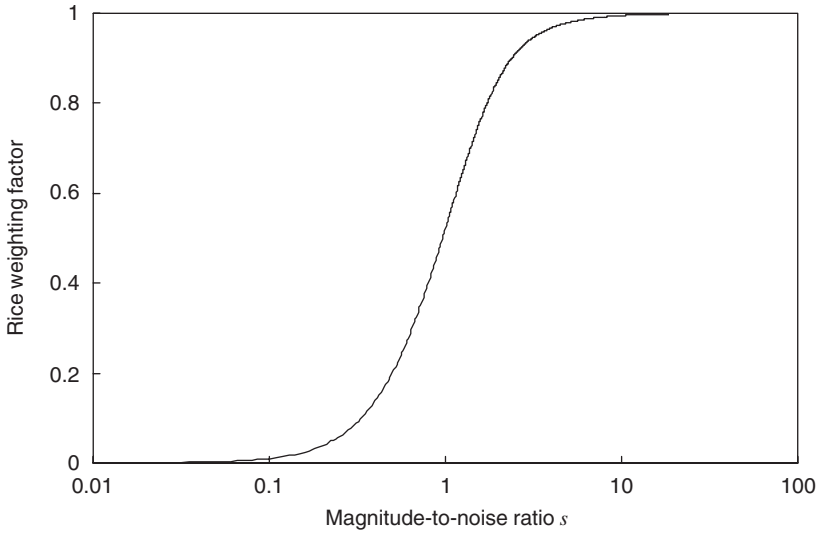

Fig. 4. Weighting factor λ, necessary for the computation of CRB with Rician distributed data, versus magnitude-to-noise ratio.

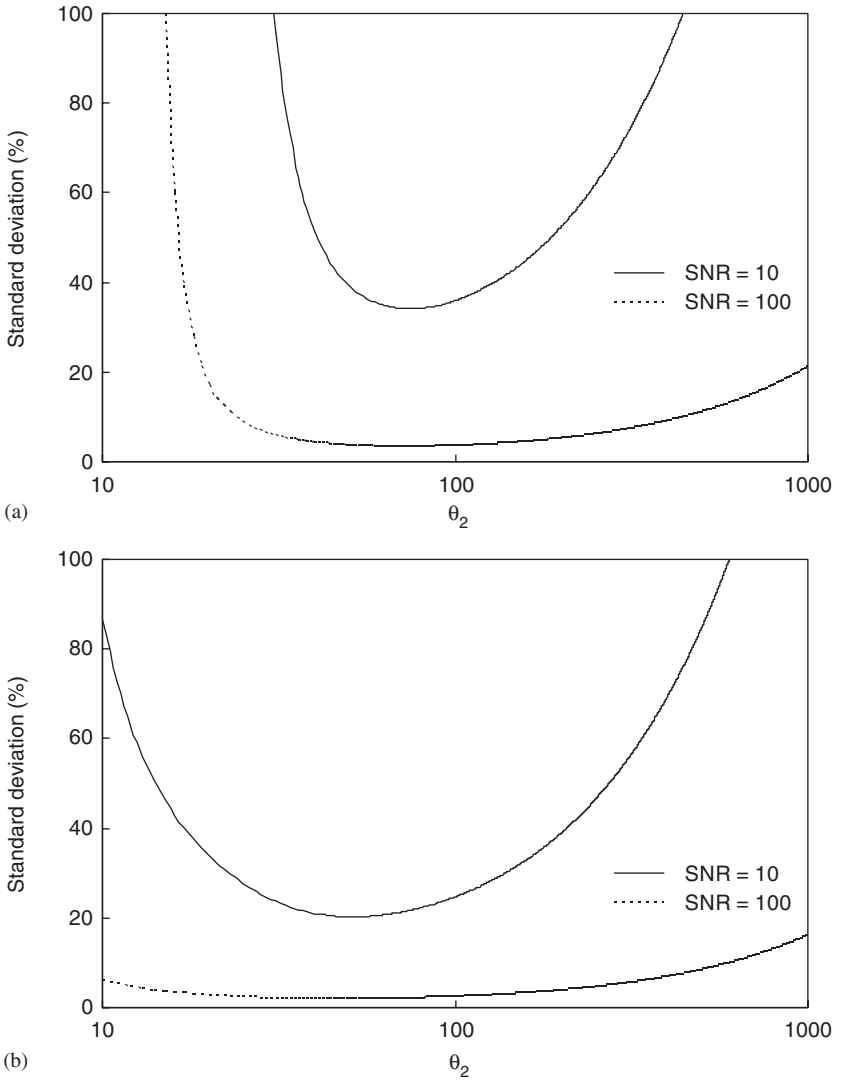

Fig. 5. CRB of the parameter θ_2 for the mono-exponential model $\eta(x;\boldsymbol{\theta}) = \theta_1 \exp(-x/\theta_2)$ for two SNR θ_1/σ. CRB computation considers the Rician behavior of the measurements due to magnitude reconstruction. The exponential curve is sampled at two points $\mathbf{x} = [10, 80]^{\mathrm{T}}$ for (a) and at $\mathbf{x} = [10, 20, 30, 40, 50, 60, 70, 80]^{\mathrm{T}}$ for (b).

This example has been chosen to show that it is possible to calculate the optimal performance of a measurement protocol in conditions close to those in the field. For a set value of θ (actually the unknown parameter) it is then possible to seek the value of $\mathbf{x}$ that minimizes CRB for a set number n. This optimization is often impossible to carry out analytically when $n > 2$ and/or when matrix $\mathbf{I}$ has a complex

form. Multidimensional methods of optimization are then used. CRB is now a well-established criterion for optimizing the choice of experimental parameters $\mathbf{x}$, for example when estimating relaxation time T_1,[33,35] parameters characterizing mono-[36,37] or multi-exponential[38] processes, diffusion tensor[39], or respective fractions of water and fat by Dixon 3-point type imaging.[40] CRB has the advantage of being an absolute criterion that does not depend on the estimator chosen, unlike, in particular, the simulations described below. In addition, the calculation of CRB is relatively simple (evaluation of partial derivatives and matrix inversion) and therefore rapid.

3.2. Strategies for the optimization of the measurement protocol

Although CRB rapidly gives an idea of the optimum that can be reached for the pdf encountered in MRI, it must be borne in mind that CRB is a valid limit only for non-biased estimators. However, the absence of bias in the estimators (consistency) and the fact that the variance of the estimations tends to CRB (efficiency) is only guaranteed asymptotically, i.e., for a large number (n) of samples, as for estimators in the sense of ML. As in practice the number of images n is limited, a prior step in optimizing protocols using CRB as criterion is therefore to check the convergence of the variance of estimations toward CRB for the estimator considered. Monte-Carlo simulations are a generic approach to carrying out this checking.

The example in Fig. 6 shows how the densities of least-squares (LS) estimators depend on the SNR. At high SNR (= 100), the simulated density of parameter $\hat{\theta}_2$ converges nicely toward a Gaussian asymptotic distribution of variance equal to the CRB, even for a reduced number of samples ($n = 2$). On the contrary, at low SNR (= 10), the simulated density is asymmetric and differs significantly from the Gaussian one. As an LS estimator is biased for Rician distributed data, CRB is an imperfect indicator of estimator performance over a wide range of SNR. This example underlines the importance of studying the validity of a CRB-based criterion over a sufficiently wide range of conditions, which should mimic experimental ones.

An extension of the CRB approach can be to minimize not only the minimal uncertainties but also both bias and variance in order to consider the use of biased estimators. Bias and variance result from a trade-off, and so it is possible to reduce the variance of estimates by tolerating an increase in the bias. For this purpose an extension of the CRB has been introduced by Hero *et al.*,[41] which represents the variance of estimates as function of the norm of the bias gradient. This curve shows the achievable trade-off between bias and variance.

If the estimator is known (unlike CRB), it is possible to compute a criterion that considers the densities of the estimates themselves rather than the asymptotic normal approximation. A generic but computationally intensive approach is based on simulating a large number of estimates, as was done to generate Fig. 6. In the case of an LS estimator, an alternative is to approximate the densities of $\hat{\boldsymbol{\theta}}_{\mathrm{LS}}$ using the analytical expression introduced by Pazman,[42] which is much more complicated to

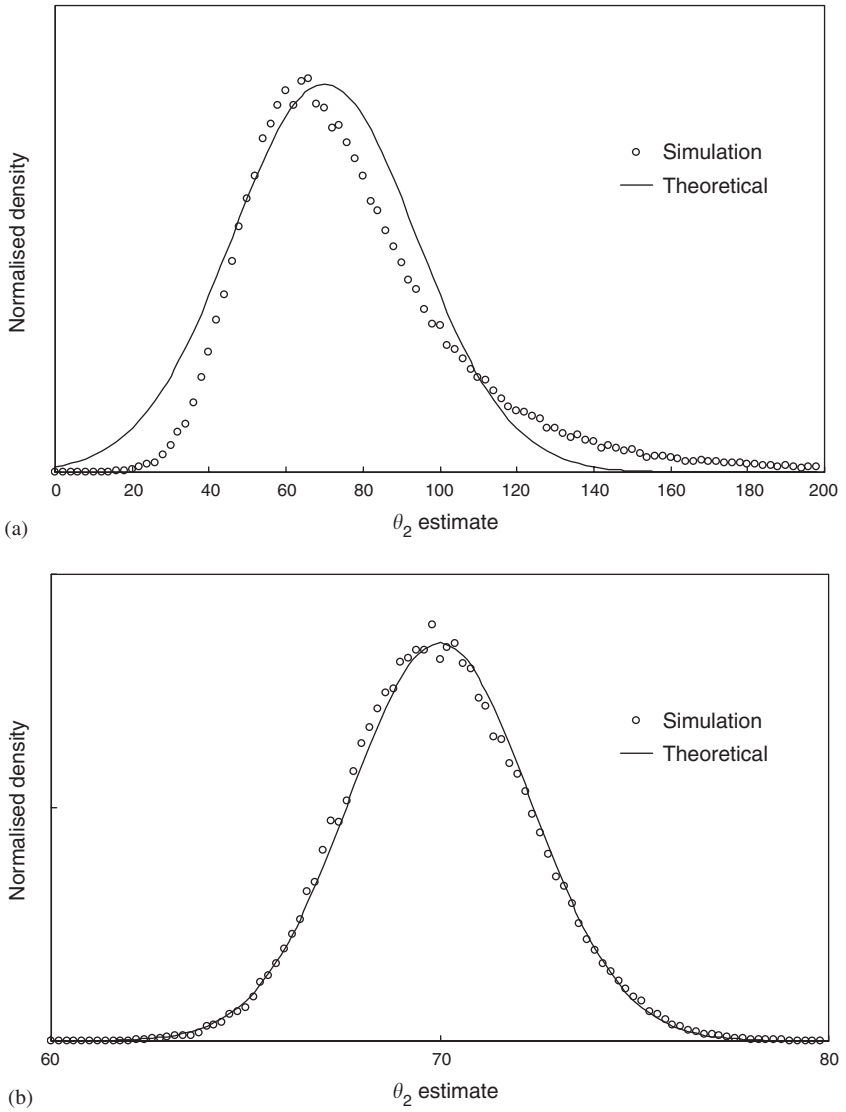

Fig. 6. Comparison of simulated and asymptotical densities of the estimated parameter $\hat{\theta}_2$ for the mono-exponential model $\eta(x;\boldsymbol{\theta}) = \theta_1 \exp(-x/\theta_2)$ for two SNR: (a) $\theta_1/\sigma = 10$ and (b) $\theta_1/\sigma = 100$. The exponential curve was sampled at two points $\mathbf{x} = [10, 80]^{\mathrm{T}}$ and the parameters of the model were obtained by LS estimator from Rician distributed samples. Simulated density results from 10^5 data vectors, the asymptotical density is a Gaussian distribution centered on the true value $\theta_2 = 70$ with a variance equal to the CRBs.

evaluate compared with the computation of CRB; or an optimization criterion can be derived from these densities in order to optimize the design of the experiment.[43] Lastly, other criteria have been defined by the theory of optimal design in non-linear models[44,45] which proposes a general mathematical framework for optimizing a measurement protocol.

4. RECONSTRUCTION OF PARAMETRIC MAPS

4.1. Preprocessing

The aim of quantitative imaging is to extract information present simultaneously in several images. Hence the first necessary condition is to have images that are perfectly aligned spatially. There are numerous programs for registrating images to correct any shifts due, for example, to movement or geometrical distortions.[46] In parametric imaging, the technique must take into account the fact that the contrast varies among the images to be aligned, as for the registration of images from different modalities. In tensor-diffusion imaging where the geometrical distortions due to eddy currents are marked, and depend on the intensity and the direction of diffusion gradients, efficient techniques have been proposed based on mutual information maximization.[47,48]

In general, the error (i.e., bias and variance) in the estimated parameter will be lower if uncertainty in the data due to noise is low. It is therefore judicious to filter the images before the estimation phase. In quantitative MRI, the filter used must first preserve the image outline; i.e., not cause smoothing outside the areas considered homogeneous. The filters must accordingly be chosen among non-linear filters. In addition, the spatial smoothing must take into account the pdf of the signal. Filters using simple spatial means assume centered additive Gaussian noise, which is not always valid in MRI, especially in the very frequent case of module reconstruction. Some non-linear quantitative filters meet these two constraints; they use approaches based on decomposition into wavelets [49–51] or anisotropic diffusion filtering.[52]

A third important property is the ability to filter the n available images simultaneously. The utility here is to define the extent of the regions to be smoothed in a robust manner, using all the available information, rather than on the basis of the contrast available on a single image. The utility is also to carry out the smoothing locally on the same areas for all the images. An adaptation of the filter of Soltanian-Zadeh *et al.*[53] has been proposed to meet these three criteria.[54] A multidimensional criterion (interframe discrimination step) is used to decide locally whether two points belong to the same region. Its principle is to position the window around the central point so as to have K-noised vectors, $\mathbf{y}^1,\ldots,\mathbf{y}^K$. To decide whether two points belong to the same region, the Euclidean distance between the central point and each point in the window is calculated and compared with a threshold. This distance is a particular case for $\gamma = 2$ in the general Minkowski metrics

defined by

$$||\mathbf{y}^i - \mathbf{y}^j||_\gamma = \left(\sum_{k=1}^{n} \left| y_k^i - y_k^j \right|^\gamma \right)^{\frac{1}{\gamma}}, \tag{14}$$

commonly used in non-linear multispectral filtering.[47] To allow for the Rician nature of the data and estimate, from the P samples selected ($P \leqslant K$), the true value η of the signal in the image of index i, several estimators are possible; the unbiased estimator $\hat{\eta}_{Quadratic}$ based on the quadratic mean given by[55,56]

$$\mu = \frac{1}{P} \sum_{j=1}^{P} y_i^{j^2} - 2\sigma_i^2 \tag{15}$$

$$\text{if } \mu \geqslant 0 \text{ then } \hat{\eta}_{Quadratic} = \sqrt{\mu} \text{ else } \hat{\eta}_{Quadratic} = 0 \tag{16}$$

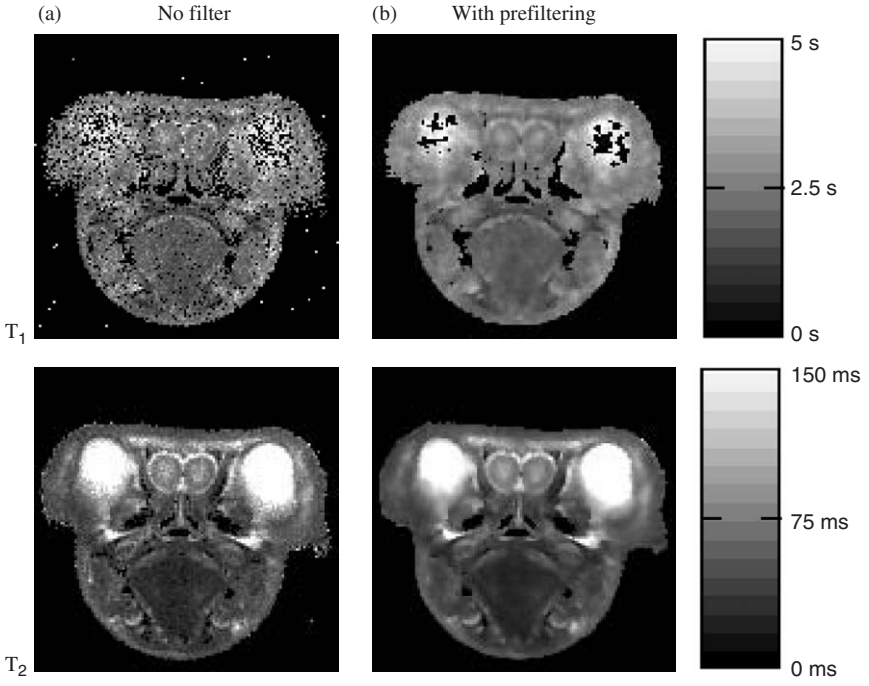

Fig. 7. T_1 and T_2 maps of the olfactory bulb of a young rabbit reconstructed directly from the noisy experimental images (a) and from the same images preliminary denoised by a quantitative multispectral non-linear edge-preserving filter (b). For T_1 mapping, the recovery curve of a Spin–Echo sequence was sampled at $n = 8$ different repetition times, $\mathbf{x} =$ [500, 1000, 1500, 2000, 2500, 3000, 4000, 5000]^T. For T_2 mapping, the decay curve of the same Spin–Echo sequence was sampled at $n = 5$ different echo times, $\mathbf{x} =$ [10, 35, 60, 85, 110]^T. For both, the model considers a single exponential term and the reconstruction is performed using LS approach.

or the ML $\hat{\eta}_{ML}$ estimator, first introduced in Ref. 29 obtained by solving

$$\hat{\eta}_{ML} - \frac{1}{P}\sum_{j=1}^{P} y_i^j \frac{I_1}{I_0}\left(\frac{y_i^j \hat{\eta}_{ML}}{\sigma_i^2}\right) = 0. \tag{17}$$

Implementation details and properties of these two approaches are discussed in Refs. 23,29,54.

The general utility of using modified multidimensional non-linear edge preserving is to improve the SNR of acquired data and reduce the bias introd uced by estimation schemes that are not designed to take into account the Rician behavior of the magnitude signal. This approach is thus useful when several regions of acquired images display a low SNR (<5) such as in analysis of T_2 decays,[54] or in the interpretation of diffusion data obtained at high b-values.[57,58] The efficiency of prefiltering the acquired data is underlined by Fig. 7 which compares parametric maps reconstructed directly from original data and from filtered ones.

4.2. Estimation of the parameters q

Obtaining parametric maps necessarily requires estimating the vector of the parameter $\boldsymbol{\theta}$ from n-noised samples. The general theory of estimation[59,60] provides solutions that can be applied in the domain of quantitative MRI. In practice, the ML approach is the most commonly used, because it concerns the estimation of non-random parameters, unlike the Bayesian approach, which is mostly applied to segment the images.[61] The LS approaches defined by

$$\hat{\boldsymbol{\theta}}_{\mathrm{LS}} = \arg\ \min \sum_{i=1}^{n} \frac{1}{\sigma_i^2}[y_i^2 - \eta(x_i;\boldsymbol{\theta})^2]^{1/2} \tag{18}$$

are very popular because of the efficacy of the minimization algorithms (e.g., Marquardt–Levenberg and Newton-type routines); and are equivalent to the ML approaches for centered additive Gaussian noise, which is valid for complex data, and those reconstructed in a module or phase when the SNR is high (*cf.* Section 2.2 Noise). Recently, ML estimators adapted to Rician data have been developed.[32] The ML estimation is then obtained by solving the following stationarity equation:

$$\sum_{i=1}^{n} \frac{1}{\sigma_i^2}\left\{ y_i \frac{I_1}{I_0}\left[\frac{y_i \cdot \eta(x_i;\boldsymbol{\theta})}{\sigma_i^2}\right] - \eta(x_i;\boldsymbol{\theta})\right\} \frac{\partial \eta(x_i;\boldsymbol{\theta})}{\partial \boldsymbol{\theta}} = \mathbf{0}. \tag{19}$$

As stated above, the utility of the ML estimators derives essentially from their asymptotic properties of consistency and optimality (i.e., $\mathrm{cov}(\hat{\boldsymbol{\theta}}_{\mathrm{ML}}) \overset{n\to\infty}{\longrightarrow} \mathbf{CRB}$). When the data exhibits significant departures from theoretical pdf (Gaussian or Rice) owing to acquisition artifacts, it may be judicious to use robust non-linear regression techniques,[62] as in parametric diffusion-tensor imaging reconstructed from echo-planar data.[63]

5. DISCUSSION/CONCLUSION

It is difficult to make an exhaustive list of the applications of quantitative imaging, because a large number of parameters are quantifiable; proton density, relaxation time (T_1, T_2, T_2^* or T_2', $T_1\rho$), data qualifying interaction of pools by magnetization transfer, apparent diffusion coefficients, indices characterizing diffusion phenomena from tensor estimation or a q-space approach, temperature difference, static magnetic field, B1 field amplitude, current density or values related to dynamic MRI contrast agent uptake.

Besides it is important to associate with these parametric maps another map giving confidence intervals for each of the parameters estimated insofar as this uncertainty strongly depends on the value of $\boldsymbol{\theta}$. This can be done by quantifying a goodness-of-fit criterion based on the classic χ^2 [64–66] or on one normalized by the total energy of the signal. The latter is sensitive not only to fitting error but also to the SNR.[67] CRB can also be an index of confidence related directly to the uncertainties of $\hat{\boldsymbol{\theta}}$.[32,66] However, the true value in the general equation (11) is still unknown and must be replaced by the estimate. This introduces a disruptive effect where the precision of the CRB-based index of confidence will itself depend on the uncertainties of the estimates.

One of the difficulties of quantitative imaging is that each of the steps that result in parametric mapping is closely dependent on the context, and especially on the model and the distortions induced by the measurement protocol. To our knowledge, no software package is currently available that will manage all the tasks described in this chapter. As efficient softwares for such optimization and reconstruction becomes more generic and commonly available, such techniques will be certainly applied with increasing frequency and efficiency.

REFERENCES

1. I. V. Mastikhin, H. Mullally, B. MacMillan and B. J. Balcom, *J. Magn. Reson.*, 2002, **156**(1), 122–130.
2. P. J. Basser, J. Mattiello and D. LeBihan, *Biophys. J.*, 1994, **66**(1), 259–267.
3. D. A. Yablonskiy, *Magn. Reson. Med.*, 1998, **39**(3), 417–428.
4. P. S. Tofts, D. Lloyd, C. A. Clark, G. J. Barker, G. J. Parker, P. McConville, C. Baldock and J. M. Pope, *Magn. Reson. Med.*, 2000, **43**(3), 368–374.
5. R. A. Lerski, D. W. McRobbie, K. Straughan, P. M. Walker, J. D. de Certaines and A. M. Bernard, *Magn. Reson. Imaging*, 1988, **6**(2), 201–214.
6. R. A. Lerski, D. W. McRobbie, K. Straughan, P. M. Walker, J. D. de Certaines and A. M. Bernard Protocols, test objects for the assessment of MRI equipment, *Magn. Reson. Imaging,*, 1988, **6**(2), 195–199.
7. C. Jones, A. MacKay and B. Rutt, *Magn. Reson. Imaging*, 1998, **16**(1), 83–85.
8. Z. Ababneh, M. Haque, S. E. Maier and R. V. Mulkern, *MAGMA*, 2004, **17**(2), 95–100.
9. E. R. McVeigh, R. M. Henkelman and M. J. Bronskill, *Med. Phys.*, 1985, **12**(5), 586–591.
10. A. A. Maudsley and S. K. Hilal, *Magn. Reson. Med.*, 1985, **2**(3), 218–233.
11. B. J. Soher, K. Young, V. Govindaraju and A. A. Maudsley, *Magn. Reson. Med.*, 1998, **40**(6), 822–831.
12. G. H. Glover and E. Schneider, *Magn. Reson. Med.*, 1991, **18**(2), 371–383.

13. Y. Ishihara, A. Calderon, H. Watanabe, K. Okamoto, Y. Suzuki, K. Kuroda and Y. Suzuki, *Magn. Reson. Med.*, 1995, **34**(6), 814–823.
14. J. De Poorter, *Magn. Reson. Med.*, 1995, **34**(3), 359–367.
15. S. Chavez, Q. S. Xiang and L. An, *IEEE Trans. Med. Imaging*, 2002, **21**(8), 966–977.
16. P. R. Moran, *Magn. Reson. Imaging*, 1982, **1**(4), 197–203.
17. J. Bittoun, O. Jolivet, A. Herment, E. Itti, E. Durand, E. Mousseaux and J. P. Tasu, *Magn. Reson. Med.*, 2000, **44**(5), 723–730.
18. J. E. Holden, J. R. Halama and B. H. Hasegawa, *Phys. Med. Biol.*, 1986, **31**(4), 383–396.
19. H. Gudbjartsson and S. Patz, *Magn. Reson. Med.*, 1995, **34**(6), 910–914 [*Erratum in Magn. Reson. Med.*, 1996, **36**(2), 332].
20. R. M. Henkelman, *Med. Phys.*, 1985, **12**(2), 232–233.
21. G. W. Hill, *ACM Trans. Math. Software*, 1981, **7**(2), 199–208.
22. J. M. Bonny, M. Zanca, J. Y. Boire and A. Veyre, *Magn. Reson. Med.*, 1996, **36**(2), 287–293.
23. J. Sijbers, A. J. den Dekker, P. Scheunders and D. Van Dyck, *IEEE Trans. Med. Imaging*, 1998, **17**(3), 357–361.
24. C. R. Rao, *Proc. Camb. Philos. Soc.*, 1946, **43**, 280–283.
25. T. E. Conturo and G. D. Smith, *Magn. Reson. Med.*, 1990, **15**(3), 420–437.
26. P. R. Bevington and D. K. Robinson, *Data Reduction and Error Analysis for the Physical Sciences*, McGraw-Hill, New York, 1992, 194–220.
27. S. J. Graham, P. L. Stanchev and M. J. Bronskill, *Magn. Reson. Med.*, 1996, **35**(3), 370–378.
28. J. Sijbers and A. J. den Dekker, *Magn. Reson. Med.*, 2004, **51**(3), 586–594.
29. J. M. Bonny, J. P. Renou and M. Zanca, *J. Magn. Reson.*, 1996, **113**(2), 136–144.
30. J. R. MacFall, N. J. Pelc and R. M. Vavrek, *Magn. Reson. Imaging*, 1988, **6**(2), 143–155.
31. J. Sijbers, A. J. den Dekker, J. Van Audekerke, M. Verhoye and D. Van Dyck, *Magn. Reson. Imaging*, 1998, **16**(1), 87–90.
32. O. T. Karlsen, R. Verhagen and W. M. Bovee, *Magn. Reson. Med.*, 1999, **41**(3), 614–623.
33. A. P. Crawley and R. M. Henkelman, *Magn. Reson. Med.*, 1988, **7**(1), 23–34.
34. S. Cavassila, S. Deval, C. Huegen, D. van Ormondt and D. Graveron-Demilly, *J. Magn. Reson.*, 2000, **143**(2), 311–320.
35. R. J. Kurland, *Magn. Reson. Med.*, 1985, **2**(2), 136–158.
36. J. A. Jones, P. Hodgkinson, A. L. Barker and P. J. Hore, *J. Magn. Reson.*, 1996, **113**, 25–34.
37. O. Brihuega-Moreno, F. P. Heese and L. D. Hall, *Magn. Reson. Med.*, 2003, **50**(5), 1069–1076.
38. A. Anastasiou and L. D. Hall, *Magn. Reson. Imaging*, 2004, **22**(1), 67–80.
39. N. G. Papadakis, D. Xing, C. L. Huang, L. D. Hall and T. A. Carpenter, *J. Magn. Reson.*, 1999, **137**(1), 67–82.
40. A. R. Pineda, S. B. Reeder, Z. Wen, H. Yu and N. J. Pelc, *Cramér-Rao Bounds for 3-point Dixon Imaging*, ISMRM, Kyoto, 2004, 2197.
41. A. O. Hero, J. A. Fessler and M. Unsman, *IEEE Trans. Signal Process.*, 1996, **44**(8), 2026–2041.
42. A. Pazman, *Statistics*, 1990, **21**, 1–33.
43. A. Pazman and L. Pronzato, *J. Stat. Plan. Infer.*, 1992, **33**(3), 385–402.
44. V. V. Fedorov, *Theory of Optimal Experiments*, Academic Press, New York, 1972.
45. A. C. Atkinson, *J. Royal Stat. Soc.*, 1996, **58**(1), 59–76.
46. V. L. Morgan, D. R. Pickens, S. L. Hartmann and R. R. Price, *Magn. Reson. Med.*, 2001, **46**(3), 510–514.
47. K. N. Plataniotis, D. Androutsos and A. N. Venetsanopoulos, *Signal Process. Image Commun.*, 1997, **9**, 143–158.
48. J. F. Nielsen, N. R. Ghugre and A. Panigrahy, *Magn. Reson. Imaging*, 2004, **22**(9), 1319–1323.
49. S. Zaroubi and G. Goelman, *Magn. Reson. Imaging*, 2000, **18**(1), 59–68.
50. R. D. Nowak, *IEEE Trans. Image Process.*, 1999, **8**(10), 1408–1419.
51. M. E. Alexander, R. Baumgartner, A. R. Summers, C. Windischberger, M. Klarhoefer, E. Moser and R. L. Somorjai, *Magn. Reson. Imaging*, 2000, **18**(2), 169–180.
52. J. Sijbers, A. J. den Dekker, A. Van der Linden, T. M. Verhoye and D. Van Dyck, *Magn. Reson. Imaging*, 1999, **17**(10), 1533–1539.

53. H. Soltanian-Zadeh, J. P. Windham and A. E. Yagle, *IEEE Trans. Image Process.*, 1995, **4**(2), 147–161.
54. J. M. Bonny, O. Boespflug-Tanguly, M. Zanca and J. P. Renou, *J. Magn. Reson.*, 2003, **161**(1), 25–34.
55. G. McGibney and M. R. Smith, *Med. Phys.*, 1993, **20**(4), 1077–1078.
56. A. J. Miller and P. M. Joseph, *Magn. Reson. Imaging*, 1993, **11**(7), 1051–1056.
57. O. Dietrich, S. Heiland and K. Sartor, *Magn. Reson. Med.*, 2001, **45**(3), 448–453.
58. D. K. Jones and P. J. Basser, *Magn. Reson. Med.*, 2004, **52**(5), 979–993.
59. H. L. VanTrees, *Detection, Estimation, and Modulation Theory: Part I*, Wiley, New York, 1968.
60. A. Papoulis, *Probability, Random Variables, and Stochastic Processes*, McGraw-Hill, New York, 1991.
61. P. A. Bromiley, N. A. Thacker, M. L. J. Scott, M. Pokric, A. J. Lacey and T. F. Cootes, *Image Vision Comput.*, 2003, **21**(10), 851–864.
62. P. Meer, D. Mintz and A. Rosenfeld, *Inter. J. Comput. Vision*, 1991, **6**(1), 59–70.
63. J. F. Mangin, C. Poupon, C. Clark, D. Le Bihan and I. Bloch, *Med. Image Anal.*, 2002, **6**(3), 191–198.
64. K. H. Cheng, *Magn. Reson. Imaging*, 1994, **12**(7), 1099–1109.
65. W. E. Reddick, R. J. Ogg, R. G. Steen and J. S. Taylor, *J. Magn. Reson. Imaging*, 1996, **6**(1), 244–249.
66. K. Young, D. Khetselius, B. J. Soher and A. A. Maudsley, *Magn. Reson. Med.*, 2000, **44**(4), 537–545.
67. N. G. Papadakis, K. M. Martin, I. D. Wilkinson and C. L. Huang, *J. Magn. Reson.*, 2003, **164**(1), 1–9.

Secondary Relaxation Processes in Molecular Glasses Studied by Nuclear Magnetic Resonance Spectroscopy

M. VOGEL[1], P. MEDICK[2] AND E.A. RÖSSLER[2]

[1]*Institut für Physikalische Chemie, Westfälische Wilhelms-Universität Münster, Correnstrasse 30, 48149 Münster, Germany*
[2]*Experimentalphysik II, Universität Bayreuth, 95440 Bayreuth, Germany*

We review nuclear magnetic resonance (NMR) studies of secondary relaxation processes in glasses. The main focus is work on molecular glasses, where the secondary relaxation is usually associated with spatially highly restricted motion. We show that NMR is well suited to study such highly hindered motion when the spatial resolution of the standard echo techniques is improved. The NMR results are discussed in the framework of findings from other experimental techniques so as to provide a comprehensive picture of secondary relaxation processes in glasses.

1. INTRODUCTION

As compared to crystalline materials, amorphous materials show distinguished physical properties, which are in widespread use in modern life. Nevertheless, the nature of the glassy state is still a matter of vigorous scientific debate. There are several routes of producing amorphous matter. A simple way is to avoid crystallization and

ANNUAL REPORTS ON NMR SPECTROSCOPY
VOLUME 56 ISSN 0066 4103
DOI 10.1016/S0066-4103(05)56005-8

super-cool a liquid. Though not always easily achieved, super-cooling a liquid results in a strong continuous increase of the viscosity. For many liquids, the viscosity increases by more than ten orders of magnitude within some tens of kelvin. Eventually, the viscous flow becomes so slow that the system can be regarded as a solid body. This viscous freezing is referred to as the glass transition, and liquids that have passed through the glass transition are called glasses. Conventionally, a value of 10^{12} Pa s is chosen to mark the glass transition temperature T_g, which is accompanied by a step in the thermal expansion coefficient. Since structural relaxation does not occur well below T_g, the system is trapped in a non-equilibrium state, where the glass essentially keeps the structure of the liquid due to the absence of a first-order phase transition while cooling. There is still no agreement on the driving forces of this extraordinary phenomenon of vitreous solidification, though important progress has been made in the last decades.

All liquids can be vitrified provided that the cooling rate is sufficiently high. For example, glasses can be prepared from polymeric or metallic melts. One group of liquids is of particular interest, namely molecular liquids, since their glass transitions can be studied by a large variety of experimental techniques. Moreover, they are models of van der Waals liquids, which are often examined in molecular dynamics simulations and theoretical approaches. There is actually only a small group of molecular liquids that can easily be super-cooled, and this group has been investigated thoroughly in recent years.

One of the most exciting properties of glasses, and not found in crystals, is the occurrence of molecular motion virtually on all time scales. On the one hand, the structural relaxation (α-process), which destroys all the correlation in time, slows down from the picosecond (ps) regime in the high-temperature liquid to about 100 s near T_g. On the other hand, basically independent of temperature, any molecular dynamics starts with attempt frequencies on the sub-ps scale. Therefore, upon cooling the liquid, a large gap opens in between the time scales of α-process and microscopic dynamics, which is filled by the emergence of secondary relaxation processes. Near T_g, more than 14 orders of magnitude in time or frequency have to be covered by the various techniques to study the nature of molecular motion.

From its very beginning nuclear magnetic resonance (NMR) was used to unravel dynamic processes in amorphous matter, where the high selectivity of this technique was exploited. Recent progress has largely benefited from the development of multidimensional NMR spectroscopy, significantly extending the traditional techniques such as spin–lattice relaxation and line-shape analyses. Modern NMR techniques helped a lot to understand the molecular dynamics in disordered systems such as the α-process.

Below T_g, structural relaxation is too slow to be observable, but secondary processes persist, which determine, e.g., the mechanical and dielectric properties of glasses. These processes have been extensively studied for polymers, where they are usually associated with polymer-specific dynamics such as side-group motion. From the point of view of glass physics, it is more interesting to investigate secondary relaxation processes in glasses comprised of rigid molecules, i.e., molecules without

any internal relaxing degrees of freedom. In this case the relaxation process is of intermolecular origin. On the one hand, these intrinsic relaxation processes are related to the glass transition phenomenon, as they already emerge above T_g; on the other hand, their investigation in the glassy state may shed light on the structure of glass, whether it is homogeneous or heterogeneous, for example. At lowest temperatures, say below 50 K, relaxation phenomena associated with the low-temperature anomalies of glasses exist. These features are well studied in inorganic systems, but work on molecular glasses is rare.

The main goal of this review is to report on progress of NMR work on relaxation processes in molecular glasses below T_g. We will demonstrate that applications of multidimensional NMR are not limited to studies of the α-process, but this technique is also well suited for the investigations of secondary relaxation processes. However, due to the spatial restrictions of molecular motion associated with secondary relaxation processes, the NMR techniques have to be pushed to their limits. Moreover, comparison with results from other techniques is very useful in order to portrait a coherent physical picture of the molecular dynamics.

There is a couple of recent NMR textbooks and review articles that focus on the main relaxation in super-cooled liquids comprised of organic molecules,[1–4] on polymer-specific dynamics,[4–9] on ionic or inorganic glasses,[10–14] or on glassy crystals[3,15] and orientational glasses.[3,16] In these contributions, the theoretical background of NMR techniques and models of molecular motion were thoroughly discussed. Therefore, we keep the theoretical part of this review as short as possible and concentrate on recent experimental results. We hope that readers being no experts in NMR will benefit from this review, too.

Many secondary relaxation processes in amorphous materials were first identified by dielectric spectroscopy (DS), as this technique allows one to probe processes with very small relaxation strengths. Although DS provides detailed information about the overall spectral density, this method does not enable straightforward analysis of the nature of a motional process, including the relevant degrees of freedom. In contrast, NMR yields direct access to the latter information. Thus, a consistent picture of the intrinsic dynamics of glasses can emerge when results from different techniques are simultaneously considered. Therefore, we find it adequate to start with a short introduction into the relaxation phenomena of glasses as compiled by various experimental methods in Section 2.1. This also offers the opportunity to become acquainted with the terminology in glass physics. Section 2.2 briefly summarizes the results of standard NMR techniques on the main relaxation in supercooled liquids. Section 3, as the main part of this review, deals with NMR studies on secondary relaxation processes in glasses. In Section 3.1, we present results of computer simulations that illustrate the potential of solid-state NMR to probe spatially highly restricted molecular dynamics. Section 3.2 focuses on NMR studies of secondary relaxations in molecular glasses, where we try to integrate the NMR findings into the body of results obtained from other methods. In Sections 3.3 and 3.4, we discuss a few examples of secondary relaxation processes in polymeric and multi-component glasses, respectively. Here, the dynamics of molecules and ions in essentially rigid glassy matrices will also be addressed. In Section 4, we take the

opportunity to briefly comment on recent progress in theoretical work on the glass transition phenomenon. Finally, conclusions are drawn in Section 5.

2. THE GLASS TRANSITION PHENOMENON

2.1. Major experimental findings

In this section, we summarize the major relaxation phenomena observed when a molecular liquid is cooled from above its melting point down to the glass transition temperature, T_g, and further below into the glass. Since DS allows one to cover a very wide frequency range and to probe relaxation processes with weak relaxation strengths, we focus on discussing DS. More detailed information about this topic can be found in Refs. 17–24.

Exploiting technical progress in instrumentation, the dielectric response of supercooled liquids ($T > T_g$) has virtually been measured completely in recent years. At least for a few paradigmatic glass formers, a frequency range $10^{-6}\,\mathrm{Hz} < \nu < 10^{13}\,\mathrm{Hz}$ was covered. This is demonstrated for the glass former glycerol (GL) in Fig. 1a, where the imaginary part of the dielectric permittivity is displayed.[22] Cooling the liquid from highest temperatures ($T = 413\,\mathrm{K}$), a minimum evolves between the main relaxation peak (α-process) in the GHz regime and the peak of the microscopic dynamics in the THz range.

When the temperature is further decreased, a power-law wing appears on the high-frequency side of the α-peak. This so-called "excess wing" can be taken as a first example of a secondary process. Usually, the α-peak is close to 10^{-2} Hz when T_g is reached. Upon cooling into the glass, this peak exits the accessible frequency window and the excess wing degenerates to what is named a nearly constant loss (NCL) behavior;[19,20,26] i.e., one observes a power-law spectrum, extending over several decades in frequency with a small exponent $\gamma = 0.1$–0.2. The temperature dependence of the NCL was found to be exponential and similar for several glass formers (*cf.* Fig. 2).[19,26,27] Thus, one can write for the NCL contribution

$$\varepsilon''(\nu) \propto \nu^{-\gamma} \exp(T/T_{\mathrm{NCL}}), \quad T < T_g. \tag{1}$$

At temperatures say, below 70 K further relaxation processes occur. There, the frequency dependence of $\varepsilon''(\nu)$ changes from a negative slope to a positive one. In this temperature range, thermally activated dynamics in asymmetric double-well potentials (ADWP) and, below 10 K, tunneling phenomena were discussed relating to the so-called low-temperature anomalies of glasses.[27,30,31]

The dielectric relaxation pattern displayed in Figs. 1a and 2 was observed for several molecular glass formers. This group has been called type A glass formers to discriminate them from type B glass formers, exhibiting a well-resolved secondary relaxation peak on the high-frequency side of the α-peak.[19] On cooling the liquid, the β-relaxation peak emerges near T_g and persists below T_g, as can be seen from the DS of the type B glass former toluene (TOL) in Fig. 1b.[19] Since Johari and Goldstein[32] first studied this secondary process in molecular glasses systematically,

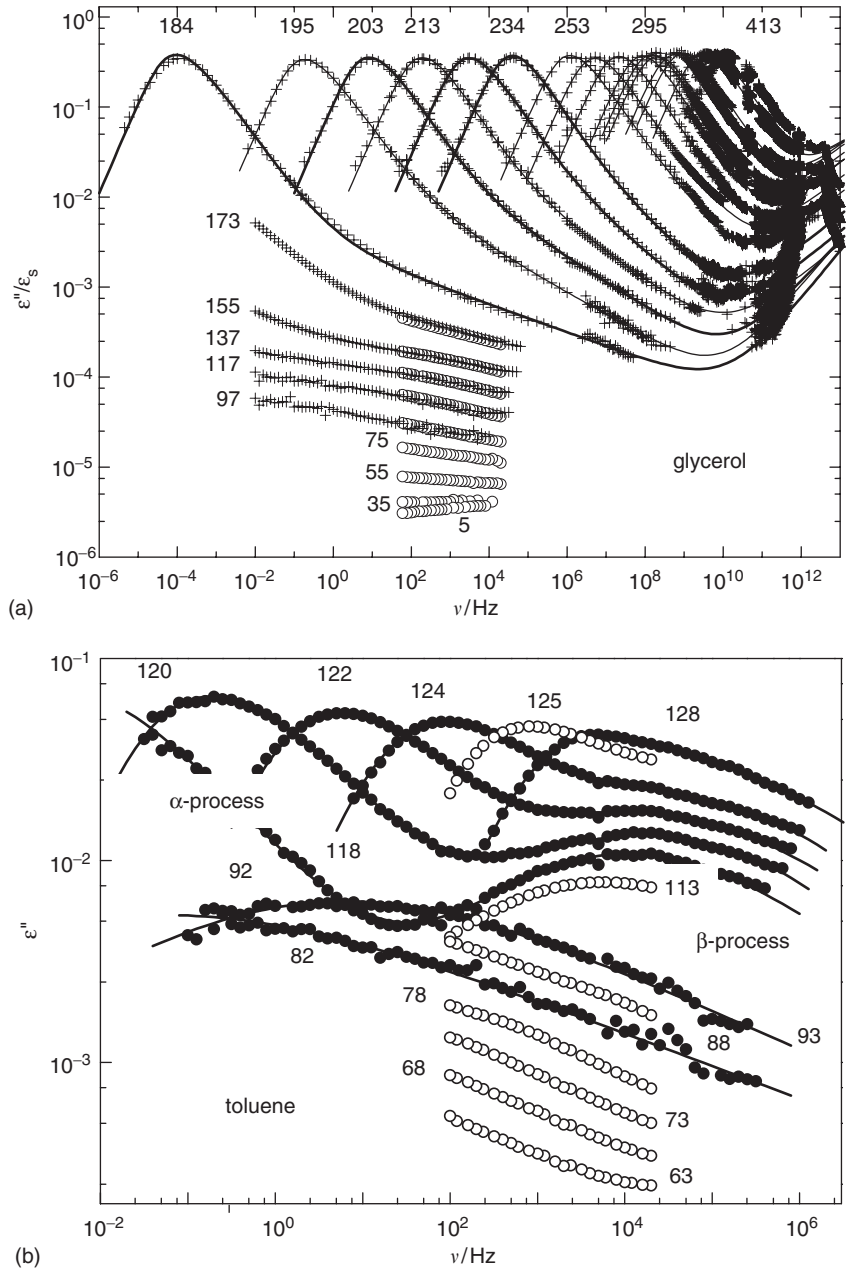

Fig. 1. Normalized imaginary part of the dielectric permittivity of (a) GL ($T_g = 189\,K$, compiled from Refs. 19, 22, 27) and (b) dielectric permittivity of TOL ($T_g = 117\,K$, compiled from Refs. 19, 28). The latter glass former shows a second relaxation peak persisting below T_g. For GL, a fit (solid line) covering all the relaxation contributions above T_g is shown.[38,39] In the case of TOL, the fit based on Eqs. (2) and (3) describes both α- and β-process.

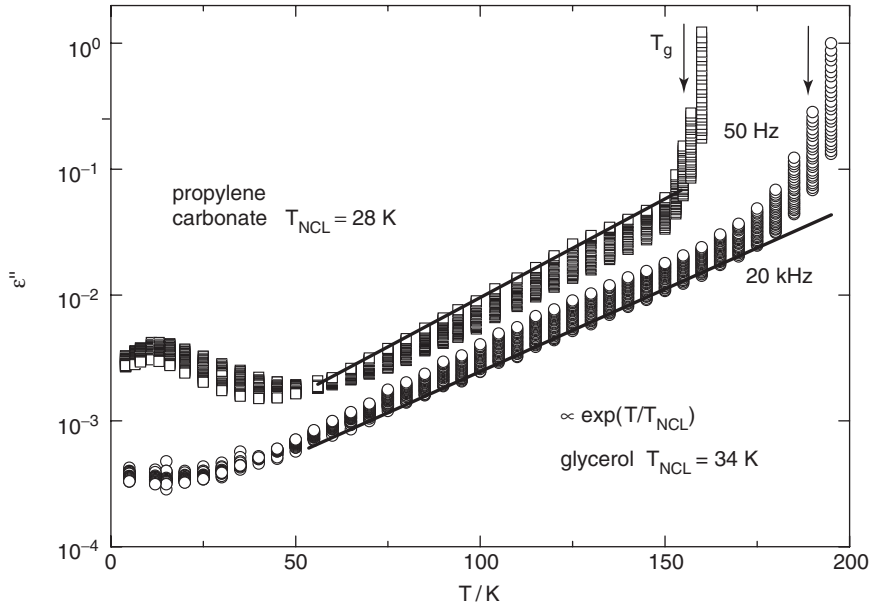

Fig. 2. Dielectric loss as a function of temperature for two glass formers (type A) measured with a high-precision bridge. A frequency range of 50 Hz to 20 kHz is covered. The lines are interpolations by Eq. (1). (Adapted from Ref. 27.)

it is often referred to as Johari–Goldstein (JG) β-process. It was also observed in mechanical relaxation[33–35] and neutron scattering (NS)[36,37] studies. We emphasize that the discrimination of type A and B glasses is a functional definition, which allows one a simple denotation of glasses with distinguishable relaxation behavior. It does not mean that clear-cut subdivision into two classes of glasses is possible. Indeed, there may be a gradual transition between both the types of glasses[25,41] (see Sections 3.2.4 and 3.4.2). On the other hand, systems exist where both a β-peak and an excess wing can be identified[19,38,40] suggesting that these are discernible relaxation phenomena.

While the time constants of the α-process as taken from the maximum of the relaxation peak exhibit a strong non-Arrhenius behavior, the β-process follows an Arrhenius law. This is shown for several glass formers in Fig. 3. The time constants of the α-process continuously change by more than 13 orders of magnitude within a small temperature interval, where the data comprises results from NMR (*cf.* Section 3.1), DS, light scattering (LS) and viscosity measurements. It is obvious that the respective time constants are very similar; i.e., the structural relaxation associated with the α-process dominates all responses of the system. The time constants of the β-process appear to merge with those of the α-process, suggesting that a single relaxation process is present at high temperatures.

Regarding the line shape of $\varepsilon''(\nu)$, numerous phenomenologic susceptibility functions have been proposed to describe the main relaxation peak, which deviates from

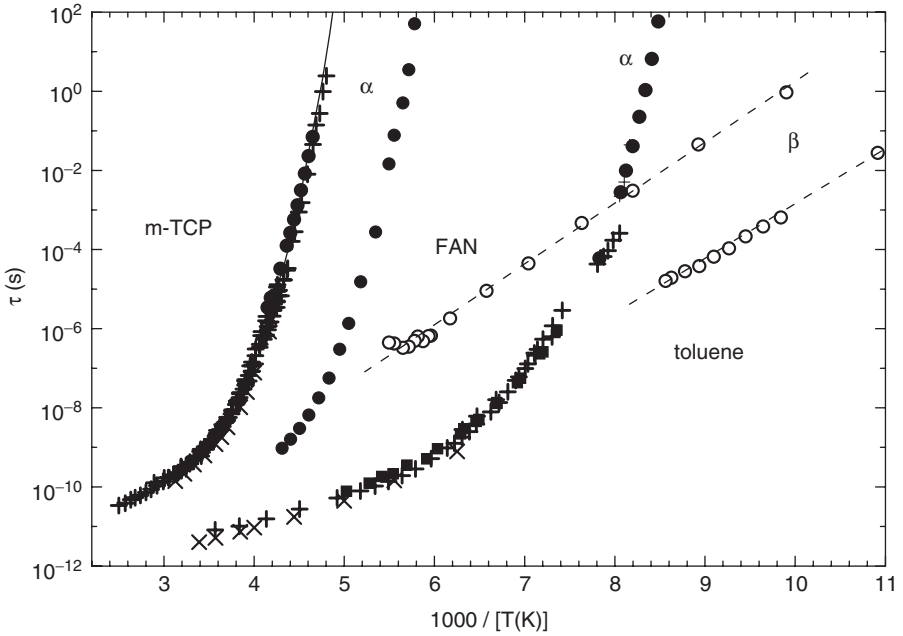

Fig. 3. Time constants of the α- and β-processes for the glass formers *m*-TCP (type A): NMR[42] (+, T_1 and T_2 for $\tau_\alpha < 10^{-4}$ s and stimulated echo for $\tau_\alpha > 10^{-4}$ s), LS (x),[43] DS[44] (circles) and viscosity (line)[45]; for *m*-FAN (type B): dielectric data (circle)[13]; for TOL (type B): NMR[46] (+, T_1, T_2 and stimulated echo), DS[19] (circles) and LS[47] (x); dashed lines: Arrhenius laws for the β-process.

Debye behavior.[17,19,21,38] A formal way to describe a non-Debye relaxation is to introduce a distribution of correlation times $G(\ln \tau_\alpha)$; e.g., the Cole–Davidson distribution. NMR[3,4] experiments among others[3,4,6,48–51,93] have demonstrated that such a distribution $G(\ln \tau_\alpha)$ is not just a formal concept, but the α-process indeed exhibits motional non-uniformities or, equivalently, dynamic heterogeneities. However, the dynamic heterogeneities are transient in nature; i.e., exchange processes within the distribution occur on the time scale of τ_α. Recently, a complete description of the dielectric response, including α-peak and excess wing, was proposed.[38,40] We show these interpolations in Fig. 1a.

The susceptibility contribution resulting from the β-process can be often described by assuming a Gaussian distribution of activation enthalpies $g(\Delta H_\beta)$.[19,52,53] Thus, one can write

$$\varepsilon(\omega) - \varepsilon_\infty = \Delta\varepsilon_\beta \int_{-\infty}^{\infty} g(\Delta H_\beta) \frac{1}{1 + i\omega\tau(\Delta H_\beta)}\, d\Delta H_\beta, \tag{2}$$

where ε_∞ is the permittivity at optical frequencies and $\Delta\varepsilon_\beta$ denotes the relaxation strength of the β-process. Further, correlation time, τ, and activation enthalpy, ΔH_β, are connected via an Arrhenius law, explicitly, $\tau(\Delta H_\beta) \propto \exp(\Delta H_\beta / RT)$. The

resulting fits are included in Fig. 1b.[19] The mean activation enthalpy $\langle \Delta H_\beta \rangle$ can be extracted from the Arrhenius plot of Fig. 3. The β-process exhibits two commonly observed features. Its relaxation strength is virtually temperature-independent below T_g, while it strongly increases with temperature above T_g, and the mean activation enthalpy $\langle \Delta H_\beta \rangle$ often correlates with T_g: i.e., $\langle \Delta H_\beta \rangle \cong 24\, RT_g$ is found for many systems.[19,54] Both the features imply that the β-process is related to the glass transition phenomenon. We emphasize that such correlations include also data for polymers.[19,33,36,55] For instance, polybutadiene (PB), a polymer without side groups, and TOL show similar β-processes, suggesting that β-processes observed for polymers can be intrinsic processes, too (see Section 3.3). Due to similar attempt frequencies and activation enthalpies, the correlation times τ_β of various glasses often fall on top of each other when plotted on a reduced temperature scale T_g/T. This is demonstrated in Fig. 4, where ethanol (ETH) is an exception from the rule.

Concerning the nature of the β-process, there are longstanding conjectures. On the one hand, Goldstein and Johari[18,32,57] postulated "islands of mobility" where loosely packed molecules undergo more or less unhindered motion; i.e., they proposed that only a fraction of molecules take part in the β-process. On the other hand, Williams and Watts[55] assumed that all molecules participate where, however, only a part of the total orientational correlation is lost due to the β-process, corresponding to a spatially restricted motion. As will be demonstrated in Chapter 3, NMR experiments clearly indicate that essentially all molecules participate in the β-process. However, there is a broad distribution of geometries of the motion.

Triggered by predictions of the mode coupling theory (MCT; see Chapter 4), the dynamics of super-cooled liquids was also studied by NS[58–60] and LS[61–65] revealing details of the susceptibility in the GHz regime. The spectra give evidence that a further fast-relaxation contribution has to be taken into account to explain in particular the shape of the susceptibility minimum, a feature also seen in the DS

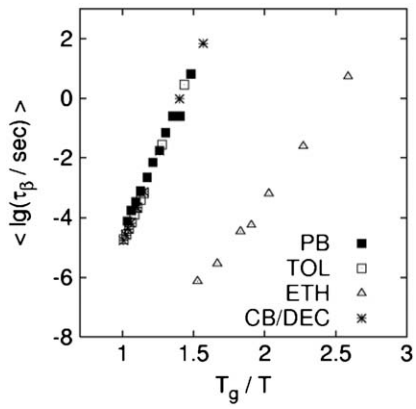

Fig. 4. Time constants of the β-process as a function of the reduced reciprocal temperature T_g/T for the glasses PB, TOL, ETH, and a mixture of CB and DEC. (Adapted from Ref. 56.)

(*cf.* Fig. 1a). Within MCT, this fast process is rationalized as "cage rattling motion" of the molecules, which are trapped in cages formed by their neighboring molecules. The characteristic temperature dependence of the corresponding relaxation strength is reflected in an anomalous temperature behavior of the Debye–Waller factor, f_Q (*cf.* Fig. 5). In the theory, the latter is taken as the non-ergodicity parameter. A cusp-like behavior is observed marking a distinguished crossover temperature $T_c > T_g$. Since $1 - f_Q$ is a measure of the mean square displacement, $\langle \Delta r^2 \rangle$, the data in Fig. 5 indicate a softening of the glass starting around T_g. This behavior is typical of all glasses.[58–60]

Fast dynamics, excess wing and β-process are intrinsic secondary relaxation processes as they are observed in glasses comprised of rigid molecules. Thus, they have to be distinguished from other secondary relaxation processes, originating from internal degrees of freedom (e.g., methyl group or phenyl-ring reorientation). Knowledge on the nature of the intrinsic secondary relaxation processes is still incomplete. While the fast dynamics may find its explanation within the frame of MCT (*cf.* Chapter 4), the excess wing ($T > T_g$) respectively NCL ($T < T_g$) behavior and the β-process still wait for an explanation. For the low-temperature properties of glasses, the standard tunneling model provides phenomenologic access;[29–31] however, the microscopic understanding is not yet complete.

Altogether, the correlation function of super-cooled liquids near T_g has to be described at least by a three-step function, reflecting relaxation processes on quite different time scales. This is schematically shown in Fig. 6.

Following an approach for polymer dynamics,[66] one may assume in first approximation that the different relaxation processes are statistically independent. Then, neglecting the microscopic dynamics, any correlation function in the super-cooled liquid can be decomposed into three factors:

$$F(t) = F_{\text{fast}}(t) F_\beta(t) F_\alpha(t), \tag{3}$$

where the normalized functions $F_{\text{fast}}(t)$, $F_\beta(t)$ and $F_\alpha(t)$ denote the correlation losses due to fast dynamics, β- and α-process, respectively. Eq. (3) agrees with what is called the Williams–Watts ansatz to describe the α- and β-process.[19,42,55] Since secondary processes yield only partial correlation losses, we can write

$$F_{\text{fast}}(t) = (1 - f) g_{\text{fast}}(t) + f, \tag{4}$$

$$F_\beta(t) = (1 - S) g_\beta(t) + S.$$

Here $(1 - f)$ and $(1 - S)$ are the losses brought about by the corresponding process and $g_{\text{fast},\beta}$ $(t \to \infty) = 0$ (see Fig. 6). The factor f can be regarded as a generalized non-ergodicity parameter and, hence, it is expected to show a similar anomaly as the Debye–Waller factor f_Q (see Fig. 5). Such decomposition of the correlation function is useful in spin–lattice relaxation studies, as will be discussed in Section 3.2.4.

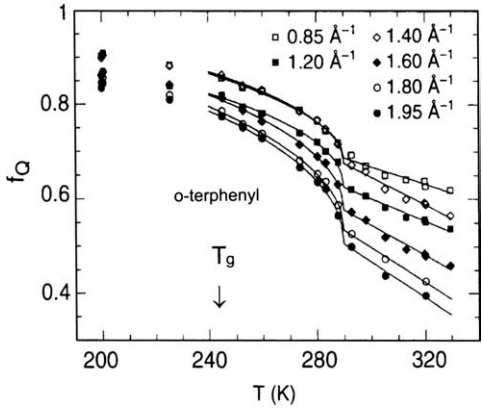

Fig. 5. Non-ergodicity parameter f_Q (Debye–Waller factor) of o-terphenyl as obtained from NS experiments for different values of the momentum transfer Q. (Adapted from Ref. 60.)

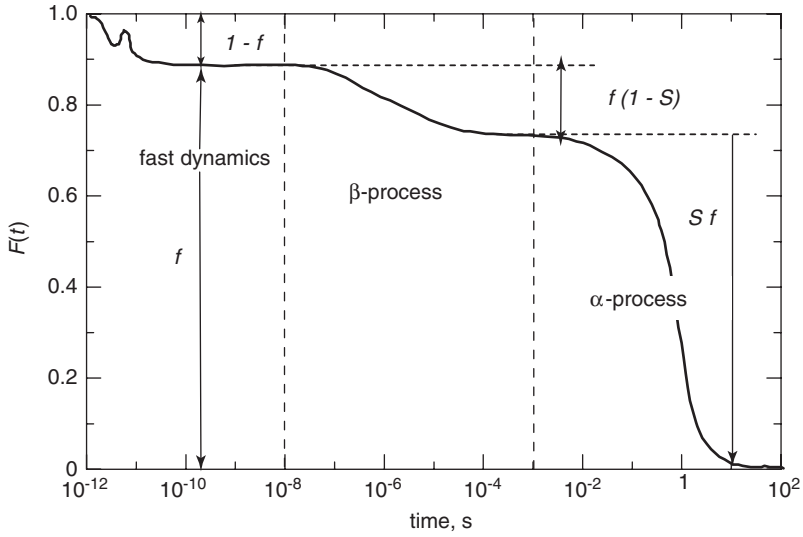

Fig. 6. Schematic correlation function close to T_g defining the relaxation strengths f and S (*cf.* Eqs. (3) and (4)).

2.2. NMR studies of the main relaxation and NMR time windows

In this section, we briefly review NMR work on the α-process in super-cooled molecular liquids. For more detailed information, the reader is referred to the review by Böhmer *et al.*[3] It will become clear that the NMR experiments that proved well suited to study the main relaxation do not provide straightforward

access to secondary relaxation processes. Instead, it is necessary to improve the spatial resolution of the experiments, as will be discussed in Chapter 3.

Various ^{2}H, ^{13}C and ^{31}P NMR techniques were used to follow the slowing down of molecular dynamics during the glass transition.[3] In particular, ^{2}H NMR proved very powerful since solely molecular reorientation is probed and isotopic labeling is easily achieved. Fig. 7 shows the correlation time windows of the major ^{2}H NMR techniques. Two reference frequencies exist: The Larmor frequency ω_L determining the sensitivity of the spin–lattice relaxation and the coupling constant δ_Q fixing the time window of line-shape experiments.

Traditional ways of probing dynamics in liquids include the measurement of the spin–lattice (T_1) and spin–spin relaxation time (T_2). Under extreme narrowing conditions ($\omega_L \tau_\alpha \ll 1$), i.e., at high temperatures in the fluid liquid, both T_1 and T_2 will provide direct access to the correlation time τ_α if the relevant coupling constant is known, e.g., from low temperature line-shape studies. In the moderate viscous regime near the T_1 minimum, a quantitative analysis depends on the proper choice of a correlation function associated with the spectral density $J_2(\omega)$entering the Bloembergen- Pound-Purcell equation [3,8]. Simultaneous analysis of T_1 and T_2 allows one to put constraints on the shape of $J_2(\omega)$. It turned out that the Cole–Davidson spectral density often yields consistent results for super-cooled liquids.[42,46,67–72] In Section 3.2.4, it will be discussed that inconsistencies at lower temperatures $T \approx T_g$ can be attributed to the appearance of the excess wing or β-process.[73] Fig. 8 presents T_1 and T_2 data of the ^{31}P nucleus in tricresyl phosphate (TCP) for two Larmor frequencies.[42] A typical asymmetric relaxation maximum is observed for $1/T_1$. The time constants τ_α obtained from analysis of T_1 and T_2 assuming a dominant chemical shift anisotropy interaction are included in Fig. 3.

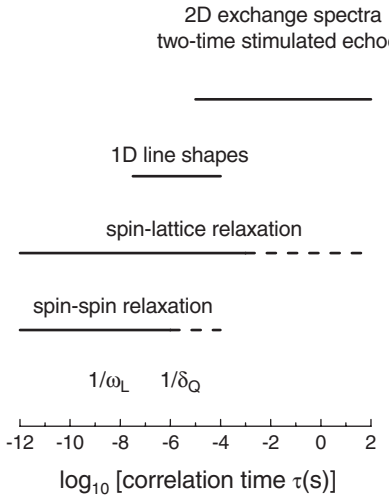

Fig. 7. Time windows of different NMR techniques; Larmor frequency ω_L and coupling constant δ as typical for ^{2}H NMR are indicated. (Adapted from Ref. 3.)

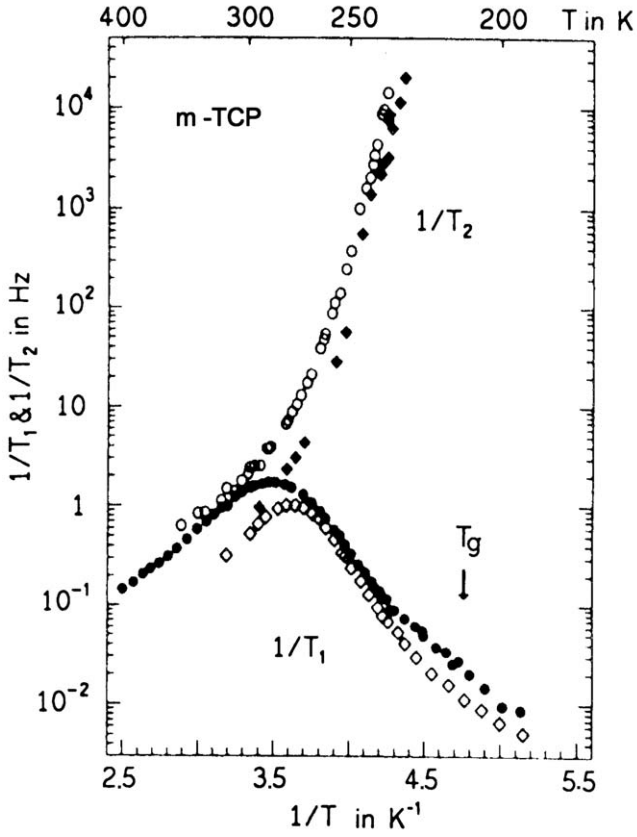

Fig. 8. Spin–lattice ($1/T_1$) and spin–spin relaxation rates ($1/T_2$) as typically found in super-cooled liquids: ^{31}P NMR data at two Larmor frequencies, 47 MHz (open symbols) and 121 MHz (solid symbols), for *m*-TCP. (Adapted from Ref. 42.)

We note that although a joint analysis of T_1 and T_2 often yields reliable correlation times the choice of the coupling constant renders some problems. Usually, its value is taken from the solid-state spectrum near T_g. However, the effective coupling constant may exhibit a discernible temperature-dependence[3] due to the fast dynamics (*cf.* Section 2.1).

Line-shape analyses are another way to investigate the dynamics in super-cooled liquids. In most cases, large spin couplings hamper direct monitoring of the free induction decay (FID) so that it is necessary to use echo techniques.[6,74–76] Fig. 9 shows solid-echo (1D) ^{2}H NMR spectra of super-cooled GL-d_5 and TOL-d_5.[77] For GL, a crossover from a Lorentzian line at high temperatures to a Pake spectrum at low temperatures is observed some 20% above T_g, where the condition $\tau_\alpha \delta \cong 1$ holds. At $T \cong T_g$ a 1D spectrum is observed, apparently not changing when the system is further cooled (see Fig. 9 right column). Although many line-shape studies were performed on viscous liquids, it was not possible to extract unambiguous

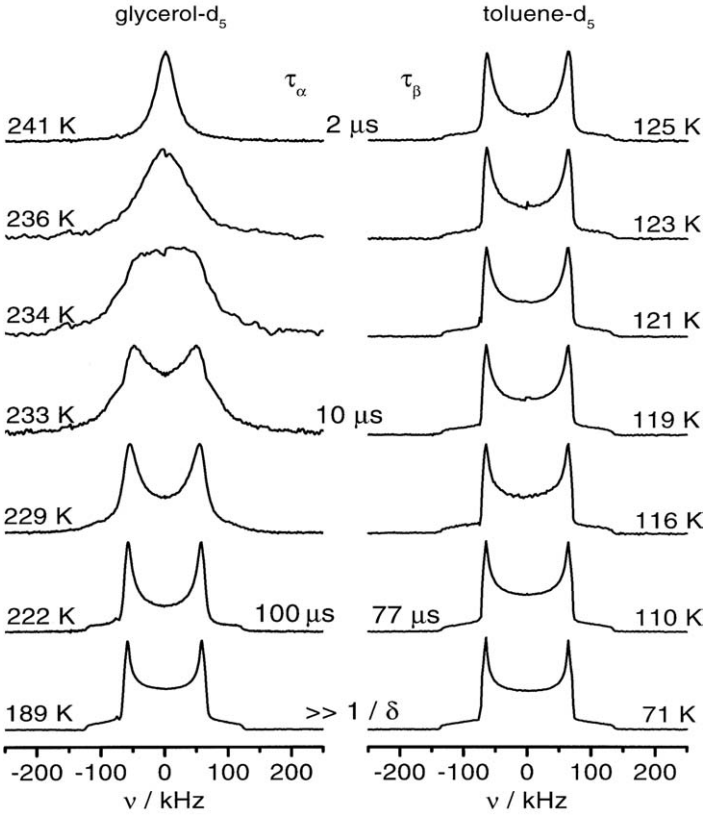

Fig. 9. Solid-echo ^{2}H NMR spectra of GL-d$_5$ ($T_g = 189$ K) and TOL-d$_5$ ($T_g = 117$ K): for GL a collapse of the solid-state spectrum is observed upon heating; for TOL only spectra near and below T_g are displayed, showing the Pake form without significant motional effects. (Adapted from Ref. 77.)

information about the reorientational process, yet the characteristic time constant was accessible.[78]

Applying the stimulated-echo technique in the most simple version[3], a three-pulse sequence is used to create an echo signal $E(t_p,t_m,t)$, which depends on the evolution time t_p, the mixing time t_m and the running or detection time t (for details *cf.* Section 3.1). Straightforward access to molecular dynamics is possible when the amplitude of the echo, which forms at $t = t_p$, is recorded as a function of t_m, resulting in an echo function $A(t_p,t_m)$. In the case $t_p \rightarrow 0$, appropriate phase cycling allows one to directly monitor the reorientational correlation function $F_2(t)$ associated with the second Legendre polynomial, explicitly, $A(t_p \rightarrow 0,\ t_m) \propto F_2(t_m)$. Performing stimulated-echo experiments, correlation functions in the time window $100\,\mu s < \tau_\alpha < T_1$ can be measured.[3,42,70,79–81] An example is given in Fig. 10. It is evident that the non-exponential correlation functions $F_2(t)$ can be interpolated by a

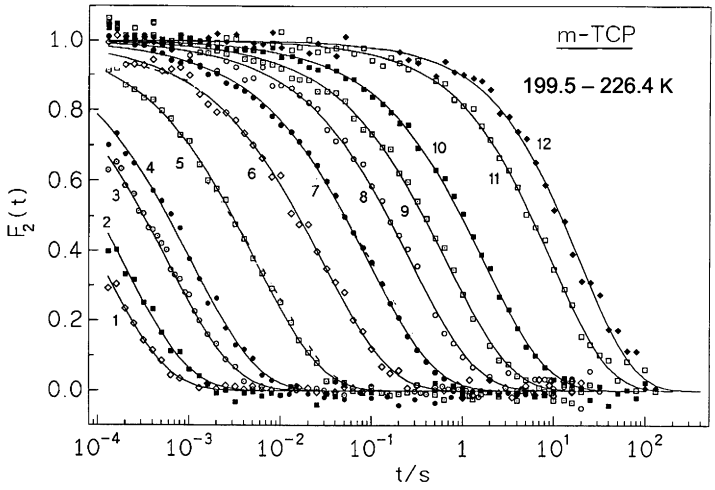

Fig. 10. ^{31}P NMR stimulated-echo decays for *m*-TCP ($T_g = 214$ K) at short t_p, measuring the correlation function $F_2(t)$. The numbers correspond to a temperature range 199.5–226.4 K. The decay curves are fitted with a Kohlrausch stretched exponential. The corresponding time constants are shown in Fig. 3. At lowest temperatures (Nos. 11 and 12) the decay is influenced by spin diffusion. (Adapted from Ref. 42.)

stretched exponential decay, $\exp[-(t/\tau)^{\beta}]$. We emphasize that the degree of non-exponentiality does not change, consistent with an essentially temperature-independent width of the α-peak in the DS. The time constants obtained from the stimulated-echo decay curves are included in Fig. 3. Note that correlation times spanning a very large range 10^{-12} s to 10^{2} s can be determined when different NMR methods are applied.

Details of the dynamical process can be revealed, when stimulated-echo decays are measured for a series of t_p values. Specifically, the resulting time constants and stretching parameters exhibit characteristic t_p dependences, which are a fingerprint of the geometry of the motion. Several studies on super-cooled liquids[79,82–86] reported that the crossover from $A(t_p \rightarrow 0, t_m)$ to $A(t_p \rightarrow \infty, t_m)$ can be reproduced when a bimodal jump angle distribution is assumed. Small angles in the range 2–3° and large angles in the range 30–50° were found, although the weight of the respective fraction may vary among the glass formers and with temperature.[87] However, attention has to be given whether secondary relaxation processes also contribute to the correlation loss. Finally, we note that the time constants of correlation functions $A(t_p \rightarrow 0, t_m)$ and $A(t_p \rightarrow \infty, t_m)$ become similar in the case of large angle motion, as present in crystalline rotor phases, for example, so that a detailed study of their t_p dependence does not yield further information.[88,89]

While the merits of the stimulated-echo technique lie in the resolution of small-jump angles, measurement of two-dimensional (2D) NMR spectra is best suited to

study large angular displacements. For example, jumps about well-defined angles lead to characteristic elliptical off-diagonal intensity, which yields straightforward access to the jump angle. The method found numerous applications to study rotor phases, polymers or side-group motion.[6] In contrast, dynamics involved in the α-process results in complete randomization of the molecular orientation so that the NMR frequencies at $t_m = 0$ and $t_m \gg \tau_\alpha$, respectively, are uncorrelated. In the case $I = 1/2$, we can thus write for the 2D NMR spectrum[90]

$$S(\omega_1, \omega_2, t_m \to \infty) = P(\omega_1)P(\omega_2) = S_{iso}(\omega_1, \omega_2), \tag{5}$$

where $P(\omega)$ is proportional to the one-dimensional (1D) spectrum. In the case $I = 1$, one has to add the contributions $S_{iso}(-\omega_1, -\omega_2)$ resulting from the second allowed NMR transitions. An experimental example is given in Fig. 11. At long mixing time t_m, we see a "box-like" 2D spectrum with off-diagonal intensity spread all over the frequency plane defined by the singularities of the spectrum.

Information about the time evolution of the spectral correlation and, hence, about the course of the motional process is available when 2D spectra are measured for different mixing times t_m, *cf.* Fig. 11. However, such experiments are time consuming and the interpretation is often not straightforward since an appropriate motional model for reorientation in super-cooled liquids is missing, and as said, sensitivity to small-angle processes is small.[81,92] A number of multidimensional NMR experiments were carried out to explore the nature of dynamic heterogeneities in super-cooled liquids. Detailed information is found in several review articles.[3,4,51,93,94] As expected for a liquid, the dynamic heterogeneities are found to be transient in nature, and most NMR studies agree that the lifetime of the heterogeneities is on the order of τ_α. Further, multidimensional NMR was used to show that dynamics in super-cooled liquids are spatially heterogeneous and to determine the length scale associated with this heterogeneity.[95,96]A typical length scale of about 1nm was reported.

The NMR results discussed so far gave no evidence for the presence of secondary relaxation processes. For example, the ^{2}H NMR spectra of TOL at $T \leqslant T_g$ in Fig. 9b do not indicate the presence of motion, although DS documents a strong β-process lying right in the NMR time window (see Fig. 1b).[97] Likewise, inspecting the 2D ^{2}H NMR spectrum of PB in Fig. 12,[98] we see that the β-process of this glass former leads only to minor broadening of the diagonal intensity. Thus, at $T \leqslant T_g$, the vast majority of molecules do not show large angle motion during secondary relaxation processes, suggesting that highly hindered motion is involved in these processes. Unless the spatial resolution is improved, such restricted motion is not probed by standard NMR experiments (see Section 3.1).

Finally, we present the mean spin–lattice relaxation times $\langle T_1 \rangle$ of several glass formers as a function of the reduced reciprocal temperature T_g/T in Fig. 13.[100,101] Since the relaxation becomes non-exponential near T_g, the time constant $\langle T_1 \rangle$ as given by the integral over the normalized spin–lattice relaxation function is plotted. Well above T_g, a minimum associated with the α-process is observed for both type A and B glass formers. When approaching T_g, the relaxation of type A glass

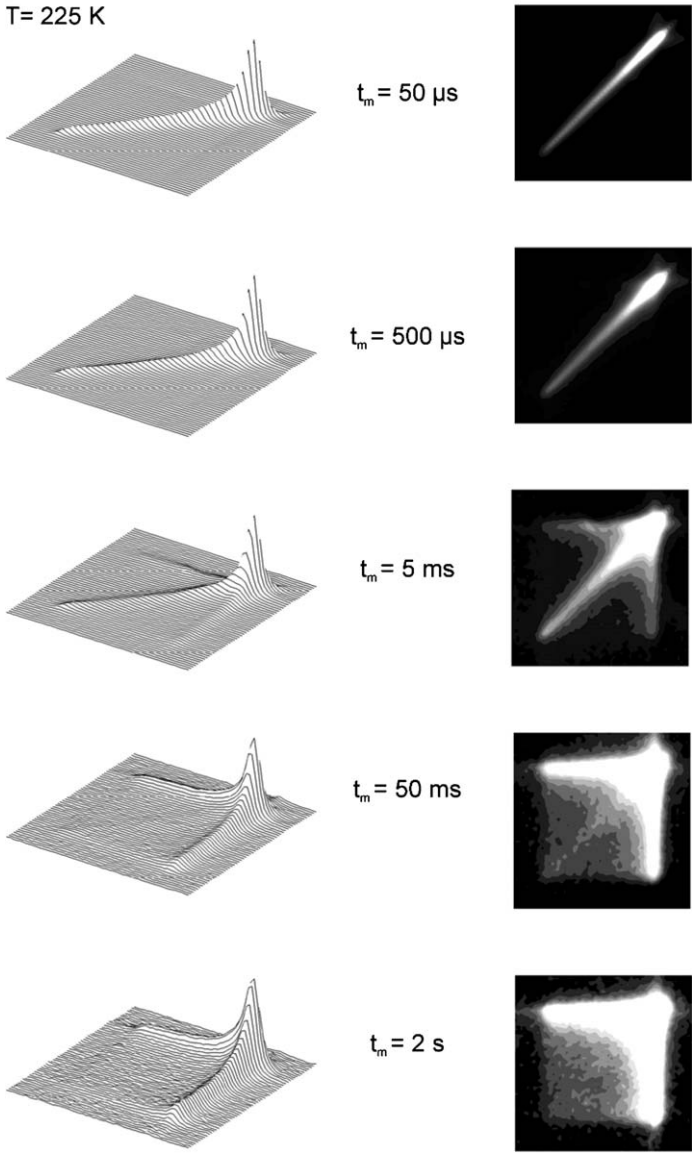

Fig. 11. 2D ^{31}P NMR spectra of the glass former *m*-TCP close to $T_g = 214\,K$ for several mixing times.[91]

formers is by a factor of about 10 slower than that of type B glass formers, indicating that the spectral density of type B systems is significantly enhanced due to the presence of the β-process. Hence, these results provide an example that secondary relaxation processes can be probed in NMR. In Section 3.2.4, we will discuss relaxation studies in more detail. It is the goal of the next chapter to

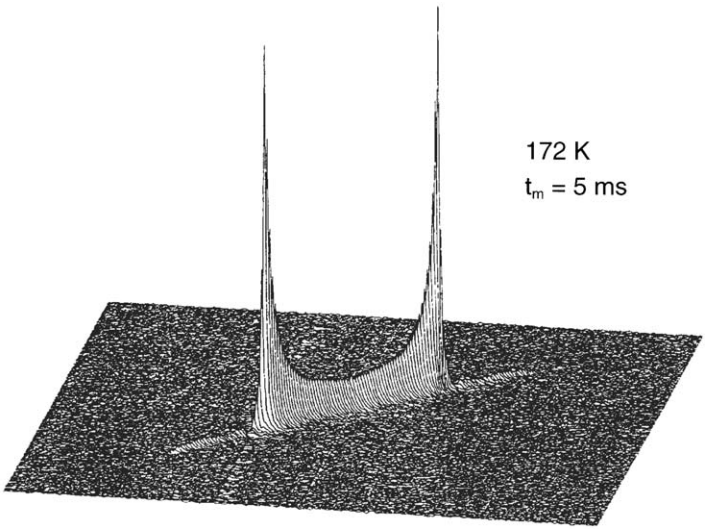

Fig. 12. 2D ^{2}H NMR spectrum of PB–d_6 near T_g. At the studied temperature, the dielectrically observed β-process lies right in the time window of the experiment. However, hardly any motional effects are observed, but the spectral intensity is essentially restricted to the diagonal.[98]

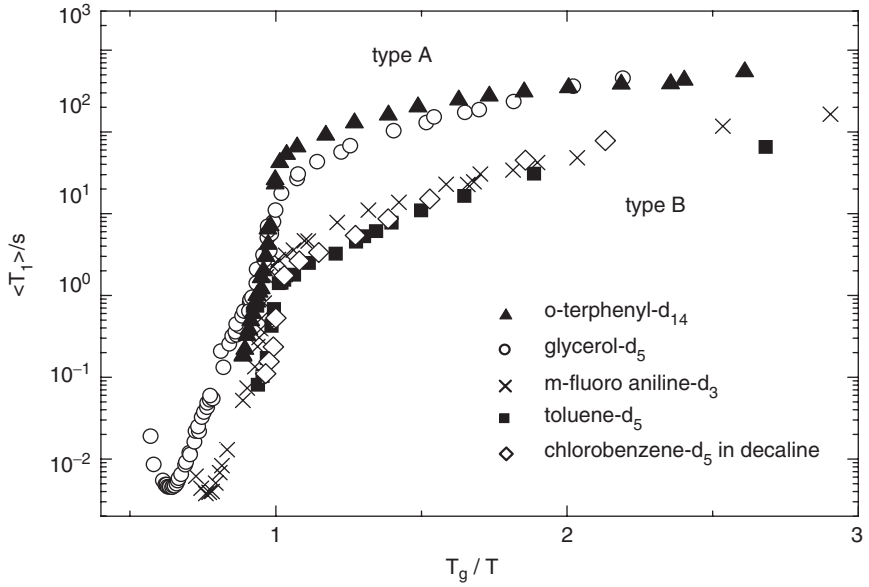

Fig. 13. Mean^{2}H spin–lattice relaxation time $\langle T_1 \rangle$ for several glass formers as a function of the reduced reciprocal temperature T_g/T (compiled from Refs. 68, 69, 100, 146). It is evident that types A and B glass formers can be distinguished based on their relaxation behavior; however, see comment in Section 3.2.4.

demonstrate that detailed information can also be obtained from 1D and 2D experiments provided the spatial resolution is systematically enhanced.

3. NMR STUDIES OF SECONDARY RELAXATION PROCESSES

Secondary relaxation processes were first investigated for polymers,[33] where rotational jumps of side groups are usually involved in these relaxation processes, i.e., there are specific intramolecular origins (see Section 3.3). This review focuses on secondary relaxation processes of molecular glasses. In particular, we discuss results for presumably rigid molecules so that side-group motion is excluded, but there are intermolecular origins of the relaxation phenomena. One expects that these origins are intrinsic to the glassy state, as was pointed out by Goldstein and Johari more than 30 years ago.[18,32,57] Consistently, various molecular glass formers exhibit a similar JG-β-process (see Section 2.1).

Valuable information about the nature of molecular dynamics in glasses was extracted from ^{2}H NMR studies. Therefore, we will give a brief introduction into this method in Section 3.1. In particular, we discuss results of random-walk (RW) simulations that illustrate that the use of suitable experimental parameters renders ^{2}H NMR a powerful tool to probe spatially highly restricted dynamics. This knowledge was exploited in 1D and 2D ^{2}H NMR work on the β-process of molecular glasses, which will be reviewed in Section 3.2. The major results of ^{2}H and ^{13}C NMR investigations on the secondary relaxation of polymers will be summarized in Section 3.3. This will allow us to compare the secondary relaxation of molecular and macromolecular glass formers. Finally, we will address relaxation processes in multi-component glasses in Section 3.4. Specifically, we will revisit NMR studies on the dynamical behavior of molecules and ions in glassy matrices, including the case of glassy ion conductors.

3.1. Probing highly hindered motion by ^{2}H NMR: theoretical background and random walk simulations

3.1.1. *Theoretical background*

^{2}H NMR proved well suited to investigate the molecular dynamics of organic compounds. Since theoretical and experimental aspects of this method were described in detail in the literature,[3,6] we restrict ourselves to a brief discussion of the basic ideas, where we concentrate on aspects important for studies of small-amplitude motion. Although we focus on ^{2}H NMR, we emphasize that similar arguments are valid for many other nuclei. The ^{2}H nucleus exhibits spin $I = 1$ and, thus, shows a quadrupolar interaction, H_Q, describing the coupling of the electric quadrupole moment Q of the nucleus with the electric field gradient tensor at the site of the nucleus. While this interaction is much stronger than other internal interactions, it is much weaker than the Zeeman interaction. Then, the orientation

of the principal axes system of the quadrupolar coupling tensor with respect to the static magnetic flux density $\mathbf{B_0}$ determines the NMR frequency (in the rotating frame), ω_Q. In the following, we assume an axially symmetric coupling tensor ($\eta = 0$), which is a good approximation, e.g., for aliphatic C–^{2}H bonds. In this case, frequencies

$$\omega_Q = \pm\delta/2(3\cos^2\theta - 1), \tag{6}$$

are observed for the two allowed transitions of the $I = 1$ nucleus, where θ is the angle between $\boldsymbol{B_0}$ and the unique axis of the coupling tensor, which in molecular systems is given by the orientation of the bond axis. Hence, Eq. (6) shows that the frequency ω_Q directly reflects the orientation of the C–^{2}H bond and molecular rotational jumps render ω_Q time dependent. The anisotropy parameter δ is proportional to the quadrupolar coupling constant, $2\pi \cdot e^2qQ/h$, where we use $\delta = 2\pi 125\,\mathrm{kHz}$ in the following.

The broad ^{2}H NMR, solid-state spectra correspond to short time signals so that large parts of the FID are not accessible due to the dead time of the receiver following the excitation radio frequency pulse. Therefore, it is necessary to use an echo technique, i.e., two pulses separated by an inter-pulse delay t_p are applied. After the first pulse, acting on the equilibrium magnetization at time $t = 0$, the spin system evolves under the quadrupolar interaction until a suited second pulse at time $t = t_p$ reverses the time evolution, leading to formation of an echo at $t = 2t_p$. For properly chosen t_p, the echo lies outside the dead time so that an undistorted spectrum is obtained from Fourier transformation of the time signal at $t \geqslant 2t_p$. ^{2}H NMR spectra can be measured with the solid-echo pulse sequence $(\pi/2)_x - t_p - (\pi/2)_y$. Neglecting spin–spin and spin–lattice relaxation, the resulting time signal at $t \geqslant 2t_p$ can be written as[74]

$$A_{tp}(t) = \langle\cos[\Phi(0, t_p) - \Phi(t_p, 2t_p) - \Phi(2t_p, t)]\rangle, \tag{7}$$

where the brackets $\langle \ldots \rangle$ denote the ensemble average and the phases Φ are calculated according to

$$\Phi(t_1, t_2) = \int_{t_1}^{t_2} \omega_Q(t)\,dt. \tag{8}$$

If molecular dynamics is absent and, hence, ω_Q is time independent, the signal can be rewritten as $A_{tp}(t) \propto \langle\cos[(t - 2t_p)\omega_Q]\rangle$. Consequently, the signal is refocused at $t = 2t_p$, the time evolution at $t \geqslant 2t_p$ reflects the FID, and the line shape does not depend on the inter-pulse delay. On the other hand, molecular reorientation during the solid-echo sequence, i.e., dynamics with correlation times in the μs-regime, leads to an attenuation of the echo height and to deviations from the rigid–lattice spectrum so that analysis of the line shape reveals details about the type of the motion.[74] In particular, the line shape shows a t_p dependence that contains valuable information about the geometry of the dynamical process. As will be demonstrated below, the inter-pulse delay t_p is of particular importance in studies of highly restricted motions since variation of t_p allows one to adjust the spatial resolution of the experiment.

2D ^{2}H NMR experiments in both frequency and time domain are well suited to investigate ultraslow motion with correlation times in the ms-s regime.[3,6] Here, we discuss the time-domain or, equivalently, stimulated-echo experiment. For this purpose, we consider the three-pulse sequence $(\pi/2)_x - t_p - (\pi/2)_{-x} - t_m - (\pi/2)_x$, where the various delays are chosen according to $t_p \ll t_m \approx \tau \ll T_1$. In this case, a stimulated echo is created at a time t_p after the third pulse. Evaluating the height of the stimulated echo for different mixing times t_m, but for a constant evolution time t_p, the following NMR correlation function can be measured:

$$F^{\cos}(t_m; t_p) = \langle \cos[\omega_Q(t=0)t_p] \cdot \cos[\omega_Q(t=t_m)t_p] \rangle / \langle \cos[\omega_Q(t=0)t_p] \cdot \cos[\omega_Q(t=0)t_p] \rangle. \quad (9)$$

We see that the NMR frequencies at two times separated by the mixing time t_m and, thus, the corresponding orientations of the C–^{2}H bonds, are correlated via cosine functions. The correlation function $F^{\sin}(t_m;t_p)$ where the cosine functions are replaced by sine functions is accessible when the pulse lengths and pulse phases in the above three-pulse sequence are modified in a suitable way.[102,103] Rotational jumps of C–^{2}H bonds during the mixing time t_m lead to $\omega_Q(0) \neq \omega_Q(t_m)$ and, hence, to a decay of $F^{\cos,\sin}(t_m;t_p)$. Therefore, these correlation functions provide straightforward access to molecular dynamics. The evolution time t_p acts as a geometrical filter similar to the momentum transfer $|\boldsymbol{Q}|$ in scattering experiments.[104,105] In the limit $t_p \to 0$, the rotational correlation function of the second Legendre polynomial is measured due to $F^{\sin}(t_m;t_p \to 0) \propto \langle \omega_Q(0) \cdot \omega_Q(t_m) \rangle$, whereas highly hindered motion can be resolved when sufficiently long t_p are used, as will be discussed below.

Due to the dead time, the correlation functions $F^{\cos,\sin}(t_m;t_p)$ for short t_p cannot be measured with three-pulse sequences, but a further pulse is necessary to refocus the stimulated echo, leading to four-pulse sequences such as $(\pi/2)_x - t_p - (\pi/2)_{-x} - t_m - (\pi/2)_x - \Delta - (\pi/2)_y$, where the echo forms at a time $t_p + \Delta$ after the last pulse.[6,102] So far, we assumed $\tau \gg t_p$ so that molecular dynamics during the evolution time can be neglected. In the studies of relaxation processes in glasses, this assumption is not justified since very broad distributions of correlation times $G(\ln \tau)$ exist. Then, it is necessary to explicitly calculate the phases $\Phi(t_1, t_2)$ according to Eq. (8) so that, in general, correlation functions resulting from the above four-pulse sequence can be written as

$$F^{\cos}(t_m; t_p) \propto \langle \cos[\Phi(0, t_p)] \cdot \cos[\Phi(t_p + t_m, t_p + t_m + \Delta) - \Phi(t_p + t_m + \Delta, t_m + 2t_p + 2\Delta)] \rangle, \quad (10)$$

where at $t = t_m + t_p$ the third pulse is applied.

3.1.2. *Technique of random walk simulations*

In the field of the glass transition, the molecular orientation/position is often considered as a stochastic process and the dynamics is described in the framework of the Ivanov model, i.e., the molecular orientation/position is assumed to be constant

between jumps of negligible duration. Then, the motion can be regarded as a continuous time random walk (RW), which is the basis of RW simulations, where the dynamical process is mimicked on a computer calling in a random-number generator.[84] Specifically, a large number of trajectories describing the molecular orientation/position as a function of time are generated within a suitable model of the motion. Based on these trajectories, it is straightforward to calculate the corresponding time dependence of the NMR frequencies, which in turn allows one to compute the results of NMR experiments from an ensemble average.[3,76,84] Thus, this approach uses the very definition of a stochastic process to simulate experimental results, like NMR correlation functions. When a first order Markov process applies to the dynamics, such calculations can also be performed by setting up the exchange matrix for a given model of the motion and solving the master equation.[106,107] However, the exchange matrix formalism is commonly restricted to simple models and, hence, applications are limited for disordered materials. In contrast, it is straightforward to implement various models of complex dynamics in RW simulations. For example, isotropic rotational jumps governed by distributions of jump angles and correlation times can be simulated, which is regarded as a realistic model of the α-process in super-cooled liquids. In addition, it is possible to consider stochastic processes that are not described by a Markov process. Also, it proved very useful to calculate trajectories from RW simulations of activated jump dynamics in energy landscapes featuring sites with different site energies that are separated by barriers of various heights.[108,109] The resulting dynamics are complex, as typical of disordered materials, including the canonical feature of short-lived dynamical heterogeneities. Thus, exchange within a distribution of correlation times can be modeled.

In general, three steps are required to create trajectories by means of RW simulations,[76,84]: (i) determination of an initial orientation/position so that the equilibrium distribution is obeyed, (ii) random selection of a waiting time t_w between two subsequent jumps from a suitable distribution and (iii) calculation of the new orientation/position after the jump. After step (i), the steps (ii) and (iii) are performed alternately until a trajectory of sufficient length in time is obtained. While the time scale of the motion is determined by the distribution of waiting times $g(t_w)$ in step (ii), the geometry of the motion comes into play in step (iii). For example, the new orientation θ_{i+1} after a γ-degree-rotational jump of a C–^{2}H bond can be obtained from the old orientation θ_i according to

$$\cos\theta_{i+1} = \sin(\theta_i)\sin(\gamma)\cos(\psi) + \cos(\theta_i)\cos(\gamma), \tag{11}$$

where the angle ψ is randomly drawn from the interval $[0,2\pi]$.

3.1.3. *RW simulations of ^{2}H NMR data*

RW simulations were performed to demonstrate that the use of suited inter-pulse delays t_p in ^{2}H NMR solid- and stimulated-echo experiments allows one to resolve spatially highly restricted reorientations.[76] For this purpose, it was assumed that C–^{2}H bonds ($\eta = 0$) show rotational random jumps (*cf.* Fig. 25) where all possible

orientations describe the slant part of a cone with a full opening angle $\chi = 6^\circ$. Corresponding to a Markov process, an exponential distribution of waiting times, $g(t_w) \propto \exp(-t_w/\tau_j)$, is assumed. For any random-jump model, the correlation time τ and the so-called jump correlation time τ_j are identical since, on average, each jump leads to the maximum possible loss of orientational correlation, the latter being determined by the geometry of the motion. Based on the trajectories $\theta(t)$ resulting from this cone model, the time dependence $\omega_Q(t)$ and the "experimental" results can be calculated using the above equations. In doing so, experimental imperfections should be taken into account to obtain "realistic" ^{2}H NMR spectra, i.e., effects due to dipolar broadening and finite pulse length should be considered.[6]

First, we discuss jump dynamics on the cone characterized by a single time constant $\tau = \tau_j$. Fig. 14a shows ^{2}H NMR spectra for various solid-echo delays t_p.[76] Although $\tau_j = 30\,\mu s$ lies well inside the time window of the experiment, the line shape for a typical delay $t_p = 20\,\mu s$ resembles a rigid–lattice spectrum, i.e., the highly hindered motion is not probed. However, when t_p is extended, the line shape changes due to the dynamics and the center of the spectrum strongly decreases with respect to the "singularities". These findings can be rationalized when we consider that highly restricted dynamics leads to small-frequency changes, $\Delta\omega_Q \equiv |\omega_Q(t = 0) - \omega_Q(t \gg \tau)|$, so that the phase accumulated during a time t_p does not substantially deviate from the rigid–lattice value $\omega_Q t_p$ until the delay is sufficiently long, i.e., $t_p \approx 1/\Delta\omega_Q$. Therefore, large t_p are required to result in a significant attenuation of the echo height and to corresponding effects in the line shape. The specific dependence of the line shape on t_p is a fingerprint of small-amplitude reorientation. When t_p is extended, the spectral intensity is strongly (weakly) reduced at positions where ω_Q depends strongly (weakly) on θ, since the dynamics results in relatively large (small) $\Delta\omega_Q$ at these positions. For example, the slope $|d\omega_Q/d\theta|$ is biggest for $\theta = 54.7^\circ$ and, thus, the spectral intensity at $\omega_Q(\theta = 54.7^\circ) = 0$ is attenuated the most. In summary, variation of the solid-echo delay allows one to adjust the spatial resolution of the ^{2}H NMR spectrum, where rotational jumps about angles as small as 1° can be resolved for sufficiently large t_p.[110]

In Fig. 14(b), we display correlation functions $F^{\cos}(t_m;t_p)$ calculated for the random jump on the cone using $\tau_j = 10\,ms$, i.e., for ultraslow motion.[3,104] Clearly, the amount of residual correlation C at $t_m \gg \tau_j$ strongly decreases and hence, the amplitude of the decay, $1 - C$, strongly increases when the evolution time t_p is extended. This reflects the well known effect that the evolution time of the stimulated-echo experiment acts as a geometrical filter.[3,104] Here, we see that, due to the spatial restriction to the surface of a cone with opening angle $\chi = 6^\circ$, a loss of correlation is not observed until large evolution times $t_p > 20\,\mu s$, say, are used. Thus, sufficiently large values of t_p are required to detect highly hindered motion in stimulated-echo experiments. In contrast, isotropic motion can already be observed for very short evolution times.[3]

The distributions of correlation times $G(\ln \tau_\beta)$ characterizing the β-process are very broad so that their widths exceed the time window of the stimulated-echo experiment. As a consequence, straightforward determination of the time constants of the dynamics from this experiment is not possible, but elaborate analysis of the

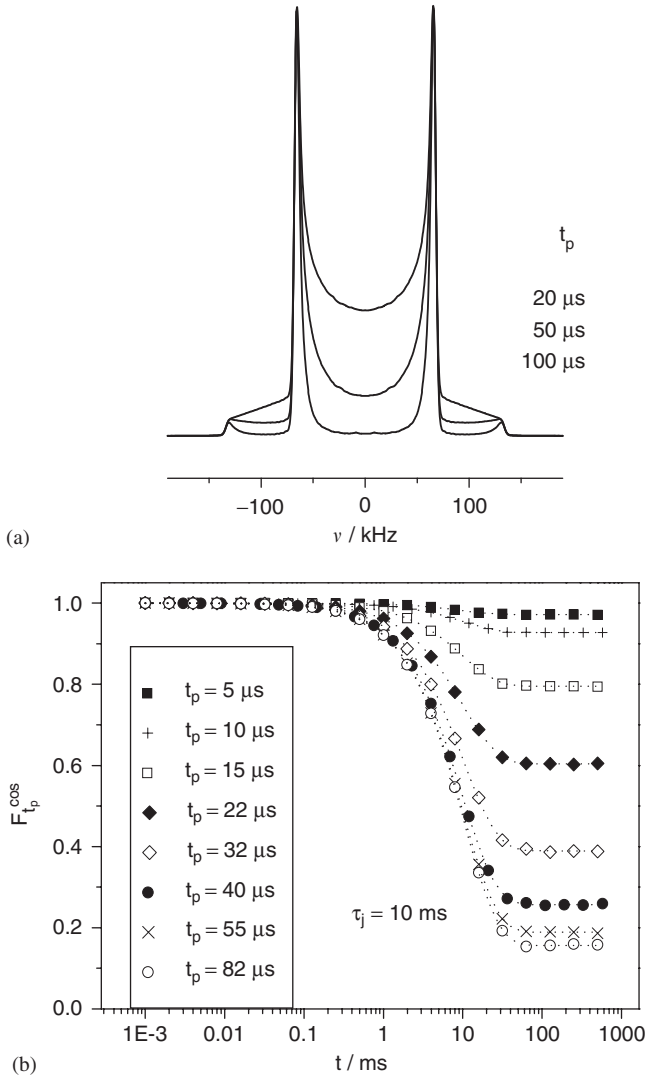

Fig. 14. Effects of small-amplitude reorientation on ^{2}H NMR experiments, as calculated by means of RW simulations. In the model, C–^{2}H bonds ($\delta = 2\pi \cdot 125\,\text{kHz}$, $\eta = 0$) perform rotational random jumps on the surface of a cone with a full opening angle $\chi = 6^\circ$. (a) ^{2}H NMR spectra for various solid-echo delays t_p ($\tau_j = \tau = 30\,\mu\text{s}$), and (b) ^{2}H NMR correlation functions $F^{\cos}(t_m)$ for various evolution times t_p ($\tau_j = \tau = 10\,\text{ms}$). (Adapted from Ref. 76.)

correlation functions is necessary. To model the situation in RW simulations, it was assumed that the random jump on the cone is subject to a logarithmic Gaussian distribution $G(\lg\tau)$ with a width $\sigma = 2.3$.[76] Fig. 15a shows the correlation functions $F^{\cos}(t_m;t_p = 30\,\mu\text{s})$ resulting for various mean logarithmic time constants $\lg\tau^m$, marking the peak positions of $G(\lg\tau)$. Due to the relatively large evolution time, the

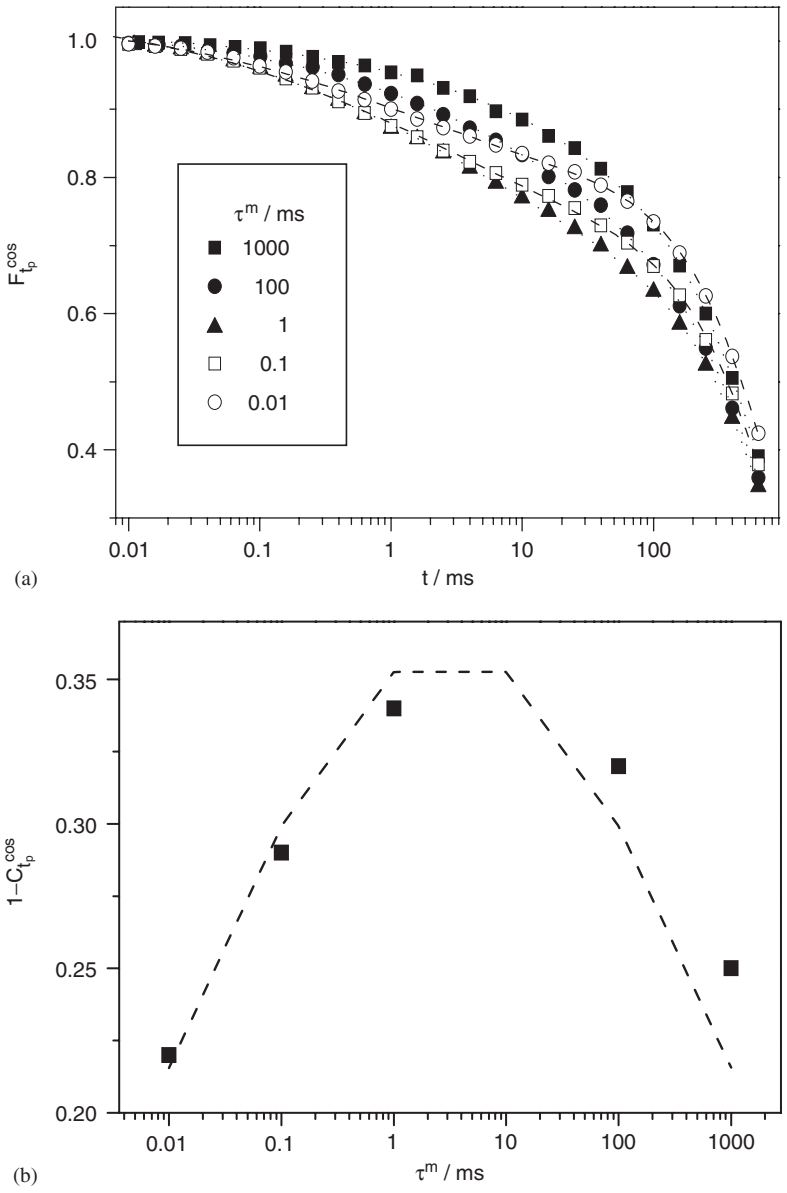

Fig. 15. Effects of small-amplitude reorientation on ^{2}H NMR stimulated-echo experiments, as calculated by means of RW simulations. The C–^{2}H bonds perform rotational random jumps on the surface of a cone with a full opening angle $\chi = 6^\circ$, which are governed by a broad logarithmic Gaussian distribution of correlation times $G(\lg\tau)$ ($\sigma = 2.3$). (a) Correlation functions $F^{\cos}(t_m;\ t_p = 30\,\mu s)$ for the indicated mean logarithmic time constants $\lg\tau^m$. The calculated data are damped by an exponential decay, $\exp[-(t_m/\tau_{SD})]$ with $\tau_{SD} = 1$ s, so as to mimic effects due to spin diffusion. The dotted lines are fits with $F^{\cos}(t_m;t_p) = \{(1–C)\exp[-(t_m/\tau)^{\beta}] + C\}\exp[-(t_m/\tau_{SD})]$. (b) Amplitude of the decays, $1–C_{tp}$, for various τ^m resulting from these fits. The dotted line is the value of the integral in Eq. (12) as a function of τ^m. (Adapted from Ref. 76).

correlation functions do not decay until $t_m \approx 100\,\mu s$, which, thus, yields the short-time limit of the experimental time window. To mimic the experimental situation, where spin diffusion eventually damps the correlation functions (see Section 3.2.2), the calculated data were multiplied by an exponential decay $\exp[-(t_m//\tau_{SD})]$ with $\tau_{SD} = 1\,s$. This damping starts to dominate the decay at $t_m \approx 100\,ms$, fixing the long time limit of the time window. Despite variation of τ^m by a factor 10^5, the curves hardly shift, but the experimental time window determines the time scale of the decay, confirming that it is not possible to extract correct correlation times. On the other hand, it was demonstrated that the amplitude of the decay, say, between 100 μs and 100 ms contains information about the time scale of the dynamics.[76,99] When $G(\lg\tau)$ shifts to shorter times, the amplitude first increases and then decreases, where it is a maximum for $\tau^m = 1$–$10\,ms$. This behavior can be understood, when we consider that neither $\tau < 100\,\mu s$ nor $\tau > 100\,ms$ lead to an observable decrease of $F^{cos}(t_m;t_p)$ so that the amplitude of the decay, $1 - C_{tp}$, is expected to be proportional to the fraction of $G(\lg\tau)$ lying in the experimental time window, i.e.,

$$1 - C_{tp} \propto \int_{100\,\mu s}^{100\,ms} G(1g\tau)d\,1g\tau \tag{12}$$

Fig. 15b shows the value of the integral and the amplitude $1 - C_{tp}$ as function of τ^m, where the latter was determined from a suitable fit of the correlation functions. The good agreement indicates that the amount of correlation lost in the experimental time window provides a measure of the location of $G(\lg\tau)$. We emphasize that these results are not limited to NMR correlation functions, but they show that any time-domain experiment will not provide straightforward access to the mean time constant of a dynamical process that is governed by a distribution $G(\lg\tau)$ broader than the experimental time window.

3.2. Secondary relaxation processes of neat molecular glasses

3.2.1. *^2H NMR solid-echo spectra: β-process in the glass ($T < T_g$)*

When the slowing down of liquid dynamics on super-cooling was followed, most studies argued that the NMR line shape reaches the rigid–lattice limit at temperatures around T_g (see Section 2.2), and consequently no t_p dependence of the solid-echo spectra was expected. While such behavior is indeed observed for type A glass formers, the situation is different for type B systems, exhibiting a discernible β-process in the DS. Some of the differences were revealed by comparison of ^2H NMR spectra for several organic glass formers at the reduced temperature $T/T_g \approx 0.85$.[56,97,99] In Fig. 16, we see that the spectra of type A systems give no evidence of dynamics below the glass transition, consistent with the absence of a secondary relaxation process in the DS.[19] In contrast, the β-process of type B glasses manifests itself in a strong dependence of the ^2H NMR spectrum on the solid-echo delay t_p (*cf.* Fig. 17). Specifically, the changes of the line shape are typical of spatially highly restricted rotational jumps, as becomes clear by comparison with

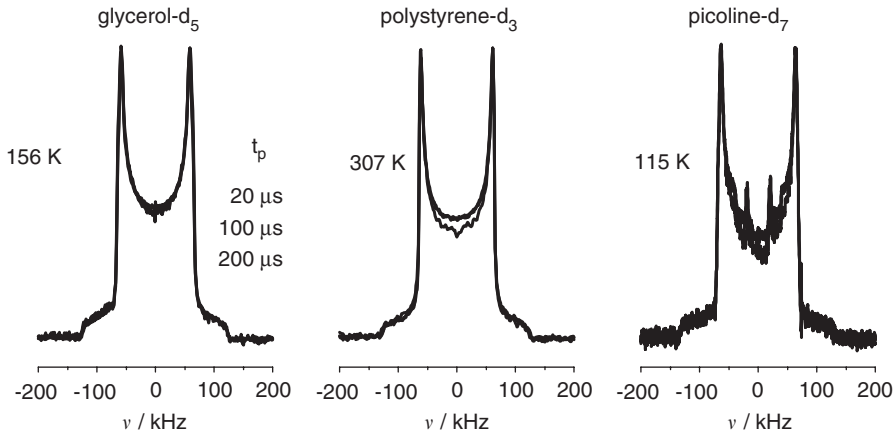

Fig. 16. ^{2}H NMR spectra for the type A glasses GL-d_5, PS-d_3 and picoline-d_7 at the reduced temperature $T/T_g \approx 0.85$. Results for solid-echo delays $t_p = 20$, 100 and 200 µs are shown. In the case of picoline-d_7, the sub-spectrum of the methyl group was removed. (Adapted from Ref. 56.)

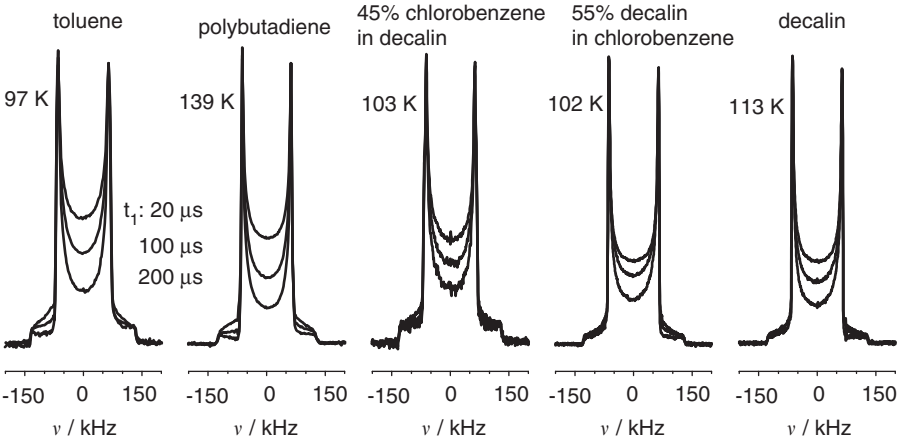

Fig. 17. ^{2}H NMR spectra for type B glasses at the reduced temperature $T/T_g \approx 0.85$. Results for the neat systems TOL-d_5, PB-d_6 and DEC-d_7 are shown together with those for the binary mixtures 45% CB-d_5 in DEC and 55% DEC-d_{18} in CB. Solid-echo delays $t_p = t_1 = 20$, 100 and 200 µs were used. (Adapted from Ref. 56.)

Fig. 14a. In Fig. 18, we present ^{2}H NMR spectra of the type B glass former TOL-d_5 for various $T < T_g$ and an echo delay $t_p = 200$ µs.[97] Strong deviations from the rigid–lattice spectrum are evident near $T_g = 117$ K, where the β-peak in the DS of TOL is located in the µs-regime (see Fig. 1b). Upon cooling, these deviations are reduced until the rigid–lattice limit is reached near $T \approx 71$ K, where the β-process

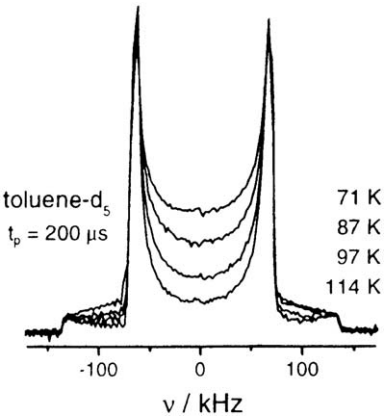

Fig. 18. ^{2}H NMR spectra of the type B glass TOL-d_5 at various temperatures $T < T_g = 117$ K. A large solid-echo delay $t_p = 200$ µs was used so as to resolve highly restricted dynamics. The methyl group rotation is not observed for the ring-deuterated compound. (Adapted from Ref. 97.)

exits the NMR time window.[12,19] These findings confirm that the ^{2}H NMR spectrum probes the β-process and effects due to spin diffusion can be neglected. Consistent with these changes of the line shape, it was found that the β-process renders the spin–spin relaxation time T_2 temperature-dependent at $T < T_g$[98,111] (*cf.* Section 3.4.2). However, quantitative analysis of T_2 is not straightforward due to interference of motional and dipolar contributions to the spin–spin relaxation.

To study the nature of the β-process in more detail, it proved useful to further increase the spatial resolution of the experiment by applying even larger solid-echo delays. In Fig. 19a, ^{2}H NMR spectra of TOL-d_5 at $T = 0.83\ T_g$ are displayed.[97] Inspecting the line shape for the largest delay $t_p = 500$ µs, we see that the intensity in the center of the spectrum nearly vanishes. Based on this finding, important conclusions about the mechanism of the motion were drawn.[99] To follow the argumentation, it is useful to recall that C–^{2}H bonds that do not show any rotational jumps in the µs-regime contribute to a rigid–lattice spectrum and, thus, yield intensity at $\nu \approx 0$. In other words, the intensity at the center of the spectrum does not vanish unless all C–^{2}H bonds move on this time scale. Since effects due to the structural relaxation can be excluded well below T_g, the results in Fig. 19a imply that basically all TOL molecules participate in the β-process. Therefore, the NMR results provide strong evidence against a model proposed by Johari[18,112] and Goldstein[57] where a fraction of molecules moves in "islands of mobility". Moreover, the data do not support the conjecture that the β-process of TOL results from a reorientation about the molecular symmetry axis,[46] because the *para*-deuteron would not participate in such type of motion, i.e., 20% of the deuterons would contribute to a rigid–lattice spectrum, a conclusion which also follows from the fact that the β-process is dielectrically active. Further information was available by comparison with the distribution of correlation times $G(\lg \tau_\beta)$ extracted for TOL

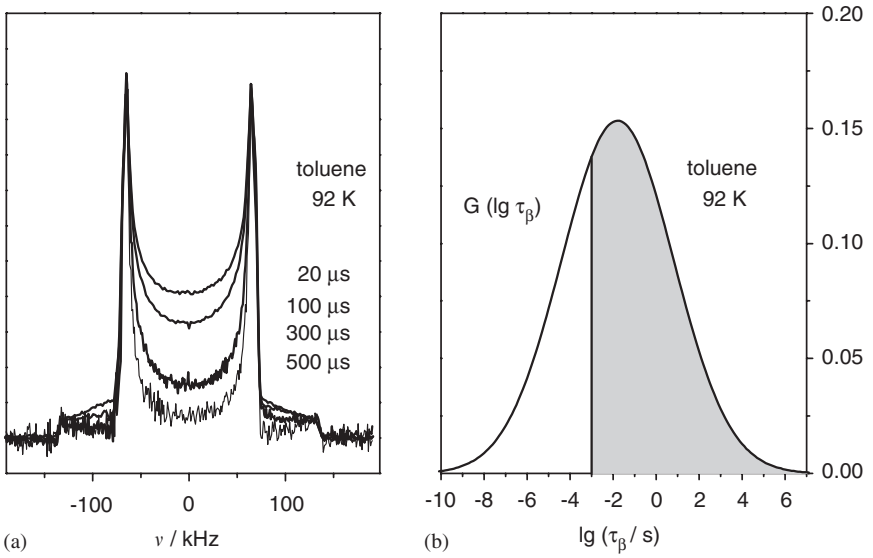

Fig. 19. (a) ^{2}H NMR spectra of the type B glass TOL-d_5 at the reduced temperature $T/T_g = 0.83$. The used solid-echo delays t_p are indicated. (b) Distribution of correlation times $G(\lg \tau_\beta)$ as obtained from DS on TOL at $T/T_g = 0.83$.[12,19] (Adapted from Ref. 99.)

from DS[19] indicating that the majority of molecules exhibit $\tau_\beta > 1$ ms at $T/T_g = 0.83$ (see Fig. 19b). Assuming a simple dynamical process, e.g., a two-site jump, these molecules would contribute to a rigid–lattice spectrum ($\tau_\beta \gg 1/\delta$) and, independent of t_p, the spectral intensity at $\nu \approx 0$ would not vanish. Thus, the findings imply that molecules characterized by correlation times $\tau_\beta \gg 1/\delta$ do show some motion already in the μs regime. Therefore, the β-process was modeled as a multi-step process so that the overall loss of correlation is not achieved until a number of elementary steps on a time scale $\tau_j \ll \tau_\beta$ are performed (see Section 3.2.3).

So far, we have discussed examples where the β-process is comparatively slow so that it is not possible to meet the condition $\delta\tau_\beta \ll 1$ for all correlation times of the distribution due to the interference of the α-process at high temperatures $T > T_g$. However, some molecular glasses show a secondary relaxation process with a comparatively low-activation enthalpy. In these cases, although it is not clear whether these relaxations are intrinsic β-processes, it is possible to shift the entire distribution $G(\lg \tau_\beta)$ from $\delta\tau_\beta \ll 1$ to $\delta\tau_\beta \gg 1$ below T_g. Figure 20(a) shows ^{2}H NMR spectra of ETH-d_1,[56,113] which exhibits such fast secondary relaxation (*cf.* Figs. 4 and 20b). Evidently, the line shape is independent of the echo delay at the highest and lowest temperatures, indicating that the fast- and slow-motion limits were reached, respectively. In contrast, a t_p dependence typical of hindered motion was found at intermediate temperatures, where the secondary relaxation occurs in the μs-regime, as revealed by DS.[114] In principle, it is possible to obtain an estimate of the amplitude of the reorientation associated with the secondary relaxation of ETH by comparison of the line widths in the fast- and slow-motion limit, respectively.

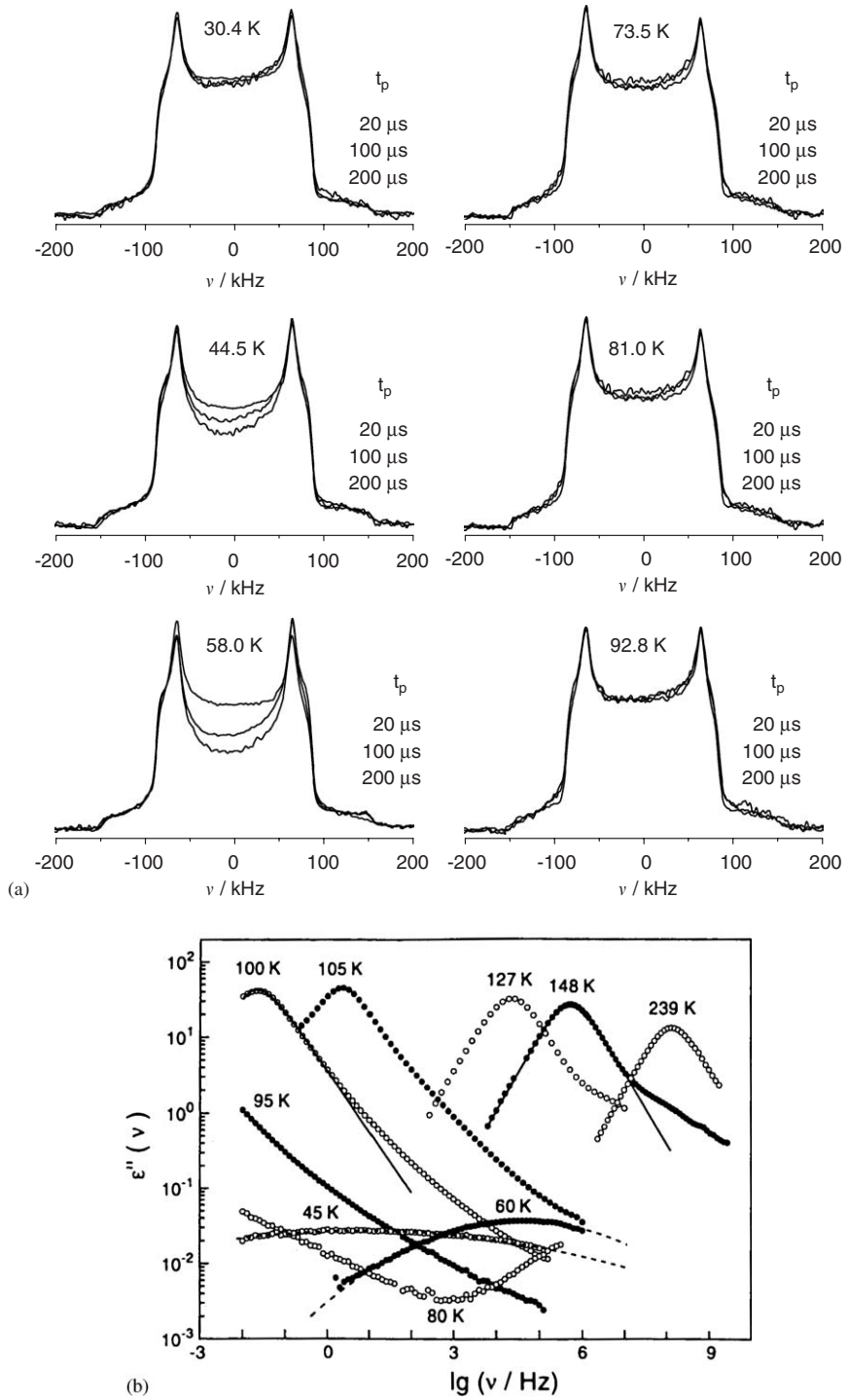

Fig. 20. (a) ^{2}H NMR spectra of the type B glass ETH-d_1[113] for various temperatures $T < T_g = 98$ K and solid-echo delays $t_p = 20$, 100 and 200 μs. (b) DS of ETH, showing a very weak secondary relaxation peak at low temperatures.[114]

The very weak reduction of the line width indicates spatially highly restricted reorientation, consistent with the above conclusions for other type B glasses, yet it is not straightforward to extract more quantitative information since fast relaxation processes and vibrations render the line width temperature-dependent as well.[3] Note that the dielectric relaxation strength of the β-process in ETH is very small (*cf.* Fig. 20b).

3.2.2. *^{2}H NMR stimulated-echo experiments: β-process in the glass ($T < T_g$)*

The stimulated-echo technique is well suited not only to investigate the primary relaxation of glass forming liquids above T_g, but also the secondary relaxation in the glassy state. In ^{2}H NMR studies on the β-process, it is advisable to measure the correlation function $F^{cos}(t_m;t_p)$ rather than $F^{sin}(t_m;t_p)$. In the former experiment, the effect of spin–lattice relaxation during the mixing time t_m can be eliminated, when the relaxation of Zeeman order, present during this period, is determined in an independent T_1 measurement. Such elimination is not possible for $F^{sin}(t_m;t_p)$ since alignment order exists during t_m, which decays with a relaxation time T_{1Q} being usually shorter than T_1. Hence, due to the possibility of correction for relaxation effects and the relationship $T_1 > T_{1Q}$, the experimental time window of the cos–cos experiment is broader, which is important due to the width of the β-process. We add that it is no drawback that $F^{cos}(t_m;t_p) = 1$ in the limit $t_p \to 0$ since, in any case, large evolution times t_p are necessary to probe the restricted dynamics.

Fig. 21 shows correlation functions $F^{cos}(t_m;t_p)$ for three type B glasses at $T/T_g \approx 0.83$, which were corrected for effects due to spin–lattice relaxation.[99] It was demonstrated that the β-process manifests itself in a stretched decay at $t_m < 100$ ms. We see that these short-time decays of $F^{cos}(t_m;t_p)$ are nearly identical for the studied glasses, in nice agreement with results in DS, where these compounds exhibit very similar β-peaks at a given value of T/T_g.[56] The amplitude of the decays up to $t_m \approx 100$ ms strongly increases when the evolution time t_p is extended, indicating the presence of spatially restricted rotational jumps. Hence, 1D and 2D ^{2}H NMR experiments yield a consistent picture of the dynamics. At times $t_m > 100$ ms, an additional process further damps the correlation functions. This long-time decay was attributed to spin diffusion as it is also present for type A glasses,[99] where a short-time decay of $F^{cos}(t_m;t_p)$ is not observed, consistent with the absence of a β-peak in the DS spectra. This conclusion is corroborated by findings that the time scale of the long-time decay strongly depends on t_p, indicating a diffusive nature of the process, but hardly depends on temperature, excluding that the long-time decay results from molecular dynamics.

For the example of TOL-d_5, the temperature dependence of $F^{cos}(t_m;t_p = 80\,\mu s)$ is presented in Fig. 22a, i.e., a large t_p is used to probe highly hindered dynamics.[1,99] When the temperature is increased, the amplitude of the short-time decay first increases and then decreases, where the amplitude is a maximum near $T \approx 97$ K. Such peculiar behavior was also reported for PB-d_6, *cf.* Fig. 22b. Further, the behavior resembles that found in simulations of a restricted reorientation governed

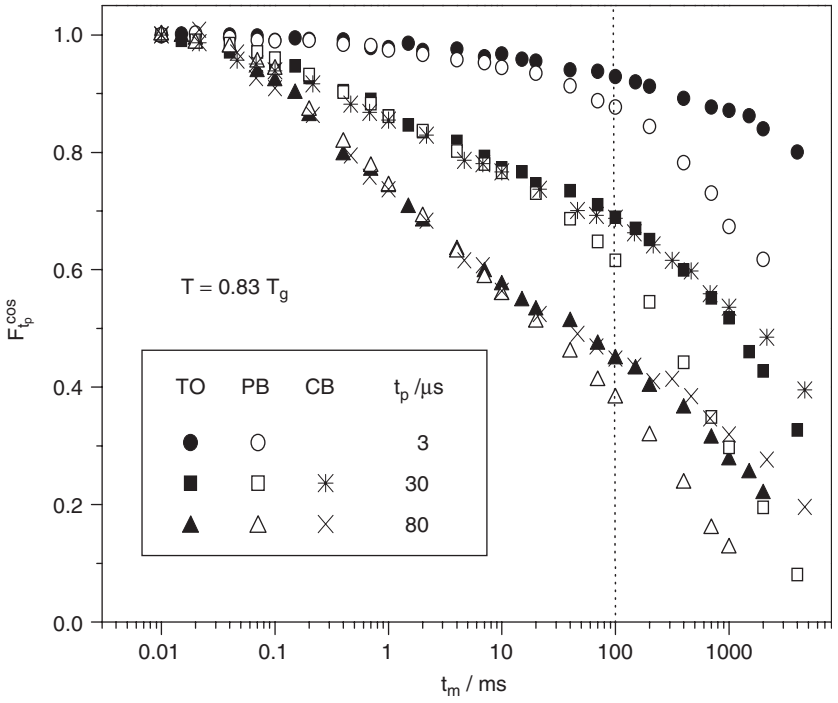

Fig. 21. Correlation functions $F^{cos}(t_m;t_p)$ for the type B glasses TOL-d_5 (TO), PB-d_6 and 45% CB-d_5 in DEC. Results for various evolution times t_p at a reduced temperature $T/T_g \approx 0.83$ are compared. (Adapted from Ref. 99.)

by a broad distribution $G(\lg \tau)$ (see Fig. 15). There, it became clear that the shift of a distribution $G(\lg \tau)$ that is much broader than the experimental time window does not lead to a corresponding shift of the correlation functions, but it manifests itself in a variation of the amplitude of the observed decay. Specifically, the amplitude is proportional to the fraction of the distribution $G(\lg \tau)$ lying in the time window of the experiment. The latter relationship was used to prove that the short-time decay observed for type B glasses results from the β-process.[99] For this purpose, the temperature-dependent amplitude of the short-time decay, $1-C_{tp}$, was determined from a suitable fit of $F^{cos}(t_m;t_p)$. For the examples of TOL and PB, we see in Fig. 23 that $1 - C_{tp}$ shows the same temperature dependence as the fraction of $G(\lg \tau_\beta)$ that is located between 100 µs and 100 ms. These limits of the experimental time window are given by the time scales of evolution time and spin diffusion, respectively, and the fractions were calculated based on the distributions $G(\lg \tau_\beta)$ obtained for TOL and PB in DS.[12,19] The nice agreement indicates that the shift of $G(\lg \tau_\beta)$ indeed determines the temperature dependence of the amplitude. Consequently, there are hardly any additional contributions to the temperature dependence of $1-C_{tp}$, implying that, for the majority of molecules, the geometry of the motion associated with the β-process is essentially independent of temperature at $T < T_g$. As will be

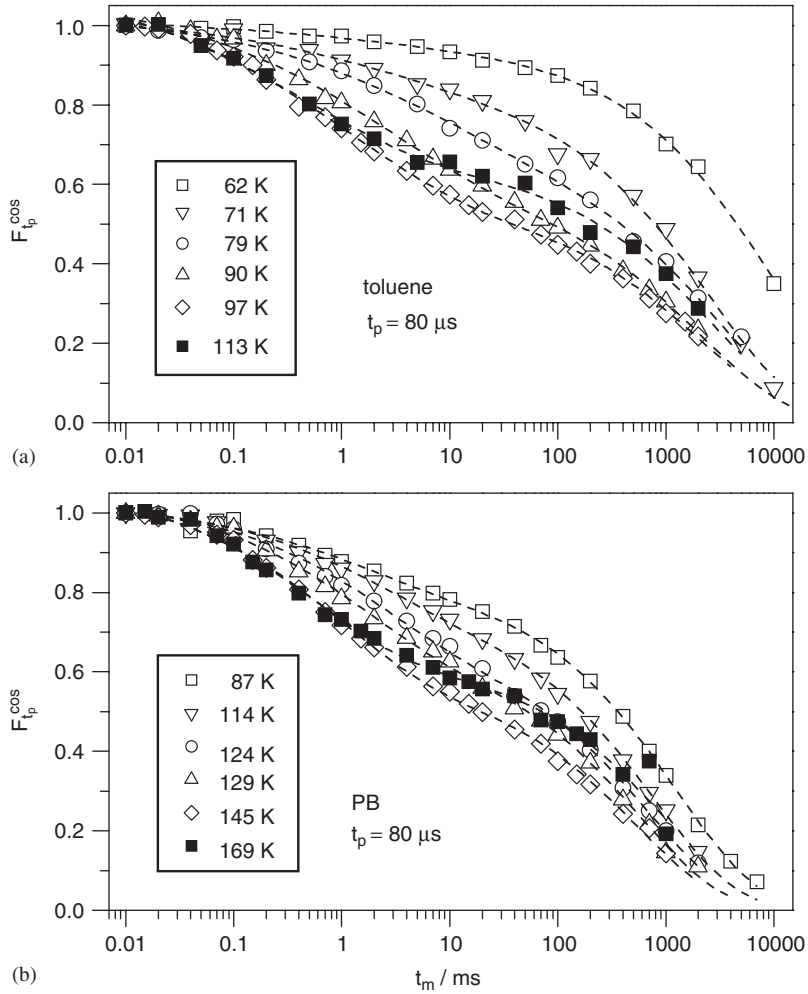

Fig. 22. Correlation functions $F^{cos}(t_m;t_p = 80\,\mu s)$ for the type B glasses (a) TOL-d_5 and (b) PB-d_6 at various temperatures $T < T_g$. The used evolution time $t_p = 80\,\mu s$ is sufficiently large so as to resolve highly hindered motion associated with the β-process of these glasses. The dashed lines are fits used to determine the amplitude of the short-time decay, $1–C_{tp}$. (Adapted from Ref. 99.)

discussed in Section 3.2.3, there may be a weak temperature dependence for a small fraction of molecules.

3.2.3. *The β-process of TOL: a model based on ^2H NMR data*

Discussing 1D and 2D ^2H NMR data, it was possible to put severe constraints on successful models of the β-process in molecular glasses. Specifically, it became clear

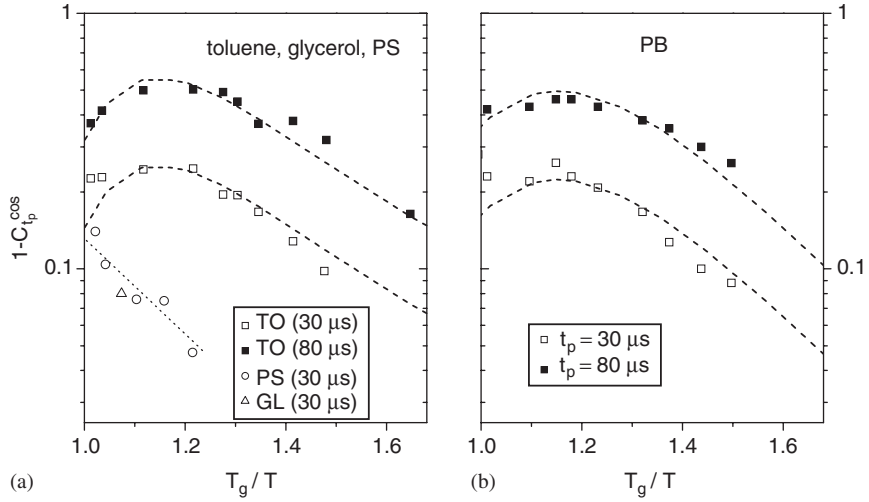

Fig. 23. Temperature-dependent amplitude $1–C_{tp}$ of the short-time decay of $F^{cos}(t_m;t_p)$ for the type B glasses (a) TOL-d_5 and (b) PB-d_6. Evolution times $t_p = 30$ and 80 µs were used. For comparison, results for the type A glasses GL-d_5 and PS-d_3 are included, indicating the absence of a short-time decay well below T_g. The dashed lines represent the respective fractions of the distribution $G(\lg \tau_\beta)$ lying in the time window of the experiments. They were calculated based on the distributions determined for TOL and PB in DS,[12,19] using Eq. (12). The fractions were multiplied with temperature-independent constants a_{tp} to match the t_p dependent values of $1–C_{tp}$. (Adapted from Ref. 99.)

that essentially all molecules participate in the β-process. Although the rotational jumps are restricted to small sections of the unit sphere for the majority of the molecules, a distribution of geometries of the motion may exist due to the disorder of the glassy state. Further, the data implied that the β-process does not result from simple dynamics, like a two-site jump, but rather from a multi-step process. Finally, there was evidence that, at $T < T_g$, the geometry of the motion is basically independent of temperature, consistent with an essentially constant dielectric relaxation strength. For the example of TOL, it was shown that these ingredients allow one to construct a model of the β-process that simultaneously describes all findings in 1D and 2D ^{2}H NMR experiments below T_g on a quantitative level.[1,110]

In this model,[110] it was assumed that all C–^{2}H bonds perform thermally activated rotational jumps within energy landscapes on the surface of a cone. Specifically, six basins were supposed to be separated by six energy barriers at positions 0, 60,…, 300° around the axis of the cone. For each cone, the barriers were drawn anew from the distribution of activation energies determined for TOL in DS.[12,19] Further, it was assumed that all positions on the surface of the cone, except for the barriers, have the same energy, i.e., a random-barrier model was considered. The thermally activated jumps lead to a random new position in one of the two neighboring basins. This means that several back-and-forth jumps occur over relatively low energy barriers until relatively high barriers are crossed. In other words, many

jumps are necessary to access all basins on the cone and, thus, the orientational correlation is lost in a multi-step process. In principle, the time scale of the jump dynamics at a given temperature is determined by the distribution of activation energies. However, the width of this distribution leads to dynamics on very different time scales so that it was not possible to simulate the resulting dynamics in a reasonable amount of time. Therefore, the low energy tail of the distribution was cut off and the fast jumps over these energy barriers were modeled by assuming an additional diffusive motion within the basins. To take into account the disorder of the glassy state, it was supposed that there is a temperature-independent distribution of geometries of the motion, i.e., a distribution of opening angles of the cone, $V(\chi)$.[110]

Adjusting the free parameters of the described energy-landscape model of the β-process, it was possible to reproduce all 1D and 2D ^{2}H NMR data of TOL below T_g.[110] Some examples are compiled in Fig. 24. Fig. 25 shows the temperature-independent distribution of the full opening angle, $V(\chi)$, which provides the good agreement between experiment and simulation. It is comprised of about 90% small angles $\chi < 10^\circ$ and 10% large angles $\chi > 10^\circ$, where the maximum is located near $\chi \approx 5^\circ$. Thus, the rotational jumps of the majority of TOL molecules are spatially highly restricted during the β-relaxation. Since the specific shape of $V(\chi)$ is not unique, the essential properties were determined.[110] First, it was assured that the basic features of the distribution are not altered when a different mechanism for the motion on the cone was assumed. Although $V(\chi)$ can be continuous, a description of results for both small and large values of t_p was found to require that angles $\chi > 10^\circ$ (10–20%) and angles $\chi < 10^\circ$ (80–90%) are present. While the values of the larger angles are somewhat ambiguous, it was argued that a maximum at $\chi = 5 \pm 1^\circ$

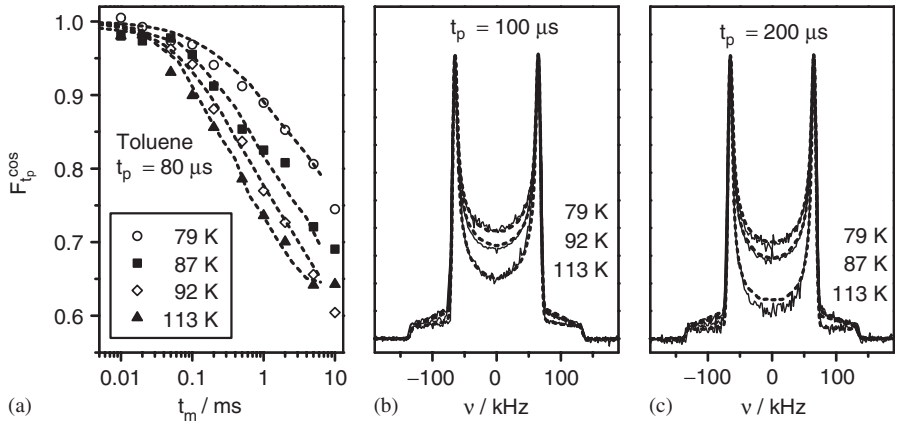

Fig. 24. ^{2}H NMR data for TOL at various temperatures $T < T_g$: (a) measured (points) and simulated within the energy-landscape model (dashed lines) correlation functions $F^{cos}(t_m;t_p = 80\,\mu s)$; (b) and (c) measured (solid lines) and simulated (dashed lines) ^{2}H NMR spectra for solid-echo delays $t_p = 100$ and $200\,\mu s$, respectively. (Adapted from Ref. 110.)

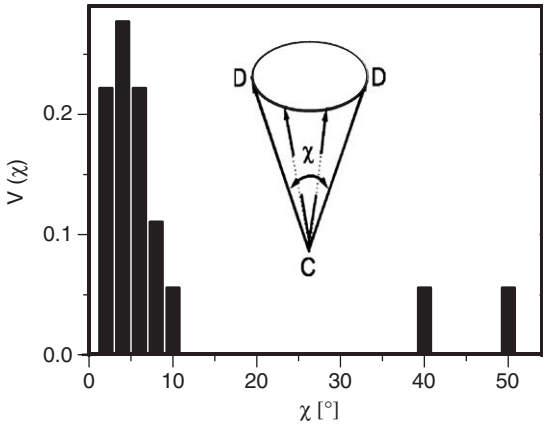

Fig. 25. Distribution $V(\chi)$ characterizing the full opening angles of the cones in the energy-landscape model of the β-process in TOL. (Adapted from Ref. 110.)

is necessary for the small-angle contribution. Since $V(\chi)$ is not varied, the temperature dependence of the simulated data is governed by the distribution of energy barriers independently determined in DS and by one adjustable parameter, namely, the diffusion coefficient that controls the additional diffusive motion within the basins, modeling jumps over otherwise neglected very small barriers of the distribution. Despite the success of this energy-landscape model, it is surely not unique. For example, in view of the structural disorder, one may expect that the energies of the basins are distributed, too. Moreover, it is not possible to exclude a weak temperature dependence of the distribution $V(\chi)$ since broad distributions hamper complete disentanglement of effects due to time scale and geometry of the motion. Strictly speaking, the discussed solid- and stimulated-echo experiments provide straightforward access to the behavior of the majority of molecules showing hindered reorientation about angles $\chi < 10^\circ$, but there is limited information about the minority of molecules undergoing less hindered reorientation about angles $\chi > 10^\circ$ and, hence, the properties of this fraction may change upon cooling. In any case, it may be of some interest that the distribution of opening angles $V(\chi)$ obtained for the β-process below T_g resembles the distributions of jump angles involved in the α-process above T_g[3,83,84] (*cf.* Section 3.2.5).

It may be appropriate to discuss the NMR findings on the β-process in the context of results from other experimental methods. Unlike ^{2}H NMR, the vast majority of experimental techniques are not capable of resolving slow reorientation about very small angles. In particular, several studies on the β-process of molecular glasses may have overlooked the small-angle contribution of the majority of molecules and concluded that a small fraction of molecules is involved in the secondary relaxation process. In contrast, straightforward analysis of ^{2}H NMR solid echo (*cf.* Section 3.2.1) and spin–lattice relaxation data (*cf.* Section 3.2.4 and in particular Ref. 115) clearly shows that essentially all molecules participate in the β-process. However, the amplitude of the reorientation differs among the molecules. The mean

amplitude of the β-process exhibits a weak temperature dependence below T_g, whereas it increases strongly when increasing the temperature above T_g. The latter finding correlates with a strong increase of the dielectric relaxation strength with temperature at $T > T_g$. Thus, in aging experiments at $T < T_g$, one may expect that the behavior of the β-process approaches that obtained from extrapolation of the strong temperature dependence at $T > T_g$, suggesting that the amplitude of the secondary relaxation decreases when the structural relaxation proceeds, as was indeed observed in DS.[112,116,117] The molecular motions associated with the β-relaxation contribute to the configurational entropy. Interestingly, it was argued[112] that the experimental values of the so-called excess entropy of glasses are smaller than the values expected for a situation where all molecules take part in the β-process. To discuss this argumentation, it useful to consider that simple calculation is limited to models where the molecules move independently between sites of equal energy. However, one can imagine that concerted motions reduce the contribution of the β-process to the configurational entropy. Also, for a disordered material, it is highly likely that a distribution of site energies exists. Indeed, the topologies of the potential-energy landscapes (PEL) of super-cooled liquids, as found in molecular dynamics simulations, provide possible explanations for the origin of the β-process (see Chapter 4). In conclusion, it may become an interesting challenge for future work to refine the above discussed energy-landscape model of the β-process – which uses the distribution of activation energies determined in DS as an external input, so as to enable not only a description of solid- and stimulated-echo experiments, but also of results from several other experimental techniques.

3.2.4. *Spin–lattice relaxation in the glass ($T < T_g$)*

Several NMR relaxation studies aimed at unraveling fluctuations persisting in glasses below T_g. Some studies on inorganic glasses discussed the NMR relaxation in terms "disorder modes", i.e., thermally activated dynamics in ADWP and at low-temperatures relaxation due to the presence of tunneling centers.[118–122] Both relaxation phenomena were identified by several techniques, in particular, by sound attenuation measurements,[27,123,124] and related to the low-temperature anomalies of glasses.[29–31] According to the so-called standard tunneling model, defects of the glass structure exist where groups of atoms move in potentials described in first approximation by an ADWP. At very low temperatures, say below 5 K, two-level systems (TLS) are assumed to be important due to tunneling in the ADWP. At higher temperatures, the model is extended so as to include thermally activated transitions over the barriers of the ADWP ("ADWP dynamics").[125–127] The TLS provide low-energetic excitations that enable explanation of the linear heat capacity of glasses at low temperatures. The barrier heights relevant for tunneling and activated jump processes are typically on the order of $0.1RT_g$ and RT_g, respectively, as compared to 10–30 RT_g for the β-process. Thus, ADWP dynamics is fast near T_g. Although the nature of the ADWP is still debated, the relaxation phenomena reported in the tunneling regime are quite universal for inorganic glasses.[124] For molecular glasses, one expects similar behavior, however, low-temperature

relaxation data from the various methods is rare.[27] For example, inspecting recent dielectric data compiled for GL in Fig. 2 one expects a crossover from the NCL behavior to some low-temperature processes around 50 K. The ^{1}H NMR spin–lattice relaxation was measured for GL down to 4 K, revealing relaxation times up to 10,000 s, where a crossover to relaxation via a coupling of the spin system to tunneling states was discussed below 10 K.[122] We add that recent high-field electron paramagnetic resonance (EPR) experiments also addressed such fast-relaxation processes in glasses.[128,129,130]

Other workers attributed the NMR relaxation in glasses to the "cage dynamics" discussed within MCT (*cf.* Sections 2.1 and 4).[69,131] For example, the cage dynamics or, more generally, the so-called fast dynamics (ps – ns) exhibits a weak temperature dependence and an anomalous increase of the corresponding mean square displacement, as monitored by NS[58–60] and LS.[47,61–65] This increase is usually found above T_g, but is also expected to be present below T_g. Therefore, assuming the extreme narrowing condition $\omega_L\tau \ll 1$, the NMR relaxation results were compared with that reported for the Debye–Waller factor in NS work (see Section 2.1).

As was discussed in Section 2.2, it is usually assumed that the NMR coupling constant, which is required for an analysis of the spin–lattice relaxation in supercooled liquids, does not depend on temperature so that it can be taken from the solid-state spectrum at $T \cong T_g$. Thus, it is neglected that fast-relaxation processes in glasses can lead to pre-averaged NMR coupling constants. A new picture may emerge from recent line-shape studies, monitoring the quadrupolar coupling constant of type A and B glass formers down to low temperatures.[3] Small changes of the coupling constant were found, which are similar for all glasses investigated. Near T_g, it appears that strong temperature dependence is present, showing similarities with the anomalous temperature dependence of the Debye–Waller factor. However, when analyzing the width of NMR spectra for type B glass formers, one has to take into account that the β-process can render the NMR line width temperature-dependent, too.

Returning to the spin–lattice relaxation studies, the relaxation behavior of type A and B glasses was systematically compared only recently.[3,100,101] It turned out that, at least down to $T \cong 0.5\ T_g$, the spin–lattice relaxation in molecular glasses (without internal relaxing degrees of freedom) is essentially determined by the "slow dynamics", namely the NCL contribution and the β-process.[70,73,100,101,115] Next, we shall briefly review these studies.

In the glassy state, non-exponential ^{2}H NMR spin–lattice relaxation is observed.[46,132,133] This effect is much stronger than that observed in crystalline materials where anisotropic reorientation leads to some non-exponentiality.[134] The differences are due to the fact that the large variety of local environments in the glass leads to broad distributions of correlation times for secondary relaxation processes. Correspondingly, there is a distribution of spin–lattice relaxation times T_1, resulting in non-exponential relaxation behavior since spin diffusion is slow in ^{2}H NMR and, hence, it does not lead to a complete averaging of the heterogeneity. This was exploited to characterize the motional non-uniformities of mobile guest molecules or of side groups in glasses.[1,3,135–137,139–141] For neat molecular glasses, it

turned out that ^{2}H spin-diffusion becomes effective at about 0.1 s.[142] On this time scale, spin–lattice relaxation near T_g is not complete so that the average relaxation time $\langle T_1 \rangle$, as given by the integral over the normalized relaxation function $\phi(t) = [M_o - M(t)]/M_o$, is spoiled by the presence of spin diffusion at long times. To extract quantitative information from relaxation data, it is thus more appropriate to analyze the average relaxation rate $\langle 1/T_1 \rangle$. Since the rate $\langle 1/T_1 \rangle$ reflects the initial slope of the relaxation function $\phi(t)$, it is not affected by spin diffusion.[143] In many cases, however, only the average relaxation time $\langle T_1 \rangle$ is available, which actually can be measured more reliably than $\langle 1/T_1 \rangle$. Assuming that the effect of spin diffusion is only weakly temperature-dependent, the relaxation rates $\langle 1/T_1 \rangle$ and $1/\langle T_1 \rangle$ are proportional to each other.

The starting point of analyzing the spin–lattice relaxation in molecular glasses ($T < T_g$) is the observation that the temperature dependence of the relaxation time $\langle T_1 \rangle$ allows one to discriminate between type A and B glasses. In Fig. 26, we once again present the ^{2}H NMR relaxation data for several molecular glasses, where, however, the data is now shown in a double logarithmic plot (see also Fig. 13). For the sake of comparison, we included results for PB-d_6[101] and ETH-d_1.[113] Clearly, the relaxation of type A glass formers is at least by a factor of 10 slower than that of type B glass formers and the temperature dependence is different. Due to the presence of the β-process, the spectral density of type B systems is significantly enhanced, resulting in a relatively fast relaxation. Moreover, one finds similar relaxation behavior among type A and B systems. For type B glass formers, this is a direct consequence of the finding that, on a T_g/T scale, the activation enthalpy ΔH_β, the amplitude 1 – S, and the shape of the β-process are often similar (see Section 2.1), leading to a comparable spectral density $J_\beta(\omega)$.[19,56] Exceptions are PB and ETH, which exhibit an even faster relaxation. While the comparatively short relaxation times $\langle T_1 \rangle$ of ETH[113,144] can be traced back to an unusually fast-secondary relaxation in this glass, *cf.* Fig. 20, the different behavior of PB can be rationalized by the presence of a further fast-relaxation process, *cf.* Fig. 29. It is important to note that the temperature dependence of the spin–lattice relaxation of type B glasses is significantly smaller than that expected based on the activation energy determined in DS (see Fig. 3). Further, a power-law behavior rather than Arrhenius temperature dependence is found.[70] The reason is that in addition to the activation energy the broadening of the distribution function $G_\beta(\ln \tau)$ affects the temperature dependence of $\langle T_1 \rangle$. For a simple thermally activated process, the width of $G_\beta(\ln \tau)$ is proportional to $1/T$. However, one has to keep in mind that also the attempt frequencies of the β-process may be governed by some distribution, corresponding to a distribution of activation entropies, leading to a different temperature dependence of the width of $G_\beta(\ln \tau)$.[145]

Following the reasoning in Section 2.1 we can write for the correlation function in the glass

$$F_{\text{glass}}(t) = f[(1 - S)g_\beta(t) + S] \quad T < T_g. \tag{13}$$

This yields the spectral density

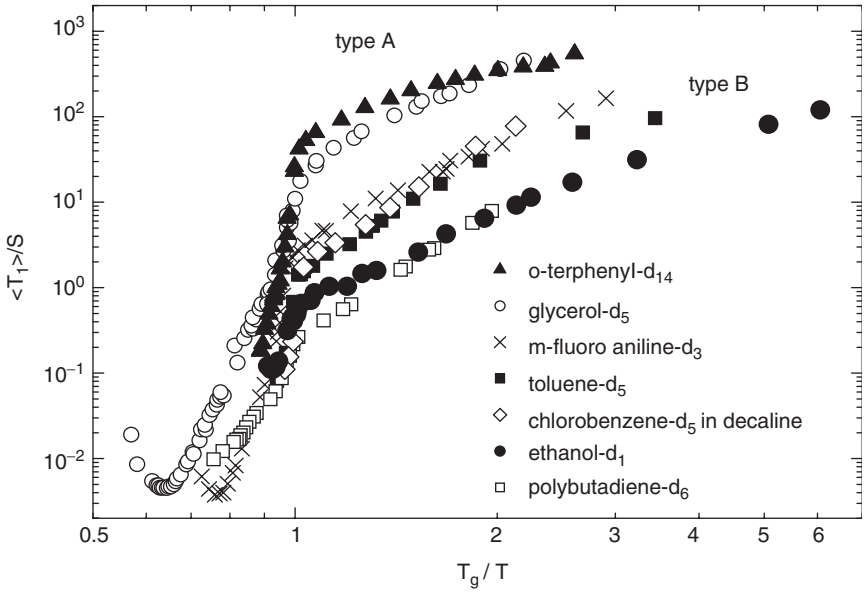

Fig. 26. ^{2}H spin–lattice relaxation times for type A and B glass formers (double-logarithmic scale, compiled from Refs. 68, 69, 100, 101, 113, 146).

$$J_{\text{glass}}(\omega) = f(1-S)J_\beta(\omega) + fS2\pi\delta(\omega) \quad T < T_g. \tag{14}$$

In most experiments, the second term of the right hand side of Eq. (14) can be ignored. Consequently, one obtains for the spin–lattice relaxation

$$1/\langle T_1\rangle \propto \langle 1/T_1\rangle \propto f(1-S)[J_\beta(\omega_L) + 4J_\beta(2\omega_L)] \tag{15}$$

Well below T_g, it is possible to neglect the temperature dependence of the non-ergodicity parameter f, and the spectral density $J_\beta(\omega_L)$ can be calculated, e.g., assuming a logarithmic Gaussian distribution $G_\beta(\ln\tau)$, corresponding to a Gaussian distribution of activation enthalpies (and entropies) as is typically done in DS[19,20,53] (*cf.* Eq. (2)).

Analyzing the ^{2}H spin–lattice relaxation of TOL, a simple two-site jump model was applied[46] to relate the relaxation strength 1 – S of the β-process to an angular displacement, resulting in a mean jump angle $<\chi>$ changing from 13° at 115 K to 9° at 75 K, which are in fair agreement with results of ^{2}H NMR solid- and stimulated-echo studies (see Section 3.2.3). However, the latter studies gave no evidence for a significant temperature dependence of the geometry of the motion, consistent with findings in DS where the relaxation strength (1 – S) is virtually temperature-independent below T_g.[19] Deuterating TOL at different positions showed[147] that, unlike above T_g, the molecular reorientation is somewhat anisotropic below T_g. A combined study of the ^{2}H spin–lattice and DS relaxation of the β-process in a homologous series of primary alcohols[72,148] reported angular displacements smaller

than $<\chi>/2/<0^{\circ}$. Further, the authors concluded that the excess wing gradually transforms into a β-process when the molecular weight is increased, rendering a distinction between type A and B glass formers questionable. Similar conclusions were drawn from a dielectric study of binary glass formers.[149] In the light of these experiments the excess wing is a quite universal limiting case of the β-process, although one should keep in mind that glass formers are known, which exhibit both phenomena excess wing and β-process.[19,38,40] In any case, various ^{2}H NMR techniques consistently show that all molecules take part in the β-process of molecular glasses (see also Sections 3.2.1 and 3.2.2).

It may be interesting to compare the relaxation strengths $1 - S_{NMR}$ extracted from NMR experiments with the values obtained in DS via $1 - S_{DS} = \Delta\varepsilon_{\beta}/\Delta\varepsilon$. In the limit of small-angle motion, $1 - S_{NMR} = 3(1 - S_{DS})$ is expected since NMR and DS probe different reorientational correlation functions.[73,150] Although the existing data is not sufficient to settle this question, there is some correlation: the spin–lattice relaxation near T_g is the faster the larger the β-peak in the DS. For example, the glass former *m*-fluoro aniline (FAN), showing the slowest spin–lattice relaxation among the type B glass formers considered in Fig. 26, exhibits also the smallest dielectric β-peak.[19] Thus, the existence of glasses exhibiting an even smaller relaxation strength of the β-process may suggest that there is a continuous crossover from type B to type A relaxation behavior. Most relaxation studies suffer from the problem that relaxation strength, mean time constant and width of the distribution of activation enthalpies determine the relaxation behavior in the glass and, hence, it is not straightforward to disentangle the effects. Moreover, competing processes are present, e.g., "fast processes" may become dominant at low temperatures. Therefore, it is necessary to compile data over a wide temperature and frequency range to separate the various contributions.

We note that, as long as effects due to spin diffusion can be neglected, analysis of the full relaxation function $\phi(t)$ can yield information that is not available from the first moments $\langle 1/T_1 \rangle$ and $\langle T_1 \rangle$. For example, it is possible to extract information about the width of the distribution of correlations times governing the β-process. Recently, such approach was used to elucidate the change of the β-process coming along with a confinement of a glass former in a nano-porous material.[100]

Though relaxation data for type B glasses at low temperatures is still rare, it may be seen in Fig. 26 that the temperature dependence of the relaxation times becomes weaker at lowest temperatures, suggesting that another relaxation mechanism starts to dominate. For type A glasses, where a β-process is absent, there is evidence that the spin–lattice relaxation is governed by the NCL phenomenon (*cf.* Figs. 2 and 27b). For GL[73] the relaxation rate $\langle 1/T_1 \rangle$ was calculated from the DS, assuming that the NMR spectral density can be expressed by the dielectric susceptibility, explicitly $J_2(\omega) = \varepsilon''(\omega)/(\Delta\varepsilon\,\omega)$. In Fig. 27a, the measured and calculated T_1 values are compared, showing nice agreement over the whole temperature range. Hence, the NCL determines the spin–lattice relaxation of GL at $T < T_g$. A crossover to the relaxation behavior associated with the low-temperature anomalies is expected below some 50 K[122] (*cf.* also Fig. 2).

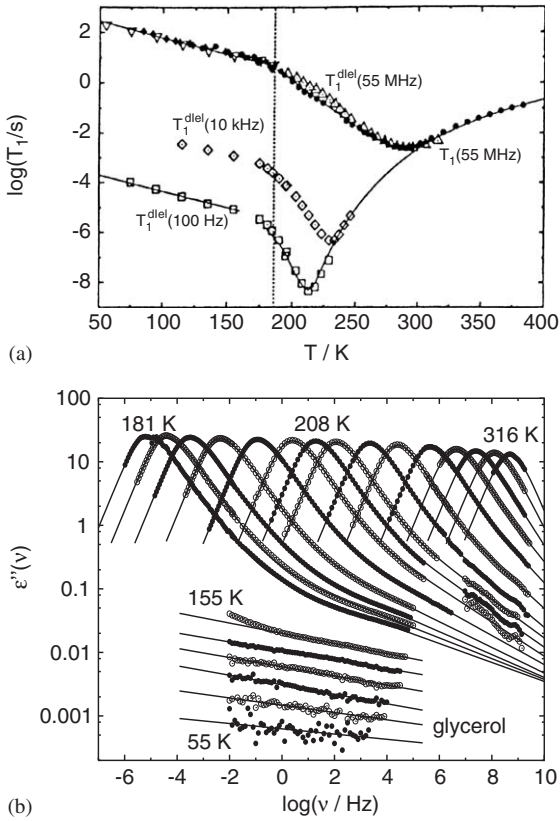

Fig. 27. (a) Spin–lattice relaxation time of GL as a function of temperature: ^{2}H NMR data at 55 MHz (solid circles) are compared with calculations for three frequencies, which are based on the dielectric loss of GL; the vertical line indicates T_g. (b) DS spectra of GL together with interpolations (solid line) used to calculate the spin–lattice relaxation times. (Adapted from Ref. 73.)

3.2.5. *Indication of small-angle motion above* T_g

In Section 3.2.3, it was demonstrated that spatially highly restricted reorientations associated with the β-process lead to characteristic changes of ^{2}H NMR spectra when the solid-echo delay t_p is augmented. These spectral changes were found well below T_g, where effects due to the α-process can be excluded. Interestingly, glass formers without discernible β-process exhibit similar spectra above T_g,[56,78,151] more precisely, at temperatures where the α-process is still too slow to completely average the anisotropy of the quadrupolar interaction. In Fig. 28,[56] we show the effects for the examples of GL and *meta*-tricresyl phosphate (*m*-TCP), in the latter case ^{31}P NMR was applied. For large solid-echo delays t_p, line-shape changes are observed even at temperatures near the glass transition, e.g., at $T = 193$ K where $\tau_\alpha = 6$ s,

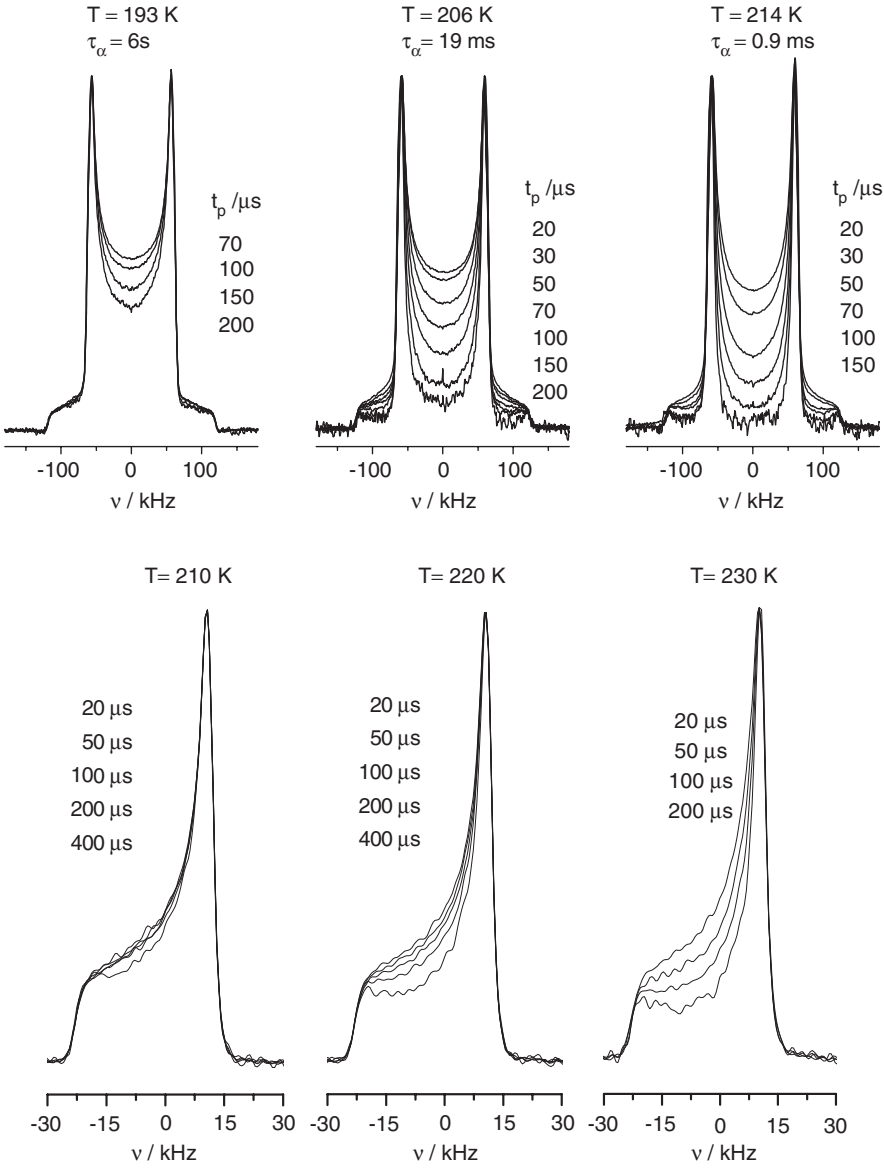

Fig. 28. (top): Solid-echo ^{2}H NMR spectra of GL (adapted from Ref. 56) ($T_g = 189\,K$), time constants of α-process are indicated; (bottom) Hahn-echo ^{31}P NMR spectra of TCP[1] ($T_g = 214\,K$) for various t_p values. Both sets of spectra were measured slightly above T_g.

indicating that molecular dynamics in the μs-regime still exists. In contrast, the ^{2}H NMR spectrum for short t_p is essentially temperature-independent up to about 225 K (*cf.* Fig. 9).

For the type A glass former polystyrene (PS)[9,78,152] similar changes of the ^{2}H NMR line shape were attributed to the α-process. Specifically, the α-process was modeled as isotropic rotational diffusion process governed by a distribution of correlation times $G(\ln \tau_\alpha)$ that strongly broadens when the temperature is lowered. In the case of rotational diffusion, i.e., for small-angle reorientation, the elementary steps of the motion occur on a time scale several orders of magnitude shorter than τ_α. Thus, despite $\tau_\alpha \gg 1/\delta$, these elementary steps can take place right in the μs-time window of the experiment. However, multidimensional NMR showed that isotropic rotational diffusion is not a realistic model of the α-process in PS[153] and the assumption of a strongly temperature-dependent width of $G(\ln \tau_\alpha)$ appears somewhat artificial (see Section 2.1). An alternative explanation may be to attribute the lineshape changes near T_g to the excess wing found for type A glass formers on the high-frequency side of the α-process (*cf.* Fig. 1), suggesting that excess wing and β-process involve similar spatially highly restricted motion. The excess wing has the character of a secondary relaxation process since, upon cooling, it emerges near T_g and - in form of the NCL behavior, it persists below T_g, just as the β-process does. However, further experiments are needed to clarify the nature of this relaxation, in particular, its relation to α- and β-process.

3.3. Secondary relaxation processes of polymers

Next, we discuss NMR results on the β-process of polymers to ascertain similarities and differences of the secondary relaxation in molecular and polymeric glasses.

In view of important technologic applications, various multidimensional NMR techniques were used to investigate the β-process of polymethyl methacrylate (PMMA) and poly(ethyl methacrylate) (PEMA).[4,154–158] It became clear that the β-process is associated with a $180° \pm 20°$ flip of a fraction of ester units that is coupled to a restricted rearrangement of the main chain. Concerning the former motion, bimodal distributions of correlation times were reported so that a temperature-dependent fraction of side groups are trapped on the timescale of the β-process. For the main chain, the dynamics in the glassy state can be described as a restricted rocking motion ($\pm 20°$) around the local chain axis, where, unlike the flip motion, all monomers participate.[154,155] Well below T_g, the geometry of the main chain motion is essentially temperature-independent, at least for PMMA,[157] whereas, above T_g, the amplitude strongly increases with temperature and a coupling of α- and β-process was proposed.[156,158] In addition, the β-process of poly(alkyl methacrylates) was studied in ^{13}C magic-angle spinning (MAS) NMR.[9,159–163] Under MAS conditions, lines of the main chain can be distinguished from those of the side chain and, hence, selective labeling is not necessary, but a single measurement is sufficient for a separate analysis of the respective dynamics. For poly(n-hexyl methacrylate), ^{13}C MAS NMR showed that, at $T > T_g$, the main chain takes part in

both the α- and β-process, while the side chain only participates in the latter.[163] Interestingly, findings of dielectrical and mechanical relaxation studies on poly(n-hexyl methacrylate), suggested that the structural relaxation at high temperatures is a continuation of the low-temperature β-process rather than the α-process, which dies out somewhat above T_g.[164,165] However, recent NMR work on poly(alkyl methacrylates) reported that the high-temperature process usually considered does not lead to isotropization of the backbone orientation, but complete structural relaxation is left to a slower process involving extended backbone chain conformations.[166]

These results for poly(alkyl methacrylates) suggest that jumps of asymmetric side groups require concomitant reorientation of the main chain to remove sterical restrictions that otherwise prohibit an accommodation of the side group in the new orientation. Consistently, reorientation of the polymer backbone was not observed, when flips of symmetric side groups are associated with β-like processes, i.e., when sterically equivalent positions are involved. Phenylene-ring flips in polycarbonate[167,168] and in PS[169] provide examples. Hence, one may speculate that side-group motion triggers a β-process of the polymer backbone. On the other hand, it was argued that it is the other way round and an intrinsic β-process of the main chain is necessary to enable side-group motion.[55] Consistently, PB, a polymer without side groups, does exhibit a β-process. Thus, it remains an open question whether side-group motion is reason or consequence of β-like backbone dynamics.

In any case, for various polymers, NMR spectra were analyzed to characterize side-group motions involved in β-like relaxation processes. In the case of PS, line-shape analysis showed that a broad, bimodal or continuous distribution of correlation times $G(\ln\tau)$ governs 180° flips of the phenyl rings,[102,169–172] which are accompanied by small-angle jumps.[1,171] Likewise, 180° flips of phenyl rings were attributed to the β-process of *bis*-phenol–C dimethylether.[173,174] In addition, ^{2}H and ^{13}C NMR line-shape analyses were performed to investigate the β-process of polyethylene terephthalate (PET, $[COO–C_6H_6–COO–(CH_2)_2]_n$) where the phenyl rings are parts of the main chain.[175] Raising the temperature at $T < T_g$, it was found that the mobility of the phenyl rings increases, where the dynamical process is comprised of fluctuations with amplitudes of about $\pm 40°$ and 180° flips for a fraction of phenyl rings. While fluctuations about $\pm 40°$ were also reported for the carbonyl moieties of PET, it was argued that the glycol units are immobile. However, a careful inspection of the data may suggest that the glycol groups show reorientations with smaller amplitudes. A comparison of NMR and dielectric investigations on secondary relaxation processes of polymers can be found in Ref. 4.

Finally, we take the opportunity to discuss some peculiarity in the case of PB. Dielectrically, PB exhibits a β-process that resembles that of TOL.[19] However, we see in Fig. 27 that $\langle T_1 \rangle$ is significantly shorter for PB than for TOL.[101] Moreover, when large solid-echo delays t_p are applied, the ^{2}H NMR line shape was found to change at low temperatures where the β-process has exited the NMR time window.[101] These findings can only be understood when a further relaxation process is assumed. Indeed, using a high-precision capacitance bridge and monitoring the dielectric loss of PB down to 4 K, a third-relaxation peaks appears near 80 K,

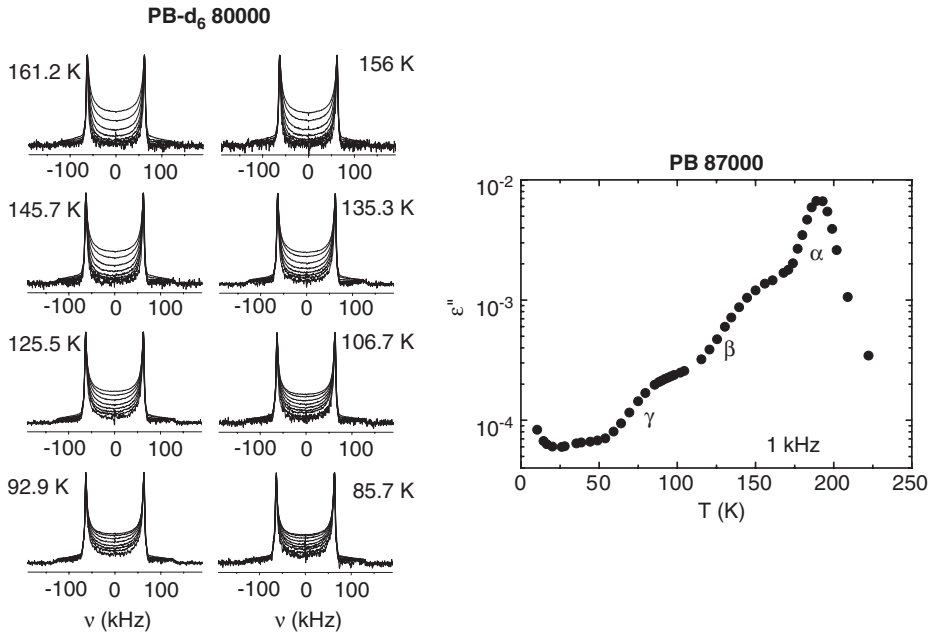

Fig. 29. (left) ^{2}H NMR spectra of PB-d_6 (molecular weight is indicated) for large solid-echo delays $t_p = 50$–$400\,\mu s$; (right) dielectric response of PB. (Adapted from Ref. 101.)

cf. Fig. 29. This is the first example that NMR studies had provided evidence for a relaxation process in the glass that only later was probed by DS.

3.4. Multi-component glasses

In the previous sections, we reviewed NMR work on neat glass formers, including studies of both main and secondary relaxation processes. Regarding the manifestation of secondary processes, it was useful to distinguish type A (without discernible β-process) and type B (with discernible β-process) glasses. However, mixing two type A glass formers, a strong secondary relaxation was observed in DS,[149] i.e., it appears that the excess wing in the neat glass former transforms into a β-process in the mixed systems. Thus, distinction between type A and B[19] may be obsolete. NMR proved well suited to study the nature of this secondary relaxation in binary glasses. In particular, it was exploited that appropriate labeling allows one to determine to which extent the two components participate in the β-process. Before we discuss such experiments we will briefly review peculiarities of the glass transition in binary systems.

3.4.1. *Glass transition of binary molecular glasses*

Doping a neat glass forming system with smaller molecules leads to a reduction of the glass transition temperature T_g.[176] In polymer research, this behavior is well known as polymer/plasticizer effect. However, it applies to any mixture provided that the T_g value of the additive is significantly lower than that of the main component.

Passing through the glass transition of binary glass formers, the large and small molecules behave differently with respect to the variation of the ^{2}H NMR line shape. The results for the large molecules[178] resemble that for neat systems (*cf.* Fig. 9), i.e., there is a continuous collapse of the rigid–lattice spectrum upon heating. In contrast, the line shape for the small molecules can be approximated by a so-called two-phase spectrum, i.e., by a superposition of a liquid spectrum and a rigid–lattice spectrum.[1,3,75,136,151,177,178–182] In Fig. 30a, the latter behavior is presented for the example of benzene in PS.[183] Two-phase spectra can be rationalized by assuming a broad distribution of correlation times $G(\ln\tau)$ so that the contribution of intermediate spectra resulting from molecules with $\tau \approx 1/\delta$ can be neglected.[136,138] Then, it is sufficient to consider spectra corresponding to the fast ($\tau \ll 1/\delta$) and slow ($\tau \gg 1/\delta$) motion limit and, hence, the total spectrum can be decomposed into

$$S(\omega; T) = S_{\text{fast}}(\omega)W(T) + S_{\text{slow}}(\omega)[1 - W(T)] \tag{16}$$

For benzene in PS, 2D ^{2}H NMR experiments confirmed the existence of a broad and continuous distribution of correlations times. From Fig. 30b[183] it is apparent that benzene molecules appearing as a static contribution in the ^{2}H NMR spectrum of Fig. 30a are not truly immobile, but show rotational jumps on a longer time scale of ms - s. It is further evident that reorientation on a time scale of 100 ms occurs well below T_g, indicating a strong decoupling of additive and polymer dynamics, where only the latter reflects the glass transition. We emphasize that such two-phase spectra are also observed for additives in low molecular weight PS (*cf.* Fig. 31), and it appears that this phenomenon is observed in any binary glass provided the components show significantly different values of T_g.[184]

While the structural relaxation in neat super-cooled liquids results from a predominantly small-angle process[3] (*cf.* Section 2.2), the reorientation of the molecularly small component in binary glasses occurs via a large angle process close to an isotropic random jump.[183] As a consequence, the 2D NMR spectra at sufficiently low temperatures can be described in analogy with the 1D NMR spectra, by the superposition of two spectral patterns, namely, a diagonal spectrum, $S_{\text{dia}}(\omega_1, \omega_2)$, representing molecules that are immobile during the mixing time and a spectrum typical of complete isotropic reorientation, $S_{\text{reo}}(\omega_1, \omega_2)$, resulting from molecules that performed large angle jumps during t_m (*cf.* Fig. 30b, 211 K).[185] In the case of a random-jump process, the dependence of the corresponding weighting factor on the mixing time directly yields the correlation function $F_2(t_m)$.[183]

At higher temperatures, a central peak $S_{\text{Lor}}(\omega_1, \omega_2)$ shows the existence of fast molecules on the NMR time scale (*cf.* Fig. 30b, 230 K).[90,183] More interestingly, there is also a cross-like pattern $S_{\text{ex}}(\omega_1, \omega_2)$, which can be understood as a product

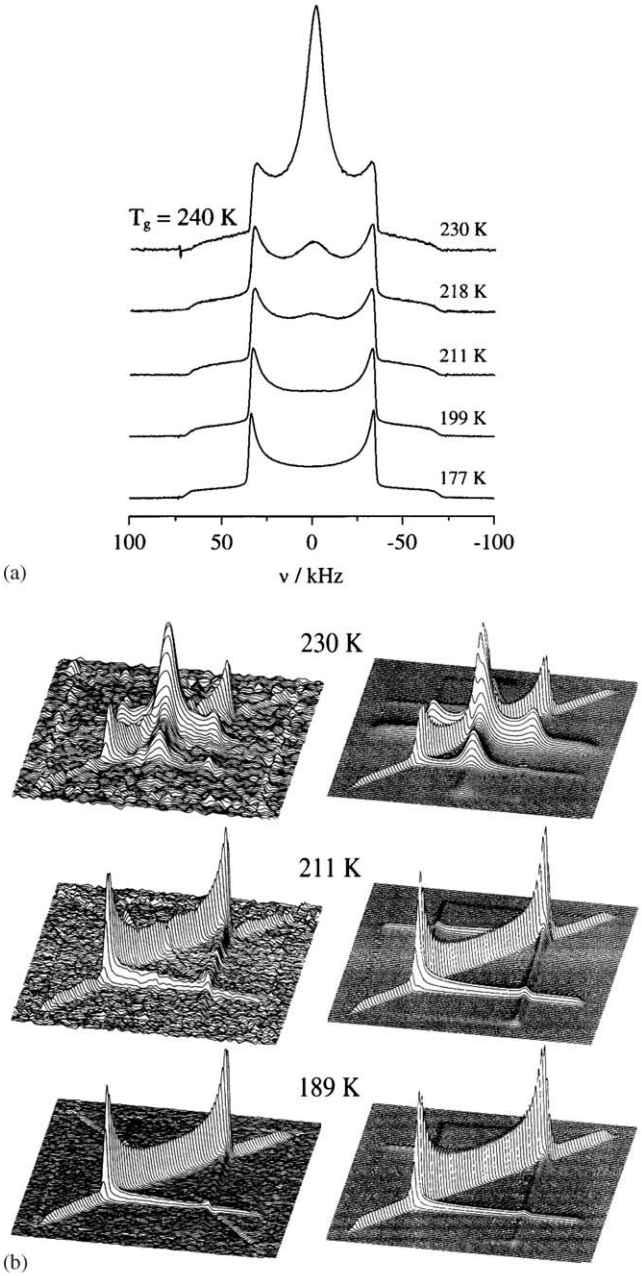

Fig. 30. ^{2}H NMR data for 26% benzene-d_6 in PS ($M = 1020$ g/mol) at different temperatures ($T_g = 240$ K): (a) 1D spectra and (b) experimental and simulated 2D spectra ($t_m = 100$ ms).[183] At the temperatures studied, the six-fold jump of the benzene molecules is fast on the NMR time scale ($\tau \ll 1/\delta$) so that its mere consequence is a pre-averaging of the quadrupolar coupling tensor.

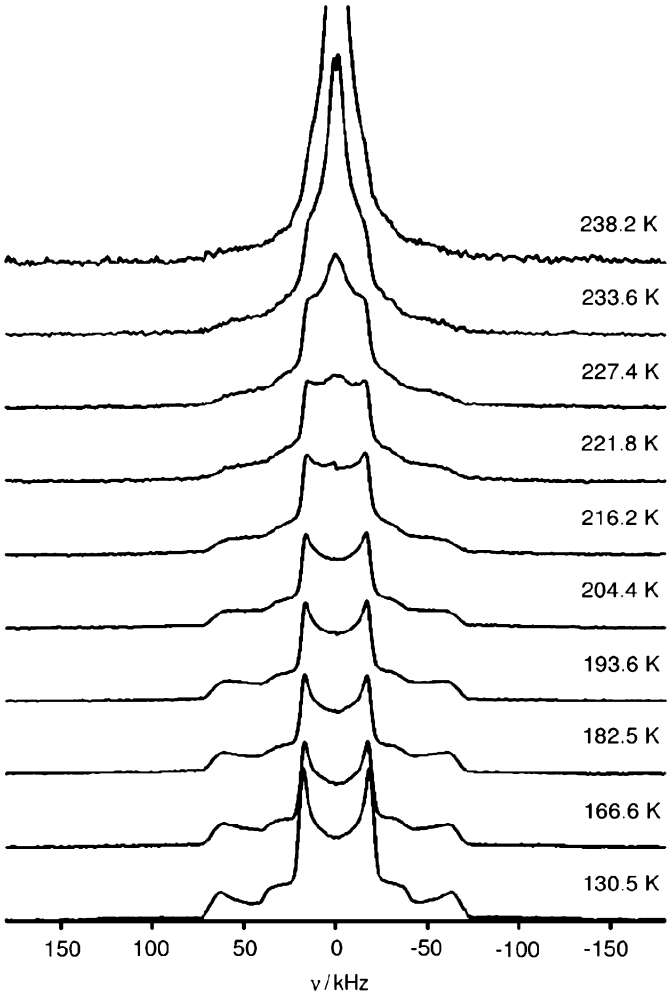

Fig. 31. ^{2}H NMR spectra of 7% picoline-d_7/tri-styrene for a solid-echo delay $t_p = 15\,\mu s$ ($T_g = 222\,K$).[189]

of a Lorentzian line in the ω_1 dimension and a Pake spectrum in the ω_2 dimension, and vice versa.[90,186] It indicates exchange processes between fast ($\tau \ll 1/\delta$) and slow ($\tau \gg 1/\delta$) molecules. Based on the four contributions $S_{dia}(\omega_1, \omega_2)$, $S_{reo}(\omega_1, \omega_2)$, $S_{L\ or}(\omega_1,\omega_2)$ and $S_{ex}(\omega_1, \omega_2)$, the 2D NMR spectra can be described as

$$S(\omega_1, \omega_2; t_m) = p_{dia} S_{dia}(\omega_1, \omega_2) + p_{reo} S_{reo}(\omega_1, \omega_2) + p_{Lor} S_{Lor}(\omega_1, \omega_2) + p_{ex} S_{ex}(\omega_1, \omega_2), \quad (17)$$

where $p_{dia} + p_{reo} + p_{Lor} + p_{ex} = 1$ and the four spectral patterns are normalized according to $\int d\omega_1 d\omega_2\ S_x(\omega_1,\omega_2) = 1$. When the mixing time dependence of the weighting factors p_i is analyzed, reorientation and exchange processes can be

studied separately. For benzene in PS, it was found that reorientation and exchange occur on the same time scale.[90,93,184] We emphasize that 4D NMR experiments have to be performed to study an exchange of the correlation time in neat systems.[3,4] Here, 2D NMR is sufficient since fast and slowly reorienting molecules can be already discriminated in the 1D NMR spectrum.

In view of these results for binary glasses composed of molecules with different masses respectively different T_g, one may speculate that the isotropic reorientation of the small molecules results from translational diffusion in an essentially rigid glassy matrix formed by the large molecules, i.e., the diffusional process may be probed by ^{2}H NMR via rotational-translational coupling.[183] Finally, we note that the stimulated-echo technique was also applied to study the main relaxation in sugar-water systems.[187,188]

3.4.2. *The secondary relaxation in binary molecular glass formers*

DS on 2-picoline/tri-styrene revealed the existence of a β-like relaxation process,[149] whereas the neat components are typical type A glass formers (see Fig. 16). To ascertain the nature of the secondary relaxation in the mixture, ^{2}H NMR was applied on 2-picoline-d_7/tristyrene.[189] In Section 3.2, it was demonstrated for neat glass formers that large solid-echo delays t_p have to be applied to be sensitive to small-angle reorientations characteristic of the β-process. Consistently, when a short t_p is used, the ^{2}H NMR spectra of 2-picoline-d_7/tri-styrene do not indicate a secondary process (see Fig. 31),[189] and they look similar as those of benzene in PS (*cf.* Fig. 30a). They are comprised of two sub-spectra originating from deuterons of the methyl group and the phenyl ring, respectively. Fig. 32a shows temperature-dependent ^{2}H NMR spectra for a large-echo delay. We see line-shape changes typical of spatially highly restricted motion, indicating that the picoline molecules participate in the β-process of the binary glass. Due to the large echo-delay, the small difference of the isotropic chemical shift of deuterons in the methyl group and phenyl ring, respectively, leads to severe distortions of the spectra, *cf.* Fig. 32b. Nevertheless, when this effect is taken into account, RW simulations based on a cone model (see Section 3.2.3) allow one to reproduce the line shape.[1,189]

Another tool to probe motion with high sensitivity is measurement of the ^{2}H spin–spin relaxation time T_2. In Fig. 32c, one recognizes for picoline-d_7/tri-styrene that T_2 exhibits a shallow minimum well below T_g. This is characteristic of a fast β-like relaxation process, similar to that observed in ETH (*cf.* Fig. 21a). This conclusion is confirmed when inspecting the time constants τ_β reported in DS work (see Fig. 32d).[149]

Fig. 33 depicts 2D ^{2}H NMR spectra of 2-picoline-d_7/tri-styrene for different temperatures.[189] The spectra at high temperatures, i.e., at 227 K and 216 K, can be understood within the dynamical scenario discussed in Section 3.4.1, namely a broad distribution of correlation times characterizing the liquid-like motion. In the spectrum at 130 K, the intensity is essentially restricted to the diagonal, although the β-like process lies right in the time window of the experiment, *cf.* Fig. 32d. Similar behavior was found for neat glass formers (see Section 2.1). It indicates that

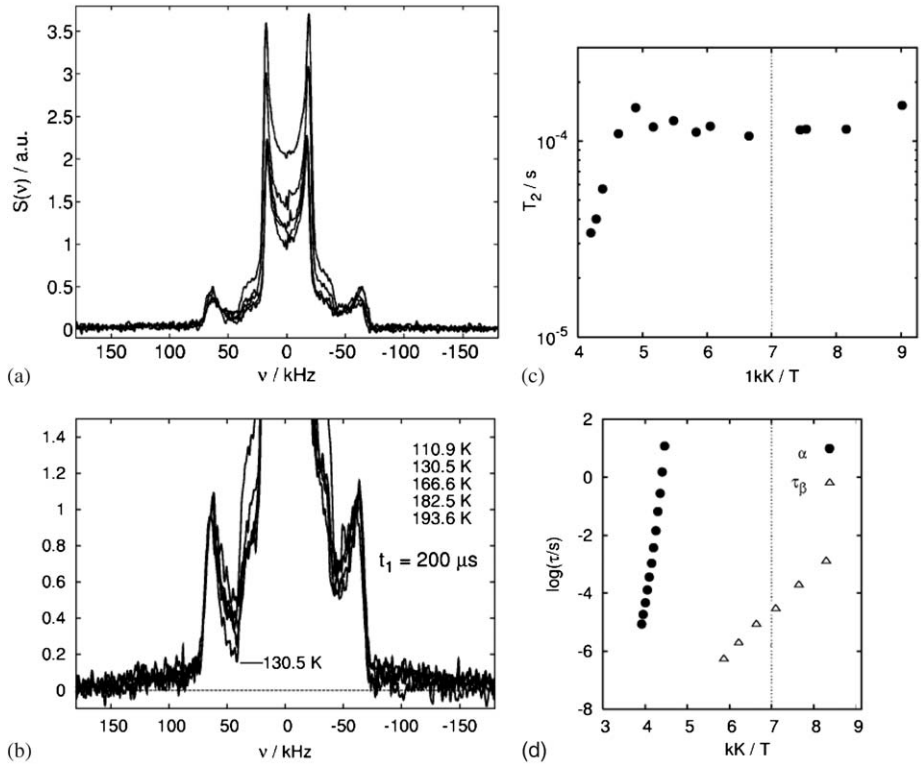

Fig. 32. (a) ^{2}H NMR spectra of 7% picoline-d_7/tri-styrene for a solid-echo delay $t_p = 200\,\mu s$ at different temperatures as indicated in (b); (b) the same spectra as in (a), but normalized to the amplitude at ± 66 kHz; (c) temperature dependence of the spin–spin relaxation time T_2 showing a shallow minimum in the glass and[189] (d) time constants τ_α and τ_β as obtained in DS (adapted from Ref. 149), vertical line indicates minimum position in (c).

large amplitude reorientation can be excluded for the vast majority of picoline molecules at temperatures well below T_g.

Using selective labeling, ^{2}H NMR revealed for the mixed glass chlorobenzene (CB)/decalin (DEC) that both components participate very similarly in the β-process of this binary glass. This is evident from Fig. 34, where ^{2}H NMR spectra of CB-d_5/DEC and CB/DEC-d_{18} are compared for various temperatures.[56] For both components, we see a t_p dependence of the line shape, which resembles that found for neat type B systems, implying that the molecular dynamics involved in the β-process are similar. Specifically, comparison with findings for TOL, suggests that the majority of CB and DEC molecules show reorientation with a typical amplitude of 4–5°. This is confirmed by ^{2}H NMR stimulated-echo experiments (see Fig. 21).

In conclusion, NMR work indicates that the dynamics underlying the secondary relaxation processes of neat and binary glasses show no principal differences with

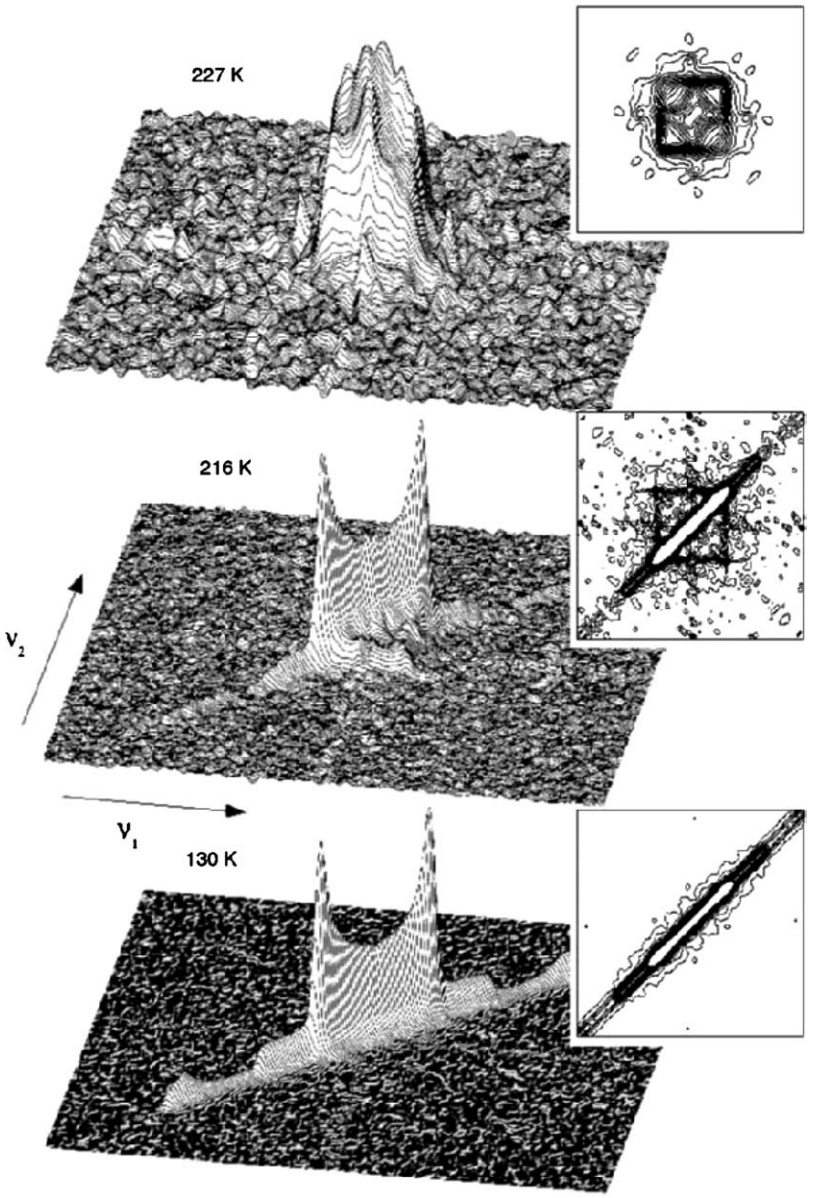

Fig. 33. 2D ^{2}H NMR spectra of 7% picoline-d_7/tri-styrene ($T_g = 222K$) for different temperatures and a mixing time $t_m = 100$ ms, oblique and contour plot.[189]

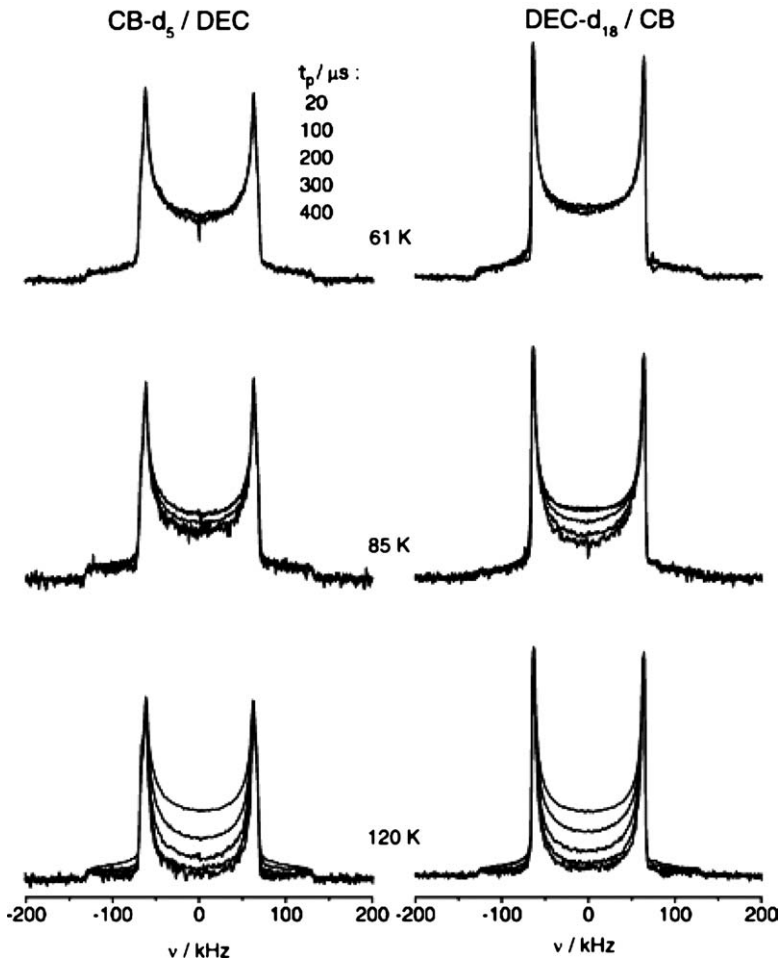

Fig. 34. ^{2}H NMR spectra for the binary glass CB/*cis*-DEC at various temperatures. The used solid-echo delays t_p are indicated. (Adapted from Ref. 56.)

respect to geometry of the motion and fraction of participating molecules. Specifically, all molecules take part where, for the vast majority, the reorientation is highly restricted. Therefore, one may argue that both classes of systems feature a comparable intrinsic secondary process.

3.4.3. *Glassy-ion conductors*

Fast ion conducting glasses are of considerable interest due to their possible applications in energy technologies, e.g., in solid-state batteries.[190–192] Such inorganic glasses can be prepared from cooling melts comprised of a network former, like SiO_2, and a network modifier, like Li_2O. The macroscopic charge transport in these

materials results from migration of mobile ions in an essentially rigid glassy matrix. There is strong evidence that the ionic diffusion can be described as a sequence of jumps between well-defined sites in the glass.[190,192] Although empirical relationships between structure and conductivity of ionic glasses have been established, the complex mechanism for the ionic hopping motion is still a matter of scientific debate. The motions of ions and guest molecules in multi-component glasses just like secondary relaxations in neat molecular and polymeric glasses are examples of dynamic processes that strongly decouple from the structural relaxation during the glass transition. Therefore, one expect that, at $T < T_g$, all these dynamic processes probe frozen density fluctuations and, hence, yield information about the local glass structure.

In NMR work, spin–lattice relaxation measurements indicated a non-exponential nature of the ionic relaxation.[10,11] While this conclusion is in harmony with results from electrical and mechanical relaxation studies, the latter techniques yielded larger activation energies for the ion dynamics than spin–lattice relaxation analysis. Possible origins of these deviations were discussed in detail.[10,193–196] The crucial point of spin–lattice relaxation studies is the choice of an appropriate correlation function of the fluctuating local fields, which in turn reflect ion dynamics. Here, we refrain from further reviewing NMR relaxation studies, but focus on recent applications of multidimensional NMR on solid-ion conductors, where well defined correlation functions can be directly measured.

In multidimensional NMR studies of organic compounds, ^{2}H, ^{13}C and ^{31}P are suitable probe nuclei.[3,4,6] For these nuclei, the time evolution of the spin system is simple due to $I \leqslant 1$ and the strengths of the quadrupolar or chemical shift interactions exceed the dipole–dipole couplings so that single-particle correlation functions can be measured. On the other hand, the situation is less favorable for applications on solid-ion conductors. Here, the nuclei associated with the mobile ions often exhibit $I > 1$ and, hence, a complicated evolution of the spin system requires elaborate pulse sequences.[197–199] Further, strong dipolar interactions often hamper straightforward analysis of the data. Nevertheless, it was shown that ^{6}Li, ^{7}Li and ^{9}Be are useful to characterize ion dynamics in crystalline ion conductors by means of 2D NMR in frequency and time domain.[200–204] For example, small translational diffusion coefficients $D \approx 10^{-20}\,m^2/s$ became accessible in ^{7}Li NMR stimulated-echo studies.[201]

Multidimensional ^{108}Ag NMR provides direct access to higher-order correlation functions of ionic jump dynamics in solids.[108,109,205,206,208] In ^{108}Ag NMR ($I = 1/2$), the chemical shift interaction dominates. In particular, dipolar interactions are negligible due to the low gyromagnetic ratio γ of the ^{109}Ag nucleus. Therefore, simple pulse sequences are sufficient to measure correlation functions, which have straightforward interpretation in view of their single-particle nature. On the other hand, the low γ results in a poor signal-to-noise ratio of ^{109}Ag NMR. However, this drawback can be overcome, as high-magnetic fields are nowadays available.

^{109}Ag NMR was used to study silver dynamics in silver phosphate glasses[108,109,205] and silver borate[208] glasses that were doped with silver iodide to

improve the ionic conductivity. As an example, ^{109}Ag NMR spectra of $(AgI)_{0.3} - (AgPO_3)_{0.7}$ glass are displayed in Fig. 35. We see a Lorentzian and a Gaussian line for high and low temperatures, respectively, while the spectra at intermediate temperatures are well described by a superposition of both line shapes, where the relative weight depends on temperature. Such superposition indicates that, on the 10–100 μs time scale of the experiment, fast and slow silver ions coexist, i.e., there is a distribution of correlation times or, equivalently, jump rates. ^{109}Ag NMR correlation functions showed that the rate distribution is continuous rather than bimodal. Due to its width, fast and slow silver ions are present at the same temperature and a shift of the distribution with temperature leads to a variation of both fractions. In ^{109}Ag NMR work on silver borate glasses, it was reported that the temperature-dependent weighting factor of both fractions provides information about the distribution of energy barriers governing the silver jumps.[208] These results resemble that for the smaller molecules in binary glasses discussed in Section 3.4.1. For example, two-phase spectra are observed for both ions and small molecules in glassy matrices.

In Fig. 36, we depict correlation functions $F^{\mathrm{sin}}(t_{\mathrm{m}})$ observed in a ^{109}Ag NMR stimulated-echo study on $(AgI)_{0.3}$–$1/3(2Ag_2O - P_2O_5)_{0.7}$ glass.[108] It was shown that such ^{109}Ag NMR correlation functions measure the probability of finding a silver ion at the same site after a time t_{m} and, hence, provide detailed information about the repopulation of the silver sites.[108,109,205,206] Obviously, the correlation functions strongly deviate from exponential behavior. Specifically, interpolations with a stretched exponential, $\exp[-(t/\tau)^{\beta}]$, yielded a small stretching exponent $\beta \approx 0.2$, in nice agreement with results from mechanical relaxation studies on silver iodide/silver phosphate glasses.[207] Likewise, small stretching exponents $\beta < 0.2$ were found to describe ^{109}Ag NMR correlation functions on AgI doped silver borate glasses.[208] The inset of Fig. 36 shows that the temperature dependence of the mean correlation time $\langle\tau\rangle$ is well described by an Arrhenius law. For several glassy and crystalline ion conductors, it was found that the activation energies determined in ^{109}Ag NMR stimulated-echo studies agree with that for the dc conductivity of the material.[108,109,205,206] Hence, ^{109}Ag NMR correlation functions probe elementary silver jumps that lead to macroscopic charge transport.

The origin of the pronounced non-exponential relaxation can be determined based on higher-order correlation functions.[3] Two fundamentally different explanations are possible. In the purely heterogeneous scenario, all particles are random walkers, but a distribution of jump rates exists. In the purely homogeneous scenario, all particles obey the same relaxation function, which is, however, intrinsically non-exponential, e.g., due to back-and-forth jumps. ^{109}Ag NMR three-time correlation functions can distinguish between both scenarios.[108,206] In these experiments, a dynamical filter meant to select slow silver ions is applied in the first-time interval (t_{m1}) and the relaxation of the selected subset is observed in the second-time interval (t_{m3}). Applications on silver phosphate[108] and silver borate glasses[208] suggested that the silver jumps are governed by dynamical heterogeneities consistent with the observation of ^{109}Ag NMR spectra comprised of a Gaussian and a Lorentzian line (see Fig. 35). However, the data analysis is not completely unambiguous

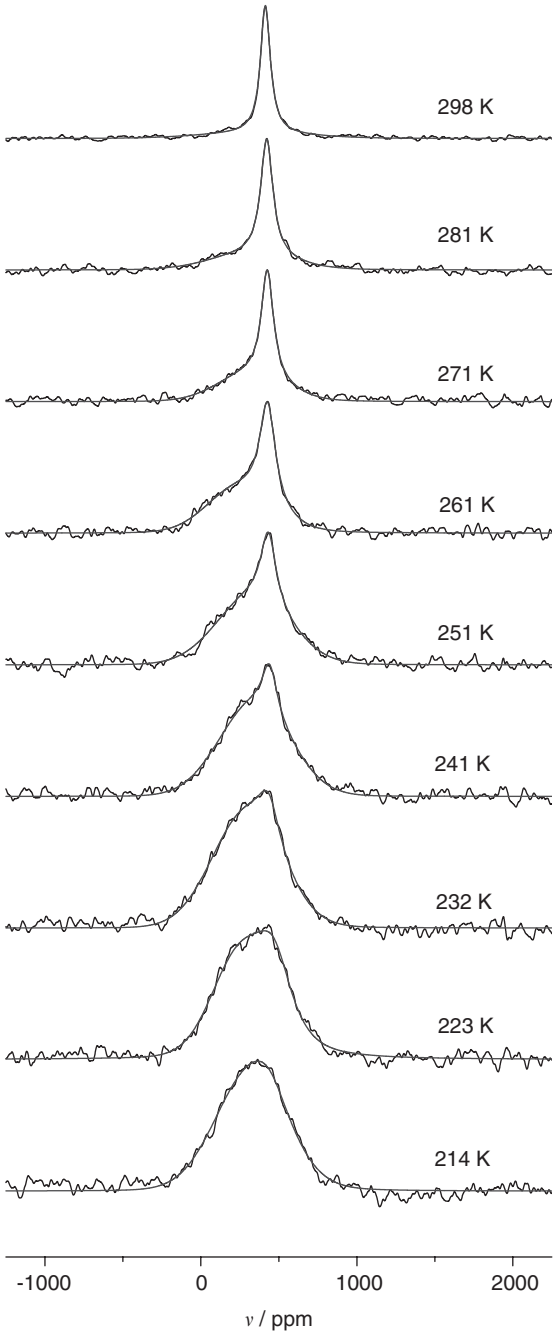

Fig. 35. ^{109}Ag NMR spectra of $(AgI)_{0.3}$–$(AgPO_3)_{0.7}$ glass together with interpolations using a weighted superposition of a Gaussian and a Lorentzian line. (Adapted from Ref. 108.)

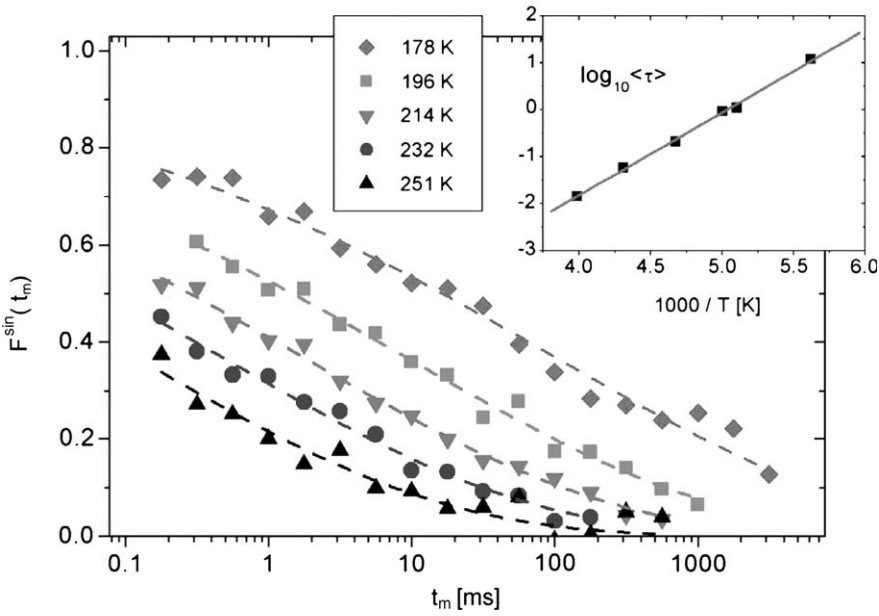

Fig. 36. ^{109}Ag NMR correlation functions $F^{\mathrm{sin}}(t_{\mathrm{m}},\ t_{\mathrm{p}} = 100\,\mu\mathrm{s})$ for $(AgI)_{0.3}$–$1/3(2Ag_2O$–$P_2O_5)_{0.7}$ glass. The dashed lines are interpolations with a stretched exponential, $\exp[-(t/\tau)^{\beta}]$, where $\beta \approx 0.2$ indicates strong deviations from exponential behavior. The inset shows the temperature dependence of the mean correlation time $\langle\tau\rangle$ (in ms) as obtained from the fits, yielding an activation energy $E_{\mathrm{a}} = 0.35\,\mathrm{eV}$. (Adapted from Ref. 108.)

due to the extreme non-exponentiality of the correlation functions. The situation is more favorable for crystalline silver ion conductors. Fig. 37 shows ^{109}Ag NMR two- and three-time correlation functions for polycrystalline $Ag_7P_3S_{11}$.[206] We see that the experimental data are well described within the purely heterogeneous scenario. Thus, the non-exponentiality is due to a distribution of jump rates rather than back-and-forth jumps. In addition, it was possible to measure the lifetime of the dynamical heterogeneities in polycrystalline $Ag_7P_3S_{11}$ using ^{109}Ag NMR four-time correlation functions.[206] All these examples demonstrate that performing multidimensional ^{109}Ag NMR experiments allows one to put severe constraints on successful models of ion transport in solids.

Altogether, it became clear that, at $T < T_{\mathrm{g}}$, the motions of molecules and ions in glassy matrices are governed by very broad distributions of correlation times, just like the β-process of neat molecular and polymeric glasses. Assuming that these distributions reflect the disorder of the glassy state, one may conclude that a broad diversity of the local glass structure exists. In particular, there is no evidence for simple "cluster-tissue models" of the glass, which would give rise to bimodal

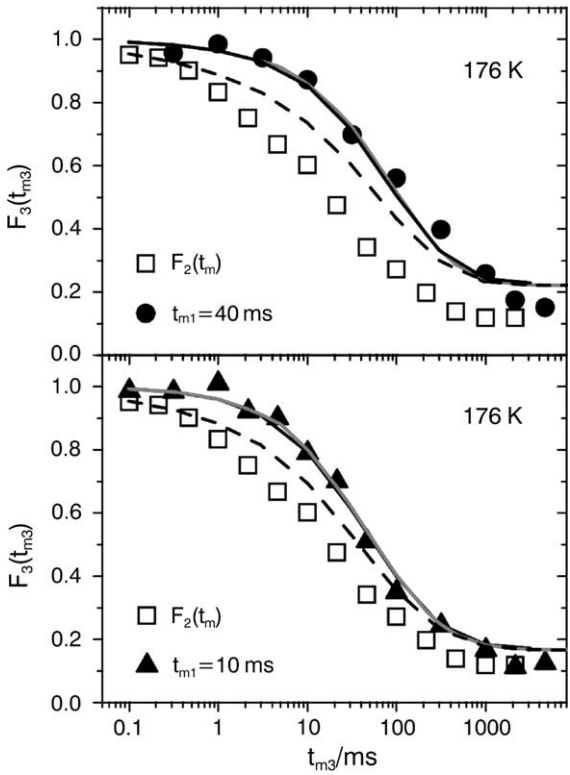

Fig. 37. ^{109}Ag NMR three-time correlation functions $F_3(t_{m1} = \text{constant}; t_{m3})$ for crystalline $Ag_7P_3S_{11}$ at $T = 176$ K. Results for $t_{m1} = 10$ ms and 40 ms (solid symbols) are compared with the two-time correlation function $F^{cos}(t_{m3})$ (open symbols). The expectations for purely homogeneous (dashed lines) and purely heterogeneous dynamics (solid lines) are included. For experimental reasons,[3,6,108] seven-pulse sequences featuring three mixing times t_{m1}, t_{m2} and t_{m3}, are used in such measurements where, however, $t_{m2} \rightarrow 0$. (Adapted from Ref. 206.)

distributions of correlation times or, equivalently, two-step decays of the correlation functions.

Finally, it is interesting whether local relaxation processes of the glassy matrix facilitate ionic diffusion. For phosphate glasses and borate glasses, ^{31}P and ^{11}B NMR spin–lattice relaxation studies gave evidence for some coupling of ion and matrix dynamics below T_g.[209–212] Moreover, it was reported that local rearrangements of phosphate networks exist, showing several features,[213,214] e.g., the time scale and temperature dependence, which resemble those of the β-process of molecular glasses and polymers. Thus, one may speculate that such type of secondary relaxation is not limited to organic glasses.

4. SOME COMMENTS ON THEORETICAL APPROACHES TO THE GLASS TRANSITION PHENOMENON

The glass transition phenomenon is a long-standing problem of condensed matter physics, and still there is no generally accepted theory in sight. Most approaches agree that the glass transition temperature T_g, though accompanied by more or less discontinuous changes of expansion coefficient and heat capacity, is not of major interest due to its cooling rate dependence. Instead, it was argued that a dynamic crossover above T_g or a hidden-phase transition below T_g are relevant, the latter being obscured by the divergence of the structural relaxation time when approaching this point. The postulate of a hidden transition results from extrapolation of the liquid entropy to low temperatures. Then, the excess entropy ΔS_{ex}, the entropy of the liquid in excess to that of the crystal, vanishes at a temperature $T_K > 0$.[215] Since an entropy of a disordered state being smaller than that of a crystal appears unphysical, a static-phase transition at the so-called Kauzmann temperature T_K was proposed. However, the conclusion is not fully compelling.[216]

The Kauzmann temperature plays an important role in the most widely applied phenomenologic theories, namely the configurational entropy[217] and the free-volume theories.[218,219] In the entropy theory, the excess entropy ΔS_{ex} obtained from thermodynamic studies is related to the temperature dependence of the structural relaxation time τ_α. A similar relation is derived in the free-volume theory, connecting τ_α with the excess free-volume ΔV_{ex}. In both cases, the excess quantity becomes zero at a distinguished temperature where, as a consequence, $\tau_\alpha(T)$ diverges. Although consistent data analyses are sometimes possible, the predictive power of these phenomenologic theories is limited. In particular, no information about the evolution of relaxation spectra is available.

On the other hand, the MCT follows a microscopic approach starting from a classical N body problem. The approach was developed by Kawasaki to describe the critical slowing down when approaching the critical point of the liquid.[220] In 1984, Bengtzelius, Götze and Sjölander[221] and Leutheusser[222] extended the theory to dense fluids, i.e., to super-cooled liquids. Thus, the theory starts from the liquid side. Many details were elaborated by Götze and co-workers.[223] Later the approach was applied to molecular liquids with rotational degrees of freedom.[224,225] MCT provides predictions for the evolution of the dynamic structure factor $S(Q, t)$. The relevant time window is the GHz regime, where the "glass dynamics" separates from the vibrational dynamics in the THz range. This regime can be easily accessed by NS and LS, but also by DS, *cf*. Fig. 1a. For details the reader is referred to Refs. 22, 223, 226, 227. The most direct support comes from molecular dynamics simulations.[228,229] However, one has to keep in mind that nowadays these simulations monitor dynamics only up to the nanosecond scale and, hence, information about the structural relaxation near T_g is not available.

In MCT, the non-ergodicity parameter $f_Q(T)$ is the crucial quantity. It describes the long-time behavior of $S(Q,t)$. In its idealized version, MCT predicts a discontinuous change at a critical temperature T_c[223]

$$f_Q(T) = 0 \quad T > T_c \tag{18}$$

$$f_Q(T) > 0 \quad T < T_c$$

Whereas the correlation function $S(Q, t)$ decays to zero in the liquid state, this is no longer the case below T_c, where the system becomes non-ergodic. Such scenario results from a generalized oscillator equation with non-linear damping. The slowing down of the molecular dynamics creates an enhanced damping, which in turn slows down the correlation function etc. The density is taken as a control parameter. In Fig. 38a, f (the Q dependence is omitted in the most simple approach) is displayed

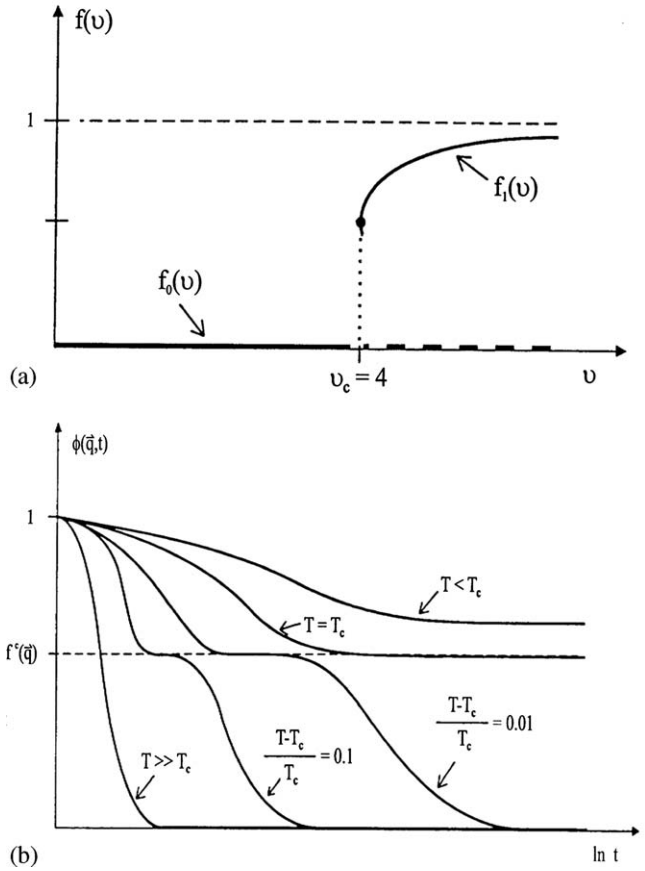

Fig. 38. (a) Long-time plateau $f(v)$ of the correlation function above and below the critical value of the control parameter, v_c. (Adapted from Ref. 216.) (b) Correlation functions at different temperatures with respect to the critical temperature T_c. From a one-step function, a two-step function emerges while cooling.

as a function of the control parameter v.[216] A control parameter $v < v_c$ yields $f_o(v) = 0$, whereas a finite value $f_1(v)$ is observed at $v \geqslant v_c$. In other words, the non-ergodicity parameter f changes discontinuously, although substantial structural changes are not observed in super-cooled liquids while cooling. This constitutes the paradigm of the glass transition being described by a dynamic phase transition. Experimentally, $f_Q(T)$ can be obtained from the temperature dependence of the Debye–Waller factor, showing indications of the expected discontinuous behavior at $T \approx T_c$, *cf.* Fig. 6.

The corresponding correlation functions are sketched for characteristic temperatures in Fig. 38b. We see that the critical temperature T_c marks the crossover from an ergodic state (liquid) to a non-ergodic state (glass). In the liquid state, a two-step process describes the decay of the correlation function, where f is the fraction relaxed by the slow process (α-process) and $1 - f$ the part decaying due to the fast dynamics. Asymptotically, the decay of the correlation function reflects different power-law regimes, and their experimental identification allows one to determine the critical temperature T_c. The cage effect provides a physical interpretation of the two-step correlation function. Molecules in the dense liquid are transiently trapped in cages formed by their neighbors. In these cages, the molecules show localized ''rattling motions'' until the cage decays at much longer times, leading to complete relaxation. The lower the temperature, the longer the molecules are trapped, and eventually at T_c, ''self-trapping'' leads to a non-ergodic state, the glass.

For molecular liquids, it turned out that T_c lies well above T_g. Therefore, the extended version of the MCT postulates that a phonon-assisted ''hopping transport'' ensures ergodicity below T_c as observed experimentally. In other words, at $T > T_g$, the transport mechanism is proposed to change from a liquid-like ($T > T_c$) to a solid-like behavior ($T < T_c$). In contrast, for colloidal glasses, it appears that the idealized MCT is sufficient to describe the glass transition.[227] Since most NMR methods probe slow dynamics, NMR tests of MCT predictions are rare. However, NMR studies revealed several features of dynamics near T_g, e.g., the existence of dynamic heterogeneities for the α-process, which are not predicted by MCT. Nevertheless, the fast dynamics associated with the first step of the correlation functions in Fig. 38b is expected to pre-average the NMR coupling constant (*cf.* Section 3.2.5).

The replica theory is another microscopic theory of the glass transition. Inspired by the spin glass theory,[230] it lends some justification to the configurational entropy theory.[216] However, details of the evolution of the dynamic susceptibility are less worked out.

In addition, potential energy landscape (PEL) approaches have shed light on the glass transition phenomenon.[231–234] In this formalism, the high-dimensional vector of all particle coordinates is considered as a point moving on the potential energy surface. Such description is useful at sufficiently low temperatures, where the time evolution of the system can be decomposed into vibrations about local minima of the PEL and infrequent transitions between these minima. The shape of the PEL was reported to depend on the fragility of the liquid, i.e., on the degree of deviation

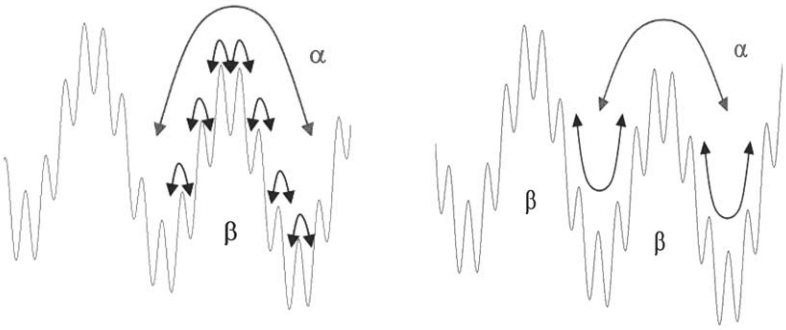

Fig. 39. Schematic picture of the PEL of a fragile glass former[231–235] suggesting that the local minima are grouped into "metabasins". It was argued that transitions between these metabasins lead to the α-process. Concerning the β-process, one can imagine that it results from either transitions between neighboring local minima[233] (left) or the exploration of metabasins, i.e., the system jumps among local minima grouped into a metabasin[236] (right).

from Arrhenius behavior.[231–234] For fragile liquids, the local minima of the PEL are grouped into so-called metabasins (see Fig. 39). In view of this organization, relations between the features of the PEL and the relaxation processes in super-cooled liquids were discussed. Molecular dynamics simulations gave evidence that transitions between metabasins are involved in the α-process.[235] Concerning the origin of the β-process, it was speculated that it results from either transitions between neighboring local minima[233] or from exploration of metabasins,[236] (see Fig. 39). In the latter picture, the β-dynamics is associated with jumps of the system among several local minima belonging to the same metabasin and the time scale separation of α- and β-process upon cooling is a consequence of the increasingly important trapping of the system in a metabasin. Moreover, the β-process is seen as a multi-step process, consistent with experimental results, as discussed in Sections 2.1 and 3.2.3. In addition, within the framework of a free-energy landscape (FEL) model, the α-process was associated with transitions between free-energy minima, while the β-process was assumed to correspond to intra-minima relaxation.[237] Using a two-site jump to model the latter process, DS and spin–lattice relaxation were calculated. Finally, the evolution of the dielectric β-peak during cooling and heating cycles was described within a double-well potential model.[238]

5. CONCLUSIONS AND OUTLOOK

The main purpose of this review was to demonstrate that the potential of multidimensional NMR, which was successfully exploited to investigate super-cooled

liquids above the glass transition temperature T_g, also provides important information about the dynamics below T_g. In particular, we focused on molecular glasses comprised of rigid molecules, where secondary relaxation processes intrinsic to the glassy state exist. It was shown that the high-angular resolution of multi-pulse experiments can be used to identify molecular motion that is highly restricted in amplitude. For example, the solid-echo technique allows one to probe angular displacements down to 1°, say. Applications of these techniques are not limited to molecular glasses, but they can also be used to study secondary relaxation process in polymeric glasses, which usually have a polymer specific origin, or more generally to internally flexible molecules. One important result from the reviewed NMR work concerns the nature of the intrinsic β-process of molecular glasses. Although this relaxation process is associated with the glass transition phenomenon of many molecular glass formers, a theoretical description is still lacking. NMR results showed that molecular dynamics underlying the β-process is complex. Specifically, though all molecules participate in the β-dynamics, broad distributions of correlation times and amplitudes of the motion exist. Further, there is evidence that simple two-site jump models are not appropriate for the β-process, but it exhibits a multi-step nature. In harmony with these features, an energy-landscape approach proved well suited to reproduce the NMR findings. To arrive at these conclusions, DS with its broad frequency range and the capability to probe weak relaxation processes can be successfully combined with NMR. At the present, it is however not clear whether the proposed energy-landscape model is sufficient to rationalize all results from the wide spectrum of experimental methods and, hence, it may become a challenge for future work to refine this model.

Based on the broad distributions characterizing molecular reorientation associated with the β-process, one may argue that this relaxation phenomenon probes the structural disorder of the glassy state. In particular, it is reasonable that the distribution of amplitudes of the motion is related to local density fluctuations of the super-cooled liquid frozen in at the glass transition temperature T_g. Then, the majority of molecules, showing reorientation with amplitudes $\chi < 10^\circ$, resides in regions of relatively high-local density, while the presence of a minority of molecules, exhibiting reorientation with amplitudes $\chi > 10^\circ$, suggests the existence of regions with somewhat reduced local density. Despite these potential density fluctuations, the glass appears to be structurally more or less homogeneous. Specifically, recalling that molecular reorientation is spatially restricted in all regions of the glass, one may argue that the distribution of local densities is continuous rather than bimodal. In other words, NMR data rule out that "islands of mobility" can be distinguished. Consistently, the dynamics of small molecules and ions in glassy matrices, which can be regarded as probes of the local glass structure, are governed by continuous rather than bimodal distributions of correlation times.

In NMR, it is possible to distinguish glass formers that do show a β-process (type B) from those that do not show a β-process (type A), but exhibit a power-law behavior (excess wing) in the dielectric loss. However, it remains an open question whether a clear-cut physical difference exists between the two relaxation processes. In view of gradual variations in the β-relaxation behavior among different glass

formers, there may be a continuous crossover from one relaxation phenomenon to the other, as was argued by several authors. Likewise, it is not straightforward to discriminate between intrinsic and non-intrinsic processes of the glassy state. For example, many polymers exhibit a secondary process where side-group motion is involved, i.e., there are specific intramolecular origins. However, it is still not clear whether side-group motion is reason or consequence of β-like backbone dynamics. Also, consensus on the cooperativeness of secondary processes has not yet been reached, i.e., how many molecules are involved. NMR studies, showing that molecules with rather different shapes and sizes mixed in a glass participate in the β-process in a similar way, hint at some cooperative motion. Of course, clarifying all these questions for a highly restricted motion is a formidable task. At cryogenic temperatures, further relaxation processes become relevant, which may be associated with the low-temperature anomalies of glasses. Although data, in particular for molecular glasses, is rare, there is some indication that these processes are probed by the spin–lattice relaxation. Progress can be expected when it will become possible to systematically study the frequency dependence of the NMR relaxation in the glassy state by means of NMR relaxometry.

Unlike crystalline materials, glasses exhibit molecular dynamics on virtually all time scales, where experimental results on the intrinsic relaxation processes of the glassy state suggest some universality. Nevertheless, descriptions of the secondary relaxation processes still rely on phenomenologic models and, hence, we think they deserve further thorough theoretical considerations. Since some secondary relaxations, e.g., the β-process, emerge in the super-cooled liquid, indicating a close relation to the glass transition phenomenon, we look forward to a theory describing both the super-cooled liquid and the glassy state.

In conclusion, understanding the nature of the glassy state is intriguing from the viewpoints of both fundamental and applied science. For example, secondary relaxation processes determine the mechanical properties of polymeric glasses, which are in widespread use in modern life. Also, numerous industrial applications rely on the transport of molecules or ions in glassy materials, where the transport process is affected by the structure and the local dynamics of the glass. Therefore, one can hope that comprehensive knowledge about the properties of glasses enables a development of tailor-made materials. NMR has proved a powerful tool to shed some light on the challenging nature of the glassy state.

ACKNOWLEDGEMENT

The authors are indebted to R. Böhmer, A. Heuer and S.A. Lusceac for helpful comments on the manuscript. We thank R. Böhmer for providing several NMR results and P. Lunkenheimer for the dielectric data of glycerol. The support by the German Research Foundation (DFG) through the grants Ro 907/2, Ro 907/4 and Ro 907/5 is acknowledged.

REFERENCES

1. E. Rössler and H. Sillescu, *Glasses and Amorphous Materials*, J. Zarzycki ed., Verlag Chemie, Weinheim, 1991, pp. 574–618.
2. G. Diezemann, G. Hinze, R. Böhmer and H. Sillescu, *Theoretical and Experimental Approaches to Supercooled Liquids: Advances and Novel Applications*, J. Fourkas, D. Kivelson, U. Mohanty and K. Nelson, eds., Washington, 1997, 154–167.
3. R. Böhmer, G. Diezemann, G. Hinze and E. Rössler, *Prog. NMR Spect.*, 2001, **39**, 191–267.
4. R. Böhmer and F. Kremer, *Broadband Dielectric Spectroscopy*, F. Kremer and A. Schönhals, eds., Springer, Berlin, 2003, 265–284.
5. V. J. McBrierty and K. J. Packer, *Nuclear Magnetic Resonance in Solid Polymers*, Cambridge University Press, Cambridge, 1993.
6. K. Schmidt-Rohr and H. W. Spiess, *Multidimensional Solid State NMR and Polymers*, Academic Press, London, 1994.
7. F. A. Bovey, *NMR of Polymers*, Academic Press, San Diego, 1996.
8. R. Kimmich, *NMR Tomography, Diffusometry, Relaxometry*, Springer, Berlin, 1997.
9. K. Schmidt-Rohr and H. W. Spiess, *Ann. Rep. NMR Spectrosc.*, 2002, **48**, 1–29.
10. D. Brinkmann, *Prog. NMR Spectrosc.*, 1992, **24**, 527–552.
11. H. Eckert, *Prog. NMR Spectrosc.*, 1992, **24**, 159–293.
12. I. Farnan, *Curr. Opin. Solid State Mater. Sci.*, 1998, **3**, 371–377.
13. J. F. Stebbins, *Chem. Rev.*, 1991, **91**, 1353–1373.
14. M. J. Duer ed., *Solid State NMR Spectroscopy*, Blackwell Science, Oxford, 2002.
15. J. N. Sherwood, ed., *The Plastically Crystalline State*, Wiley, New York, 1979.
16. U. T. Höchli, K. Knorr and A. Loidl, *Adv. Phys.*, 1990, **39**, 405–615.
17. C. J. F. Böttcher and P. Bordewijk, *Theory of Electric Polarization*, Vol. 2, Elsevier, Amsterdam, 1973.
18. G. P. Johari, *Ann. New York Acad. Sci.*, 1976, **279**, 117–140.
19. A. Kudlik, S. Benkhof, T. Blochowicz, C. Tschirwitz and E. Rössler, *J. Mol. Struct.*, 1999, **479**, 201–218.
20. K. L. Ngai, *J. Non-Cryst. Solids*, 2000, **275**, 7–51.
21. C. A. Angell, K. L. Ngai, G. B. McKenna, P. F. McMillan and S. W. Martin, *J. Appl. Phys.*, 2000, **88**, 3113–3157.
22. P. Lunkenheimer, U. Schneider, R. Brand and A. Loidl, *Contemp. Phys.*, 2000, **41**, 15–36.
23. F. Kremer and A. Schönhals, eds., *Broadband Dielectric Spectroscopy*, Springer, Berlin, 2003.
24. For recent progress see references in, *J. Non-Cryst. Solids*, 2002, 307–310.
25. K. L. Ngai and M. Paluch, *J. Chem. Phys.*, 2004, **120**, 857–873.
26. C. Hansen and R. Richert, *J. Phys. Condens. Matter*, 1997, **9**, 9661–9671.
27. C. Gainaru, A. Rivera, S. Putselyk, G. Eska and E. A. Rössler, *Phys. Rev. B.*, 2005, submitted.
28. C. Gainaru, PhD thesis, Universität Bayreuth, 2005.
29. W. A. Phillips ed., *Amorphous Solids, Low Temperature Properties*, Springer, Berlin, 1981.
30. S. Hunklinger and A. K. Raychaudhuri, *Progress in Low Temperature Physics*, D. F. Breuer ed., Amsterdam, Elsevier, 1986, Vol. 9, pp. 265–344.
31. P. Esquinazi ed., *Tunneling Systems in Amorphous and Crystalline Solids*, Springer, Berlin, 1998.
32. G. P. Johari and M. Goldstein, *J. Chem. Phys.*, 1970, **53**, 2372–2388.
33. N. G. McCrum, B. E. Read and G. Williams, *Anelastic and Dielectric Effects in Polymeric Solids*, Dover, New York, 1967.
34. A. Faivre, G. Niquet, M. Maglione, J. Fornazero, J. F. Jal and L. David, *Eur. Phys. J.*, 1999, **B10**, 277–286.
35. J. Perez, J. Y. Cavaille and L. David, *J. Molec. Struct.*, 1999, **479**, 183–194.
36. A. Arbe, D. Richter, J. Colmenero and B. Farago, *Phys. Rev.*, 1996, **E54**, 3853–3869.
37. S. Kahle, L. Willner, M. Monkenbusch, D. Richter, A. Arbe, J. Colmenero and B. Frick, *Appl. Phys. A*, 2002, **74**, S371–S373.

38. Th. Blochowicz, Ch. Tschirwitz, St. Benkhof and E. A. Rössler, *J. Chem. Phys.*, 2003, **118**, 7544–7555.
39. S. Adichtchev, T. Blochowicz, C. Tschirwitz, V. N. Novikov and E. A. Rössler, *Phys. Rev.*, 2003, **E68**, 011504-1–011504-10.
40. S. Adichtchev, T. Blochowicz, C. Gainaru, V. N. Novikov, E. A. Rössler and C. Tschirwitz, *J. Phys. Condens. Matter*, 2003, **15**, S835–S847.
41. P. Lunkenheimer and U. Schneider, *Broadband Dielectric Spectroscopy*, F. Kremer and A. schönhals, eds., Springer, Berlin, 2003, pp. 130–169.
42. E. Rössler and P. Eiermann, *J. Chem. Phys.*, 1994, **100**, 5237–5249.
43. S. Adichtchev and E. A. Rössler, unpublished data.
44. A. Kudlik, Promotionsarbeit, Bayreuth, 1998.
45. D. J. Plazek, C. A. Bero and I. -C. Chay, *J. Non-Cryst. Solids*, 1994, **172–174**, 181–190.
46. G. Hinze and H. Sillescu, *J. Chem. Phys.*, 1996, **104**, 314–319.
47. J. Wiedersich, N. V. Surovtsev and E. Rössler, *J. Chem. Phys.*, 2000, **113**, 1143–1153.
48. R. Chamberlin, *Phys. Rev. Lett.*, 1999, **83**, 5134–5137.
49. R. Böhmer and G. Diezemann, *Broadband Dielectric Spectroscopy*, F. Kremer and A. Schönhals, eds., Springer, Berlin, 2003, pp. 523–569.
50. R. Böhmer, *Curr. Opin. Solid State Mater. Sci., 3*, 1998, **3**, 378–385.
51. H. Sillescu, *J. Non-Cryst. Solids*, 1999, **243**, 81–108.
52. L. Wu, *Phys. Rev.*, 1991, **B43**, 9906–9915.
53. R. Deegan and S. R. Nagel, *Phys. Rev.*, 1992, **B52**, 5653–5656.
54. K. L. Ngai and S. Capaccioli, *Phys. Rev.*, 2004, **E69**, 031501/1–5.
55. G. Williams and D. C. Watts, *Trans. Faraday Soc.*, 1970, **66**, 80–85.
56. M. Vogel, Ch. Tschirwitz, G. Schneider, Ch. Koplin, P. Medick and E. Rössler, *J. Non-Cryst. Solids*, 2002, **307–310**, 326–335.
57. M. Goldstein, *J. Chem. Phys.*, 1968, **51**, 3728–3739.
58. E. Bartsch, F. Fujara, B. Geil, M. Kiebel, W. Petry, W. Schnauss, H. Sillescu and J. Wuttke, *Physica*, 1993, **A201**, 223–236.
59. W. Petry and J. Wuttke, *Trans. Theory Stat. Phys.*, 1995, **24**, 1075–1095.
60. A. Tölle, *Rep. Prog. Phys.*, 2001, **64**, 1473–1532.
61. G. Li, W. M. Du, A. Sakai and H. Z. Cummins, *Phys. Rev.*, 1992, **A46**, 3343–3356.
62. H. Z. Cummins, G. Li, W. M. Du, J. Hernandez and N. J. Tao, *Trans. Theory Stat. Phys.*, 1995, **24**, 981–1016.
63. G. Hinze, D. D. Brace, S. D. Gottke and M. D. Fayer, *J. Chem. Phys.*, 2000, **113**, 3723–3733.
64. R. Torre, P. Bartolini, M. Ricci and R. M. Pick, *Europhys. Lett.*, 2000, **52**, 324–329.
65. S. Adichtchev, St. Benkhof, Th. Blochowicz, V. N. Novikov, E. Rössler, C. Tschirwitz and J. Wiedersich, *Phys. Rev. Lett*., 2002, **88**, 055703/1–4.
66. R. Kimmich and E. Anoardo, *Prog. NMR Spectr.*, 2004, **44**, 257–320.
67. E. Rössler and H. Sillescu, *Chem. Phys. Lett.*, 1984, **112**, 94–98.
68. T. Dries, F. Fujara, M. Kiebel, E. Rössler and H. Sillescu, *J. Chem. Phys.*, 1988, **88**, 2139–2147.
69. W. Schnauss, F. Fujara and H. Sillescu, *J. Chem. Phys.*, 1992, **97**, 1378–1389.
70. E. Rössler, U. Warschewske, P. Eiermann, A. P. Sokolov and D. Quitmann, *J. Non-Cryst. Solids*, 1994, **172–174**, 113–125.
71. E. Rössler, J. Tauchert and P. Eiermann, *J. Phys. Chem.*, 1994, **98**, 8173–8180.
72. A. Döß, M. Paluch, H. Sillescu and G. Hinze, *Phys. Rev. Lett*., 2002, **88**, 095701/1–4.
73. T. Blochowicz, A. Kudlik, S. Benkhof, J. Senker, E. Rössler and G. Hinze, *J. Chem. Phys.*, 1999, **110**, 12011–12022.
74. H. W. Spiess and H. Sillescu, *J. Magn. Reson.*, 1981, **42**, 381–389.
75. B. J. Cauley, C. Cipriani, K. Ellis, A. K. Roy, A. A. Jones, P. T. Inglefield, B. J. McKinley and R. P. Kambour, *Macromolecules*, 1991, **24**, 403–409.
76. M. Vogel and E. Rössler, *J. Magn. Reson.*, 2000, **147**, 43–58.
77. M. Vogel and E. Rössler, *J. Phys. Chem.*, 2000, **B104**, 4285–4287.

78. U. Pschorn, E. Rössler, H. Sillescu, S. Kaufmann and H. W. Spiess, *Macromolecules*, 1991, **24**, 398–402.
79. F. Fujara, B. Geil, H. Sillescu and G. Fleischer, *Z. Phys.*, 1992, **B88**, 195–204.
80. D. van Dusschoten, U. Tracht, A. Heuer and H. W. Spiess, *J. Phys. Chem.*, 1999, **A103**, 8359–8364.
81. S. Dvinskikh, G. Benini, J. Senker, M. Vogel, J. Wiedersich, A. Kudlik and E. Rössler, *J. Phys. Chem.*, 1999, **B103**, 1727–1737.
82. B. Geil, F. Fujara and H. Sillescu, *J. Magn. Reson.*, 1998, **130**, 18–26.
83. R. Böhmer and G. Hinze, *J. Chem. Phys.*, 1998, **109**, 241–248.
84. G. Hinze, *Phys. Rev.*, 1998, **E57**, 2010–2018.
85. U. Tracht, A. Heuer and H. W. Spiess, *J. Chem. Phys.*, 1999, **111**, 3720–3724.
86. F. Qi, T. El Goresy, R. Böhmer, A. Döß, G. Diezemann, G. Hinze, H. Sillescu, T. Blochowicz, C. Gainaru, E. A. Rössler and H. Zimmermann, *J. Chem. Phys.*, 2003, **118**, 7431–7438.
87. T. Jörg, R. Böhmer, H. Sillescu and H. Zimmermann, *Europhys. Lett.*, 2000, **49**, 748–753.
88. M. Winterlich, H. Zimmermann and R. Böhmer, *Phys. Rev. Lett*., 2003, **91**, 235504/1–4.
89. S. A. Lusceac, I. Roggatz, J. Gmeiner, P. Medick and E. A. Rössler, *J. Chem. Phys.*, 2004, **121**, 4770–4780.
90. M. Vogel and E. Rössler, *J. Phys. Chem.*, 1998, **A102**, 2102–2108.
91. O. Baldus and E. A. Rössler, unpublished data.
92. K. Zemke, K. Schmidt-Rohr, J. H. Magill, H. Sillescu and H. W. Spiess, *Mol. Phys.*, 1993, **80**, 1317–1330.
93. K. Schmidt-Rohr and H. W. Spiess, *Phys. Rev. Lett.*, 1991, **66**, 3020–3023.
94. R. Böhmer, R. V. Chamberlin, G. Diezemann, B. Geil, A. Heuer, G. Hinze, S. C. Kuebler, R. Richert, B. Schiener, H. Sillescu, H. W. Spiess, U. Tracht and M. Wilhelm, *J. Non-Cryst. Solids*, 1998, **235–237**, 1–9.
95. U. Tracht, M. Wilhelm, A. Heuer, H. Feng, K. Schmidt-Rohr and H. W. Spiess, *Phys. Rev. Lett.*, 1998, **81**, 2727–2730.
96. S. A. Reinsberg, X. H. Qiu, M. Wilhelm, H. W. Spiess and M. D. Ediger, *J. Chem. Phys.*, 2001, **114**, 7299–7302.
97. M. Vogel and E. Rössler, *J. Phys. Chem.*, 2000, **104**, 4285–4287.
98. M. Vogel, PhD thesis, Universität Bayreuth, 2000.
99. M. Vogel and E. Rössler, *J. Chem. Phys.*, 2001, **114**, 5802–5815.
100. S. A. Lusceac, C. Koplin, P. Medick, M. Vogel, C. LeQuellec, C. Alba-Simionesco and E. A. Rössler, *J. Phys. Chem.*, 2004, **108**, 16601–16605.
101. S. A. Lusceac, C. Gainaru, M. Vogel, P. Medick, C. Koplin and E. A. Rössler, Macromolecules, 2005, in the press.
102. D. Schaefer, J. Leisen and H. W. Spiess, *J. Magn. Reson.*, 1995, **115**, 60–79.
103. G. Hinze, R. Böhmer, G. Diezemann and H. Sillescu, *J. Magn. Reson.*, 1998, **131**, 218–223.
104. F. Fujara, S. Wefing and H. W. Spiess, *J. Chem. Phys.*, 1986, **84**, 4579–4584.
105. G. Fleischer and F. Fujara, *NMR – Basic Princi. Progr.*, 1994, **30**, 159–207.
106. A. Abragam, *The Priciples of Nuclear Magnetism*, Clarendon Press, Oxford, 1961.
107. N. G. Van Kampen, *Stochastic Processes in Physics and Chemistry*, Elsevier, Amsterdam, 1981.
108. M. Vogel, C. Brinkmann, A. Heuer and H. Eckert, *Phys. Chem. Chem. Phys.*, 2002, **4**, 3237–3245.
109. M. Vogel, C. Brinkmann, A. Heuer and H. Eckert, *Solid State Nucl. Magn. Reson.*, 2002, **22**, 344–362.
110. M. Vogel and E. Rössler, *J. Chem. Phys.*, 2001, **115**, 10883–10891.
111. O. Kircher, G. Diezemann, R. Böhmer, G. Hinze, K. U. Schug, H. Sillescu and H. Zimmermann, *J. Chem. Phys.*, 1987, **108**, 8550–8556.
112. G. P. Johari, *J. Non-Cryst. Solids*, 2002, **307–310**, 317–325.
113. G. Schneider and E. A. Rössler, unpublished data.
114. S. Benkhof, A. Kudlik, T. Blochowicz and E. Rössler, *J. Phys. Condens. Matter*, 1998, **10**, 8155–8171.
115. R. Böhmer, G. Hinze, T. Jörg, F. Qi and H. Sillescu, *J. Phys. Condens. Matter*, 2000, **12**, A383–A390.

116. G. P. Johari, *J. Chem. Phys.*, 1982, **77**, 4619–4626.
117. H. Wagner and R. Richert, *J. Chem. Phys.*, 1999, **103**, 4071–4077.
118. M. Rubinstein, H. A. Resing, T. L. Reinecke and K. L. Ngai, *Phys. Rev. Lett.*, 1975, **34**, 1444–1447.
119. J. Szeftel and H. Alloul, *J. Non-Cryst. Solids*, 1978, **29**, 253–281.
120. A. Deville, B. Gaillard, C. Blanchard and J. Livage, *J. Phys.*, 1983, **44**, 77.
121. S. Estalji, O. Kanert, J. Steinert, H. Jain and K. L. Ngai, *Phys. Rev.*, 1991, **B43**, 7481–7486.
122. Y. Akagi and N. Nakamura, *J. Phys. Condens. Matter*, 2000, **12**, 5155–5168.
123. K. A. Topp and D. G. Cahill, *Z. Phys.*, 1996, **B101**, 235–245.
124. R. O. Pohl, Xiao Liu and Eunjoo Thompson, *Rev. Mod. Phys.*, 2002, **74**, 991–1013.
125. N. Theodorakopoulos and J. Jäckle, *Phys. Rev.*, 1976, **B14**, 2637–2641.
126. K. S. Gilroy and W. A. Phillips, *Philos. Mag.*, 1981, **B43**, 735–746.
127. J. Wiedersich, S. V. Adichtchev and E. Rössler, *Phys. Rev. Lett.*, 2000, **84**, 2718–2721.
128. G. G. Maresch, M. Weber, A. A. Dubinskii and H. W. Spiess, *Chem. Phys. Lett.*, 1992, **193**, 134–140.
129. D. Leporini, V. Schädler, Wiesner, H. W. Spiess and G. Jeschke, *J. Chem. Phys.*, 2003, **119**, 11829–11846.
130. V. Bercu, M. Martenelli, C. A. Massa, L. A. Pardi and D. Leporini, *J. Phys. Condens. Matter*, 2004, **16**, L1–L10.
131. F. Fujara, W. Petry, R. M. Diehl, W. Schnauss and H. Sillescu, *Europhys. Lett.*, 1991, **14**, 563–568.
132. W. Schnauss, F. Fujara, K. Hartmann and H. Sillescu, *Chem. Phys. Lett.*, 1990, **166**, 381–384.
133. B. Geil and G. Hinze, *Chem. Phys. Lett.*, 1993, **216**, 51–55.
134. T. Torchia and A. Szabo, *J. Magn. Reson.*, 1982, **49**, 107–121.
135. W. Müller-Warmuth and W. Otte, *J. Chem. Phys.*, 1980, **72**, 1749–1755.
136. E. Rössler, M. Taupitz, K. Börner, M. Schulz and H.-M. Vieth, *J. Chem. Phys.*, 1990, **92**, 5847–5855.
137. K. Börner, G. Diezemann, E. Rössler and H.-M. Vieth, *Chem. Phys. Lett.*, 1991, **181**, 563–568.
138. E. Rössler and M. Taupitz, *Disorder Effects on Relaxation Processes*, R. Richert and A. Blumen, eds., Springer, Berlin, 1994, pp. 361–383.
139. I. Roggatz, C. Karle, M. Taupitz and E. Rössler, Ber. Bunsenges, *Phys. Chem.*, 1996, **100**, 1554–1559.
140. A. Döß, G. Hinze, R. Böhmer, H. Sillescu, H. Kolshorn, M. Vogel and H. Zimmermann, *J. Chem. Phys.*, 2000, **112**, 5884–5892.
141. F. Qi, G. Hinze, R. Böhmer, H. Sillescu and H. Zimmermann, *Chem. Phys. Lett.*, 2002, **328**, 257–262.
142. G. Hinze, G. Diezemann and H. Sillescu, *J. Chem. Phys.*, 1996, **104**, 430–433.
143. G. Diezemann, *J. Chem. Phys.*, 1995, **103**, 6368–6384.
144. T. Eguchi, G. Soda and H. Chihara, *Mol. Phys.*, 1980, **40**, 681–696.
145. A. Kudlik, C. Tschirwitz, S. Benkhof, T. Blochowicz and E. Rössler, *J. Non-Cryst. Solids*, 1998, **235–237**, 406–411.
146. S. A. Lusceac, PhD thesis, Universität Bayreuth, 2005.
147. G. Hinze, H. Sillescu and F. Fujara, *Chem. Phys. Lett.*, 1995, **232**, 154–158.
148. A. Döß, M. Paluch, H. Sillescu and G. Hinze, *J. Chem. Phys.*, 2002, **117**, 6582–6589.
149. T. Blochowicz and E.A. Rössler, *Phys. Rev. Lett.*, 2004, **92**, 225701/1–4.
150. A. Brodin, E. A. Rössler, R. Bergman and J. Mattsson, *Eur. Phys. J.*, 2003, **B36**, 349–357.
151. E. Rössler, H. Sillescu and H. W. Spiess, *Polymer*, 1985, **26**, 203–207.
152. Comment: For polystyrene, a β-like relaxation process was attributed to phenyl-ring flips, while the main chain does not participate, see Section 3.3. Hence, when the backbone motion of a selectively labeled compound is studied, polystyrene can be regarded as a type A glass former.
153. A. Heuer, J. Leisen, S. C. Kuebler and H. W. Spiess, *J. Chem. Phys.*, 1996, **105**, 7088–7096.
154. S. Kulik, H. W. Beckham, K. Schmidt-Rohr, D. Radloff, U. Pawelzik, C. Boeffel and H. W. Spiess, *Macromolecules*, 1994, **27**, 4746–4754.
155. K. Schmidt-Rohr, A. S. Kulik, H. W. Beckham, A. Ohlemacher, U. Pawelzik, C. Boeffel and H. W. Spiess, *Macromolecules*, 1994, **27**, 4733–4745.

156. S. C. Kuebler, A. Heuer and H. W. Spiess, *Macromolecules*, 1996, **29**, 7089–7096.
157. S. C. Kuebler, D. J. Schaefer, C. Boeffel, U. Pawelzik and H. W. Spiess, *Polym. Prepr. Am. Chem. Soc., Div. Polym. Chem.*, 1997, **38**, 821.
158. S. C. Kuebler, D. J. Schaefer, C. Boeffel, U. Pawelzik and H. W. Spiess, *Macromolecules*, 1997, **30**, 6597–6609.
159. E. R. deAzevedo, W.-G. Hu, T. J. Bonagamba and K. Schmidt-Rohr, *J. Chem. Phys.*, 2000, **112**, 8988–9001.
160. W. Domberger, D. Reichert, F. Garwe, H. Schneider and E. Donth, *J. Phys. Condens. Matter*, 1995, **7**, 7419–7426.
161. Z. Luz, P. Tekely and D. Reichert, *Prog. Nucl. Magn. Reson. Spectrosc.*, 2002, **41**, 83–113.
162. F. Laupretre, *NMR – Basic Princ. Progr.*, 1994, **30**, 63–109.
163. O. Pascui, M. Beiner and D. Reichert, *Macromolecules*, 2003, **36**, 3992–4003.
164. F. Garwe, A. Schönhals, H. Lockwenz, M. Beiner, K. Schröter and E. Donth, *Macromolecules*, 1996, **29**, 247–253.
165. M. Beiner, S. Kahle, E. Hempel, K. Schröter and E. Donth, *Europhys. Lett.*, 1998, **44**, 321–327.
166. M. Wind, R. Graf, A. Heuer and H. W. Spiess, *Phys. Rev. Lett*., 2003, **91**, 155702.
167. M. T. Hansen, B. Blümich, C. Boeffel, H. W. Spiess, L. Morbitzer and A. Zembrod, *Macromolecules*, 1992, **25**, 5542–5544.
168. M. Wehrle, G. P. Hellmann and H. W. Spiess, *Colloid Polym., Sci.*, 1987, **265**, 815–822.
169. A. S. Kulik and K. O. Prins, *Polymer*, 1993, **34**, 4635–4641.
170. J. Schaefer, M. D. Sefcik, E. D. Stejskal, R. A. McKay, W. T. Dixon and R. E. Cais, *Macromolecules*, 1984, **17**, 1107–1118.
171. H. W. Spiess, *Colloid Polym. Sci.*, 1983, **261**, 193–209.
172. J. Zhao, Y. H. Chin, Y. Liu, A. A. Jones, P. T. Inglefield, R. P. Kambour and D. W. White, *Macromolecules*, 1995, **28**, 3881–3889.
173. G. Meier, G. D. Boese and E. W. Fischer, *J. Chem. Phys.*, 1991, **94**, 3050–3059.
174. A. K. Roy, A. A. Jones and P. T. Inglefield, *J. Magn. Reson.*, 1985, **64**, 441–450.
175. A. S. Maxwell, I. M. Ward, F. Laupretre and L. Monnerie, *Polymer*, 1998, **39**, 6835–6849.
176. J. D. Ferry, *Viscoelastic Properties of Polymers*, J. Wiley, New York, 1980.
177. P. Kosfeld, *Adv. Chem. Ser.*, 1965, **48**, 49.
178. E. Rössler, *Lecture Notes in Physics 277*, Th. Dorfmüller and G. Williams, eds., Springer, Berlin, 1987, 144–154.
179. P. Bergquist, Y. Zhu, A. A. Jones and P. T. Inglefield, *Macromolecules*, 1999, **32**, 7925–7931.
180. Y. Liu, M. M. Turnbull, A. A. Jones, P. T. Inglefield and R. P. Kambour, *Solid State NMR*, 1993, **2**, 289–306.
181. C. Zhang, P. Wang, A. A. Jones and P. T. Inglefield, *Macromolecules*, 1991, **24**, 338–340.
182. Y. H. Chin, P. T. Inglefield and A. A. Jones, *Macromolecules*, **26**, 5372–5378.
183. P. Medick, M. Vogel and E. Rössler, *J. Magn. Reson.*, 2002, **159**, 126–136.
184. T. Blochowicz, C. Karle, A. Kudlik, P. Medick, I. Roggatz, M. Vogel, C. Tschirwitz, J. Wolber, J. Senker and E. Rössler, *J. Phys. Chem.*, 1999, **B103**, 4032–4044.
185. P. Medick, T. Blochowicz, M. Vogel and E. Rössler, *J. Non-Cryst. Solids*, 2002, **307–310**, 565–572.
186. M. Vogel, P. Medick and E. Rössler, *J. Molec. Liquids*, 2000, **86**, 103–108.
187. G. R. Moran and K. R. Jeffrey, *J. Chem. Phys.*, 1999, **110**, 3472–3483.
188. A. W. Wachner and K. R. Jeffrey, *J. Chem. Phys.*, 1999, **111**, 10611–10615.
189. P. Medick, PhD thesis, Universität Bayreuth, 2005.
190. A. Bunde, M. D. Ingram and P. Maass, *J. Non-Cryst. Solids*, 1994, **172–174**, 1222–1236.
191. K. L. Ngai, *J. Non-Cryst. Solids*, 1996, **203**, 232–245.
192. A. Bunde, K. Funke and M. D. Ingram, *Solid State Ionics*, 1998, **105**, 1–13.
193. S. R. Elliot and A. P. Owens, *Phys. Rev.*, 1991, **B44**, 47–59.
194. O. Kanert, J. Steinert, H. Jain and K. Ngai, *J. Non-Cryst. Solids*, 1991, **131–133**, 1001–1010.
195. M. Tatsumisago, C. A. Angell and S. W. Martin, *J. Chem. Phys.*, 1992, **97**, 6968–6974.
196. K. Ngai, *J. Chem. Phys.*, 1993, **98**, 6424–6430.
197. J. Bowden, W. D. Hutchison and J. Khachan, *J. Magn. Reson.*, 1986, **67**, 415–437.

198. X.-P. Tang and Y. Wu, *J. Magn. Reson.*, 1998, **133**, 155–165.
199. R. Böhmer, *J. Magn. Reson.*, 2000, **147**, 78–88.
200. Z. Xu and J. F. Stebbins, *Science*, 1995, **270**, 1332–1334.
201. R. Böhmer, T. Jörg, F. Qi and A. Titze, *Chem. Phys. Lett.*, 2000, **316**, 419–424.
202. V. M. J. Verhoeven, I. M. de Schepper, G. Nachtegaal, A. P. M. Kentgens, E. M. Kelder, J. Schoonman and F. M. Mulder, *Phys. Rev. Lett.*, 2001, **86**, 4314–4317.
203. F. Qi, T. Jörg and R. Böhmer, *Solid State Nucl. Magn. Reson.*, 2002, **22**, 484–500.
204. F. Qi, G. Diezemann, H. Böhm, J. Lambert and R. Böhmer, *J. Magn. Reson.*, 2004, **169**, 225–239.
205. M. Vogel, C. Brinkmann, H. Eckert and A. Heuer, *J. Non-Cryst. Solids*, 2002, **307–310**, 971–980.
206. M. Vogel, C. Brinkmann, H. Eckert and A. Heuer, *Phys. Rev.*, 2004, **B69**, 094302/1–5.
207. C. Liu and C. A. Angell, *J. Non-Cryst. Solids*, 1986, **83**, 162–184.
208. S. Berndt, K. R. Jeffrey, R. Küchler and R. Böhmer, *Solid State Nucl. Magn. Reson.*, 2005, **27**, 122–131.
209. M. Trunell, D. R. Torgeson, S. W. Martin and F. Borsa, *J. Non-Cryst. Solids*, 1992, **139**, 257–262.
210. S. Sen and J. F. Stebbins, *Phys. Rev.*, 1997, **B55**, 3512–3519.
211. S. Berger, J. Roos, A. Y. Zavidov and D. Brinkmann, *Solid State NMR*, 1998, **10**, 197–203.
212. C. Tomasi, P. Mustarelli, A. Magistris and M. P. I. Garcia, *J. Non-Cryst. Solids*, 2001, **293–295**, 785–791.
213. B. Ruffĺe, S. Beufils and J. Gallier, *Chem. Phys.*, 1995, **195**, 339–350.
214. V. Blache, J. Förster, H. Jain, O. Kanert, R. Küchler and K. L. Ngai, *Solid State Ionics*, 1998, **113–115**, 723–731.
215. W. Kauzmann, *Chem. Rev.*, 1948, **43**, 219–256.
216. R. Schilling, *Collective Dynamics of Non-linear and Disordered Systems*, G. Radons, W. Just and P. Häussler, eds., Springer, Berlin, 2003.
217. G. Adams and J. H. Gibbs, *J. Chem. Phys.*, 1965, **43**, 139–146.
218. M. H. Cohen and D. Turnbull, *J. Chem. Phys.*, 1959, **31**, 1164–1169.
219. M. H. Cohen and G. S. Grest, *Phys. Rev.*, 1979, **B20**, 1077–1098.
220. K. Kawasaki, *Phase Transitions and Critical Phenomena*, C. Domb and M. S. Green, eds., Academic Press, London, 1976.
221. U. Bengtzelius, W. Götze and A. Sjölander, *J. Phys. Solid State Phys.*, 1984, **C17**, 5915–5934.
222. E. Leutheusser, *Phys. Rev.*, 1984, **A29**, 2765–2773.
223. W. Götze and L. Sjögren, *Rep. Prog. Phys.*, 1992, **55**, 241–376.
224. R. Schilling and T. Scheidsteger, *Phys. Rev.*, 1997, **E56**, 2932–2949.
225. A. Winkler, A. Latz and C. R. Schilling, *Theis, Phys. Rev.*, 2000, **E62**, 8004–8015.
226. S. Yip, ed., *Trans. Theory Stat. Phys.*, 24, 1995.
227. W. Götze, *J. Phys. Condens. Matter.*, 1999, **11**, A1–A45.
228. W. Kob and H. C. Andersen, *Trans. Theory Stati. Phy.*, 1995, **24**, 1179–1198.
229. W. Kob, *J. Phys. Condens. Matt.*, 1999, **11**, R85–R115.
230. M. Mezard and G. Parisi, *J. Phys.*, 1996, **A29**, 6515–6524.
231. C. A. Angell, *J. Non-Cryst. Solids*, 1991, **131–133**, 13–31.
232. C. A. Angell, *Science*, 1995, **267**, 1924–1934.
233. F. H. Stillinger, *Science*, 1995, **267**, 1935–1939.
234. P. G. Debenedetti and F. H. Stillinger, *Nature (London)*, 2001, **410**, 259–267.
235. B. Doliwa and A. Heuer, *Phys. Rev. Lett.*, 2003, **91**, 235501/1–4.
236. M. Vogel, B. Doliwa, A. Heuer and S. C. Glotzer, *J. Chem. Phys.*, 2004, **120**, 4404–4414.
237. G. Diezemann, U. Mohanty and I. Oppenheim, *Phys. Rev.*, 1999, **E59**, 2067–2083.
238. J. Dyre and N. B. Olsen, *Phys. Rev. Lett.*, 2003, **91**, 155703.

Index

Italicized page numbers denote that the keywords are taken from figures, tables or schemes.